Proceedings of

RAGtime 6/7: Workshops on black holes and neutron stars

16–18/18–20 September ’04/’05
Opava, Czech Republic

Editors
S. Hledík
Z. Stuchlík

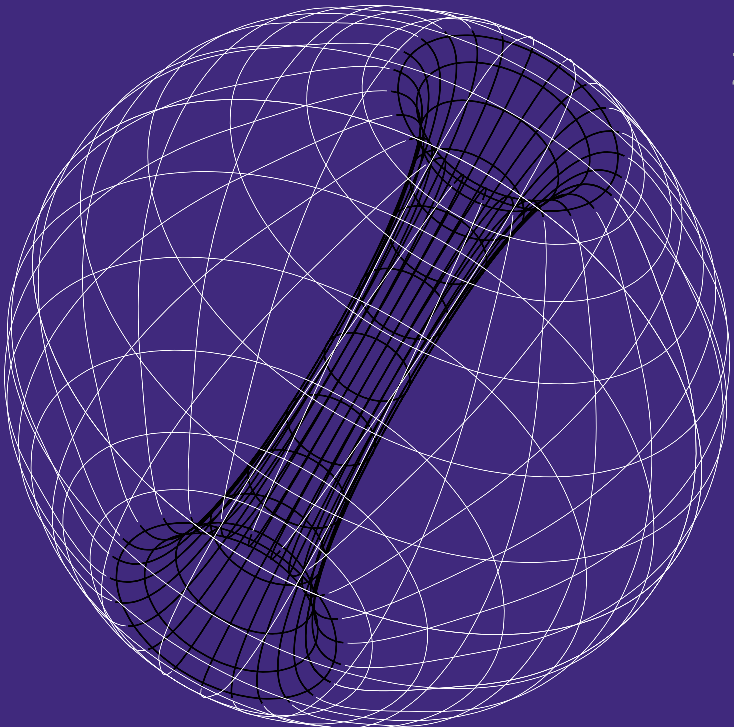

SILESIAN UNIVERSITY IN OPAVA

Publications of the Institute of Physics No. 4

RAG time 6

WORKSHOP ON BLACK HOLES AND NEUTRON STARS, 16–18TH SEPT 2004

Relativistic Astrophysics Group
at the Institute of Physics
Faculty of Philosophy & Science
Silesian University at Opava
Bezručovo nám. 13, CZ- 746 01
Opava, Czech Republic

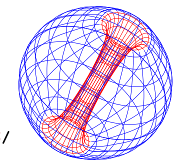

http://uf.fpf.slu.cz/rag/time6/

RAG time 7

WORKSHOP ON BLACK HOLES AND NEUTRON STARS, 18–20TH SEPT 2005

Relativistic Astrophysics Group
at the Institute of Physics
Faculty of Philosophy & Science
Silesian University in Opava
Bezručovo nám. 13, CZ-746 01
Opava, Czech Republic

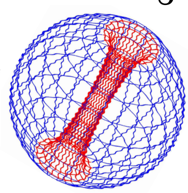

http://www.physics.cz/rag/time7/

Sponsored by

- Statutory City of Opava http://www.opava-city.cz/
- Ing. J. Ricka – Turnkey Interiors
- Mr. Milan Čajan *Property Owner*
- Ing. Vít Škrobánek – Cargo Design
  Conversions, extensions and adaptations of lorries
  http://www.czechcontact.com/CARGO_DESIGN_SKROBANEK

Proceedings of RAGtime 6/7:
Workshops on black holes and neutron stars
16–18/18–20 September 2004/2005
Opava, Czech Republic

S. Hledík and Z. Stuchlík, editors

Opava 2005

Annotation: In this Proceedings, the talks presented during workshops *RAGtime 6/7: Workshops on black holes and neutron stars, Opava, 16–18/18–20 September 2004/2005* are collected.

ISBN 80-7248-334-X

PREFACE

Relativistic Astrophysics Group (RAG) at the Institute of Physics, the Faculty of Philosophy and Science of the Silesian University in Opava, started a series of Workshops on Black Holes and Neutron Stars called *RAGtime* in 1999. The purpose of the workshops was to provide an opportunity for the presentation and discussion of recent developments in the field of relativistic astrophysics related to accretion processes onto black holes and neutron stars, and to general physical phenomena connected to the properties of black holes and their vicinity, and the internal structure of neutron stars or quark stars, as they were obtained by collaborating research groups at the Silesian University in Opava, the Faculty of Mathematics and Physics of Charles University in Prague, the International School for Advanced Studies in Trieste, the Institute of Astrophysics at University of Oxford, the Department of Astrophysics of Göteborg University, the Institute of Physics at the University of Bergen, the Institute of Astronomy of the Polish Academy of Science, and other remarkable institutes.

The *RAGtime* workshops are also vitally important for students of theoretical physics and/or astrophysics at the Silesian University in Opava, because they have a unique opportunity to be regularly in direct contact with the most recent results of relativistic astrophysics and they also have a possibility to discuss problems with leading astrophysicists of world-wide reputation like Marek Abramowicz, John Miller, Jeff McClintock, Ron Remillard, Shoji Kato, Luciano Rezzolla, Vladimír Karas, Petr Hadrava, Jiří Grygar and others.

We would like to thank all the authors for careful preparation of their contributions. We are also indebted to Mayor of the Statutory City of Opava Ing. Zbyněk Stanjura, Deputy Mayor doc. RNDr. Ing. Jan Mrázek, CSc., and all other sponsors for providing financial support for the successful course of the last RAGtime meeting.

Opava, December 2005

S. Hledík and Z. Stuchlík
editors

CONTENTS

M. A. Abramowicz, D. Barret, M. Bursa, J. Horák, W. Kluźniak, P. Rebusco and G. Török
A note on the slope-shift anticorrelation in the neutron star kHz QPOs data 1

P. Bakala, P. Čermák, S. Hledík, Z. Stuchlík and K. Truparová Plšková
A virtual trip to the Schwarzschild–de Sitter black hole: Computer simulation of extreme gravitational lensing in Schwarzschild–de Sitter spacetimes 11

K. Beckwith
Observational effects of strong gravity 29

M. Bursa
High-frequency QPOs in GRO J1655−40: Constraints on resonance models by spectral fits 39

M. Dovčiak, V. Karas, G. Matt and A. Martocchia
Polarization of radiation from AGN accretion discs – the lamp-post model 47

P. Hadrava
Kinetic model of quasiperiodic oscillations of gaseous rings 55

J. Horák
On polarization of light scattered on hot electron clouds 63

V. Karas
An introduction to relativistic magnetohydrodynamics I. The force-free approximation 71

J. Kovář and Z. Stuchlík
Embedding diagrams of optical reference geometry of Kerr–de Sitter spacetimes 81

J. Miller
Computations of primordial black hole formation 101

K. Mrázová, S. Hledík and Z. Stuchlík
Games with polytropes and adiabates 109

W. G. Newton
Subnuclear matter in neutron stars and supernovae: nuclear pasta and beyond 119

T. Pecháček, M. Dovčiak and V. Karas
The relativistic shift of spectral lines from black-hole accretion discs 137

J. Schee, Z. Stuchlík and J. Juráň
Light escape cones and raytracing in Kerr geometry 143

J. Schovancová, L. Šubr, V. Karas, Z. Stuchlík and J. Kovář
Some aspects of the Störmer problem within strong gravitational fields 157

P. Slaný and Z. Stuchlík
Perfect fluid tori in the Kerr–de Sitter naked singularity backgrounds 167

Z. Stuchlík and S. Hledík
Excitation of oscillations by a small inhomogeneity on the surface of a neutron star 189

Z. Stuchlík and S. Hledík
Radial pulsations and dynamical stability of spherically symmetric perfect fluid configurations in spacetimes with a nonzero cosmological constant 209

Z. Stuchlík and M. Kološ
Friedman models with the superstring dark energy 223

Z. Stuchlík and M. Kološ
Swiss cheese model with the superstring dark energy 231

Z. Stuchlík and J. Kovář
Equilibrium of spinning test particles in equatorial plane of Kerr–de Sitter spacetimes 241

Z. Stuchlík and G. Török
On the possibility of precise determination of black hole spin in the framework of resonance models 253

Z. Stuchlík, M. Urbanec and G. Török
Trapping of neutrinos in the internal Schwarzschild–(anti-)de Sitter spacetimes 265

L. Šubr and V. Karas
A manifestation of the Kozai mechanism in the galactic nuclei 281

J. Svoboda
On time-dependent spectra of black-hole accretion discs 295

P. A. Taylor
Long gamma-ray bursts: (current) theory and observation 301

G. Török and Z. Stuchlík
Epicyclic frequencies of Keplerian motion in Kerr spacetimes 315

K. Truparová Plšková and Z. Stuchlík
The latitudinal and radial geodetical motion in Kerr–de Sitter spacetime 339

M. Urbanec, J. C. Miller and J. Říkovská Stone
Matching of equations of state: Influence on calculated neutron star models 357

J. Miller
The Double Pulsar J0737−3039 363

S. Hledík and Z. Stuchlík, editors, Silesian University in Opava, Czech Republic, 2005, pp. 1–9

A note on the slope-shift anticorrelation in the neutron star kHz QPOs data

Marek A. Abramowicz,[1,2,3,4] Didier Barret,[5]
Michal Bursa,[1,6] Jiří Horák,[1,6] Włodek Kluźniak,[1,4,7]
Paola Rebusco[1,8] and Gabriel Török[1,3,5]

[1] Nordita, Blegdamsvej 17, 2100 Copenhagen, Denmark
[2] Department of Physics, Göteborg University, S 412 96 Göteborg, Sweden
[3] Institute of Physics, Faculty of Philosophy & Science, Silesian University in Opava, Bezručovo nám. 13, CZ-746 01 Opava, Czech Republic
[4] Copernicus Astronomical Centre, Warszawa, Poland
[5] Centre d'Etude Spatiale des Rayonnements, CNRS/UPS, 9 Avenue du Colonel Roche, 31028 Tolouse Cedex 04, France
[6] Astronomical Institute, Czech Academy of Sciences, Boční II 1401, CZ-141 31 Praha 4, Czech Republic
[7] Zielona Góra University, Lubuska 2, 65-265 Zielona Góra, Poland
[8] Max-Planck-Institute für Astrophysik, D-85741 Garching, Germany

ABSTRACT
Observations show that the upper ν_{U} and lower ν_{L} of the "twin peak" high frequency QPOs in neutron star sources vary along lines $\nu_{\mathrm{U}} = A\nu_{\mathrm{L}} + B$ in a frequency-frequency plot, and that their ratios $\nu_{\mathrm{U}}/\nu_{\mathrm{L}}$ cluster near the value 3/2. This behaviour is well consistent with the predictions of the non-linear resonance model for QPOs. In this Note, we further explore our recent finding that the coefficients A, B of the frequency-frequency lines for individual sources are anticorrelated. In the (A, B) plane, they occupy rather a narrow region along the line $A = 3/2 - B/600\,\mathrm{Hz}$. We show that this observational property of QPOs also follows from the resonance model.

Keywords: LMXRB – neutron stars – X-ray variability – observations – theory

1 THE BURSA LINE

The Fourier power spectra of X-ray variability from Galactic neutron star and black hole sources often reveal twin peaks corresponding to two physically connected frequencies – upper ν_{U} and lower ν_{L}. These twin peak frequencies are rather high – from hundreds to thousands of Hertz – i.e., in the range of ISCO frequencies. Thus, most likely, the oscillations, which produce them, occur very near the central compact source, in the strong Einstein gravity.

80-7248-334-X

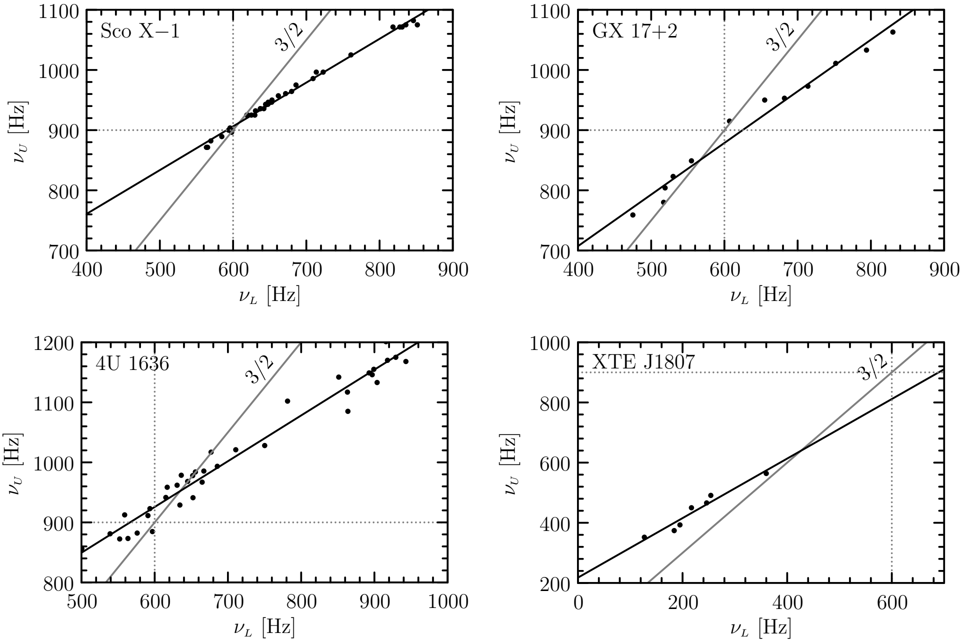

Figure 1. The behaviour of individual sources in a frequency-frequency plot. The two Z-sources (Sco X-1, GX 17+2), one atoll source (4U 1636) and the millisecond pulsar XTE J1807 are shown. The slopes and shifts A and B of their best linear fits are listed in the Table 1. Note that all the Bursa lines come close to the point [600 Hz, 900 Hz] shown as the intersection of two dotted lines.

In black hole sources, ν_U and ν_L appear to be fairly fixed, and in addition to have a well defined rational ratio $\nu_U/\nu_L = 3/2$ (pointed out in Abramowicz and Kluźniak, 2001). In neutron star sources ν_U and ν_L vary by hundreds of Hertz, along "Bursa lines,"[1]

$$\nu_U = A\nu_L + B\,. \tag{1}$$

It was demonstrated by Abramowicz et al. (2003b); Rebusco (2004); Horák (2004) that variations of ν_U and ν_L along the line (1) can be explained within the Kluźniak & Abramowicz non-linear resonance model for QPOs, as we shortly recall in Section 3.

The four examples shown in Fig. 1 illustrate another important general observational feature of the neutron star QPOs. The sectors occupied by data points on the individual lines typically cross the "3/2" straight line. This underlines in another way the relevance of the 3/2 ratio not only for the black hole QPOs but for the neutron star QPOs as well – the clustering around 3/2 value (and less often around other rational ratios) was examined by Abramowicz et al. (2003a) and later also by Belloni et al. (2005) and Bulik (2005).

[1] It was first shown by Psaltis et al. (1998), although in a different context, that frequency pairs of all sources cluster along a single line. Its importance was later noticed by Bursa (2002), unpublished, who also pointed that each source follows a slightly different line.

2 THE SLOPE-SHIFT ANTICORRELATION

Recently, Abramowicz et al. (2005) discovered another interesting feature of the frequency-frequency plots. They noticed that for *individual* lines (best linear fits through frequency points) $\nu_U = A\,\nu_L + B$ the coefficients A, B are anticorrelated.

Here, we follow our previous analysis and add six more sources, including Z-sources and a millisecond pulsar. All twelve sources are listed in Table 1, where we also give the resulting A and B. Table 2 compares the relation between A and B obtained by the least squares method for a coherent set of six sources analysed in Abramowicz et al. (2006) and

Table 1. Best linear fits and their errors for the frequency-frequency correlation for several atoll and Z sources (A and Z, respectively) and for the millisecond pulsar (P). The references: 1–6: Abramowicz et al. (2006), 7: Boirin et al. (2000), 8: Linares et al. (2005), 9: Homan et al. (2002), 10: Jonker et al. (2000), 11: Jonker et al. (2002), 12: Belloni et al. (2005).

	Source	Type	A	ΔA	B [Hz]	ΔB [Hz]
(1)	4U 0614	A	1.04	0.11	286.8	69.6
(2)	4U 1728	A	0.92	0.04	399.4	30.4
(3)	4U 1820	A	0.90	0.08	346.7	65.0
(4)	4U 1608	A	0.76	0.03	451.9	18.8
(5)	4U 1636	A	0.70	0.01	520.1	9.7
(6)	4U 1735	A	0.61	0.05	593	39
(7)	4U 1915	A	1.13	0.03	266	16
(8)	XTE J1807	P	1.11	0.11	181	26
(9)	GX 17+2	Z	0.86	0.04	364	28
(10)	GX 34+0	Z	0.84	0.07	391	26
(11)	GX 5-1	Z	0.83	0.04	386	14
(12)	Sco X-1	Z	0.786	0.002	432.5	1.5

Table 2. Anticorrelation between the slope and shift for 12 sources. The first two lines compare best linear fits $A(B)$ separately for coherent set of sources (Table 1: 1–6) analysed in Abramowicz et al. (2006) and for six other sources (Table 1: 7–12) examined by different authors. The second pair of lines cover all the sources and compare the $A(B)$ best linear fit vs. fit with intercept 1.5 shown in Fig. 2. Note that these two fits have almost the same quality (see also Fig. 3 for conjunctions).

Sources	Best fit $A(B)$	χ^2/dof
1–6	$A = 1.46(\pm0.17) - 0.0015(\pm0.0003)B$	0.28
7–12	$A = 1.58(\pm0.09) - 0.0018(\pm0.0002)B$	0.60
1–12	$A = 1.45(\pm0.07) - 0.0015(\pm0.0002)B$	1.33
1–12	$A = 1.5 - 0.0016B$	1.51

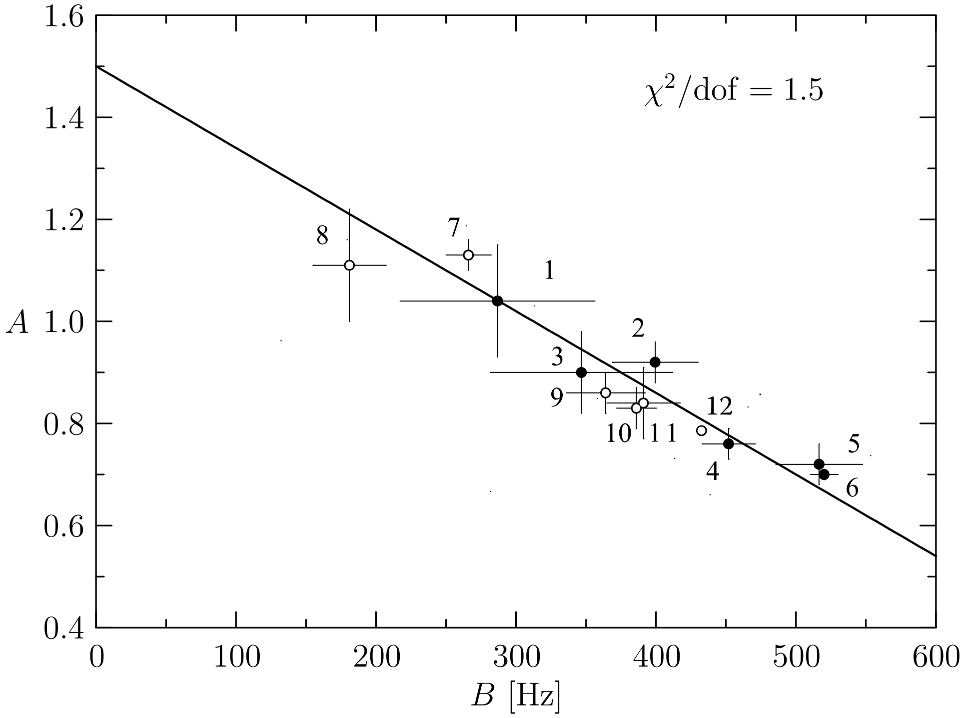

Figure 2. The anticorrelation between slopes and shifts. The points correspond to the individual sources listed in the Table 1; sources 1–6 (7–12) are denoted by filled (open) circles. We also show the best fit for the line going through the point [0, 1.5] and the corresponding value of χ^2.

for six other sources analysed by different authors using different methods, as well as the best linear fit for the whole set of 12 sources. This comparison shows that these 12 sources lie in the (A, B) plane close to the line

$$A = 1.5 - 0.0016B\,, \tag{2}$$

which is illustrated in Fig. 2.

3 A POSSIBLE THEORETICAL EXPLANATION IN THE FRAMEWORK OF THE RESONANCE MODEL

The frequency and the amplitude of a non-linear oscillator are not independent. In the lowest order with respect to the small amplitude α, the actual (observed) frequency ν differs from the eigenfrequency ν^0 of the oscillator by a correction $\Delta\nu$ proportional to the squared dimensionless amplitude, $\nu - \nu^0 = \Delta\nu \sim \nu^0 a^2$. Consider a very general system that has two coupled oscillation modes, whose eigenfrequencies are ν^0_{L} and ν^0_{U}. The frequencies of non-linear oscillations may be written in the form

$$\nu_{\rm L} = \nu_{\rm L}^0 + \Delta\nu_{\rm L}\,, \quad \nu_{\rm U} = \nu_{\rm U}^0 + \Delta\nu_{\rm U}\,, \tag{3}$$

$$\Delta\nu_{\rm L} = \nu_{\rm L}^0(\kappa_{\rm L}a_{\rm L}^2 + \kappa_{\rm U}a_{\rm U}^2)\,, \quad \Delta\nu_{\rm U} = \nu_{\rm U}^0(\lambda_{\rm L}a_{\rm L}^2 + \lambda_{\rm U}a_{\rm U}^2)\,, \tag{4}$$

where $\kappa_{\rm L}$, $\kappa_{\rm U}$, $\lambda_{\rm L}$ and $\lambda_{\rm U}$ are constants depending on non-linearities in the system and $a_{\rm L}$ and $a_{\rm U}$ are amplitudes of the oscillators.

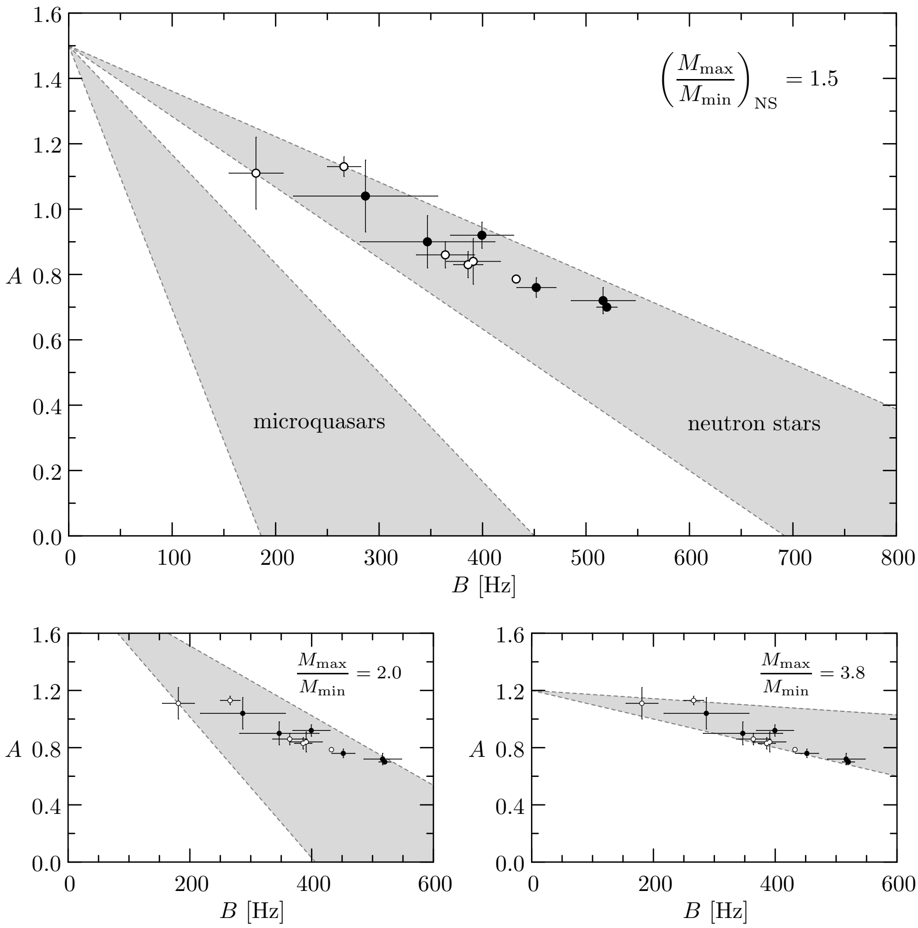

Figure 3. The $1/M$ scaling and the slope-shift anticorrelations. The characteristic frequencies scale inversely with the neutron star mass. On the other hand, the ratio $\tilde{\nu}_{\rm U}/\tilde{\nu}_{\rm L}$ should be close to the particular value $A_0 = 3/2$ for the resonance. The shaded regions give us the spread of the neutron star masses and expected region of black hole sources (see the text). We consider three cases: $A_0 = 3/2$ (top), 2.0 (bottom-left) and 1.2 (bottom-right). Note the rather unrealistic ratio between expected maximum and minimum neutron star masses in the sample for the values $A_0 \lesssim 1.2$.

It is natural to suppose that due to an interplay between the resonance excitation mechanism and the dissipation of the energy in the system, the two amplitudes $a_{\rm L}$ and $a_{\rm U}$ are correlated, i.e., one may consider the amplitudes as functions of a single parameter s,

$$a_{\rm L} = a_{\rm L}(s)\,, \quad a_{\rm U} = a_{\rm U}(s)\,. \tag{5}$$

Expanding with respect to s, we obtain from Eq. (3)

$$\nu_{\rm L} = \tilde{\nu}_{\rm L} + sF\,, \quad \tilde{\nu}_{\rm L} = \nu^0_{\rm L}\left(1 + \tilde{\alpha}^2_{\rm L}\right)\,, \quad F = f_0 + f_1 s + \cdots\,, \quad \tilde{\alpha}^2_{\rm L} \ll 1\,, \tag{6}$$

$$\nu_{\rm U} = \tilde{\nu}_{\rm U} + sG\,, \quad \tilde{\nu}_{\rm U} = \nu^0_{\rm U}\left(1 + \tilde{\alpha}^2_{\rm U}\right)\,, \quad G = g_0 + g_1 s + \cdots\,, \quad \tilde{\alpha}^2_{\rm G} \ll 1\,, \tag{7}$$

Isolating the parameter s from the two last equations, we get the Bursa line, i.e., a linear correlation between the observed frequencies $\nu_{\rm U} = A\nu_{\rm L} + B$, with the slope A and the shift B given by,

$$A = \frac{\tilde{\nu}_{\rm U}}{\tilde{\nu}_{\rm L}} X\,, \quad B = \tilde{\nu}_{\rm U}(1 - X)\,, \quad X \equiv \frac{G}{F}\,. \tag{8}$$

Any particular value of X leads to particular values of the slope and the shift. By solving Eqs (8) for the parameter X, one gets

$$A = \frac{\tilde{\nu}_{\rm U}}{\tilde{\nu}_{\rm L}} - \frac{1}{\tilde{\nu}_{\rm L}} B = A_0 - \frac{1}{\tilde{\nu}_{\rm L}} B\,. \tag{9}$$

Note that *for a given type of resonance* $A_0 = {\rm const} + \mathcal{O}(a^2)$, as it depends only on the ratio of the amplitude corrected eigenfrequencies. Of course, $\tilde{\nu}_{\rm L} \neq$ const even for a given resonance, as the eigenfrequencies themselves may differ from a system to system. Note also that if one includes more terms in expansions (6) and (7), the Bursa lines will deviate from straight lines.

Therefore, Eq. (9) predicts that the slope A and the shift B are anticorrelated. For a given type of resonance, the individual pairs A, B should be located on lines inside a triangle with a quite well determined vertex at [0, A_0], and with the size of its base proportional to the scatter in $\tilde{\nu}_{\rm L}$. In particular, for the 3 : 2 resonance the vertex should be very close to the point [0, 1.5], which indeed seems to be the case, as Fig. 3 shows.

4 MASSES AND ROTATION RATES OF NEUTRON STARS

The neutron star masses M must enter the discussion because of the $1/M$ scaling of QPOs frequencies predicted by the Kluźniak & Abramowicz resonance model, and by *all models* that assume strong gravity origin of QPOs. Indeed, in a strong gravity, a typical size is of the order of the gravitational radius, $r_{\rm G} \sim M$, a typical velocity is of the order of the light speed c and therefore typical frequency is $\nu \sim c/r_{\rm G} \sim 1/M$. So QPOs frequencies should scale inversely with the mass if a mass is the main difference between neutron stars.

Accordingly, the $\tilde{\nu}_{\rm L}$ frequency of Eq. (9) should roughly scale inversely with the mass of individual neutron stars corresponding to an individual A, B point. If all neutron star masses were equal, all the $\tilde{\nu}_{\mathrm{L}}$ frequencies would be equal as well, and individual frequency-frequency lines would cross at one point. However, the masses of neutron stars are not equal and therefore this intersection spreads into a region with the size proportional to the range of masses of the neutron star sources involved – the smaller the range, the more point-like the region is.

It is easy to see that the slope-shift anticorrelation line is steeper or softer for more massive or less massive sources respectively. Assuming the frequencies $\tilde{\nu}_{\mathrm{U}}$ and $\tilde{\nu}_{\mathrm{L}}$ are connected to the generic mass M^0 and scale inversely with the mass M, we can rewrite the Eq. (9) in the form

$$A = A_0 - \frac{1}{\tilde{\nu}_{\mathrm{L}}}\frac{M}{M^0}B\,. \tag{10}$$

This is illustrated in Fig. 3. The issue is more complicated because the $1/M$ scaling is not exact – it is also affected by rotation and by the internal structure of neutron stars. For this reason, the anticorrelation has a potential to provide observational constrains for masses, rotation rates, and multipole momenta for neutron stars. At the moment, the theory does not predict the exact form of $F(S)$, $G(S)$. The hope is that more accurate frequency-frequency fits may determine these functions better.

5 BLACK HOLE SOURCES

Our theory is also applicable to the case of black hole QPOs. The apparently steady frequencies reported in these systems can be attributed to smaller eigenfrequencies and amplitudes of oscillations. In our view the oscillation modes of an accretion disk are the same for black holes and neutron stars. Therefore, the dimensionless coefficients λ_{L}, λ_{U}, κ_{L} and κ_{U} in Eqs (4) are of the same order. The frequencies observed from black holes differ from the typical ones of neutron stars by a factor of ≈ 2. The same can be applied to the eigenfrequencies.[2] If the amplitudes of black hole QPOs were smaller than those of the neutron stars by a factor of ~ 5, the range of observed frequencies would be shorter by a factor of ~ 50 with respect to the range of the neutron stars, since it is proportional to the squares of the amplitudes.

The reported rms amplitudes of black hole QPOs are only a few per cent, contrary to neutron star QPOs rms amplitudes that usually exceed ten percent. The question is, how the observed rms amplitudes of QPOs in X-ray flux relate to the intrinsic amplitudes of oscillations. This is obviously connected to the modulation mechanism that may be different in the two classes of objects. If, similarly, the intrinsic amplitudes differ by such a large factor, it should not be surprising that the QPOs frequencies appear stable, since the predicted range of their variations correspond to a few Hertz. Such small variations can not be ruled out, more to the contrary, Miller et al. (2001) reported systematic motion of the upper high-frequency peak towards lower frequencies in the source XTE J1550-564. At

[2] The direct application of the $1/M$ scaling rule gives a factor of ~ 5. However, large differences in spins between black holes and neutron stars influence strongly the simple scaling, the five times heavier black hole may have QPOs frequencies only twice lower than a typical neutron star (see Fig. 7 in Török and Stuchlík, 2005).

this general level, the black hole QPOs can be understood as rescaled version of the neutron star QPOs and the corresponding region (180–450 Hz for microquasars) in the slope-shift plot is also denoted in Fig. 3.

6 DISCUSSION AND CONCLUSIONS

We have examined carefully the sources 1–6 from Table 1 and obtained good linear fit in the (A, B) plane. Rough comparison with not so coherent data for six other sources indicates that the trend would be valid as well.

The fact that observations of the neutron stars QPOs show both the Bursa line and the slope-shift anticorrelation, which are generic (and very general) consequences of non-linearity and coupling of oscillation modes, supports the clue that the QPOs are due to non-linear, coupled oscillations. Another observational clue is that the eigenfrequency ratio is close to the rational ratio, $\nu_{\mathrm{U}}^0/\nu_{\mathrm{L}}^0 = 3/2$, which suggests a 3 : 2 resonance. At the moment, it is not possible to firmly conclude anything more than that from the observational data.

ACKNOWLEDGEMENTS

This work has been supported by Nordita's Nordic Project *QPOs in black hole and neutron star sources*. M. A. and G. T. were supported by the Czech grant MSM 4781305903. M. B. and J. H. were supported by the Czech grant IAA 300030510.

REFERENCES

Abramowicz, M. A., Barret, D., Bursa, M., Horák, J., Kluźniak, W., Rebusco, P. and Török, G. (2006), to be submitted to Astrophys. J. Lett.

Abramowicz, M. A., Barret, D., Bursa, M., Horák, J., Kluźniak, W., Rebusco, P. and Török, G. (2005), The correlations and anticorrelations in QPO data, *Astronom. Nachr.*, **326**(9), pp. 864–866.

Abramowicz, M. A., Bulik, T., Bursa, M. and Kluźniak, W. (2003a), Evidence for a 2 : 3 resonance in Sco X-1 kHz QPOs, *Astronomy and Astrophysics*, **404**, pp. L21–L24.

Abramowicz, M. A., Karas, V., Kluźniak, W., Lee, W. and Rebusco, P. (2003b), Non-Linear Resonance in Nearly Geodesic Motion in Low-Mass X-Ray Binaries, *Publ. Astronom. Soc. Japan*, **55**(2), pp. 467–471, URL `http://pasj.asj.or.jp/v55/n2/550214/550214-frame.html`.

Abramowicz, M. A. and Kluźniak, W. (2001), A precise determination of black hole spin in GRO J1655−40, *Astronomy and Astrophysics*, **374**, p. L19, `astro-ph/010507`.

Belloni, T., Méndez, M. and Homan, J. (2005), The distribution of kHz QPO frequencies in bright low mass X-ray binaries, *Astronomy and Astrophysics*, **437**, pp. 209–216.

Boirin, L., Barret, D., Olive, J. G., Bloser, P. F. and Grindlay, J. E. (2000), Low and High Frequency Quasi-Periodic Oscillations in 4U1915-05, `astro-ph/0007071`.

Bulik, T. (2005), The statistics of Sco X-1 kHZ QPOs, *Astronom. Nachr.*, **326**(9), pp. 861–863.

Homan, J., van der Klis, M., Jonker, P. G., Wijnands, R., Kuulkers, E., Méndez, M. and Lewin, W. H. G. (2002), RXTE Observations of the Neutron Star Low-Mass X-Ray Binary GX 17+2: Correlated X-Ray Spectral and Timing Behavior, *Astrophys. J.*, **568**(2), pp. 878–900.

Horák, J. (2004), General aspects of nonlinear resonance 3 : 2 in QPO context, in S. Hledík and Z. Stuchlík, editors, *Proceedings of RAGtime 4/5: Workshops on black holes and neutron stars, Opava, 14–16/13–15 October 2002/2003*, pp. 91–110, Silesian University in Opava, Opava, ISBN 80-7248-242-4, `astro-ph/0408092`.

Jonker, P. G., van der Klis, M., Homan, J., Méndez, M., Lewin, W. H. G., Wijnands, R. and Zhang, W. (2002), The Power Spectral Properties of the Z Source GX 340+0, *Monthly Notices Roy. Astronom. Soc.*, **333**, p. 665.

Jonker, P. G., van der Klis, M., Wijnands, R., van Paradijs, J., Méndez, M., Ford, E. C., Kuulkers, E. and Lamb, F. K. (2000), The Power Spectral Properties of the Z Source GX 340+0, *Astrophys. J.*, **537**(1), pp. 374–386.

Linares, M., van der Klis, M., Altamiro, D. and Markwardt, C. B. (2005), Discovery of Kilohertz Quasi-periodic Oscillations and Shifted Frequency Correlations in the Accreting Millisecond Pulsar XTE J1807-294, *Astrophys. J.*, **634**(2), pp. 1250–1260.

Miller, J. M., Wijnands, R., Homan, J., Belloni, T., Pooley, D., Corbel, S., Kouveliotou, C., van der Klis, M. and Lewin, W. H. G. (2001), High-Frequency Quasi-Periodic Oscillations in the 2000 Outburst of the Galactic Microquasar XTE J1550-564, *Astrophys. J.*, **563**(2), pp. 928–933.

Psaltis, D., Mendez, M., Wijnands, R., Homan, J., Jonker, P. G., van der Klis, M., Lamb, F. K., Kuulkers, E., van Paradijs, J. and Lewin, W. H. G. (1998), The Beat-Frequency Interpretation of Kilohertz Quasi-periodic Oscillations in Neutron Star Low-Mass X-Ray Binaries, *Astrophys. J. Lett.*, **501**, p. L95, `astro-ph/9805084`.

Rebusco, P. (2004), Twin Peaks kHz QPOs: Mathematics of the 3:2 Orbital Resonance, *Publ. Astronom. Soc. Japan*, **56**(3), pp. 553–557.

Török, G. and Stuchlík, Z. (2005), Epicyclic frequencies of Keplerian motion in Kerr spacetimes, pp. 315–338, this volume.

Proceedings of *RAGtime 6/7: Workshops on black holes and neutron stars, Opava, 16–18/18–20 September, 2004/2005*
S. Hledík and Z. Stuchlík, editors, Silesian University in Opava, Czech Republic, 2005, pp. 11–28

A virtual trip to the Schwarzschild–de Sitter black hole

Computer simulation of extreme gravitational lensing in Schwarzschild–de Sitter spacetimes

Pavel Bakala,[1,a] Petr Čermák,[2] Stanislav Hledík,[1]
Zdeněk Stuchlík[1] and Kamila Truparová Plšková[1]

[1] Institute of Physics, Faculty of Philosophy & Science, Silesian University in Opava, Bezručovo nám. 13, CZ-746 01 Opava, Czech Republic
[2] Institute of Computer Science, Faculty of Philosophy & Science, Silesian University in Opava, Bezručovo nám. 13, CZ-746 01 Opava, Czech Republic
[a] pavel.bakala@fpf.slu.cz

ABSTRACT
We describe a new method to developing a realistic fully general relativistic model and computer code of optical projection in a strong, spherically symmetric gravitational field. Classical theoretical analysis of optical projection for an observer in the vicinity of a Schwarzschild black hole was extended to black hole spacetimes with a repulsive cosmological constant (Schwarzschild–de Sitter spacetimes). In our simulation we consider both null geodesics beyond and ahead of the turning point. Simulation takes care of frequency shift effects, as well as the amplification of intensity. Our code generates static images of sky for static observers and movie simulation for free-falling observers. We use techniques of parallel programming to get high performance and fast run of our code.

1 INTRODUCTION

This work is devoted to the following "virtual astronomy" problem: What is the view of distant universe for an observer in the vicinity of a black hole (neutron star) like? Nowadays, this problem can be hardly tested by real astronomy, however, it gives an impressive illustration of differences between optics in a strong gravity field and between flat spacetime optics as we experience it in our everyday life.

In this paper we compute and display the appearance of distant universe to an observer near the black hole. We will study this problem for the spherically symmetric Schwarzschild–de Sitter spacetime with a repulsive (positive) cosmological constant. We consider two classes of observers for which we will compute the appearance of sources in the distant universe. The first class are static observers, i.e., observers who (for example thanks to its rocket) sit at rest in the external field of the hole (with world lines of $r, \theta, \phi = \text{const}$).

80-7248-334-X

The second class are radially falling observers, i.e., observers who fall freely from a given radius onto the black hole.

In pure Schwarzschild case we assume free-fall observers falling from infinity and distant source located in infinity too (Cunningham, 1975). In Schwarzschild–de Sitter case it is useful to choose the starting point for the radially moving observers at the static radius, where the gravitational attraction of the hole is balanced by the cosmological repulsion (Stuchlík and Hledík, 1999; Stuchlík and Plšková, 2004). Hereafter, in this case we assume distant sources located at the static radius.

2 SCHWARZSCHILD–DE SITTER GEOMETRY

The line element of the Schwarzschild–de Sitter spacetime in the standard Schwarzschild coordinates in geometric units ($c = G = 1$) has the form

$$\mathrm{d}s^2 = -\left(1 - \frac{2M}{r} - \frac{\Lambda}{3}r^2\right)\mathrm{d}t^2 + \left(1 - \frac{2M}{r} - \frac{\Lambda}{3}r^2\right)^{-1}\mathrm{d}r^2 + r^2(\mathrm{d}\theta^2 + \sin^2\theta\,\mathrm{d}\phi^2)\,, \quad (1)$$

where M is mass of the central black hole, $\Lambda \sim 10^{-56}\,\mathrm{cm}^{-2}$ is the repulsive cosmological constant. It is advantageous to introduce dimensionless cosmological parameter y by the relation

$$y = \tfrac{1}{3}\Lambda M^2\,. \quad (2)$$

The event horizons of the spacetime are given by condition

$$g_{tt} \equiv -\left(1 - \frac{2}{r} - yr^2\right) = 0\,. \quad (3)$$

The location of events horizons is determined by the relation

$$y = y_{\mathrm{h}}(r) \equiv \frac{r-2}{r^3}\,. \quad (4)$$

In the Schwarzschild–de Sitter spacetimes there exists a critical value of the parameter y, given by the relation $y_{\mathrm{crit}} = y_{\mathrm{h}}(r = 3) = 1/27$, corresponding to the local maximum of $y_{\mathrm{h}}(r)$. For $0 < y < y_{\mathrm{crit}}$, there exists two events horizons. The black-hole horizon and the cosmological horizon are located at

$$r_{\mathrm{h}} = \frac{2}{\sqrt{3y}}\cos\frac{\pi + \xi}{3}\,, \qquad r_{\mathrm{c}} = \frac{2}{\sqrt{3y}}\cos\frac{\pi - \xi}{3}\,, \quad (5)$$

where

$$\xi = \cos^{-1} 3\sqrt{3y}\,. \quad (6)$$

The static radius, the hypersurface where the gravitational attraction of the hole is balanced by the cosmological repulsion, is given by the condition

$$y = y_{\mathrm{s}}(r) \equiv \frac{1}{r^3}\,. \quad (7)$$

The spacetime is dynamic at $r < r_{\mathrm{h}}$ and $r > r_{\mathrm{c}}$. If $y = y_{\mathrm{crit}} = 1/27$, the horizons and static radius coincide at $r_{\mathrm{h}} = 3$. If $y > 1/27$, the spacetime is dynamic at $r > 0$ and describes a naked singularity (Stuchlík and Hledík, 1999). We consider only spacetimes with possibility of static observers existence, consequently with $y < 1/27$.

It follows from the central symmetry of the geometry (1) that the geodetical motion of test particles and photons is allowed in the central planes only.The existence of Killing vector fields $\xi_{(t)}$ and $\xi_{(\phi)}$ of the SdS spacetime implies the existence of two constants of motion

$$p_t = g_{t\mu} p^{\mu} = -\mathcal{E} \, , \qquad p_{\phi} = g_{\phi\mu} p^{\mu} = \Phi \, , \tag{8}$$

but the motion is determined by the impact parameter

$$b \equiv \frac{\Phi}{\mathcal{E}} \, . \tag{9}$$

The 4-momentum of the photon reads

$$p_t = -\mathcal{E} \, , \qquad p_r = \pm \frac{\sqrt{1 - \frac{b^2}{r^2}\left(1 - \frac{2}{r} - yr^2\right)}}{\left(1 - \frac{2}{r} - yr^2\right)} \mathcal{E} \, , \qquad p_{\phi} = b\mathcal{E} = \Phi \, . \tag{10}$$

The "+" sign corresponds to photons receding from the black hole, the "−" sign corresponds to photons infalling into the black hole.

3 TETRADS AND DIRECTLY MEASURED QUANTITIES

In order to calculate directly measured quantities, one has to transform the 4-momentum of the photon into local coordinate system of the observer. Local components of 4-momentum for the observer located at a given r can be obtained using appropriate tetrad of 1-form $p^{(\alpha)} = \omega^{(\alpha)}_{\mu} p^{\mu}$. An observer (located at $r < r_{\mathrm{s}}$) will see the photons coming from the directional angle α related to the outward radial direction as given by the general relation

$$\cos\alpha = -\frac{p^{(r)}_{\mathrm{obs}}}{p^{(t)}_{\mathrm{obs}}} \, , \tag{11}$$

and frequency shift g of the photon (the ratio of observed and emitted energy) is given by the relation

$$g = \frac{p^{(t)}_{\mathrm{obs}}}{p^{(t)}_{\mathrm{source}}} \, . \tag{12}$$

Indexes "obs" (observer) and "source" denote the components locally measured by a observer or a source located on a given r_{obs} or r_{source}, respectively.

3.1 Static observers

Let us consider static observers who are located at rest at $r = \text{const}, \theta = \text{const}, \phi = \text{const}$. The observers are endowed by a proper reference system with an orthonormal tetrad of one-forms (Stuchlík and Plšková, 2004)

$$\omega^{(t)} = B(r, y)\,\mathrm{d}t\,, \tag{13}$$
$$\omega^{(r)} = B(r, y)^{-1}\,\mathrm{d}r\,, \tag{14}$$
$$\omega^{(\theta)} = r\,\mathrm{d}\theta\,, \tag{15}$$
$$\omega^{(\phi)} = r\sin\theta\,\mathrm{d}\phi\,, \tag{16}$$

where we denote

$$B^2(r, y) \equiv 1 - 2r^{-1} - yr^2\,. \tag{17}$$

If we will consider motion of photons in the equatorial plane only, the components of 4-momentum of the photon measured by a static observer located at a given r_{obs} are given by the relations

$$p_t = -\mathcal{E}\,, \qquad p_r = \frac{A(r_{\mathrm{obs}}, y; b)}{B^2(r_{\mathrm{obs}}, y)}\mathcal{E}\,, \qquad p_\phi = b\mathcal{E} = \Phi\,, \tag{18}$$

where

$$A(r, y; b) = \pm\sqrt{1 - B^2(r, y)\frac{b^2}{r^2}}\,. \tag{19}$$

The directional angle and frequency shift are given by formulas

$$\cos\alpha_{\mathrm{stat}} = -A(r_{\mathrm{obs}}, y; l) = \pm\sqrt{1 - \frac{b^2}{r_{\mathrm{obs}}^2}\left(1 - \frac{2}{r_{\mathrm{obs}}} - yr_{\mathrm{obs}}^2\right)}\,, \tag{20}$$

$$g_{\mathrm{stat}} = \sqrt{\frac{g_{tt}\,(r_{\mathrm{source}})}{g_{tt}\,(r_{\mathrm{obs}})}}\,. \tag{21}$$

3.2 Radially falling observers

The orthonormal tetrad of 1-forms of the radially falling observers has the form (Stuchlík and Plšková, 2004)

$$\omega^{(\tilde{t})} = \sqrt{1 - 3y^{1/3}}\,\mathrm{d}t + Z(r, y)B^{-2}(r, y)\,\mathrm{d}r\,, \tag{22}$$

$$\omega^{(\tilde{r})} = Z(r, y)\,\mathrm{d}t + \sqrt{1 - 3y^{1/3}}B^{-2}(r, y)\,\mathrm{d}r\,, \tag{23}$$

$$\omega^{(\tilde{\theta})} = r\,\mathrm{d}\theta\,, \tag{24}$$
$$\omega^{(\tilde{\phi})} = r\sin\theta\,\mathrm{d}\phi\,, \tag{25}$$

where we introduced a new variable

$$Z(r, y) \equiv \sqrt{\frac{2}{r} + yr^2 - 3y^{1/3}}\,. \tag{26}$$

The components of 4-momentum of the photon measured by a radially falling observers at a given $r_{\rm obs}$ are given by the relations

$$p^{(\tilde{t})}_{\rm obs} = \frac{\mathcal{E}}{B^2(r_{\rm obs}, y)}\left(\sqrt{1 - 3y^{1/3}} + Z(r_{\rm obs}, y)A(r_{\rm obs}, y; b)\right)\,, \tag{27}$$

$$p^{(\tilde{r})}_{\rm obs} = \frac{\mathcal{E}}{B^2(r_{\rm obs}, y)}\left(Z(r, y) + \sqrt{1 - 3y^{1/3}}A(r_{\rm obs}, y; b)\right)\,, \tag{28}$$

$$p^{(\tilde{\phi})}_{\rm obs} = \frac{\mathcal{E}b}{r_{\rm obs}} = \frac{\Phi}{r_{\rm obs}}\,. \tag{29}$$

The directional angle and frequency shift will be given by formulas

$$\cos\tilde{\alpha} = -\frac{Z(r_{\rm obs}, y) + \sqrt{1 - 3y^{1/3}}A(r_{\rm obs}, y; b)}{\sqrt{1 - 3y^{1/3}} + Z(r_{\rm obs}, y)A(r_{\rm obs}, y; b)}\,, \tag{30}$$

$$\tilde{g} \equiv \frac{p^{(\tilde{t})}_{\rm obs}}{p^{(t)}_{\rm source}} = \frac{B(r_{\rm source}, y)}{Z(r_{\rm obs}, y)\cos\tilde{\alpha} + \sqrt{1 - 3y^{1/3}}}\,. \tag{31}$$

4 FORMULATION OF THE PROBLEM

As shown in Fig. 1, projections of virtual images on the observer sky are given by tangential vectors of corresponding geodesics. The vantage choice of tangential vector is the space part of 4-momentum of photons on the geodesic. Due to the spherical symmetry of the problem we can consider (only for simplicity of calculations) and sources located on equatorial plane ($\theta = \pi/2$) and the observers with ($\phi = 0$). In this case space coordinates of sources are $(r_{\rm source}, \phi_{\rm source}, \pi/2)$ and $\Delta\phi$ along the geodesics is given by

$$\Delta\phi = \phi_{\rm source} + 2k\pi\,, \tag{32}$$

where the parameter k takes values of $0, 1, 2, \ldots, +\infty$ for geodesics orbiting clockwise, $-1, -2, \ldots, -\infty$ for geodesics orbiting counter-clockwise. First direct image corresponds to $k = 0$, first indirect one corresponds to $k = -1$ case. Infinite values of k correspond to a photon captured on the circular photon orbit. Direction of space part of the photon 4-momentum is given only by impact parameter b, so we need b as the function of locations of source and observer. In order to calculate proper impact parameter b for given $\Delta\phi$ and $r_{\rm source}$ we will start from following "Binet formula" for Schwarzschild–de Sitter spacetime:

$$\frac{\mathrm{d}\phi}{\mathrm{d}u} = \pm\frac{\mathrm{d}u}{\sqrt{b^{-2} - u^2 + 2u^3 + y}}\,, \qquad u = r^{-1}\,. \tag{33}$$

Required positivity of term under the square root defines motion condition for photons, which can be written as

$$C(b, u, y) \equiv \left(b^{-2} - u^2 + 2u^3 + y\right) \geq 0\,. \tag{34}$$

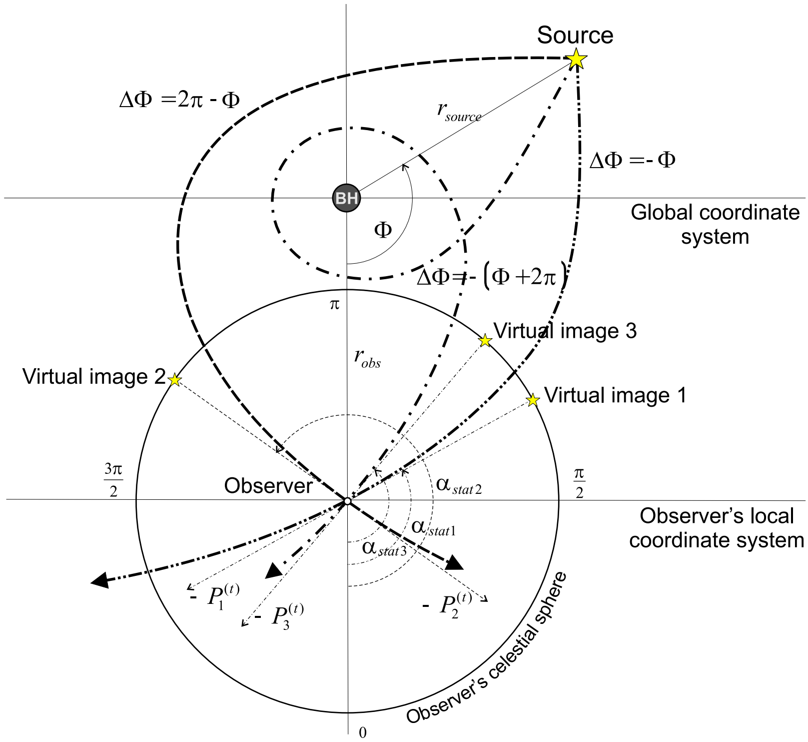

Figure 1. Simulated situation.

5 CONSEQUENCES OF MOTION CONDITION

As shown in Fig. 2, there exist two types of geodesics. The first one corresponds with the positive motion condition satisfied in whole range of u. Photons going from infinity along these geodesics must fall to the central singularity. The second type corresponds to restricted interval of u allowed for the motion. The boundary of the interval of allowed radii defines the turning point r_{turn} for photons going from infinity and it is clear that geodesic with turn point at the observer's position ($r_{\text{obs}} = r_{\text{turn}}$) must have the highest value $b_{\max}(r_{\text{obs}})$ of impact parameters for given r_{obs}. Geodesics with $b > b_{\max}$ never achieve r_{obs}. Straightforward calculation yields the relation

$$r_{\text{turn}} = \frac{2}{\sqrt{3(y+b^{-2})}} \cos\left[\frac{1}{3}\arccos\left(-3\sqrt{3(y+b^{-2})}\right)\right], \tag{35}$$

and

$$b_{\max} = \frac{1}{\sqrt{u_{\text{obs}}^2 - 2u_{\text{obs}}^3 - y}}. \tag{36}$$

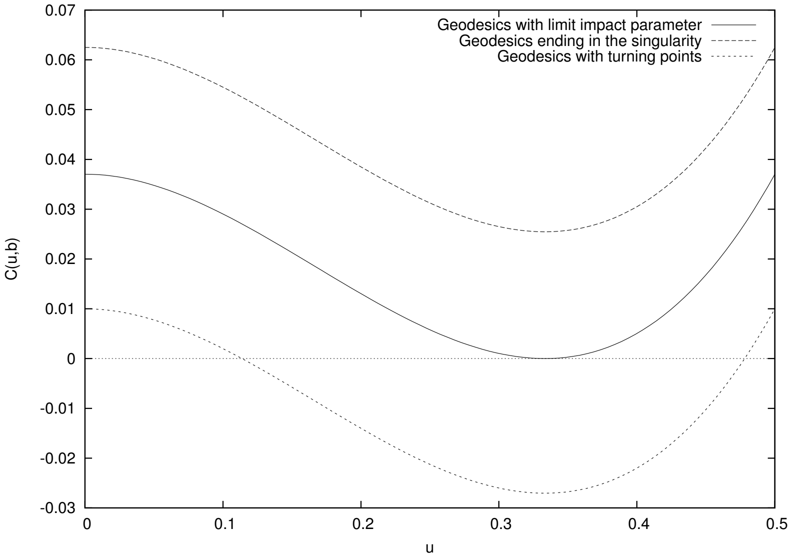

Figure 2. Motion condition as a function of u.

The limit case is the geodesic with the motion condition touching the the zero level at one point only. This case corresponds to the photon capture on the circular photon orbit and the impact parameter of the circular photon geodesic will be called "critical impact parameter." The circular photon orbit corresponds to the minimum of the motion condition function $C(b, u, y)$. Using conditions $\mathrm{d}C(b, u, y)/\mathrm{d}u = 0$ and $C(b, u, y) = 0$ simultaneously we obtain formula for limit impact parameter b_{c} and location of circular photon orbit r_{ph}. The circular photon orbit is located at $r = 3$ for arbitrary value of the dimensionless parameter y. However the critical impact parameter depends on y by the relation

$$b_{\mathrm{c}}(y) = \sqrt{\frac{27}{1 - 27y}}\,. \tag{37}$$

For observers located under circular photon orbit we have to consider geodesics with $b < b_{\mathrm{c}}$ only, because all turning points are located above the circular photon orbit. For observers located above the circular photon orbit one have to consider both types of geodesics.

6 THREE KINDS OF NULL GEODESICS

Finally, due the character of the motion condition, we have to consider three types of null geodesics passing an observer's position. The first one has impact parameter $b < b_{\mathrm{c}}$. Photons going from infinity along these geodesics finish in the singularity. The second one has $b < b_{\mathrm{c}}$, and the observer is located above the turning point of the geodesics. For both these types of null geodesics we can write the integral form of the “Binet formula” in the form

$$\Delta\phi(u_{\rm obs}) = \pm \int_{u_{\rm source}}^{u_{\rm obs}} \frac{\mathrm{d}u}{\sqrt{b^{-2} - u^2 + 2u^3 + y}} . \tag{38}$$

The last one has $b < b_{\rm c}$ and the observer is located under the turning point. Therefore, we can express the integral form of the “Binet formula” in the form

$$\Delta\phi(u_{\rm obs}) = \pm \int_{u_{\rm turn}}^{u_{\rm obs}} \frac{\mathrm{d}u}{\sqrt{b^{-2} - u^2 + 2u^3 + y}} \mp \Delta\phi(u_{\rm turn}) , \tag{39}$$

where

$$\Delta\phi(u_{\rm turn}) = \left| \int_{u_{\rm source}}^{u_{\rm turn}} \frac{\mathrm{d}u}{\sqrt{b^{-2} - u^2 + 2u^3 + y}} \right| . \tag{40}$$

Integral equations (39) and (40) provide an expression for $\Delta\phi$ along the photon path as a function $F(b, u_{\rm obs}, u_{\rm source}, y)$. Therefore, we can rewrite the Eq. (32) for observers with space coordinates $(r_{\rm obs}, 0, \pi/2)$ in the following way:

$$F\,(b, u_{\rm obs}, u_{\rm source}, y) - \phi_{\rm source} - k2\pi = 0 . \tag{41}$$

Final equation expresses b as an implicit function of the boundary conditions and cosmological constant. The function $F(b, u_{\rm obs}, u_{\rm source}, y)$ can be given in term of elliptic integrals. However, here we shall use a direct numerical methods to solve Eq. (41). We used Romberg integration and trivial bisection method. Faster root finding methods (e.g., Newton–Raphson method) may unfortunately fail here.

7 SIMULATIONS

Our code computes a view of the distant universe, which is represented by a nondistorted picture of an object on the observer sky in the flat spacetime. We assume that the image is a parallel mapping of hemisphere of sky toward the black hole. The code generates two images, parallel mappings of both hemispheres of the observer sky, because optical projection in strong gravity field can shift images of sources from a hemisphere of the sky to the opposite one. For this simulation we used a picture of M104 Sombrero galaxy provided by VLT (Very Large Telescope Interferometry Array) ESO Cerro Paranal, Chile downloaded from www site (Katedra fyziky, Fakulta elektrotechnická, ČVUT Praha, 2005).

7.1 Simulation for the static observer above the photon orbit

For observers above the photon orbit we have to consider both type of null geodesics, with and without turning points. The left panel of Fig. 4 shows impact parameter b and a directional angle $\alpha_{\rm stat}$ as a functions of $\Delta\phi$ along the geodesic line. The geodesics with $\Delta\phi < \Delta\phi(b_{\rm max})$ have no turning points ahead of observer position, some of them with

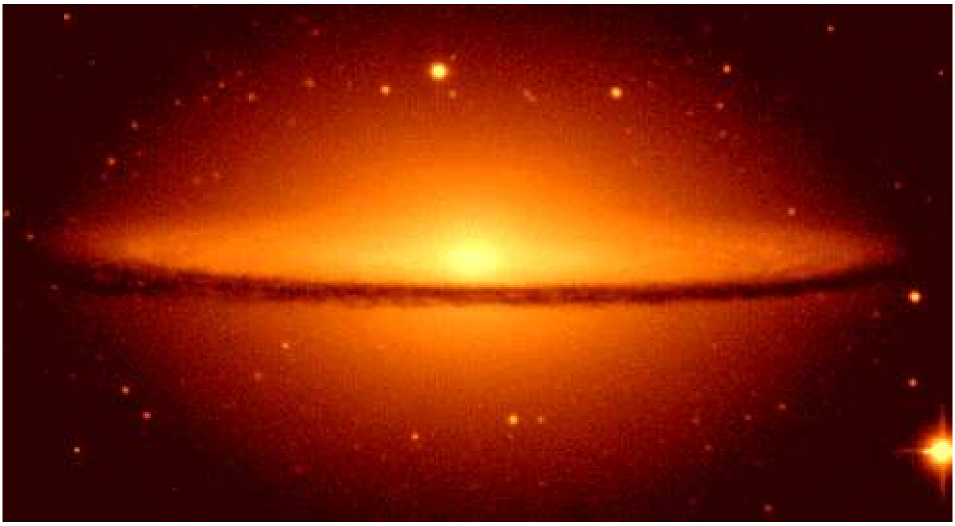

Figure 3. Optical appearance of the Sombrero galaxy as seen from the Earth.

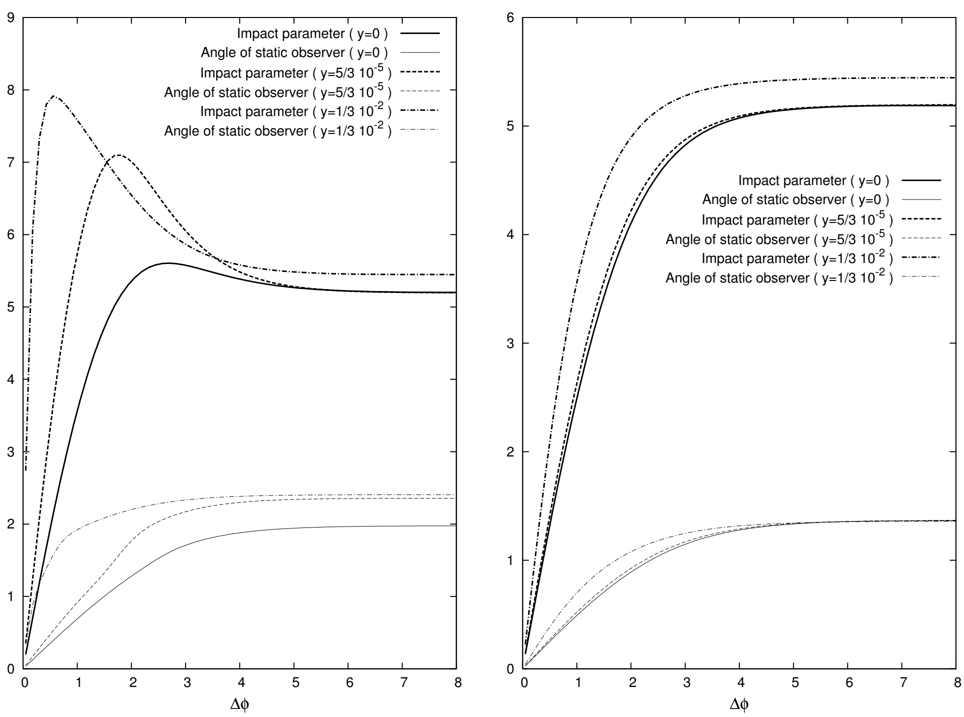

Figure 4. Impact parameter and directional angle as a function of $\Delta\phi$ for different values of cosmological constant. *Left panel:* Above the photon orbit. *Right panel:* Under the photon orbit.

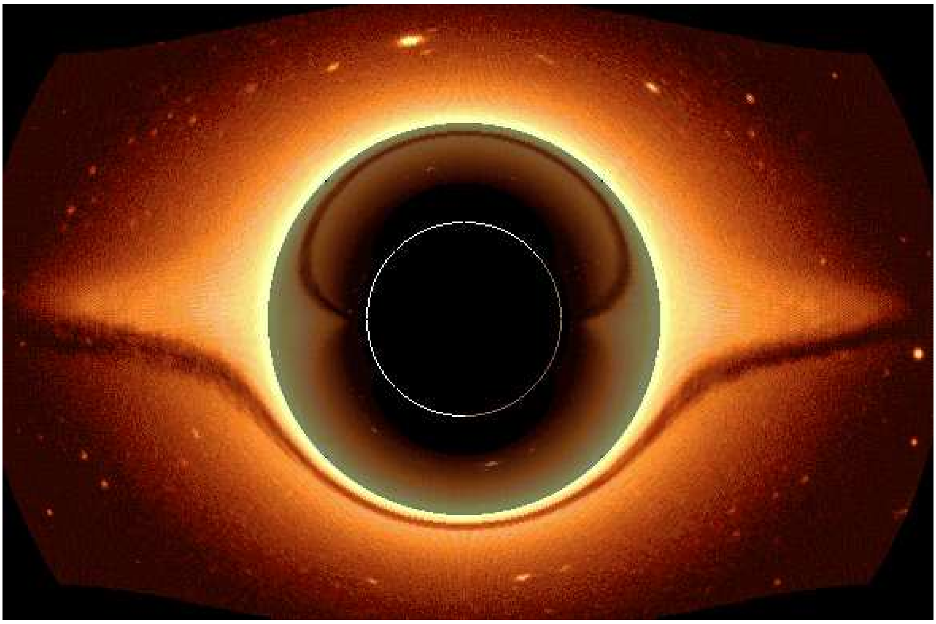

Figure 5. Sombrero observed from $r_{\rm obs} = 25M$ in pure Schwarzschild case.

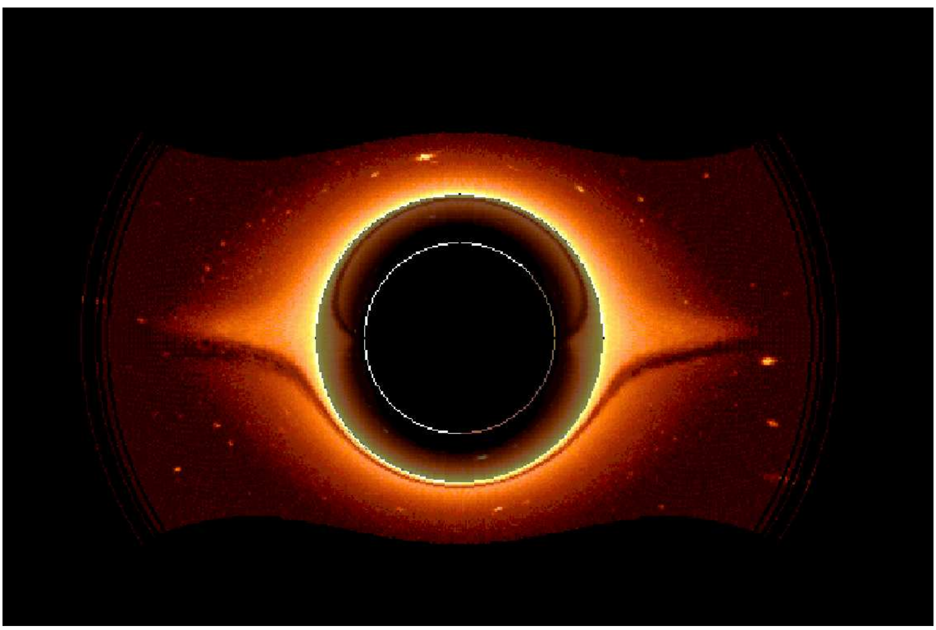

Figure 6. Sombrero observed from $r_{\rm obs} = 25M$ with the cosmological constant $\Lambda = 10^{-5}\,{\rm cm}^{-2}$.

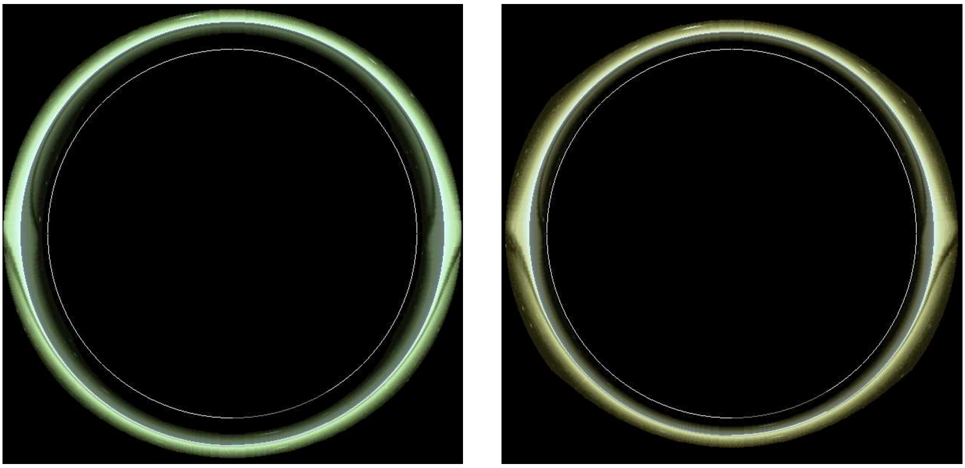

Figure 7. Sombrero observed from $r_{\rm obs} = 5M$. *Left panel:* Without the cosmological constant. *Right panel:* With the cosmological constant $\Lambda = 10^{-5}\,\rm cm^{-2}$.

$b < b_{\rm c}$ will finish in the central singularity, other ones have turning points beyond the observer position. All geodesics with $\Delta\phi > \Delta\phi(b_{\rm max})$ have a turning point ahead of the observer's position and escape to infinity. Geodesics with $\Delta\phi = \Delta\phi(b_{\rm max})$ have turning points just at the observer's radius and, of course escape to infinity too. The impact parameter b increases with $\Delta\phi$ up to $b_{\rm max}$, after which it decreases and asymptotically approaches $b_{\rm c}$ from above. The directional angle $\alpha_{\rm stat}$ monotonically increases with $\Delta\phi$ up to its maximum value, which defines the black region on the observer's sky. The black region increases with decreasing radial coordinate of the observer. Simulation outputs in Figs 5, 6 and 7 illustrate these effects for different values of $r_{\rm obs}$ and the cosmological constant.

7.2 Simulation for the static observer under the photon orbit

The situation is qualitatively different for observer position under the photon orbit. There exist only geodesics without turning points finishing in the central singularity, therefore those with $b < b_{\rm c}$. The right panel of Fig. 4 shows the impact parameter b and the directional angle $\alpha_{\rm stat}$ as a functions of $\Delta\phi$ along the geodesic. The impact parameter b increases with $\Delta\phi$ and asymptotically approaches to $b_{\rm c}$ from below. The angle $\alpha_{\rm stat}$ monotonically increases with $\Delta\phi$ up to its maximum value, which defines a black region on the observer sky. The black region occupies a more than half of the observer sky. Due to the strong gravity field the images are strongly blueshifted. In case of an observer near the event horizon, the whole universe is displayed as a small spot around the intersection point of the observer sky and the optical axis, the straight line defined by an observer's position and the central singularity. Simulation outputs in Fig. 8 illustrate those effects for different values of the cosmological constant.

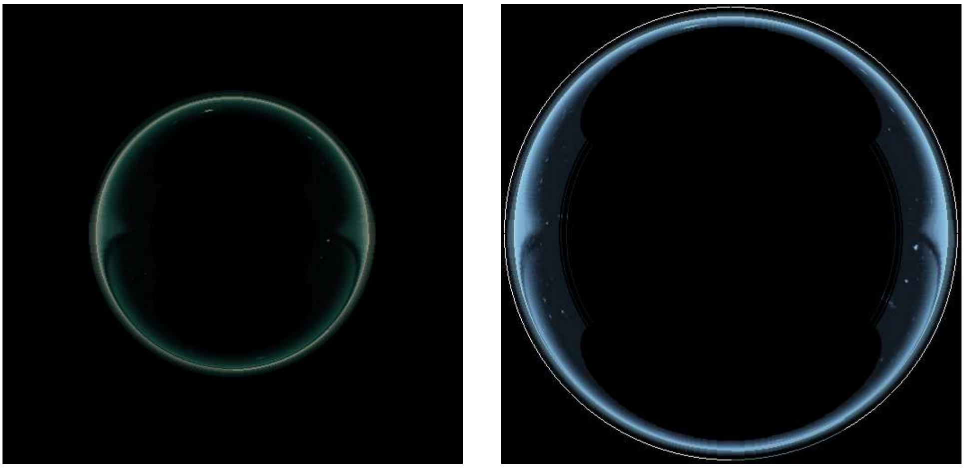

Figure 8. Sombrero observed from $r_{\rm obs} = 2.8M$ – outward direction view. *Left panel:* Without the cosmological constant. *Right panel:* With the cosmological constant $\Lambda = 10^{-5}\ {\rm cm}^{-2}$.

7.3 Simulation for the free-falling observer

Simulation for free-falling observer generates a sequence of images with defined frame rate per second. The sequence can be merged in a demonstration movie. The left side of the movie screen is the view of the hemisphere of the observer sky toward the black hole, the right panel is the view of the opposite hemisphere. The movie also displays the proper time and the radial coordinate of the free-falling observer. This movie can be downloaded from our www site (Silesian University in Opava, 2005–2009). Some time cuts of the movie for pure Schwarzschild case are shown in Fig. 9. The main difference in comparison with the static observer is dependency of frequency shift on ϕ coordinate of the source.

7.4 Other properties of the optical projection

7.4.1 Einstein rings

A source on the optical axis, straight line defined by the observer's position and the central singularity, has no defined plane of the photon motion and it is displayed as infinitesimally thin rings. As in case of standard images, there is an infinite number of Einstein rings generated as borders between the images of different order, but all higher order rings and images merge in the one bright ring on the border of the black region in the observer sky (Nemiroff, 1993). The physical reason for this is an infinite number of equivalent null geodesics.

7.4.2 Intensity changes

The strong gravity field makes time, frequency and space redistribution of radiation flux from the whole observer sky (Cunningham, 1975). Intensity of higher order images de-

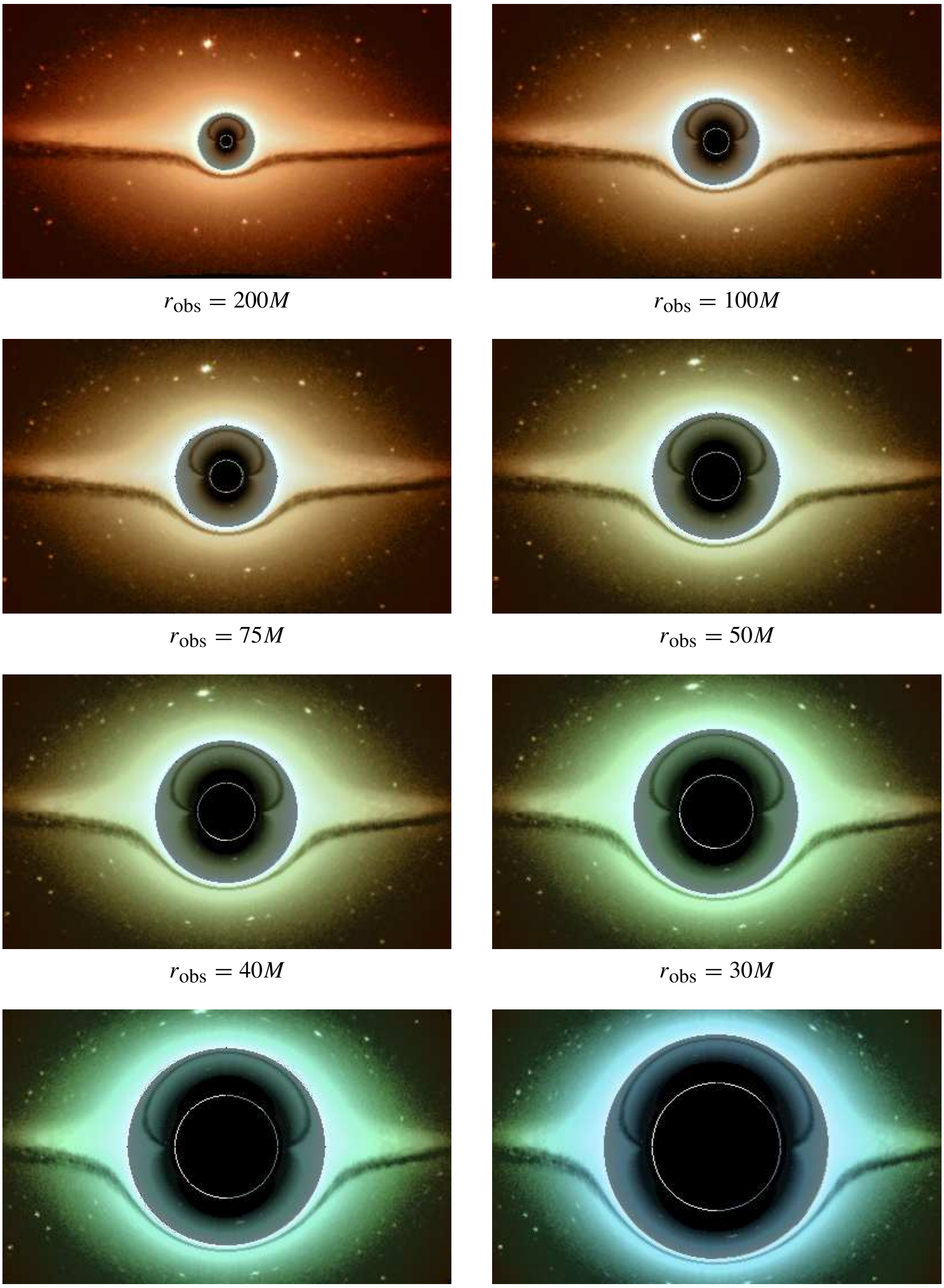

$r_{\text{obs}} = 200M$ $r_{\text{obs}} = 100M$

$r_{\text{obs}} = 75M$ $r_{\text{obs}} = 50M$

$r_{\text{obs}} = 40M$ $r_{\text{obs}} = 30M$

$r_{\text{obs}} = 20M$ $r_{\text{obs}} = 15M$

Figure 9. Simulation for radially free-falling observer in pure Schwarzschild case. View of Sombrero galaxy on different radiuses of free-falling observer.

creases very rapidly, except for the Einstein rings where intensity theoretically (in our geometrical approach) goes to infinity (Ohanian, 1987). Therefore, Einstein rings will be well detectable and observable.

7.4.3 Geometry of the optical projection

The optical projection conserves spherical symmetry. The rings in the imaginary sky with centre on optical axis in the flat spacetime is transformed into rings with centre on the optical axis and different radii. But all images generated by counter-clockwise orbiting geodesics are inverted in both angular coordinates ϕ and θ.

8 INFLUENCE OF COSMOLOGICAL CONSTANT

It is possible to define an apparent angular size of the black hole as an angular size of the black region on the observer sky. This angular size depend on the value of the cosmological constant and it is useful as an illustration of the influence of the cosmological constant on the geometry of the optical projection. For observers above the circular photon orbit the

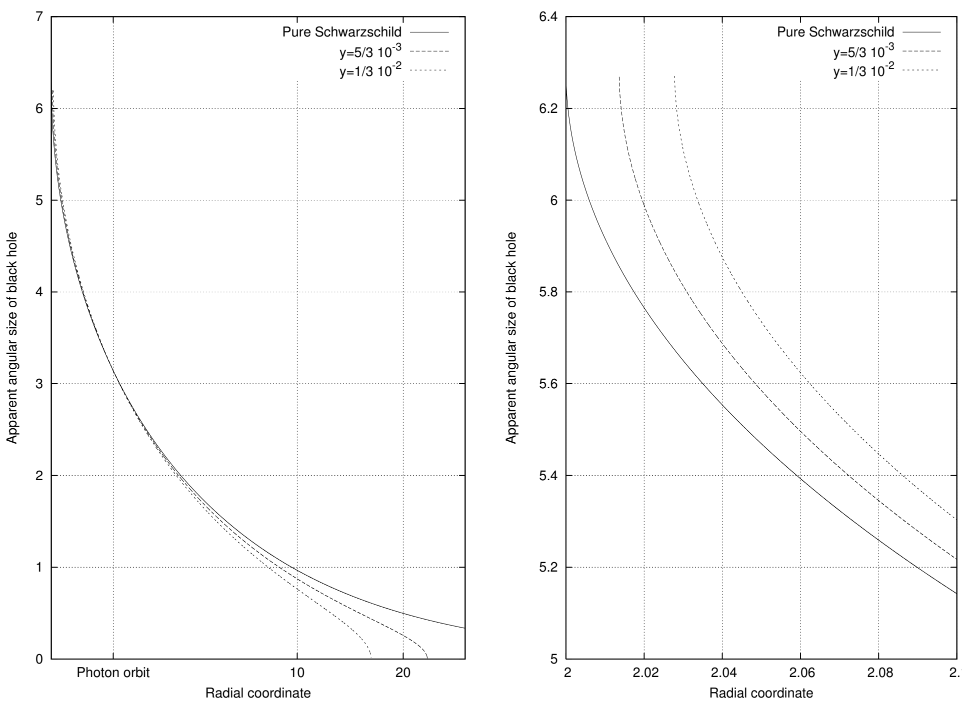

Figure 10. Apparent angular size of black hole as a function of r for different values of cosmological constant. *Left panel:* Under and above photon orbit. *Right panel:* Zoom near event horizon.

maximum directional angle $\alpha_{\max}$ corresponds to the outgoing geodesics with the directional angle

$$\alpha_{\max} = \lim_{b \to b_c^+} \alpha_{\text{stat}}(b, y, r_{\text{obs}}) \, . \tag{42}$$

For observers under the circular photon orbit the maximum directional angle $\alpha_{\max}$ corresponds to the ingoing geodesics with the directional angle

$$\alpha_{\max} = \lim_{b \to b_c^-} \alpha_{\text{stat}}(b, y, r_{\text{obs}}) \, , \tag{43}$$

see Fig. 4 and Eqs (20) and (30). In the area with $\alpha > \alpha_{\max}$, the sky seems to be black. Any radiation observed in this region must originate at close vicinity of the black hole. The dependency of the apparent angular size of the black hole is different above and under the circular photon orbit. Above the photon orbit the cosmological constant causes downsizing of the black region on the sky. The biggest black region exists in pure Schwarzschild case. Situation is opposite under the photon orbit. For observers under the photon orbit cosmological constant causes upsizing of the black region on the observer sky. In the limit case, for observer on the circular photon orbit, the apparent angular size of the black hole is independent on the cosmological constant, and it is invariably π, always one half of the observer sky. This interesting behaviour is shown in Fig. 10. Of course, the cosmological constant has the influence onto the frequency shift too, see Eqs (21) and (31).

9 SOFTWARE IMPLEMENTATION

The code BHC is developed in C language, compiled under the gcc and mpicc compilers on GNU/Linux operating system. Libraries Numerical Recipes (Press et al., 2002) and MPI were used. The simulation runs on SGI ALTIX 350 with eight Itanium II CPUs and IBM Blade Server with six Xeon CPUs. Only the first three images are generated by the simulation. Intensity of higher order images rapidly decrease and its positions merge with the second Einstein ring. However, the intensity ratio between images with different orders is nonrealistic. Computer displays have no required bright resolution. For modelling of frequency shift we used software routine from LightSpeed! (Daniel, 2005) special relativity simulator.

Simulation for free-falling observer requires a great deal of computational time. Therefore, parallelization is essential. For parallelization BHC was selected library Message Passing Interface (MPI), commonly used on most multiprocessor platforms and supported by most manufacturers like HP, IBM, SUN, etc. The main advantage of MPI is great scalability and great portability. The MPI library contains functions for sending and receiving messages in blocked and non blocked modes between processes, namely `MPI_Send`, `MPI_Receive` and `MPI_Wait`. For scattering and gathering messages from or to multiple processes are available functions `MPI_Scatter` and `MPI_Gather`. For process synchronization is used Function `MPI_Barrier`. Those functions are used in parallelization described below. Let assume, that hardware platform contain k processors. Each process belongs to one processor is denoted by index k and identification `ID` $= (k-1)$. We have also Video

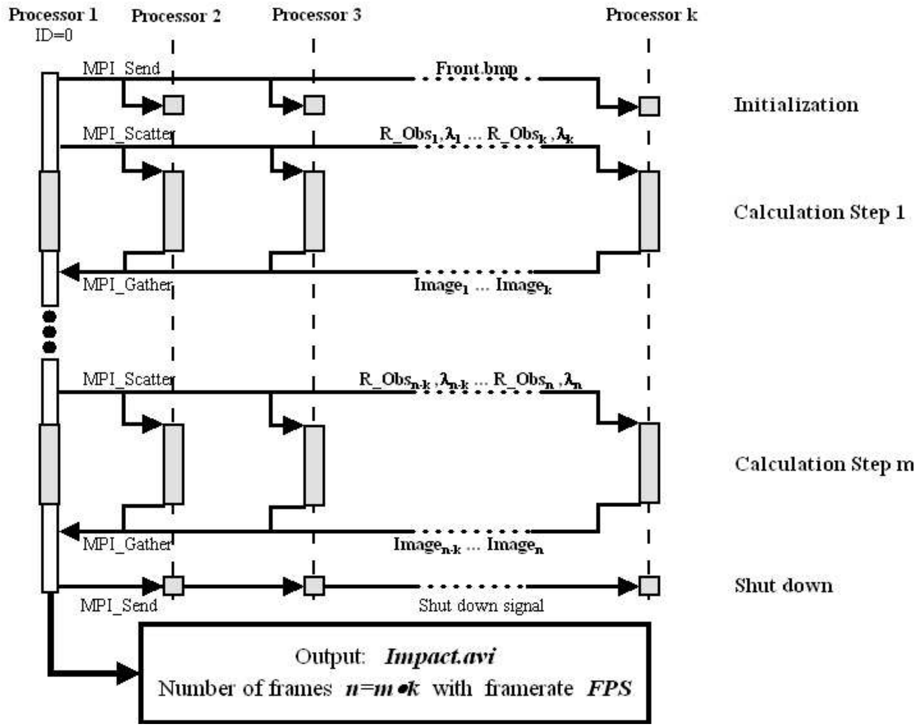

Figure 11. Parallelization of BHC code.

(AVI) frame rate given in Frame Rate per Second (FPS) and front undistorted image in BMP format. Dimension of front image can be up to 1024x1024 pixels. Parallelization of BHC routine is shown in Fig. 11 The algorithm consists of following steps:

- Front image is read and distributed via function `MPI_Send` to other $1, \ldots, k$ processes.
- Process with $\mathtt{ID} = 0$ determine Parameters `R_Obs` and `Lambda` for Calculation Step 1 for all processes.
- `R_Obs` and `Lambda` for each k are distributed by function `MPI_Scatter` to all processes and Images Calculations are initiated.
- Images with parameters `R_Obs` and `Lambda` are calculated with using BHC routine.
- Resulting images from all processes are collected by process with $\mathtt{ID} = 0$ using Function `MPI_Gather` and fed into compression codec.
- Simulation is finished by execution m steps. The final AVI file is stored on HDD. The shutdown signal is initiated and all processes are terminated.

The result is AVI file with number of frames $m \times k$ and frame rate FPS. Execution of BHC Simulation is initiated by command:

```
mpirun -np k impact R_Observer_Start FPS
```

where `k` is number of processors on HW Platform, `Impact` is name of code binary File, `R_Observer_Start` is starting radial coordinate of free-falling observer, `FPS` is frame rate in final AVI file.

10 CONCLUSIONS

In this work we present first studies of computer modelling and simulation of optical effects in the Schwarzschild–de Sitter spacetimes. Our results shows different influence of the cosmological constant on the geometry of the optical projection for observers located above and under the circular photon orbit. This influence vanishes for observers located just at the circular photon orbit. In future we plan to extend our method and the code in order to include the influence of the black hole rotation. In future we also assume extension our studies onto the influence of the cosmological constant onto quasi periodical oscillation and related optical phenomena in the vicinity of supermassive black holes in active galactic nuclei (Török, 2005b,a; Bursa, 2004). For these kinds of extensions it will be useful to solve parallelization BHC code on huge supercomputer systems, which contain units with different computational parameters and HW and OS platforms.

ACKNOWLEDGEMENTS

The present work was supported by the Czech grant MSM 4781305903. We thank Jiří "Dron" Sléžka for help with computer processing of the images.

REFERENCES

Bursa, M. (2004), Variability of accreting sources at very high time resulution, in Hledík and Stuchlík (2004), pp. 25–32.

Cunningham, C. T. (1975), Optical appearance of distant objects to observer near and inside a Schwarzschild black hole, *Phys. Rev. D*, **12**, pp. 323–328.

Daniel, R. G. (2005), Program LightSpeed!, URL `http://lightspeed.sourceforge.net/`.

Einstein, A. (1936), Lens-like action of a star by the deviation of light in the gravitational field, *Science*, **84**, p. 506.

Hledík, S. and Stuchlík, Z., editors (2004), *Proceedings of RAGtime 4/5: Workshops on black holes and neutron stars, Opava, 14–16/13–15 October 2002/2003*, Silesian University in Opava, Opava, ISBN 80-7248-242-4.

Katedra fyziky, Fakulta elektrotechnická, ČVUT Praha (2005), Aldebaran homepage, URL `http://www.aldebaran.cz/`.

Misner, C. W., Thorne, K. S. and Wheeler, J. A. (1973), *Gravitation*, Freeman, San Francisco.

Nemiroff, R. J. (1993), Visual Distortions Near a Black Hole and Neutron Star, *Amer. J. Phys.*, **61**, pp. 619–631, provided by the NASA Astrophysics Data System, `astro-ph/9312003`, URL `http://adsabs.harvard.edu/cgi-bin/nph-bib_query?bibcode=1993A%mJPh..61..619N&db_key=AST`.

Ohanian, H. C. (1987), The black hole as a gravitational "lens", *Amer. J. Phys.*, **55**(5), pp. 428–432.

Press, W. H., Flannery, B. P., Teukolsky, S. A. and Vetterling, W. T. (2002), *Numerical Recipes Multi-Language Code CD ROM with LINUX or UNIX Single-Screen License Revised Version*, Cambridge University Press, Cambridge, 2nd edition, ISBN 0-521-75036-9, source Code for the second edition versions of C, C++, Fortran 77, Fortran 90, and the first edition versions of Pascal, BASIC, Lisp and Modula 2 plus many extras, URL `http://www.nr.com/`.

Press, W. H., Teukolsky, S. A., Vetterling, W. T. and Flannery, B. P. (1997), *Numerical Recipes in C: The Art of Scientific Computing*, Cambridge University Press, Cambridge, 2nd edition, ISBN 0-521-43108-5, URL `http://www.nr.com/`.

Silesian University in Opava (2005–2009), Relativistic and particle physics and its astrophysical aplications, Czech research project MSN 4781305903, URL `http://www.physics.cz/research/`.

Stuchlík, Z. and Hledík, S. (1999), Some properties of the Schwarzschild–de Sitter and Schwarzschild–anti-de Sitter spacetimes, *Phys. Rev. D*, **60**(4), p. 044006 (15 pages), URL `http://ojps.aip.org/journal_cgi/dbt?KEY=PRVDAQ&Volume=60&Issu%e=4`.

Stuchlík, Z. and Plšková, K. (2004), Optical appearance of isotropically radiating sphere in the Schwarzschild–de Sitter spacetime, in Hledík and Stuchlík (2004), pp. 167–185.

Török, G. (2005a), A possible 3 : 2 orbital epicyclic resonance in QPO frequencies of Sgr A*, *Astronomy and Astrophysics*, **440**(1), pp. 1–4.

Török, G. (2005b), QPOs in microquasars and Sgr A*: measuring the black hole spin, *Astronom. Nachr.*, **326**(9), pp. 856–860, `astro-ph/0510669`.

Žára, J., Beneš, B., Sochor, J. and Felkel, P. (2004), *Moderní počítačová grafika*, Computer Press, Brno, 1. edition, ISBN 80-251-0454-0.

Proceedings of *RAGtime 6/7: Workshops on black holes and neutron stars, Opava, 16–18/18–20 September, 2004/2005*
S. Hledík and Z. Stuchlík, editors, Silesian University in Opava, Czech Republic, 2005, pp. 29–38

Observational effects of strong gravity

Kris Beckwith

Department of Physics, University of Durham, South Road, Durham DH1 3LE, UK
k.r.c.beckwith@durham.ac.uk

ABSTRACT
The current paradigm of high energy spectroscopy tells us that light emitted from a wide variety of objects has its origin close to the black hole event horizon. As such, these photons are subject to general relativistic effects such as light-bending, gravitational lensing and redshift, time-dilation, etc. These gravitational effects are well-understood from a theoretical standpoint and therefore provide a natural mechanism to test the properties of strong gravitational fields. To this end, we have developed a new (semi-analytic) strong gravity code, capable of describing the contribution of photons that perform multiple orbits of the hole. We apply this code to a simple Keplerian accretion disk in order to understand the role played by the angular emissivity, black hole spin and higher order images in forming the line profile.

1 INTRODUCTION

Black holes are the ultimate test of strong gravity, spacetime so warped that not even light can escape. By definition they have no emission (apart from Hawking radiation), yet their immense gravitational potential energy can be tapped by any infalling material. This can power a luminous accretion flow where the emission has its origin close to the black hole event horizon, as is seen in many objects including Active Galactic Nuclei, Galactic black hole binaries, Ultra-Luminous X-ray Sources and Gamma Ray Bursts. Photons emitted in this region are subject to general relativistic effects such as light-bending, gravitational lensing and redshift, as well as special relativistic effects as the emitting material will be moving rapidly (e.g., Fabian et al., 2000). These are well-understood from a theoretical standpoint, so accreting objects provide a natural laboratory to test the properties of strong gravitational fields.

Calculations of the relativistic corrections to photon properties have been ongoing for nearly three decades, starting with the classic work of Cunningham (1975) who calculated the distortions expected on the spectrum of a geometrically thin, optically thick, Keplerian accretion disc orbiting a Kerr black hole. Interest in these calculations dramatically increased with the realisation that the accretion disc could emit *line* as well as continuum radiation. Iron Kα fluorescence resulting from X-ray irradiation of the accretion disc can give a narrow feature, on which the relativistic distortions are much more easily measured than on the broad accretion disc continuum (Fabian et al., 1989). Since then, several

80-7248-334-X

groups have developed numerical codes that are capable of determining these effects both for standard discs (Dovčiak et al., 2004) and alternative emission geometries (Bursa et al., 2004).

Observationally, evidence for a relativistically smeared iron line first came from the ASCA observation of the active galactic nuclei (AGN) MCG-6-30-15 (Tanaka et al., 1995). Further observations showed evidence for the line profile being so broad as to require a maximally spinning black hole (Iwasawa et al., 1996). More recent data from XMM are interpreted as showing that the line is even wider than expected from an extreme Kerr disk, requiring direct extraction of the spin energy from the central black hole as well as the immense gravitational potential (Wilms et al., 2001).

Such results are incredibly exciting, but X-ray spectral fitting is not entirely unambiguous. There is a complex reflected continuum as well as the line (Nayakshin et al., 2000; Ballantyne et al., 2001). For an ionised disk (as inferred for MCG-6-30-15) the current models in general use (`pexriv` in the `XSPEC` spectral fitting package) are probably highly incomplete (Ross et al., 1999). Complex ionised absorption also affects AGN spectra (see, e.g., Kaspi et al., 2002) and the illuminating continuum itself can have complex curvature rather than being a simple power law.

However, in MCG-6-30-15 these issues have been examined in detail, and the results on the dramatic line width appear robust (Fabian and Vaughan, 2003; Reynolds et al., 2004). Thus there is a clear requirement that the extreme relativistic effects are well modelled. There are two models which are currently widely available to the observational community, within the `XSPEC` spectral fitting package, `diskline` (based on Fabian et al., 1989) and `laor` (Laor, 1991). The analytic `diskline` code models the line profile from an accretion disc around a Schwarzschild black hole (so of course cannot be used to describe the effects in a Kerr geometry). Also, it does not include the effects of lightbending (although Fabian et al. (1989) outline a scheme for incorporating this) and hence does not accurately calculate all the relativistic effects for $r < 20r_{\rm g}$ (where $r_{\rm g} = GM/c^2$). By contrast, the `laor` model numerically calculates the line profile including lightbending for an extreme Kerr black hole, but uses a rather small set of tabulated transfer functions which limit its resolution and accuracy (Beckwith and Done, 2004a).

In response to these limitations, we have developed a fast, semi-analytic code to calculate relativistic corrections to photons properties in the gravitational field of the Kerr black hole (Beckwith and Done, 2004a,b). Here, we briefly introduce the method implemented by the code to perform these calculations and apply this technique to a simple Keplerian accretion disk in order to understand the role played by the angular emissivity, black hole spin and higher order images in forming the line profile.

2 CALCULATING RELATIVISTIC LINE PROFILES

Line emission from a patch of disc with rest energy $E_{\rm int}$ subtends a solid angle $\mathrm{d}\Xi = r_{\rm o}^{-2}\,\mathrm{d}\alpha\mathrm{d}\beta$ on the observers sky at an energy $E_{\rm o}$. This observer then measures the amount of flux at the energy $E_{\rm o}$ to be:

$$F_{\rm o}(E_{\rm o}) = r_{\rm o}^{-2} \iint g^4 \epsilon(r_{\rm e}, \mu_{\rm e}) \delta(E_{\rm o} - gE_{\rm int})\,\mathrm{d}\alpha\mathrm{d}\beta\,, \tag{1}$$

where $g = E_o/E_{int}$ is the redshift factor and $d\alpha d\beta$ is the solid angle subtended by each small patch of the disc in the observers frame of reference. The total amount of flux at an energy E_o is then found by summing all $d\alpha d\beta$ that fall within some dE of $E_o$and the overall line profile is then generated by scanning over all possible E_o.

An additional complication to this calculation is due to the dependence of the observed radiation pattern on the emissivity law $\epsilon(x_i)$ $(i = 1, \ldots, n)$. Here, we choose the emissivity law to have a two parameter dependence, (i) the radial coordinate from which the photon is emitted, r_e and (ii) the initial direction of the photon with respect to the z-axis of the local disc frame, μ_e (see Fig. 1). We assume that the dependence of the emissivity law is separable, that is we can write $\epsilon(r_e, \mu_e) = \mathcal{E}(r_e) f(\mu_e)$. We choose $\mathcal{E}(r_e) \propto r_e^{-q}$ and take

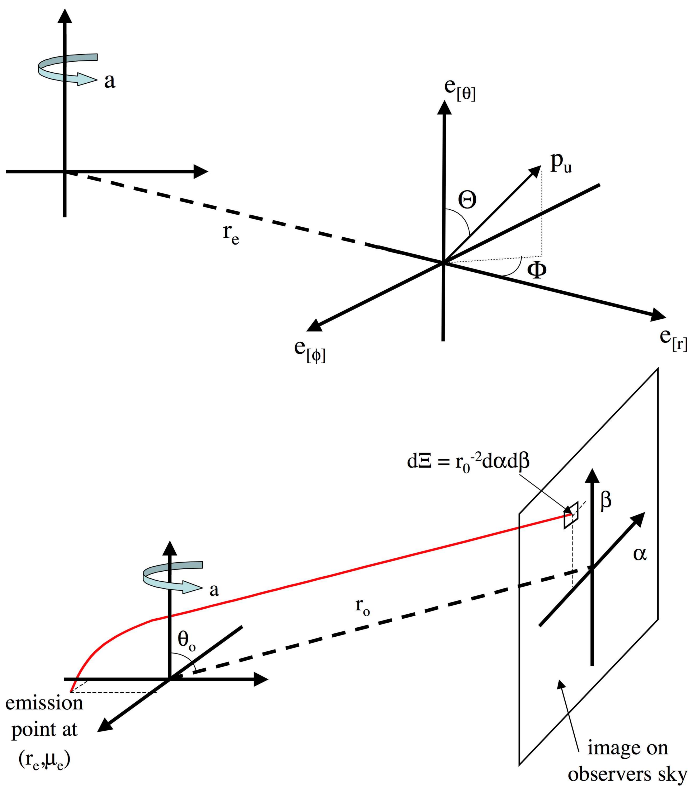

Figure 1. *Top panel:* The coordinate system used for the disc. The emission is defined in the rest frame of the disc material. The polar and azimuthal emission angles Θ, Φ are obtained by taking the dot-products of the photon four-momentum with the basis vectors of this frame, where $\mu_e = \cos\Theta$. This disc frame can be connected to the frame which co-rotates with the black hole spacetime via a simple boost which depends on the velocity. *Bottom panel:* Diagram showing the link between the observers frame of reference and the global coordinate system defined by the black hole. Photons that are emitted from the disc at some distance r_e from the hole are seen at coordinates α, β on the image of the disc at the observer.

$q = 3$, consistent with gravitational energy release within the disc (Życki et al., 1999). The choice of the angular dependence is far more complex however, as it depends on the (poorly understood) vertical structure of the accretion disc, in particular the ionization state of the material and so the choice of this dependence is not unique.

3 THE ROLE OF ANGULAR EMISSIVITY & BLACK HOLE SPIN

Different angular emissivity laws can have striking effects on the form of the relativistic line profile, which we illustrate in Fig. 2 for a maximal Kerr black hole ($a = 0.998$) viewed at an inclination $\theta_o = 30°$. The line profiles here all implement the standard radial emissivity law of r_e^{-3} and we show the line profiles generated by three different angular emissivities, (i) $f(\mu_e) = 1$ (solid lines), corresponding to an optically thick disk; (ii) $f(\mu_e) \propto (1 + 2.06\mu_e)$ (long dashed lines) corresponding to an optically thick, limb-darkened disk (Laor, 1991); (iii) $f(\mu_e) \propto \mu_e^{-1}$ (short dashed lines) corresponding to an optically thin, limb-brightened disk (the limiting case of ionized material). In the left-hand panel of the figure, the disc extends from the marginally stable orbit, $r_{ms} = 1.235r_g$ to $r_{out} = 20r_g$. There is a $\sim 35\%$ difference in the height of the blue peak depending of the form of the angular emissivity used.

However, such a limited range of radii is probably not very realistic. The disc should extend out to much greater distances from the black hole, where the relativistic effects (including lightbending) are less extreme. However, realistic emissivities strongly weight the contribution from the innermost regions, so the effective dilution of the relativistic effects by including the outer disc is not overwhelming. The centre panel of Fig. 2 shows the line profiles generated using the same angular emissivity laws for a disc extending from 1.235–$400r_g$, again with $\theta_o = 30°$. There are still significant differences in the line profiles, with a $\sim 25\%$ difference in the height of the blue peak while the red wing slope changes from $F_o(E_o) \propto E_o^{3.5}$ (limb darkened) to $\propto E_o^{2.5}$ (limb brightened).

Despite the expectation of an extended disc, some recent observational studies (e.g., Reynolds et al., 2004) have tentatively suggested that the disc is very small, from ~ 1.235–$6r_g$. This enhances the importance of lightbending. The right-hand panel of Fig. 2 shows the line profiles for a disc extending from 1.235–$6r_g$. The blue peak height differences are $\sim 40\%$, and the red wing slopes are different. For comparison we also show a limb darkened profile obtained from a very different *radial* emissivity of $r_e^{-4.5}$ (dotted line). This is very similar to the extreme limb brightened profile obtained from the r_e^{-3} radial weighting. We caution that uncertainties in the angular distribution of the line emissivity can change the expected line profile due to lightbending effects even at low/moderate inclinations, and that this can affect the derived radial emissivity.

Currently, the only available models in `XSPEC` have either zero or maximal spin. A zeroth order approximation to spacetimes with different spins is to use the maximal Kerr results but with a disc with inner radius given by the minimum stable orbit for the required value of a (e.g., Laor, 1991). We test this for the most extreme case of $a = 0$ modelled by a maximal Kerr spacetime with $r_{min} = 6r_g$. Figure 3 (left-hand panel) compares this with a true Schwarzschild calculation for a disc extending from 6–$400r_g$ with $\theta_o = 30°$ for a range of angular emissivities. The differences between the spacetimes (for a given angular

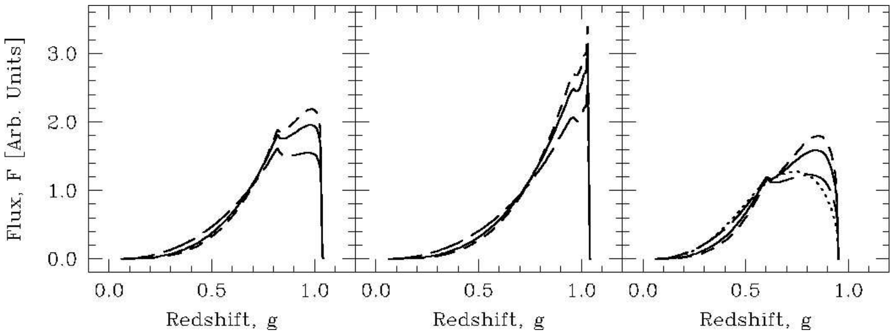

Figure 2. Comparison of the relativistic line profiles generated for a maximal Kerr black hole ($a = 0.998$) viewed at an inclination $\theta_o = 30°$ with the inner edge of the disc located at $r_{ms} = 1.235 r_g$. The line profiles here all implement the standard radial emissivity law of r_e^{-3} and we show the line profiles generated by three different angular emissivities, (i) $f(\mu_e) = 1$ (solid lines); (ii) $f(\mu_e) \propto (1 + 2.06\mu_e)$ (long dashed lines); (iii) $f(\mu_e) \propto \mu_e^{-1}$ (short dashed lines). In the left-hand panel, the outer edge of the disc is located at $20r_g$ and there is a $\sim 35\%$ difference in the height of the blue peak. In the centre panel, the outer edge of the disc is located at $400r_g$, which reduces the difference in the height of the blue peak to $\sim 25\%$. Finally, in the right-hand panel, the outer edge of the disc is located at $6r_g$, (the formal best fit to the MCG-6-30-15 data set), resulting in a difference in the height of the blue beak of $\sim 40\%$. For comparison we also show a limb darkened profile obtained from a very different *radial* emissivity of $r_e^{-4.5}$ (dotted line), which is very similar in characteristic to the r_e^{-3} optically thin, limb-brightened case (short dashed line).

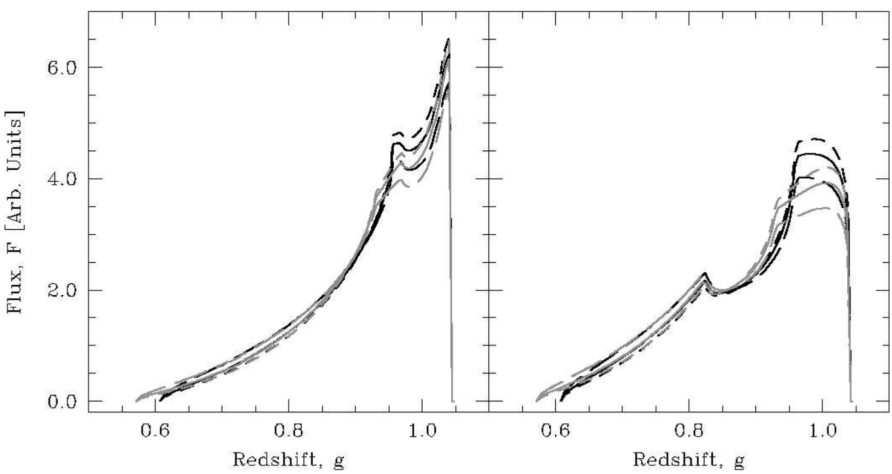

Figure 3. As in Fig. 2 for maximal Kerr ($a = 0.998$, black lines) and Schwarzschild ($a = 0$, grey lines) black holes. Here, the disc extends from the minimum stable orbit for the Schwarzschild black hole, $r_{ms} = 6r_g$ to $400r_g$ (left-hand panel) and $20r_g$ (right-hand panel). For the extended disc, the differences between the line profiles produced for the same sized disc in different assumed spacetimes is of order $\sim 5\%$ for a given angular emissivity. Reducing the radial extent of the disc enhances these differences to $\sim 15\%$ (left-hand panel).

emissivity) are at most $\sim 5\%$. This is roughly on the same order as the effect of changing the angular emissivity, which is much reduced here compared to Fig. 2 due to the larger $r_{\rm min}$. Assumptions about both spin and angular emissivity become somewhat more important for smaller outer disc radii. Figure 3 (right-hand panel) shows this for a disc between 6–20$r_{\rm g}$.

4 THE CONTRIBUTION OF HIGHER ORDER IMAGES

The contribution of higher order images to the observed flux is dependent both on the location of the observer and the angular momentum of the hole itself, together with the assumed geometry and emissivity of the accretion flow. For an optically thick accretion disc then any photons which re-intersect the disc after emission will be either absorbed (and then re-emitted) or reflected by the material. Figure 4 shows the contributions of both the direct ($N = 0$) and higher order ($N = 1, 2$) images of a geometrically thin disc extending

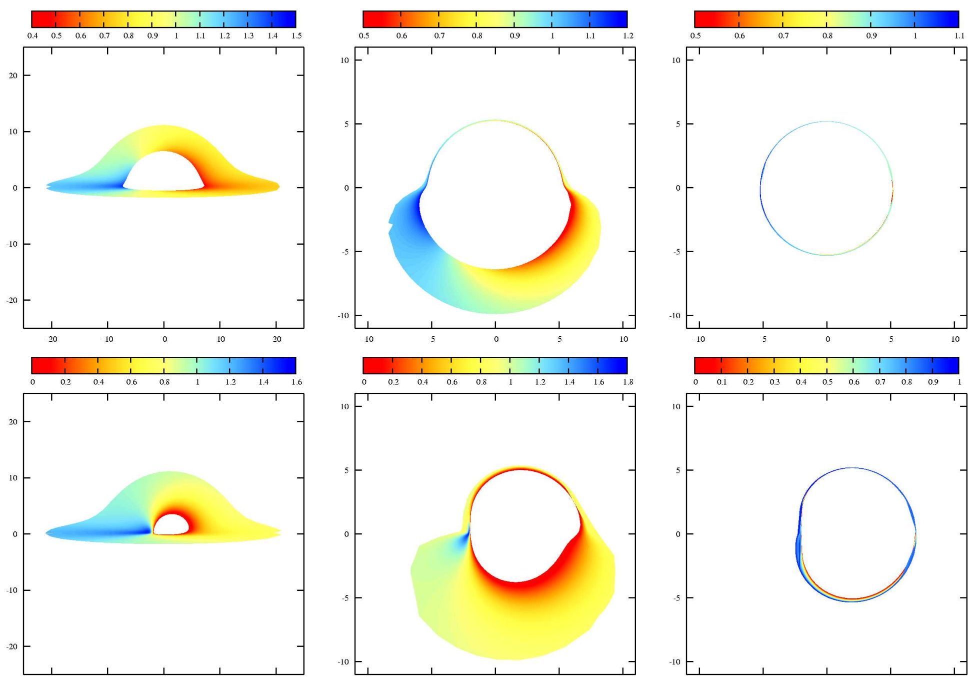

Figure 4. The contribution of orbiting photons (higher order images) to a distant observers image of a geometrically thin, optically thick, Keplerian accretion disc around Schwarzschild (top row) and extreme Kerr (bottom row) black holes. In both cases the observer is located at radial infinity with $\theta_{\rm o} = 85°$, the disc extends from the marginally stable orbit (6$r_{\rm g}$ for Schwarzschild, 1$r_{\rm g}$ for extreme Kerr) to 20$r_{\rm g}$ and the images are coloured by the associated value of the redshift parameter, $g = E_{\rm o}/E_{\rm e}$. From left to right, the panels show the contributions from (i) the direct ($N = 0$) image, (ii) the first order ($N = 1$) image and (iii) the second order ($N = 2$) image.

from r_{ms} to $20r_g$, viewed at $\theta_o = 85°$ for both Schwarzschild and maximal Kerr black holes. The principle effect of black hole spin for the accretion disk dynamics is to move the location of the marginally-stable orbit, r_{ms} and hence the location of the inner edge of the accretion disc. In the case of the Schwarzschild hole, the inner edge of the accretion disc is located at $6r_g$, above the radius of the unstable photon orbits ($3r_g$) so higher order image photons which cross the equatorial plane below $6r_g$ are not absorbed by the disc and may be able to freely propagate to the observer. This contrasts with the extreme Kerr hole behaviour, where the accretion disc extends down to $1r_g$, intersecting the allowed radial range of the unstable photon orbits ($1r_g \leq r_c \leq 4r_g$) and hence a large fraction of these orbiting photons return to the disc in the case of a rotating black hole.

To understand how the astrophysical properties of the accretion flow couple to the gravitational field of the black hole, we generate relativistically smeared line profiles, applying the same emissivity laws that were described in the preceding section (Fig. 5). The top and bottom rows of the figure again correspond to the Schwarzschild and extreme Kerr cases, respectively with the image order running from $N = 0 \to 2$, left to right.

Turning our attention to the Schwarzschild case, we see that, for the direct image, limb darkening boosts the effects of gravitational lensing, enhancing the flux from the far side

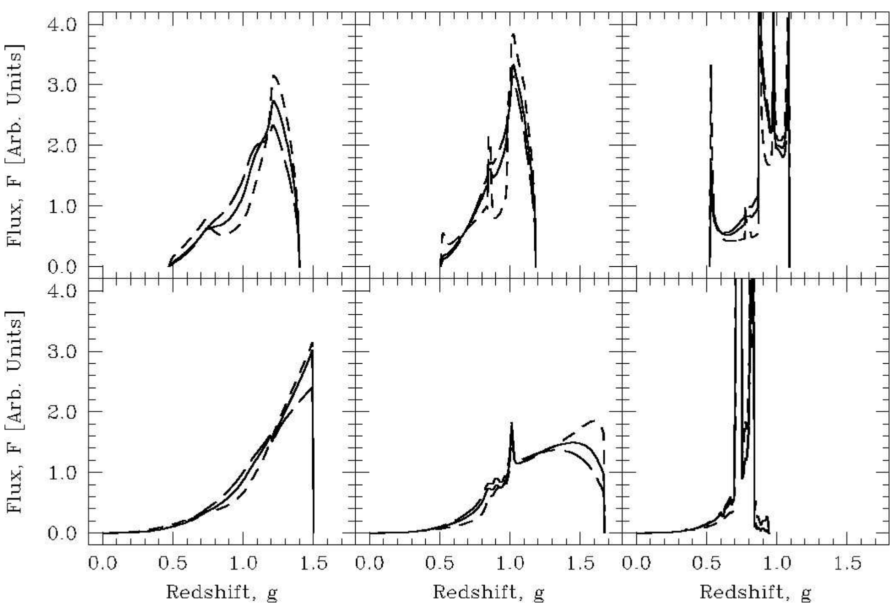

Figure 5. Relativistic line profiles generated from the images shown in Fig. 4 using the emissivity laws described in Fig. 2. As in Fig. 4, lines generated by the Schwarzschild black hole are shown on the top row, extreme Kerr on the bottom and from left to right the panels show the contributions from the $N = 0, \ldots, 2$ images. Line profiles generated by the zeroth order photons have the standard skewed, double peaked structure. Those generated by the first order photons have a similar structure, whilst those from the second order photons are far more complex.

of the hole. This is because these photons are strongly bent, i.e., are emitted from a lower inclination angle than that at which they are observed, so a limb darkening law means that the flux here is higher (Beckwith and Done, 2004a). The Dopper shifts are rather small for this material, so this lensing enhances the flux in the middle of the line. Since the line profiles are normalized to unity, this means that the blue wing is less dominant.

The first order spectra retains the characteristic double peaked and skewed shape, and again the principle effect of the different angular emissivities is to alter the balance between the blue wing and lensed middle of the line. However, there is some new behaviour for the limb brightened emissivity. This has the largest change in emissivity with angle, and this combined with the exquisite sensitivity of lensed paths means that this picks out only a small area on the disc, leading to a discrete feature in the spectrum. The profile also shows enhancement of the extreme red wing of the line, as the photons which orbit generally are emitted from the very innermost radii of the disc.

The discrete features are completely dominant for all emissivities at second order. These are images of the top of the disc where the photons have orbited the black hole, so the paths are even more sensitive to small changes than first order. Thus the profiles are significantly more complex in structure, being dominated by lensing. There are blue and red features at the extreme ends of the line profile which are picking out the maximum projected velocity of the innermost radii of the disc. These have the standard blue peak enhancement. However, the two strong features redward of this are a pair of lensed features, from the near and far side of the disc.

For the direct image of the extreme Kerr hole, the line exhibits the characteristic triangular shape previously reported by, e.g., Laor (1991), with the variation in angular emissivity acting to alter the balance between the different regions of the line on a $\sim 5\%$ level. The line associated with the first order image exhibits a marked difference in comparison to those associated with the Schwarzschild black hole, being both broader and resembling a skewed Gaussian combined with a narrow line (due to caustic formation) at $g \approx 1.0$. Here the principle effect of changes in the angular emissivity is to alter the height of the blue wing, relative to the rest of the line. Again, the line profile associated with the second order image are completely dominated by discrete features, as in the Schwarzschild case.

5 CONCLUSION

Recent observational studies have provided evidence for highly broadened fluorescent iron Kα lines. While there are a variety of line profiles seen (e.g., Lubiński and Zdziarski, 2001), there are some objects where the line implies that there is material down to the last stable orbit in a maximally spinning Kerr spacetime (most notably MCG-6-30-15: see Wilms et al., 2001). However, the strong gravity codes generally used to model these effects are now over a decade old. Increased computer power means that it is now possible to improve on these models. We describe our new code to calculate these effects, which uses uses fully adaptive gridding to map the image of the disc at the observer using the analytic solutions of the light travel paths. This is a very general approach, so the code can easily be modified to incorporate different emission geometries.

Relativistically smeared line profiles are generated by convolving the observed area of the disc (at a given energy) with an emissivity law describing energy release in the rest frame of the emitter. This emissivity law is not only dependent on the location of the emitter within the disc, but also the initial direction that a photon is emitted in. Lightbending means that a range of initial photon directions contribute to the observed radiation spectrum at a given inclination. As such, the emissivity law convolves together the effects of strong gravity and the astrophysics of the accretion flow, which in the most extreme case can play a $\sim 40\%$ role in shaping the internal structure of the line profile. By contrast, black hole spin plays at most a $\sim 15\%$ role in shaping the internal structure (keeping the inner edge of the disc fixed).

Our code is capable of calculating both the imaging and spectral contributions of higher order images to the standard picture of relativistically smeared line profiles. As has long been known, the major amplification effects of gravitational lensing are for the first order paths from the far side of the underneath of the disc viewed at high inclination, i.e., photons initially emitted downwards on the far side of the black hole, which are bent by gravity up above the disc plane. For a disc viewed edge-on, the spectral signature of these first order photons retains the characteristic skewed, double-peaked shape in the Schwarzschild case, whilst in the extreme Kerr case, the line resembles a skewed Gaussian. By contrast, the spectra of the second order image is dominated by discrete spectral features in both cases.

REFERENCES

Ballantyne, D. R., Ross, R. R. and Fabian, A. C. (2001), *Monthly Notices Roy. Astronom. Soc.*, **327**, p. 10.

Beckwith, K. and Done, C. (2004a), *Monthly Notices Roy. Astronom. Soc.*, **352**, p. 353.

Beckwith, K. and Done, C. (2004b), *Monthly Notices Roy. Astronom. Soc.*, submitted.

Bursa, M., Abramowicz, M. A., Karas, V. and Kluźniak, W. (2004), The Upper Kilohertz Quasi-periodic Oscillation: A Gravitationally Lensed Vertical Oscillation, *Astrophys. J. Lett.*, **617**, pp. L45–L48, `astro-ph/0406586`.

Cunningham, C. T. (1975), *Astrophys. J.*, **202**, p. 788.

Dovčiak, M., Karas, V. and Yaqoob, T. (2004), *Astrophys. J. Suppl.*, **153**, p. 205.

Fabian, A. C., Iwasawa, K., Reynolds, C. S. and Young, A. J. (2000), *Publ. Astronom. Soc. Pacific*, **112**, p. 1145.

Fabian, A. C., Rees, M. J., Stella, L. and White, N. E. (1989), *Monthly Notices Roy. Astronom. Soc.*, **238**, p. 729.

Fabian, A. C. and Vaughan, S. (2003), *Monthly Notices Roy. Astronom. Soc.*, **340**, p. L28.

Iwasawa, K., Fabian, A. C., Reynolds, C. S., Nandra, K., Otani, C., Inoue, H., Hayashida, K., Brandt, W. N., Dotani, T., Kunieda, H., Matsuoka, M. and Tanaka, Y. (1996), *Monthly Notices Roy. Astronom. Soc.*, **282**, p. 1038.

Kaspi, S., Brandt, W. N., George, I. M., Netzer, H., Crenshaw, D. M., Gabel, J. R., Hamann, F. W., Kaiser, M. E., Koratkar, A., Kraemer, S. B., Kriss, G. A., Mathur, S., Mushotzky, R. F., Nandra, K., Peterson, B. M., Shields, J. C., Turner, T. J. and Zheng, W. (2002), The Ionized Gas and Nuclear Environment in NGC 3783. I. Time-averaged 900 Kilosecond Chandra Grating Spectroscopy, *Astrophys. J.*, **574**(2), pp. 643–662, `astro-ph/0203263`.

Laor, A. (1991), *Astrophys. J.*, **376**, p. 90.

Lubiński, P. and Zdziarski, A. A. (2001), *Monthly Notices Roy. Astronom. Soc.*, **323**, p. 37.

Nayakshin, S., Kazanas, D. and Kallman, T. R. (2000), *Astrophys. J.*, **537**, p. 833.

Reynolds, C. S. and Begelman, M. C. (1997), *Astrophys. J.*, **488**, p. 109.

Reynolds, C. S., Wilms, J., Begelman, M. C., Staubert, R. and Kendziorra, E. (2004), On the deep minimum state in the Seyfert galaxy MCG-6-30-15, *Monthly Notices Roy. Astronom. Soc.*, **349**(4), pp. 1153–1166, `astro-ph/0401305`.

Ross, R. R., Fabian, A. C. and Young, A. J. (1999), *Monthly Notices Roy. Astronom. Soc.*, **306**, p. 461.

Tanaka, Y., Nandra, K., Fabian, A. C., Inoue, H., Otani, C., Dotani, T., Hayashida, K., Iwasawa, K., Kii, T., Kunieda, H., Makino, F. and Matsuoka, M. (1995), *Nature*, **375**, p. 659.

Wilms, J., Reynolds, C. S., Begelman, M. C., Reeves, J., Molendi, S., Staubert, R. and Kendziorra, E. (2001), *Monthly Notices Roy. Astronom. Soc.*, **328**, p. L27.

Życki, P. T., Done, C. and Smith, D. A. (1999), *Monthly Notices Roy. Astronom. Soc.*, **305**, p. 231.

Proceedings of *RAGtime 6/7: Workshops on black holes and neutron stars, Opava, 16–18/18–20 September, 2004/2005*
S. Hledík and Z. Stuchlík, editors, Silesian University in Opava, Czech Republic, 2005, pp. 39–45

High-frequency QPOs in GRO J1655−40: Constraints on resonance models by spectral fits

Michal Bursa

Astronomical Institute, Czech Academy of Sciences, Boční II 1401, CZ-141 31 Praha 4, Czech Republic
bursa@astro.cas.cz

ABSTRACT
A class of resonance models has been proposed to explain the high-frequency quasi-periodic oscillations observed from Galactic black-hole sources. The spin predictions given by these models are compared with the recent angular momentum estimate for GRO J1655−40. It is found that none of the present resonance models is consistent with the value of the spin obtained by spectral fits of the X-ray continuum. Instead, observational constraints seem to favour another, so far not considered resonance between the vertical epicyclic frequency and the periastron precession frequency.

1 INTRODUCTION

The spectral and timing X-ray observations of Galactic black-hole binary systems provide us with information about physical processes that occur in accretion disks near black hole event horizons. One of the main goals of these studies is to obtain constraints on black hole masses and spins using predictions of general relativity in the regime of strong gravity. RXTE observations of some microquasars have revealed an interesting kind of quasi-periodic modulation of the incoming X-ray flux at frequencies ranging from 100 to 450 Hz. These high-frequency quasi-periodic oscillations (HFQPOs) are the fastest QPOs that have been confirmed in black-hole systems. Their properties are in some aspects similar to the kHz QPOs observed in neutron stars: they appear in the range of frequencies that Keplerian orbits very close to compact stars would have, they come in pairs. Other properties differ from kHz QPOs: they always stay at fixed positions, the ratio of the two frequencies is sharply $\nu_2 : \nu_1 = 3 : 2$, the signal modulation is much weaker. See a comprehensive review by McClintock and Remillard (2004) for details.

80-7248-334-X

2 HIGH-FREQUENCY QPO'S AS A NON-LINEAR RESONANCE

The rational ratio of the frequencies originally lead Kluźniak and Abramowicz (2000) to an idea of a resonance that may be responsible for generating HFQPOs. In the resonance model (see a recent review in Abramowicz and Kluźniak, 2004, and references therein) a non-linear coupling in the motion of accreting fluid is made responsible for the twin QPOs. At particular radii in the disk, commensurabilities between certain combinations of epicyclic and orbital frequencies can lead to an excitement of a resonance between the particular types of motions. In this way, general relativity itself picks up certain frequencies at preferred radii in the disk regardless of properties of the source.

Unlike Newtonian $1/r$ gravity, general relativity predicts independent frequencies for different types of periodic motion in the strong gravitational field of a rotating compact object (Nowak and Lehr, 1998; Merloni et al., 1999). The condition $\nu_{\mathrm{K}} > \nu_z > \nu_r$ is always satisfied for the Keplerian orbital, vertical epicyclic and radial epicyclic frequencies, respectively. The radial epicyclic frequency ν_r reaches a maximum at a particular radius and goes to zero at the marginally stable circular orbit (Kato, 2001). This allows for two of the three frequencies (or a combination) to be in a ratio of small natural numbers somewhere in the disk.

A whole class of relativistic resonance models has been be constructed with different combinations of frequencies (see, e.g., Abramowicz and Kluźniak, 2004; Abramowicz et al., 2004b for a detailed description of possible models). The most natural is the parametric resonance between the vertical and radial epicyclic frequency: $\nu_2 = \nu_z$, $\nu_1 = \nu_r$, $2\nu_z = 3\nu_r$ (3 : 2 resonance). Another possibility is a forced resonance between the epicyclic modes, which gives two solutions: $\nu_2 = \nu_z$, $\nu_1 = \nu_z - \nu_r$, $\nu_z = 3\nu_r$ (3 : 1 resonance) and $\nu_2 = \nu_z + \nu_r$, $\nu_1 = \nu_z$, $\nu_z = 2\nu_r$ (2 : 1 resonance). Finally, models with coupling between the orbital Keplerian motion and the radial epicyclic motion can be considered: $\nu_2 = \nu_{\mathrm{K}}$, $\nu_1 = \nu_r$, $2\nu_{\mathrm{K}} = 3\nu_r$ (Keplerian 3 : 2 resonance); $\nu_2 = \nu_{\mathrm{K}}$, $\nu_1 = \nu_{\mathrm{K}} - \nu_r$, $\nu_{\mathrm{K}} = 3\nu_r$ (Keplerian 3 : 1 resonance) and $\nu_2 = \nu_{\mathrm{K}} + \nu_r$, $\nu_1 = \nu_{\mathrm{K}}$, $\nu_{\mathrm{K}} = 2\nu_r$ (Keplerian 2 : 1 resonance).

3 SPIN ESTIMATES

For each resonance model Török et al. (2005) have made fits to the observational data for the three microquasars with known masses in order to constrain values of their spins. They compare the observed upper QPO frequency of each source with frequencies predicted by individual resonance models. Based on the knowledge of mass they calculate the range for the black hole angular momentum required by each model to work. Their results are summarized in Table 1.

The observational data already excludes the Keplerian 3 : 2 resonance in the case of two sources. If it is assumed that the HFQPOs are produced by the same type of resonance in all black-hole sources, then this model can be ruled out as incompatible with observations. Other models discussed in their paper are so far consistent with measured masses, but as they note, future observations or developments in accretion theory can narrow down the choice. In this context, direct measurements of black-hole spins may especially be useful to limit the selection.

Table 1. Summary of angular momentum estimates as they are predicted by different resonance models for the three microquasars with known masses. The uncertainty in the spin estimates is due to uncertainties in the black-hole mass measurements. [Adopted from (Török, 2005).]

Resonance	XTE 1550−564	GRO J1655−40	GRS 1915+105
Standard:			
3 : 2	+0.89 – +0.99	+0.96 – +0.99	+0.69 – +0.99
2 : 1	+0.12 – +0.42	+0.31 – +0.42	−0.41 – +0.44
3 : 1	+0.32 – +0.59	+0.50 – +0.59	−0.15 – +0.61
Keplerian:			
3 : 2	–	–	+0.79 – +1.0
2 : 1	+0.12 – +0.43	+0.31 – +0.42	−0.41 – +0.44
3 : 1	+0.29 – +0.54	+0.45 – +0.53	−0.13 – +0.55

4 THE SPIN OF GRO J1655−40 AND IMPLICATIONS FOR RESONANCE MODELS

Shafee et al. (2005) have recently published an analysis of X-ray spectral data from ASCA and RXTE of the two black hole candidates, GRO J1655−40 and 4U 1543−47, where they estimate the angular momenta of these sources. Here, GRO J1655−40 (hereafter J1655) is of a high interest, because it also shows the twin HFQPOs.

Their analysis is based on fitting the X-ray thermal continuum spectra using a fully relativistic model of a thin accretion disk around a Kerr black hole (Li et al., 2005). The model includes all relativistic effects as well as self-irradiation of the disk, limb-darkening effects and the spectral hardening factor. It, however, strongly relies on the assumed value of the spectral hardening factor, which cannot be obtained from the data and must be estimated independently. The state-of-the-art non-LTE disk atmosphere model of Davis et al. (2005) is used to estimate the factor.

The spin of J1655, according to Shafee et al. (2005), is $a \simeq 0.65$–0.75. It can be compared with the predictions of the resonance theory given by Török et al. (2005) and listed in Table 1. We find that it is not compatible with any of the "basic" six models (3 : 2, 2 : 1, 3 : 1; see Fig. 1), as well as with models with "higher" resonances 5 : 1, 5 : 2, 5 : 3. The models predict spins either too high (> 0.96) or too low (< 0.6). The one with the closest approach is the 3 : 1 forced resonance, which predicts spin in the range 0.50–0.59.

5 THE VERTICAL-PRECESSION RESONANCE

A new model can be assumed to satisfy the observational evidence, which has not been considered so far: the resonance between the vertical epicyclic frequency and the periastron precession frequency. These two frequencies are in the 3 : 2 ratio typically very near the marginally stable orbit. For a black hole with spin $a = 0.75$ it occurs around $r = 4.3\,r_{\mathrm{g}}$, while marginally stable orbit is at $r_{\mathrm{ms}} = 3.16\,r_{\mathrm{g}}$. The occurrence of HFQPOs may then

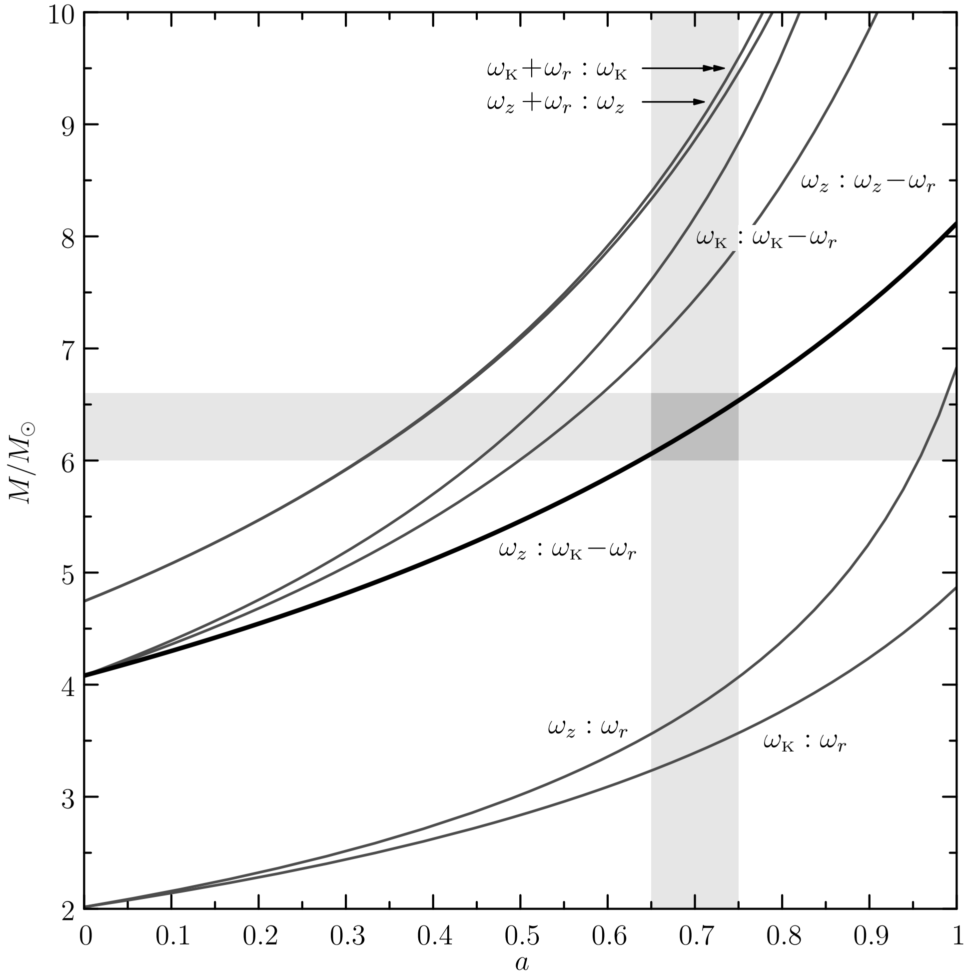

Figure 1. Possible combinations of mass and angular momentum predicted by individual resonance models for the HFQPO frequencies observed from GRO J1655−40. Thin lines represent predictions of the standard 3 : 2, 3 : 1 and 2 : 1 resonances. The thick line shows the prediction of the vertical-precession resonance. Shaded regions indicate the likely ranges for the mass (inferred from optical measurements of radial curves) and the dimensionless angular momentum (inferred from the X-ray spectral data fitting) of J1655.

correspond to a formation of an slightly eccentric fluid slender torus at the end of the accretion flow. This torus would oscillate in the vertical direction either rigidly or in a "snake-like" mode (Abramowicz et al., 2005). It has been shown (Bursa et al., 2004; Bursa, 2005) that strong gravity effects can cause sufficient modulation of the radiation produced in a vertically oscillating torus. It is, however, not clear what physical situation would couple the vertical and the precession modes to the 3 : 2 ratio.

Figure 1 shows the predictions of the standard resonance models and of the vertical-precession model in the mass-spin plane. It shows possible combinations of mass and spin of J1655 as they are predicted by individual resonance models. It is clear that the only model, which matches the observational constraints, is the vertical-precession resonance.

6 APPLICATIONS TO MICROQUASARS AND SGR A*

Based on the measured HFQPO frequencies and mass of J1655, the vertical-precession model predicts the spin of the black hole to be $a = 0.64$–0.76, which is an excellent match with the estimated value 0.65–0.75. For the other two microquasars with known masses, no spin estimates are yet available, mainly because large uncertainties in their distances. The model predicts spins to be in the range 0.41–0.77 for XTE 1550−564 and in the range −0.09 to 0.78 for GRS 1915+105. The predicted spin values are summarized in Table 2.

In the case of Sgr A* – the super massive black hole in the centre of our Galaxy – three QPO periodicities 700 s, 1150 s and 2250 s have been reported by Aschenbach et al. (2004) in the two brightest X-ray flares from the Galactic centre. Although the quality of the used light curves is very low and the results have not been so far independently confirmed, the ratio of the reported periodicities is 3.21 : 1.96 : 1, i.e., the "Keplerian" frequencies found in Sgr A* are close to form a commensurable sequence 3 : 2 : 1, similar to 3 : 2 HFQPOs in microquasars (Abramowicz et al., 2004a,b; Aschenbach, 2004). Assuming the mass of Sgr A* $3.6 \times 10^6\,M_\odot$,[1] Török et al. (2005) give its spin $a \simeq 0.8$–0.9, whereas 3 : 2 parametric resonance models (both standard and Keplerian) are not consistent with observed frequencies. The vertical-precession model does not match these observations as well.

[1] From the analysis of orbits of proximate stars within 10–1000 light hours of Sgr A*, the current best estimate of the central mass is $(3.7 \pm 0.2) \times 10^6\,(R_*/8\,\mathrm{kpc})^3\,M_\odot$ (Ghez et al., 2005), where the uncertainty in the Galactic centre distance adds an additional 19% error. This gives the mass of the black hole in Sgr A* most likely to be in the interval $(2.8$–$4.6) \times 10^6\,M_\odot$.

Table 2. Summary of angular momentum estimates as they are predicted by the vertical–precession model for the three microquasars with known masses. QPO frequencies observed from Sgr A* are not consistent with the model.

Source	Measured mass [$M_\odot$]	Measured spin	Predicted spin
XTE 1550−564	8.4 – 10.8	–	0.41 – 0.77
GRO 1655−40	6.0 – 6.6	0.65 – 0.75	0.64 – 0.76
GRS 1915+105	10 – 18	–	−0.09 – 0.78
Sgr A*	$(2.8 - 4.6) \times 10^6$	–	–

7 CONCLUSIONS

None of the resonance models listed in Abramowicz and Kluźniak (2004) and Török et al. (2005) predicts the spin of J1655 to be in the range given by Shafee et al. (2005) This could mean that none of these models is able to explain the origin of HFQPOs in black hole sources.

Although the spectral fitting analysis has been done very carefully, it has some weak points. The assumed value of the spectral hardening factor is one of them. Next, the analysis assumes that the disk terminates at the marginally stable orbit in the thermal dominant state and that it has zero torque at the inner edge. However, in face of these points the method is very reliable and gives good results. Improved disk atmosphere models may change the estimated value of spin, but not significantly. Relaxing the assumption of the zero torque and the disk terminal radius may, as argued by Shafee et al. (2005), only decrease the spin estimate.

Observational constraints seem to favour a newly proposed resonance model, where the upper and lower QPO frequencies correspond to the vertical epicyclic frequency and the periastron precession frequency, respectively. We have checked that the measured spin of J1655 is consistent with the prediction of the model. In the case of the other two microquasars with known masses, we have given the likely ranges of their spins. Unfortunately, current knowledge of their distances and large errors in mass measurements do not allow to accurately use the spectral fitting method to constrain the angular momenta of those black holes.

We have also noted that the vertical-precession model does not match with the QPO frequencies reported from Sgr A*. This may put some doubt about whether the QPOs from the Galactic centre have the same origin as the HFQPOs in microquasars.

ACKNOWLEDGEMENTS

I wish to thank to the organizers of the Opava RAGtime conference. I am also grateful to Marek Abramowicz and Vladimír Karas for reading the manuscript and for useful comments. This work was supported by the Czech GAAV grant IAA 300030510. The Astronomical Institute is operated under the project AV0Z10030501.

REFERENCES

Abramowicz, M. A., Blaes, O. M., Horák, J., Kluźniak, W. and Rebusco, P. (2005), Epicyclic oscillations of fluid bodies: Paper II. Strong gravity, submitted to Classical Quantum Gravity, `astro-ph/0511375`.

Abramowicz, M. A. and Kluźniak, W. (2004), Interpreting black hole QPOs, in P. Karet, F. K. Lamb and J. H. Swank, editors, *X-ray Timing 2003: Rossi and Beyond.*, volume 714, pp. 21–28, NY: American Institute of Physics, Melville, `astro-ph/0312396`.

Abramowicz, M. A., Kluźniak, W., McClintock, J. E. and Remillard, R. A. (2004a), The Importance of Discovering a 3 : 2 Twin-Peak Quasi-periodic Oscillation in an Ultraluminous X-Ray Source, or How to Solve the Puzzle of Intermediate-Mass Black Holes, *Astrophys. J. Lett.*, **609**, pp. L63–L65.

Abramowicz, M. A., Kluźniak, W., Stuchlík, Z. and Török, G. (2004b), Twin peak QPOs frequencies in microquasars and Sgr A*. The resonance and other orbital models, in S. Hledík and Z. Stuchlík, editors, *Proceedings of RAGtime 4/5: Workshops on black holes and neutron stars, Opava, 14–16/13–15 October 2002/2003*, pp. 1–23, Silesian University in Opava, Opava, ISBN 80-7248-242-4.

Aschenbach, B. (2004), Measuring mass and angular momentum of black holes with high-frequency quasi-periodic oscillations, *Astronomy and Astrophysics*, **425**, pp. 1075–1082, `astro-ph/0406545`.

Aschenbach, B., Grosso, N., Porquet, D. and Predehl, P. (2004), X-ray flares reveal mass and angular momentum of the Galactic Center black hole, *Astronomy and Astrophysics*, **417**, pp. 71–78.

Bursa, M. (2005), Global oscillations of a fluid torus as a modulation mechanism for black-hole high-frequency QPOs, *Astronom. Nachr.*, **326**, pp. 849–855, `astro-ph/0510460`.

Bursa, M., Abramowicz, M. A., Karas, V. and Kluźniak, W. (2004), The Upper Kilohertz Quasi-periodic Oscillation: A Gravitationally Lensed Vertical Oscillation, *Astrophys. J. Lett.*, **617**, pp. L45–L48, `astro-ph/0406586`.

Davis, S. W., Blaes, O. M., Hubeny, I. and Turner, N. J. (2005), Relativistic Accretion Disk Models of High-State Black Hole X-Ray Binary Spectra, *Astrophys. J.*, **621**, pp. 372–387, `astro-ph/0408590`.

Ghez, A. M., Salim, S., Hornstein, S. D., Tanner, A., Lu, J. R., Morris, M., Becklin, E. E. and Duchêne, G. (2005), Stellar Orbits around the Galactic Center Black Hole, *Astrophys. J.*, **620**, pp. 744–757.

Kato, S. (2001), Trapping of Non-Axisymmetric g-Mode Oscillations in Thin Relativistic Disks and kHz QPOs, *Publ. Astronom. Soc. Japan*, **53**, pp. L37–L39.

Kluźniak, W. and Abramowicz, M. A. (2000), The physics of kHz QPOs – strong gravity's coupled anharmonic oscillators, submitted in Phys. Rev. Lett., `astro-ph/0105057`.

Li, L.-X., Zimmerman, E. R., Narayan, R. and McClintock, J. E. (2005), Multitemperature Blackbody Spectrum of a Thin Accretion Disk around a Kerr Black Hole: Model Computations and Comparison with Observations, *Astrophys. J. Suppl.*, **157**, pp. 335–370, `astro-ph/0411583`.

McClintock, J. E. and Remillard, R. A. (2004), Black Hole Binaries, in W. H. G. Lewin and M. van der Klis, editors, *Compact Stellar X-Ray Sources*, Cambridge University Press, Cambridge, `astro-ph/0306213`.

Merloni, A., Vietri, M., Stella, L. and Bini, D. (1999), On gravitomagnetic precession around black holes, *Monthly Notices Roy. Astronom. Soc.*, **304**, pp. 155–159, `astro-ph/9811198`.

Nowak, M. A. and Lehr, D. E. (1998), Stable oscillations of black hole accretion discs, in M. A. Abramowicz, G. Björnsson and J. E. Pringle, editors, *Theory of Black Hole Accretion Disks*, pp. 233–253, Cambridge University Press, Cambridge, `astro-ph/9812004`.

Shafee, R., McClintock, J. E., Narayan, R., Davis, S. W., Li, L.-X. and Remillard, R. A. (2005), Estimating the Spin of Stellar-Mass Black Holes via Spectral Fitting of the X-ray Continuum, `astro-ph/0508302`.

Török, G. (2005), QPOs in microquasars and Sgr A*: measuring the black hole spin, *Astronom. Nachr.*, **326**(9), pp. 856–860, `astro-ph/0510669`.

Török, G., Abramowicz, M. A., Kluźniak, W. and Stuchlík, Z. (2005), The orbital resonance model for twin peak kHz quasi periodic oscillations in microquasars, *Astronomy and Astrophysics*, **436**(1), pp. 1–8, `astro-ph/0401464`.

Proceedings of *RAGtime 6/7: Workshops on black holes and neutron stars, Opava, 16–18/18–20 September, 2004/2005*
S. Hledík and Z. Stuchlík, editors, Silesian University in Opava, Czech Republic, 2005, pp. 47–54

Polarization of radiation from AGN accretion discs – the lamp-post model

Michal Dovčiak[1], Vladimír Karas[2], Giorgio Matt[3] and Andrea Martocchia[4]

[1]Astronomical Institute, Czech Academy of Sciences, Boční II 1401, CZ-141 31 Praha 4, Czech Republic
[2]Charles University in Prague, Faculty of Mathematics and Physics, V Holešovičkách 2, Praha, Czech Republic
[3]Dipartimento di Fisica, Università degli Studi "Roma Tre," I-00146 Roma, Italy
[4]UPS/Centre d'Etude Spatiale des Rayonnements, Toulouse, France

ABSTRACT
The effects of strong gravity on the polarization of the Compton reflection from an X-ray illuminated accretion disc are studied. The gravitational field of a rotating black hole influences Stokes parameters of the radiation along the propagation to a distant observer. Assuming the lamp-post model, the degree and the angle of polarization are examined as functions of the energy, observer's inclination angle, height of the primary source and inner radius of the disc emitting region.

1 INTRODUCTION

In this contribution we show that polarimetric studies in the X-ray domain could provide additional information about accretion discs in a strong gravity regime, which may be essential to discriminate between different possible geometries of the source. The idea of using polarimetry to gain additional information about accreting compact objects is not a new one. In this context it was proposed by Rees (1975) that polarized X-rays are of high relevance. Pozdnyakov et al. (1979) studied spectral profiles of iron X-ray lines that result from multiple Compton scattering. Later on, various processes affecting polarization (due to magnetic fields, absorption as well as strong gravity) were examined for black-hole accretion discs (Agol and Blaes, 1996). Temporal variations of polarization were also discussed, in particular the case of orbiting spots near a black hole (Connors et al., 1980; Bao et al., 1996). With the promise of new polarimetric detectors (Costa et al., 2001), quantitative examination of specific models becomes timely.

Since the reflecting medium has a disc-like geometry, a substantial amount of linear polarization is expected in the resulting spectrum because of Compton scattering. Polarization properties of the disc emission are modified by the photon propagation in a gravitational field, providing additional information on its structure. Here we calculate the observed polarization of the reflected radiation assuming the lamp-post model for the stationary power-law illuminating source (Martocchia and Matt, 1996; Petrucci and Henri, 1997).

80-7248-334-X

2 ASSUMPTIONS

We assume a rotating (Kerr) black hole as the only source of the gravitational field, having a common symmetry axis with an accretion disc. The disc is also assumed to be stationary and we restrict ourselves to the time-averaged analysis. In other words, we examine processes that vary at a much slower pace than the light-crossing time at the corresponding radius. Intrinsic polarization of the emerging light can be computed locally, assuming a plane-parallel scattering layer which is illuminated by light radiated from the primary source. This problem was studied extensively in various approximations (e.g., Chandrasekhar, 1960; Sunyaev and Titarchuk, 1985). Here we employ the Monte Carlo computations (Matt et al., 1991; Matt, 1993) to determine the intrinsic emissivity of an illuminated disc. The exact form of the local Stokes parameters can be found in (Dovčiak et al., 2004a, section describing the kyl1cr model). We integrate contributions to the total signal across the disc emitting region using a general relativistic ray-tracing technique described in (Dovčiak, 2004; Dovčiak et al., 2004a) and we compute the polarization angle and degree as measured by a distant observer. We show the polarization properties of scattered light as a function of energy and model parameters, namely, the height $z = h$ of the primary source on the symmetry axis, the dimensionless angular momentum a of the black hole, and the viewing angle θ_{o} of the observer.

3 RESULTS

In the first set of figures (Figs 1 and 2) we show the energy dependence of the polarization angle and degree due to reflected and reflected-plus-direct radiation for different inclination angles and different heights of the primary source. One can see that the polarization of reflected radiation can be as high as thirty percent or even more for small inclinations and small heights. Polarization of the reflected radiation does not depend on energy very much except for the region close to the iron edge at approximately 7.2 keV, where it either decreases for small inclinations or increases for large ones.

In order to compute observable characteristics one has to combine the primary power-law continuum with the reflected component. The polarization degree of the resulting signal depends on the mutual proportion of the two components and also on the energy range in which the signal is integrated. The net degree of polarization increases with energy (see bottom panels in Figs 1 and 2) due to the fact that the intensity of radiation from the primary source decreases exponentially, the intensity of the reflected radiation increases with energy (in the energy range 3–15 keV) and the polarization of the reflected light alone is more or less constant. In our computations we assumed that the irradiating source emits isotropically and its light is affected only by gravitational redshift and lensing, according to the source location at $z = h$ on axis. This results in a dilution of primary light by factor $\sim g_{\mathrm{h}}^2(h, \theta_{\mathrm{o}})\, l_{\mathrm{h}}(h, \theta_{\mathrm{o}})$, where $g_{\mathrm{h}} = [1 - 2h/(a^2 + h^2)]^{1/2}$ is the redshift of primary photons reaching directly the observer, l_{h} is the corresponding lensing factor. Here, the redshift is the dominant relativistic term, while lensing of primary photons is a few percent at most and it can be safely ignored. Anisotropy of primary radiation may further attenuate or amplify the polarization degree of the final signal, while the polarization angle is rather independent of this effect as long as the primary light is itself unpolarized.

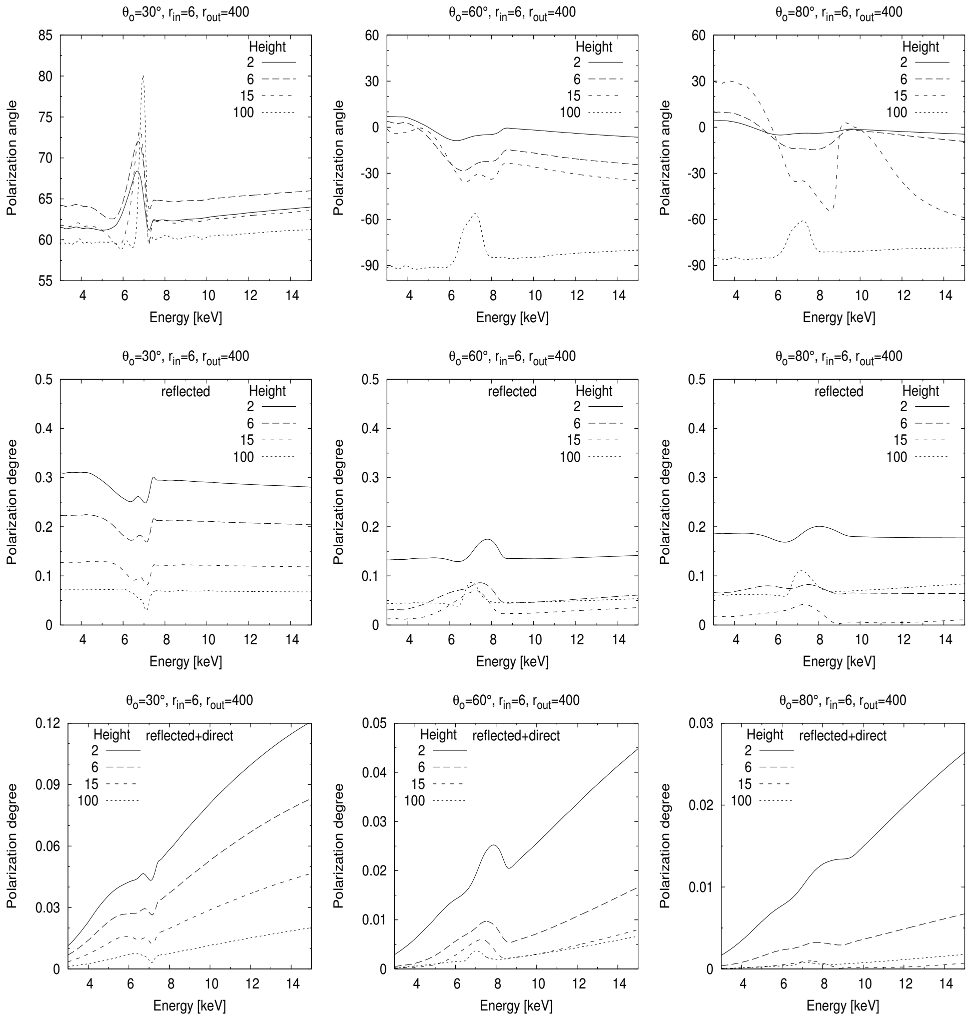

Figure 1. Energy dependence of polarization angle (top panels) and polarization degree (middle panels) due to reflected radiation for different observer's inclination angles ($\theta_{\rm o} = 30°, 60°$ and $80°$) and for different heights of the primary source ($h = 2, 6, 15$ and 100). Polarization degree for reflected-plus-direct radiation is also plotted (bottom panels). The emission comes from a disc within $r_{\rm in} = 6$ and $r_{\rm out} = 400$. Isotropic primary radiation with photon index $\Gamma = 2$ and angular momentum of the central black hole $a = 0.9987$ were assumed.

The polarization of scattered light is also shown in Fig. 3, where we plot the polarization degree and the change of the polarization angle as functions of h. Notice that in the Newtonian case only polarization angles of $0°$ or $90°$ would be expected for reasons of symmetry. The two panels in the figure correspond to different locations of the inner disc edge: $r_{\rm in} = 6$ and $r_{\rm in} = 1.20$, respectively. The curves are strongly sensitive to $r_{\rm in}$ and h,

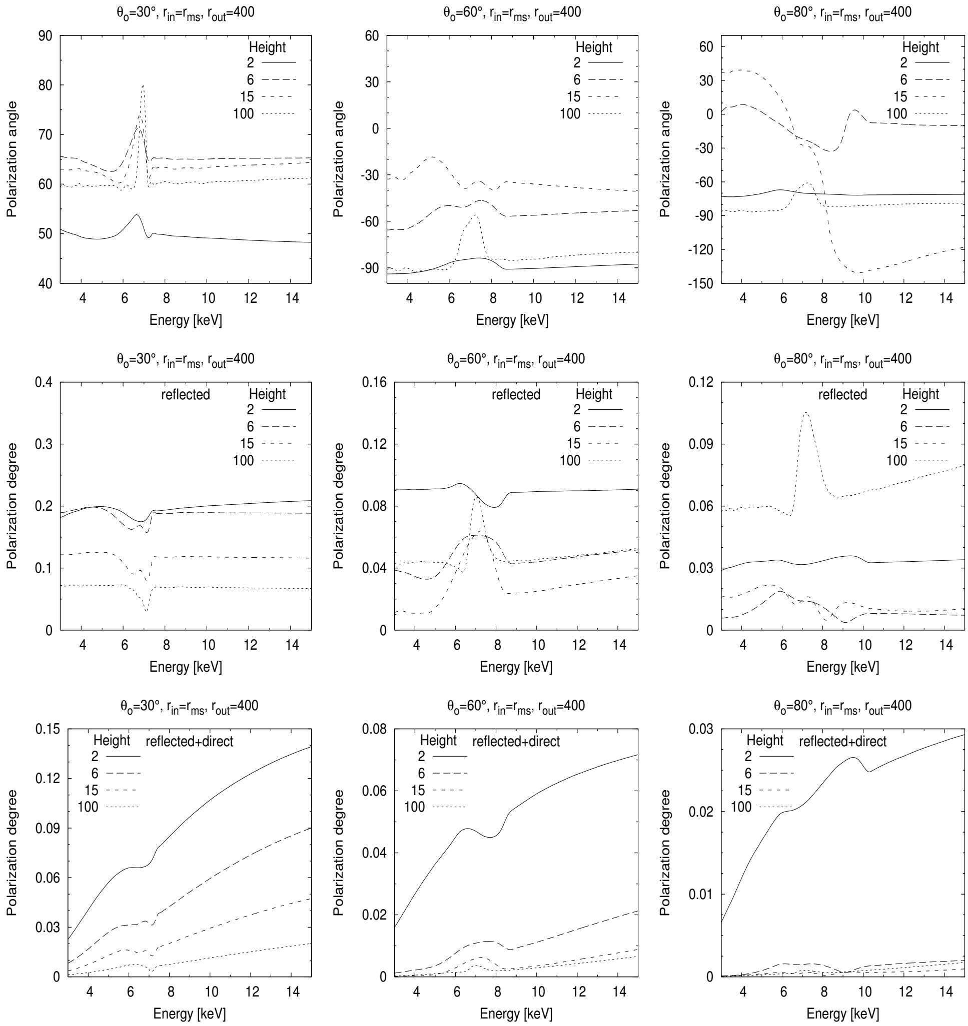

Figure 2. Same as in the previous Fig. 1 but for disc starting at $r_{\rm in} = 1.20$.

while the dependence on $r_{\rm out}$ is weak for a large disc (here $r_{\rm out} = 400$). Sensitivity to $r_{\rm in}$ is particularly appealing if one remembers the practical difficulties in estimating $r_{\rm in}$ by fitting spectra. The effect is clearly visible up to $h \sim 10$ for polarization degree and even higher for polarization angle (for larger inclination angles of the observer). Graphs corresponding to $r_{\rm in} = 6$ and $a = 0.9987$, resemble, in essence quite closely, the non-rotating case ($a = 0$) because dragging effects are most prominent near the horizon.

Figure 4 shows the polarization degree and angle as functions of the observer's inclination. Again, by comparing the two cases of different $r_{\rm in}$ one can clearly recognize that the polarization is sensitive to details of the flow near the inner disc boundary.

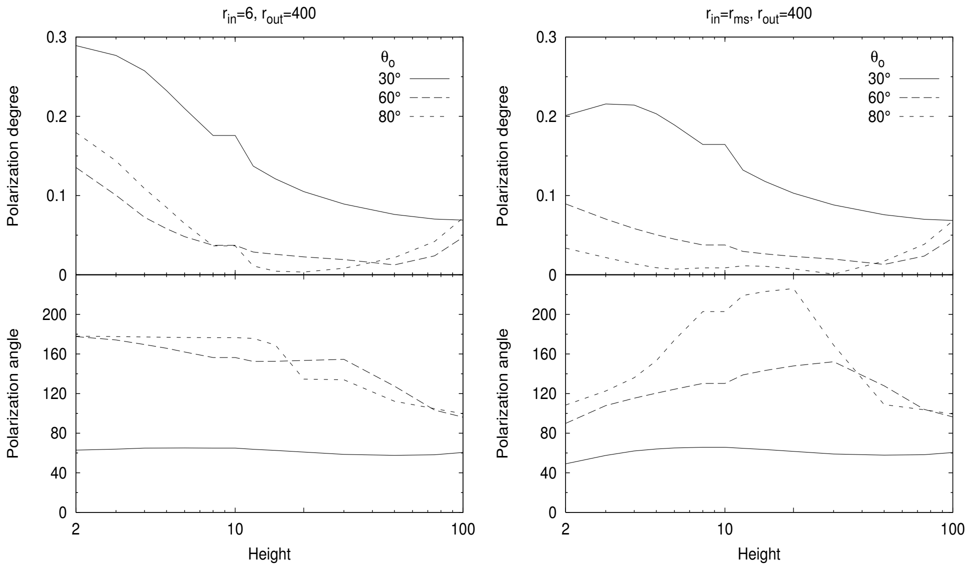

Figure 3. Polarization degree and angle due to reflected radiation integrated over the whole surface of the disc and propagated to the point of observation. Dependence on height h is plotted. *Left panel:* $r_{\rm in} = 6$. *Right panel:* $r_{\rm in} = 1.20$. In both the panels the energy range was assumed 9–12 keV, the photon index of incident radiation $\Gamma = 2$, the angular momentum $a = 0.9987$. The figure is taken from (Dovčiak et al., 2004b).

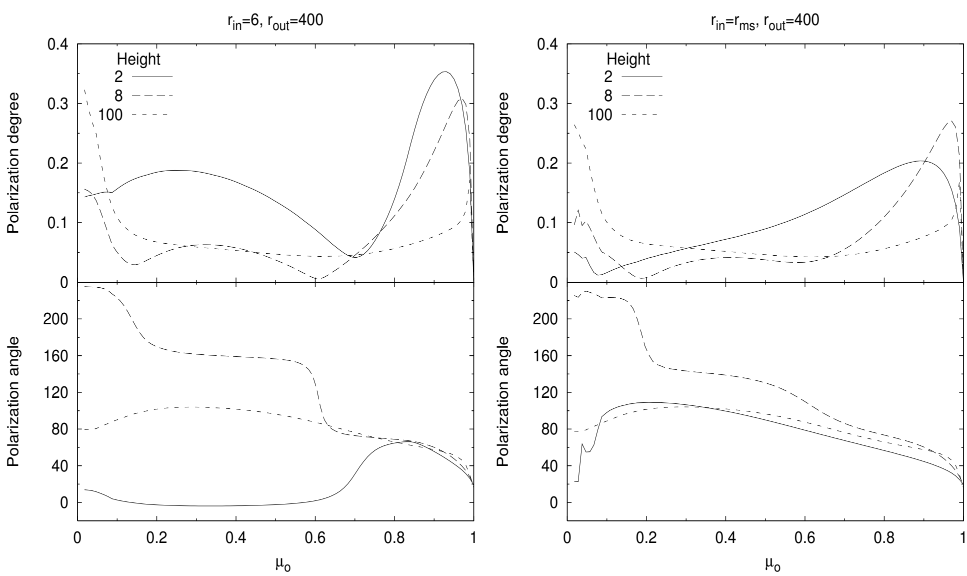

Figure 4. Polarization degree and angle as functions of $\mu_{\rm o}$ (cosine of observer inclination, $\mu_{\rm o} = 0$ corresponds to the edge-on view of the disc). The same model is shown as in the previous Fig. 3. The figure is similar to Fig. 2 in (Dovčiak et al., 2004b) but computed with higher resolution.

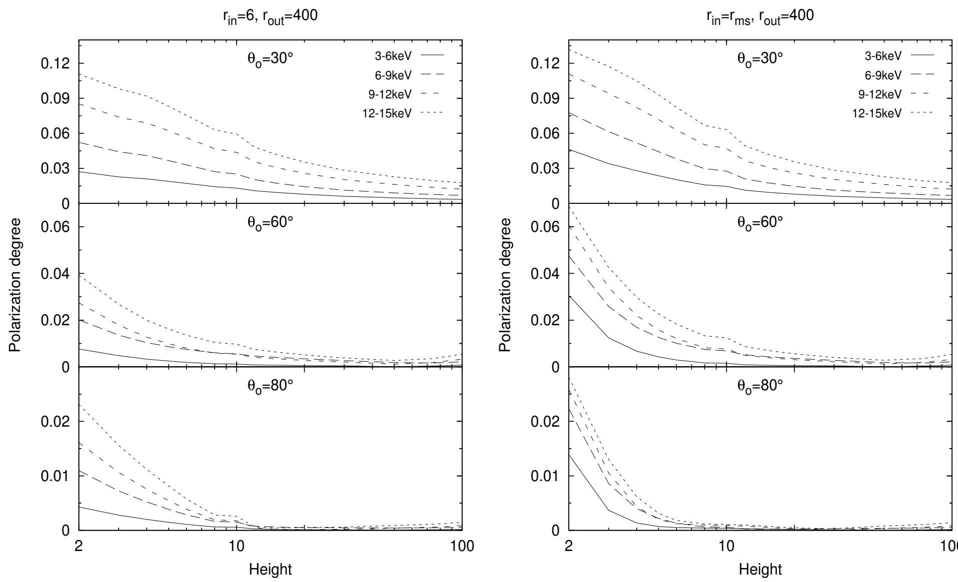

Figure 5. Net polarization degree of the total (primary plus reflected) signal as a function of h. *Left panel:* $r_{\rm in} = 6$. *Right panel:* $r_{\rm in} = 1.20$.

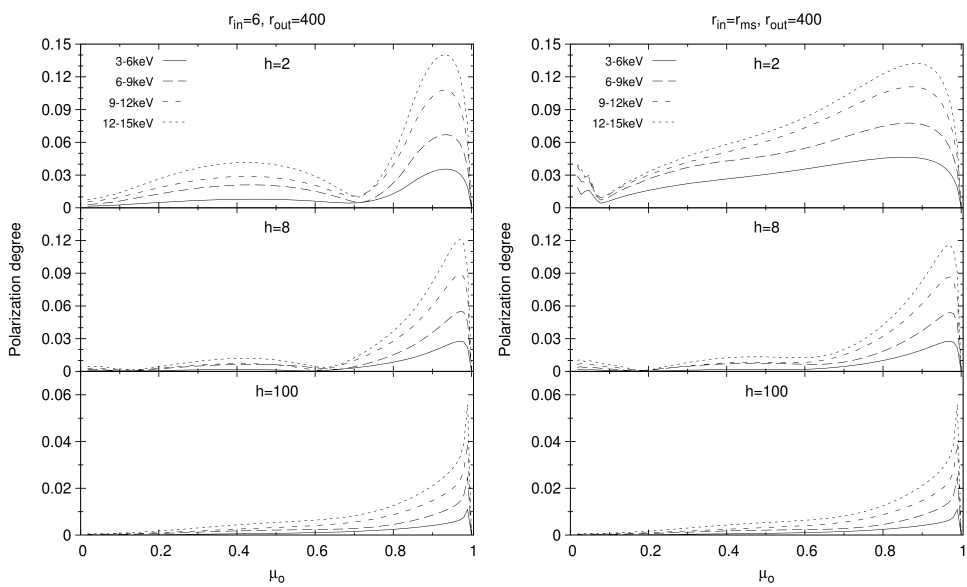

Figure 6. Net polarization degree of the total (primary plus reflected) signal as a function of $\mu_{\rm o}$. The same model is shown as in the previous Fig. 5.

The dependence of the polarization degree of overall radiation (primary plus reflected) on the height of the primary source and the observer inclination in different energy ranges is shown in Figs 5 and 6.

4 CONCLUSIONS

We examined the polarimetric properties of X-ray illuminated accretion discs in the lamp-post model. From the figures shown it is clear that observed values of polarization angle and degree are rather sensitive to the model parameters. The adopted approach provides additional information with respect to traditional X-ray spectroscopy and so it has great potential for discriminating between different models. It offers an improved way of measuring rotation of the black hole because the radiation properties of the inner disc region most likely reflect the value of the black-hole angular momentum. One should stress here, that firstly, the estimation of the black hole spin in spectroscopy is usually based on assuming that the innermost line- or continuum-emitting orbit coincides with the innermost stable orbit, and secondly, there are always several unknown variables at play. Therefore it would be better to get the value of the inner edge of the disc and the spin of the black hole on the base of both the spectroscopy and polarimetry.

While our calculations have been performed assuming a stationary situation, in reality it is likely that the height of the illuminating source changes with time, and indeed such variations have been invoked by Miniutti et al. (2003) to explain the primary and reflected variability patterns of MCG-6-30-15. A complete time-resolved analysis (including all consequences of the light travel time in curved space-time) is beyond the scope of this contribution and we defer it to future work, assuming that the primary source varies on a time-scale longer than light-crossing time in the system. This is also a well-substantiated assumption from a practical point of view, since feasible techniques will anyway require sufficient integration time (i.e., order of several ksec). Once full temporal resolution is possible, the analysis described above can be readily extended. Here, it suffices to note that a variation of h implies a variation of the observed polarization angle of the reflected radiation. As it is hard to imagine a physical and/or geometrical effect giving rise to the same effect, time variability of the polarization angle can be considered (independently of the details) a very strong signature of strong-field general relativity effects at work.

New generation photoelectric polarimeters (Costa et al., 2001) in the focal plane of large area optics (such as those foreseen for *Xeus*) can probe polarization degrees of the order of one percent in bright AGNs, making polarimetry, along with timing and spectroscopy, a tool for exploring the properties of the accretion flows in the vicinity of black holes.

ACKNOWLEDGEMENTS

Two of authors (M. D. and V. K.) gratefully acknowledge support from Czech Science Foundation grants 205/05/P525 and 205/03/0902, and from Charles University in Prague (GAUK 299/2004). G. M. acknowledges financial support from Agenzia Spaziale Italiana (ASI) and Ministero dell'Istruzione, dell'Università e della Ricerca (MIUR), under grant COFIN-03-02-23.

REFERENCES

Agol, E. and Blaes, O. (1996), Polarization from magnetized accretion discs in active galactic nuclei, *Monthly Notices Roy. Astronom. Soc.*, **282**, pp. 965–976.

Bao, G., Wiita, P. J. and Hadrava, P. (1996), Energy-Dependent Polarization Variability as a Black Hole Signature, *Phys. Rev. Lett.*, **77**, pp. 12–15.

Chandrasekhar, S. (1960), *Radiative Transfer*, Dover Publications, New York.

Connors, P. A., Piran, T. and Stark, R. F. (1980), Polarization features of X-ray radiation emitted near black holes, *Astrophys. J.*, **235**, pp. 224–244.

Costa, E., Soffitta, P., Bellazzini, R., Brez, A., Lumb, N. and Spandre, G. (2001), An efficient photoelectric X-ray polarimeter for the study of black holes and neutron stars, *Nature*, **411**, pp. 662–665.

Dovčiak, M. (2004), *Radiation of accretion discs in strong gravity*, Ph.D. thesis, Charles University at Prague, Faculty of Mathematics and Physics, Prague, `astro-ph/0411605`.

Dovčiak, M., Karas, V., Martocchia, A., Matt, G. and Yaqoob, T. (2004a), An XSPEC model to explore spectral features from black-hole sources, in S. Hledík and Z. Stuchlík, editors, *Proceedings of RAGtime 4/5: Workshops on black holes and neutron stars, Opava, 14–16/13–15 October 2002/2003*, pp. 33–73, Silesian University in Opava, Opava, ISBN 80-7248-242-4, `astro-ph/0407330`.

Dovčiak, M., Karas, V. and Matt, G. (2004b), Polarization signatures of strong gravity in active galactic nuclei accretion discs, *Monthly Notices Roy. Astronom. Soc.*, **355**, pp. 1005–1009.

Martocchia, A. and Matt, G. (1996), Iron K-alpha line intensity from accretion discs around rotating black holes, *Monthly Notices Roy. Astronom. Soc.*, **282**, pp. L53–L57.

Matt, G. (1993), X-ray polarization properties of a centrally illuminated accretion disc, *Monthly Notices Roy. Astronom. Soc.*, **260**, pp. 663–674.

Matt, G., Perola, G. C. and Piro, L. (1991), The iron line and high energy bump as X-ray signatures of cold matter in Seyfert 1 galaxies, *Astronomy and Astrophysics*, **274**, pp. 25–34.

Miniutti, G., Fabian, A. C., Goyder, R. and Lasenby, A. N. (2003), The lack of variability of the iron line in MCG-6-30-15: general relativistic effects, *Monthly Notices Roy. Astronom. Soc.*, **344**, pp. L22–L26.

Petrucci, C. O. and Henri, G. (1997), Anisotropic illumination of AGN's accretion disk by a non thermal source. II. General relativistic effects, *Astronomy and Astrophysics*, **326**, pp. 99–107.

Pozdnyakov, L. A., Sobol, I. M. and Sunyaev, R. A. (1979), The profile evolution of X-ray spectral lines due to Comptonization – Monte Carlo computations, *Astronomy and Astrophysics*, **75**, pp. 214–222.

Rees, J. M. (1975), Expected polarization properties of binary X-ray sources, *Monthly Notices Roy. Astronom. Soc.*, **171**, pp. 457–465.

Sunyaev, R. A. and Titarchuk, L. G. (1985), Comptonization of low-frequency radiation in accretion disks: angular distribution and polarization of hard radiation, *Astronomy and Astrophysics*, **143**, pp. 374–388.

Proceedings of *RAGtime 6/7: Workshops on black holes and neutron stars, Opava, 16–18/18–20 September, 2004/2005*
S. Hledík and Z. Stuchlík, editors, Silesian University in Opava, Czech Republic, 2005, pp. 55–62

Kinetic model of quasiperiodic oscillations of gaseous rings

Petr Hadrava

Astronomical Institute, Academy of Sciences, Prague, Czech Republic
had@pleione.asu.cas.cz

ABSTRACT
In context of 3 : 2 resonant quasiperiodic oscillations, a method of "$1 + \frac{1}{2}$"-dimensional non-ideal gas-dynamics is used to model axisymmetric oscillations of an orbiting ring. It is shown that the characteristic frequencies of the oscillations are influenced by the degree of freedom in the inner shear of the ring and by the rate of relaxation.

1 INTRODUCTION

One of theoretical models explaining the quasiperiodic oscillations (QPOs) in high-energy sources has been suggested by Kluźniak and Abramowicz (2001). It is based on assumption of non-linear resonant oscillations (mostly in ratio of frequencies 3 : 2) in accretion disks around a central compact object (for a recent review cf. Abramowicz et al., 2004; Török et al., 2005). The resonance occurs at a particular radius of axially symmetric potential of the central body (mirror symmetry with respect to the equatorial plane is also assumed) between the orbital frequency of vertical perturbations and epicyclic frequency of radial perturbations of the gas motion. To explain the quasiperiodicity and frequency variations of the oscillations a non-linear coupling of the oscillation modes is required. This can be due to different effects. One of them is the non-linearity caused by the higher terms in Taylor expansion of the effective potential. Another one, investigated here, may consist in relaxation processes in the gas itself. In reality both these and possibly also some other (e.g., electromagnetic) processes may take place simultaneously.

In the present contribution a kind of the so called "$1+\frac{1}{2}$"-dimensional hydrodynamic models will be used to study axially symmetric oscillations of a gaseous ring shaped as circular torus with elliptical cross-section, which orbits in an axially symmetric potential. This method is based on the kinetic theory of the gas so that it is convenient to treat a non-ideal gas and its viscosity. The problem of QPOs requires only a modest generalization (namely to replace a spherically symmetric by axially symmetric potential) of example chosen for its simplicity to illustrate the method when it was originally introduced (Hadrava, 1983, Paper I henceforth). Because of numerous mistypes in Paper I, the method will be briefly summarized here again, first for the linear case of collisionless particles (Section 2) and

80-7248-334-X

then for the non-linear problem of relaxation in a gas (Section 3). Finally, the method will be applied to the study of ring oscillations (Section 4).

2 EVOLUTION OF A CLOUD OF NON-INTERACTING PARTICLES

Let us treat a cloud of non-interacting particles; the motion of each particle being given by the same one-particle Hamiltonian H with an external potential and let the cloud be described by a distribution function F in one-particle phase space with coordinates ξ. The evolution of F in time t is then given by Boltzmann equation

$$\frac{\partial}{\partial t}F + [F, H] = \frac{\partial}{\partial t}F(\xi, t) + \dot{\xi}\frac{\partial}{\partial \xi}F(\xi, t) = 0\,. \tag{1}$$

Our method is based on the assumption that F can be approximated in the form of 6-dimensional Gaussian function

$$F(\xi, t) = F_0 \exp\left[-(\xi - \xi_0(t))^{\mathrm{T}} \boldsymbol{A}(t)(\xi - \xi_0(t))\right]\,. \tag{2}$$

This assumption is motivated by the fact that it generalizes the Maxwellian distribution in the momentum subspace, which can be, e.g., for a free expansion in vacuum, imprinted on the density distribution in space also. Tidal forces may result in an anisotropic expansion and, for inefficient energy redistribution, also in an anisotropic cooling. This is why the shape of F is given by a general symmetric matrix $\boldsymbol{A}$.

It follows from Boltzmann equation (1), that the maximum of F moves along a phase trajectory $\xi_0(t)$ satisfying the equations of Hamiltonian motion

$$\frac{\mathrm{d}}{\mathrm{d}t}\xi(t) = [\xi, H] \tag{3}$$

and consequently (following the Liouville theorem) that the maximum value F_0 along this trajectory is constant. Next, it can be shown (cf. Paper I) that to keep the second derivatives $\partial^2/\partial\xi^2$ of F along $\xi_0(t)$ consistent with (1), the matrix $\boldsymbol{A}$ must satisfy differential equation

$$\frac{\mathrm{d}}{\mathrm{d}t}\boldsymbol{A}(t) = -\boldsymbol{C}^{\mathrm{T}}\boldsymbol{A} - \boldsymbol{A}\boldsymbol{C}\,, \tag{4}$$

where the matrix $\boldsymbol{C}$ corresponding to tidal forces is given by second-order derivatives of H

$$\boldsymbol{C} = \left[\frac{\partial\dot{\xi}}{\partial\xi}\right]_{\xi_0} = [\xi, \partial_\xi H]\,. \tag{5}$$

Solving (either numerically or, in simpler cases, also analytically) the set of ordinary differential equations (4) along with the equation (3) of motion of the centre of a cloud of particles, we get within the assumption (2) complete information about the distribution of the particles. Obviously, in the course of evolution the higher order derivatives of F, which we do not solve explicitely, will generally violate the Gaussian form (2) of F even if it is satisfied by the initial conditions. However, because most of the particles are grouped within the characteristic width of this distribution and only a negligible part of them forms a high-energy tail of the Maxwellian distribution in momentum space and an outer halo of the dense core of the cloud, we can expect that this method gives a good insight into the behaviour of the cloud core provided its size does not exceed the characteristic scale of inhomogeneities of the external field.

If we split the space and momentum components of ξ and $\boldsymbol{A}$

$$\xi - \xi_0 = \begin{pmatrix} x \\ p \end{pmatrix}, \qquad \boldsymbol{A} = \begin{pmatrix} \boldsymbol{c} & \boldsymbol{b}^{\mathrm{T}} \\ \boldsymbol{b} & \boldsymbol{a} \end{pmatrix}, \tag{6}$$

$\boldsymbol{C}$ can be expressed in a block form as

$$\boldsymbol{C} = \begin{pmatrix} \boldsymbol{\gamma} & \boldsymbol{\delta} \\ \boldsymbol{\beta} & \boldsymbol{\alpha} \end{pmatrix} = \begin{pmatrix} \frac{\partial^2 H}{\partial p \partial x} & \frac{\partial^2 H}{\partial p \partial p} \\ -\frac{\partial^2 H}{\partial x \partial x} & -\frac{\partial^2 H}{\partial x \partial p} \end{pmatrix}, \tag{7}$$

where obviously $\boldsymbol{\gamma} = -\boldsymbol{\alpha}^{\mathrm{T}}$, and Eq. (4) can be written as

$$\frac{\mathrm{d}}{\mathrm{d}t}\boldsymbol{a} = -\boldsymbol{\alpha}^{\mathrm{T}}\boldsymbol{a} - \boldsymbol{a}\boldsymbol{\alpha} - \boldsymbol{\delta}^{\mathrm{T}}\boldsymbol{b}^{\mathrm{T}} - \boldsymbol{b}\boldsymbol{\delta}, \tag{8}$$

$$\frac{\mathrm{d}}{\mathrm{d}t}\boldsymbol{b} = -\boldsymbol{a}\boldsymbol{\beta} - \boldsymbol{\alpha}^{\mathrm{T}}\boldsymbol{b} + \boldsymbol{b}\boldsymbol{\alpha}^{\mathrm{T}} - \boldsymbol{\delta}^{\mathrm{T}}\boldsymbol{c}, \tag{9}$$

$$\frac{\mathrm{d}}{\mathrm{d}t}\boldsymbol{c} = -\boldsymbol{\beta}^{\mathrm{T}}\boldsymbol{b} - \boldsymbol{b}^{\mathrm{T}}\boldsymbol{\beta} + \boldsymbol{\alpha}\boldsymbol{c} + \boldsymbol{c}\boldsymbol{\alpha}^{\mathrm{T}}. \tag{10}$$

Provided the parameters F_0, ξ_0 and $\boldsymbol{A}$ of distribution function F in the form (2) are known, the distribution of macroscopic characteristics of the cloud in space can be calculated by integration on the momentum space. The density is given by

$$\rho = mF_0 \det{}^{1/2}(\pi\bar{\boldsymbol{a}}) \exp\left[-x^{\mathrm{T}}\bar{\boldsymbol{c}}x\right], \tag{11}$$

the velocity by

$$v = -\bar{\boldsymbol{b}}x \tag{12}$$

and the stress tensor by

$$\boldsymbol{\tau} = \frac{\rho}{2m}\bar{\boldsymbol{a}}, \tag{13}$$

where the matrices

$$\bar{\boldsymbol{a}} = \boldsymbol{a}^{-1}, \qquad \bar{\boldsymbol{b}} = \boldsymbol{a}^{-1}\boldsymbol{b}, \qquad \bar{\boldsymbol{c}} = \boldsymbol{c} - \boldsymbol{b}^{\mathrm{T}}\boldsymbol{a}^{-1}\boldsymbol{b} \tag{14}$$

are nonlinear functions of submatrices $\boldsymbol{a}$, $\boldsymbol{b}$ and $\boldsymbol{c}$. It is thus obvious from Eq. (11) that the assumption (2) allows to describe a cloud with Gaussian density profile of the shape of triaxial ellipsoid. This ellipsoid may also be elongated to a tube with elliptic cross-section or to a plane-parallel structure if the matrix $\bar{\boldsymbol{c}}$ is singular in one or two directions. According to Eq. (12), the cloud may have an internal velocity field linear in space, i.e., an anisotropic expansion with constant gradient and constant rotation and shear. Finally, following Eq. (13) the stress tensor is constant in the whole cloud, but generally anisotropic and non-diagonal.

The dynamics of non-interacting particles is linear, which means Eq. (4) determining the evolution of matrix $\boldsymbol{A}$ is linear. Consequently, its solution for any initial conditions can be written in the form

$$\boldsymbol{A}(t) = \boldsymbol{B}^{\mathrm{T}}(t)\boldsymbol{A}(0)\boldsymbol{B}(t)\,, \tag{15}$$

where[1]

$$\boldsymbol{B}(t) = \exp\left[-\int_0^t \boldsymbol{C}(t')\,\mathrm{d}t'\right] \tag{16}$$

is matrix satisfying equation

$$\frac{\mathrm{d}}{\mathrm{d}t}\boldsymbol{B} = -\boldsymbol{B}\boldsymbol{C}\,, \quad \boldsymbol{B}(0) = \boldsymbol{1}\,. \tag{17}$$

3 EVOLUTION OF A CLOUD WITH A RELAXATION

As the matrices $\bar{\boldsymbol{a}}$, $\bar{\boldsymbol{b}}$ and $\bar{\boldsymbol{c}}$ are of our direct interest rather than $\boldsymbol{a}$, $\boldsymbol{b}$ and $\boldsymbol{c}$, we can solve differential equations

$$\frac{\mathrm{d}}{\mathrm{d}t}\bar{\boldsymbol{a}} = \left(\frac{\delta\bar{\boldsymbol{a}}}{\delta t}\right)_{\mathrm{c}} + \boldsymbol{\alpha}\bar{\boldsymbol{a}} + \bar{\boldsymbol{a}}\boldsymbol{\alpha}^{\mathrm{T}} + \bar{\boldsymbol{b}}\boldsymbol{\delta}\bar{\boldsymbol{a}} + \bar{\boldsymbol{a}}\boldsymbol{\delta}^{\mathrm{T}}\bar{\boldsymbol{b}}^{\mathrm{T}}\,, \tag{18}$$

$$\frac{\mathrm{d}}{\mathrm{d}t}\bar{\boldsymbol{b}} = -\boldsymbol{\beta} - \boldsymbol{\alpha}\bar{\boldsymbol{b}} + \bar{\boldsymbol{b}}\boldsymbol{\alpha}^{\mathrm{T}} + \bar{\boldsymbol{b}}\boldsymbol{\delta}\bar{\boldsymbol{b}} - \bar{\boldsymbol{a}}\boldsymbol{\delta}^{\mathrm{T}}\bar{\boldsymbol{c}}\,, \tag{19}$$

$$\frac{\mathrm{d}}{\mathrm{d}t}\bar{\boldsymbol{c}} = \boldsymbol{\alpha}\bar{\boldsymbol{c}} + \bar{\boldsymbol{c}}\boldsymbol{\alpha}^{\mathrm{T}} + \bar{\boldsymbol{c}}\boldsymbol{\delta}\bar{\boldsymbol{b}} + \bar{\boldsymbol{b}}^{\mathrm{T}}\boldsymbol{\delta}^{\mathrm{T}}\bar{\boldsymbol{c}}\,, \tag{20}$$

instead of Eqs (8), (9) and (10). It is not surprising that these equations are non-linear, because Eq. (14) is also non-linear.

In addition to the direct consequence of Eqs (8), (9), (10) and (14) we have added now the first so called collisional term on the right-hand side of Eq. (18), which accounts for relaxation of non-equilibrium components of the stress tensor. Even with the very simple BGK-model

$$\left(\frac{\delta\bar{\boldsymbol{a}}}{\delta t}\right)_{\mathrm{c}} = \frac{\bar{\boldsymbol{a}}_0 - \bar{\boldsymbol{a}}}{\tau}\,, \qquad \bar{\boldsymbol{a}}_0 = \frac{\mathrm{Tr}(\bar{\boldsymbol{a}})}{3}\boldsymbol{1}\,, \tag{21}$$

of this collisional term, which assumes an exponential damping of deviation of the distribution function from equilibrium with relaxation time[2] τ and which is a linear function of $\bar{\boldsymbol{a}}$,

[1] Cf. Paper I for calculation of this integral by means of Jordan's decomposition for constant $\boldsymbol{C}$.

[2] Different relaxation times for non-diagonal components and for differences between the diagonal components of the stress-tensor can be also assumed.

the complete problem becomes to be inherently non-linear.[3] The equivalent set of equations for matrices $\boldsymbol{a}$, $\boldsymbol{b}$ and $\boldsymbol{c}$ reads

$$\frac{\mathrm{d}}{\mathrm{d}t}\boldsymbol{a} = -\boldsymbol{a}\left(\frac{\delta\bar{\boldsymbol{a}}}{\delta t}\right)_{\mathrm{c}}\boldsymbol{a} - \boldsymbol{\alpha}^{\mathrm{T}}\boldsymbol{a} - \boldsymbol{a}\boldsymbol{\alpha} - \boldsymbol{\delta}^{\mathrm{T}}\boldsymbol{b}^{\mathrm{T}} - \boldsymbol{b}\boldsymbol{\delta}\,, \tag{22}$$

$$\frac{\mathrm{d}}{\mathrm{d}t}\boldsymbol{b} = -\boldsymbol{a}\left(\frac{\delta\bar{\boldsymbol{a}}}{\delta t}\right)_{\mathrm{c}}\boldsymbol{b} - \boldsymbol{a}\boldsymbol{\beta} - \boldsymbol{\alpha}^{\mathrm{T}}\boldsymbol{b} + \boldsymbol{b}\boldsymbol{\alpha}^{\mathrm{T}} - \boldsymbol{\delta}^{\mathrm{T}}\boldsymbol{c}\,, \tag{23}$$

$$\frac{\mathrm{d}}{\mathrm{d}t}\boldsymbol{c} = -\boldsymbol{b}^{\mathrm{T}}\left(\frac{\delta\bar{\boldsymbol{a}}}{\delta t}\right)_{\mathrm{c}}\boldsymbol{b} - \boldsymbol{\beta}^{\mathrm{T}}\boldsymbol{b} - \boldsymbol{b}^{\mathrm{T}}\boldsymbol{\beta} + \boldsymbol{\alpha}\boldsymbol{c} + \boldsymbol{c}\boldsymbol{\alpha}^{\mathrm{T}}\,, \tag{24}$$

i.e., the collisional term is non-linear in this representation.

In the approximation of a nearly ideal gas we can assume that the relaxation is sufficiently efficient to diminish the non-equilibrium components of the stress tensor to a small perturbations of the isotropic equilibrium one, and we can write (up to the higher order terms)

$$\boldsymbol{a} = a\mathbf{1} + \delta\boldsymbol{a} + a^{-1}\delta\boldsymbol{a}\delta\boldsymbol{a} + \mathcal{O}(\delta\boldsymbol{a})^3\,, \qquad \bar{\boldsymbol{a}} = a^{-1}\mathbf{1} - a^{-2}\delta\boldsymbol{a}\,, \tag{25}$$

where $\delta\boldsymbol{a}$ is a trace-free matrix, and in the BGK-approximation (21)

$$\left(\frac{\delta\bar{\boldsymbol{a}}}{\delta t}\right)_{\mathrm{c}} = \frac{1}{\tau a^2}\,\delta\boldsymbol{a}\,. \tag{26}$$

Substituting this collisional term into Eq. (22), it gets the form

$$\frac{\mathrm{d}}{\mathrm{d}t}\boldsymbol{a} = -\frac{1}{\tau}\left(\delta\boldsymbol{a} + \frac{2}{a}\,\delta\boldsymbol{a}\delta\boldsymbol{a} + \cdots\right) - \boldsymbol{\alpha}^{\mathrm{T}}\boldsymbol{a} - \boldsymbol{a}\boldsymbol{\alpha} - \boldsymbol{\delta}^{\mathrm{T}}\boldsymbol{b}^{\mathrm{T}} - \boldsymbol{b}\boldsymbol{\delta}\,. \tag{27}$$

Regarding Eq. (25) and neglecting the terms quadratic and higher-order in $\delta\boldsymbol{a}$, we get from the trace of this equation an equation for pressure (temperature)

$$\frac{\mathrm{d}}{\mathrm{d}t}a = -\frac{1}{3}\,\mathrm{Tr}\left(\boldsymbol{\alpha}^{\mathrm{T}}\boldsymbol{a} + \boldsymbol{a}\boldsymbol{\alpha} + \boldsymbol{\delta}^{\mathrm{T}}\boldsymbol{b}^{\mathrm{T}} + \boldsymbol{b}\boldsymbol{\delta}\right)\,. \tag{28}$$

If the relaxation time τ is much shorter than the characteristic dynamical time of the studied problem, Eq. (27) gives an exponential relaxation of $\delta\boldsymbol{a}$ to the instantaneous value

$$\delta\boldsymbol{a} = -\tau\left(\boldsymbol{\alpha}^{\mathrm{T}}\boldsymbol{a} + \boldsymbol{a}\boldsymbol{\alpha} + \boldsymbol{\delta}^{\mathrm{T}}\boldsymbol{b}^{\mathrm{T}} + \boldsymbol{b}\boldsymbol{\delta}\right)\,. \tag{29}$$

In analogy with Eq. (27) we get from Eqs (23) and (24) differential equations

$$\frac{\mathrm{d}}{\mathrm{d}t}\boldsymbol{b} = -\frac{1}{\tau a}\left(\delta\boldsymbol{a} + \frac{1}{a}\delta\boldsymbol{a}\delta\boldsymbol{a} + \cdots\right)\boldsymbol{b} - \boldsymbol{a}\boldsymbol{\beta} - \boldsymbol{\alpha}^{\mathrm{T}}\boldsymbol{b} + \boldsymbol{b}\boldsymbol{\alpha}^{\mathrm{T}} - \boldsymbol{\delta}^{\mathrm{T}}\boldsymbol{c}\,, \tag{30}$$

$$\frac{\mathrm{d}}{\mathrm{d}t}\boldsymbol{c} = -\frac{1}{\tau a^2}\boldsymbol{b}^{\mathrm{T}}\delta\boldsymbol{a}\boldsymbol{b} - \boldsymbol{\beta}^{\mathrm{T}}\boldsymbol{b} - \boldsymbol{b}^{\mathrm{T}}\boldsymbol{\beta} + \boldsymbol{\alpha}\boldsymbol{c} + \boldsymbol{c}\boldsymbol{\alpha}^{\mathrm{T}}\,. \tag{31}$$

[3] General consequences of non-linear coupling of resonant modes in context of QPOs have been discussed, e.g., by Horák (2004).

4 DYNAMICS OF AN ORBITING GASEOUS RING

Let us investigate now in the framework of Newtonian mechanics evolution of a cloud of particles with Hamiltonian given in cylindrical coordinates r, φ and z as

$$H = \tfrac{1}{2}(p_r^2 + r^{-2}p_\varphi^2 + p_z^2) + \Phi(r, z)\,. \tag{32}$$

If we choose a circular orbit $p_r = p_z = 0$, $p_\varphi^2 = r^3\partial_r\Phi$, as the pivoting trajectory of the centre of our cloud (torus), the corresponding matrix $\boldsymbol{C}$

$$\boldsymbol{C} = \frac{\partial(\dot r, \dot\varphi, \dot z, \dot p_r, \dot p_\varphi, \dot p_z)}{\partial(r, \varphi, z, p_r, p_\varphi, p_z)} = \begin{pmatrix} 0 & 0 & 0 & 1 & 0 & 0 \\ -\chi & 0 & 0 & 0 & r^{-2} & 0 \\ 0 & 0 & 0 & 0 & 0 & 1 \\ -\omega^2 & 0 & 0 & 0 & \chi & 0 \\ 0 & 0 & 0 & 0 & 0 & 0 \\ 0 & 0 & -\psi^2 & 0 & 0 & 0 \end{pmatrix}, \tag{33}$$

where

$$\chi = 2r^{-3/2}\left[\frac{\partial\Phi}{\partial r}\right]^{1/2}, \qquad \omega = r^{-3/2}\left[\frac{\partial}{\partial r}\left(r^3\frac{\partial\Phi}{\partial r}\right)\right]^{1/2}, \qquad \psi = \left[\frac{\partial^2\Phi}{\partial z^2}\right]^{1/2}, \tag{34}$$

is constant. Its exponential $\boldsymbol{B} = \exp(-\boldsymbol{C}t)$ thus reads

$$\boldsymbol{B} = \begin{pmatrix} \cos\omega t & 0 & 0 & -\frac{\sin\omega t}{\omega} & \frac{\chi(1-\cos\omega t)}{\omega^2} & 0 \\ \frac{\chi\sin\omega t}{\omega} & 1 & 0 & -\frac{\chi(1-\cos\omega t)}{\omega^2} & \left(\frac{\chi^2}{\omega^2} - \frac{1}{r^2}\right)t - \frac{\chi^2\sin\omega t}{\omega^3} & 0 \\ 0 & 0 & \cos\psi t & 0 & 0 & -\frac{\sin\psi t}{\psi} \\ \omega\sin\omega t & 0 & 0 & \cos\omega t & -\frac{\chi\sin\omega t}{\omega} & 0 \\ 0 & 0 & 0 & 0 & 1 & 0 \\ 0 & 0 & \psi\sin\psi t & 0 & 0 & \cos\psi t \end{pmatrix}. \tag{35}$$

It is obvious from this matrix that for non-interacting particles the motion in vertical direction z is separated from the motion in the orbital plane and that it corresponds to simple harmonic oscillations with frequency ψ. Similarly, the perturbations of motion in r-direction have characteristic frequencies ω, however, due to angular-momentum conservation, they are coupled with perturbations in ϕ-direction. This degree of freedom complicates a bit the analogy between a simple non-linear coupling of two harmonic oscillators and QPOs of an orbiting ring. The term $B_{25} \equiv B_{\varphi p_\varphi}$ diverges linearly in time (unless the potential $\Phi \sim r^2$) what means that a cloud initially limited in φ ($A_{22}(t = 0) \neq 0$) cools in p_φ ($A_{55}(t) \to \infty$). It can be shown that the term $\bar c_{22} \equiv \bar c_{\varphi\varphi} \sim t^{-2} \to 0$, i.e., the cloud expands along its central circular trajectory (cf. Fig. 1 in Paper I) and asymptotically reaches the shape of axially symmetric ring (torus). It is important to note that even if we choose this shape *ab initio* ($A_{22} = 0$, as we shall assume in the following), in which case the coordinate φ can be suppressed, this degree of freedom still influences the oscillations in direction of coordinate r due to coupling with variations of the radial gradient of orbital velocity (shear) in the flow. The oscillations are no more sinusoidal, what means that the observed resonances need not correspond necessarily to the ratio of frequencies ω and ψ, but also multiples of ω can cause the resonance.

In the opposite approximation of ideal gas, i.e., the extremely strong relaxation with $\tau \to 0$, the orbiting ring can be described by matrix

$$\boldsymbol{A} = \begin{pmatrix} X & 0 & 0 & R & S & 0 \\ 0 & 0 & 0 & 0 & 0 & 0 \\ 0 & 0 & Z & 0 & 0 & T \\ R & 0 & 0 & P & 0 & 0 \\ S & 0 & 0 & 0 & P & 0 \\ 0 & 0 & T & 0 & 0 & P \end{pmatrix} . \tag{36}$$

The corresponding Eqs (28), (30) and (31) read

$$\dot{P} = \tfrac{2}{3}(R + T) , \tag{37}$$
$$\dot{R} = X - \omega^2 P , \tag{38}$$
$$\dot{S} = \chi R , \tag{39}$$
$$\dot{T} = Z - \psi^2 P , \tag{40}$$
$$\dot{X} = 2\omega^2 R , \tag{41}$$
$$\dot{Z} = 2\psi^2 T . \tag{42}$$

This linear set of equations has eigenvalues λ satisfying the relation

$$0 = \det\left(\frac{\partial(\dot{P}, \dot{R}, \dot{S}, \dot{T}, \dot{X}, \dot{Z})}{\partial(P, R, S, T, X, Z)} - \lambda\mathbf{1}\right) = \lambda^2(2\omega^2 - \lambda^2)\left(\frac{4}{3}\psi^2 - \lambda^2\right) . \tag{43}$$

The first two roots $\lambda = 0$ correspond to the stationary ring with radial and vertical dimensions given by $X = \omega^2 P$ and $Z = \psi^2 P$. The other roots $\lambda = \pm\sqrt{2}\,\omega$ and $\lambda = \pm\sqrt{4/3}\,\psi$

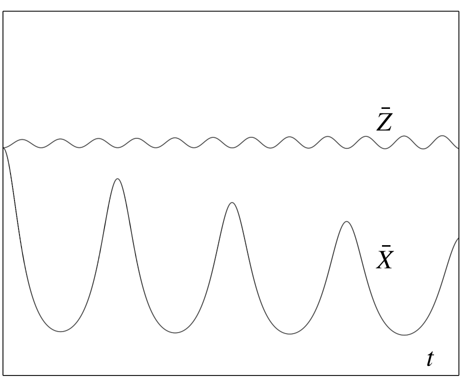

Figure 1. Oscillations of radial ($\bar{X}$) and vertical ($\bar{Z}$) widths of a gaseous torus with a weak relaxation in a potential with $\psi : \omega = 3 : 2$.

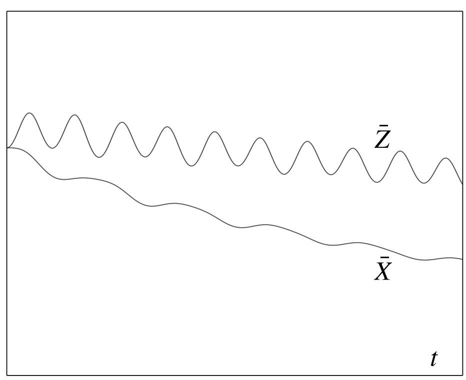

Figure 2. Oscillations of radial ($\bar{X}$) and vertical ($\bar{Z}$) widths of a gaseous torus with a strong relaxation.

correspond to the ring oscillations with these frequencies. Possible resonance of these oscillations occurs at different ratio $\omega : \psi$ and hence at a different radius of the ring than for the gas of non-interacting particles.

In the general non-linear case of moderately interacting particles we get a smooth transition between the two above described cases. In addition to the oscillations, the ring undergoes a secular enlargement in the radial direction due to angular-momentum transport, by which it approaches the shape of accretion disk with a small inner and large outer edge. Examples of results obtained by numerical integration of equations of the type of (18)–(20) are shown in Figs 1 and 2.

ACKNOWLEDGEMENTS

This work has been supported by grant GAČR 202/02/0735 and by project AV0Z 10030501.

REFERENCES

Abramowicz, M. A., Kluźniak, W., Stuchlík, Z. and Török, G. (2004), Twin peak QPOs frequencies in microquasars and Sgr A*. The resonance and other orbital models, in Hledík and Stuchlík (2004), pp. 1–23.

Hadrava, P. (1983), Simple kinetic model of a multi-particle cloud, *Bull. Astronom. Inst. Czechoslovakia*, **34**, pp. 234–241.

Hledík, S. and Stuchlík, Z., editors (2004), *Proceedings of RAGtime 4/5: Workshops on black holes and neutron stars, Opava, 14–16/13–15 October 2002/2003*, Silesian University in Opava, Opava, ISBN 80-7248-242-4.

Horák, J. (2004), General aspects of nonlinear resonance 3 : 2 in QPO context, in Hledík and Stuchlík (2004), pp. 91–110, `astro-ph/0408092`.

Kluźniak, W. and Abramowicz, M. A. (2001), Strong-field gravity and orbital resonance in black holes and neutron stars – kHz quasi-periodic oscillations (QPO), *Acta Phys. Polon. B*, **32**, pp. 3605–3612.

Török, G., Abramowicz, M. A., Kluźniak, W. and Stuchlík, Z. (2005), The orbital resonance model for twin peak kHz quasi periodic oscillations in microquasars, *Astronomy and Astrophysics*, **436**(1), pp. 1–8, `astro-ph/0401464`.

Proceedings of *RAGtime 6/7: Workshops on black holes and neutron stars, Opava, 16–18/18–20 September, 2004/2005*
S. Hledík and Z. Stuchlík, editors, Silesian University in Opava, Czech Republic, 2005, pp. 63–70

On polarization of light scattered on hot electron clouds

Jiří Horák

Astronomical Institute, Czech Academy of Sciences, Boční II 1401, CZ-141 31 Praha 4, Czech Republic

ABSTRACT
In this note we study polarization properties of radiation scattered on relativistic electrons in a hot cloud. The electron distribution is considered isotropic in the cloud comoving frame. We derive simple formulae for frequency-integrated Stokes parameters I, Q and U of the scattered radiation. The last parameter V vanishes because the resulting polarization is linear. The Stokes parameters are evaluated in the polarization frame comoving with the cloud, whose one basis vector is pointed along the direction of the scattered radiation and the two other basis vectors lie in the perpendicular observation plane. The incident unpolarized radiation comes into the formulae as components of the stress-energy tensor with respect to this reference frame. Our results are illustrated on a simple example of a cloud illuminated by a single beam of radiation.

1 INTRODUCTION

Electron scattering is an important phenomenon that influences observed radiation as well as dynamics of electrons in different types of astrophysical objects. Between 'classical' systems of interest are relativistic jets in active galactic nuclei. Many authors have studied an effect of Thomson scattering on jet velocity profiles (see, e.g., Noerdlinger, 1974; O'Dell, 1981; Sikora and Wilson, 1981; Phinney, 1982 for pioneering papers). The deceleration by ambient radiation field (also called radiation drag) has been recognized as an important factor that determines terminal speeds of jets (Sikora et al., 1996; Fukue, 2005). These ideas were more recently reconsidered in a connection with jets emerging from several galactic X-ray binaries (e.g., Renaud and Henri, 1998).

In some sources, light scattered by fast moving jets represent an important component of observed radiation. The scattering on relativistic electrons increases the photon energy up to X-rays or γ-rays and contributes to a non-zero linear polarization. Because of a small optical depth $\tau \ll 1$, one usually considers only single scattering. One of the first calculations of the polarization due to Thomson scattering in blazars was given by Begelman and Sikora (1987). The relative importance of the synchrotron and Compton scattered radiation in the polarized radiation from blazars was discussed by Poutanen (1994). The polarimetry may be important also in the case of radiation from gamma-ray bursts since it can help to discriminate between various geometries of their sources (Lazzati et al., 2004).

80-7248-334-X

Here, we consider intensity and polarization of light scattered on a hot optically thin cloud. The scatterers are relativistic electrons moving randomly in the cloud reference frame. This problem was extensively studied by Nagirner and Poutanen (1993), who considered scattering in an isotropic electron gas with Maxwellian or power-law energy distribution. Their rigorous formalism uses Klein–Nishina cross-section formula and allows to consider highly energetic as well as polarized incident radiation. On the other hand, in some astrophysical applications a single Thomson scattering provides sufficient approximation. The main results of the work presented here are three very simple formulae for the *frequency-integrated* Stokes parameters of the scattered radiation. The incident radiation field is included in terms of the relativistic stress-energy tensor $T^{\mu\nu}$. The derivation of the formulae is described in Section 2. Section 3 is devoted to a particular example of scattering on a cloud with monoenergetic electron distribution. Discussion and some concluding remarks follow in Section 4.

2 STOKES PARAMETERS OF THE SCATTERED LIGHT

We consider Thomson scattering in electrons of a warm cloud. The cloud is assumed to be optically thin so that it is sufficient to consider only single scattering. The Compton optical depth is $\tau = n\sigma_{\mathrm{T}}R$, where n is the electron number density, σ_{T} is the total Thomson cross-section and R is the size of the cloud. Electrons are moving with random velocity and their distribution is isotropic in the rest frame of the cloud (referred to as CF). The frame is defined by the orthonormal tetrad $\{\boldsymbol{u}, \boldsymbol{X}, \boldsymbol{Y}, \boldsymbol{Z}\}$, where the time-like four-vector $\boldsymbol{u}$ denotes cloud four-velocity. The observer is located along the $\boldsymbol{Z}$-vector that is introduced as a spatial projection of the four-momentum $\boldsymbol{p}$ of scattered photons, $\boldsymbol{Z} = \boldsymbol{u} - \boldsymbol{p}/\nu$, where $\nu = -\boldsymbol{p}\cdot\boldsymbol{u}$ is the frequency of the scattered radiation in CF.[1] The remaining two four-vectors, $\boldsymbol{X}$ and $\boldsymbol{Y}$ can be chosen arbitrary in the calculations. They form the polarization basis with respect to which the Stokes parameters of the scattered radiation are calculated. Spatial components of vectors and tensors with respect to CF are denoted by capital letters and indices are raised/lowered using the special-relativistic metric tensor $\eta_{\alpha\beta} = \mathrm{diag}(-1, 1, 1, 1)$.

The Lorentz factor γ and the relative velocity $\boldsymbol{\beta}$ of an electron with a four-velocity $\tilde{\boldsymbol{u}}$ measured by an observer in CF are given by $\gamma = -\tilde{\boldsymbol{u}}\cdot\boldsymbol{u}$ and $\boldsymbol{\beta} = \boldsymbol{u} - \tilde{\boldsymbol{u}}/\gamma$. Because $\boldsymbol{\beta}$ is a projection of $\tilde{\boldsymbol{u}}$ onto the three-space perpendicular to $\boldsymbol{u}$, its time component vanishes in CF. The non-vanishing components can be expressed as

$$\beta^X = \beta\sin\theta\cos\phi\,, \quad \beta^Y = \beta\sin\theta\sin\phi\,, \quad \beta^Z = \beta\cos\theta\,, \tag{1}$$

where θ and ϕ are referred to as the polar and azimuthal angle. One can easily check that $\gamma = (1-\beta^2)^{-1/2}$, where $\beta^2 \equiv \boldsymbol{\beta}\cdot\boldsymbol{\beta}$.

The isotropic electron distribution in the cloud frame is described by the electron distribution function $n(\boldsymbol{\beta}) = nf(\gamma)$, where n is the electron number density and the function $f(\gamma)$ is normalized to unity. Due to their additivity, the total Stokes parameters[2] $S = I, Q, U$

[1] We use units where $c = h = 1$.

[2] We remove the circularity V-parameter from our discussion because the Thomson scattering produces strictly linear polarization for which $V = 0$.

can be expressed as an integral

$$S = \int_{\gamma} f(\gamma) \int_{\phi} \int_{\theta} s(\gamma, \phi, \theta)\, \mathrm{d}\gamma\, \mathrm{d}\phi\, \mathrm{d}\theta\,, \tag{2}$$

where $s(\gamma, \phi, \theta)$ are Stokes parameters ($s = i, q, u$) of the radiation scattered by a swarm of electrons moving with the Lorentz factors from the interval $\langle\gamma, \gamma + \mathrm{d}\gamma\rangle$ in the direction described by the azimuthal and polar angles in the intervals $\langle\phi, \phi + \mathrm{d}\phi\rangle$ and $\langle\theta, \theta + \mathrm{d}\theta\rangle$. The Stokes parameters are measured in CF and the swarm has electron number density n (the same as the density of the whole cloudlet).

For the swarm we introduce a comoving frame with the orthonormal tetrad $\{\tilde{\boldsymbol{u}}, \tilde{\boldsymbol{X}}, \tilde{\boldsymbol{Y}}, \tilde{\boldsymbol{Z}}\}$ (referred to as swarm frame, SF), where the time-like four-vector $\tilde{\boldsymbol{u}}$ is the electron four-velocity and $\tilde{\boldsymbol{Z}}$ is projected four-momentum $\boldsymbol{p}$ onto the three-space perpendicular to $\tilde{\boldsymbol{u}}$, $\tilde{\boldsymbol{Z}} = \tilde{\boldsymbol{u}} - \boldsymbol{p}/\tilde{\nu}$. The frequency of the scattered radiation measured in SF is $\tilde{\nu} = -\boldsymbol{p} \cdot \tilde{\boldsymbol{u}}$. In addition, we chose the $\tilde{\boldsymbol{Y}}$-vector so that it is perpendicular to all three fourvectors $\boldsymbol{u}, \tilde{\boldsymbol{u}}, \boldsymbol{p}$.

The Stokes parameters of the scattered radiation $\tilde{\imath}$, $\tilde{q}$, $\tilde{u}$ with respect to SF can be expressed in terms of the stress-energy tensor of the incident radiation field as (Sobolev, 1963; Beloborodov, 1998; see also Horák and Karas, 2005)

$$\tilde{\imath} = A\left(\tilde{T}^{tt} + \tilde{T}^{ZZ}\right), \quad \tilde{q} = A\left(\tilde{T}^{YY} - \tilde{T}^{XX}\right), \quad \tilde{u} = A\left(\tilde{T}^{XY} + \tilde{T}^{YX}\right), \tag{3}$$

where $A \equiv 3\tau/16\pi$ and $\tilde{T}^{\mu\nu}$ denotes components of the stress-energy tensor in SF. They can be expressed in terms of the CF-components $T^{\mu\nu}$ using a Lorentz transform $\Lambda^{\mu}_{\nu}(\gamma, \theta, \phi)$ between CF and SF. With the aid of the transformation, Eqs (3) can be uniformly written as

$$\tilde{s} = A\, \tilde{M}^{(s)}_{\rho\sigma}\, T^{\rho\sigma} \tag{4}$$

with

$$\tilde{M}^{(i)}_{\rho\sigma} = \Lambda^{t}_{\rho}\Lambda^{t}_{\sigma} + \Lambda^{Z}_{\rho}\Lambda^{Z}_{\sigma}\,, \quad \tilde{M}^{(q)}_{\rho\sigma} = \Lambda^{Y}_{\rho}\Lambda^{Y}_{\sigma} - \Lambda^{X}_{\rho}\Lambda^{X}_{\sigma}\,, \quad \tilde{M}^{(u)}_{\rho\sigma} = \Lambda^{X}_{\rho}\Lambda^{Y}_{\sigma} + \Lambda^{Y}_{\rho}\Lambda^{X}_{\sigma}\,. \tag{5}$$

Let us consider a special case when the relative velocity of the electron swarm $\boldsymbol{\beta}$ lies in the $\boldsymbol{X}$-$\boldsymbol{Z}$ plane in CF (the azimuthal angle $\phi = 0$). The $\boldsymbol{Y}$-vector is perpendicular to all three four-vectors $\boldsymbol{u}$, $\tilde{\boldsymbol{u}}$ and $\boldsymbol{p}$ so that the Y-axes of the both reference frames are aligned, $\tilde{\boldsymbol{Y}} = \boldsymbol{Y}$. In that case all three Stokes parameters are transformed in the same way as the integrated intensity, keeping the fraction s/ν^4 invariant (Cocke and Holm, 1972). In a general case, when the velocity $\boldsymbol{\beta}$ has non-zero Y-component in CF, we perform a rotation of the frame about the Z-axis by angle ϕ. Applying the well known transformation rules of Stokes parameters under rotations (e.g., Rybicki and Lightman, 1979), we find that

$$i = \delta^4 \tilde{\imath}\,, \quad q = \delta^4 \left(\tilde{q}\cos 2\phi - \tilde{u}\sin 2\phi\right), \quad u = \delta^4 \left(\tilde{q}\sin 2\phi + \tilde{u}\cos 2\phi\right), \tag{6}$$

where $\delta \equiv \nu/\tilde{\nu} = [\gamma(1 - \beta\cos\theta)]^{-1}$ is Doppler factor.

The above transformations are valid if the source moves *as a whole* with respect to the observer. In our case, however, the source is *stationary* in the sense that it contains electrons with fast individual motions in random directions and a direction of motion of an individual electron is frequently changed. Hence, photons are essentially radiated from the constant place. In the former case, the Lorentz transformation contains also a contribution of the aberration effect. The Stokes parameters are expressed per time of observation $\mathrm{d}t$ in CF and per time of emission $\mathrm{d}\tilde{t}$ in SF. These two time intervals are related by $\mathrm{d}\tilde{t} = \gamma \mathrm{d}t$ if the source is stationary and radiates essentially from the same point or by $\mathrm{d}\tilde{t} = \gamma(1-\beta\cos\theta)\mathrm{d}t$ if the source is in a bulk motion and its distance from the observer is changing as $ct(1-\beta\cos\theta)$. For this reason, we complete the Lorentz transformation by an extra factor $(1-\beta\cos\theta) = 1/(\gamma\delta)$ (see also Begelman and Sikora, 1987; Blumenthal and Gould, 1970; and Rybicki and Lightman, 1979, sec. 4.8).

The expressions for the transformed Stokes parameters i, q and u can be written as

$$s = AM^{(s)}_{\rho\sigma}T^{\rho\sigma} \tag{7}$$

with matrices $M^{(s)}$ defined as

$$M^{(i)} = \frac{\delta^3}{\gamma}\,\tilde{M}^{(i)}\,, \tag{8}$$

$$M^{(q)} = \frac{\delta^3}{\gamma}\left(\tilde{M}^{(q)}\cos 2\phi - \tilde{M}^{(u)}\sin 2\phi\right)\,, \tag{9}$$

$$M^{(u)} = \frac{\delta^3}{\gamma}\left(\tilde{M}^{(q)}\sin 2\phi + \tilde{M}^{(u)}\cos 2\phi\right)\,, \tag{10}$$

and the matrices $\tilde{M}^{(s)}$ defined in Eq. (5).

The total Stokes parameters I, Q, U can be obtained by substituting Eq. (7) into the expression (2). The dependence of the Stokes parameters s on the Lorentz factor γ and direction of motion (angles ϕ and θ) is hidden in the matrix $M^{(s)}$ in Eq. (7). Hence, the stress-energy tensor of the incident radiation can be put outside the integral and knowing the distribution function $f(\gamma)$ the rest can be integrated. The Lorentz transformation $\Lambda^{\alpha}_{\beta}(\gamma,\theta,\phi)$ is derived in the Appendix A.

By integrating $M^{(i)}$, we find

$$\int_\gamma\int_\phi\int_\theta f M^{(i)}\,\mathrm{d}\theta\,\mathrm{d}\phi\,\mathrm{d}\gamma = \begin{pmatrix} 1+\mathcal{A} & 0 & 0 & -\mathcal{A} \\ 0 & \mathcal{B} & 0 & 0 \\ 0 & 0 & \mathcal{B} & 0 \\ -\mathcal{A} & 0 & 0 & 1+\mathcal{A}-2\mathcal{B} \end{pmatrix}, \tag{11}$$

where we define quantities

$$\mathcal{A} \equiv \frac{4}{3}\left\langle\gamma^2\beta^2\right\rangle, \quad \mathcal{B} \equiv 1 - \left\langle\frac{\ln[\gamma(1+\beta)]}{\beta\gamma^2}\right\rangle, \tag{12}$$

with notation $\langle x\rangle \equiv \int x f(\gamma)\,\mathrm{d}\gamma$ for averaging over the electron Lorentz factor γ. According to Eq. (2), the total intensity scattered into the direction $\boldsymbol{Z}$ in CF can be expressed as

$$I = A\left[(1+\mathcal{A})\left(T^{tt}+T^{ZZ}\right) + \mathcal{B}\left(T^{tt}-3T^{ZZ}\right) - 2\mathcal{A}T^{tZ}\right], \tag{13}$$

where we use the identity $T^{XX} + T^{YY} = T^{tt} - T^{ZZ}$.

Similar calculations lead to the formulae for two other Stokes parameters,

$$Q = A\left(T^{YY} - T^{XX}\right) \quad \text{and} \quad U = -2\,A\,T^{XY}\,. \tag{14}$$

These are, however, same as if the radiation was scattered by a cold cloud.

3 EXAMPLE: A MONOENERGETIC ELECTRON DISTRIBUTION

We illustrate our results on a simple example. The electron distribution function in CF is monoenergetic, $f(\gamma) = \delta(\gamma - \gamma_0)$. All electrons have the same energy $\gamma_0 m_e$, with m_e being the electron rest mass. The averaging in expressions (12) is trivial. We obtain

$$\mathcal{A} = \frac{4}{3}(\gamma_0^2 - 1)\,, \quad \mathcal{B} = 1 - \frac{\ln\left[\gamma_0 + \sqrt{\gamma_0^2 - 1}\right]}{\gamma_0\sqrt{\gamma_0^2 - 1}}\,. \tag{15}$$

We consider a narrow beam of incident radiation that propagates in the direction $\boldsymbol{n}$ in the cloud reference frame.[3] This four-vector and the direction of observation $\boldsymbol{Z}$ make the angle ϑ. Obviously, all properties of the scattered radiation depend only on this angle and we can assume without any loss of generality that $n^Y = 0$. The two other components are $n^X = \sin\vartheta$ and $n^Z = \cos\vartheta$. The integrated intensity of the incident radiation is I_0 and the nonzero components of the stress-energy tensor of the incident radiation are

$$T^{tt} = I_0\,, \quad T^{tZ} = I_0\,n^Z\,, \quad T^{ZZ} = I_0\,n^Z n^Z\,, \quad T^{XX} = I_0\,n^X n^X\,. \tag{16}$$

The total amount of radiation scattered on the cloud is proportional to τI_0. We use it to introduce normalized Stokes parameters $I_\star$ and $Q_\star$ of the scattered radiation. The remaining parameter U is zero because of the symmetry with respect to the $X - Z$ plane. Using Eqs (13), (14) and (16) we find

$$I_\star \equiv \frac{I}{\tau I_0} = \frac{3}{16\pi}\left[(1 + \mathcal{A} - 3\mathcal{B})\cos^2\vartheta - 2\mathcal{A}\cos\vartheta + (1 + \mathcal{A} + \mathcal{B})\right]\,, \tag{17}$$

$$Q_\star \equiv \frac{Q}{\tau I_0} = -\frac{3}{16\pi}\sin^2\vartheta\,. \tag{18}$$

The angular dependence of the scattered intensity $I_\star$ on the angle of observation ϑ for different values of γ_0 is shown in the left panel of Fig. 1. In the case of a cloud containing cold electrons ($\gamma_0 = 1$) both $\mathcal{A}$ and $\mathcal{B}$ are zero and the angular dependence of the scattered intensity reduces to $I \propto 1 + \cos^2\vartheta$ – the same as for Thomson scattering on a single electron. The scattering on a cold cloud is symmetric with respect to the plane perpendicular to the direction of the incident radiation beam. On the other hand, if the cloud contains

[3] The fourvector $\boldsymbol{n}$ is a projection of the incident photon four-momentum onto the three-space perpendicular to the four-velocity $\boldsymbol{u}$.

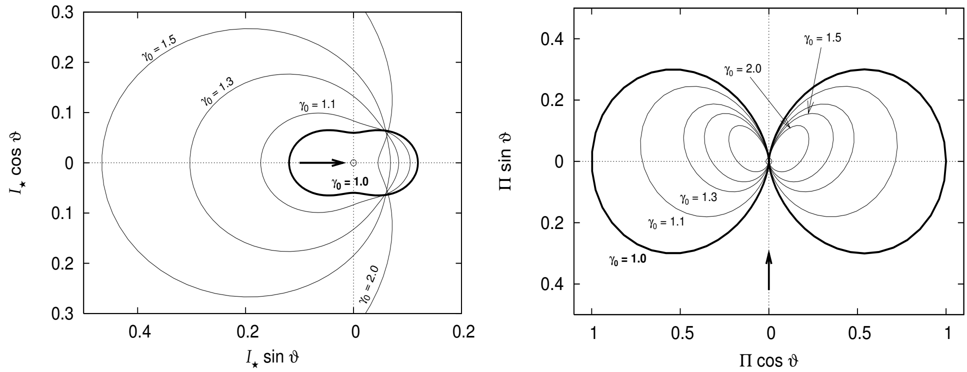

Figure 1. *Left:* the normalized scattered intensity $I_\star$ as a function of the scattering angle ϑ between the direction of the incident radiation beam and the direction of observation. The scattering occurs on the hot electron cloud. Different curves corresponds to different values of the electron Lorentz factor measured in the blob reference frame. The case of cold electron corresponds to $\gamma_0 = 1$. *Right:* the magnitude of transversal polarization Π as a function of the scattering angle for several values of the electron Lorentz factor. The depolarization effect of the electron motions and the shift of the angle of maximal polarization are apparent.

ultrarelativistic electrons with $\gamma_0 \gg 1$, we have $\mathcal{A} \approx 4/3\gamma_0^2$, $\mathcal{B} \approx 1$ and Eq. (13) gives the angular dependence $I \propto \gamma_0^2(1 - \cos\vartheta)^2$, which is highly asymmetric. Most of the radiation is scattered in the backward direction. This is important regarding a dynamics of the cloud: the scattered radiation transports momentum from the electrons in the backward direction so that the hot clouds are more strongly accelerated by the incident radiation. This effect called *Compton rocket*, was firstly studied by O'Dell (1981) and later reconsidered by Phinney (1982).

The direction of polarization of the scattered radiation is parallel to the $\boldsymbol{Y}$-vector in CF because $Q_\star < 0$ (see a discussion of the polarization direction in Horák and Karas, 2005). The polarization magnitude is given as a ratio $\Pi = |Q_\star|/I_\star$, because both U and V vanish. The angular dependence of the polarization magnitude is shown in the right panel of Fig. 1. In the case of the cold cloud, the expression for the polarization is identical with the well known expression for the scattering on a single electron, $\Pi = (1 - \cos^2\vartheta)/(1 + \cos^2\vartheta)$ giving the maximal value of unity for a completely polarized radiation when $\vartheta_{\mathrm{m,cold}} = \pi/2$. However, the polarization is reduced by a factor $\sim \gamma_0^2$ if the cloud contains relativistic electrons. The maximal polarization occurs closer to the direction of the incident radiation, because of the asymmetric profile of the scattered intensity. Simple algebra gives the angle ϑ_{m} along which an observer receives radiation with the highest polarization

$$\cos\vartheta_{\mathrm{m}} = \frac{1}{\mathcal{A}}\left[1 + \mathcal{A} - \mathcal{B} - \sqrt{(1 - \mathcal{B})(1 + 2\mathcal{A} - \mathcal{B})}\right]. \tag{19}$$

This angle approaches zero as the electron Lorentz factor increases. However, the polarization is strongly reduced in that case.

4 CONCLUSIONS

In this note we studied polarization properties of the Thomson-scattered radiation on the cloud with relativistic electrons. The frequency-integrated Stokes parameters are given by Eqs (13) and (14). The incident unpolarized radiation comes into the formulae as components $T^{\alpha\beta}$ of the stress-energy tensor with respect to the comoving polarization frame. The same quantity determines also a dynamics of the cloud (see, e.g., Phinney, 1982). Our results are useful when one considers the polarization effect on the scattered radiation together with the dynamical effects on the cloud (see, e.g., Horák and Karas, 2005).

ACKNOWLEDGEMENTS

This work was supported by GAČR grant 205/06/P415.

REFERENCES

Begelman, M. C. and Sikora, M. (1987), *Astrophys. J.*, **322**, p. 650.

Beloborodov, A. M. (1998), *Astrophys. J.*, **496**, p. L105.

Blumenthal, G. R. and Gould, R. J. (1970), *Rev. Modern Phys.*, **42**, p. 237.

Cocke, W. J. and Holm, D. A. (1972), *Nature Physical Science*, **240**, p. 161.

Fukue, J. (2005), *PASJ*, **57**, p. 691.

Horák, J. and Karas, V. (2005), *Monthly Notices Roy. Astronom. Soc.*, **365**, p. 813.

Lazzati, D., Rossi, E., Ghisellini, G. and Rees, M. J. (2004), *Monthly Notices Roy. Astronom. Soc.*, **347**, p. L1.

Nagirner, D. I. and Poutanen, J. (1993), *Astronomy and Astrophysics*, **275**, p. 325.

Noerdlinger, P. D. (1974), *Astrophys. J.*, **192**, p. 529.

O'Dell, S. L. (1981), *Astrophys. J.*, **243**, p. L147.

Phinney, E. S. (1982), *Monthly Notices Roy. Astronom. Soc.*, **198**, p. 1109.

Poutanen, J. (1994), *Astrophys. J. Suppl.*, **92**, p. 607.

Renaud, N. and Henri, G. (1998), *Monthly Notices Roy. Astronom. Soc.*, **300**, p. 1047.

Rybicki, G. B. and Lightman, A. P. (1979), *Radiative Processes in Astrophysics*, Wiley, New York.

Sikora, M., Sol, H., Begelman, M. C. and Madejski, G. M. (1996), *Monthly Notices Roy. Astronom. Soc.*, **280**.

Sikora, M. and Wilson, D. B. (1981), *Monthly Notices Roy. Astronom. Soc.*, **198**, p. 529.

Sobolev, V. V. (1963), *A treatise on radiative transfer*, Van Nostrand, Princeton, N.J.

APPENDIX A: LORENTZ TRANSFORM

Here, we derive the Lorentz transform $\Lambda^{\alpha}_{\beta}(\theta, \phi)$ between CF and SF. First, let us consider the case $\phi = 0$. The Y-axes of both frames are aligned ($\boldsymbol{Y} = \tilde{\boldsymbol{Y}}$) as it was discussed in Section 2. The remaining tetrad four-vectors $\boldsymbol{X}$, $\tilde{\boldsymbol{X}}$, $\boldsymbol{Z}$ and $\tilde{\boldsymbol{Z}}$ of both frames can be expressed as linear combinations of $\boldsymbol{u}$, $\tilde{\boldsymbol{u}}$ and $\boldsymbol{p}$. The components of the Lorentz transform matrix can be expressed as scalar products

$$\Lambda^{\alpha}_{\beta} = \tilde{\boldsymbol{e}}^{(\alpha)} \cdot \boldsymbol{e}_{(\beta)}\,, \tag{A1}$$

of corresponding covariant and contravariant basis four-vectors $\tilde{\boldsymbol{e}}^{(\alpha)} = \{\tilde{\boldsymbol{u}}, \tilde{\boldsymbol{X}}, \tilde{\boldsymbol{Y}}, \tilde{\boldsymbol{Z}}\}$ and $\boldsymbol{e}_{(\alpha)} = \{-\boldsymbol{u}, \boldsymbol{X}, \boldsymbol{Y}, \boldsymbol{Z}\}$, respectively. We find

$$\Lambda^{\alpha}_{\beta}(\theta) = \begin{pmatrix} \gamma & -\gamma\beta\sin\theta & 0 & -\gamma\beta\cos\theta \\ -k & 1 & 0 & k \\ 0 & 0 & 1 & 0 \\ l & -\gamma\beta\sin\theta & 0 & m \end{pmatrix} \tag{A2}$$

with

$$k = \gamma\delta\beta\sin\theta\,, \quad l = \gamma^2\beta\delta(\beta - \cos\theta)\,, \quad m = \delta - \gamma\beta\cos\theta\,. \tag{A3}$$

In the more general case when the three-velocity $\vec{\beta}$ and $\boldsymbol{Y}$-vector make nonzero azimuthal angle ϕ, we make the rotation about the $\boldsymbol{Z}$-axis through angle ϕ. The final Lorentz transform is given by $\Lambda(\theta, \phi) = \Lambda(\theta)R_Z(\phi)$. We find

$$\Lambda^{\alpha}_{\beta}(\phi, \theta) = \begin{pmatrix} \gamma & -\gamma\beta\sin\theta\cos\phi & -\gamma\beta\sin\theta\sin\phi & -\gamma\beta\cos\theta \\ -k & \cos\phi & \sin\phi & k \\ 0 & -\sin\phi & \cos\phi & 0 \\ l & -\gamma\beta\sin\theta\cos\phi & -\gamma\beta\sin\theta\sin\phi & m \end{pmatrix}. \tag{A4}$$

Proceedings of *RAGtime 6/7: Workshops on black holes and neutron stars, Opava, 16–18/18–20 September, 2004/2005*
S. Hledík and Z. Stuchlík, editors, Silesian University in Opava, Czech Republic, 2005, pp. 71–80

An introduction to relativistic magnetohydrodynamics I. The force-free approximation

Vladimír Karas

Astronomical Institute, Czech Academy of Sciences, Boční II 1401, CZ-141 31 Praha 4, Czech Republic
Charles University in Prague, Faculty of Mathematics and Physics, V Holešovičkách 2, Praha, Czech Republic

ABSTRACT
This lecture summarizes basic equations of relativistic magnetohydrodynamics (MHD). The aim of the lecture is to present important relations and approximations that have been often employed and found useful in the astrophysical context, namely, in situations when plasma motion is governed by magnetohydrodynamic and gravitational effects competing with each other near a black hole.

1 INTRODUCTION

Different arguments can be put forward in order to demonstrate that magnetohydrodynamic effects dominate the behaviour of cosmic plasma and must be taken into account. Near compact bodies, black holes in particular, the gravitational terms cannot be ignored, and so the general-relativity MHD needs be employed. This is a daunting task. As a starting point in this lecture we describe basic equations that have been developed by various authors during past three to four decades. The main intention is to give premises and to suggest selected references that would help entering the complex subject. Only axially symmetric and stationary flows will be considered here.

The field of astrophysical MHD has been covered in textbooks and review articles (see, e.g., Cowling, 1976; Melrose, 1980; Zel'dovich et al., 1983; Lynden-Bell, 1994). The applications relate to entire astrophysics, ranging from solar physics to accretion discs; in our case, the original motivation comes from the studies of partical acceleration near neutron stars where strong electromagnetic fields and inertial effects are present (Pacini, 1968; Goldreich and Julian, 1969; Michel, 1982). Strength of the magnetic intensity is maintained and considerably increased near an accreting object. Magnetic fields can be amplified by the dynamo action in the disk (Balbus and Hawley, 1992; Krause et al., 1992; Balbus, 2003). It is quite understandable that complications arising from the inclusion of electromagnetic effects can be accommodated only under various simplifying assumptions.

80-7248-334-X

Maxwell's and Euler's equations are the relevant prerequisites for this paper. They adopt the following form. Maxwell's equations (i.e., Ampere's law and Faraday's law) are written here in the form of non-vacuum equations:

$$\nabla \times \boldsymbol{B} = \frac{4\pi}{c}\boldsymbol{j} + \frac{1}{c}\frac{\partial \boldsymbol{D}}{\partial t}\,, \qquad \nabla \cdot \boldsymbol{B} = 0\,, \tag{1}$$

$$\nabla \times \boldsymbol{E} = -\frac{1}{c}\frac{\partial \boldsymbol{B}}{\partial t}\,, \qquad \nabla \cdot \boldsymbol{E} = 4\pi\rho_{\mathrm{e}}\,, \tag{2}$$

with ρ_{e} and $\boldsymbol{j}$ being density of all electric charges and currents. Euler's equation adopts the appropriate form:

$$\rho\frac{\partial \boldsymbol{v}}{\partial t} + \rho\,\boldsymbol{v}\cdot\nabla\boldsymbol{v} = -\nabla P + \boldsymbol{f} \tag{3}$$

with

$$\boldsymbol{f} = \boldsymbol{f}_{\mathrm{L}} + \boldsymbol{f}_{\mathrm{g}} = \rho_{\mathrm{e}}\boldsymbol{E} + c^{-1}\boldsymbol{j}\times\boldsymbol{B} - \rho\boldsymbol{g} \tag{4}$$

being the Lorentz and gravitational terms, respectively. Finally, for the sake of simplification, the assumptions about axial symmetry and stationarity are imposed. The above is the "usual" form of the equations (i.e., without general relativity taken into account), however, reformulation is possible in which the look of these equations remains familiar also when strong gravitational fields are present (Thorne et al., 1986).

The primary distinction between the models with and without a black hole consists in different boundary conditions imposed upon the electromagnetic field, which threads the black hole horizon. The relevant Maxwell equations describing the field outside the black hole horizon can be solved by introducing appropriate imaginary currents flowing on the surface of the horizon. These are defined in such a way that the boundary conditions are satisfied. Currents flowing along the field lines can thus close a circuit and the energy extraction is then described in an analogous way as in our previous discussion of magnetized disks or as in the theory of pulsar emission (Blandford, 1976; Camenzind, 1986a).

2 FORCE-FREE AXISYMMETRIC MHD

Let us first start by employing the traditional three-vector formalism. The equations given above are further simplified by assuming the force-free approximation, which adopts a simple mathematical formulation:

$$\rho_{\mathrm{e}}\boldsymbol{E} + c^{-1}\boldsymbol{j}\times\boldsymbol{B} = \boldsymbol{0}\,. \tag{5}$$

The physical interpretation and consequences of the above relation require a thorough discussion. Equation (5) tells us that inertia of the material is neglected. In other words, the influence of the Lorentz force acting on plasma in the comoving frame gets neutralized immediately by induced electric currents; perfect conductivity is thus assumed. (A dimension-less condition for the validity of the force-free approximation is $\rho\Gamma v^2/B^2 \ll 1$.) This is similar to the assumption of ideal MHD,

$$\boldsymbol{E}' \equiv \boldsymbol{E} + c^{-1}\boldsymbol{v}\times\boldsymbol{B} = \boldsymbol{0} \tag{6}$$

(where $\boldsymbol{E}'$ is the electric field in the system attached to plasma). Both approximations are equivalent if the current density is proportional to the velocity of the medium, $\boldsymbol{j} = \rho_{\mathrm{e}}\boldsymbol{v}$. (A more general formula for the current density that still satisfies the force-free assumption Eq. (5) has a form $\boldsymbol{j} = \rho_{\mathrm{e}}\boldsymbol{v} + \mu\boldsymbol{B}$; μ is a scalar function to be determined.) Both the force-free and the perfect MHD fields are degenerate, i.e., $\boldsymbol{E} \cdot \boldsymbol{B} = 0$. The approximation of ideal MHD can be understood as an assumption about perfect electric conductivity of the material. Substituting

$$\boldsymbol{j} = \sigma\boldsymbol{E}' \tag{7}$$

for the vector of electric field from Ohm's law (σ designates specific conductivity of the medium) and assuming perfect conductivity ($\sigma \to \infty$), we find

$$\nabla \times (\boldsymbol{v} \times \boldsymbol{B}) = \frac{\partial \boldsymbol{B}}{\partial t}\,. \tag{8}$$

Equation (8) expresses the freezing of the magnetic field in plasma material. The reason for this denomination is evident upon realizing that the magnetic flux across an imaginary loop $\mathcal{L}$ flowing together with the medium can be written as a sum of two terms, the first one being determined by motion of the loop,

$$\int_{\mathcal{S}} \nabla \times (\boldsymbol{v} \times \boldsymbol{B}) \cdot \mathrm{d}\boldsymbol{\mathcal{S}} = \oint_{\mathcal{L}} (\boldsymbol{v} \times \boldsymbol{B}) \cdot \mathrm{d}\boldsymbol{\mathcal{L}} = -\oint_{\mathcal{L}} \boldsymbol{B} \cdot (\boldsymbol{v} \times \mathrm{d}\boldsymbol{\mathcal{L}})\,. \tag{9}$$

The term $\partial\boldsymbol{B}/\partial t$ on the right-hand side of (8) corresponds to the change of the magnetic flux due to the explicit time-dependence of $\boldsymbol{B}$,

$$\int_{\mathcal{S}} \frac{\partial \boldsymbol{B}}{\partial t} \cdot \mathrm{d}\boldsymbol{\mathcal{S}}\,. \tag{10}$$

Equation (8) thus expresses the fact that the magnetic flux across any arbitrary closed loop remains constant. As we have seen before, one can also understand this equation as a condition for the electric field to vanish in the rest frame of plasma. The validity of the above approximations must always be verified separately in each given situation.

We will now examine the basic relations valid for axially symmetric magnetohydrodynamic equilibrium configurations under forces of gravity. It should be noted that relevant equations are capable of describing, for example, aligned rotators of the pulsar theory, magnetized disks or magnetized outflows and inflows of matter as special cases (Camenzind, 1986b; Lovelace et al., 1986). Again, we adopt the assumption of axial symmetry and stationarity and we set $\partial/\partial\phi = 0$, $\partial/\partial t = 0$ in all formulae. Starting equations are: mass conservation law (the continuity equation); momentum conservation law – the Euler equation (supplemented by the relation for the external force $\boldsymbol{f} = c^{-1}\boldsymbol{j} \times \boldsymbol{B} - \rho\boldsymbol{g}$; we assume an electrically neutral plasma, $\rho_{\mathrm{e}} = 0$); Maxwell's equations; perfect MHD condition; formula for gravitational acceleration $\boldsymbol{g}$ (e.g., in the form of Poisson's equation $\Delta\Phi = 4\pi G\rho$); the first law of thermodynamics; and the equation of state.

It follows from Faraday's law and conditions of axial symmetry and stationarity ($\nabla \times \boldsymbol{E} = \boldsymbol{0}$) that the toroidal part $\boldsymbol{E}_{\mathrm{T}}$ of electric field (the component in the azimuthal direction, the value of which is given by $E_{\phi}^2 = \boldsymbol{E}_{\mathrm{T}} \cdot \boldsymbol{E}_{\mathrm{T}}$) vanishes:

$$E_{\phi} = 0\,. \tag{11}$$

Perfect MHD condition implies the relation for the poloidal flow velocity

$$\boldsymbol{v}_{\mathrm{P}} = \xi \boldsymbol{B}_{\mathrm{P}} \,, \tag{12}$$

where $\xi(R,z)$ is a (yet undetermined) scalar function. It is advantageous at this point to introduce into the Maxwell equations the vector potential $\boldsymbol{A}$ and the scalar magnetic flux function, $\Psi(R,z) \equiv RA_{\phi}$. Components of $\boldsymbol{B}_{\mathrm{P}}$ in terms of Ψ read $B_R = -\Psi_{,z}/R$, $B_z = \Psi_{,R}/R$, where the coma denotes partial differentiation. It is now evident from Eq. (12) that

$$4\pi\rho\xi = F_1(\Psi) \,, \tag{13}$$

where $F_1(\Psi)$ is an arbitrary function to be specified by the boundary conditions and symmetries of the required solution. (We have applied the Maxwell equation $\nabla\cdot\boldsymbol{B} = \nabla\cdot\boldsymbol{B}_{\mathrm{P}} = 0$ and the continuity equation.) We will see that there is a set of such functions of Ψ that determine a specific solution. Each function can be identified with some conserved quantity (derivation of F_1 utilizes the mass conservation equation). The existence of flux functions, which remain constant on magnetic surfaces $\Psi = $ const, is crucial in investigating axisymmetric hydromagnetic flows (Chandrasekhar, 1961).

It follows from $\boldsymbol{v}_{\mathrm{P}} = \xi\boldsymbol{B}_{\mathrm{P}}$ [Eq. (12)] that

$$\boldsymbol{v} \times \boldsymbol{B} = \boldsymbol{v}_{\mathrm{T}} \times \boldsymbol{B}_{\mathrm{P}} + \boldsymbol{v}_{\mathrm{P}} \times \boldsymbol{B}_{\mathrm{T}} = \frac{v_{\phi} - \xi B_{\phi}}{R}\,\nabla\Psi \,. \tag{14}$$

Curl of the last equation vanishes in accordance with the perfect MHD condition and Faraday's law so that another stream function, F_2, can be introduced in the following way:

$$\frac{v_{\phi} - \xi B_{\phi}}{R} = F_2(\Psi), \qquad \boldsymbol{E} = -c^{-1}F_2(\Psi)\nabla\Psi \,. \tag{15}$$

Further relations are obtained by projections of the Euler equation and can be derived via straightforward but lengthy manipulations. The toroidal part reads

$$\boldsymbol{B}_{\mathrm{P}} \cdot \nabla(RB_{\phi} - F_1 R v_{\phi}) \,. \tag{16}$$

For analogous reasons as those that have been presented with Eq. (12), the term in parentheses is also a function of Ψ only, say $F_3(\Psi)$. Other two independent relations can be obtained by projecting the Euler equation into the poloidal plane. The projection along $\boldsymbol{B}_{\mathrm{P}}$ yields the Bernoulli equation

$$\frac{1}{2}v^2 + \int_{\Psi=\mathrm{const}} \frac{\mathrm{d}P}{\rho} + \Phi - Rv_{\phi}F_3 = F_4(\Psi) \,. \tag{17}$$

Compared to the hydrodynamical form of Bernoulli integral, in which electromagnetic effects are not been considered, the additional term $Rv_{\phi}F_3$ corresponds to the electromagnetic (Poynting) energy transport. The projection of the poloidal component of the Euler equation to the direction parallel to $\nabla\Psi$ (the third independent projection) is known as the Grad–Shafranov equation (Beskin and Kuznetsova, 2000; Ioka and Sasaki, 2003). This is a non-linear differential equation for Ψ, the explicit form of which naturally depends on the equation of state and on stream functions F_k. For example, we set $F_1 = 0$ if no poloidal flow of material is required *a priori* (the case of disks). Force-free approximation to the Grad–Shafranov equation is equivalent to the self-consistent form of the pulsar equation from the astrophysical literature (Cohen et al., 1973; Scharlemann and Wagoner, 1973). Within the general relativity framework, its applications to rotating compact stars and black holes have been discussed recently examined by Kim et al. (2005). On the other hand, laboratory plasma is often described within the approximation of a vanishing material flow, $F_1 = F_2 = 0$, and negligible gravity, $\Phi = 0$ (tokamaks).

Electromagnetic forces act on charged particles and may substantially modify the structure of accretion disks (Michel, 1982, 1983). The inclusion of electromagnetic effects makes the disk theory much more complex. A simplified approach is possible in terms of self-similar solution of axially symmetric MHD equations (Königl, 1989). Here we will illustrate the basic assumptions of simple analytical models, which are not realistic but can train our intuition. The procedure for constructing magnetized disk solutions can go as follows: (i) Choose cylindrical polar coordinates $\{R, \phi, z\}$. (ii) Assume a steady electric current $\boldsymbol{j} = j_\phi \boldsymbol{e}_\phi$ at $z = 0$ (the equatorial plane) with a corresponding structure of magnetic induction – $B_R, B_z \neq 0$, and $B_\phi = 0$. The distribution of $j_\phi(R)$ then determines the structure of the magnetic field lines. The system under discussion is axially symmetric and stationary, and thus emits no electromagnetic radiation.

Consider a magnetized disk in the equatorial plane and assume that the magnetic field is frozen into the disk. The toroidal part of the field arises from the dragging of the magnetic field by the disk material. It follows that $\boldsymbol{B}_{\rm T} = B_\phi \boldsymbol{e}_\phi$, $\boldsymbol{B}_{\rm P} = \boldsymbol{B} - \boldsymbol{B}_{\rm T} = B_R \boldsymbol{e}_R + B_z \boldsymbol{e}_z$. One proceeds analogously in deriving the electric intensity $\boldsymbol{E}$ but in this case $\boldsymbol{E}_{\rm T} = \boldsymbol{0}$ [cf. Eq. (11)].

Basic relations adopt the following form: The Maxwell equation $\nabla \cdot \boldsymbol{B} = 0$ together with the consequence of axial symmetry, $\nabla \cdot \boldsymbol{B}_{\rm T} = 0$, yield $\nabla \cdot \boldsymbol{B}_{\rm P} = 0$. This means that both the poloidal and the toroidal components can be separately associated with unending field lines. The value of $\boldsymbol{E}_{\rm P}$ follows from the force-free condition:

$$\boldsymbol{0} = \boldsymbol{E}' = \boldsymbol{E}_{\rm P} + c^{-1}(\boldsymbol{\Omega} \times \boldsymbol{r}) \times \boldsymbol{B}\,, \tag{18}$$

where $\boldsymbol{\Omega} = \Omega^{\rm F} \boldsymbol{e}_\phi$ means the angular velocity of each field line and $\boldsymbol{r}$ is the radius vector. Charged particles move along field lines. Using $\nabla \times \boldsymbol{E}_{\rm P} = \boldsymbol{0}$ and $\nabla \cdot \boldsymbol{B}_{\rm P} = 0$ we find

$$\boldsymbol{B}_{\rm P} \cdot \nabla \Omega^{\rm F} = 0\,. \tag{19}$$

In other words, the angular velocity of each field line remains constant along its curve; thus $\Omega^{\rm F}$ does not change along poloidal field lines. This result is called Ferraro's law of iso-rotation (Ferraro and Plumpton, 1961).

The light surface is the locus of points where the velocity of the field lines approaches the speed of light. Charged particles cannot corotate with field lines beyond the light surface; instead, they are forced to move away and this is the basis of particle acceleration around pulsars and possibly formation of jets in extragalactic sources. The disk itself can serve as a source of particles. Assuming the perfect MHD condition inside the disk, we obtain for the particle density

$$n = \frac{1}{4\pi q_e} \nabla \cdot \boldsymbol{E} = -\frac{1}{4\pi q_e c} \nabla \cdot (\boldsymbol{v} \times \boldsymbol{B}) = -\frac{1}{2c}\, \Omega B_\phi\,. \tag{20}$$

Non-zero charge-density generates an electric field, which pulls charged particles out of the disk.

Magnetic field lines threading the disk exert a torque on its material

$$\boldsymbol{G} = \boldsymbol{R} \times (\boldsymbol{j} \times \boldsymbol{B})\,, \tag{21}$$

and are thus a source of effective viscosity. Such a disk does not radiate (remember that we are considering axisymmetric stationary configurations) but it can still transmit energy in a direct-current flux.

Consider now a circle of radius R centred on the symmetry axis. Ampere's law yields

$$B_\mathrm{T} = \frac{2J}{cR}\,. \tag{22}$$

We have already mentioned that in the force-free region currents flow along magnetic surfaces, but in the disk and in the far region the force-free condition is violated and dissipation occurs. The density of the electromagnetic energy flowing through the force-free region is given by

$$\boldsymbol{P} = c\boldsymbol{E} \times \boldsymbol{B} \approx c\boldsymbol{E}_\mathrm{P} \times \boldsymbol{B}_\mathrm{T}\,. \tag{23}$$

Substituting for $\boldsymbol{E}_\mathrm{P}$ from Eq. (18) we estimate the magnitude of this vector as

$$\mathcal{P} \approx \Omega R B_\mathrm{P} B_\mathrm{T}\,. \tag{24}$$

B_P and B_T are to be determined in accordance with the boundary conditions.

3 MHD IN THE GENERAL RELATIVITY FRAMEWORK

The following discussion is a general relativistic generalization of axially symmetric MHD flows that have been treated in previous chapters. We will employ the standard notation of general relativity with geometrized units, $c = G = 1$, and the signature of metric $- + ++$ in this chapter. The set of equations of perfect magnetohydrodynamics can be written in the following form (Anile and Choquet-Bruhat, 1989; Lichnerowitz, 1967).

Conservation of the particle number:

$$\left(\rho_0 u^\alpha\right)_{;\alpha} = 0\,, \qquad \rho_0 = mn\,; \tag{25}$$

m is the particle rest mass, n numerical density, u^α four-velocity. Here we do not consider a possibility of creation of pairs, which would break this conservation law.

Normalization condition for four-velocity:

$$u^\alpha u_\alpha = -1\,. \tag{26}$$

Energy-momentum conservation and the definition of energy-momentum tensor in terms of material density ρ, pressure P, and electromagnetic field tensor $F_{\mu\nu}$:

$$T^{\alpha\beta}{}_{;\beta} = 0\,, \tag{27}$$
$$T^{\alpha\beta} = T^{\alpha\beta}_{\mathrm{matter}} + T^{\alpha\beta}_{\mathrm{EMG}}\,, \tag{28}$$
$$T^{\alpha\beta}_{\mathrm{matter}} = (\rho + p)u^\alpha u^\beta + p g^{\alpha\beta}\,, \tag{29}$$
$$T^{\alpha\beta}_{\mathrm{EMG}} = \frac{1}{4\pi}\left(F^{\alpha\mu}F^\beta_\mu - \frac{1}{4}F^{\mu\nu}F_{\mu\nu}g^{\alpha\beta}\right), \tag{30}$$
$$F_{\mu\nu} = A_{\nu,\mu} - A_{\mu,\nu}\,. \tag{31}$$

In the fluid rest frame, electric field is assumed to vanish completely:

$$F_{\alpha\beta}u^\beta = 0\,. \tag{32}$$

The axial symmetry and stationarity guarantee the existence of two Killing vectors, $k^\alpha = \delta^\alpha_t$ and $m^\alpha = \delta^\alpha_\phi$, which satisfy relations

$$0 = k_\alpha T^{\alpha\beta}{}_{;\beta} = \left(k_\alpha T^{\alpha\beta}\right)_{;\beta}\,, \tag{33}$$
$$0 = m_\alpha T^{\alpha\beta}{}_{;\beta} = \left(m_\alpha T^{\alpha\beta}\right)_{;\beta}\,. \tag{34}$$

Let us now turn to the consequences of the above Eqs (25)–(34), which are particularly relevant for the theory of black hole magnetospheres (Blandford and Znajek, 1977; Hirotani et al., 1992; Znajek, 1976). Equation (32) has four components that can be written in explicit way:

$$A_{t,r}u^r + A_{t,\theta}u^\theta = 0\,, \tag{35}$$
$$A_{t,r}u^t + A_{\phi,r}u^\phi + F_{r\theta}u^\theta = 0\,, \tag{36}$$
$$A_{t,\theta}u^t + A_{\phi,\theta}u^\phi + F_{\theta r}u^r = 0\,, \tag{37}$$
$$A_{\phi,r}u^r + A_{\phi,\theta}u^\theta = 0\,. \tag{38}$$

It follows from Eqs (35) and (38) that

$$\frac{A_{t,r}}{A_{\phi,r}} = \frac{A_{t,\theta}}{A_{\phi,\theta}} \equiv -\Omega^{\mathrm{F}}\,, \tag{39}$$

and therefore

$$\frac{\Omega^{\mathrm{F}}_{,r}}{\Omega^{F}_{,\theta}} = \frac{A_{\phi,r}}{A_{\phi,\theta}}\,. \tag{40}$$

Equation (39) is an exact analogy to Eq. (18) and Ω^{F} has thus again the interpretation of the angular velocity of magnetic field lines (a deep and pedagogical exposition of these relations can be found in Phinney, 1983). The last two equations imply that the Jacobians

$$\frac{\partial(A_t, A_\phi)}{\partial(r,\theta)} = 0\,, \qquad \frac{\partial(\Omega^{\mathrm{F}}, A_\phi)}{\partial(r,\theta)} = 0 \tag{41}$$

vanish, and thus $A_t \equiv A_t(A_\phi)$ and $\Omega^{\mathrm{F}} \equiv \Omega^{\mathrm{F}}(A_\phi)$. The flow stream-lines and the magnetic field-lines lie in the level surfaces of A_ϕ, i.e., $\vec{u} \cdot \nabla A_\phi = \vec{B} \cdot \nabla A_\phi = 0$, where $B = ({}^*F) \cdot u$. The arrow denotes two-component space-like vectors defined in the (r, θ)-plane.

One can define the stream function $k(r,\theta) \equiv k(A_\phi)$ satisfying

$$\frac{u^r}{A_{\phi,\theta}} = -\frac{u^\theta}{A_{\phi,r}} \equiv \frac{k(r,\theta)}{4\pi\sqrt{-g}\,\rho_0}\,. \tag{42}$$

Equations (36), (39) and (42) can be solved with respect to the azimuthal component of velocity,

$$u^\phi = \Omega^{\mathrm{F}} u^t + \frac{k}{4\pi R^2 \rho_0} B_{\mathrm{T}}\,, \tag{43}$$

where $R^2 = g_{t\phi}^2 - g_{tt}g_{\phi\phi}$, $B_{\mathrm{T}} = -({}^*F)_{\phi t}$. Equation (43) describes to what degree particles fail to corotate with field lines. Two additional stream functions can be obtained by inserting the explicit form of $T^{\alpha\beta}$ into Eqs (33)–(34). Axial symmetry thus yields a relation for the specific angular momentum at infinity, $\mathcal{L}$:

$$0 = \rho_0 u^\beta \left(\frac{\rho + p}{\rho_0}\, u_\phi\right)_{,\beta} + \frac{1}{\sqrt{-g}} \left(\sqrt{-g}\, T^{\beta}_{\phi\ \mathrm{EMG}}\right)_{,\beta}\,, \tag{44}$$

$$(k\mathcal{L})_{,r} A_{\phi,\theta} - (k\mathcal{L})_{,\theta} A_{\phi,r} = 0\,, \tag{45}$$

where

$$\mathcal{L} = \frac{\rho + P}{\rho_0}\, u_\phi - \frac{B_{\mathrm{T}}}{k} \equiv \mathcal{L}(A_\phi)\,. \tag{46}$$

After a completely analogous derivation, stationarity gives the relation for the specific energy at infinity:

$$e = -\frac{\rho + P}{\rho_0}\, u_t - \frac{B_{\mathrm{T}}\Omega^{\mathrm{F}}}{k} \equiv e(A_\phi)\,. \tag{47}$$

Discussion proceeds now analogously to the analysis, which we have carried out within the non-relativistic limit when projections of the Euler equations in different direction were employed (for the original derivation and for further discussion, see Lovelace et al., 1986; Phinney, 1983; Nitta et al., 1991). The above derived stream functions are not completely independent – they must satisfy boundary conditions.

Finally, we are still left with the two equations, $T^{r\beta}{}_{;\beta} = 0$ and $T^{\theta\beta}{}_{;\beta} = 0$, but also these relations are not independent. We have already imposed a restriction on projection by u_α – the first law of thermodynamics $T^{\alpha\beta}{}_{;\beta} u_\alpha = 0$, which is included in the equation of state for $P(\rho_0)$. The last required equation can thus be obtained by contracting $T^{\alpha\beta}{}_{;\beta} = 0$ with any poloidal four-vector which is linearly independent of poloidal projection of u_α. The result is a non-linear second-order differential equation which is a generalization of the Grad–Shafranov equation within general relativity (Kim et al., 2005).

Our discussion has been restricted to weak, electromagnetic test-fields in a given, fixed background spacetime; we have neglected the influence of the electromagnetic field on the spacetime metric. This approach was employed by a number of authors to address the problem of electromagnetic effects near a rotating (Kerr) black hole (Takahashi et al., 1990; Thorne et al., 1986; Wagh and Dadhich, 1989). On the other hand, self-consistent solutions of coupled Einstein–Maxwell equations for black holes immersed in electromagnetic fields have been studied only within stationary, axially symmetric, vacuum models (Díaz and Baez, 1989; Dokuchaev, 1987; Gal'tsov, 1986; Ernst and Wild, 1976; Hiscock, 1981; Karas and Vokrouhlický, 1991e.g.,). It appears that the test electromagnetic field approximation is fully adequate for modelling astrophysical sources, however, the long-term evolution of magnetospheres of rotating black holes, consequences of non-ideal MHD and the effects of oscillatory motion of the central body are still open to further work (Okamoto, 1992; Park and Vishniac, 1989; Rezzolla et al., 1991; Rezzolla and Ahmedov, 2004; Kudoh and Kaburaki, 1996).

ACKNOWLEDGEMENTS

The author acknowledges financial support from the Czech Science Foundation grant No. 205/03/0902.

REFERENCES

Anile, A. M. and Choquet-Bruhat, Y. (1989), Relativistic Fluid Dynamics, *Lect. Notes Math.*, **1385**, ISSN 0075-8434.

Balbus, S. A. (2003), Relativistic Fluid Dynamics, *Annual Review of Astronomy and Astrophysics*, **41**, p. 555.

Balbus, S. A. and Hawley, J. F. (1992), *Astrophys. J.*, **400**, p. 610.

Beskin, V. S. and Kuznetsova, I. V. (2000), *Astrophys. J.*, **541**, p. 257.

Blandford, R. D. (1976), *Monthly Notices Roy. Astronom. Soc.*, **176**, p. 465.

Blandford, R. D. and Znajek, R. L. (1977), *Monthly Notices Roy. Astronom. Soc.*, **179**, p. 433.

Camenzind, M. (1986a), *Astronomy and Astrophysics*, **156**, p. 137.

Camenzind, M. (1986b), *Astronomy and Astrophysics*, **162**, p. 32.

Chandrasekhar, S. (1961), *Hydrodynamic and Hydromagnetic Stability*, Oxford University Press, Oxford.

Cohen, R. H., Coppi, B. and Treves, A. (1973), , *Astrophys. J.*, **179**, p. 269.

Cowling, T. G. (1976), *Magnetohydrodynamics*, A. Hilger, London.

Díaz, A. G. and Baez, N. B. (1989), *J. Math. Phys.*, **30**, p. 1310.

Dokuchaev, V. I. (1987), *Soviet Phys. JETP*, **65**, p. 1079.

Ernst, F. J. and Wild, W. J. (1976), *J. Math. Phys.*, **17**, p. 182.

Ferraro, V. C. A. and Plumpton, C. (1961), *An Introduction to Magneto-fluid Mechanics*, Oxford University Press, New York.

Gal'tsov, D. V. (1986), *Particles and fields around black holes*, Moscow University Press, Moscow.

Goldreich, P. and Julian, W. H. (1969), *Astrophys. J.*, **157**, p. 869.

Hirotani, K., Takahashi, M., Nitta, S.-Y. and Tomimatsu, A. (1992), *Astrophys. J.*, **386**, p. 455.

Hiscock, W. A. (1981), *J. Math. Phys.*, **22**, p. 1828.

Ioka, K. and Sasaki, M. (2003), *Phys. Rev. D*, **67**, p. 124026.

Karas, V. and Vokrouhlický, D. (1991), *J. Math. Phys.*, **32**, p. 714.

Kim, H., Lee, H. M., Lee, C. H. and Lee, H. K. (2005), *Monthly Notices Roy. Astronom. Soc.*, **358**, p. 998.

Krause, F., Rädler, K.-H. and Rüdiger, G. (1992), *The Cosmic Dynamo; Proceedings of the IAU Symposium No. 157*, Kluwer Academic Publishers, Dordrecht.

Kudoh, T. and Kaburaki, O. (1996), *Astrophys. J.*, **461**, p. 565.

Königl, A. (1989), *Astrophys. J.*, **342**, p. 208.

Lichnerowitz, A. (1967), *Relativistic Hydrodynamics and Magnetohydrodynamics*, Benjamin, New York.

Lovelace, R. V. E., Mehanian, C., Mobarry, C. M. and Sulkanen, M. E. (1986), *Astrophys. J. Suppl.*, **62**, p. 1.

Lynden-Bell, D., editor (1994), *Cosmical Magnetism*, Kluwer Academic Publishers, Dordrecht.

Melrose, D. B., editor (1980), *Plasma Astrophysics*, Gordon and Breach, Science Publishers.

Michel, F. C. (1982), *Rev. Modern Phys.*, **54**, p. 1.

Michel, F. C. (1983), *Astrophys. J.*, **266**, p. 188.

Nitta, S.-Y., Takahashi, M. and Tomimatsu, A. (1991), *Phys. Rev. D*, **44**, p. 2295.

Okamoto, I. (1992), *Monthly Notices Roy. Astronom. Soc.*, **254**, p. 192.

Pacini, F. (1968), *Nature*, **219**, p. 145.

Park, S. J. and Vishniac, E. T. (1989), *Astrophys. J.*, **337**, p. 78.

Phinney, E. S. (1983), *A Theory of Radio Sources*, Ph.D. thesis, Cambridge University.

Rezzolla, L. and Ahmedov, B. J. (2004), *Monthly Notices Roy. Astronom. Soc.*, **352**, p. 1161.

Rezzolla, L., Ahmedov, B. J. and Miller, J. C. (1991), *Monthly Notices Roy. Astronom. Soc.*, **322**, p. 723, ibid. (2003), **338**, p. 816.

Scharlemann, E. T. and Wagoner, R. V. (1973), *Astrophys. J.*, **182**, p. 951.

Takahashi, M., Nitta, S., Tatematsu, Y. and Tomimatsu, A. (1990), *Astrophys. J.*, **363**, p. 206.

Thorne, K. S., Price, R. H. and MacDonald, D. A. (1986), *Black Holes: The Membrane Paradigm*, Yale University Press, New Haven.

Wagh, S. M. and Dadhich, N. (1989), *Phys. Rep.*, **183**, p. 137.

Zel'dovich, Y. B., Ruzmaikin, A. A. and Sokoloff, D. D. (1983), *Magnetic Fields in Astrophysic*, Gordon and Breach, Science Publishers, New York.

Znajek, R. L. (1976), *Black Hole Electrodynamics*, Ph.D. thesis, Cambridge University.

S. Hledík and Z. Stuchlík, editors, Silesian University in Opava, Czech Republic, 2005, pp. 81–99

Embedding diagrams of optical reference geometry of Kerr–de Sitter spacetimes

Jiří Kovář [a] and Zdeněk Stuchlík [b]

Institute of Physics, Faculty of Philosophy & Science, Silesian University in Opava,
Bezručovo nám. 13, CZ-746 01 Opava, Czech Republic
[a] Jiri.Kovar@fpf.slu.cz
[b] Zdenek.Stuchlik@fpf.slu.cz

ABSTRACT
Embedding diagrams of the equatorial plane of the Kerr–de Sitter black-hole or naked-singularity spacetimes are constructed for the optical reference geometry. The embedding diagrams do not cover whole stationary parts of the Kerr–de Sitter spacetimes. Hence, limits of embeddability are discussed. The Kerr–de Sitter spacetimes are then classified according to the number of embeddable regions and the number of the turning points of the diagrams.

1 INTRODUCTION

The optical reference geometry introduced by Abramowicz et al. (1988, 1993, 1995) enables to introduce the concept of inertial forces in the framework of general relativity in a natural way. It provides a description of relativistic dynamics in accordance with our natural Newtonian intuition. The optical reference geometry results from an appropriate conformal $(3 + 1)$ splitting, reflecting some hidden properties of spacetimes under consideration through its geodesic structure. The geodesics of the optical geometry related to the static spacetimes coincide with trajectories of light, thus being "optically straight." Moreover, the geodesics are "dynamically straight," because test particles moving along them are kept by a velocity independent force. Many important properties of relativistic dynamics can be then effectively illustrated by the properties of embedding diagrams of the optical geometry, because the centrifugal force is closely related to the diagrams (Stuchlík et al., 2000). The radii of turning points of the diagrams coalesce with the radii where the centrifugal force vanishes independently of the velocity and also with the radii of gyration (Stuchlík et al., 2000). Unfortunately, some spacetimes cannot be entirely embedded into the 3-dimensional Euclidean space, therefore the limits of embeddability must be established.

We present the embedding diagrams of the optical geometry in the case of physically relevant stationary and axially symmetric spacetimes around rotating black holes or naked singularities in the universe with recently indicated repulsive cosmological constant, i.e.,

80-7248-334-X

in the Kerr–de Sitter (KdS) spacetimes. We use the standard approach enabling a systematic treatment of the turning points and embeddability limits of the diagrams (Hledík, 2002). In Section 2, we briefly summarize features of the KdS geometry and classify the KdS spacetimes into black-hole and naked-singularity spacetimes. This way we introduce the "Chinese box" technique, which is used later in a more complicated classification. In Section 3, the definition of the optical reference geometry in the case of the general stationary spacetimes is introduced and applied to the KdS spacetimes. Section 4 turns to the embedding diagrams of the optical geometry of these spacetimes. There is detailed discussion concerning the limits of embeddability of the optical geometry and the number of turning points of the embedding diagrams, concluded with the full classification of the KdS spacetimes according to the properties of the optical geometry. Examples of some typical embedding diagrams are also included. Some concluding remarks are given in Section 5.

2 KERR–DE SITTER SPACETIMES

KdS spacetimes are stationary and axially symmetric solutions of Einstein's equations with a non-zero cosmological constant Λ. In the standard Boyer–Lindquist coordinates (t, r, θ, ϕ) and geometric units ($c = G = 1$), the line element of the KdS geometry is given by the relation

$$\begin{aligned} \mathrm{d}s^2 = &- \frac{\Delta_r}{I^2\rho^2}(\mathrm{d}t - a\sin^2\theta\,\mathrm{d}\phi)^2 + \frac{\Delta_\theta \sin^2\theta}{I^2\rho^2}[a\,\mathrm{d}t - (r^2+a^2)\,\mathrm{d}\phi]^2 \\ &+ \frac{\rho^2}{\Delta_r}\,\mathrm{d}r^2 + \frac{\rho^2}{\Delta_\theta}\,\mathrm{d}\theta^2\,, \end{aligned} \tag{1}$$

where

$$\Delta_r = r^2 - 2Mr + a^2 - \tfrac{1}{3}\Lambda r^2(r^2+a^2)\,, \tag{2}$$

$$\Delta_\theta = 1 + \tfrac{1}{3}\Lambda a^2\cos^2\theta\,, \tag{3}$$

$$I = 1 + \tfrac{1}{3}\Lambda a^2\,, \tag{4}$$

$$\rho^2 = r^2 + a^2\cos^2\theta \tag{5}$$

and the mass M, specific angular momentum a, and cosmological constant Λ are parameters of the spacetime. Using the dimensionless cosmological parameter

$$y = \tfrac{1}{3}\Lambda M^2 \tag{6}$$

and putting $M = 1$, the coordinates t, r, the line element $\mathrm{d}s$, and the parameter a are expressed in units of M and become dimensionless.

Stationary regions of the KdS spacetimes, determined by the relation $\Delta_r(r; a^2, y) \geq 0$, are limited by the inner and outer black-hole horizons at $r_{\mathrm{h}-}$ and $r_{\mathrm{h}+}$ and by the cosmological horizon at r_{c}. Spacetimes containing three horizons are black-hole spacetimes, while spacetimes containing one horizon (the cosmological horizon exists for any choice of the spacetime parameters) are naked-singularity spacetimes (Stuchlík and Slaný, 2004). It follows from the relation $\Delta_r(r; a^2, y) = 0$ that for given values of the rotational and cosmological parameters a^2 and y, the loci of horizons are given by solutions of the equation

$$y = y_{\rm h}(r; a^2) \equiv \frac{r^2 - 2r + a^2}{r^2(r^2 + a^2)}\,, \tag{7}$$

whereas, because of the repulsive cosmological constant, the solutions are restricted by the condition

$$y_{\rm h}(r; a^2) > 0\,. \tag{8}$$

The investigation of the function $y_{\rm h}(r; a^2)$, following the "Chinese box" method, leads to the classification of the KdS spacetimes into the black-hole and naked-singularity spacetimes (see Fig. 1). The asymptotic behaviour of $y_{\rm h}(r; a^2)$ is given by $y_{\rm h}(r \to \infty; a^2) \to +0$

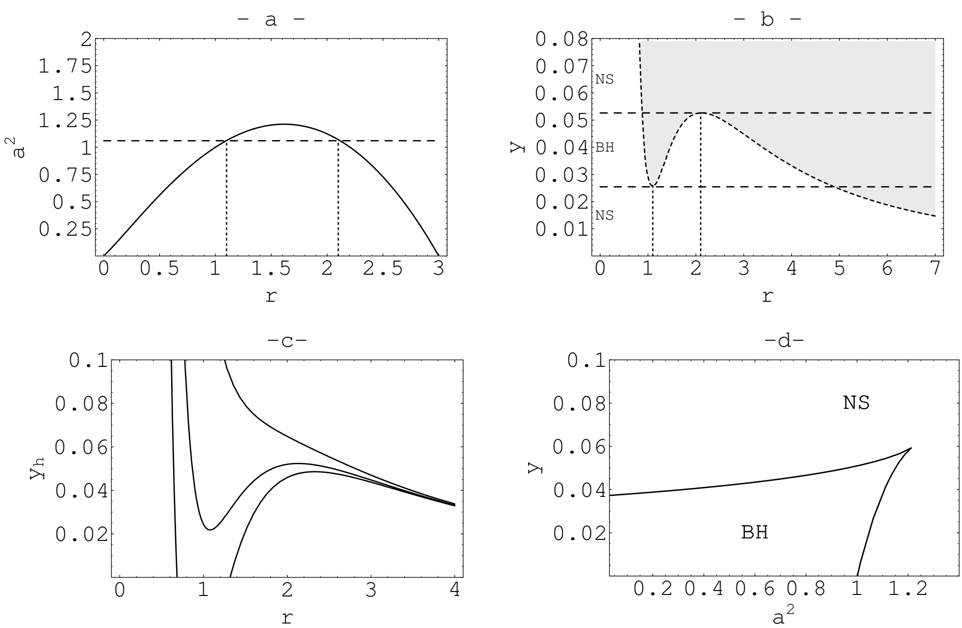

Figure 1. Classification of the KdS spacetimes by using the "Chinese box" method. (a) The characteristic function $a^2_{\rm he}(r)$ governing the location of extrema of the function $y_{\rm h}(r; a^2)$. For given a^2, the extrema of $y_{\rm h}(r; a^2)$ are determined by the solutions of $a^2 = a^2_{\rm he}(r)$ (note the dashed line $a^2 = 1.06$ and compare with Fig. 1b). (b) The function $y_{\rm h}(r; a^2)$ determining the loci of event horizons of the KdS spacetimes and limiting the dynamic regions (gray). The function is given for $a^2 = 1.06$. For given y and a^2, the horizons are determined by solutions of $y = y_{\rm h}(r; a^2)$. In the parameter line (y) of the spacetimes, the extrema of $y_{\rm h}(r; a^2)$ separate regions corresponding to the black-hole (BH) spacetimes and naked-singularity (NS) spacetimes for given values of the rotational parameter a^2. (c) The functions $y_{\rm h}(r; a^2)$ in three specific cases $a^2 = 0.9$ (with one positive and one negative extrema), $a^2 = 1.05$ (with two positive extrema) and $a^2 = 1.4$ (with no extrema). (d) Functions $y_{\rm h,min}(a^2)$ and $y_{\rm h,max}(a^2)$ separating the parametric plane (a^2, y) into two regions corresponding to the BH and NS spacetimes.

and $y_{\mathrm{h}}(r \to 0; a^2) \to \infty$. The local extrema of $y_{\mathrm{h}}(r; a^2)$ are determined (due to the condition $\partial_r y_{\mathrm{h}}(r; a^2) = 0$) by the relation

$$a^2(r) = a^2_{\mathrm{he}}(r) \equiv \frac{1}{2}\left(-2r^2 + \sqrt{8r+1}\,r + r\right), \tag{9}$$

whereas the maximum of the function $a^2_{\mathrm{he}}(r)$ is located at $r \doteq 1.6160$ and takes the value $a^2_{\mathrm{he,max}} \doteq 1.2120$ (see Fig. 1a).

We can distinguish three different types of the behaviour of the function $y_{\mathrm{h}}(r; a^2)$ (see Fig. 1c).

- For $a^2 < a^2_{\mathrm{he,max}}$, $y_{\mathrm{h}}(r; a^2)$ has two local extrema $y_{\mathrm{h,min}}(a^2)$ and $y_{\mathrm{h,max}}(a^2)$ determined by relations (7) and (9) (see Fig. 1b). The black-hole spacetimes exist for $y_{\mathrm{h,min}}(a^2) \le y < y_{\mathrm{h,max}}(a^2)$ and $y > 0$, while the naked-singularity spacetimes exist for $0 < y < y_{\mathrm{h,min}}(a^2)$ or $y \ge y_{\mathrm{h,max}}(a^2)$.
- For $a^2 = a^2_{\mathrm{he,max}}$, the extrema $y_{\mathrm{h,min}}(a^2)$ and $y_{\mathrm{h,max}}(a^2)$ coincide at $y_{\mathrm{h,crit}} = 0.0592$, which is the limiting value for the black-hole spacetimes.
- For $a^2 > a^2_{\mathrm{he,max}}$, $y_{\mathrm{h}}(r; a^2)$ has no extrema and there are only the naked-singularity spacetimes (Stuchlík and Slaný, 2004).

The parameter plane (a^2, y) separated by the functions $y_{\mathrm{h,min}}(a^2)$ and $y_{\mathrm{h,max}}(a^2)$ into the regions corresponding to the black-hole and naked-singularity spacetimes is illustrated in Fig. 1d.

3 OPTICAL REFERENCE GEOMETRY

3.1 General case

In stationary spacetimes described by a metric g_{ik} (with signature $+2$), the definition of the optical reference geometry requires introducing of family of special observers with the timelike, unit, and hypersurface orthogonal 4-velocity field n^i and with its 4-acceleration field equal to the gradient of a scalar function. Such a vector field, satisfying the mentioned conditions

$$n^k n_k = -1\,, \quad n^i \nabla_i n_k = \nabla_k \Phi\,, \quad n_{[i} \nabla_j n_{k]} = 0\,, \tag{10}$$

can be found in the form

$$n^i = \mathrm{e}^{-\Phi} \iota^i\,, \quad \Phi = \tfrac{1}{2} \ln\left(-\iota^i \iota_i\right), \tag{11}$$

whereas it corresponds to the unit 4-velocity field of stationary observers parallel to a timelike Killing vector field ι^i, which exists due to the spacetime stationarity. Note that the scalar function Φ is called *gravitational potential* and e^{Φ} is the norm coefficient here. The equations (10) also implies

$$n^i \nabla_i \Phi = 0\,, \tag{12}$$

i.e., the special observers with the 4-velocity n^i observe no change in the gravitational potential as their proper time passes, thus they are fixed with respect to the *gravitational* *field*. The local instantaneous 3-dimensional (n^i orthogonal) space of the observers is described by the metric

$$h_{ik} = g_{ik} + n_i n_k \, , \tag{13}$$

the so-called *directly projected geometry*. The conformally adjusted metric of the directly projected geometry

$$\tilde{h}_{ik} = \mathrm{e}^{-2\Phi} h_{ik} \, , \tag{14}$$

is the so-called *optical reference geometry*.

3.2 Kerr–de Sitter case

KdS spacetimes, being stationary and axially symmetric, admit two Killing vector fields: the timelike vector field $\boldsymbol{\eta} = \partial/\partial t$ and the spacelike vector field $\boldsymbol{\xi} = \partial/\partial\phi$. These Killing vector fields are not orthogonal in general and $\eta^i\eta_i = g_{tt}$, $\eta^i\xi_i = g_{t\phi}$, $\xi^i\xi_i = g_{\phi\phi}$. Their linear combination, especially $\iota^i = \eta^i + \Omega_{\mathrm{LNRF}}\xi^i$, where $\Omega_{\mathrm{LNRF}} = -\eta^i\xi_i/\xi^i\xi_i$, can be used for the definition of the special observers with the 4-velocity

$$n^i = \mathrm{e}^{-\Phi}(\eta^i + \Omega_{\mathrm{LNRF}}\xi^i) \, , \tag{15}$$

$$\Phi = \tfrac{1}{2}\ln\left[-(\eta^i + \Omega_{\mathrm{LNRF}}\xi^i)(\eta_i + \Omega_{\mathrm{LNRF}}\xi_i)\right] . \tag{16}$$

This 4-velocity, relevant for the construction of the ordinary projected geometry, corresponds to the 4-velocity of the locally non-rotating frames moving along circular orbits with the angular velocity $\mathrm{d}\phi/\mathrm{d}t = \Omega_{\mathrm{LNRF}}$. The timelike vector field (15) is the unit and hypersurface orthogonal vector field, whereas its 4-acceleration equals to the gradient of the scalar function Φ, just as required in the equations (10).

The metric coefficients of the optical reference geometry necessary for the construction of the embedding diagrams of the equatorial plane are given by the relations

$$\tilde{h}_{rr} = \frac{r(1+a^2y)^2[r^3 + a^4ry + a^2(2+r+r^3y)]}{\Delta_r^2} \, , \tag{17}$$

$$\tilde{h}_{\phi\phi} = \frac{[r^3 + a^4ry + a^2(2+r+r^3y)]^2}{r^2\Delta_r} \, . \tag{18}$$

4 EMBEDDING DIAGRAMS

Properties of the optical reference geometry can be represented by the embedding of the equatorial plane into the 3-dimensional Euclidean space with the line element expressed in the cylindrical coordinates (ρ, z, α) in the form

$$\mathrm{d}\sigma^2 = \mathrm{d}\rho^2 + \rho^2\,\mathrm{d}\alpha^2 + \mathrm{d}z^2 \, . \tag{19}$$

4.1 Embedding formula

The embedding diagram is characterized by the embedding formula $z = z(\rho)$ determining a surface in the Euclidean space with the line element

$$\mathrm{d}l^2_{(\mathrm{E})} = \left[1 + \left(\frac{\mathrm{d}z}{\mathrm{d}\rho}\right)^2\right] \mathrm{d}\rho^2 + \rho^2\,\mathrm{d}\alpha^2\,, \tag{20}$$

isometric to the 2-dimensional equatorial plane of the optical space determined by the line element

$$\mathrm{d}\tilde{l}^2 = \tilde{h}_{rr}\,\mathrm{d}r^2 + \tilde{h}_{\phi\phi}\,\mathrm{d}\phi^2\,. \tag{21}$$

The azimuthal coordinates can be identified ($\phi = \alpha$) and we can put $\rho^2 = \tilde{h}_{\phi\phi}$. Thus the differential form of embedding formula is governed by the relation

$$\left(\frac{\mathrm{d}z}{\mathrm{d}\rho}\right)^2 = \tilde{h_{rr}} \left(\frac{\mathrm{d}r}{\mathrm{d}\rho}\right)^2 - 1\,. \tag{22}$$

It is convenient to transfer it into a parametric form $z(\rho) = z(r(\rho))$ with r being the parameter, i.e.,

$$\frac{\mathrm{d}z}{\mathrm{d}r} = \pm\sqrt{\tilde{h}_{rr} - \left(\frac{\mathrm{d}\rho}{\mathrm{d}r}\right)^2}\,, \tag{23}$$

whereas the sign in this formula is irrelevant, leading to isometric surfaces (Hledík, 2001).

Using the relation $\rho^2 = \tilde{h}_{\phi\phi}$ and the metric coefficients (17) and (18), we obtain the differential form of the embedding formula in the form

$$\frac{\mathrm{d}z}{\mathrm{d}r} = \pm\sqrt{\frac{L}{-\Delta_r{}^3 r^4}}\,, \tag{24}$$

where

$$L = Ay^4 + By^3 + Cy^2 + Dy + E \tag{25}$$

and

$$A = a^6 r^6 (a^2 + r^2)^3\,, \tag{26}$$
$$B = a^4 r^5 (a^2 + r^2)^2 [3r^3 + a^2(3r + 10)]\,, \tag{27}$$
$$\begin{aligned} C = {} & -a^2 r^3 (a^2 + r^2)[-3r^7 - a^2(6r^2 + 16r + 9)r^3 \\ & - a^4 r(3r^2 + 12r + 37) + 4a^6]\,, \end{aligned} \tag{28}$$
$$\begin{aligned} D = {} & r^2\{r^{10} + a^2 r^6(3r^2 + 2r - 18) + a^4 r^3[r(3r^2 - 4r - 16) + 36] \\ & + a^6 r[r(r^2 - 14r - 18) + 60] - 4a^8(2r + 5)\}\,, \end{aligned} \tag{29}$$
$$\begin{aligned} E = {} & 4a^8 - 4a^6 r[r(r - 3) + 6] - 3a^4(r - 2)r^2[r(4r - 3) + 6] \\ & - 2a^2 r^5[r(6r - 17) + 18] + (9 - 4r)r^8\,. \end{aligned} \tag{30}$$

4.2 Features of embedding diagrams

From the differential form of the embedding formula (24), it is clear that due to the condition $(\mathrm{d}z/\mathrm{d}r)^2 \geq 0$, the equatorial plane of the optical geometry is not entirely embeddable into the 3-dimensional Euclidean space. The embeddable regions are determined by the condition $L(r; a^2, y) \leq 0$, whereas the equality in this relation determines limits of the embeddability. Due to the relation

$$\frac{\mathrm{d}z}{\mathrm{d}\rho} = \frac{\mathrm{d}z}{\mathrm{d}r}\frac{\mathrm{d}r}{\mathrm{d}\rho}\,, \tag{31}$$

the radii of turning points of the embedding diagrams, i.e., their bellies and throats, are determined by the condition $\mathrm{d}\rho/\mathrm{d}r = 0$.

4.2.1 Limits of embeddability

The equation $L(r; a^2, y) = 0$ implicitly defines two functions $y_{\mathrm{L}\pm}(r; a^2)$, whereas $y_{\mathrm{L}-}(r; a^2) < y_{\mathrm{L}+}(r; a^2)$ for all values of a^2 and r. Instead of giving long explicit expressions for the functions $y_{\mathrm{L}\pm}(r; a^2)$, we only present their properties and examples of different types of their behaviour (see Figs 2 and 3). For given values of a^2 and y, the limits of embeddability are determined by solutions of the equations

$$y = y_{\mathrm{L}\pm}(r; a^2)\,. \tag{32}$$

Because of the reality condition $\Delta_r(r; a^2, y) > 0$ and the repulsive cosmological constant, the solutions are restricted by the conditions

$$0 < y_{\mathrm{L}\pm}(r; a^2) < y_{\mathrm{h}}(r; a^2)\,. \tag{33}$$

Thus the embeddable regions are given by the conditions $0 < y_{\mathrm{L}-}(r; a^2) \leq y$ and $y \leq y_{\mathrm{L}+}(r; a^2)$.

The zero points of functions $y_{\mathrm{L}\pm}(r; a^2)$ are determined by the condition $E(r; a^2) = 0$ (see Eq. (25)), i.e., by the equation

$$\begin{aligned}4a^8 - 4a^6 r[r(r-3)+6] - 3a^4(r-2)r^2[r(4r-3)+6]\\ - 2a^2r^5[r(6r-17)+18] + (9-4r)r^8 = 0\,,\end{aligned} \tag{34}$$

which we consider as the implicit form of functions $a^2_{\mathrm{L0}\pm}(r)$. The function $a^2_{\mathrm{L0}+}(r)$ has two local maxima $a^2_{\mathrm{L0+,max1}} \doteq 1.1354$ and $a^2_{\mathrm{L0+,max2}} \doteq 1.0754$ located at $r \doteq 0.6895$ and at $r = 1.3317$. There is also one local minimum $a^2_{\mathrm{L0+,min}} = 1$ located at $r = 1$. On the other hand, the function $a^2_{\mathrm{L0}-}(r)$ has no local extrema.

The number of solutions of the equation (32) depends on the number of extrema of the functions $y = y_{\mathrm{L}\pm}(r; a^2)$. They are given by the functions $a^2_{\mathrm{Le1}}(r)$ and $a^2_{\mathrm{Le2}\pm}(r)$, which are defined implicitly by eliminating y from the equations $L(r; a^2, y) = 0$ and $\partial_r L(r; a^2, y) = 0$. Since this expression is too large to be presented here, we only show the behaviour of the functions $a^2_{\mathrm{Le1}}(r)$ and $a^2_{\mathrm{Le2}\pm}(r)$ (see Fig. 2). The function $a^2_{\mathrm{Le1}}(r)$ is identical with the function $a^2_{\mathrm{he}}(r)$ (see the relation (9)) governing the extrema of $y_{\mathrm{h}}(r; a^2)$. Thus two extrema

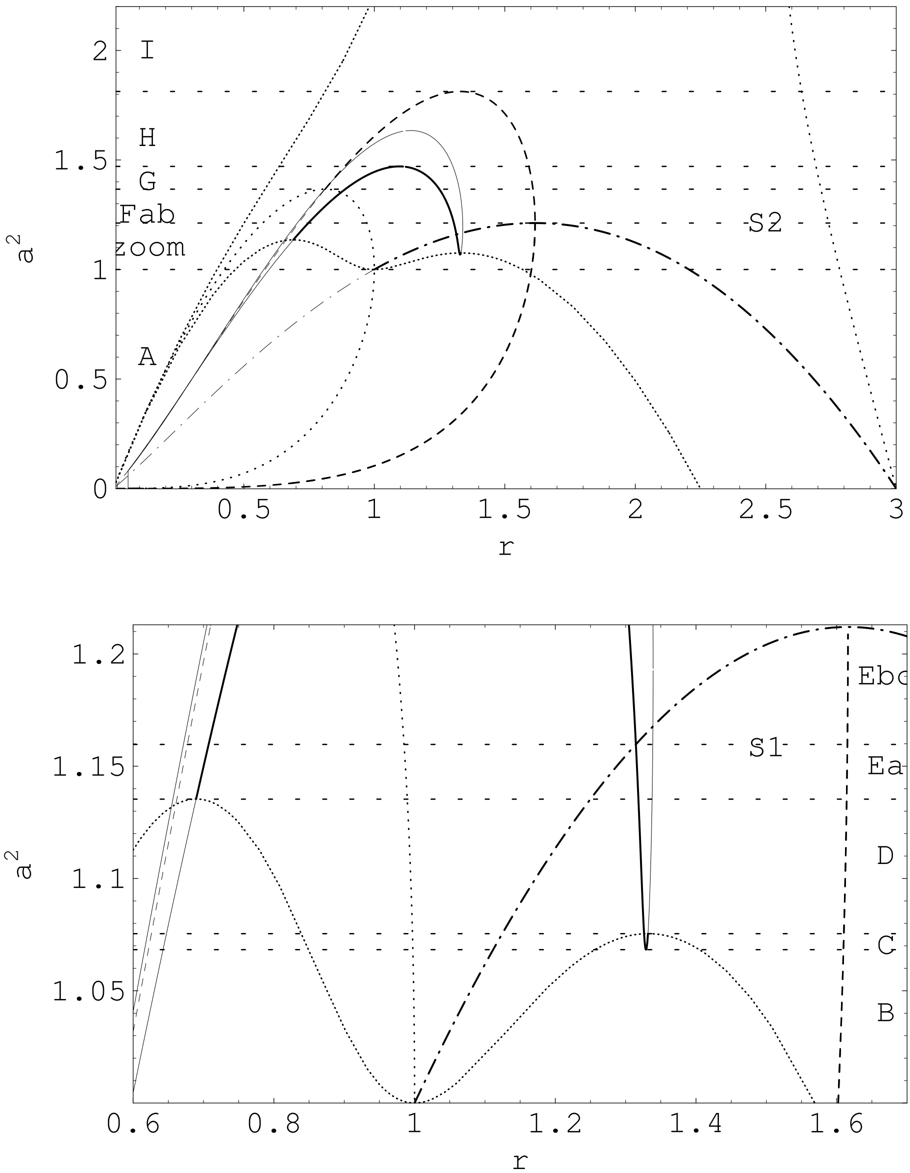

Figure 2. Characteristic functions $a^2_{\mathrm{L0}\pm}(r)$ (closely dotted) governing zeros of the function $y_{\mathrm{L}\pm}(r;a^2)$; $a^2_{\mathrm{Le1}}(r)$ (dashed-dotted) and $a^2_{\mathrm{Le2}\pm}(r)$ (solid) governing extrema of $y_{\mathrm{L}\pm}(r;a^2)$; $a^2_{\mathrm{T0}\pm}(r)$ (dotted) governing zeros of the function $y_{\mathrm{T}}(r;a^2)$; $a^2_{\mathrm{Te}\pm}(r)$ (dashed) governing extrema of $y_{\mathrm{T}}(r;a^2)$. The thick parts of the dashed-dotted and solid curves govern positive extrema of $y_{\mathrm{L}\pm}(r;a^2)$. In the parameter line (a^2) of the spacetimes, the extrema and common points of the characteristic functions separate fourteen regions corresponding to the different types of behaviour of $y_{\mathrm{L}\pm}(r;a^2)$ (see Fig. 3).

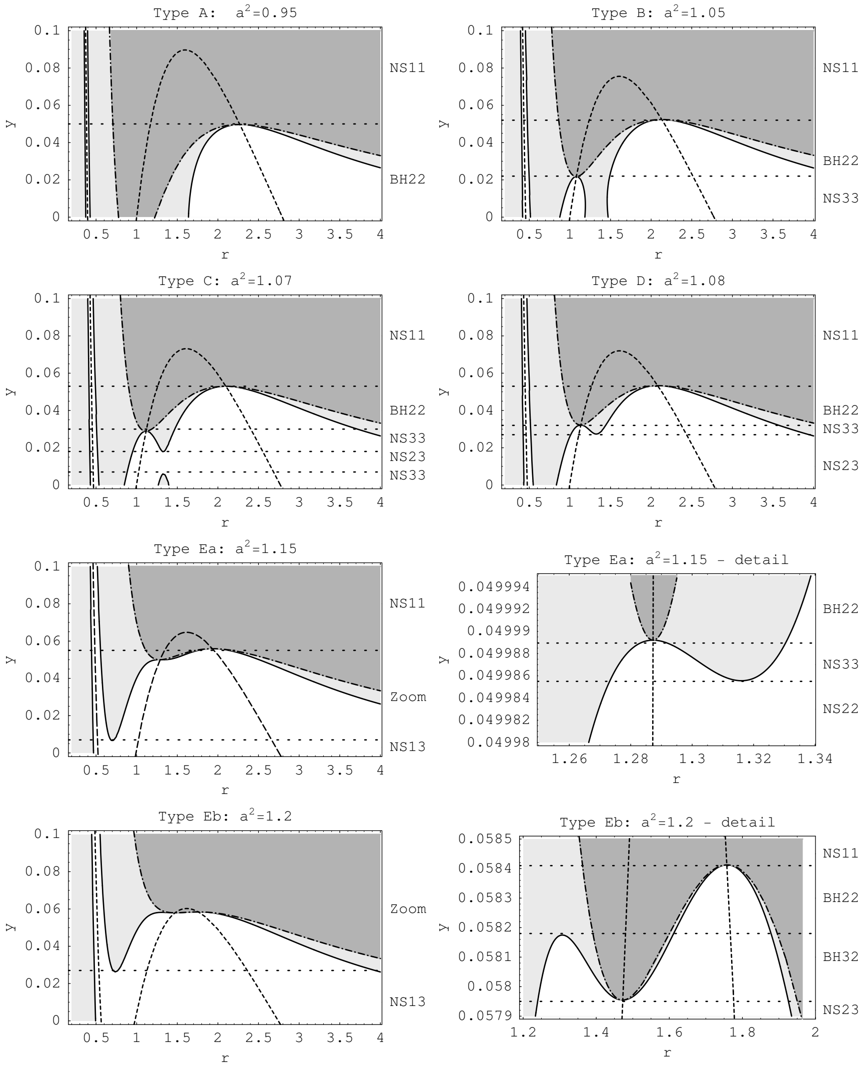

Figure 3. Functions $y_{\mathrm{L}\pm}(r; a^2)$ (solid) limiting embeddable regions (white); $y_{\mathrm{T}}(r; a^2)$ (dashed) determining turning points of embedding diagrams; $y_{\mathrm{h}}(r; a^2)$ (dashed-dotted) determining locations of event horizons and limiting the dynamic regions (gray). For given y and a^2, limits of embeddability are determined by solutions of $y = y_{\mathrm{L}\pm}(r; a^2)$. Turning points of the embedding diagrams are determined by solutions of $y = y_{\mathrm{T}}(r; a^2)$ and restricted by the condition $0 < y < y_{\mathrm{h}}(r; a^2)$. In the parameter line (y) of the KdS spacetimes, extrema of $y_{\mathrm{L}\pm}(r; a^2)$ and $y_{\mathrm{T}}(r; a^2)$ separate regions corresponding to different classes of the spacetimes differing in the number of embeddable regions (first digit) and turning points of the embedding diagrams (second digit). Note that in the case of the classes NS12 and NS22, the second digits exceptionally denote one turning point and one inflexion point of the diagrams, i.e., not two turning points.

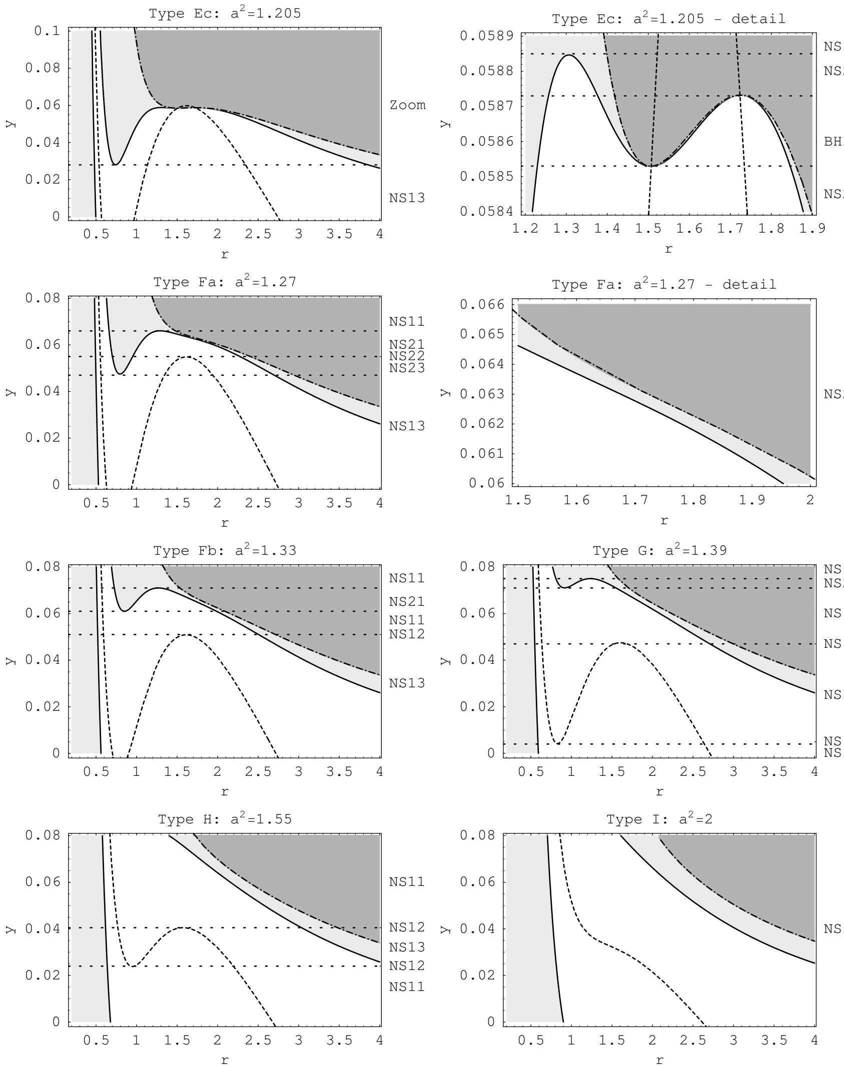

Figure 3. (Continued from page 89.)

of $y_{\mathrm{L}\pm}(r;\,a^2)$ coalesce with two extrema of $y_{\mathrm{h}}(r;\,a^2)$. These two extrema of $y_{\mathrm{L}\pm}(r;\,a^2)$ are the only common points of $y_{\mathrm{L}\pm}(r;\,a^2)$ and $y_{\mathrm{h}}(r;\,a^2)$ and there is $y_{\mathrm{L}\pm}(r;\,a^2) < y_{\mathrm{h}}(r;\,a^2)$ for the other points. The maximum of the function $a^2_{\mathrm{Le1}}(r)$ takes the value $a^2_{\mathrm{Le1,max}} \doteq 1.2120$ and is located at $r \doteq 1.6160$. The common point of $a^2_{\mathrm{Le1}}(r)$ and $a^2_{\mathrm{L0+}}(r)$ coalesces with the local minimum of $a^2_{\mathrm{L0+}}(r)$ and divides the function $a^2_{\mathrm{Le1}}(r)$ into two parts governing positive (relevant for the classification) and negative extrema of $y_{\mathrm{L}\pm}(r;\,a^2)$. The function $a^2_{\mathrm{Le2+}}(r)$ has local maximum $a^2_{\mathrm{Le2+,max}} \doteq 1.4706$ located at $r \doteq 1.0961$ and local minimum

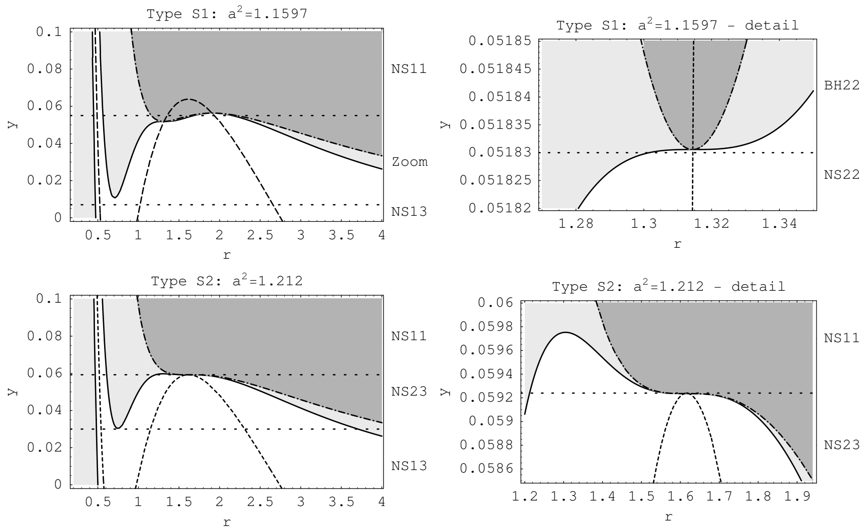

Figure 3. (Continued from page 89.)

$a^2_{\mathrm{Le2+,min}} \doteq 1.0683$ at $r \doteq 1.3289$. Two of three common points of $a^2_{\mathrm{Le2+}}(r)$ and $a^2_{\mathrm{L0+}}(r)$ coalesce with local maxima of $a^2_{\mathrm{L0+}}(r)$ and divide the function $a^2_{\mathrm{Le2+}}(r)$ into two parts governing positive and negative extrema of $y_{\mathrm{L\pm}}(r; a^2)$. The function $a^2_{\mathrm{Le2-}}(r)$ completely governs negative local extrema of $y_{\mathrm{L\pm}}(r; a^2)$, which we do not consider here.

All the characteristic functions $a^2_{\mathrm{L0\pm}}(r)$, $a^2_{\mathrm{Le1\pm}}(r)$ and $a^2_{\mathrm{Le2}}(r)$ are illustrated in Fig. 2. These functions enable us to understand the behaviour of the functions $y_{\mathrm{L\pm}}(r; a^2)$ and classify the KdS spacetimes according to the number of embeddable regions.

4.2.2 Turning points of the embedding diagrams

Since there is

$$\frac{\mathrm{d}\rho}{\mathrm{d}r} = \left\{r^2 \Delta_r^{3/2}\right\}^{-1} \left\{r^3 a^4 (a^2 + r^2) y^2 + r^2 a^2 [(2r + 5)a^2 + r^2(2r + 3)] y \right. \\ \left. + r^4(r - 3) + r a^2 [r(r - 3) + 6] - 2a^4 \right\} , \quad (35)$$

for given values a^2 and y, the radii of turning points of the embedding diagrams determined by the condition $\mathrm{d}\rho/\mathrm{d}r = 0$, are given by solutions of the equation

$$y = y_{\mathrm{T}}(r; a^2) \equiv \left\{2a^2 r^2 (a^2 + r^2)\right\}^{-1} \left\{-(2r + 5) r a^2 - r^3 (2r + 3) \right. \\ \left. + \sqrt{r(a^2 + 3r^2)[8a^4 + r a^2 (16r + 1) + r^3 (8r + 3)]}\right\} . \quad (36)$$

The solutions are restricted by the conditions

$$0 < y_{\mathrm{L-}}(r; a^2) < y_{\mathrm{T}}(r; a^2) < y_{\mathrm{L+}}(r; a^2) . \quad (37)$$

The zeros of the function $y_{\rm T}(r;\,a^2)$ are given by the relation

$$r^4(r-3)+ra^2[r(r-3)+6]-2a^4=0\,, \tag{38}$$

which we consider as the implicit form of the functions $a^2_{\rm T0\pm}(r)$. The maximum of this function takes the value $a^2_{\rm T0\pm,max} \doteq 1.3667$ and is located at $r \doteq 0.8116$.

The number of solutions of the equation (36) depends on the number of the extrema of the function $y_{\rm T}(r;\,a^2)$. They are determined (due to the condition $\partial_r y_{\rm T}(r;\,a^2)=0$) by the equation

$$\begin{aligned}
&-\left\{\sqrt{a^4r^3(a^2+3r^2)[8a^4+r(16r+1)a^2+r^3(8r+3)]}\right\}^{-1}\\
&\times\left\{r[12a^8+r(48r+1)a^6+3r^3(24r+1)a^4+3r^5(16r+1)a^2\right.\\
&\qquad\left.+\,3r^7(4r+3)]a^2\right\}+5a^4+12r^2a^2+3r^4=0\,,
\end{aligned} \tag{39}$$

which we consider as the implicit form of functions $a^2_{\rm Te\pm}(r)$ with the maximum $a^2_{\rm Te+,max} \doteq 1.8126$ at $r \doteq 1.3285$.

The characteristic functions $a^2_{\rm Te\pm}(r)$ and $a^2_{\rm T0\pm}(r)$ are illustrated in Fig. 2 and enable us to understand the behaviour of the functions $y_{\rm T}(r;\,a^2)$ and classify the KdS spacetimes according to the number of turning points of the embedding diagrams.

4.3 Classification of the Kerr–de Sitter spacetimes

The number of embeddable regions and turning points of the embedding diagrams is determined by the number of solutions of equations (32) and (36), which depends on the number of the extrema of the functions $y_{\rm L\pm}(r;\,a^2)$ and $y_{\rm T}(r;\,a^2)$. We therefore denote $y_{\rm L-,max}(a^2)$ as the only maximum of the function $y_{\rm L-}(r;\,a^2)$ which becomes positive (relevant for the classification) for some a^2 and r, $y_{\rm L+,e1}(a^2)$, $y_{\rm L+,e2}(a^2)$ as the extrema of the function $y_{\rm L+}(r;\,a^2)$ coalescent with the minimum and maximum of the function $y_{\rm h}(r;\,a^2)$; $y_{\rm L+,e3}(a^2)$, $y_{\rm L+,e4}(a^2)$ as the remaining two extrema of the function $y_{\rm L+}(r;\,a^2)$. Finally we denote $y_{\rm T,min}(a^2)$ and $y_{\rm T,max}(a^2)$ as the minimum and maximum of the function $y_{\rm T}(r;\,a^2)$. Using the characteristic functions $a^2_{\rm Te\pm}(r)$, $a^2_{\rm T0\pm}(r)$, $a^2_{\rm L0\pm}(r)$, $a^2_{\rm Le1}(r)$ and $a^2_{\rm Le2\pm}(r)$, we can distinguish fourteen different types of behaviour of the functions $y_{\rm L\pm}(r;\,a^2)$ and $y_{\rm T}(r;\,a^2)$ differing in the number of their extrema satisfying the conditions $0<y\leq y_{\rm h}(r;\,a^2)$ (see Fig. 3). We represent the obtained fourteen different types of KdS spacetimes in Table 1.

The classification of the KdS spacetimes according to the number of embeddable regions and turning points can be now given in the following way. We step by step discuss the number of embeddable regions using the number of solutions of the equation (32) restricted by the conditions (33) for given a^2 and y and the number of turning points of embedding diagrams given by the solutions of the equation (36) restricted by the conditions (37) for each type of the KdS spacetimes separately.

In the spacetimes of type A, for $0<y<y_{\rm L+,e2}(a^2)$, there are four solutions of the equation (32) satisfying the conditions (33) and then two embeddable regions. There are two solutions of the equation (36) satisfying the conditions (37), i.e., two turning points of

Table 1. Different types of the KdS spacetimes determined by the different types of behaviour of the functions $y_{L\pm}(r; a^2)$ and $y_T(r; a^2)$. The number of extrema $y_{L+,e1}(a^2)$, $y_{L+,e2}(a^2)$, $y_{L+,e3}(a^2)$, $y_{L+,e4}(a^2)$, $y_{L-,max}(a^2)$, $y_{T,min}(a^2)$, and $y_{T,max}(a^2)$ of the functions $y_{L\pm}(r; a^2)$ and $y_T(r; a^2)$ satisfying the conditions $0 < y \leq y_h(r; a^2)$ are subsequently expressed by the digits in the last column. The types Ea, Eb, and Ec differ in the relation among the values of extrema $y_{L+,e2}(a^2)$, $y_{L+,e3}(a^2)$, and $y_{L+,e4}(a^2)$ and the types Fa and Fb differ in the relation among the values of extrema $y_{L+,e3}(a^2)$ and $y_{T,max}(a^2)$.

Type	Range of a^2	Extrema	Type	Range of a^2	Extrema
A	$(0, 1\rangle$	0,1,0,0,0,0,0	Fa	$(1.2120, 1.2938)$	0,0,1,1,0,0,1
B	$(1, 1.0683)$	1,1,0,0,0,0,0	Fb	$\langle 1.2938, 1.3667\rangle$	0,0,1,1,0,0,1
C	$\langle 1.0683, 1.0754)$	1,1,0,1,1,0,0	G	$(1.3667, 1.4706)$	0,0,1,1,0,1,1
D	$\langle 1.0754, 1.1354\rangle$	1,1,0,1,0,0,0	H	$\langle 1.4706, 1.8126)$	0,0,0,0,0,1,1
Ea	$(1.1354, 1.1597)$	1,1,1,1,0,0,0	I	$\langle 1.8126, \infty)$	0,0,0,0,0,0,0
Eb	$(1.1597, 1.2032)$	1,1,1,1,0,0,0	S1	1.1597	0,1,1,0,0,0,0
Ec	$\langle 1.2032, 1.2120)$	1,1,1,1,0,0,0	S2	1.2120	0,0,1,1,0,0,1

the embedding diagrams. Moreover there are three solutions of the equation (7) determining three even horizons and thus two stationary regions of the spacetimes. We denote the obtained class as BH22, i.e., black-hole KdS spacetimes with two embeddable regions and two turning points. For $y \geq y_{L+,e2}(a^2)$ there are two solutions of the equation (32) satisfying the conditions (33) and thus only one embeddable region. The only solution of the equation (36) satisfying the conditions (37) determines one turning point of the embedding diagrams. Moreover there is one solution of the equation (7), i.e., one cosmological horizon separating one stationary and one dynamic region. We denote the obtained class as NS11, i.e., naked-singularity KdS spacetimes with one embeddable region and one turning point. Note that although there are two horizons and two stationary regions in the case of $y = y_{L+,e2}(a^2)$, the outer stationary region coincides with the outer horizon where the geometry is not embeddable and thus we cannot consider it. Using the same way, we can sort the remaining types of the spacetimes obtaining the classification of all KdS spacetimes (see Table 2).

Now it is clear, that the functions $y_{L+,e1}(a^2)$, $y_{L+,e2}(a^2)$, $y_{L+,e3}(a^2)$, $y_{L+,4}(a^2)$, $y_{L-,max}(a^2)$, $y_{T,min}(a^2)$, and $y_{T,max}(a^2)$ separate the parametric plane (a^2, y) into nine regions (see Fig. 4) corresponding to two classes of KdS black-hole spacetimes and to seven classes of naked-singularity spacetimes differing in the number of embeddable regions and number of turning points of the embedding diagrams. Qualitatively different types of the embedding diagrams corresponding to the presented classification are illustrated in Figs 5–10.

5 CONCLUSIONS

The embedding diagrams of the optical reference geometry of the KdS spacetimes were presented and the classification of the spacetimes according to the number of embeddable

Table 2. Classification of the KdS spacetimes according to the number of embeddable regions (first digit) and turning points of the embedding diagrams (second digit). Limits of the ranges of the parameter y (functions of the parameter a^2) are illustrated in Fig. 4.

Class	Range of y
Type A	
BH22	$(0;\ y_{\mathrm{L+,e2}}(a^2))$
NS11	$\langle y_{\mathrm{L+,e2}}(a^2);\ \infty)$
Type B	
NS33	$(0;\ y_{\mathrm{L+,e1}}(a^2))$
BH22	$\langle y_{\mathrm{L+,e1}}(a^2);\ y_{\mathrm{L+,e2}}(a^2))$
NS11	$\langle y_{\mathrm{L+,e2}}(a^2);\ \infty)$
Type C	
NS33	$(0;\ y_{\mathrm{L-,max}}(a^2))$
NS23	$\langle y_{\mathrm{L-,max}}(a^2);\ y_{\mathrm{L+,e4}}(a^2))$
NS33	$(y_{\mathrm{L+,e4}}(a^2);\ y_{\mathrm{L+,e1}}(a^2))$
BH22	$\langle y_{\mathrm{L+,e1}}(a^2);\ y_{\mathrm{L+,e2}}(a^2)$
NS11	$\langle y_{\mathrm{L+,e2}}(a^2);\ \infty)$
Type D	
NS23	$(0;\ y_{\mathrm{L+,e4}}(a^2)\rangle$
NS33	$(y_{\mathrm{L+,e4}}(a^2);\ y_{\mathrm{L+,e1}}(a^2))$
BH22	$\langle y_{\mathrm{L+,e1}}(a^2);\ y_{\mathrm{L+,e2}}(a^2))$
NS11	$\langle y_{\mathrm{L+,e2}}(a^2);\ \infty)$
Type Ea	
NS13	$(0;\ y_{\mathrm{L+,e3}}(a^2)\rangle$
NS22	$(y_{\mathrm{L+,e3}}(a^2);\ y_{\mathrm{L+,e4}}(a^2)\rangle$
NS33	$(y_{\mathrm{L+,e4}}(a^2);\ y_{\mathrm{L+,e1}}(a^2))$
BH22	$\langle y_{\mathrm{L+,e1}}(a^2);\ y_{\mathrm{L+,e2}}(a^2))$
NS11	$\langle y_{\mathrm{L+,e2}}(a^2);\ \infty)$
Type Eb	
NS13	$(0;\ y_{\mathrm{L+,e3}}(a^2)\rangle$
NS23	$(y_{\mathrm{L+,e3}}(a^2);\ y_{\mathrm{L+,e1}}(a^2))$
BH32	$\langle y_{\mathrm{L+,e1}}(a^2);\ y_{\mathrm{L+,e4}}(a^2)\rangle$
BH22	$(y_{\mathrm{L+,e4}}(a^2);\ y_{\mathrm{L+,e2}}(a^2))$
NS11	$\langle y_{\mathrm{L+,e2}}(a^2);\ \infty)$
Type Ec	
NS13	$(0;\ y_{\mathrm{L+,e3}}(a^2)\rangle$
NS23	$(y_{\mathrm{L+,e3}}(a^2);\ y_{\mathrm{L+,e1}}(a^2))$
BH32	$\langle y_{\mathrm{L+,e1}}(a^2);\ y_{\mathrm{L+,e2}}(a^2))$
NS21	$\langle y_{\mathrm{L+,e2}}(a^2);\ y_{\mathrm{L+,e4}}(a^2)\rangle$
NS11	$(y_{\mathrm{L+,e4}}(a^2);\ \infty)$

Class	Range of y
Type Fa	
NS13	$(0;\ y_{\mathrm{L+,e3}}(a^2)\rangle$
NS23	$(y_{\mathrm{L+,e3}}(a^2);\ y_{\mathrm{T,max}}(a^2))$
NS22	$y = y_{\mathrm{T,max}}(a^2)$
NS21	$(y_{\mathrm{T,max}}(a^2);\ y_{\mathrm{L+,e4}}(a^2)\rangle$
NS11	$(y_{\mathrm{L+,e4}}(a^2);\ \infty)$
Type Fb	
NS13	$(0;\ y_{\mathrm{T,max}}(a^2))$
NS12	$y = y_{\mathrm{T,max}}(a^2)$
NS11	$(y_{\mathrm{T,max}}(a^2);\ y_{\mathrm{L+,e3}}(a^2)\rangle$
NS21	$(y_{\mathrm{L+,e3}}(a^2);\ y_{\mathrm{L+,e4}}(a^2)\rangle$
NS11	$(y_{\mathrm{L+,e4}}(a^2);\ \infty)$
Type G	
NS11	$(0;\ y_{\mathrm{T,min}}(a^2))$
NS12	$y = y_{\mathrm{T,min}}(a^2)$
NS13	$(y_{\mathrm{T,min}}(a^2);\ y_{\mathrm{T,max}}(a^2))$
NS12	$y = y_{\mathrm{T,max}}(a^2)$
NS11	$(y_{\mathrm{T,max}}(a^2);\ y_{\mathrm{L+,e3}}(a^2)\rangle$
NS21	$(y_{\mathrm{L+,e3}}(a^2);\ y_{\mathrm{L+,e4}}(a^2)\rangle$
NS11	$(y_{\mathrm{L+,e4}}(a^2);\ \infty)$
Type H	
NS11	$(0;\ y_{\mathrm{T,min}}(a^2))$
NS12	$y = y_{\mathrm{T,min}}(a^2)$
NS13	$(y_{\mathrm{T,min}}(a^2);\ y_{\mathrm{T,max}}(a^2))$
NS12	$y = y_{\mathrm{T,max}}(a^2)$
NS11	$(y_{\mathrm{T,max}}(a^2);\ \infty)$
Type I	
NS11	$(0;\ \infty)$
Type S1	
NS13	$(0;\ y_{\mathrm{L+,e3}}(a^2)\rangle$
NS22	$(y_{\mathrm{L+,e3}}(a^2);\ y_{\mathrm{h,min}}(a^2))$
BH22	$\langle y_{\mathrm{h,min}}(a^2);\ y_{\mathrm{L+,e2}}(a^2))$
NS11	$\langle y_{\mathrm{L+,e2}}(a^2);\ \infty)$
Type S2	
NS13	$(0;\ y_{\mathrm{L+,e3}}(a^2)\rangle$
NS23	$(y_{\mathrm{L+,e3}}(a^2);\ y_{\mathrm{T,max}}(a^2))$
NS21	$\langle y_{\mathrm{T,max}}(a^2);\ y_{\mathrm{L+,e4}}(a^2)\rangle$
NS11	$(y_{\mathrm{L+,e4}}(a^2);\ \infty)$

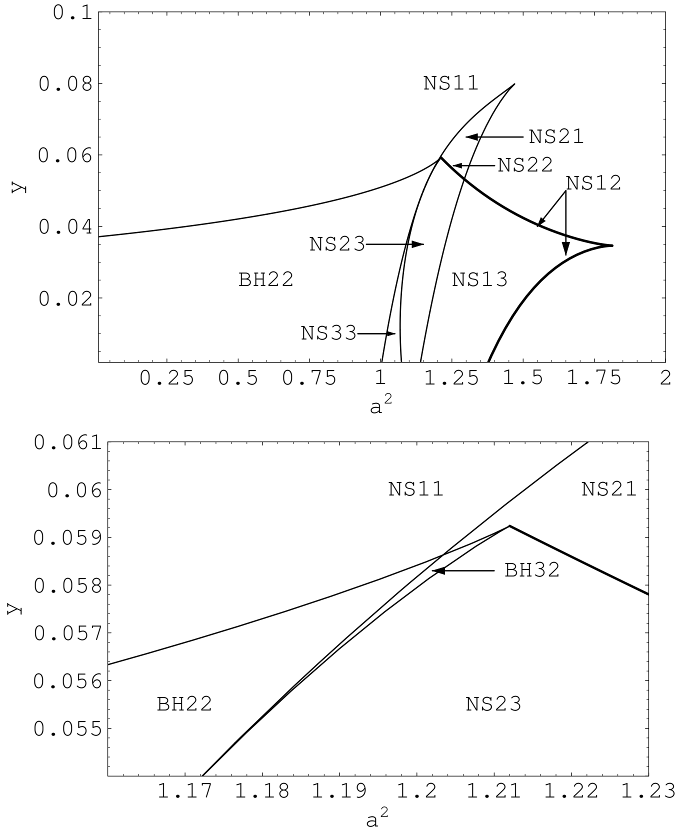

Figure 4. Classification of the KdS spacetimes according to the number of embeddable regions (first digit) and turning points of embedding diagrams (second digit). In the parameter plane (a^2, y), there are two classes BH22 and BH32 of the KdS black-hole spacetimes and seven classes NS11, NS12, NS13, NS23, NS21, NS22, NS23, NS33 of the KdS naked-singularity spacetimes. Note that in the case of the classes NS12 and NS22, the second digits exceptionally denote one turning point and one inflexion point, i.e., not two turning points. The classes NS2 and NS12 are denoted by the thick solid curves.

regions of the geometry (first digit) and number of turning points of the embedding diagrams (second digit) was given:

	BH spacetimes	NS spacetimes
KdS	BH22, BH32	NS11, NS12, NS13, NS21, NS22, NS23, NS33
K	BH22	NS11, NS12, NS13, NS23, NS33
SdS	BH11	–

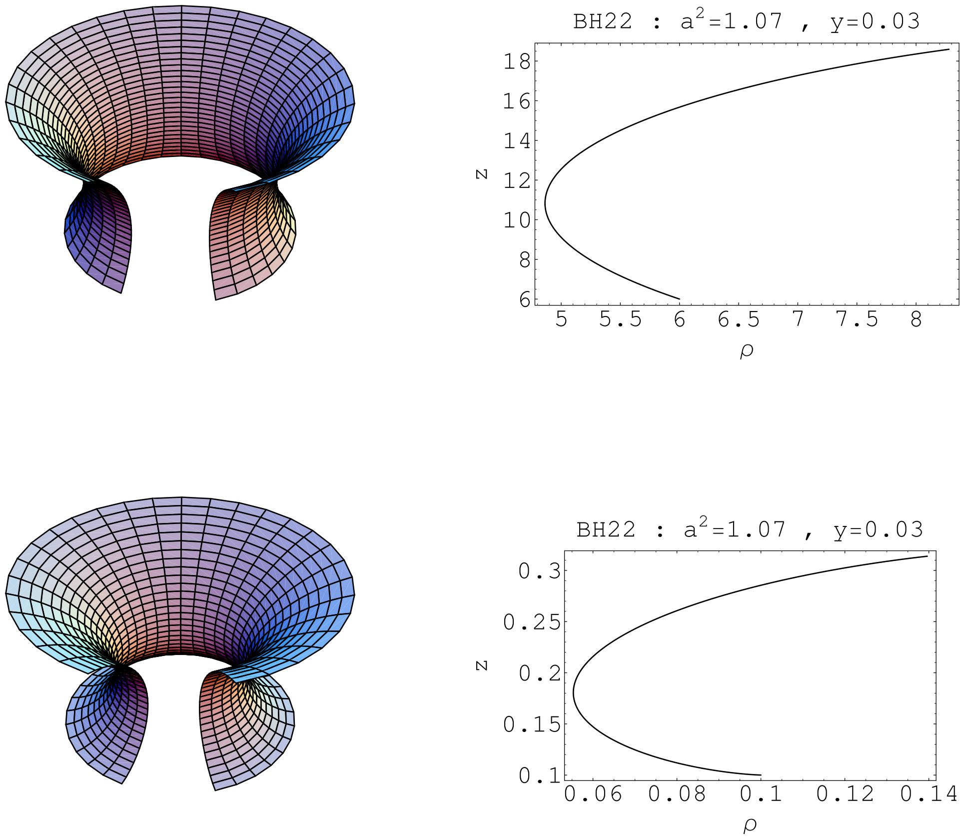

Figure 5. Embedding diagram (two parts) of the optical reference geometry of the KdS spacetime of the class BH22.

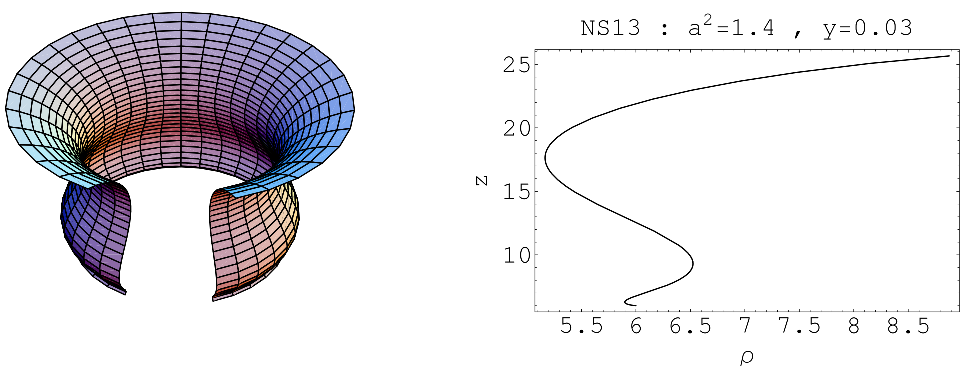

Figure 6. Embedding diagram of the optical reference geometry of the KdS spacetime of the class NS13.

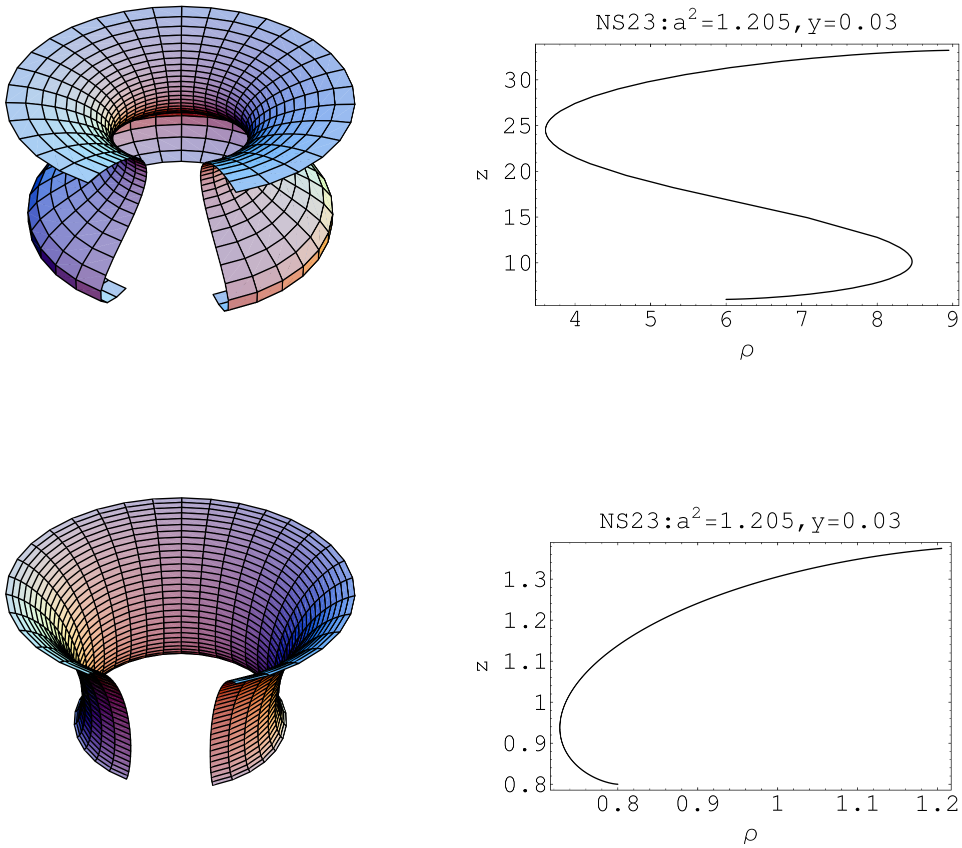

Figure 7. Embedding diagram (two parts) of the optical reference geometry of the KdS spacetime of the class NS23.

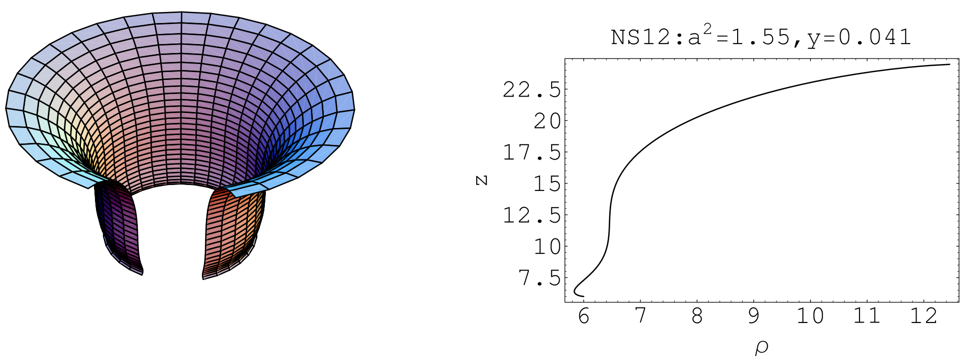

Figure 8. Embedding diagram of the optical reference geometry of the KdS spacetime of the class NS12.

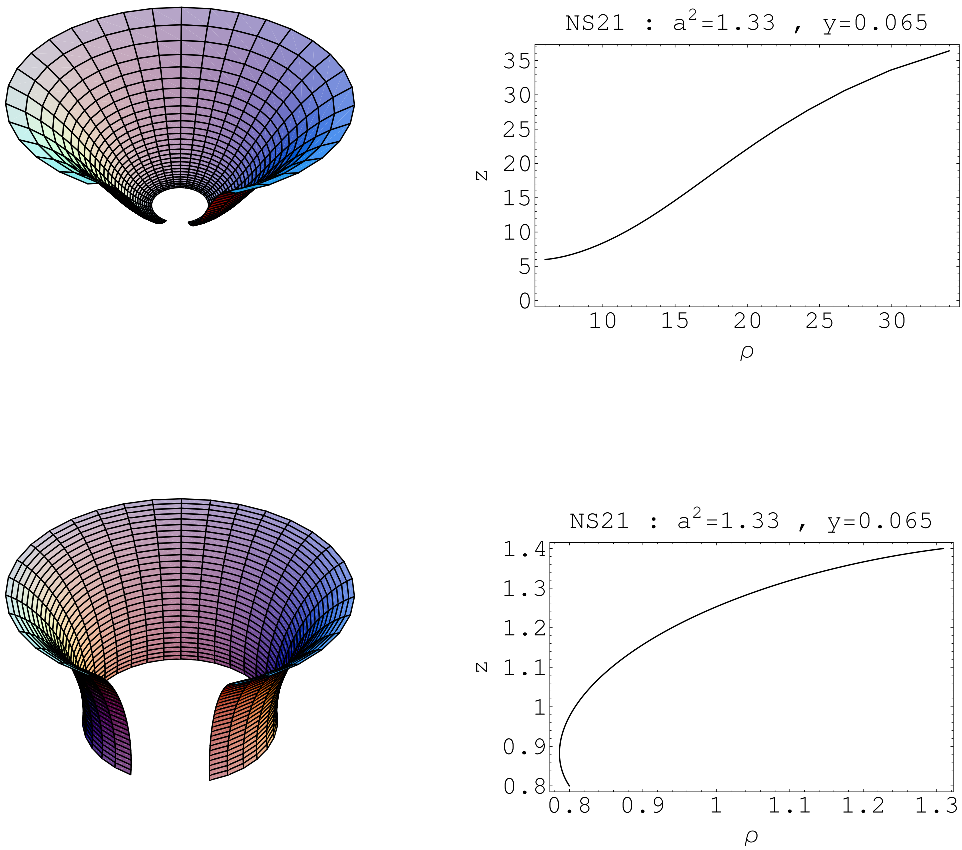

Figure 9. Embedding diagram (two parts) of the optical reference geometry of the KdS spacetime of the class NS21.

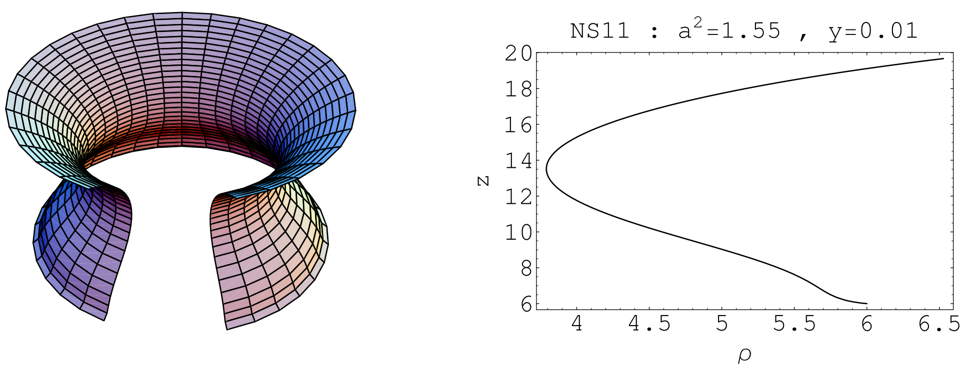

Figure 10. Embedding diagram of the optical reference geometry of the KdS spacetime of the class NS11.

As well as in the case of the pure Kerr spacetimes ($y = 0$) (Stuchlík and Hledík, 1999a), it is a complex classification compared to the Schwarzschild–de Sitter spacetimes ($a = 0$, Stuchlík and Hledík, 1999b), because of the rotation of the source of the gravitation, theoretically allowing the existence of the naked-singularity spacetimes. Of course, intuitively, the centrifugal force, closely related to the embedding diagrams, must be also heavily dependent on the rotation. On the other hand, the cosmological repulsion manifests mainly in the behaviour of the gravitational inertial force, which is not directly related to the embedding diagrams (for the detailed analysis of the inertial forces in the KdS spacetimes, see Kovář and Stuchlík, 2004).

ACKNOWLEDGEMENTS

The present work was supported by the Czech grant MSM 4781305903.

REFERENCES

Abramowicz, M. A., Carter, B. and Lasota, J. (1988), *Gen. Relativity Gravitation*, **20**, p. 1173.

Abramowicz, M. A., Nurowski, P. and Wex, N. (1993), Covariant definition of inertial forces, *Classical Quantum Gravity*, **10**(10), p. L183, URL `http://www.iop.org/EJ/S/UNREG/1NOryEzmtf2ZMVyFDaUGbw/toc/0264%-9381/10/10`.

Abramowicz, M. A., Nurowski, P. and Wex, N. (1995), Optical reference geometry for stationary and axially symmetric spacetimes, *Classical Quantum Gravity*, **12**(6), p. 1467, URL `http://www.iop.org/EJ/S/UNREG/1NOryEzmtf2ZMVyFDaUGbw/toc/0264%-9381/12/6`.

Hledík, S. (2001), Embedding diagrams of the ordinary and optical reference geometry of black-hole spacetimes and their astrophysical relevance, in S. Hledík and Z. Stuchlík, editors, *Proceedings of RAGtime 2/3: Workshops on black holes and neutron stars, Opava, 11–13/8–10 October 2000/2001*, pp. 25–52, Silesian University in Opava, Opava, ISBN 80-7248-131-2.

Hledík, S. (2002), Optical geometry, inertial forces, and embedding diagrams, in O. Semerák, J. Podolský and M. Žofka, editors, *Gravitation: Following the Prague Inspiration (A Volume in Celebration of the 60th Birthday of Jiří Bičák)*, pp. 161–192, World Scientific, New Jersey, London, Singapore, Hong Kong, ISBN 981-238-093-0.

Kovář, J. and Stuchlík, Z. (2004), Inertial forces in Kerr–de Sitter spacetimes, in S. Hledík and Z. Stuchlík, editors, *Proceedings of RAGtime 4/5: Workshops on black holes and neutron stars, Opava, 14–16/13–15 October 2002/2003*, pp. 111–**??**, Silesian University in Opava, Opava, ISBN 80-7248-242-4.

Stuchlík, Z. and Hledík, S. (1999a), Embedding diagrams of the optical geometry of Kerr backgrounds, *Acta Phys. Slovaca*, **49**(5), pp. 795–803, ISSN 0323-0465/99.

Stuchlík, Z. and Hledík, S. (1999b), Some properties of the Schwarzschild–de Sitter and Schwarzschild–anti-de Sitter spacetimes, *Phys. Rev. D*, **60**(4), p. 044006 (15 pages), URL `http://ojps.aip.org/journal_cgi/dbt?KEY=PRVDAQ&Volume=60&Issu%e=4`.

Stuchlík, Z., Hledík, S. and Juráň, J. (2000), Optical reference geometry of Kerr–Newman spacetimes, *Classical Quantum Gravity*, **17**(14), pp. 2691–2718, ISSN 0264-9381/00, URL `http://www.iop.org/EJ/S/UNREG/u57x46uofSBK94ysqmdKSg/toc/0264%-9381/17/14`.

Stuchlík, Z. and Slaný, P. (2004), Equatorial circular orbits in the Kerr–de Sitter spacetimes, *Phys. Rev. D*, **69**, p. 064001, ISSN 1094-1622, `gr-qc/0307049`.

Proceedings of *RAGtime 6/7: Workshops on black holes and neutron stars, Opava, 16–18/18–20 September, 2004/2005*
S. Hledík and Z. Stuchlík, editors, Silesian University in Opava, Czech Republic, 2005, pp. 101–107

Computations of primordial black hole formation

John Miller

SISSA, International School for Advanced Studies, Trieste, Italy
INFN, Trieste, Italy
Department of Physics (Astrophysics), University of Oxford, England
miller@sissa.it

1 INTRODUCTION

At the present epoch of the universe, there is a minimum mass for naturally forming black holes which is somewhere in the region of $2\,\mathrm{M}_\odot$. If a very dense object with a mass smaller than this starts collapsing towards the black hole state, the collapse will be halted by neutron degeneracy pressure. The situation was different in the very early universe. Consider, for example, the conditions a few microseconds after the Big Bang (around the time of the cosmological quark-hadron transition): the temperatures then were $\gtrsim 100\,\mathrm{MeV}$ (10^{12} K), densities $\gtrsim 10^{15}\,\mathrm{g\,cm^{-3}}$, the horizon scale $\lesssim 10\,\mathrm{km}$ (or $1\,\mathrm{M}_\odot$) and the energy density of the universe was dominated by relativistic particles and radiation. This is deeply inside the radiation-dominated era. At this time, the equation of state could be roughly approximated by

$$p = \frac{1}{3}\left(e - \frac{\Lambda}{2\pi}\right) , \tag{1}$$

where e and p are the total energy density and pressure and Λ is an effective cosmological constant term representing the behaviour of vacuum energy which may be present in addition to the relativistic particles (quarks, pions, leptons, photons). In the absence of vacuum energy, (1) reduces to the standard expression for a radiation dominated fluid. An equation of state of this general form can be used at *any* time during the radiation-dominated era, up to around the time of equivalence between radiation and matter ($\sim 10^4$ years after the Big Bang). In contrast with high-density matter today (where the hadrons are in the form of non-relativistic baryons), this matter in the early universe does not stiffen when compressed and so it was possible then to form smaller black holes than could be produced today.

It has been suggested by Niemeyer and Jedamzik (1998, 1999) that black holes formed from density fluctuations in the early universe might have masses following a *scaling law* of the form

$$M_{\mathrm{BH}} = K\,(\delta - \delta_{\mathrm{c}})^{\gamma} , \tag{2}$$

80-7248-334-X

where K and γ are constants, δ is the amplitude of the perturbation and δ_c is the critical threshold value for δ (perturbations with amplitudes larger than this would produce black holes while smaller perturbations would disperse into the surrounding medium). The sort of behaviour represented by (2) is known as *critical collapse* and has been demonstrated (theoretically) to occur for *scale-free* situations involving scalar fields and fluids. It was open to question whether a similar behaviour would arise in the early universe where there *are* some relevant scales, most notably the horizon scale.

The work which I am reporting on here has been done in collaboration with Ilia Musco and Luciano Rezzolla of SISSA, Trieste and has the aim of investigating various aspects of the formation of these *primordial black holes* (PBHs) in the early universe. Cosmological structure formation is thought to have resulted from the growth and evolution of small perturbations initiated at the time of inflation (see Liddle and Lyth, 2000, and references therein). Inflationary models give rise to a spectrum of super horizon-scale fluctuations which then start to re-enter the horizon in the radiation-dominated era and PBHs could be formed at this stage in extreme cases where the fluctuation amplitude exceeds a critical threshold value (Zel'dovich and Novikov, 1966, 1967; Hawking, 1971; Carr and Hawking, 1974). The masses of these PBHs could, in principle, span many orders of magnitude, from the Planck mass up to the horizon mass at the time of equivalence between radiation and matter. We have carried out GR numerical simulations of spherical PBH formation in the background of an expanding universe in the radiation-dominated era. Our work builds on previous investigations by a number of authors including: Carr (1975); Nadezhin et al. (1978a,b); Bicknell and Henriksen (1979); Niemeyer and Jedamzik (1998, 1999); Shibata and Sasaki (1999); Hawke and Stewart (2002). Our aim was to re-visit the subject area, trying to clarify various issues. A particular point is that we have used, as initial conditions, perturbations representing growing-mode over-densities with length-scales greater than the horizon scale and still within the linear regime. Their evolution was then followed as they subsequently become nonlinear. A convenient parameter for measuring the perturbation amplitude δ is the fractional mass-excess within the overdense region. Determining the critical threshold value of this (δ_c), above which PBHs are formed, is clearly important for cosmological considerations (Carr et al., 1994; Green and Liddle, 1997; Liddle and Green, 1998).

2 MATHEMATICAL FORMULATION & CALCULATION METHOD

As with most of the other literature on this subject, we have restricted attention to spherical symmetry, which very greatly simplifies the calculations, and we have used the formulations of the relativistic hydrodynamical equations given by Misner and Sharp (1964); Hernandez and Misner (1966). Both of these are Lagrangian formulations (with a co-moving radial coordinate), the first using a diagonal metric (with the time referred to as "cosmic time" which reduces to the familiar Friedmann–Robertson–Walker time coordinate in the absence of perturbations), and the second using an outward null slicing where the time coordinate is an "observer time" (the clock time as measured by a distant fundamental observer viewing the evolution proceeding).

The spherical matter distribution is divided into a sequence of concentric spherical shells and we label each one with a co-moving radial coordinate which we denote by r. The general form of the metric can then be written as

$$ds^2 = -A^2\,dt^2 - 2AB\,dr\,dt + C^2\,dr^2 + R^2(d\theta^2 + \sin^2\theta\,d\varphi^2)\,, \tag{3}$$

where R, A, B and C are functions of r and the time coordinate t; $2\pi R$ is the proper circumference of a circle with comoving radial coordinate r and R is the radial coordinate used in the Schwarzschild metric. (We are using units in which $c = G = 1$.) One is free to define a new time coordinate t_c as

$$a\,dt_c = A\,dt + B\,dr\,, \tag{4}$$

and inserting this into (3) then gives

$$ds^2 = -a^2\,dt_c^2 + b^2\,dr^2 + R^2(d\theta^2 + \sin^2\theta\,d\varphi^2)\,, \tag{5}$$

(with $b^2 = B^2 + C^2$). This is a diagonal metric (no cross term in $dr\,dt$) and t_c is the cosmic time. This formulation is particularly simple and has the advantage of using a slicing which many people find intuitive; this was the approach used by May and White (1966) in their classic paper studying spherically-symmetric gravitational collapse. However, this approach has a well-known drawback for studying black hole formation in that singularities are typically formed rather early in calculations of continuing collapse and it is not then possible to follow the subsequent evolution (although this problem can be avoided by using an excision technique). Another possibility is to use the freedom in time-slicing to avoid the singularity formation. In spherical symmetry, using an outgoing *null slicing* is an attractive option. On a radial light ray (or *null* ray)

$$ds^2 = -a^2\,dt_c^2 + b^2\,dr^2 = 0\,, \tag{6}$$

giving

$$a\,dt_c = \pm b\,dr\,, \tag{7}$$

with the plus sign corresponding to an outgoing ray and the minus sign to an ingoing one. We can define an *observer time* coordinate t_o which is constant along an outgoing null ray:

$$f\,dt_o = a\,dt_c - b\,dr\,, \tag{8}$$

where f is an integrating factor. With suitable normalization, t_o is the proper time as measured by a distant observer. In terms of this, the metric then becomes

$$ds^2 = -f^2\,dt_o^2 - 2fb\,dr\,dt_o + R^2(d\theta^2 + \sin^2\theta\,d\varphi^2)\,, \tag{9}$$

which is the general form (3) with C set equal to zero. The observer-time approach is particularly convenient for calculations involving black hole formation in spherical symmetry: anything which could not be seen by a distant observer (including singularity formation) does not occur within finite coordinate time while all observable behaviour can be calculated. This is, in some sense, the optimal approach for studying black hole formation in spherical symmetry (being linked directly to potential observations rather than coming from an abstract mathematical prescription) although more sophisticated slicing conditions have advantages for calculations away from spherical symmetry.

For both the cosmic time and observer time approaches, one then has a system of equations for the metric functions and hydrodynamic variables. We will not repeat these here but refer the reader to the original papers (Misner and Sharp, 1964; Hernandez and Misner, 1966). Our calculations of PBH formation have been made using a code based on that of Miller and Motta (1989) but with the grid organized in a way similar to that in the code of Miller and Rezzolla (1995), which was designed for calculations in an expanding cosmological background.

In general, the calculation proceeds in two stages: first, initial data is specified on a space-like slice at constant cosmic time, specifying the energy density e and the radial four-velocity component U as functions of R at the initial time t_{i}. This data is then evolved using the cosmic-time equations so as to generate a second set of initial data on a null slice (at constant observer time). To do this, an outgoing radial light ray is traced out from the centre and parameter values are noted as it passes the boundary of each grid zone. This second set of initial data, constructed in this way, is then evolved using the observer-time equations.

The initial model consists of an unperturbed background, represented by the spatially-flat Friedmann–Robertson–Walker solution, together with a density perturbation and a corresponding velocity perturbation satisfying the conditions for a growing-mode. For the results presented in the next section, the initial perturbations had the well-known Mexican hat profile (with a central over-density surrounded by a compensating under-density) and were specified with a length-scale of several horizon-scales and small amplitudes well within the linear regime. Once the initial conditions have been specified, the data is then evolved forwards in time and the perturbation parameter δ is calculated at the moment when the overdensity enters the horizon. For further details of the methods used, see Musco et al. (2005).

3 SOME RESULTS FROM THE CALCULATIONS

In this section, we present some results from our calculations (all with $\Lambda = 0$ except where otherwise stated). Further details can be found in Musco et al. (2005).

Figure 1 shows the worldlines of fluid elements during a typical evolution leading to black hole formation. The initial perturbation had a Mexican-hat profile with a length-scale of 5 horizon-scales and gave rise to a black hole with mass $M_{\mathrm{BH}} = 0.4415\, M_{\mathrm{H}}$ where M_{H} is the horizon mass at the time of horizon crossing. The perturbation amplitude was rather close to the critical value: $\delta - \delta_{\mathrm{c}} = 2.37 \times 10^{-3}$ measured at horizon crossing (with $\delta_{\mathrm{c}} = 0.43$). Note the cut between the worldlines of material going to form the black hole and the material continuing to move outwards with the expansion of the universe. In between, a relative void forms although a small amount of material is continuing to be accreted across this up to the end of the calculation. For cases closer to the critical limit, the void becomes deeper and a shock appears at its outer edge.

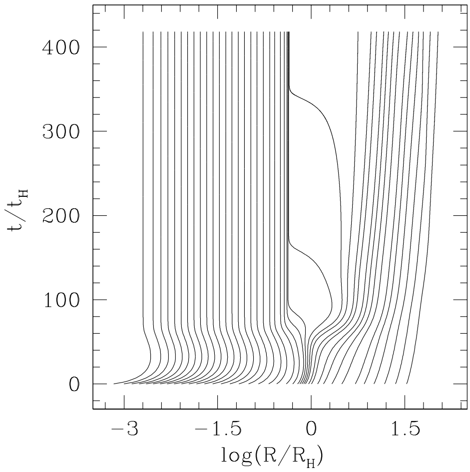

Figure 1. A typical evolution resulting in the formation of a black hole: the plot shows the behaviour of fluid-element worldlines. The time is measured in units of the horizon crossing time t_H and the horizontal scale shows the log of the Schwarzschild circumference coordinate measured in units of the horizon radius at time t_H.

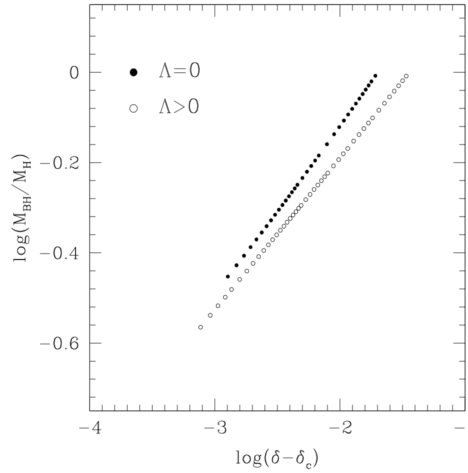

Figure 2. Scaling behaviours for $M_{\rm BH}$ as a function of $\delta - \delta_c$ calculated for growing-mode Mexican hat perturbations specified within the linear regime. The filled circles correspond to $\Lambda = 0$ while the open circles are for a positive Λ giving $\Lambda M_{\rm H}^2 = 2.25 \times 10^{-3}$.

Figure 2 shows scaling laws obtained for the mass of the black hole $M_{\rm BH}$ as a function of $\delta - \delta_c$ for a standard case with zero Λ and a representative case with $\Lambda > 0$. For zero Λ, we find $\delta_c \simeq 0.43$ and $\gamma \simeq 0.36$. Comparing with previous calculations made for initial perturbations which were not specified as purely growing modes (Niemeyer and Jedamzik, 1999), the values of γ are the same but the previous calculations gave $\delta_c \simeq 0.67$ which is substantially different. We note that our present result is consistent with that of Green et al. (2004) who used a different method. The results for positive Λ show γ decreasing with increasing Λ (as expected, because a positive Λ hinders collapse with the effect being strongest for the higher masses) and δ_c increasing with increasing Λ. Both relations are approximately linear in $\Lambda M_{\rm H}^2$ for small enough Λ.

Noting the work of Hawke and Stewart (2002), we do not expect that the linear scaling laws will continue to indefinitely small values of $M_{\rm BH}$ and $\delta - \delta_c$ but instead will level off at a minimum value of $M_{\rm BH}$ (they found a minimum value of $\sim 10^{-4}$ of the horizon mass which they interpreted as being caused by the effects of strong shocks breaking the scale-free behaviour). This is beyond the regime that we can treat at present with our code. It will be important however to check these results because they were obtained for non-linear initial perturbations which were not purely growing modes.

Figure 3 shows worldlines for a particular case of subcritical collapse starting with a Mexican hat perturbation specified in the linear regime, with δ being as close to δ_c as can be well-handled by the code ($\delta - \delta_c = -3.0 \times 10^{-3}$). This is representative of the more extreme cases of subcritical collapse; for less extreme cases, the perturbation subsides

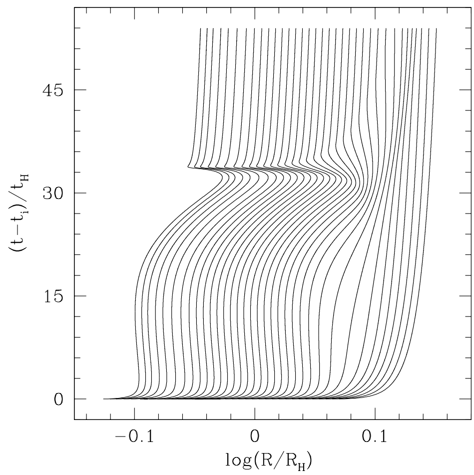

Figure 3. Worldlines for a subcritical Mexican hat perturbation with $\delta - \delta_c = -3.0 \times 10^{-3}$. This plot shows alternating collapse and expansion of the perturbed region while the outer material continues to expand uniformly. For sub-critical cases, the cosmic time formulation is used throughout; the time is measured in units of the horizon crossing time with t_i being the initial time from which the calculation started.

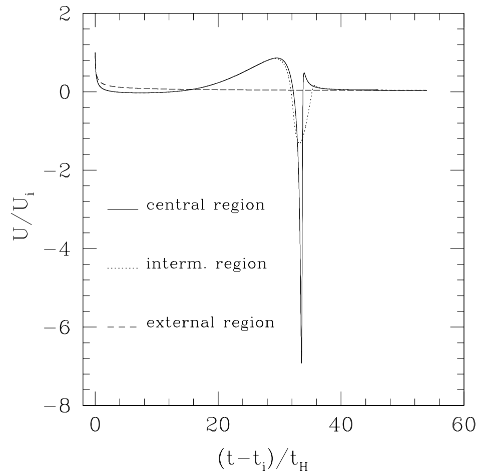

Figure 4. The evolution of the radial velocity U is plotted as a function of time at three (comoving) locations: near to the centre of the perturbation, at an intermediate region (mid-way through the collapsing matter) and at the edge of the grid where the fluid is unperturbed. U is measured in units of its initial value at the same co-moving location and the time is measured in units of the horizon crossing time.

into the background medium in an uneventful way. Figure 4 shows the behaviour of the radial component of four-velocity at three locations: near to the centre of the perturbation; in the outer unperturbed medium and at an intermediate location. It is helpful to view Figs 3 and 4 in conjunction. At first, the material in the central region is continuing to expand but is decelerating. It then has a very gentle collapse followed by a similarly gentle bounce and re-expansion. This continues until it encounters the surrounding material which was not originally perturbed and it then rebounds from this more strongly, propelled by a compression. The following bounce is then far more dramatic since it follows a collapse nearly in free-fall, largely unopposed by internal pressure. Unlike the situation for a similar perturbation within a non-expanding uniform background, there are then no further cycles of expansion and collapse because the expansion of the background prevents further compressions arising. However, for perturbations with δ closer to δ_c further cycles might be seen.

4 CONCLUSION AND FUTURE PERSPECTIVES

The main results of our work so far have been: (i) confirmation of previous results about the existence of scaling laws; (ii) calculation of the revised value of δ_c for calculations starting with purely growing mode perturbations; (iii) calculations including the effects of a non-zero vacuum energy; (iv) demonstration of the quite dramatic hydrodynamic behaviour which can occur in sub-critical collapse.

Topics for future work include the following:

- Use of the code to investigate different prescriptions for perturbation spectra coming from inflation to see whether some prescriptions can be ruled out on the grounds that their PBH production would be in conflict with observations.
- Improvement of the code to enable study of cases with smaller $\delta - \delta_c$ so as to check on the result about the scaling law levelling off at a minimum mass.
- Investigation of the possibility that intermediate mass black holes (10^2–10^3 $M_\odot$) might have a primordial origin rather than coming from Population III stars as commonly thought.

REFERENCES

Bicknell, G. V. and Henriksen, R. N. (1979), *Astrophys. J.*, **232**, p. 670.

Carr, B. J. (1975), *Astrophys. J.*, **201**, p. 1.

Carr, B. J., Gilbert, J. H. and Lidsey, J. E. (1994), *Phys. Rev. D*, **50**, p. 4853.

Carr, B. J. and Hawking, S. W. (1974), *Monthly Notices Roy. Astronom. Soc.*, **168**, p. 399.

Green, A. M. and Liddle, A. R. (1997), *Phys. Rev. D*, **56**, p. 6166.

Green, A. M., Liddle, A. R., Malik, K. A. and Sasaki, M. (2004), *Phys. Rev. D*, **70**, p. 041502.

Hawke, I. and Stewart, J. M. (2002), *Classical Quantum Gravity*, **19**, p. 3687.

Hawking, S. W. (1971), *Monthly Notices Roy. Astronom. Soc.*, **152**, p. 75.

Hernandez, W. C. and Misner, C. W. (1966), *Astrophys. J.*, **143**, p. 452.

Liddle, A. R. and Green, A. M. (1998), *Phys. Rep.*, **307**, p. 125.

Liddle, A. R. and Lyth, D. H. (2000), *Cosmological Inflation and Large-Scale Structure*, Cambridge University Press.

May, M. M. and White, R. H. (1966), *Phys. Rev.*, **141**, p. 1232.

Miller, J. C. and Motta, S. (1989), *Classical Quantum Gravity*, **6**, p. 185.

Miller, J. C. and Rezzolla, L. (1995), *Phys. Rev. D*, **51**, p. 4017.

Misner, C. W. and Sharp, D. H. (1964), *Phys. Rev.*, **136**, p. B571.

Musco, I., Miller, J. C. and Rezzolla, L. (2005), *Classical Quantum Gravity*, **22**, p. 1405, `gr-qc/0412063`.

Nadezhin, D. K., Novikov, I. D. and Polnarev, A. G. (1978a), *Astronom. Zh.*, **55**, p. 216.

Nadezhin, D. K., Novikov, I. D. and Polnarev, A. G. (1978b), *Soviet Astronom.*, **22**(2), p. 129.

Niemeyer, J. C. and Jedamzik, K. (1998), *Phys. Rev. Lett.*, **80**, p. 5481.

Niemeyer, J. C. and Jedamzik, K. (1999), *Phys. Rev. D*, **59**, p. 124013.

Shibata, M. and Sasaki, M. (1999), *Phys. Rev. D*, **60**, p. 084002.

Zel'dovich, Y. B. and Novikov, I. D. (1966), *Astronom. Zh.*, **43**, p. 758.

Zel'dovich, Y. B. and Novikov, I. D. (1967), *Soviet Astronom.*, **10**, p. 602.

Proceedings of *RAGtime 6/7: Workshops on black holes and neutron stars, Opava, 16–18/18–20 September, 2004/2005*
S. Hledík and Z. Stuchlík, editors, Silesian University in Opava, Czech Republic, 2005, pp. 109–117

Games with polytropes and adiabates

Kristina Mrázová, Stanislav Hledík and Zdeněk Stuchlík

Institute of Physics, Faculty of Philosophy & Science, Silesian University in Opava,
Bezručovo nám. 13, CZ-746 01 Opava, Czech Republic

ABSTRACT

Equilibrium configurations that are solutions of spherically symmetric hydrostatic equations of General Relativity for an ideal fluid obeying a polytropic (or adiabatic) equation of state are given in the framework of general relativity. The equilibrium configurations are given in terms of the polytropic index n and the so called relativistic parameter σ (for polytropes) or α (for adiabates).

First, simple models of polytropic and adiabatic spheres for non-relativistic and ultra-relativistic case of the equation of state are introduced. Then, the comparison of polytropic and adiabatic spheres is given in some special characteristic cases and the influence of the relativistic parameter on the structure of the spheres and the gravitational and binding energy.

1 INTRODUCTION

We assume static spherically symmetric, equilibrium perfect-fluid configurations obeying the polytropic and adiabatic equation of state (EoS). We are going to discuss non-relativistic (i.e., $n = 1.5$) and ultrarelativistic (i.e., $n = 3.0$) case of polytropic and adiabatic spheres. I'll show you differences in behaviour of quantities for different polytropic and adiabatic EoS (i.e., for different value of polytropic index n). We compare polytropic and adiabatic configuration in the case when central pressure and central density of both configurations are equal and in the case when central pressures and central rest densities are equal.

2 POLYTROPIC AND ADIABATIC SPHERES

We assume perfect-fluid configuration obeying polytropic and adiabatic EoS (Iben, 1963; Chandrasekhar, 1964; Stuchlík and Hledík, 2005). The matter inside the sphere is described by the perfect-fluid stress-energy tensor

$$T^{\mu}{}_{\nu} = (P + \rho c^2) U^{\mu} U^{\nu} + P \delta^{\mu}_{\nu} \, . \tag{1}$$

The energy-momentum tensor is related to the spacetime geometry by Einstein's gravitational equations in the standard form

$$G_{\mu\nu} \equiv R_{\mu\nu} - \tfrac{1}{2} R g_{\mu\nu} = \frac{8\pi G}{c^4} T_{\mu\nu} \tag{2}$$

80-7248-334-X

and the law of local energy-momentum conservation is described by

$$T^{\mu\nu}{}_{;\nu} = 0\,. \tag{3}$$

The r-component (which is the only non-zero component in the static case) of this conservation law is

$$\frac{\mathrm{d}P}{\mathrm{d}r} + \frac{1}{2}(P + \rho c^2)\frac{\mathrm{d}\nu}{\mathrm{d}r} = 0\,. \tag{4}$$

Pressure P and mass-energy density ρ are connected by polytropic or adiabatic EoS

$$P_{(\mathrm{p})} = K_{(\mathrm{p})}\rho_{(\mathrm{p})}^{1+\frac{1}{n}}\,, \qquad P_{(\mathrm{a})} = K_{(\mathrm{a})}\rho_{\mathrm{g(a)}}^{1+\frac{1}{n}}\,, \tag{5}$$

where ρ_{g} is rest mass-energy density, K is a constant to be determined by the thermal characteristics of a given fluid sphere and n is the polytropic index. Subscript (p) denotes polytropic quantities, subscript (a) denotes adiabatic quantities. The rest and total mass-energy density are related by $\rho = \rho_{\mathrm{g}} + nP/c^2$ (Tooper, 1964, 1965).

We derive the general relativistic equations of equilibrium for a spherically symmetric distribution of fluid obeying a polytropic and adiabatic EoS. In spherical coordinate system at rest with respect of the fluid and chosen such that the metric reduces to the standard form

$$\mathrm{d}s^2 = -\mathrm{e}^{2\Phi}c^2\,\mathrm{d}t^2 + \mathrm{e}^{2\Psi}\,\mathrm{d}r^2 + r^2(\mathrm{d}\theta^2 + \sin^2\theta\,\mathrm{d}\phi^2)\,. \tag{6}$$

The equations of hydrostatic equilibrium in these coordinates are (Oppenheimer and Volkoff, 1939)

$$\frac{\mathrm{d}P_{(\mathrm{p})}}{\mathrm{d}r_{(\mathrm{p})}} = -\left(\rho_{(\mathrm{p})}c^2 + P_{(\mathrm{p})}\right)\frac{\frac{G}{c^2}M_{(\mathrm{p})}(r_{(\mathrm{p})}) + \frac{4\pi G}{c^4}P_{(\mathrm{p})}r_{(\mathrm{p})}^3}{r_{(\mathrm{p})}\left[r_{(\mathrm{p})} - \frac{2G}{c^2}m_{(\mathrm{p})}(r_{(\mathrm{p})})\right]}\,, \tag{7}$$

$$\frac{\mathrm{d}M_{(\mathrm{p})}(r_{(\mathrm{p})})}{\mathrm{d}r} = 4\pi r_{(\mathrm{p})}^2\rho_{(\mathrm{p})}\,. \tag{8}$$

(This is Tolman–Oppenheimer–Volkoff equation of hydrostatic equilibrium for the polytropic case. The equation of hydrostatic equilibrium for adiabatic case has the same form, only the total mass-energy density $\rho_{(\mathrm{p})}$ is changed to rest mass-energy density $\rho_{\mathrm{g(a)}}$ and (p) $\rightarrow$ (a).)

We introduce new variable θ (Tooper, 1964) which is connected with density as

$$\rho_{(\mathrm{p})} = \rho_{\mathrm{c(p)}}\theta^n\,, \qquad \rho_{\mathrm{g(a)}} = \rho_{\mathrm{gc(a)}}\theta^n\,, \tag{9}$$

and is connected with pressure as

$$P_{(\mathrm{p})} = K\rho_{\mathrm{c(p)}}^{1+\frac{1}{n}}\theta^{n+1} = P_{\mathrm{c(p)}}\theta^{n+1}\,, \qquad P_{(\mathrm{a})} = K\rho_{\mathrm{gc(a)}}^{1+\frac{1}{n}}\theta^{n+1} = P_{\mathrm{c(a)}}\theta^{n+1}, \tag{10}$$

Relativity parameter σ for polytropes or α for adiabates are defined as

$$\sigma = \frac{K_{(\mathrm{p})}\rho_{\mathrm{c(p)}}^{\frac{1}{n}}}{c^2} = \frac{P_{\mathrm{c(p)}}}{\rho_{\mathrm{c(p)}}c^2}\,, \qquad \alpha = \frac{K_{(\mathrm{a})}\rho_{\mathrm{gc(a)}}^{\frac{1}{n}}}{c^2} = \frac{P_c(a)}{\rho_{\mathrm{gc(a)}}c^2}\,. \tag{11}$$

Physical interpretation of the parameter σ is the ratio of pressure to energy density at the centre of the sphere and physical interpretation of α is the ratio of pressure to rest energy density at the centre of the sphere.

With transformations to new variables ξ, θ, v defined by

$$r_{(p)} = \frac{\xi}{A_{(p)}}\,, \qquad A^2_{(p)} = \frac{4\pi G\rho_{c(p)}}{(n+1)\sigma c^2} \tag{12}$$

$$M_{(p)}(r_{(p)}) = \frac{4\pi\rho_{c(p)}}{A^3_{(p)}} v_{(p)}(\xi_{(p)})\,, \tag{13}$$

(in the adiabatic case $\rho_{c(p)} \to \rho_{gc(a)}$ and $\sigma \to \alpha$), the equations of hydrostatic equilibrium for polytropes become

$$\frac{d\theta}{d\xi_{(p)}} = -\frac{\left(\sigma\xi^3_{(p)}\theta^{n+1} + v_{(p)}\right)(1+\sigma\theta)}{\xi^2_{(p)}} g_{(p)rr}\,, \tag{14}$$

$$\frac{dv_{(p)}}{d\xi_{(p)}} = \xi^2_{(p)}\theta^n\,, \tag{15}$$

and the equations of hydrostatic equilibrium for adiabates become

$$\frac{d\theta}{d\xi_{(a)}} = -\frac{\left(\alpha\xi^3_{(a)}\theta^{n+1} + v_{(a)}\right)[1+\alpha(n+1)\theta]}{\xi^2_{(a)}} g_{(a)rr}\,, \tag{16}$$

$$\frac{dv_{(a)}}{d\xi_{(a)}} = \xi^2_{(a)}\theta^n(1+n\alpha\theta)\,, \tag{17}$$

where the radial metric coefficient for polytropes is given by

$$g_{(p)rr}(\xi_{(p)}, v_{(p)}; n, \sigma, \lambda_{(p)}) \equiv \frac{1}{1 - 2\sigma(n+1)\frac{v_{(p)}}{\xi_{(p)}}} \tag{18}$$

and the radial metric coefficient for adiabates may be obtained by simple replacement $\sigma \to \alpha$.

3 CASE OF $P_{c(a)} = P_{c(p)}$ AND $\rho_{c(a)} = \rho_{c(p)}$

When we want to compare quantities in this special case we have to compute relation between adiabatic and polytropic relativistic parameter

$$\alpha = \frac{\sigma}{1-n\sigma}\,, \qquad \sigma = \frac{\alpha}{1+n\alpha}\,. \tag{19}$$

We will focus to behaviour of masses, radiuses, binding energy and gravitational potential energy. Relation between masses $M_{(a)}$ and $M_{(p)}$ is

$$M_{(p)} = M_{(a)}\left[\frac{(1-n\alpha)^3}{1+n\alpha}\right]^{1/2}\frac{v_{(p)}}{v_{(a)}}\,. \tag{20}$$

The relation between radii $R_{(a)}$ and $R_{(p)}$ is

$$R_{(p)} = R_{(a)} \left(\frac{1 - n\alpha}{1 + n\alpha} \right)^{1/2} \frac{\xi_{(p)1}}{\xi_{(a)1}} . \tag{21}$$

The relation between binding energies $E_{b(a)}$ and $E_{b(p)}$ is

$$E_{b(p)} = E_{b(a)} \frac{1 - \frac{v_{(p)}}{u_{g(p)}}}{1 - \frac{v_{(a)}}{u_{g(a)}}} \frac{u_{g(p)}}{u_{g(a)}} , \tag{22}$$

where $u_{g(a)}$ and $u_{g(p)}$ are defined by the following integrals:

$$u_{g(a)} = \int_0^{\xi_{(a)1}} \frac{\xi_{(a)}^2 \theta^n}{\left[1 - 2(n+1)\alpha \frac{v_{(a)}}{\xi_{(a)}}\right]^{1/2}} \, d\xi_{(a)} , \tag{23}$$

$$u_{g(p)} = \int_0^{\xi_{(p)1}} \frac{\xi_{(p)}^2 \theta^n}{\left[1 - 2(n+1)\sigma(1+n\sigma)^n + \frac{v_{(p)}}{\xi_{(p)}}\right]^{1/2}} \, d\xi_{(p)} . \tag{24}$$

The relation between gravitational potential energies $\Omega_{(a)}$ and $\Omega_{(p)}$ is

$$\Omega_{(p)} = \Omega_{(a)} (1 + n\alpha)^{\frac{n-3}{2}} \frac{(1 + n\alpha)[1 + n\alpha(1 + \theta)] - \frac{v_{(p)}}{u_{g(p)}}}{1 + n\alpha\theta - \frac{v_{(a)}}{u_{g(a)}}} \frac{u_{g(p)}}{u_{g(a)}} . \tag{25}$$

4 CASE OF $P_{c(a)} = P_{c(p)}$ AND $\rho_{gc(a)} = \rho_{gc(p)}$

When we want to compare quantities in this special case we have to compute relation between adiabatic and polytropic relativistic parameter

$$\alpha = \sigma(1 + \sigma)^n . \tag{26}$$

We will focus to behaviour of masses, radiuses, binding energy and gravitational potential energy. Relation between masses $M_{(a)}$ and $M_{(p)}$ is

$$M_{(a)} = M_{(p)} \left[\frac{(1 - n\sigma)(1 + \sigma)^{4n/3}}{1 - n\sigma(1 + \sigma)^n} \right]^{3/2} \frac{v_{(a)}}{v_{(p)}} . \tag{27}$$

Relation between radiuses $R_{(a)}$ and $R_{(p)}$ is

$$R_{(a)} = R_{(p)} \frac{(1 - n\sigma)^{1/2}(1 + \sigma)^{3n/2}}{[1 - n\sigma(1 + \sigma)^n]^{1/2}} \frac{\xi_{(a)1}}{\xi_{(p)1}} . \tag{28}$$

Relation between binding energies $E_{b(a)}$ and $E_{b(p)}$ is

$$E_{b(a)} = E_{b(p)} \frac{1 - \frac{v_{(a)}}{u_{g(a)}}}{1 - \frac{v_{(p)}}{u_{g(p)}}} (1 + \sigma)^{\frac{n(3-n)}{2}} \frac{u_{g(a)}}{u_{g(p)}} . \tag{29}$$

Relation between gravitational potential energies $\Omega_{(\mathrm{a})}$ and $\Omega_{(\mathrm{p})}$ is

$$\Omega_{(\mathrm{a})} = \Omega_{(\mathrm{p})}(1+\sigma)^{\frac{n(3-n)}{2}} \frac{1 + n\theta\sigma(1+\sigma)^n - \frac{v_{(\mathrm{a})}}{u_{\mathrm{g(a)}}}}{1 + n\theta\sigma - \frac{v_{(\mathrm{p})}}{u_{\mathrm{g(p)}}}} \frac{u_{\mathrm{g(a)}}}{u_{\mathrm{g(p)}}} \,. \tag{30}$$

5 CONCLUSIONS

The structure of sphere (adiabatic or polytropic) is different for non-relativistic or ultra-relativistic case (as we can see in the Fig. 1). Radius of spheres grows with increasing polytropic index n. Non-relativistic star has the smallest radius and ultra-relativistic has the bigger one. For ultra-relativistic example has more than $5/6$ of the star nearly zero density – it is unphysical effect but this is extreme condition. Mass and gravitational potential energy are also increasing with increasing polytropic index. Binding energy is decreasing and for limit ultra-relativistic case is in whole radius negative. (This behaviour is similar in case of polytropic spheres).

In Fig. 2 we can see comparison between polytropes and adiabates in non-relativistic and ultra-relativistic case. Radius and mass of spheres are smaller for adiabates and binding energy is smaller for polytropes. In ultra-relativistic case are differences between polytropes and adiabates greater than for non-relativistic case. Characteristic of changes are the same as in non-relativistic case.

Figure 3 shows the differences between quantities for special case when $\rho_{\mathrm{c(a)}} = \rho_{\mathrm{c(p)}}$ and $P_{\mathrm{c(a)}} = P_{\mathrm{c(p)}}$. From Eqs (19) it is obvious that polytropic parameter σ has limits. For $n = 1.5$ has to be $\sigma < 2/3$ and for $n = 3.0$ has to be $\sigma < 1/3$. Ratio of masses $M_{\mathrm{a}}/M_{\mathrm{p}}$ and gravitational potential energies $\Omega_{\mathrm{a}}/\Omega_{\mathrm{p}}$ are increasing, i.e., mass and gravitational potential energy of adiabates grows with polytropic parameter σ more quickly than for polytropes. Ratio of radiuses $R_{\mathrm{a}}/R_{\mathrm{p}}$ is increasing too but for ultra-relativistic case appears something like "shoulder." Ratio of binding energy $E_{\mathrm{b(a)}}/E_{\mathrm{b(p)}}$ is for $n = 1.5$ decreasing and for $n = 3.0$ increasing. The peaks in non-relativistic case are probably just numerical artefacts lacking any physical meaning.

In Fig. 4 are shown dependencies of adiabatic and polytropic index for case $\rho_{\mathrm{c(a)}} = \rho_{\mathrm{c(p)}}$, $P_{\mathrm{c(a)}} = P_{\mathrm{c(p)}}$ (left panel) and for case $\rho_{\mathrm{gc(a)}} = \rho_{gc(p)}$, $P_{\mathrm{c(a)}} = P_{\mathrm{c(p)}}$ (right panel).

Figure 5 shows dependencies of different quantities for special case $\rho_{\mathrm{gc(a)}} = \rho_{gc(p)}$ and $P_{\mathrm{c(a)}} = P_{\mathrm{c(p)}}$. We can see dependencies of ratios $M_{\mathrm{a}}/M_{\mathrm{p}}$, $\Omega_{\mathrm{a}}/\Omega_{\mathrm{p}}$ and $R_{\mathrm{a}}/R_{\mathrm{p}}$ in the left site and zoom part of non-relativistic case in the right site. Quantities have similar behaviour as in previous special case. In graphs of ratio of binding energies to polytropic parameter we can see some instability in ultra-relativistic case for $\sigma \sim 0.62$. It can be connected with ratio of causality.

ACKNOWLEDGEMENTS

The present work has been supported by the Czech grant MSM 4781305903.

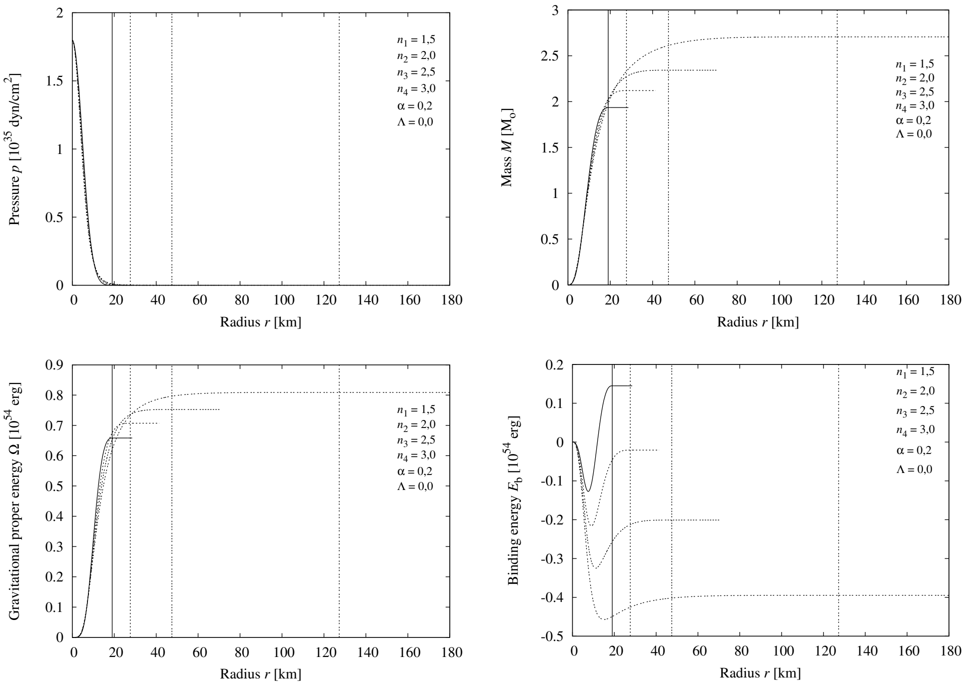

Figure 1. Graphs of the dependence of pressure P, mass M, gravitational potential energy Ω and binding energy $E_{\rm b}$ on radius r of the adiabatic spheres for different value of polytropic index n (continuous line denotes non-relativistic case ($n = 1.5$), dotted line denotes quantities with $n = 2.0$, dash-and-dot line denotes quantities with $n = 2.5$ and broken line denotes ultra-relativistic case $n = 3.0$).

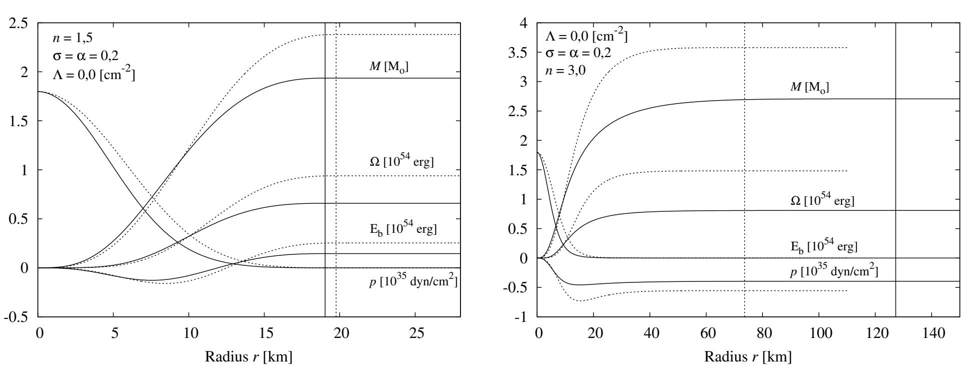

Figure 2. Comparison of polytropic and adiabatic spheres for non-relativistic and ultra-relativistic case.

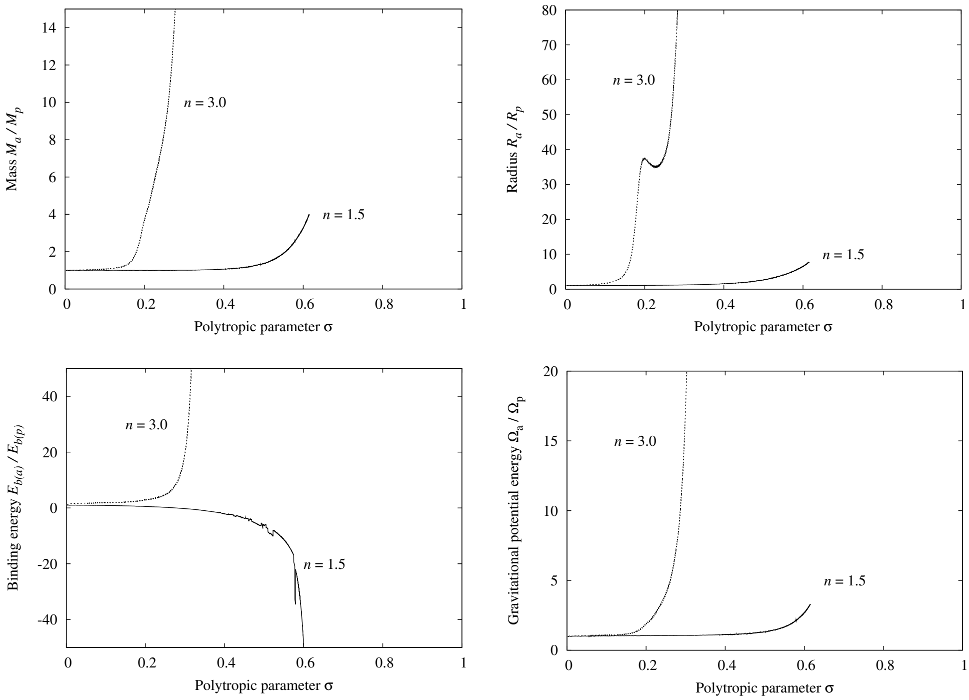

Figure 3. Graphs of comparison of the ratio of different quantities for adiabates and polytropes to polytropic parameter σ.

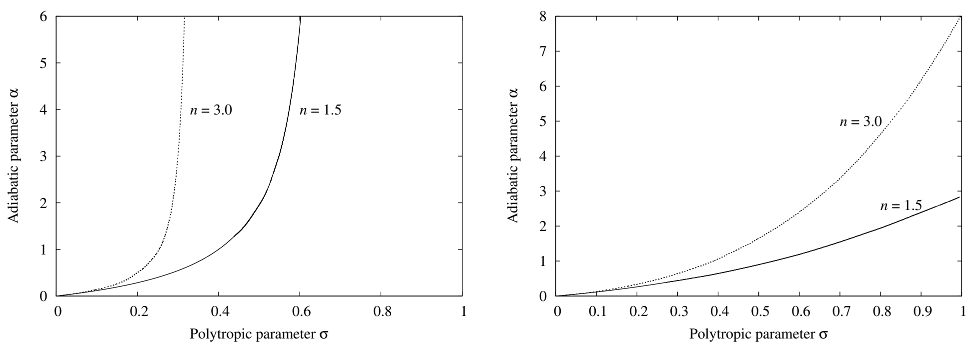

Figure 4. Graphs of comparison of the ratio of different quantities for adiabates and polytropes to polytropic parameter σ.

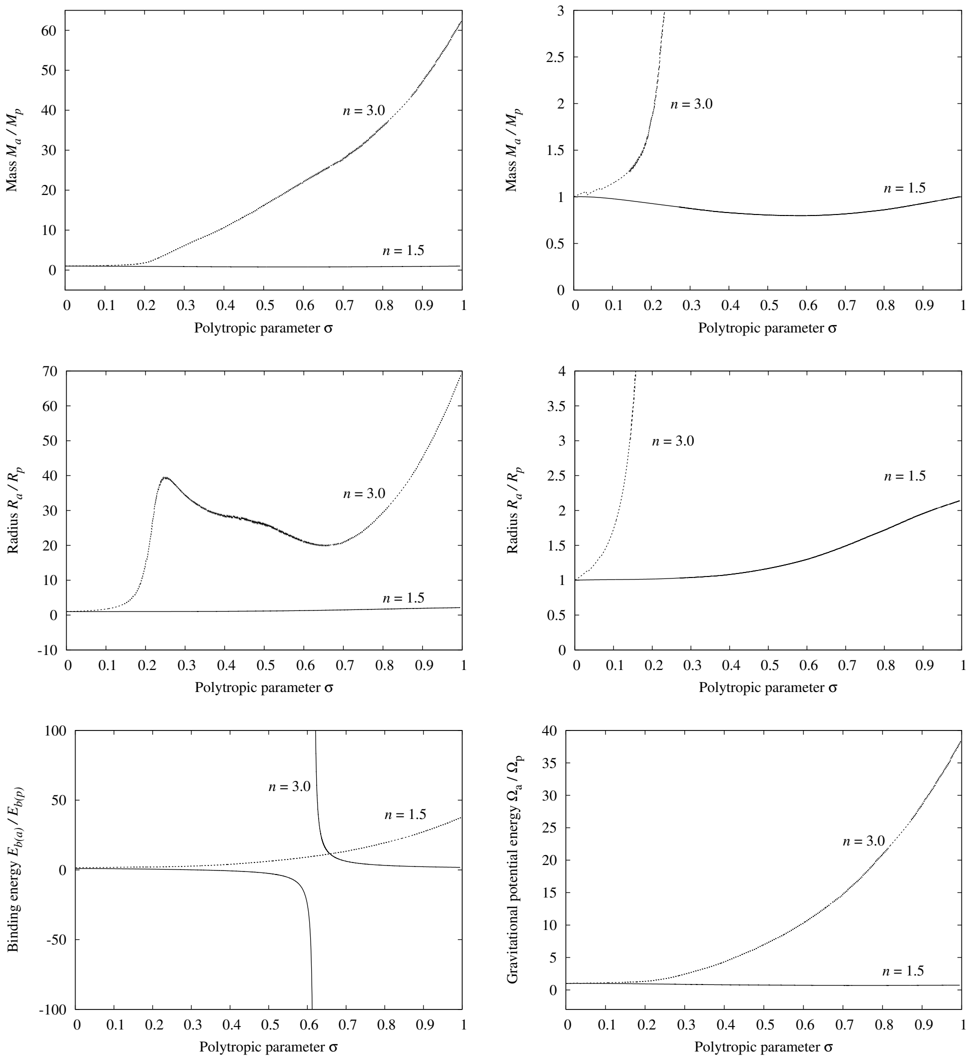

Figure 5. Graphs of comparison of the ratio of different quantities for adiabates and polytropes to polytropic parameter σ.

REFERENCES

Chandrasekhar, S. (1964), The dynamical instability of gaseous masses approaching the Schwarzschild limit in general relativity, *Astrophys. J.*, **140**, p. 417.

Iben, I. (1963), Massive stars in quasi-static equilibrium, *Astrophys. J.*, **138**, p. 1090.

Oppenheimer, J. R. and Volkoff, G. M. (1939), On Massive Neutron Cores, *Phys. Rev.*, **55**, p. 375.

Stuchlík, Z. (2000), Spherically symmetric static configurations of uniform density in spacetimes with a non-zero cosmological constant, *Acta Phys. Slovaca*, **50**(2), pp. 219–228, ISSN 0323-0465/00.

Stuchlík, Z. (2002), The role of a repulsive cosmological constant in astrophysical processes, in O. Semerák, J. Podolský and M. Žofka, editors, *Gravitation: Following the Prague Inspiration (A Volume in Celebration of the 60th Birthday of Jiří Bičák)*, pp. 27–83, World Scientific, New Jersey, London, Singapore, Hong Kong, ISBN 981-238-093-0.

Stuchlík, Z. and Hledík, S. (2005), in preparation.

Tooper, R. F. (1964), General relativistic polytropic fluid spheres, *Astrophys. J.*, **140**(2), pp. 434–459.

Tooper, R. F. (1965), Adiabatic fluid spheres in general relativity, *Astrophys. J.*, **142**(4), pp. 1541–1562.

Proceedings of *RAGtime 6/7: Workshops on black holes and neutron stars, Opava, 16–18/18–20 September, 2004/2005*
S. Hledík and Z. Stuchlík, editors, Silesian University in Opava, Czech Republic, 2005, pp. 119–135

Subnuclear matter in neutron stars and supernovae: nuclear pasta and beyond

William G. Newton

Clarendon Laboratory, Oxford OX1 3PU, UK
w.newton1@physics.ox.ac.uk

ABSTRACT
We review the current status of models of matter at subnuclear density as it appears in astrophysical contexts; namely, during core collapse of supernovae and in the inner crusts of neutron stars. We discuss the main observational probes of this regime, and present preliminary results of our own studies of the so-called nuclear pasta that appears in this density regime.

1 INTRODUCTION

The evolution of a star with a mass of between $\approx 10\,\mathrm{M}_\odot$–$30\,\mathrm{M}_\odot$ ends when the material of the core, which has been processed to iron via a series of fusion reactions throughout its lifetime, reaches the Chandrasekhar mass. At this point electron degeneracy pressure can no longer support the core against its own gravity. The core becomes unstable to radial oscillations and collapses. Electron captures onto protons and photodisintegration of iron nuclei rapidly remove electron and radiation pressure and the collapse proceeds on a timescale of milliseconds (Woosley et al., 2002; Bethe, 1990). The core shrinks by a factor of ≈ 1000 to a radius of 100 km, at which point the density at the centre has reached the order of magnitude that is found in the nuclei of atoms. A convenient density scale on which to describe such matter is set by nuclear saturation density $\rho_\mathrm{s} \approx 3 \times 10^{14}\,\mathrm{g\,cm^{-3}} \equiv 0.16\,\mathrm{baryons\,fm^{-3}} = n_\mathrm{s}$ (1 fm $= 10^{-15}$ m) which is defined as the density at which the energy per nucleon of infinite, symmetric (proton fraction $y_\mathrm{p} = 0.5$) nuclear matter (SNM) has a minimum. In the inner part of the core, the collapse overshoots nuclear saturation density and is halted and reversed by the strongly repulsive short range nucleon-nucleon interaction. This rebound meets matter still falling inwards and a shock develops. What happens next is still a matter being explored through simulation (Janka et al., 2004) but it is thought that the shock stalls as it passes through and interacts with the material of the outer core, only to be revived by the massive neutrino flux emergent from the inner core. The outer material of the star is ejected, and a supernova (SN) explosion becomes visible through electromagnetic (which carries away $\approx 1\%$ of the energy) and neutrino radiation (which carries away the other $99\% \approx 10^{51}$ ergs). The high density core becomes a neutron star (NS). Thus begins a new stage in the star's life, whose properties largely depend on the properties of bulk matter around nuclear saturation density (Janka et al., 2001).

80-7248-334-X

The bulk nuclear matter generated in the collapse of the star is initially hot (10^{10}–10^{12} K $\equiv$ 1–100 MeV). The neutrinos are initially trapped; that is, their mean free path through the matter is much smaller than the dimensions of the core itself, and this inhibits electron capture onto protons (inverse beta decay) (Langanke and Martinez-Pinedo, 2003). The fraction of protons is thus locked at ≈ 0.3. Below nuclear matter densities nucleons still cluster into nuclei and, as we shall see, other shapes. The matter is in nuclear statistical equilibrium (NSE) – equilibrium with respect to the strong nuclear force. Subsequently the matter cools mainly through the loss of neutrinos and the proton fraction falls as inverse beta decay becomes possible again. A cold neutron star has temperatures below 10^9 K $\equiv 0.1$ MeV and a core proton fraction of around 0.1. Since this temperature is small compared to the nuclear energy scale, it can be considered as effectively at zero temperature.

Much theoretical effort has been expended examining the nature of bulk matter at nuclear densities and above so as to supply more realistic physical inputs to the modelling of core collapse SNe and to understand the properties of neutron stars. These inputs usually come in the form of an equation of state (EoS) which describes the pressure of the matter as a function of density and temperature $P = P(\rho, T)$ and from which the mechanical and thermodynamical properties of the matter can be derived. These studies can be broadly divided into two groups: those that include exotic components in the matter (where we define exotic as non-nucleonic), and those that do not.

The dominant theoretical input to those studies without exotic components is the nucleon-nucleon interaction in a many-body context. The nuclear interaction cannot be obtained from QCD exactly, and models obtained indirectly from QCD have limited applicability. All widely used nuclear models are phenomenological, fit to data from nucleon-nucleon scattering and nuclei (systems of up to 300 nucleons and proton fractions around 0.5) (Machleidt, 2001). Their extrapolation to the regime of an (effectively) infinite number of nucleons and a much smaller proton fraction, where no laboratory data exists, is very model dependent and uncertain. Heavy ion collisions are the closest we can come to creating systems of many nucleons at the densities and temperatures of NSs and SNe, and may shed some light on their properties.

A range of exotic components have been postulated to come into existence in stellar nuclear matter. They include hyperons (nucleons with strange quarks in them), meson condensates and, at the highest densities, quark matter (Glendenning, 2000). Many models of stellar nuclear matter include one or more of them. However, our knowledge of the way these particles interact with nucleons and with themselves is far smaller than our knowledge of the nucleon-nucleon interaction alone. Laboratory data is scant or non-existent: some of these effects are based heavily on theoretical speculation.

The hope is that detailed observations of neutron stars and supernovae might constrain our models of nuclear matter at zero and non-zero temperatures and help us understand better both the nature of the nucleon-nucleon interaction in this unfamiliar environment and, through this and the more exotic phenomena postulated, the fundamental theory of the strong interaction.

As a result of the theoretical uncertainties outlined above, we do not have a good idea of the density at which various exotic components appear in the star and of what their effects will be. Thus in the central parts of stellar core collapse and neutron stars it is very difficult to separate the effects on potential observables of exotic and non-exotic components.

At densities just below nuclear saturation ($0.1–1\rho_s$), there exists an inhomogeneous phase (or phases) of matter in which some bulk matter – nuclei or nuclear clusters of various shapes – coexists with a gas of nucleons. The nuclear shapes present have been termed "pasta." The theoretical uncertainties in this regime are limited solely to those in non-exotic physics such as the nucleon-nucleon interaction. The study of matter in this density regime, and astrophysical observations of phenomena influenced by it, could help us constrain the our models of the nucleon physics alone, which in turn would allow us to better disentangle the uncertainties in the physics of matter above nuclear saturation density *if the same description of nuclear matter is used there*.

We will refer to matter in the density regime $0.1–1\rho_s$ as "subnuclear matter." Whereas uniform nuclear matter is expected to be fluid like, subnuclear matter may exist in a variety of phases ranging from solid to liquid crystal. Its mechanical and thermodynamic properties are expected to be quite different to the uniform phase and probably vary quite substantially with density and temperature within the subnuclear phase.

In this paper we review our current understanding of subnuclear matter and its observational implications, and give some preliminary results from our efforts to simulate it.

2 SUBNUCLEAR MATTER AND NUCLEAR PASTA

Let us place our studies in physical context by examining the anatomy of a neutron star. For the following description we will not mention the pasta phase; we will later explain where it fits in.

We are dealing with a system of $\approx 10^{57}$ baryons (equivalent to one solar mass). At zero temperature and pressure, the equilibrium (ground state) configuration of a system of about 90 baryons is $^{56}_{26}$Fe. Its energy cannot be lowered by changing its composition through the strong, weak or electromagnetic interactions. For 10^{57} baryons at zero temperature and pressure, and ignoring gravity, the ground state is a large integer number of iron nuclei arranged in a lattice so as to minimise the configurational energy. The electrons are in a ferromagnetic state.

Adding gravity, the system will be arranged in a spherically symmetric configuration so as to minimise the gravitational energy. The outer surface will be at zero density, and the density will increase to a central density. The iron lattice will form the outermost layer; let us now move inwards towards the centre.

At a density of $\rho \sim 10^7\,\mathrm{g\,cm^{-3}}$ the electrons will become relativistically degenerate and their Fermi energy ($\sim 1\,\mathrm{MeV}$) allows inverse beta decay to occur: electrons at the Fermi surface combine with protons to produce a neutron and anti-neutrino (which escapes), lowering the energy:

$$\mathrm{n} \rightarrow \mathrm{p} + \mathrm{e}^- + \bar{\nu}_\mathrm{e}\,. \tag{1}$$

The reverse process is inhibited because the electrons fill the Fermi sea, leaving no place for an extra electron to go. Thus as one moves inwards, and the density increases, the equilibrium nuclei move step by step away from iron nuclei and towards more neutron rich nuclei. In addition, the reduction in the proportion of protons in the nuclei decreases internal Coulomb repulsion and allows larger nuclei to form.

At a density of $\rho \sim 4 \times 10^{11}\,\mathrm{g\,cm^{-3}}$ the ratio of neutrons to protons in the nuclei reaches a critical level: the nuclei have become so large that the nuclear force only weakly binds the outermost neutrons, and *neutron drip* occurs. Neutrons leak out of the nuclei and a two phase system develops in which nuclei and free neutrons co-exist and together form the ground state of matter at this density.

At densities of $\rho \sim 4 \times 10^{12}\,\mathrm{g\,cm^{-3}}$ the number of free neutrons has grown so large that their pressure exceeds that of the free electrons, and the neutron fluid now controls the properties of this system.

At a density of $\rho \sim 2.5 \times 10^{14}\,\mathrm{g\,cm^{-3}}$ (nuclear saturation density), nuclei are so close that they touch one another. Beyond this density, the nuclei merge into a fluid of neutrons and protons. This fluid is in beta equilibrium with the electrons. When the electron chemical potential exceeds the muon rest mass, it becomes energetically favourable for neutrons to decay into protons plus muons (a new decay channel has opened up), and so muons exist in beta equilibrium too.

The density region below neutron drip point is termed the outer crust. Above neutron drip point but below the point at which the nucleons form a homogeneous fluid is the inner crust. Above this point is the core. The inner and outer crusts combined form the outer $\lesssim 1$ km of the star, but their rigidity compared with the fluid core means they are expected to play a large part in the neutron star dynamics.

2.1 Complexity, frustration and the appearance of pasta

Matter on Earth is made of atoms: the short range, attractive nuclear interaction binds nucleons into a nucleus on a scale of a few fm, and nuclei are separated of by distances of the order 1000 fm. In subnuclear matter, the separation of nuclei and hence their coulomb repulsion has become comparable to the scale over which the attractive nuclear interaction operates. Matter is frustrated: it is impossible to minimize the energy of the system with respect to all microscopic interactions simultaneously, and the result is a very large number of low energy states into which the matter can arrange itself (Horowitz and Perez-Garcia, 2004). In this case, the competition between coulomb repulsion and the nuclear surface tension results in a large number of possible nuclear configurations very different from "ordinary" spherical nuclei. These shapes are termed nuclear pasta. The subnuclear system shares many similarities with more familiar, complex fluids such as solutions of polymers. See (Watanabe and Sonoda, 2005) for a more detailed exploration of this.

Finally it is important to note the major difference between the pasta phase in neutron stars (zero temperature, proton fraction ~ 0.1) and supernovae (finite temperature, proton fraction ~ 0.3): in neutron stars the pasta phase coexists with a significant density of external neutron gas. This gas is mostly absent or very low in density in the pasta phase in supernovae (Watanabe and Sonoda, 2005).

2.2 Pasta studies with nuclear degrees of freedom

The nuclear pasta regime was first studied using the semi-classical liquid drop model, in which the degrees of freedom are nuclear rather than nucleonic, and within the Wigner–Seitz approximation which places restrictions on the nuclear shapes describable by assuming that a unit cell of the regular pasta structure can be replaced by a spherical cell of the same volume. In the liquid drop model the matter is broken down into elements such as the bulk (the matter inside and outside of the pasta), the surface, and so on. Their properties are supplied by fitting results of microphysical calculations of infinite nuclear matter to a semi-empirical mass formula and, depending on the model used, they can vary quite widely. This affects predictions of, for example, the density of transition to uniform matter, and most of the studies cited below can accommodate a range of such values.

Ravenhall et al. (1983) first established the basic shapes that one might expect to find in subnuclear matter, and named them after types of pasta, giving birth to the nomenclature that has been retained up to the present day. They found that within their formalism, nucleons arrange themselves into the following shapes: with increasing density, spheres, cylinders (spaghetti), slabs (lasagna), cylindrical holes (tubes, or penne), spherical holes (breaking the pasta theme, bubbles or Swiss cheese) and finally uniform matter.

The nuclear and subnuclear equation of state of supernova matter has been most extensively studied using the liquid drop formalism; indeed, the most widely used EoS used today in supernova simulations is the Lattimer and Swesty (LS) EoS (Lattimer et al., 1985; Lattimer and Swesty, 1991). The advantage of such a formalism is the speed with which one can obtain the pressure at any given density and temperature during the simulation rather than interpolate between points on an EoS table.

The effect of thermal fluctuations on the pasta shapes in NSs and SNe has been studied in the liquid drop framework, and it has been found that even at temperatures in neutron star crusts the long range order of the shapes may be destroyed. For example, one study finds that individual lasagna shapes extend only for ≈ 100–1000 fm before becoming disrupted (Watanabe et al., 2000a,b).

It is mostly assumed that the pasta forms a rigid lattice (e.g., bcc[1] for spherical nuclei), but Pethick and Potekhin (1998) have pointed out that along the extension of the shapes, there exists translational invariance and thus it behaves more like a fluid in that direction, whilst remaining in a lattice structure transverse to the extension. The pasta shapes seem likely, therefore, to exist somewhere between a solid phase and liquid phase, much like a liquid crystal, and their mechanical and thermal properties will probably vary significantly from one shape region to another. This has not been the subject of much consideration.

2.3 Pasta studies with nucleonic degrees of freedom

2.3.1 Quantum molecular dynamics

Studies using the liquid drop model neglect the microscopic degrees of freedom. However, the microscopic scale (nucleons) is not far separated from the semi-macroscopic scale (pasta), and microscopic degrees of freedom could play an important role and should be taken into consideration.

The technique of quantum molecular dynamics (QMD) and similar (Maruyama et al., 1998) are semi-classical microscopic approaches that leads to an improved treatment of the

[1] Abbreviation "bcc" stands for the lattice type "body centred cubic."

pasta regime. Each nucleon, represented by a Gaussian wavefunction, is evolved according to Newtonian equations of motion

$$\dot{\boldsymbol{R}}_i = \frac{\partial H}{\partial \boldsymbol{P}_i}, \qquad \dot{\boldsymbol{P}}_i = -\frac{\partial H}{\partial \boldsymbol{R}_i} \tag{2}$$

and a stochastic two-body term. Here H is the two body Hamiltonian which describes the nuclear force, and includes a term to mimic the Pauli exclusion principle, and $\boldsymbol{R}_i$ and $\boldsymbol{P}_i$ are the position and momentum of the ith particle.

Pasta has been studied using this method by placing A nucleons in a large cubic box, volume V (with A and V adjusted to give the appropriate baryon number density), with periodic boundary conditions. No assumption on the nuclear shape had to be made, and the box can be made large enough to include the effects of electron screening.

The pasta's dynamical response to a neutrino flux has been calculated in this framework (Horowitz and Perez-Garcia, 2004; Horowitz et al., 2004), and significant strength at low energies from excitations of the internal degrees of freedom of the pasta has been found. This may be an important effect in the treatment of neutrino interactions with matter in SN simulations, especially concerning shock revival.

The pasta shapes themselves and their sequence have also been studied in detail using QMD at zero and finite temperature (Watanabe et al., 2002, 2004). It is found that more complicated shapes intermediate between the canonical pasta shapes may exist, and display rubberlike or spongelike mechanical qualities. It was also shown that pasta can be formed on a timescale much smaller than NS cooling by cooling a uniform nucleon distribution, and that it can also form by compression of a bcc lattice of spherical nuclei on a timescale much smaller than that of core collapse.

2.3.2 Hartree–Fock

Although QMD does describe matter in terms of the nucleonic degrees of freedom, it does not contain some important quantum effects that are seen in nuclear systems such as the discrete shell like distribution of the single particle energies of nucleons confined to a nucleus. The simplest way of incorporating these effects into the study of subnuclear matter is through the Hartree–Fock (HF) method, in which the problem of solving the A body Schrödinger equation with a two-body nuclear potential is reduced to solving A coupled one body Schrödinger equations with a common one-body mean field.

The subnuclear phase was first studied in the HF approximation by Bonche and Vautherin (1981), who in one dimension, in the Wigner–Seitz approximation, used it to calculate the EoS of SN matter below saturation density. They were able to observe the nuclei and external neutron gas emerge self-consistently.

Recently, NS matter was studied in the HF approximation in a cubic box, free of the Wigner–Seitz approximation (Magierski and Heenen, 2002). The basic pasta shapes coexisting with the external neutron gas emerged naturally, and in addition other exotic shapes were observed. An additional, important effect was uncovered to do with the scattering of the free neutrons comprising the external neutron gas off the nuclear clusters. The effect is two-fold: the energy distribution of the free neutrons is discretized like those of the bound nucleons, forming a shell structure; and the scattering causes an effective interaction between nuclear clusters analogous to the Casimir effect in quantum field theory. It has thus been dubbed the Fermionic Casimir effect (Magierski et al., 2002). The energy of this interaction is comparable to the energy difference between the different shape phases. As a result, the order in which the shape changes occur may be different to the simple sequence initially thought, and several shapes may coexist at the same density in different areas of the star. The effects this coexistence might have on crustal dynamics have yet to be explored.

Dynamical response of pasta has been studied using a modified HF method in one dimension in the Wigner–Seitz approximation (Khan et al., 2005). It is found that low energy supergiant resonances occur across two Wigner–Seitz cells which would affect significantly the thermodynamics of the inner crust of NSs and the interactions of neutrinos with SN matter.

2.4 Superfluidity

At a critical temperature of $\approx 10^9$–10^{10} K neutrons and protons in the core and neutrons in the external gas in the NS inner crust are expected to pair up and form a superfluid. Superfluids have zero viscosity, and as a result cannot support bulk rotation. In order to retain its angular momentum, the neutron superfluid has to arrange itself into quantized vortices aligned with the rotation axis, with a cross-sectional density of $\approx 10^4/P\,\mathrm{cm}^{-2}$ where P is the rotational period of the star in seconds. Various stages of the neutron star's life see it spinning down or up (see next section), resulting in the vortices moving outwards or inwards from the centre of the star. Such behaviour in spinning superfluids has been observed in the laboratory (see, for example, the work on sodium gas cooled to a Bose–Einstein condensate in Abo-Shaeer et al., 2001). However, the critical temperature and properties of the various superfluids in neutron stars are still to be determined accurately because of the uncertainties in extrapolating the nucleon pairing interaction to the regime of extremely neutron rich, bulk matter (see Dean and Hjorth-Jensen, 2003 for a review). The effect of pairing on nuclear pasta, and the effect of pasta on vortices, is still to be explored.

3 OBSERVATIONAL IMPLICATIONS

We now briefly review some phenomena associated with NSs and SNe that have been observed or may potentially be observed and could act as probes of the pasta regime.

3.1 Supernova simulations

Properties of core collapse supernovae and their mechanism may be deduced from their observational characteristics: light curves and spectra from the explosion and its remnant provide information about its energetics and the distribution of elements created. The events of the core of the explosion, however, are not accessible optically, although they may be probed through neutrino and gravitational wave observations.

To deduce the mechanisms and properties of matter in the core collapse, one must develop theoretical models to be confronted by the observations. The most realistic supernova simulations so far, however, suffer from the following drawback: the shockwave that is created when the core bounces stalls before it can eject the outer envelope – in other words, there is no explosion (Janka et al., 2001). However, these models do not include a realistic treatment of the interaction of neutrinos with the nuclei and pasta phase of the subnuclear medium. It is generally accepted that the shock will be revived by such interactions, so it is essential to examine them carefully. For example, the large number of low energy configurations that are be available in the pasta regime may allow significant transfer of energy from the neutrinos to the nuclear medium (Horowitz et al., 2004), and yet are only just starting to be studied in detail.

3.2 Young neutron stars: cooling

A newly born neutron star cools very quickly through neutrino emission, while the crust stays hot a lot longer, cooling on its thermal conduction timescale mainly through heat flow into the core which can thought of in terms of a cooling wave flowing from the centre of the star, during which time the effective temperature stays constant at $\approx 2 \times 10^9$ K. As the cooling wave reaches the edge of the star, the effective temperature drops sharply. The magnitude of the drop and duration of this thermal relaxation process depends mainly on the thermal conductivity and heat capacity of the inner crust (Gnedin et al., 2001). Observations of young neutron stars ($\lesssim 100$ yrs) during the period of the emergence of the cooling wave would thus constrain the properties of the inner crust, including the nature of the superfluidity and its critical temperature there. There have not been any studies of this epoch that take into account the effects of pasta.

Thermal emission has been detected from several young ($\approx 10^4$ yrs), isolated neutron stars and may help constrain neutrino and thermal cooling models (Page et al., 2004). There are suggestions also that the properties of pasta can allow the more efficient direct Urca process for neutrino cooling where spherical nuclei may suppress it.

3.3 Adolescent neutron stars: spin down and glitches

Neutron stars enter a phase of spin down after their birth due to torque exerted by their magnetic fields. The spin down rate can measured very accurately by observing their pulsed radio emission. Most radio pulsars exhibit the glitch phenomenon in which it is observed the star's spin frequency increases suddenly before relaxing back to its prior spin down rate. In recent years it has become apparent that glitches vary greatly in their magnitude and the nature and timescale of the relaxation (Horvath, 2004, and references therein).

There have been two major models put forward to explain the glitch phenomenon. The first is the starquake theory, in which the solid crust of the neutron star develops stresses as the spin down decreases centrifugal support from the core. When the stresses reach a certain magnitude, the crust cracks and rearranges itself into a configuration with smaller moment of inertia, increasing the rotational frequency. The viability of this mechanism depends on the amount of elastic energy that can be stored in the crust, and this will be influenced by the mechanical properties of subnuclear matter. A second model involves the interaction of the superfluid vortices with nuclei in the inner crust: it has been suggested that in certain circumstance it is energetically favourable for vortices to *pin* to the nuclei, impeding their movement radially outwards as the star spins down. Thus there develops a rotational velocity difference between the lattice of nuclei and the neutron superfluid. Then there is either a catastrophic unpinning of vortices and sudden motion of them outwards when the rotational velocity difference reaches a critical value (mechanical models) or the vortices unpin when a large input of thermal energy into the inner crust occurs from, for example, a starquake (thermal models) (Horvath, 2004; Larson and Link, 2002; Crawford and Demiański, 2003). Others suggest pinning does not occur at all, and that we should look elsewhere to explain glitches (Jones, 1998). One thing is for certain: the nature of pinning, and indeed whether or not it occurs at all, depends critically on the properties of the nuclei and pasta in the inner crust and their interaction with superfluid neutrons and vortices.

3.4 Mature neutron stars: accretion powered spin up and X-ray emission

Later on in its life a neutron star with a binary companion enters a phase of its life during which it accretes material off its companion, gaining angular momentum and spinning up, eventually to periods of order milliseconds. The accreted material reaches the surface of the neutron star and, when its density and temperature are great enough, undergoes thermonuclear burning. The observational properties of such binaries are many and varied (Campana et al., 1998; Wijnands, 2005).

If accretion occurs at near to super Eddington rates, burning can occur stably on the surface and no material is ejected. The weight of the accreted material compresses the crust, forcing the bottom layers into the core. If accretion continues for long enough in a stable way, the whole crust can be forced into the core, dissolving into uniform nuclear matter, replaced by the accreted matter. Whereas the original crust was composed of material processed through to nuclear statistical equilibrium, the new crust will not be. The properties of the pasta in the new crust may have changed quite considerably.

Energy generated by nuclear burning at the surface can diffuse inwards, heating the interior. If one assumes the inner crust is completely crystalline in its nature, with a well defined sequence of nuclei with increasing density that may not be monotonic with respect to the nucleon number A, one can apply the Lindemann melting criterion to determine at what temperature the lattice will melt at various densities (Haensel and Zdunik, 2003; Brown, 2000). One finds that it melts in layers: liquid sandwiched between solid. This obviously has an impact on the mechanical properties of the crust. The effect of heating on the non-crystalline phases of pasta has not been studied to our knowledge.

During the quiescent phase of soft X-ray transients (SXRTs), neutron stars that accrete off a low mass companion, X-ray radiation is observed that is greater than one would expect from an old, cooling neutron star. It has been suggested by Haensel and Zdunik (2003) that this radiation comes from the crust, heated during the last accretion episode. These observations could help us constrain the thermal conductivity of the crust.

3.5 Neutron star oscillations and mergers: gravitational waves

With a network of gravitational wave observatories across the world reaching operational sensitivities, we are about to embark on a new era of observational astronomy using gravitational waves to probe events that would otherwise be inaccessible to us. Some observations should allow us to constrain our theories of nuclear matter.

Gravitational wave asteroseismology – the examination of gravitational waves from oscillation modes in young and old neutron stars – should prove a fruitful method of constraining the EoS of nuclear matter (Andersson and Kokkotas, 2004; Ferrari et al., 2003; Benhar et al., 1999). Such oscillations should be sensitive to the mechanical properties of subnuclear matter in the inner crust.

The final moments of the inspiral of a binary neutron star system offer a potentially powerful source of gravitational waves, the observation of which would allow a determination of the binary parameters and other parameters such as the innermost stable circular orbit (ISCO) which are particularly sensitive to the properties of the crustal EoS (Bejger et al., 2005).

3.6 Multifragmentation reactions

Finally we mention the possibility of studying nuclear matter at subnuclear densities in labs here on Earth. The multifragmentation stage of heavy ion collisions produces, at high densities and temperatures, similar structures to those predicted for nuclear pasta, albeit briefly and at a higher proton fraction (Botvina and Mishustin, 2005), and may allow some constraints to be imposed on properties of the pasta phases.

4 A NEW STUDY OF SUBNUCLEAR MATTER

We have presented a basic review of the present state of inner crust theory. We believe there is sufficient motivation for a further study of the pasta phases, one focused on an in depth examination of microphysical effects (involving the nucleon degrees of freedom and quantum effects) and their implications for thermal and mechanical properties and for the EoS. Magierski and Heenen (2002) demonstrated the existence of the Fermionic Casimir effect using the Hartree–Fock (HF) method, but their study was limited to very few densities and only considered neutron star matter at zero temperature. We would like to use the same HF method in three dimensions, extending it to a full survey of the neutron star inner crust and subnuclear matter in supernovae, and examining the sequence of phases we find, their energies, their responses to neutrinos and to mechanical perturbations and their thermal properties. We would also like to calculate the EoS of subnuclear matter. We have previously calculated the EoS of uniform nuclear matter in the HF approximation, so we will be able to join the two together self-consistently. This would be advantageous for applications to hydrodynamical simulations of SNe and NSs, as there would be no discontinuities arising from artificial joins in the EoS. It is also desirable to have as self-consistent an EoS as possible from the point of view of constraining our nuclear models using observations. Finally we note that, while the HF method more suited than, say, QMD, to include quantum microphysical effects, it lacks the ability that QMD simulations have to study long range effects such as thermal fluctuations and lattice vibrations, since to extend our simulation volume to sufficient sizes is computationally unfeasible. Thus our method should be viewed as complementary to QMD until computer technology catches up with our theoretical ambitions!

The Hartree–Fock method is used in conjunction with phenomenological effective two-nucleon potentials such as the Skyrme force (which we use here) and is extensively described in nuclear physics literature (see, e.g., Bender et al., 2003). We briefly review the method in Appendix A.

We consider density, temperature and proton fraction y_{p} as parameters of the matter in bulk, and are interested in the following ranges:

- $0.001\,\mathrm{fm}^{-3} < n_{\mathrm{b}} < 0.16\,\mathrm{fm}^{-3}$
- $0\,\mathrm{MeV} < T < 10\,\mathrm{MeV}$
- $0 < y_{\mathrm{p}} < 0.5$

We make the following *assumption* about the matter we are attempting to describe: at a given temperature and density the matter is arranged in a periodic structure through a sufficiently large region for a unit cell to be identified. Given this, we may calculate only one unit cell and obtain from this both the bulk and microscopic properties of the matter self consistently, and directly see how the one affects the other.

Each unit cell will contain a certain number of neutrons N and protons Z, making a total baryon number of $A = N + Z$. In the lower density limit ($n_{\mathrm{b}} \lesssim 0.0001\,\mathrm{fm}^{-3}$), these particles will be arranged in what we would recognize as a roughly spherical (but large) nucleus at the centre of the cell. As the density is increased, however, the shape will deform, neutrons and protons will become unbound, and the distinction between the nucleus and the unbound neutrons and protons will be lost, and we will be forced to think of the contents of the cell as a single entity, the nuclear configuration.

Finally, we note that we have freedom to increase the cell volume V and number of nucleons A and still describe the same density. In our first approach to this study, we would like to determine a single representative cell size. This is done by calculating configurations at constant density, temperature and proton fraction, varying cell size, and selecting the configuration that gives the minimum free energy.

4.1 Preliminary results

We are still at the testing stages of our simulations, but we present some preliminary results. In the four figures that we show we have integrated the proton and neutron densities in the cell over the z direction for display purposes.

Figures 1 and 2 show the proton and neutron distributions from a sequence of configurations obtained at eight densities, from $0.0195\,\mathrm{fm}^{-3}$ to $0.0976\,\mathrm{fm}^{-3}$ (nuclear saturation density being $0.16\,\mathrm{fm}^{-3}$) and at zero temperature and a proton fraction of $y_{\mathrm{p}} = 0.03$. Note, we have not minimized with respect to cell volume at each density: we have used the same volume throughout. One can see the development of the central nucleus and neutron gas; notice that any distinction between the two is quite arbitrary. One can also see that at the highest density we have essentially uniform matter, illustrating the ability of our simulation to bridge the interface between subnuclear and nuclear matter self-consistently.

Figures 3 and 4 show the proton and neutron distributions from a sequence of configurations obtained at four temperatures, from 0 MeV to 9 MeV, and at a density of $0.06\,\mathrm{fm}^{-3}$

and a proton fraction of $y_{\mathrm{p}} = 0.1$. Here we see nuclear configurations quite different to a single nucleus in a cell: at 0 and 2 MeV we see configurations that might be classified as

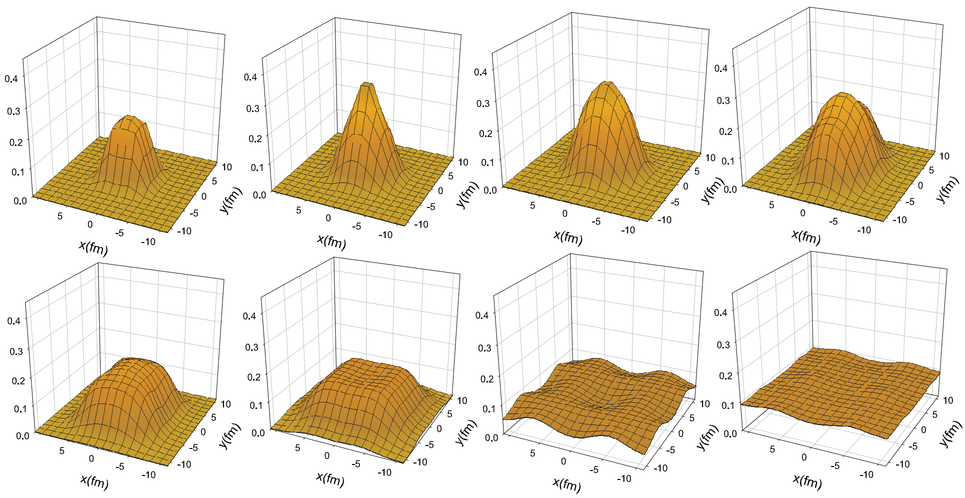

Figure 1. Sequence of proton densities integrated over the z direction at increasing densities. The densities are, from left to right, top to bottom, 0.0195, 0.0312, 0.0390, 0.0507, 0.0585, 0.0702, 0.0780 and 0.0976 fm^{-3}. The scale along the vertical axis is fm^{2}.

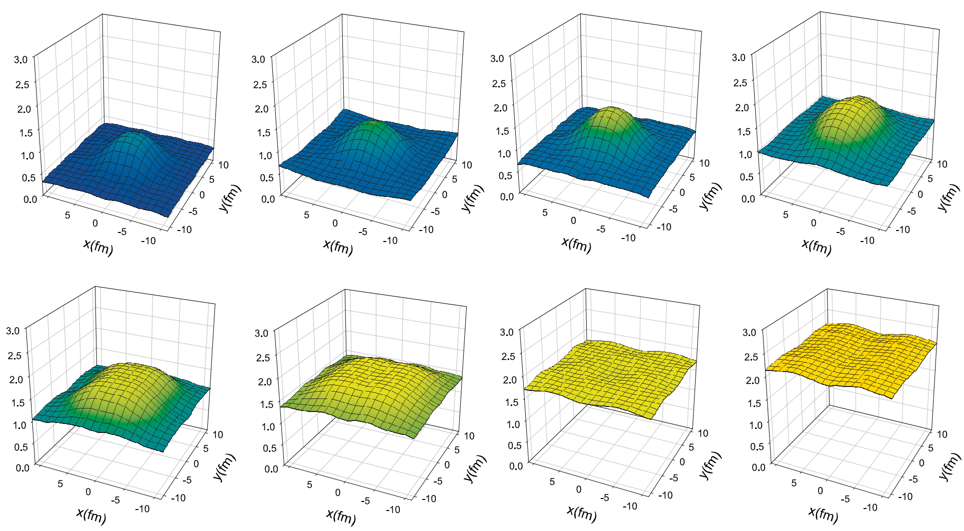

Figure 2. Sequence of neutron densities integrated over the z direction at increasing densities. The densities are, from left to right, top to bottom, 0.0195, 0.0312, 0.0390, 0.0507, 0.0585, 0.0702, 0.0780 and 0.0976 fm^{-3}. The scale along the vertical axis is fm^{2}.

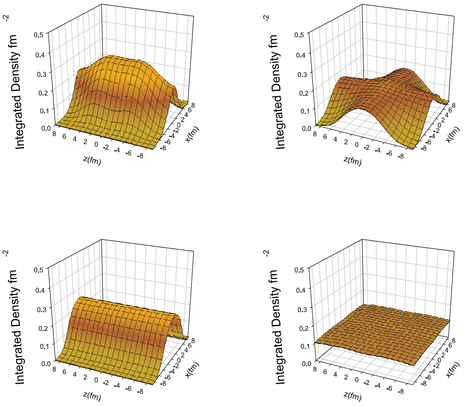

Figure 3. Sequence of proton densities integrated over the z direction at increasing temperatures. The temperatures are, from left to right, top to bottom, 0, 1, 2 and 9 MeV. The scale along the vertical axis is fm^2.

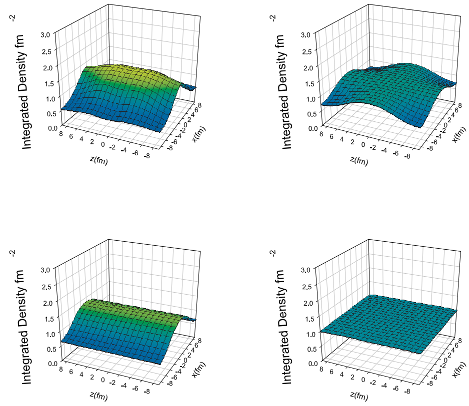

Figure 4. Sequence of neutron densities integrated over the z direction at increasing densities. The densities are, from left to right, top to bottom, 0, 1, 2 and 9 MeV. The scale along the vertical axis is fm^2.

cylindrical in the pasta scheme; at 1 MeV we have a configuration that does not appear in the pasta scheme at all. As we push the temperature to 9 MeV ($\approx 10^{11}$ K) we again see dissolution to uniform matter.

We conclude by emphasizing again that these results are preliminary. They have been calculated at arbitrary cell sizes and there are still tests to be done. However, we hope they demonstrate our ability to self-consistently produce a range of nuclear shapes with no prior assumptions on the nuclear geometry except tri-axiality, and that we can smoothly model the transition to uniform matter.

APPENDIX A: SKYRME–HARTREE–FOCK THEORY

We use the Skyrme interaction, which is a two body interaction between particles i and j,

$$
\begin{aligned}
V_{ij,\mathrm{Skyrme}} = {} & t_0(1+x_0P_\sigma)\delta(\boldsymbol{r}_i-\boldsymbol{r}_j) \\
& + \tfrac{1}{2}t_1(1+x_1P_\sigma)\left[\boldsymbol{p}_{12}^2\delta(\boldsymbol{r}_i-\boldsymbol{r}_j)+\delta(\boldsymbol{r}_i-\boldsymbol{r}_j)\boldsymbol{p}_{12}^2\right] \\
& + t_2(1+x_2P_\sigma)\boldsymbol{p}_{12}\cdot\delta(\boldsymbol{r}_i-\boldsymbol{r}_j)\boldsymbol{p}_{12} \\
& + \tfrac{1}{6}t_3(1+x_3P_\sigma)\rho^\alpha(\bar{\boldsymbol{r}})\delta(\boldsymbol{r}_i-\boldsymbol{r}_j) \\
& + \mathrm{i}t_4\boldsymbol{p}_{12}\cdot\delta(\boldsymbol{r}_i-\boldsymbol{r}_j)(\boldsymbol{\sigma}_i+\boldsymbol{\sigma}_j)\times\boldsymbol{p}_{12}\,,
\end{aligned}
\tag{A1}
$$

where ρ is the baryon number density, $\boldsymbol{p}_{12}=\boldsymbol{p}_i-\boldsymbol{p}_j$ is the relative momentum, P_σ is the spin exchange operator, $\boldsymbol{\sigma}$ is the vector of Pauli spin matrices and $\bar{\boldsymbol{r}}=(\boldsymbol{r}_i+\boldsymbol{r}_j)/2$. t_0, t_1, t_2, t_3, t_4, x_0, x_1, x_2, x_3 and α are parameters which are adjusted so that the results of many body calculations using this potential match experimental properties of nuclei.

Using this potential we have to solve the many-body Schrödinger equation for A nucleons

$$\hat{H}\Psi = \left(\sum_{i=1}^{A} \frac{\hbar^2 \boldsymbol{p}_i^2}{2m} + \sum_{i<j}^{A} V_{ij,\mathrm{Skyrme}}\right)\Psi = E\Psi\,. \tag{A2}$$

What is the form of the many body wavefunction Ψ? Well, many body fermion wavefunctions must be constructed from *Slater determinants* Φ, which are antisymmetric products of the single particle wavefunctions ψ:

$$\Phi_{k_1,\ldots,k_A}(\boldsymbol{r}_1,\ldots,\boldsymbol{r}_A) = \frac{1}{\sqrt{A!}}\begin{vmatrix} \phi_{k_1}(\boldsymbol{r}_1) & \ldots & \phi_{k_1}(\boldsymbol{r}_A) \\ \vdots & & \vdots \\ \phi_{k_A}(\boldsymbol{r}_1) & \ldots & \phi_{k_A}(\boldsymbol{r}_A) \end{vmatrix}\,. \tag{A3}$$

$\phi_k(\boldsymbol{r}_i)$ is the single particle wavefunction of the ith nucleon in momentum state k. The momentum states $k_1,\ldots,k_A$ are taken from the infinity of available states.

In general, the solution to equation (A2) is a linear combination of all possible Slater determinants:

$$\Psi(\boldsymbol{r}_1,\ldots,\boldsymbol{r}_A) = \sum_{k_1,\ldots,k_A} c_{k_1,\ldots,k_A}\Phi_{k_1,\ldots,k_A}(\boldsymbol{r}_1,\ldots,\boldsymbol{r}_A)\,, \tag{A4}$$

where the sum is over all possible combinations of A momentum states selected from the infinite number available. Then the probability of finding the nucleons in a certain combination of states if given by the corresponding coefficient c.

As one might guess at this point, finding such a solution is an intractable problem, and we must make an approximation, which is exactly what we do.

A1 The Hartree–Fock approximation

The Hartree–Fock approximation states that *the ground state wavefunction for a nuclear configuration is given by a single Slater determinant*, and not a linear combination of all possible ones. In other words, there is a definite set of states $k_1,\ldots,k_A$ that are occupied by individual nucleons with an occupation probability of 1.

How do we find this wavefunction? Well, we use the variational principle which states that *the best approximation to the ground state for the Hamiltonian $\hat{H}$ is obtained for that wave function Φ whose energy expectation value is minimal.* Mathematically, we write

$$\delta E[\Phi] = \delta\langle\Phi|\hat{H}|\Phi\rangle = 0\,. \tag{A5}$$

Carrying out this variational procedure with respect to the single particle wavefunctions of a single Slater determinant, the two body Skyrme potential becomes a one body density-dependent potential and the A-body Schrödinger equation for the A-body wavefunction becomes A single body Schrödinger equations for the single particle wavefunctions:

$$h_{\mathrm{HF}}\phi_{i,q} = \left[-\nabla\frac{\hbar^2}{2m_q^*}\nabla + u_q(r) + w_q(r)\frac{(\nabla\times\boldsymbol{\sigma})}{i}\right]\phi_{i,q} = \epsilon_{i,q}\phi_{i,q}\,. \tag{A6}$$

Here, $q = \mathrm{p, n}$ labels the isospin states, i the single particle states, w_q is the spin-orbit potential (which we currently set to zero), u_q is the single particle potential, and m_q^* is the effective mass.

Physically, in making this approximation we are making the assumption that the nucleons in a nucleus or a nuclear configuration move independently of each other in an average potential created by all the other nucleons.

The one body potentials derived from the Skyrme interaction are given by

$$\begin{aligned} u_q = {} & t_0\left(1+\tfrac{1}{2}x_0\right)\rho - t_0\left(\tfrac{1}{2}+x_0\right)\rho_q \\ & + \frac{1}{12}t_3\rho^\alpha\left[(2+\alpha)\left(1+\tfrac{1}{2}x_3\right)\rho - 2\left(\tfrac{1}{2}+x_3\right)\rho_q - \alpha\left(\tfrac{1}{2}+x_3\right)\frac{\rho_\mathrm{p}^2+\rho_n^2}{\rho}\right] \\ & + \frac{1}{4}\left[t_1\left(1+\tfrac{1}{2}x_1\right)+t_2\left(1+\tfrac{1}{2}x_2\right)\right]\tau - \frac{1}{4}\left[t_1\left(\tfrac{1}{2}+x_1\right)-t_2\left(\tfrac{1}{2}+x_2\right)\right]\tau_q \\ & - \frac{1}{8}\left[3t_1\left(1+\tfrac{1}{2}x_1\right)-t_2\left(1+\tfrac{1}{2}x_2\right)\right]\nabla^2\rho \\ & + \frac{1}{8}\left[3t_1\left(\tfrac{1}{2}+x_1\right)+t_2\left(\tfrac{1}{2}+x_2\right)\right]\nabla^2\rho_q \\ & - \frac{1}{2}t_4\left(\nabla\cdot\boldsymbol{J}+\nabla\cdot\boldsymbol{J}_q\right)+U_\mathrm{Coul} \end{aligned} \tag{A7}$$

and the effective mass is

$$\begin{aligned} \frac{\hbar^2}{2m_q^*} = \frac{\hbar^2}{2m_q} & + \frac{1}{4}\left[t_1\left(1+\tfrac{1}{2}x_1\right)+t_2\left(1+\tfrac{1}{2}x_2\right)\right]\rho \\ & - \frac{1}{4}\left[t_1\left(\tfrac{1}{2}+x_1\right)-t_2\left(\tfrac{1}{2}+x_2\right)\right]\rho_q \end{aligned} \tag{A8}$$

with the following densities and currents depending on the single particle wavefunctions ϕ_i

$$\rho_{\mathrm{n,p}}(\boldsymbol{r}) = \sum_{i=1}^{N,Z} n_i\phi_i^*(\boldsymbol{r})\phi_i(\boldsymbol{r}), \tag{A9}$$

$$\boldsymbol{j}_{\mathrm{n,p}}(\boldsymbol{r}) = \frac{\mathrm{i}}{2}\sum_{i=1}^{N,Z} n_i\left[\nabla\phi_i^*(\boldsymbol{r})\phi_i(\boldsymbol{r}) - \phi_i^*(\boldsymbol{r})\nabla\phi_i(\boldsymbol{r})\right], \tag{A10}$$

$$\tau_{\mathrm{n,p}}(\boldsymbol{r}) = \sum_{i=1}^{N,Z} n_i\nabla\phi_i^*(\boldsymbol{r})\cdot\nabla\phi_i(\boldsymbol{r}), \tag{A11}$$

$$\nabla\boldsymbol{J}_{\mathrm{n,p}}(\boldsymbol{r}) = -\mathrm{i}\sum_{i=1}^{N,Z} n_i\nabla\phi_i^*(\boldsymbol{r})\cdot\nabla\times\boldsymbol{\sigma}\phi_i(\boldsymbol{r}), \tag{A12}$$

n_i is the occupation probability of each state. It is 1 or 0 in a pure Hartree–Fock basis at zero temperature. At finite temperature, the occupation probabilities are given by the

Fermi–Dirac distribution:

$$n_{i,q} = \frac{1}{e^{\frac{\epsilon_{i,q}-\mu_q}{k_B T}} + 1}, \tag{A13}$$

where μ is the chemical potential of the relevant species. The Hartree–Fock (binding) energy E is given by

$$E = \sum_i \epsilon_i + \int d^3x \left\{ -\alpha t_3 (\rho_p + \rho_n)^\alpha \left[\left(1 + \tfrac{1}{2}x_3\right)(\rho_p + \rho_n)^2 - \left(\tfrac{1}{2} + x_3\right)(\rho_p^2 + \rho_n^2) \right] \right\} . \tag{A14}$$

Thus we are presented with a series of A coupled non-linear differential equations to solve. Note that the potentials in the Hamiltonian, which determine the single particle wavefunctions, are themselves composed of the single particle wavefunctions. This type of problem must be solved iteratively. Basically we want to start with an initial guess of the wavefunctions of all the states that might conceivably contribute to the total ground state wavefunction, form the potentials out of them, calculate $\hat{h}_{HF}\phi_{i,q} - \epsilon_{i,q}\phi_{i,q} = \delta\phi_{i,q}$, form new wavefunctions $\phi_{i,q,\mathrm{new}} = \phi_{i,q} + \delta\phi_{i,q}$ and repeat. In practice this iteration is unstable and we use more sophisticated schemes based on it.

ACKNOWLEDGEMENTS

This research was supported by EPSRC grant 02300018.

REFERENCES

Abo-Shaeer, J. R., Raman, C., Vogels, J. M. and Ketterle, W. (2001), *Science*, **292**, p. 476.

Andersson, N. and Kokkotas, K. D. (2004), `astro-ph/0403087`.

Bejger, M., Gondek-Rosińska, D., Gourgoulhon, E., Haensel, P., Taniguchi, K. and Zdunik, J. L. (2005), *Astronomy and Astrophysics*, **431**, p. 297.

Bender, M., Heenen, P.-H. and Reinhard, P.-G. (2003), *Rev. Modern Phys.*, **75**, p. 121.

Benhar, O., Berti, E. and Ferrari, V. (1999), *Monthly Notices Roy. Astronom. Soc.*, **310**, p. 797.

Bethe, H. A. (1990), *Rev. Modern Phys.*, **62**, p. 801.

Bonche, P. and Vautherin, D. (1981), *Nuclear Phys. A*, **372**, p. 496.

Botvina, A. S. and Mishustin, I. N. (2005), *Phys. Rev. C*, **72**, p. 048801.

Brown, E. F. (2000), *Astrophys. J.*, **531**, p. 988.

Campana, S., Colpi, M., Mereghetti, S., Stella, L. and Tavani, M. (1998), *Astronom. and Astrophys. Rev.*, **8**, p. 279.

Crawford, F. and Demiański, M. (2003), *Astrophys. J.*, **595**, p. 1052.

Dean, D. J. and Hjorth-Jensen, M. (2003), *Rev. Modern Phys.*, **75**, p. 607.

Ferrari, V., Miniutti, G. and Pons, J. A. (2003), *Monthly Notices Roy. Astronom. Soc.*, **342**, p. 629.

Glendenning, N. K. (2000), *Compact Stars: Nuclear Physics, Particle Physics, and General Relativity*, Springer-Verlag, New York.

Gnedin, O. Y., Yakovlev, D. G. and Potekhin, A. Y. (2001), **324**, p. 725.

Haensel, P. and Zdunik, J. L. (2003), *Astronomy and Astrophysics*, **404**, p. L33.

Horowitz, C. J. and Perez-Garcia, M. A. (2004), *Phys. Rev. C*, **69**, p. 045804.

Horowitz, C. J., Perez-Garcia, M. A., Carriere, J., Berry, D. K. and Piekarewicz, J. (2004), *Phys. Rev. C*, **70**, p. 065806.

Horvath, J. A. (2004), *Internat. J. Modern Phys. D*, **13**, p. 1327.

Janka, H.-T., Buras, R., Kifonidis, K., Marek, A. and Rampp, M. (2004), `astro-ph/0401461`.

Janka, H.-T., Kifonidis, K. and Rampp, M. (2001), `astro-ph/0103015`.

Jones, P. B. (1998), *Monthly Notices Roy. Astronom. Soc.*, **296**, p. 217.

Khan, E., Sandulescu, N. and Giai, N. V. (2005), *Phys. Rev. C*, **71**, p. 042801.

Langanke, K. and Martinez-Pinedo, G. (2003), *Rev. Modern Phys.*, **75**, p. 819.

Larson, M. B. and Link, B. (2002), *Monthly Notices Roy. Astronom. Soc.*, **333**, p. 613.

Lattimer, J. M., Pethick, C. J. and Ravenhall, D. G. (1985), *Nuclear Phys. A*, **432**, p. 646.

Lattimer, J. M. and Swesty, F. D. (1991), *Nuclear Phys. A*, **535**, p. 331.

Machleidt, R. (2001), *Nuclear Phys. A*, **689**, p. 11c.

Magierski, P., Bulgac, A. and Heenen, P.-H. (2002), *Internat. J. Modern Phys. A*, **17**, p. 1059.

Magierski, P. and Heenen, P.-H. (2002), *Phys. Rev. C*, **65**, p. 045804.

Maruyama, T., Niita, K., Oyamasu, K., Maruyama, T., Chiba, S. and Iwamoto, A. (1998), *Phys. Rev. C*, **57**, p. 655.

Page, D., Lattimer, J. M., Prakash, M. and Steiner, A. W. (2004), *Astrophys. J. Suppl.*, **155**, p. 623.

Pethick, C. J. and Potekhin, A. Y. (1998), *Phys. Lett. B*, **427**, p. 7.

Ravenhall, D. G., Pethick, C. J. and Wilson, J. R. (1983), *Phys. Rev. Lett.*, **50**, p. 2066.

Watanabe, G., Iida, K. and Sato, K. (2000a), *Nuclear Phys. A*, **676**, p. 455.

Watanabe, G., Iida, K. and Sato, K. (2000b), *Nuclear Phys. A*, **687**, p. 512.

Watanabe, G., Sato, K., Yasuoka, K. and Ebisuzaki, T. (2002), *Progr. Theoret. Phys. Suppl.*, **146**, p. 638.

Watanabe, G., Sato, K., Yasuoka, K. and Ebisuzaki, T. (2004), *Phys. Rev. C*, **69**, p. 055805.

Watanabe, G. and Sonoda, H. (2005), `cond-mat/0502515`.

Wijnands, R. (2005), `astro-ph/0501264`.

Woosley, S. E., Heger, A. and Weaver, T. A. (2002), *Rev. Modern Phys.*, **74**, p. 1015.

S. Hledík and Z. Stuchlík, editors, Silesian University in Opava, Czech Republic, 2005, pp. 137–141

The relativistic shift of spectral lines from black-hole accretion discs

Tomáš Pecháček,[1,a] Michal Dovčiak[2] and Vladimír Karas[1,2]

[1]Charles University in Prague, Faculty of Mathematics and Physics, V Holešovičkách 2, Praha, Czech Republic
[2]Astronomical Institute, Czech Academy of Sciences, Boční II 1401, CZ-141 31 Praha 4, Czech Republic
[a]pechacek_t@seznam.cz

ABSTRACT
We present a simple approximate analytical formulae describing relativistic shift of a spectral line, produced by a small bright spot on a thin accretion disc around a non-rotating black hole. For the redshift factor we employ similar approach as Zhang, X.-H. and Bao, G. (1991), The rotation of accretion disks and the power spectra of X-ray 'flickering', *Astronomy and Astrophysics*, **246**, pp. 21–31, improved in terms of Beloborodov, A. M. (2002), Gravitation Bending of Light Near Compact Objects, *Astrophys. J.*, **586**, pp. L85–L88 approximation for light bending and Pecháček, T., Dovčiak, M., Karas, V. and Matt, G. (2005b), The relativistic shift of narrow spectral features from black-hole accretion discs, *Astronomy and Astrophysics*, **441**, pp. 855–861 account for aberration effects. Approximation is used also for calculating light-travel time. Results are compared with an exact solution obtained by numerical integration of null geodesics.

1 INTRODUCTION

The X–ray spectroscopy of Active Galactic Nuclei (AGN) and galactic black hole candidates is a powerful method for experimental study of accretion onto black holes. In this paper we discuss a simple toy-model of a bright spot orbiting a black hole. Our results can be used to simplify calculations of line profiles from thin Keplerian discs.

Let us consider a monochromatic point source on a circular orbit around a black hole. This source is assumed to be isotropically emitting photons of constant frequency $\nu_{\rm s}$ in its rest frame. We derive an approximate formula for time dependency of observed frequency as seen by an observer with inclination i at infinity,

$$\nu_{\rm o} = \nu_{\rm o}(t, r, i)\,, \tag{1}$$

where r is orbital radius of the spot and t is time measured by observer's clock. It is useful to decompose the problem into two parts and calculate the observed frequency and time in terms of two independent functions of the source position. Position of the source is

80-7248-334-X

described by its orbital radius r and azimuthal angle ϕ (measured from the nearest point to the observer). Change of the frequency is described by the redshift factor, i.e., the ratio $\nu_{\mathrm{o}}/\nu_{\mathrm{s}} \equiv g(r,\phi,i)$. The assumption of a circular orbit means that

$$r(t) = \text{const}, \qquad \phi(t) = \Omega t\,, \tag{2}$$

where Ω is the orbital frequency of the source. Time t describes a delay between arrivals of a photon emitted from the nearest point $(r, \phi = 0)$ and another photon emitted from some ϕ. Time can be generally written in the form

$$t(r,\phi,i) = \frac{\phi}{\Omega} + \delta t(r,\phi,i)\,, \tag{3}$$

where δt is a time delay due to the geometrical and gravitational effects. Preliminary results of this investigation have been published in Pecháček et al. (2005a).

2 APPROXIMATION OF THE REDSHIFT FACTOR

The redshift factor can be, within the approximation of geometrical optics, written in the form,

$$g = \frac{u_{\mathrm{o}}^{\alpha} p_{\mathrm{o}\alpha}}{u_{\mathrm{s}}^{\alpha} p_{\mathrm{s}\alpha}}\,, \tag{4}$$

where u^{α} and p^{α} are four-velocities and four-momenta of the observer and source, respectively. The gravitational field of a nonrotating black hole can be made dimensionless and expressed in Schwarzschild's coordinates,

$$\mathrm{d}s^2 = -\left(1-\frac{2}{r}\right)\mathrm{d}t^2 + \left(1-\frac{2}{r}\right)^{-1}\mathrm{d}r^2 + r^2\,\mathrm{d}\theta^2 + r^2\sin^2\theta\,\mathrm{d}\phi^2\,, \tag{5}$$

where r is measured in units of M. Equation (4) can be in this metric written in the form

$$g = \frac{\sqrt{1-2/r-\Omega^2 r^2\sin^2\theta}}{1-\Omega\lambda}\,, \tag{6}$$

where $\Omega(r)$ is the orbital frequency of the source. Impact parameter $\lambda \equiv L/E$ is connected with the direction of emission by equation

$$\lambda = \frac{n^{(\phi)}e^{t}_{(t)} + e^{t}_{(\phi)}}{n^{(\phi)}e^{\phi}_{(t)} + e^{\phi}_{(\phi)}}\,, \tag{7}$$

where $e^{\alpha}_{(a)}$ is an orthonormal tetrad of the source and $n^{(a)} \equiv p^{(a)}/p^{(t)}$ is a null directional four-vector with respect to this tetrad.

Let ψ be an angle measured in the orbital plane of light, so that $\psi = 0$ is for the observer. A photon is emitted from the point (r, ψ) at some angle α with respect to the radial direction in static local frame. According to Beloborodov (2002), α can be approximately calculated from the relation

$$1 - \cos\alpha = (1 - \cos\psi)\left(1 - \frac{2}{r}\right) . \tag{8}$$

For the ϕ-component of the directional four-vector we obtain

$$n^{(\phi)} = -\sqrt{\frac{1 - \cos^2\alpha}{1 - \cos^2\psi}}\, \sin i \, \sin\phi \,, \tag{9}$$

where $\cos\psi = \sin i \cos\phi$. From Eqs (6), (7) and (9) and from an assumption of Keplerian orbital frequency $\Omega(r) = r^{-3/2}$ we obtain

$$g(r, \phi, i) = \frac{\sqrt{r(r-3)}}{r + \sin\phi \sin i \sqrt{r - 2 + 4(1 + \cos\phi \sin i)^{-1}}} . \tag{10}$$

For further details, see Pecháček et al. (2005b).

3 APPROXIMATION OF TIME DELAY

Time of flight of photons is influenced by presence of the black hole, even if the light bending is negligible. In Pecháček et al. (2005a) we use a similar approach as Shapiro (1964) improved for stronger gravitational fields. In this paper we examine the following elliptic integral for time of flight. From normalizations of photons four-momentum ($p^{\mu} p_{\mu} = 0$) and from conservation laws it follows

$$\mathrm{d}t = \frac{2}{(1-u)u^2\sqrt{1 - (1-u)u^2 b^2}}\, \mathrm{d}u \,, \tag{11}$$

where $u = 2/r$ and $b = \lambda/2$ is a dimensionless impact parameter. The integration of (11) leads to an elliptic integral. We can rearrange the integrand in a more suitable form,

$$\begin{aligned} \int \frac{1}{(1-u)u^2\sqrt{1-(1-u)u^2b^2}}\, \mathrm{d}u = &- \frac{\sqrt{1-(1-u)u^2b^2}}{u} \\ &+ \frac{b^2}{2}\int \frac{u}{\sqrt{1-(1-u)u^2b^2}}\, \mathrm{d}u \\ &+ \int \frac{1}{(1-u)u\sqrt{1-(1-u)u^2b^2}}\, \mathrm{d}u \,. \end{aligned} \tag{12}$$

The first term is equal to $-\cos\alpha/u$. Using the approximation (8) we obtain

$$-\frac{\cos\alpha}{u} = -\frac{r}{2}\cos\psi - (1 - \cos\psi) \,. \tag{13}$$

Approximating the Equation (12) for light-travel time in a similar way as Beloborodov (2002) did for the spatial shape of light rays, we can expand the remaining integrals in

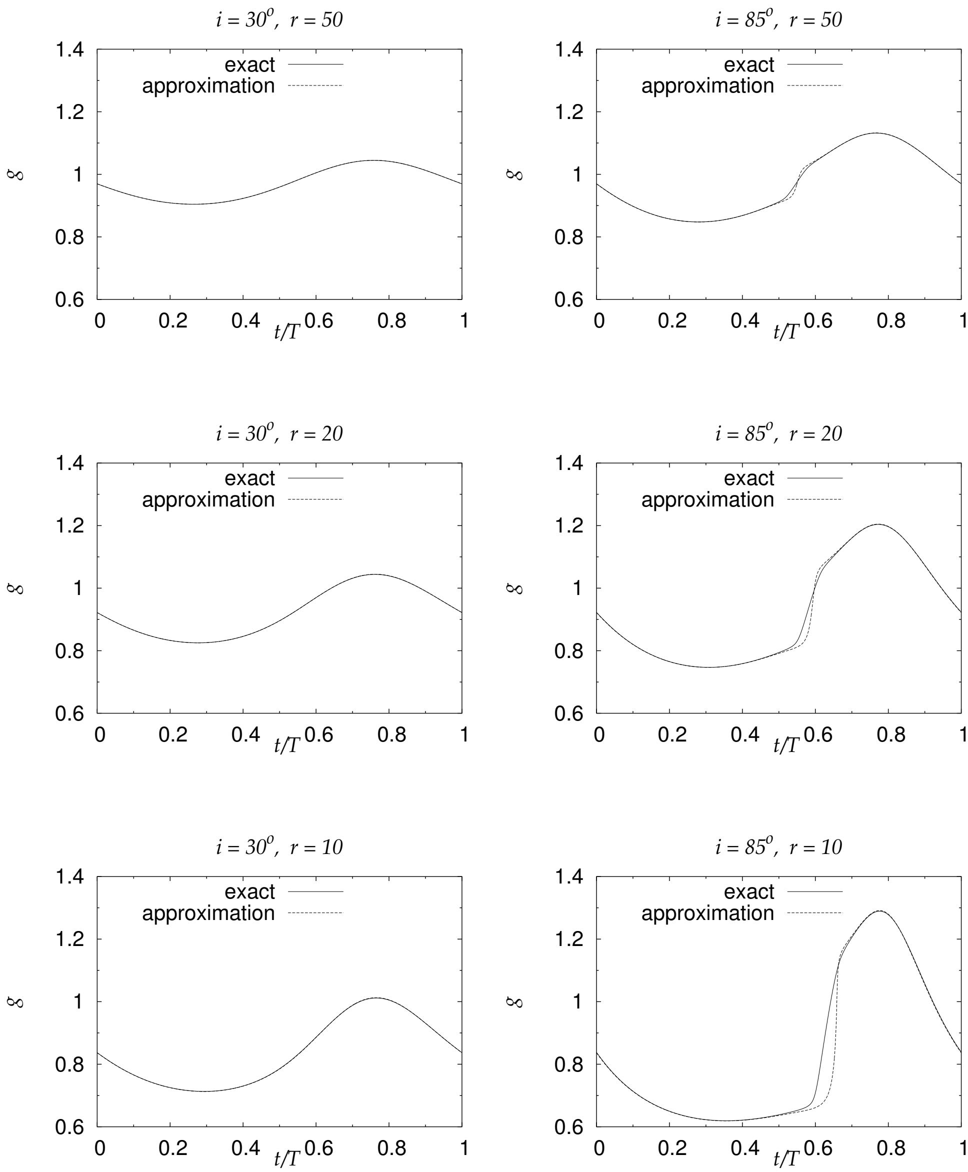

Figure 1. Dependence of g on time t for some combinations of values of source orbital radius r and observer inclination i. Every point of the approximative curve corresponds to $g(\phi)$ and $t(\phi)$ calculated from formulae (3), (10) and (15) for the same value of $\phi \in \langle 0,\ 2\pi \rangle$. The exact solution is obtained in an analogous way by direct numerical integration of geodesic equation. The time is plotted as a fraction of orbital period $T = 2\pi/\Omega$.

$x \equiv (1 - \cos\alpha)/(1 - u)$ and collect terms with the same power of u. Each of these terms is in itself a power series in x. In our approximation we use only the leading terms from the described expansion.

For $\delta t(r, \phi, i)$ we can formulate the following simple algorithm:

- Introduce

$$\cos\psi_1 = \sin i, \quad \cos\psi_2 = \sin i \cos\phi \,. \tag{14}$$

- For $j = 1, 2$ calculate

$$T_j = -r\cos\psi_j - (1 - \cos\psi_j) - 2\ln\left(\frac{1 + \cos\psi_j}{2}\right) . \tag{15}$$

- The result is $\delta t(r, \phi, i) = T_2 - T_1$.

4 CONCLUSION

In this paper we use the same approximation for the g-factor as in Pecháček et al. (2005b,a). This approximation is quite precise. The relative error of g as a function of ϕ is only $\delta g < 8\%$ at $r_{\mathrm{ms}} = 6$. Accuracy of the approximation of extremal values of g is even higher and the relative error for that is better than 0.1%. The approximation of time delay is different from the formula used in Pecháček et al. (2005a). In contrast to that work, our present approximation is applicable for all combinations of parameters r, i and ϕ.

ACKNOWLEDGEMENTS

The authors have been supported by the Czech Science Foundation under the grants 205/03H144 (T. P.), 205/05/P525 (M. D.) and 205/03/0902 (V. K.).

REFERENCES

Beloborodov, A. M. (2002), Gravitation Bending of Light Near Compact Objects, *Astrophys. J.*, **586**, pp. L85–L88.

Misner, C. W., Thorne, K. S. and Wheeler, J. A. (1973), *Gravitation*, Freeman, San Francisco.

Pecháček, T., Dovčiak, M. and Karas, V. (2005a), The Relativistic Shift of Spectral Lines from Black-Hole Accretion Discs, in J. Šafránková, editor, *WDS'05 Proceedings of Contributed Papers: Part III – Physics*, pp. 475–479, Matfyzpress, Prague.

Pecháček, T., Dovčiak, M., Karas, V. and Matt, G. (2005b), The relativistic shift of narrow spectral features from black-hole accretion discs, *Astronomy and Astrophysics*, **441**, pp. 855–861.

Shapiro, I. I. (1964), Fourth Test of General Relativity, *Phys. Rev. Lett.*, **13**, pp. 789–791.

Zhang, X.-H. and Bao, G. (1991), The rotation of accretion disks and the power spectra of X-ray 'flickering', *Astronomy and Astrophysics*, **246**, pp. 21–31.

Proceedings of *RAGtime 6/7: Workshops on black holes and neutron stars, Opava, 16–18/18–20 September, 2004/2005*
S. Hledík and Z. Stuchlík, editors, Silesian University in Opava, Czech Republic, 2005, pp. 143–155

Light escape cones and raytracing in Kerr geometry

Jan Schee, Zdeněk Stuchlík and Josef Juráň

Institute of Physics, Faculty of Philosophy & Science, Silesian University in Opava,
Bezručovo nám. 13, CZ-746 01 Opava, Czech Republic

ABSTRACT
The integrals of photon motion in the Kerr spacetimes are given in terms of the emission angles related to emitters moving along the circular geodesic orbits. The local frames of the circular geodesic emitters are given in relation to the locally nonrotating frames and local directional angles of the escape cones are given in terms of the motion constants of photons.

1 INTRODUCTION

Studies of the optical phenomena in the field of Schwarzschild and Kerr black holes are of high importance in understanding of many astrophysical phenomena related to accretion discs rotating around the holes in the Galactic binary systems or quasars and active galactic nuclei (Bardeen, 1973; Novikov and Thorne, 1973).

A lot of work is devoted to the modelling of light curves and profiled spectral lines generated in the vicinity of black holes (Laor, 1991; Bao and Stuchlík, 1992; Stuchlík and Bao, 1992; Karas et al., 1992; Viergutz, 1993; Fabian et al., 1975). The recent results include also the phenomena of polarization of the radiation (Horák, 2005; Horák and Karas, 2005). The modelling of the light curves of sources on accretion discs around black holes can be very important in understanding the quasiperiodic oscillations observed in microquasars (Bursa et al., 2004; Bursa, 2005). The high frequency QPO's enable us to predict the black hole spin in the microquasars (Török et al., 2005; Török, 2005a) and in the centre of the Galaxy (Török, 2005a,b), and they are relevant for the binary systems with neutron stars (Abramowicz et al., 2005b,a).

In the investigations of the black-hole optical phenomena, two approaches of integration of the Carter equations of photon motion can be used-namely, direct numerical integration (Cunningham, 1975; Cunningham and Bardeen, 1972), and more sophisticated approach based on the elliptic integrals (Rauch and Blandford, 1994; Kraniotis, 2004).

Here, we propose a modification of the elliptic integral approach by introducing the photon directional angles as measured in the emitter's frame into the elliptic integrals of the photon geodetical motion. In Section 2, the frames of the geodesic circular observers (emitters) GF are introduced by Lorentz transforming the locally nonrotating frames. In

80-7248-334-X

Section 3, the directional angles of photons in the GF are given in terms of the Carter constants of motion and the escape photon cones are determined. In Section 4, the raytracing of photons is discussed, and the integrals of motion are given in terms of the elliptic integrals involving the photon directional angles. In Section 5, some concluding remarks are presented and examples of the rays are shown.

2 THE FRAME OF OBSERVERS ON CIRCULAR GEODESICS (GF)

A GF is moving along a circular geodetical orbit in the equatorial plane of Kerr geometry. We shall construct its frame, i.e., tetrad of 1-forms, starting from the locally nonrotating frames (LNRF), which are generally non-geodetical accelerated frames (Misner et al., 1973). The LNRF rotate with the geometry in such a way that the directions $-\varphi$ and φ are equivalent. The tetrad of the LNRF 1-forms is given by the relations

$$\omega^{(r)} = \left\{0, \sqrt{\frac{\Sigma}{\Delta}}, 0, 0\right\} , \tag{1}$$

$$\omega^{(\theta)} = \left\{0, 0, \sqrt{\Sigma}, 0\right\} , \tag{2}$$

$$\omega^{(t)} = \left\{\sqrt{\frac{\Delta\Sigma}{A}}, 0, 0, 0\right\} , \tag{3}$$

$$\omega^{(\varphi)} = \left\{-\Omega_{\rm LNRF}\sqrt{\frac{A}{\Sigma}}\,\sin\theta, 0, 0, \sqrt{\frac{A}{\Sigma}}\,\sin\theta\right\} , \tag{4}$$

while the constants of motion E (energy) and ϕ (axial angular momentum) and the angular velocity $\Omega_{\rm LNRF}$ are given by

$$E = \sqrt{\frac{\Delta\Sigma}{A}} , \tag{5}$$

$$\phi = 0 , \tag{6}$$

$$\Omega_{\rm LNRF} = \pm\frac{2aMr}{A} . \tag{7}$$

where

$$\Delta = r^2 - 2Mr + a^2 , \tag{8}$$

$$\Sigma = r^2 + a^2\cos^2\theta , \tag{9}$$

$$A = (r^2 + a^2)^2 - a^2\Delta\sin^2\theta . \tag{10}$$

The tetrad of 1-forms corresponding to the GF is obtained by a special Lorentz transformation of the LNRF tetrad. GF is moving with respect to the LNRF in φ direction with velocity $V_{\rm GF_\pm}$, where the $\pm$ sign corresponds to the corotating and counterrotating circular geodesic, respectively. The relevant transformation matrix has the standard form

$$\Lambda(V) = \begin{pmatrix} \gamma & 0 & 0 & -\gamma V \\ 0 & 1 & 0 & 0 \\ 0 & 0 & 1 & 0 \\ -\gamma V & 0 & 0 & \gamma \end{pmatrix}, \tag{11}$$

where

$$\gamma = \frac{1}{\sqrt{1-V^2}}. \tag{12}$$

The magnitude of the velocity V is determined by the relation

$$V = \frac{U^{(\varphi)}}{U^{(t)}} = \frac{\omega^{(\varphi)}_{\mu} U^{\mu}}{\omega^{(t)}_{\mu} U^{\mu}}, \tag{13}$$

where U^{μ} is four-velocity of GF (observer) and $\omega^{(\mu)}$ is the tetrad of LNRF observer. Using Eq. (13), one arrives to

$$V_{\mathrm{GF}\pm} = \frac{\omega^{(\varphi)}_{t} + \omega^{(\varphi)}_{\varphi}(U^{\varphi}/U^{t})}{\omega^{(t)}_{t}} = \frac{A}{\Sigma\sqrt{\Delta}}(\Omega_{\mathrm{GF}\pm} - \Omega_{\mathrm{LNRF}}), \tag{14}$$

where Ω_{LNRF} is given by the relation (7) and

$$\Omega_{\mathrm{GF}\pm} = \pm\frac{\sqrt{Mr}}{r^2 \pm a\sqrt{Mr}}. \tag{15}$$

We obtain

$$V_{\mathrm{GF}\pm} = \pm\frac{(r^2+a^2)\sqrt{Mr} \mp 2aMr}{\sqrt{\Delta}\,(r^2 \pm a\sqrt{Mr})}. \tag{16}$$

The special Lorentz transformation $\tilde{\omega}^{(\mu)} = \omega^{(\alpha)}\Lambda_{\alpha}{}^{\mu}(V)$ gives us the 1-form tetrad of GF

$$\tilde{\omega}^{(r)} = \left\{0, \sqrt{\frac{\Sigma}{\Delta}}, 0, 0\right\}, \tag{17}$$

$$\tilde{\omega}^{(\theta)} = \left\{0, 0, \sqrt{\Sigma}, 0\right\}, \tag{18}$$

$$\tilde{\omega}^{(t)}_{\pm} = \left\{\frac{r^2 - 2Mr \pm a\sqrt{Mr}}{Z_{\pm}}, 0, 0, \mp\frac{(r^2+a^2)\sqrt{Mr} \mp 2Mar}{Z_{\pm}}\right\}, \tag{19}$$

$$\tilde{\omega}^{(\varphi)}_{\pm} = \left\{\mp\frac{\sqrt{Mr\Delta}}{Z_{\pm}}, 0, 0, \frac{\sqrt{\Delta}\,(r^2 \pm a\sqrt{Mr})}{Z_{\pm}}\right\}. \tag{20}$$

where the "±" distinguish between corotating and counterrotating observers, again, and

$$Z_{\pm} = r\sqrt{r^2 - 3Mr \pm 2a\sqrt{Mr}}, \tag{21}$$

The constants of motion of GF, E, ϕ are given by the relations (Bardeen, 1973)

$$E_{\pm} = \frac{r^2 - 2Mr \pm a\sqrt{Mr}}{Z_{\pm}}\,, \tag{22}$$

$$\phi_{\pm} = \pm\frac{(r^2 + a^2)\sqrt{Mr} \mp 2Mar}{Z_{\pm}}\,, \tag{23}$$

and its angular velocity $\Omega_{\mathrm{GF}_{\pm}}$ is given by Eq. (15).

3 LOCAL ESCAPE CONES OF GF'S

Motion of a photon in the Kerr geometry is determined by the *Carter equations* (Carter, 1973), which read

$$\Sigma k^r = \pm\sqrt{R(r)}\,, \tag{24}$$

$$\Sigma k^\theta = \pm\sqrt{W(\theta)}\,, \tag{25}$$

$$\Sigma k^\varphi = -\frac{P_W}{\sin^2\theta} + \frac{aP_R}{\Delta}\,, \tag{26}$$

$$\Sigma k^t = -aP_W + \frac{(r^2 + a^2)P_R}{\Delta}\,, \tag{27}$$

where

$$R(r) = P_R^2 - \Delta K\,, \tag{28}$$

$$W(\theta) = K - \left(\frac{P_W}{\sin\theta}\right)^2\,, \tag{29}$$

$$P_R(r) = E(r^2 + a^2) - a\phi\,, \tag{30}$$

$$P_W(\theta) = aE\sin^2\theta - \phi\,. \tag{31}$$

Usually, it is convenient to introduce a new constant $Q = K - (\phi - aE)^2$ which can be expressed in the form $Q = p_\theta^2 + \cos^2\theta(\phi^2\csc^2\theta - a^2E^2)$. The aim of this section is to construct *light escape cones* for GF. The geodetical motion of photons can conveniently be given in terms of the constant of motion $L = Q + \phi^2$. Then we can define the two impact parameters.

The impact parameter λ is defined by the relation

$$\lambda \equiv \frac{\phi}{E} = \frac{k_\varphi}{-k_t} = -\frac{\omega^{(\mu)}_\varphi k_{(\mu)}}{\omega^{(\mu)}_t k_{(\mu)}}\,. \tag{32}$$

The impact parameter $\mathcal{L}$ is determined by $\mathcal{L} \equiv L/E^2$. For a given λ one obtains an effective potential of the radial motion $\mathcal{L}(r;\lambda,a)$. The function $\mathcal{L}(r;\lambda,a)$ determining the effective potential reads

$$\mathcal{L} = \frac{L}{E^2} = \mathcal{L}(r;\lambda,a) \equiv \frac{(a\lambda - 2r)^2}{\Delta} + r(r+2)\,. \tag{33}$$

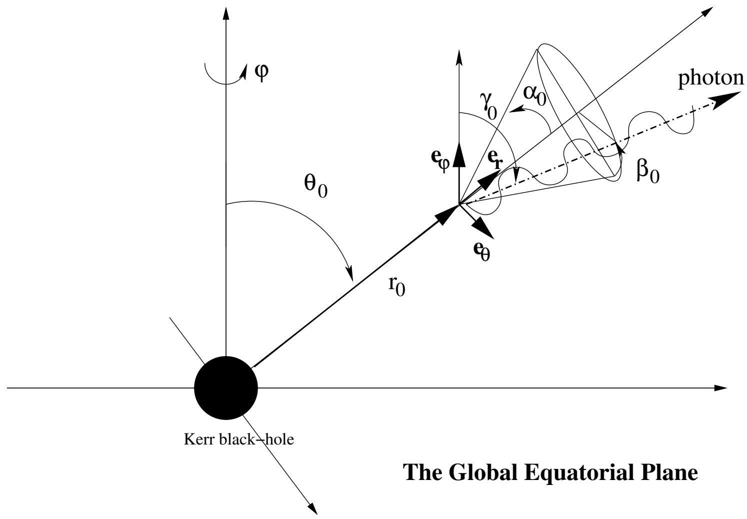

Figure 1. The local escape cone. A schematic drawing of α, β and γ definition. An observer at $[r_0; \theta_0]$ in a given spacetime with parameter a is shooting a photon in the direction characterized by any double of angles from the set $\{\alpha_0, \beta_0, \gamma_0\}$. (The third angle is related to the other two by the relation (38).) Angles are measured locally. Angle α_0 is subtended by tetrad vector $\boldsymbol{e}_r$; angle β_0 is measured in the plane perpendicular to radial direction; angle γ_0 is subtended by tetrad vector $\boldsymbol{e}_\varphi$.

Using the *effective potential*, we can construct light escape cones which enable us to determine whether a photon can escape to infinity or fall below a black-hole horizon.

The constants of motion of a photon λ and $\mathcal{L}$ fully characterize a photon geodesic and are fully determined by any double of angles from the set $\{\alpha_0, \beta_0, \gamma_0\}$ defined by the relations (see Fig. 1)

$$k^{(t)} = -k_{(t)} = 1\,, \tag{34}$$

$$k^{(r)} = k_{(r)} = \cos\alpha_0\,, \tag{35}$$

$$k^{(\theta)} = k_{(\theta)} = \sin\alpha_0\cos\beta_0\,, \tag{36}$$

$$k^{(\varphi)} = k_{(\varphi)} = \sin\alpha_0\sin\beta_0 = \cos\gamma_0\,. \tag{37}$$

For directional angle γ_0 (see Fig. 1), there is

$$\cos\gamma_0 = \frac{k^{(\varphi)}}{k^{(t)}} = \frac{\omega^{(\varphi)}_\mu k^\mu}{\omega^{(t)}_\mu k^\mu}\,. \tag{38}$$

For the GF one obtains from (24),(26) and (38) the relation between the impact parameter λ and the angle γ_0, which reads

$$\lambda = \frac{\left[(a^2+r^2)\sqrt{Mr} - 2aMr\right]\sqrt{Mr} + \left(r^2 + a\sqrt{Mr}\right)\Delta\cos\gamma_0}{\left(r^2 - 2Mr + a\sqrt{Mr}\right)\sqrt{\Delta} + \sqrt{Mr}\,\Delta\cos\gamma_0}\,. \tag{39}$$

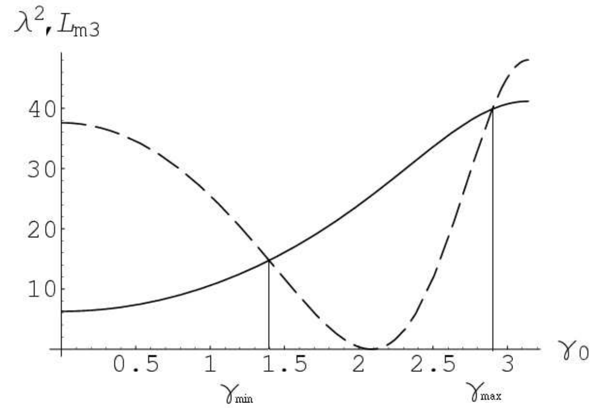

Figure 2. Plot of $\mathcal{L}_{m3}$ and λ^2 for $\gamma_0 \in \langle 0, \pi \rangle$; GF_+ observer is at radius $r_0 = 5$ and rotation parameter of black-hole is $a = 0.6$. Intersections of both functions determine values of γ_{min} and γ_{max}.

By setting the angle γ_0, we get impact parameter λ and also the behaviour of $\mathcal{L}$ is given. To find whether a photon can escape to infinity, we need to calculate minimum of $\mathcal{L}$ (denoted $\mathcal{L}_{m3}$). From equation $\partial\mathcal{L}/\partial r = 0$ one finds that the minimum $\mathcal{L}_{m3}$ is located at the radius

$$r_{m3} = \sqrt{a\lambda - a^2} \qquad \text{for} \qquad \lambda \geq a\,, \tag{40}$$

$$r_{m3} = 1 - \frac{k_1}{k_2} + \frac{k_2}{3} \qquad \text{for} \qquad \lambda < a\,, \tag{41}$$

where

$$k_1 = a^2 + a\lambda - 3\,, \tag{42}$$

$$k_2 = \left[27(1-a^2) + 3\sqrt{3}\sqrt{27(1-a^2)^2 + k_1^3}\right]^{1/3}\,. \tag{43}$$

For GF only r_{m3} given by (41) is relevant. Values of minima $\mathcal{L}_{m3}$ at radius r_{m3}, given by relation (40), lie in the region forbidden for the radial motion. For λ and given r_0, we have behaviour of the minimum for the radial motion $\mathcal{L}_{m3}$ and behaviour of the minimal value of $\mathcal{L}$ which follows from the restriction on the latitudinal motion and is given by formulae (Bičák and Stuchlík, 1976)

$$\mathcal{L} = \lambda^2 \qquad \text{for} \qquad |\lambda| \geq 0\,, \tag{44}$$

$$\mathcal{L} = 2a\lambda - a^2 \qquad \text{for} \qquad |\lambda| \leq 0\,. \tag{45}$$

The intersection of minimal value of $\mathcal{L}$ and $\mathcal{L}_{m3}$ give us γ_{min} and γ_{max} (see Fig. 2). For every value of $\gamma_0 \in \langle \gamma_{min}, \gamma_{max} \rangle$ we calculate α_0^{max} from the relation

$$\alpha_0^{max} = \arccos\left[\operatorname{sign}(r_0 - r_{m3})\frac{k^{(r)}}{k^{(t)}}\right]\,, \tag{46}$$

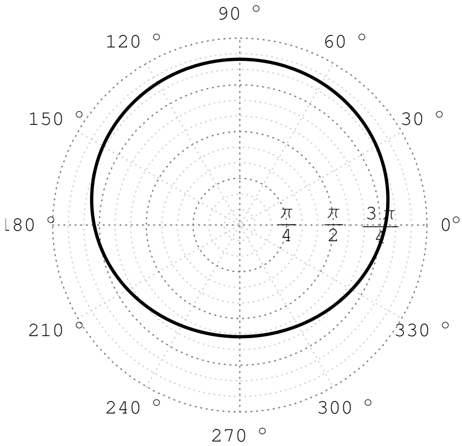

(a)

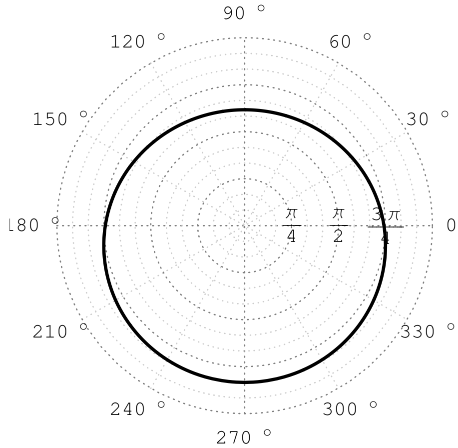

(b)

Figure 3. Light escape cones for the GF on a circular orbit corotating with the Kerr spacetime (plot (a)) and for the GF counterrotating in the Kerr spacetime (plot (b)). Both observers are at the radius $r_0 = 5$. Rotating parameter $a = 0.2$ in both cases. Angle $\beta = 90°$ corresponds to a photon moving in the equatorial plane in the direction of observer's revolution. Angle $\beta = 270°$ corresponds to a photon moving in the equatorial plane in the opposite direction of observer's revolution.

where

$$\frac{k^{(r)}}{k^{(t)}} = \frac{r\sqrt{(r^2 - 3r + 2a\sqrt{r})[(a^2 - a\lambda + r^2)^2 - (a^2 - 2a\lambda + \mathcal{L})\Delta]}}{\sqrt{r^2\Delta}\,[r^2 + (a^2 - \lambda)\sqrt{r}\,]}. \tag{47}$$

Angle β_0 can be obtained from the relation

$$\cos\gamma_0 = \sin\alpha_0^{\max}\sin\beta_0\,. \tag{48}$$

For all $\gamma_0 \in \langle\gamma_{\min}, \gamma_{\max}\rangle$, we obtain a set of doubles $[\alpha_0^{\max}, \beta_0]$. This set separates angle space into two regions. Parameters from the region "below" the border identify photons that fall into the black-hole, while parameters from the region "above" the border identify photons that escape to infinity. For a given β, it means that if $\alpha < \alpha_0^{\max}$, then photon with $[\alpha, \beta]$ can escape to infinity, when $\alpha \geq \alpha_0^{\max}$, then photon with $[\alpha, \beta]$ will asymptotically wind on to the photon circular orbit or fall below black-hole horizon.

4 RAYTRACING AND LIGHT ESCAPE CONES

Let us consider a source of radiation on a circular orbit in the vicinity of a Kerr black-hole. In order to calculate optical effect which influence the radiation radiated from the source we use raytracing algorithm. It means that we consider all photons radiated from that source at some instant t_e and track them. But not all of the radiated photons will reach distant observer. Some of the radiated photons will fall into the black-hole or will asymptotically wind onto the photon circular orbit. Only photons that escape to infinity are worth to track in considering the observable optical phenomena. The *light escape cones* are very useful tool to select only photons, that can escape to infinity and be possibly observed by a distant observer.

With transformation $u \equiv 1/r$ and $\mu \equiv \cos\theta$, we rewrite the Carter equations (24)–(27) into the form (Rauch and Blandford, 1994)

$$\Sigma k^u = u_{\mathrm{sgn}}\sqrt{U}\,, \tag{49}$$

$$\Sigma k^\mu = \mu_{\mathrm{sgn}}\sqrt{M}\,, \tag{50}$$

$$\Sigma k^\varphi = -a + \frac{\lambda}{1-\mu^2} + \frac{a}{\Delta}(u^{-2}+a^2-a\lambda)\,, \tag{51}$$

$$\Sigma k^t = -a[a(1-\mu^2)-\lambda] + \frac{u^{-2}+a^2}{\Delta}(u^{-2}+a^2-a\lambda)\,, \tag{52}$$

where

$$U = 1 + (a^2-q-\lambda^2)u^2 + 2[(a-\lambda)^2+q]u^3 - a^2qu^4\,, \tag{53}$$

$$M = q + (a^2-q-\lambda^2)\mu^2 - a^2\mu^4\,. \tag{54}$$

Signs $u_{\mathrm{sgn}} = \pm 1$ and $\mu_{\mathrm{sgn}} = \pm 1$ change when a relevant turning point is reached. Turning points in u and μ are solutions of $U(u) = 0$ and $M(\mu) = 0$.

The Carter equations (49)–(52) can be rewritten into the following integral form (Rauch and Blandford, 1994)

$$\int_{\mu_0}^{\mu(u)} \frac{\mathrm{d}\mu'}{\sqrt{M(\mu')}} = u_{\mathrm{sgn}}\mu_{\mathrm{sgn}}\int_{u_0}^{u}\frac{\mathrm{d}u'}{\sqrt{U(u')}}\,, \tag{55}$$

$$\varphi(u) = \varphi_0 + \mu_{\mathrm{sgn}}\int_{\mu_0}^{\mu(u)} \frac{\lambda\mu'^2}{1-\mu'^2}\frac{\mathrm{d}\mu'}{\sqrt{M(\mu'^2)}} + u_{\mathrm{sgn}}\int_{u_0}^{u}\frac{2(a-\lambda)u'+\lambda}{(u/u_+-1)(u/u_--1)}\frac{\mathrm{d}u'}{\sqrt{U(u')}}\,, \tag{56}$$

$$t(u) = t_0 + \mu_{\mathrm{sgn}}\int_{\mu_0}^{\mu(u)} a^2\mu^2\frac{\mathrm{d}\mu'}{\sqrt{M(\mu')}} + u_{\mathrm{sgn}}\int_{u_0}^{u}\frac{2a(a-\lambda)u^3+a^2u^2+1}{u^2(u/u_-1)(u/u_--1)}\frac{\mathrm{d}u'}{\sqrt{U(u')}}\,. \tag{57}$$

Here the u coordinate is taken for a free parameter $u \in \langle 0, u_{\mathrm{turn}}\rangle$. For a given u_0, u, μ_0 we calculate value of μ from Eq. (55). Suppose for the moment that $a^2 > 0, q^2 \neq 0 (M_- > 0)$; then we can write

$$M(\mu) = a^2(\mu^2 - M_+)(\mu^2 - M_-)\,, \tag{58}$$

where $M_- = \mu_-^2$ and $M_+ = \mu_+^2$. Denoting the r.h.s. of Eq. (55) as

$$I \equiv \mu_{\mathrm{sgn}}u_{\mathrm{sgn}}\int_{u_0}^{u}\frac{\mathrm{d}u'}{\sqrt{U(u')}} \tag{59}$$

and rearranging Eq. (55), one obtains

$$\int_{\mu}^{\mu_+} \frac{d\mu'}{\sqrt{M(\mu')}} = \int_{\mu_0}^{\mu_+} \frac{d\mu'}{\sqrt{M(\mu')}} - I\,. \tag{60}$$

Substituting from Eq. (58) to Eq. (60), we arrive at the relation

$$\mu_+ \int_{\mu}^{\mu_+} \frac{d\mu'}{|a|\sqrt{(\mu'^2 - M_+)(\mu'^2 - M_-)}} = \mu_+ \int_{\mu_0}^{\mu_+} \frac{d\mu'}{|a|\sqrt{(\mu'^2 - M_+)(\mu'^2 - M_-)}} - \mu_+ I\,. \tag{61}$$

Using the standard formulae (Abramowitz and Stegun, 1964; Rauch and Blandford, 1994)

$$a\int_{y}^{a} \frac{dt}{\sqrt{(a^2 - t^2)(t^2 - b^2)}} = F(\phi|m_1) = \mathrm{dn}^{-1}\left(\frac{y}{a}\middle| m_1\right), \tag{62}$$

where we are using complementary parameter $m_1 = 1 - m$ and $x = \tan\phi$; $\sin\phi = (a^2 - y^2)/(a^2 - b^2)$, and $m = (a^2 - b^2)/a^2$; we obtain the formula

$$x(\mu_+, I) = F\left(\sqrt{\frac{M_+ - \mu_0^2}{\mu_0^2 - M_-}}\,\middle|\, \frac{M_-}{M_+}\right) - \mu_+|a|I\,. \tag{63}$$

The value of μ is determined from the Jacobi function dn by the relation

$$\mu = \mu_+\,\mathrm{dn}\left(x(\mu_+, I)\,\middle|\,\frac{M_-}{M_+}\right). \tag{64}$$

For other cases, depending on values of M_- and q, we proceed analogically. One finally obtains a table of relations to calculate μ (see Rauch and Blandford, 1994).

The photon trajectory is uniquely determined by the constants of motion λ and $q \equiv Q/E^2$ which for the $\mathrm{GF}_\pm$ take the form

$$\lambda_\pm = -\frac{\mp 2aMu^{-1} + (a^2 + u^{-2})\sqrt{Mu^{-1}} + \left(\pm u^{-2} + a\sqrt{Mu^{-1}}\right)\sqrt{\Delta}\,\sin\alpha\sin\beta}{u^{-1}(u^{-1} - 2M) + \sqrt{Mu^{-1}}\,(a + \sqrt{\Delta}\,\sin\alpha\sin\beta)}\,, \tag{65}$$

$$\begin{aligned} q_\pm = {} & \frac{u^{-2}\left[u^{-1}(u^{-1} - 3M) \pm 2a\sqrt{Mu^{-1}}\right](u^{-2} + a^2\mu^2)\cos^2\beta\sin^2\alpha}{\left[u^{-1}(u^{-1} - 2M) + \sqrt{Mu^{-1}}\,(a + \sqrt{\Delta}\,\sin\alpha\sin\beta)\right]^2} - a^2\mu^2 \\ & + \frac{\left[(a^2 - u^{-2})\sqrt{Mu^{-1}} \mp 2aMu^{-1} + \left(\pm u^{-2} + a\sqrt{Mu^{-1}}\right)\sqrt{\Delta}\sin\alpha\sin\beta\right]^2}{\sqrt{1 - \mu^2}\left[u^{-1}(u^{-1} - 2M) + \sqrt{Mu^{-1}}\,(a + \sqrt{\Delta}\,\sin\alpha\sin\beta)\right]^2}\,, \end{aligned} \tag{66}$$

where α and β are determined by the light escape cone, as described in previous Section 3.

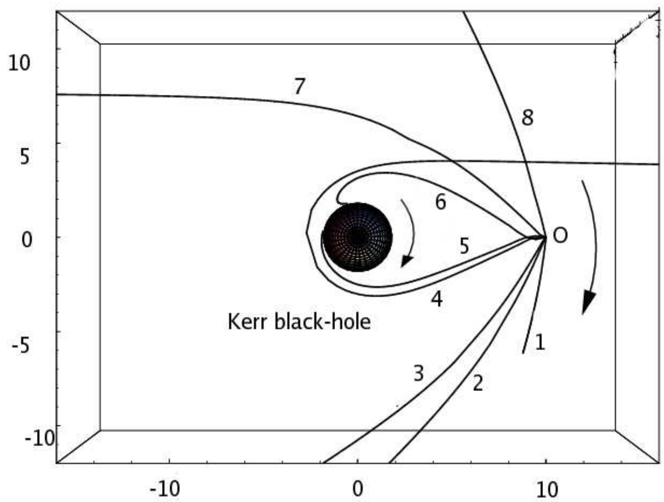

Figure 4. Trajectories of photons emitted by GFs orbiting a Kerr black hole with $a = 0.6$ at radius $r_0 = 10$. The directional angles of photons are (from left to right; doubles $[\alpha^0_{\max}, \beta_0]$): [100°,90°], [125°,90°], [135°,90°], [178°,90°], [100°,270°], [125°,270°], [135°,270°], [178°,270°].

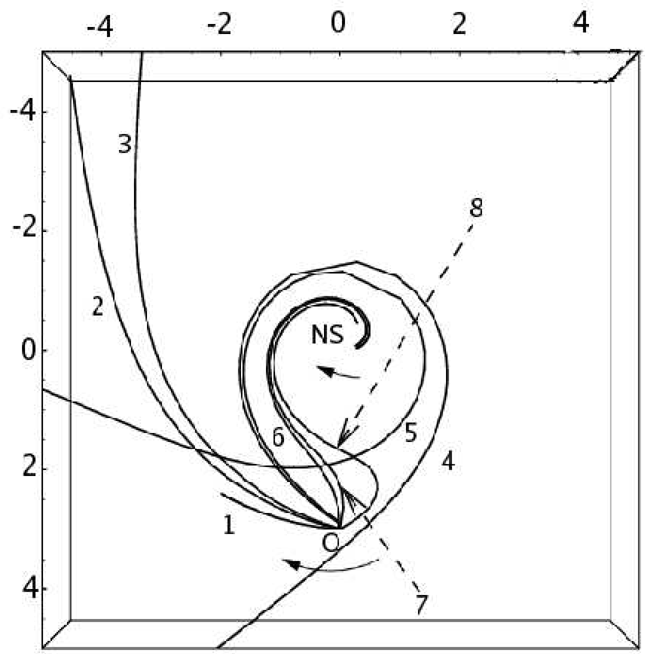

Figure 5. Trajectories of photons emitted by GFs orbiting a Kerr naked singularity with $a = 1.1$ at radius $r_0 = 3$. The directional angles of photons are (from left to right; doubles $[\alpha^0_{\max}, \beta_0]$): [100°,90°], [125°,90°], [135°,90°], [178°,90°], [100°,270°], [125°,270°], [135°,270°], [178°,270°].

When μ and u are known, we can compute values of φ and t from (56) and (57). Integrals in that relations can be also expressed in terms of elliptic integrals; this we are preparing for our next work. Here, these integrals are computed numerically.

We can conclude that for given, locally measured, angles α, β, we calculate values of impact parameters of λ and q. From Eqs (55)–(57), we obtain the geodesic of a photon for a given radial parameter $u \in [0, u_{\mathrm{turn}}]$. We have a set of coordinates (t, u, μ, φ) which can be used to calculate photon 4-momentum from the Carter Eqs (24)–(27). From this point, we can calculate physical quantities like redshift of a photon, lensing parameter of radiation passing by the black-hole (naked singularity), its light curve, etc., that characterize the optical phenomena in the black-hole backgrounds.

The raytracing can now be implemented by the procedure presented above. Some typical plots of the photon trajectories, are given in Figs 4 and 5, for different parameters α and β.

5 CONCLUSIONS

We have discussed the relation of the light escape cones of the GFs to the raytracing of photons in the Kerr spacetimes. The results of our study can be represented in the following way. The boundary between photons that can escape to infinity and those captured by a Kerr black-hole (naked singularity) is determined by the light escape cone and relations between α^0_{max} and β_0, as illustrated for the case of black holes (naked singularities) in Fig. 6 (Fig. 7).

The examples of typical photon trajectories starting at GFs orbiting in the field of Kerr black holes (naked singularities) are determined by the raytracing in terms of elliptic integrals using the local directional angles at GFs and are illustrated in Fig. 4 (Fig. 5).

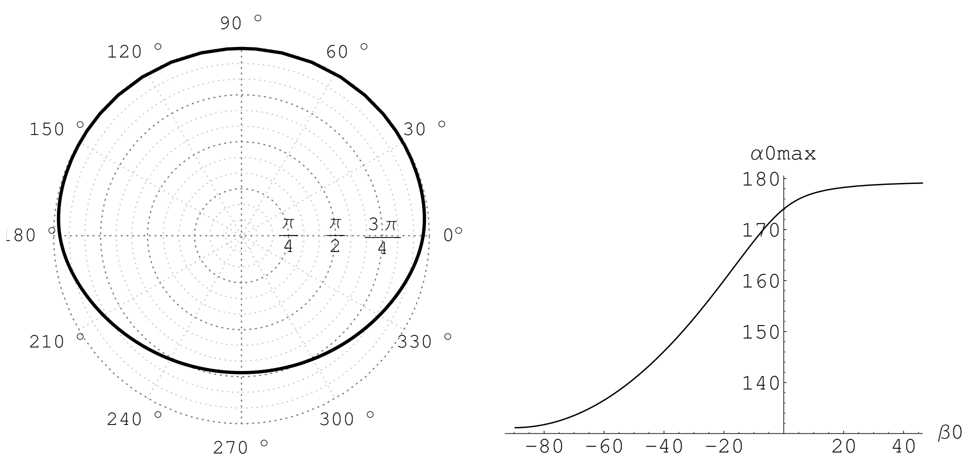

(a) (a)

Figure 6. The light escape cone (a) of the GF_+ orbiting a Kerr black hole with $a = 0.6$ at $r_0 = 10$. The relevant angle relation $\alpha^0_{\mathrm{max}}(\beta_0)$ is given in (b).

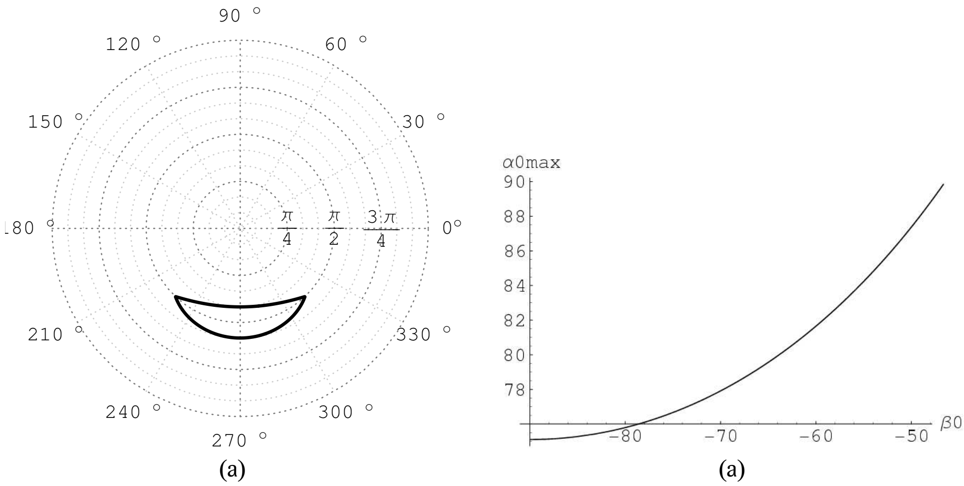

Figure 7. The light escape cone (a) of the GF_+ orbiting a Kerr naked singularity with $a = 1.1$ at $r_0 = 3$. At (b), the relation $\alpha^0_{max}(\beta_0)$ is plotted.

The presented approach to the raytracing in terms of elliptic integrals will be used in further investigations of the optical phenomena in the field of Kerr black holes and naked singularities. We expect to obtain a procedure that will enable to compute all the optical characteristics (the redshift, luminosity, ...) along any ray at any point of the photon trajectory. Further, it is important to make generalization from the stationary situations, when emitters moving along circular geodesic orbits are considered, to dynamical, time-dependent situations.

ACKNOWLEDGEMENTS

The presented work was supported by the Czech grant MSM 4781305903.

REFERENCES

Abramowicz, M. A., Barret, D., Bursa, M., Horák, J., Kluźniak, W., Rebusco, P. and Török, G. (2005a), A note on the slope-shift anticorrelation in the neutron star kHz QPOs data, pp. 1–9, this volume.

Abramowicz, M. A., Barret, D., Bursa, M., Horák, J., Kluźniak, W., Rebusco, P. and Török, G. (2005b), The correlations and anticorrelations in QPO data, *Astronom. Nachr.*, **326**(9), pp. 864–866.

Abramowitz, M. and Stegun, I. A. (1964), *Handbook of Mathematical Functions With Formulas, Graphs, and Mathematical Tables*, Applied Mathematics Series, National Bureau of Standards, Washington, D.C., ISBN 761-919-0-65-67.

Bao, G. and Stuchlík, Z. (1992), *Astrophys. J.*, **400**, p. 163.

Bardeen, J. M. (1973), Timelike and null geodesics in the Kerr metric, in C. D. Witt and B. S. D. Witt, editors, *Black Holes*, p. 215, Gordon and Breach, New York–London–Paris.

Bičák, J. and Stuchlík, Z. (1976), On the latitudinal and radial motion in the field of a rotating black hole, *Bull. Astronom. Inst. Czechoslovakia*, **27**(3), pp. 129–133.

Bursa, M. (2005), High-frequency QPOs in GRO J1655−40: Constraints on resonance models by spectral fits, pp. 39–45, this volume.

Bursa, M., Abramowicz, M. A., Karas, V. and Kluźniak, W. (2004), The Upper Kilohertz Quasi-periodic Oscillation: A Gravitationally Lensed Vertical Oscillation, *Astrophys. J. Lett.*, **617**, pp. L45–L48, `astro-ph/0406586`.

Carter, B. (1973), Black hole equilibrium states, in C. D. Witt and B. S. D. Witt, editors, *Black Holes*, p. 57, Gordon and Breach, New York–London–Paris.

Cunningham, C. T. (1975), Optical appearance of distant objects to observer near and inside a Schwarzschild black hole, *Phys. Rev. D*, **12**, pp. 323–328.

Cunningham, C. T. and Bardeen, J. M. (1972), *Astrophys. J.*, **173**, p. L137.

Fabian, A. C., Pringle, J. E. and Rees, M. J. (1975), *Monthly Notices Roy. Astronom. Soc.*, **172**, p. 15P.

Horák, J. (2005), On polarization of light scattered on hot electron clouds, pp. 63–70, this volume.

Horák, J. and Karas, V. (2005), *Monthly Notices Roy. Astronom. Soc.*, **365**, p. 813.

Karas, V., Vokrouhlický, D. and Polnarev, A. G. (1992), *Monthly Notices Roy. Astronom. Soc.*, **259**, p. 569.

Kraniotis, G. V. (2004), Precise relativistic orbits in Kerr and Kerr–(anti-)de Sitter spacetimes, *Classical Quantum Gravity*, **21**, pp. 4743–4769.

Laor, A. (1991), Line profiles from a disk around a rotating black hole, *Astrophys. J.*, **376**, pp. 90–94.

Misner, C. W., Thorne, K. S. and Wheeler, J. A. (1973), *Gravitation*, Freeman, San Francisco.

Novikov, I. D. and Thorne, K. S. (1973), Black hole astrophysics, in C. D. Witt and B. S. D. Witt, editors, *Black Holes*, p. 436, Gordon and Breach, New York–London–Paris.

Rauch, K. P. and Blandford, R. D. (1994), Optical caustics in a Kerr space-time and the origin of rapid X-ray variability in active galactic nuclei, *Astrophys. J.*, **421**, p. 46.

Stuchlík, Z. and Bao, G. (1992), Radiation from hot spots orbiting an extreme Reissner–Nordström black hole, *Gen. Relativity Gravitation*, **24**, pp. 945–957.

Török, G. (2005a), A possible 3 : 2 orbital epicyclic resonance in QPO frequencies of Sgr A*, *Astronomy and Astrophysics*, **440**(1), pp. 1–4.

Török, G. (2005b), QPOs in microquasars and Sgr A*: measuring the black hole spin, *Astronom. Nachr.*, **326**(9), pp. 856–860, `astro-ph/0510669`.

Török, G., Abramowicz, M. A., Kluźniak, W. and Stuchlík, Z. (2005), The orbital resonance model for twin peak kHz quasi periodic oscillations in microquasars, *Astronomy and Astrophysics*, **436**(1), pp. 1–8, `astro-ph/0401464`.

Viergutz, S. U. (1993), *Astrophys. and Space Sci.*, **205**, pp. 155–161.

Proceedings of *RAGtime 6/7: Workshops on black holes and neutron stars, Opava, 16–18/18–20 September, 2004/2005*
S. Hledík and Z. Stuchlík, editors, Silesian University in Opava, Czech Republic, 2005, pp. 157–166

Some aspects of the Störmer problem within strong gravitational fields

Jaroslava Schovancová,[1,a] Ladislav Šubr,[1]
Vladimír Karas,[2] Zdeněk Stuchlík[3] and Jiří Kovář[3]

[1]Astronomical Institute of the Charles University in Prague, Czech Republic
[2]Astronomical Institute, Czech Academy of Sciences, Boční II 1401, CZ-141 31 Praha 4, Czech Republic
[3]Institute of Physics, Faculty of Philosophy & Science, Silesian University in Opava, Bezručovo nám. 13, CZ-746 01 Opava, Czech Republic
[a]`schovan@sirrah.troja.mff.cuni.cz`

ABSTRACT
We examine halo orbits of electrically charged particles near a magnetized compact star. We compare the Newtonian and Pseudo-Newtonian approaches to the Störmer problem as a preliminary discussion of the full general relativistic approach. We show the differences in the effective potential that arise due to strong gravity near a gravitating body.

1 INTRODUCTION

Near compact objects (black holes and neutron stars), strong gravity acts on particles and fluids and its influence competes with electromagnetic forces. Basic aspects of the motion are identical as they are in the limit of weak gravitational field, e.g., near planets of the Solar system, however, strong gravity brings modifications and some new aspects.

On the way to understanding radiation belts surrounding magnetized planets, including the Earth, one meets Störmer's analysis (Störmer, 1955) of the charged particle motion in the pure magnetic dipole field. The radiation belts consist of individual ions and electrons; their motion is governed mainly by the magnetic force. In the case of dust grains the charge-to-mass ratio is smaller and dynamics is more complex. We cannot consider just the magnetic force in the equations of motion, instead we have to include also the planet's gravity and rotation of the magnetic dipole.

In this paper we present a brief introduction to the Störmer problem and discuss its modification due to the general relativity. First, in Section 2 we discuss the Newtonian approach based on Dullin et al. (2002). The main aim of this section is to summarize the weak gravitational field formalism and to prepare for the discussion of differences that will be brought by strong-gravity. In order to facilitate the transition to general relativity formalism we first discuss the Störmer problem in terms of the Pseudo-Newtonian model

80-7248-334-X

of Paczyński and Wiita (1980). In Section 3 we compare the Newtonian and the Pseudo-Newtonian approaches to the Störmer problem.

2 SUMMARY OF DULLIN'S ET AL. ANALYSIS IN THE NEWTONIAN APPROACH

Dullin et al. (2002) developed a general approach that incorporates both gravitational and electromagnetic forces near a planet. General discussion of charged particle motion can begin with axisymmetric geometry assumption, which describes motion of charged grains in the aligned magnetosphere of a rotating planet. Let's study motion of a particle of mass m and charge q in three-dimensional space. In the inertial frame equations of motion are

$$m\ddot{\boldsymbol{r}} = \frac{q}{c}\,\dot{\boldsymbol{r}} \times \boldsymbol{B} - \nabla U(\boldsymbol{r})\,, \tag{1}$$

where the scalar potential $U(\boldsymbol{r})$ includes gravitational potential and potential of electric field induced by the rotation of the dipole. Dullin et al. (2002) make an assumption that the magnetic field $\boldsymbol{B}$ and potential U are symmetric with respect to rotation around the z axis.

In order to express co-rotational electric field let's transform the equations of motion to a rotating coordinate system using a rotation matrix R corresponding to the angular velocity $\boldsymbol{\Omega} = (0, 0, \Omega)^{\mathrm{T}}$. The transformed equations of motion read

$$m\ddot{\boldsymbol{q}} = \left(\frac{q}{c}\boldsymbol{B} - 2m\boldsymbol{\Omega}\right) \times \dot{\boldsymbol{q}} - m\boldsymbol{\Omega} \times (\boldsymbol{\Omega} \times \boldsymbol{q}) + \frac{q}{c}\boldsymbol{B} \times (\boldsymbol{\Omega} \times \boldsymbol{q}) - \nabla U(\boldsymbol{q})\,, \tag{2}$$

where we can recognize the Coriolis force $-2m\boldsymbol{\Omega} \times \dot{\boldsymbol{q}}$ and the centrifugal force $-m\boldsymbol{\Omega} \times (\boldsymbol{\Omega} \times \boldsymbol{q})$. Comparing the transformed equations of motion (2) to the non-transformed one (1), it is possible to see that there is no term $\boldsymbol{B} \times (\boldsymbol{\Omega} \times \boldsymbol{q})$ in (1). Consequently, there must be such term in ∇U in order to cancel it. This term gives rise to co-rotational electric field:

$$\boldsymbol{E} = \frac{q}{c}\boldsymbol{B} \times (\boldsymbol{\Omega} \times \boldsymbol{q}) = \frac{q}{c}\mathcal{M}\Omega\nabla\left(\frac{x^2 + y^2}{r^3}\right)\,, \tag{3}$$

where $\mathcal{M}$ is strength of a centred magnetic dipole. The electric field $\boldsymbol{E}$ is unipolar, therefore it is not induced by a changing magnetic field, it is perpendicular to the magnetic field and the divergence of the electric field is nonzero, which gives rise to a space charge distribution originating from the plasma rotation.

In order to distinguish the impact of the charge-to-mass ratio of the particle and to stress the significance or negligence of the gravitational or co-rotational electric forces we introduce two parameters – "switches" – which can adopt values 0 or 1 : σ_{g} is connected to the gravitational field, its value is $\sigma_{\mathrm{g}} = 1$ if the gravity is more significant than the co-rotational electric force, or otherwise $\sigma_{\mathrm{g}} = 0$. The switch σ_{r} is connected to the co-rotational electric field, its value is $\sigma_{\mathrm{r}} = 1$ in case the co-rotational electric field is significant and $\sigma_{\mathrm{r}} = 0$ if it is negligible.

According to four possible values of $\sigma_{\mathrm{g}}, \sigma_{\mathrm{r}}$ pairs we introduce four distinct flavours of the problem (Dullin et al., 2002): the *Classical Störmer Problem* (CSP, $\sigma_{\mathrm{g}} = 0, \sigma_{\mathrm{r}} = 0$) in which the particle moves under the pure magnetic dipole field conditions, the *Rotational Störmer*

Problem (RSP, $\sigma_g = 0$, $\sigma_r = 1$) which includes the planetary co-rotational electric field, the *Gravitational Störmer Problem* (GSP, $\sigma_g = 1, \sigma_r = 0$) with Keplerian-gravity included and co-rotational electric field excluded, and the most general *Rotational-Gravitational Störmer Problem* (RGSP, $\sigma_g = 1, \sigma_r = 1$), which includes both planetary gravitational and co-rotational electric field.

For each of these four cases we must consider charge sign in prograde or retrograde orbits. Here follows the Dullin et al. (2002) results résumé: (1) CSP: There are no stable circular orbits, equatorial or non-equatorial (halo). (2) RSP: There exist stable equatorial orbits for both charge-signs. There are no halo orbits. (3) GSP: There are stable orbits for both charge signs. Retrograde stable halo orbits for positive charges, prograde stable halo orbits for negative charges. (4) RGSP: There are stable equatorial orbits for both charge signs. There is a range of positive charge-to-mass ratios without stable equatorial orbits. There are prograde halo orbits for negative charges. There are pro- or retrograde halo orbits for positive charges. For stability the frequency must be sufficiently different from twice the planetary rotation rate.

2.1 Equations of motion

In an inertial frame we can split the potential into two parts: the first part corresponding to the gravity and the other part corresponding to the co-rotational electric field:

$$U(\boldsymbol{r}) = -\sigma_g \frac{\mu m}{r} + \sigma_r \frac{q}{c} \mathcal{M} \Omega \left(\frac{x^2 + y^2}{r^3} \right) . \tag{4}$$

We can distinguish three types of constants:

- Parameters connected with the planet: the mass $\mu = GM$ and the spin rate Ω.
- Parameters connected with dust particle: the mass m and an electric charge measured in $q\mathcal{M}/c$.
- Constants of motion: angular momentum p_φ and total energy $h = H$ of the particle. We can define a region in configuration space by fixing these two parameters.

In order to reduce the number of parameters we scale distances and masses. Distances are measured in terms of radius of Keplerian synchronous orbit R and masses are scaled to the particle mass m. Then we introduce two dimensionless parameters p and δ:

$$p \equiv p_\varphi \frac{R\delta c}{q\mathcal{M}} \qquad \text{and} \qquad \delta \equiv \frac{\Omega q \mathcal{M}}{mc\mu} = \frac{\omega_c \Omega}{\omega_K^2} , \tag{5}$$

where $\omega_c = qB_0/mc$ is the cyclotron frequency, B_0 is the planetary equatorial magnetic field and $\omega_K = (GM/R_s^3)^{1/2}$ is the Kepler frequency at the planetary radius R_s. The parameter p is the scaled angular momentum and the parameter δ corresponds to the charge-to-mass ratio.

Finally, we use the effective potential method in order to derive relation between circular orbits radii and previously introduced parameters p and δ. The scaled Hamiltonian of the above equations of motion in spherical coordinates reads

$$H = \frac{1}{2}\left(p_r^2 + \frac{p_\theta^2}{r^2}\right) + U_{\mathrm{eff}}\,. \tag{6}$$

2.2 Equatorial orbits

Assuming the motion in the equatorial plane, Dullin et al. (2002) consider the effective potential U_{eff} is that part of Hamiltonian (6) independent of non-constant momenta p_r and p_θ:

$$U_{\mathrm{eff}}(r,\theta,p) = \frac{(pr - \delta\sin^2\theta)^2}{2r^4\sin^2\theta} - \frac{\sigma_{\mathrm{g}}}{r} + \frac{\sigma_{\mathrm{r}}\delta\sin^2\theta}{r}\,. \tag{7}$$

Since we know the Hamiltonian (6) we can express the equations of motion:

$$\dot{r} = p_r\,, \qquad \dot{\theta} = p_\theta\,, \qquad \dot{\varphi} = \frac{\partial U_{\mathrm{eff}}}{\partial p}\,, \tag{8}$$

$$\dot{p}_r = -\frac{\partial U_{\mathrm{eff}}}{\partial r}\,, \qquad \dot{p}_\theta = -\frac{\partial U_{\mathrm{eff}}}{\partial \theta}\,, \qquad \dot{p}_\varphi = 0\,. \tag{9}$$

In order to simplify the partial derivatives of U_{eff} calculation we introduce the frequency $\omega(r,\theta)$:

$$\omega(r,\theta) = \dot{\varphi} = \frac{\partial U_{\mathrm{eff}}}{\partial p} = \frac{p}{r^2\sin^2\theta} - \frac{\delta}{r^3}\,. \tag{10}$$

This frequency is measured in terms of planetary spin Ω, thence $\omega = 1$ means synchronous motion. Now we eliminate p in equations in terms of ω:

$$U_{\mathrm{eff}} = \frac{1}{2}\omega^2 r^2\sin^2\theta - \frac{\sigma_{\mathrm{g}}}{r} + \frac{\sigma_{\mathrm{r}}\delta\sin^2\theta}{r}\,. \tag{11}$$

Assuming the circular orbits in the equatorial plane, Dullin et al. (2002) have to solve polynomial

$$P(r,\omega) = \omega^2 r^3 - \omega\delta + \sigma_{\mathrm{r}}\delta - \sigma_{\mathrm{g}}\,. \tag{12}$$

Solving the equation for equatorial orbits $P = 0$ we get a generalized Kepler's third law for equatorial orbits:

$$r_{\mathrm{e}}(\omega)^3 = \frac{\sigma_{\mathrm{g}} + \delta(\omega - \sigma_{\mathrm{r}})}{\omega^2}\,. \tag{13}$$

The equation for equatorial orbits (12) can be solved for δ as a function of $\omega(r)$:

$$\delta = \frac{r^3\omega^2 - \sigma_{\mathrm{g}}}{\omega - \sigma_{\mathrm{r}}}\,. \tag{14}$$

Now we have two parameters describing particle motion and we are able to figure out "phase space (ω,δ)" trajectories. Consider an equatorial circular orbit of given radius r_{e}.

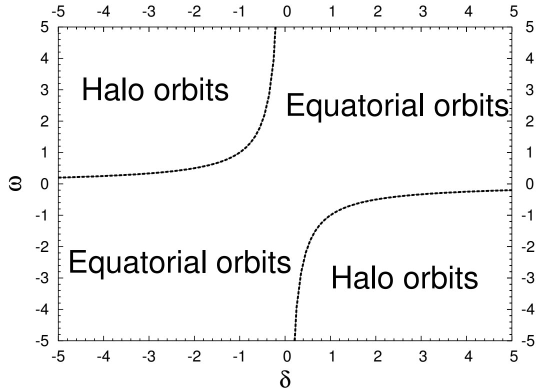

Figure 1. Possible (ω, δ)-parameterization for equatorial orbits and for halo orbits.

The corresponding angular momentum $p_{\rm e}$ can be calculated from (10). The radius $r_{\rm e}$ is positive if (see Fig. 1)

$$\omega \leq \sigma_{\rm r} - \frac{\sigma_{\rm g}}{\delta} \qquad \text{and} \qquad \delta \leq 0\,, \qquad \text{or} \tag{15}$$

$$\omega \geq \sigma_{\rm r} - \frac{\sigma_{\rm g}}{\delta} \qquad \text{and} \qquad \delta \geq 0\,. \tag{16}$$

Finally, we can choose the radius of equatorial orbit r and frequency $\omega(r)$ and according to the equation (14) we obtain value of δ parameter as function of r, ω. Moreover, by choosing just the orbital radius, we obtain "phase space trajectories" of such dust grain (see Fig. 3 in Dullin et al., 2002). Each curve on figure shows possible $(\omega(r), \delta(r))$ parameterization of the equatorial orbit of radius r for distinct Störmer problem.

2.2.1 Stability of the equatorial orbits

From the second derivatives of the effective potential $U_{\rm eff}$ (11) Dullin et al. (2002) get the stability constraint on ω. The equatorial orbits are stable if ω lies in following ranges:

$$\begin{aligned} \delta < 0 \;&:\; \omega_{\rm e}^{-} < \omega < \omega_{\rm PF}\,, \\ 0 < \delta < \delta_{\rm e}^{-} \;&:\; \omega_{\rm PF} < \omega < \omega_{\rm e}^{-}\,, \\ \delta > \delta_{\rm e}^{+} \;&:\; \omega_{\rm PF} < \omega < \omega_{\rm e}^{+}\,, \end{aligned}$$

where

$$\omega_{\rm e}^{\pm} = \frac{1 \pm \sqrt{3}}{2}\left(\sigma_{\rm r} - \frac{\sigma_{\rm g}}{\delta}\right)\,, \qquad \omega_{\rm PF} = \sigma_{\rm r} - \frac{\sigma_{\rm g}}{3\delta}\,, \qquad \delta_{\rm e}^{\pm} = \frac{\sigma_{\rm g}}{\sigma_{\rm r}}\frac{5 \pm 2\sqrt{3}}{3}\,.$$

2.3 Halo orbits

Halo orbits are defined as orbits which do not cross the equatorial plane. According to Dullin et al. (2002) we can find such halo orbits, which occur in a plane parallel to the equatorial plane. Our first aim is to find circular halo orbits. In case of equatorial orbits we solved Eq. (12). The non-equatorial orbits are described by solution of set of equations $Q(r,\omega)=0$ and $A(\theta,\omega)=0$, where

$$Q(r,\omega) = \omega^2 r^3 + 2\omega\delta - 2\sigma_{\rm r}\delta\,, \tag{17}$$
$$A(\theta,\omega) = \sigma_{\rm g} + 3\delta(\omega-\sigma_{\rm r})\sin^2\theta\,. \tag{18}$$

The non-equatorial (halo) orbits for charged dust grains are completely described by these functions A and Q. Solutions for orbits with constant radius and/or at constant height above/beneath the equatorial plane are given by

$$r_{\rm h}^3(\omega) = 2\delta\frac{\sigma_{\rm r}-\omega}{\omega^2}\,, \tag{19}$$
$$\sin^2\theta_{\rm h}(\omega) = \frac{\sigma_{\rm g}}{3\delta(\sigma_{\rm r}-\omega)}\,. \tag{20}$$

Similar conditions for halo orbits as Eqs (15) and (16) for equatorial orbits are given by (see Fig. 1)

$$\omega \geq \sigma_{\rm r} - \frac{\sigma_{\rm g}}{3\delta} \qquad \text{and} \qquad \delta \leq 0\,, \qquad \text{or} \tag{21}$$
$$\omega \leq \sigma_{\rm r} - \frac{\sigma_{\rm g}}{3\delta} \qquad \text{and} \qquad \delta \geq 0\,. \tag{22}$$

Under conditions of the equations (19) and (20) the parameter δ can be expressed as a function of r and $\omega(r)$:

$$\delta|_{r=\rm const} = \frac{r^3\omega^2}{2(\sigma_{\rm r}-\omega)}\,, \tag{23}$$
$$\delta|_{\theta=\rm const} = \frac{\sigma_{\rm g}}{3(\sigma_{\rm r}-\omega)\sin^2\theta}\,. \tag{24}$$

Finally, let's chose the radius of equatorial orbit r and frequency $\omega(r)$ and according to the equation (23) we obtain "phase space trajectories" of such dust grain. Each curve in figure shows possible $(\omega(r),\delta(r))$ parameterization of equatorial orbit of radius r for distinct Störmer problem. Moreover, we can fix height above/beneath the equatorial plane according to (24) in order to obtain curves of constant θ. Or, we can merge these two types of curves together and get a set of parameters (ω,δ) for circular trajectories (constant r) at constant height (constant θ) – see Fig. 6 in Dullin et al. (2002). From Eq. (24) we can see gravity is necessary for orbits in planes parallel to the equatorial plane (planes of constant θ).

2.3.1 Stability of the halo orbits

From the second derivatives of the effective potential U_{eff} (11) Dullin et al. (2002) got the stability constraint on ω. The halo orbits are stable if ω lies in following ranges:

$$\begin{aligned}
\delta < \delta_{\mathrm{h}}^{-} &: \quad \omega > \omega_{\mathrm{h}}^{+}\,, \\
\delta_{\mathrm{h}}^{-} < \delta < 0 &: \quad \omega > \omega_{\mathrm{PF}}\,, \\
0 < \delta < \delta_{\mathrm{h}}^{+} &: \quad \omega < \omega_{\mathrm{PF}}\,, \\
\delta > \delta_{\mathrm{h}}^{-} &: \quad \omega < \omega_{\mathrm{h}}^{-}\,,
\end{aligned}$$

where

$$\omega_{\mathrm{h}}^{\pm} = \sigma_{\mathrm{r}}\left(2 \pm \sqrt{3}\right)\,, \qquad \delta_{\mathrm{h}}^{\pm} = \frac{\sigma_{\mathrm{g}}}{\sigma_{\mathrm{r}}}\frac{1 \pm \sqrt{3}}{6}\,.$$

3 THE STÖRMER PROBLEM IN PSEUDO-NEWTONIAN APPROACH

On our way to find circular orbits we can either use (ω, δ) parameters, or alternatively, we can inspect the poloidal (ρ, z) plane around the planet in order to search for the effective potential minima. Complete discussion of the problem requires general relativity, however, basic aspects of the motion can be examined in terms of the Pseudo-Newtonian model. In order to compare the Newtonian and the Pseudo-Newtonian approaches we use the effective potential (Howard et al., 1999) (note the potentials $U_{\mathrm{eff,N}}$ and $U_{\mathrm{eff,PW}}$ are scaled by the dust grain mass m):

$$U_{\mathrm{eff,N}} = \frac{1}{2\rho^2}\left(p_{\varphi} - \frac{\omega_{\mathrm{c}}\rho^2}{r^3}\right)^2 - \sigma_{\mathrm{g}}\frac{\omega_{\mathrm{K}}^2}{r} + \sigma_{\mathrm{r}}\frac{\Omega\,\omega_{\mathrm{c}}\rho^2}{r^3}\,, \tag{25}$$

where $r = (\rho^2 + z^2)^{1/2}$, $p_{\varphi} = \omega\rho_0^2 + \omega_{\mathrm{c}}\rho_0^2/r_0^3$ is the constant of motion, (ρ_0, z_0) is the position of the equilibria circular orbit, $\omega_{\mathrm{K}} = (GM/Rp^3)^{1/2}$ is the Keplerian frequency and $\omega_{\mathrm{c}} = qB_0/mc$ is the cyclotron frequency. In the Pseudo-Newtonian approach the effective potential reads

$$U_{\mathrm{eff,PW}} = \frac{1}{2\rho^2}\left(p_{\varphi} - \frac{\omega_{\mathrm{c}}\rho^2}{r^3}\right)^2 - \sigma_{\mathrm{g}}\frac{\omega_{\mathrm{K}}^2}{r - \frac{2GM}{c^2 R_{\mathrm{p}}}} + \sigma_{\mathrm{r}}\frac{\Omega\,\omega_{\mathrm{c}}\rho^2}{r^3}\,. \tag{26}$$

Introducing the gravitational radius GM/c^2 in the denominator of the middle term on the right-hand side is a simple trick that captures certain features of motion very near compact stars and black holes. In (25) and (26) we use “scaled lengths” notation – all the length quantities are expressed in terms of planetary radius R_{p}.

We study two systems in order to compare effects of the object’s compactness to the effective potentials (25) and (26) of planet, in this case Saturn, and of a compact object – the neutron star. For the system with planet Saturn we use these parameters: $M_{\mathrm{SAT}} = 5.6 \times 10^{29}$ g, $R_{\mathrm{SAT}} = 6.03 \times 10^9$ cm, $\Omega_{\mathrm{SAT}} = 1.69 \times 10^{-4}$ Hz, $B_{\mathrm{SAT}} = 0.21$ G,

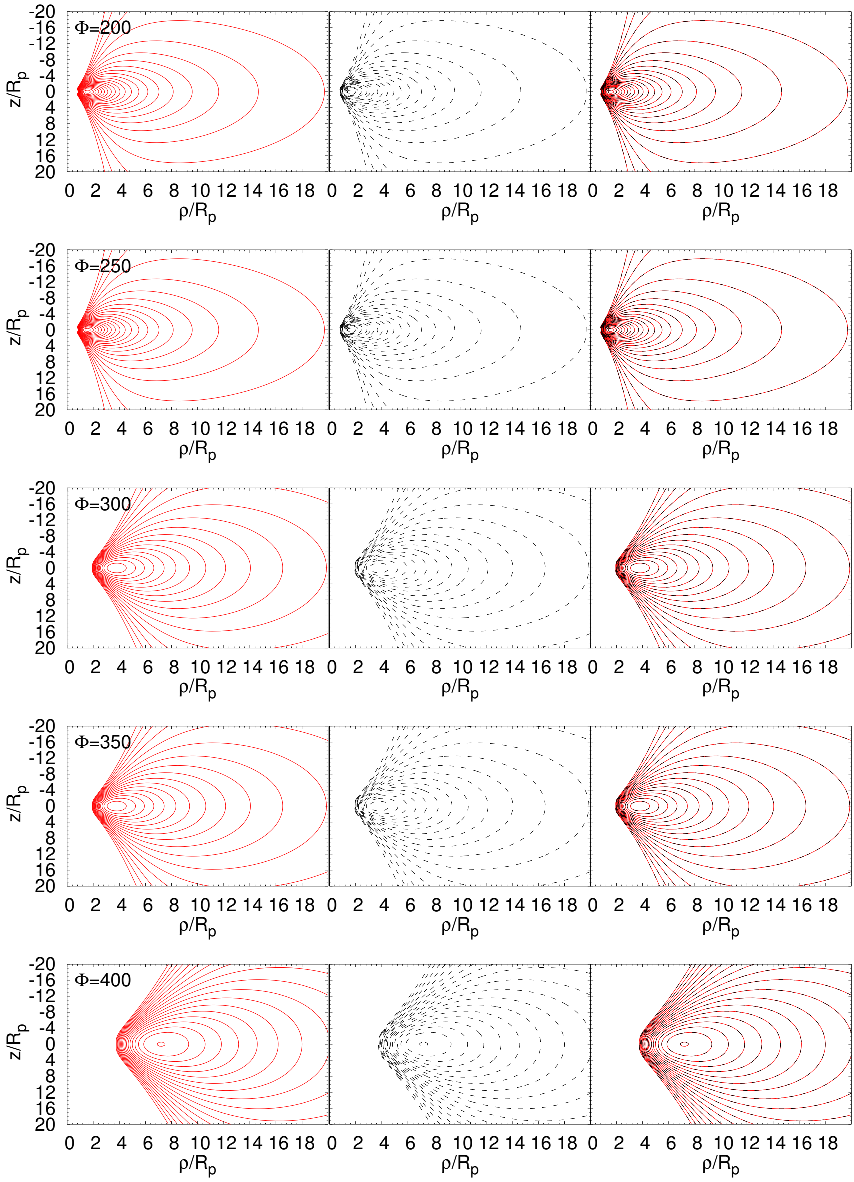

Figure 2. Iso-contours of the effective potential in the Newtonian approach (*left*) and in the Pseudo-Newtonian approach (*middle*) and comparison of both approaches (*right*) by over-plotting the two graphs on top of each other. The case of the Rotational-Gravitational ($\sigma_g = \sigma_r = 1$) Störmer Problem for Saturn ($R_g/R_p = 6.88 \times 10^{-6}$). Each row of pictures differs by the dust-grains surface potential – here from $\Phi = 200\,\mathrm{V\,cm^{-2}}$ to $\Phi = 400\,\mathrm{V\,cm^{-2}}$. As expected, the Newtonian and the Pseudo-Newtonian results are almost indistinguishable because of small compactness of the central body in this example.

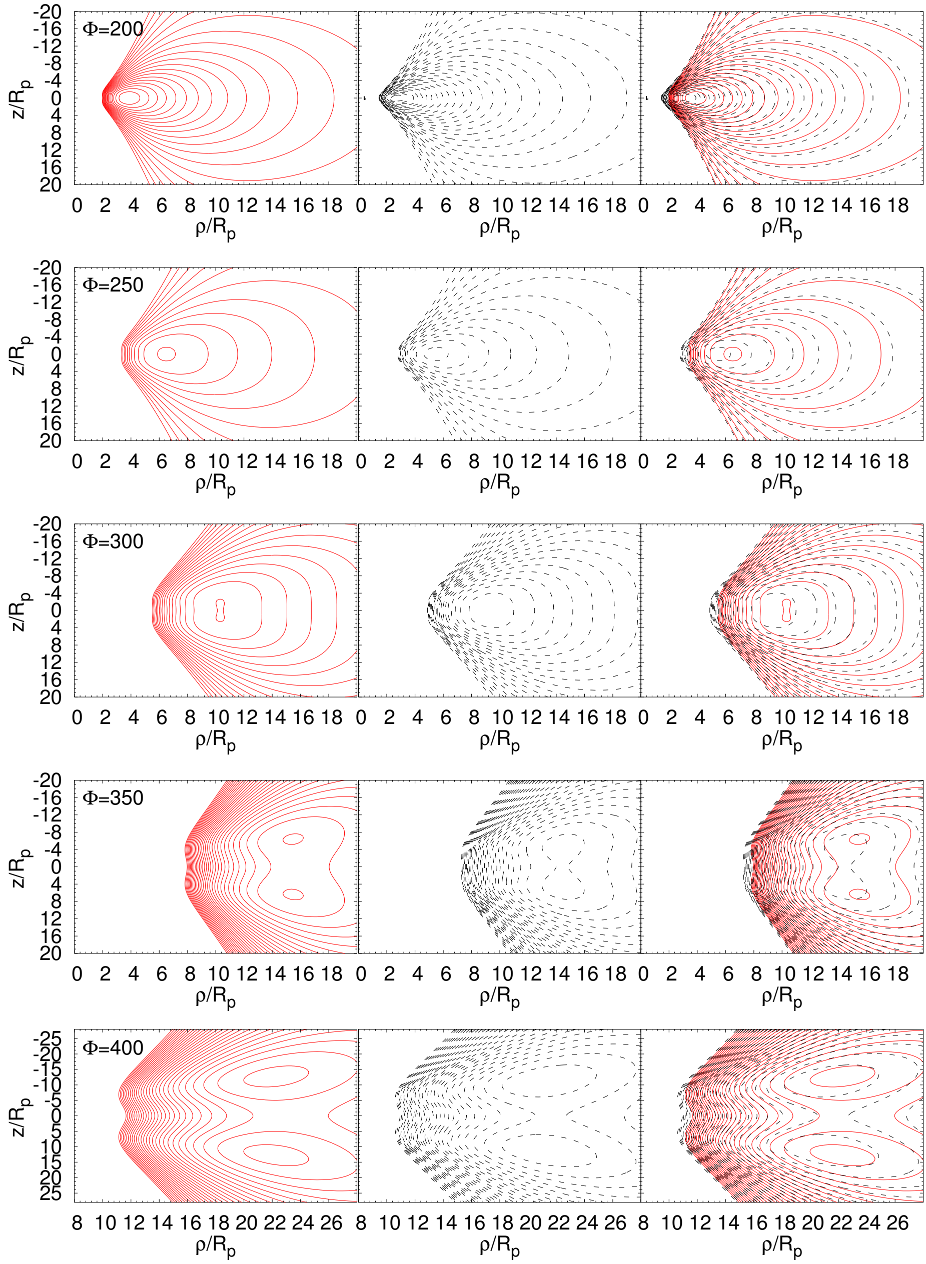

Figure 3. The same as in Fig. 2, but for the case of a highly compact neutron star ($R_g/R_p = 0.201$). In contrast to the previous figure, minima of the effective potential have developed for $\Phi \geq 292\,\mathrm{V\,cm^{-2}}$ in case of the Newtonian approach (25) and for $\Phi \geq 317\,\mathrm{V\,cm^{-2}}$ in case of the Pseudo-Newtonian approach (26). These correspond to halo orbits.

$R_g/R_{SAT} = 6.88 \times 10^{-9}$. For the system with the neutron star we use these parameters: $M_{NS} = 4.0 \times 10^{33}$ g, $R_{NS} = 1.47 \times 10^6$ cm, $\Omega_{NS} = 5.0 \times 10^3$ Hz, $B_{NS} = 6.88 \times 10^6$ G, $R_g/R_{NS} = 2.01 \times 10^{-1}$.

Iso-contours of the effective potentials (25) and (26) are shown in Fig. 2 for the case of Saturn. In the left column we can see the iso-contours of the effective potential (25), in the middle column we can see the iso-contours of the effective potential (26) and in the right column we compare the Newtonian and the Pseudo-Newtonian approaches. From the Fig. 2 we can see that the difference between the Newtonian and the Pseudo-Newtonian approaches in case of non-compact object is negligible. Each set of pictures (each line) in the Fig. 2 means different surface potential of a studied dust grain. We choose to study dust grains with surface potential from $\Phi = 200\,\mathrm{V\,cm^{-2}}$ to $\Phi = 400\,\mathrm{V\,cm^{-2}}$. The local minima of the effective potential of chosen dust grains are located in the equatorial plane on radial distance from 2 R_{SAT} to 7 R_{SAT}.

However, near a compact object the difference between the iso-contours of the two potentials, (25) versus (26), are not negligible. This can be seen in Fig. 3, which has been constructed in a similar way as Fig. 2. The chosen dust grains surface potential is the same as in the previous case: from $\Phi = 200\,\mathrm{V\,cm^{-2}}$ to $\Phi = 400\,\mathrm{V\,cm^{-2}}$. In case the surface potential is lower than $\Phi = 292\,\mathrm{V\,cm^{-2}}$ for the Newtonian approach (25) or is lower than $\Phi = 317\,\mathrm{V\,cm^{-2}}$ for the Pseudo-Newtonian approach (26) there are equatorial circular orbits. Otherwise, there are non-equatorial circular orbits near the neutron star.

4 CONCLUSIONS

Results of the Newtonian and the Pseudo-Newtonian approaches coincide in the case of weak gravitational fields (see Fig. 2). There are several differences between the results of the Newtonian and the Pseudo-Newtonian approaches in the case of compact objects (see Fig. 3). We have verified that similarly to the Newtonian case, both equatorial and halo orbits can occur near a compact star, depending on the dust grain surface potential.

However, it can be inferred from the Fig. 3 that general relativistic corrections to the gravity of the central body have a tendency to bring the halo orbits closer to the equatorial plane. Further investigation of these corrections is a subject of our ongoing project.

ACKNOWLEDGEMENTS

This work was prepared as a part of the student's project (J. S.) and it was supported by the grant 299/2004 of the Charles University in Prague. J. K. and Z. S. were supported by Czech grant MSM 4781305903.

REFERENCES

Dullin, H. R., Horányi, M. and Howard, J. E. (2002), *Physica D*, **171**, pp. 178–195.

Howard, J. E., Horányi, M. and Stewart, G. R. (1999), *Phys. Rev. Lett.*, **83**(20), p. 3993.

Paczyński, B. and Wiita, P. J. (1980), *Astronomy and Astrophysics*, **88**(1–2), pp. 23–31.

Störmer, C. (1955), *The Polar Aurora*, Clarendon Press, Oxford.

Proceedings of *RAGtime 6/7: Workshops on black holes and neutron stars, Opava, 16–18/18–20 September, 2004/2005*
S. Hledík and Z. Stuchlík, editors, Silesian University in Opava, Czech Republic, 2005, pp. 167–187

Perfect fluid tori in the Kerr–de Sitter naked singularity backgrounds

Petr Slaný and Zdeněk Stuchlík

Institute of Physics, Faculty of Philosophy & Science, Silesian University in Opava, Bezručovo nám. 13, CZ-746 01 Opava, Czech Republic

ABSTRACT

Perfect fluid tori with uniform distribution of the specific angular momentum, $\ell(r,\theta) = \text{const}$, orbiting the Kerr–de Sitter naked singularities are discussed. Closed equipotential surfaces corresponding to stationary thick discs are allowed only in the spacetimes admitting stable circular geodesics. The last closed surface crosses itself in the cusp(s) enabling outflows of matter from the torus due to the violation of hydrostatic equilibrium. The inner cusp enables the accretion onto the ring singularity. Influence of the repulsive cosmological constant, $\Lambda > 0$, resides in the existence of the outer cusp enabling the *excretion* (outflow of matter from the torus into the outer space) and gives rise to completely new type of a disc called the *excretion disc*. The plus-family accretion and excretion discs can be both the corotating or counterrotating discs, the minus-family ones are always the counterrotating discs, as related to locally non-rotating frames. If the parameters of naked-singularity spacetimes are very close to the parameters of the extreme black-hole spacetimes, the family of possible disc-like configurations includes members with two isolated discs where the inner one is always a counterrotating accretion disc, while the outer one can be the corotating or counterrotating excretion disc, as well as the counterrotating accretion disc.

1 INTRODUCTION

Observations give strong evidence that accretion discs orbiting massive black holes are the energy sources in quasars and active galactic nuclei. Since the existence of naked singularities is not excluded on the present state of knowledge (e.g., de Felice and Yunqiang, 2001), accretion onto a naked singularity could still be regarded as the power engine of the most energetic phenomena in the Universe, despite of the cosmic censorship hypothesis (Penrose, 1969). Basic properties of geometrically thin accretion discs with low accretion rates and negligible pressure are given by the circular geodesic motion in the black-hole backgrounds (Novikov and Thorne, 1973), while for geometrically thick accretion discs with high accretion rates and pressure being relevant they are determined by equipotential surfaces of test perfect fluid rotating in the background (see, e.g., Abramowicz, 1998). Attention is focused on the configurations containing closed equipotential surfaces, as they correspond to stationary tori, which occur only in the backgrounds admitting stable circular

80-7248-334-X

orbits. An outflow of matter from the torus induced by a violation of hydrostatic equilibrium is possible, if the last closed equipotential surface self-crossing in the cusp(s) can exist in the background. (In fact, in the centre of any equilibrium toroidal configuration the matter follows stable equatorial circular geodesic, while in the cusps it follows unstable equatorial circular geodesics.) The so-called Paczyński mechanism (Abramowicz et al., 1978, 1980) is very similar to the one well-known from the binary systems where the matter overfilling the "Roche lobe" can flow from the normal star onto the companion through the Lagrange point L1 or even out from the system through the Lagrange point L2 (see, e.g., Novikov and Thorne, 1973).

The presence of a repulsive cosmological constant or, equivalently, a positive vacuum energy, indicated by a wide range of independent cosmological tests giving the present value $\Lambda_0 \sim 10^{-56}\,\mathrm{cm}^{-2}$ (see, e.g., Spergel et al., 2003; Bahcall et al., 1999; Kolb and Turner, 1990), leads to very important consequences for the properties of both the thin and thick discs.

It was shown that thin discs orbiting the Schwarzschild–de Sitter (SdS) black holes have, besides the standard inner edge at the inner marginally stable circular orbit, an outer edge at the outer marginally stable circular orbit located slightly under the static radius (Stuchlík and Hledík, 1999). Similarly, thick discs orbiting the SdS black hole have, besides the standard inner cusp enabling accretion inflow of matter from the disc onto the black hole, an outer cusp located nearby the static radius and enabling an outflow of matter from the system of the black hole and its accretion disc into the outer space; such a process is called *excretion*. Rezzolla et al., analysing the dynamics of thick discs in the SdS backgrounds (Rezzolla et al., 2003; Rezzolla, 2004), suggested that the repulsive vacuum energy can have a stabilizing effect on dynamics of thick discs, as the mass outflow through the outer cusp is able to efficiently suppress the so-called runaway instability of the disc, which can develop in some dynamical models of accretion disc (see Abramowicz et al., 1983; compare with Wilson, 1984; Nishida et al., 1997). Moreover, for current value of the cosmological constant , $\Lambda = \Lambda_0 \doteq 1.3 \times 10^{-56}\,\mathrm{cm}^{-2}$, and supermassive black holes of mass $M \sim 10^9\,\mathrm{M}_\odot$, the location of the outer cusp, and the outer edge of the disc, is about 110 kpc that is smaller than but comparable to the extension of giant galaxies with such massive central black holes, indicating that the repulsive cosmological constant could play an important role in the formation and evolution of large galaxies.

Another feature connected with the cosmic repulsion consists in strong collimation of open equipotential surfaces near the axis of rotation, being evident nearby and behind the static radius, suggesting a certain role of $\Lambda > 0$ in the collimation of jets far away from the maternal disc (Stuchlík et al., 2000; Stuchlík, 2005). It is curious, if the influence of the repulsive cosmological constant will be relevant for the radial and vertical epicyclic oscillations that are expected as a source of quasiperiodic variability at quasars and active galactic nuclei as predicted by Török (2005a,b).

Studies of rotating backgrounds are crucial to understand astrophysically realistic situations in active galactic nuclei because their central engines are assumed to be fast rotating due to the matter trapped from the accretion disc. Our work analyses the combined effect of a repulsive vacuum energy and rotation of the black hole/naked singularity on the properties of accretion discs. The equatorial circular geodesics of the Kerr–de Sitter spacetimes and their relevance for the geometrically thin accretion discs were discussed in Stuchlík and

Slaný (2004b). As in the Schwarzschild–de Sitter spacetimes, the outer marginally stable orbit always exists in those Kerr–de Sitter spacetimes admitting any stable circular orbits. Because the Kerr–de Sitter spacetimes are asymptotically de Sitter, not flat, the notion of corotating or counterrotating motion cannot be related to the observers at infinity but only to the locally non-rotating observers/frames (LNRF). As in the Kerr spacetimes, the circular geodesics of the Kerr–de Sitter spacetimes can be separated into two families (see Stuchlík and Slaný, 2004b). The minus-family orbits are all counterrotating, while the plus-family orbits are usually corotating relative to the LNRF. However, the plus-family orbits become counterrotating in the vicinity of the static radius in all Kerr–de Sitter spacetimes (these orbits are unstable), and also near the ring singularity in Kerr–de Sitter naked-singularity spacetimes with the rotational parameter low enough (these orbits can even be stable down to the inner marginally stable orbit). In such spacetimes, the efficiency of the conversion of rest energy into heat energy in the geometrically thin plus-family accretion discs, given by the difference of energies of a particle at the outer and the inner marginally stable orbit ($\eta = E_{\mathrm{ms(o)}} - E_{\mathrm{ms(i)}}$), can reach extremely high values exceeding the efficiency of the annihilation process. It should be noted, however, that in all Kerr–de Sitter spacetimes containing stable circular orbits, the accretion efficiency η is smaller in comparison with the one for pure Kerr case ($y = 0$). Moreover, it was shown that transformation of a Kerr–de Sitter naked singularity into an extreme black hole, caused by the accretion process, leads to an abrupt instability of the innermost parts of the plus-family accretion discs that can have strong observational consequences (Stuchlík and Slaný, 2004b; Stuchlík, 1980).

Studies of equilibrium configurations of barotropic perfect fluid orbiting the Kerr–de Sitter black holes have revealed qualitatively the same properties of the tori as in the Schwarzschild–de Sitter backgrounds allowing stable circular geodesics (Stuchlík and Slaný, 2004a; Slaný and Stuchlík, 2005). In fact, in black-hole backgrounds we can distinguish three kinds of discs:

Accretion discs Toroidal equipotential surfaces are bounded by the marginally closed critical equipotential surface self-crossing in the inner cusp and enabling outflow of matter from the disc into the black hole. Another critical surface self-crossing in the outer cusp is open. Matter filling the region between the critical surfaces cannot remain in hydrostatic equilibrium and contributes to the accretion flow along the inner cusp and a throat formed by open surfaces. Moreover, if the potential levels corresponding to the critical surfaces are comparable, i.e., $W_{\mathrm{crit(i)}} \lesssim W_{\mathrm{crit(o)}}$, huge overfilling of the critical surface with the inner cusp causing the accretion could be combined with the excretion, having a capability to regulate the accretion.

Marginally bound accretion discs Such configurations exist only for the uniform distribution of the specific angular momentum in the disc $\ell(r, \theta) = \ell_{\mathrm{mb}}$, where ℓ_{mb} corresponds to the Keplerian specific angular momentum on the marginally bound circular orbit. Toroidal equipotential surfaces are bounded by the marginally closed critical equipotential surface self-crossing in both the cusps. Any overfilling of the critical surface causes the accretion inflow through the inner cusp as well as the excretion outflow through the outer cusp.

Excretion discs Toroidal equipotential surfaces are bounded by the marginally closed critical equipotential surface self-crossing in the outer cusp and enabling outflow of matter from the disc into the outer space by a violation of hydrostatic equilibrium. The equipotential surface with the inner cusp, if such a surface exists, is open (cylindrical) and separated from the critical surface with the outer cusp by other cylindrical surfaces which, in fact, disable accretion into the black hole.

Due to the existence of non-zero pressure-gradients in the fluid, the inner edge of the accretion discs (corresponding to the inner cusp of equipotential surfaces) is shifted under the inner marginally stable orbit up to the inner marginally bound orbit, $r_{\mathrm{mb(i)}} < r_{\mathrm{in}} < r_{\mathrm{ms(i)}}$. Similarly, the outer edge of the excretion discs (corresponding to the outer cusp of equipotential surfaces) is located between the outer marginally stable and outer marginally bound orbit, $r_{\mathrm{ms(o)}} < r_{\mathrm{out}} < r_{\mathrm{mb(o)}}$. Marginally bound accretion discs have, thus, naturally determined both edges by the location of the cusps of the only critical surface, $r_{\mathrm{in}} \approx r_{\mathrm{mb(i)}}$, $r_{\mathrm{out}} \approx r_{\mathrm{mb(o)}}$, and correspond to maximally extended discs. Moreover, potential difference between the boundary (determined by the marginally closed critical surface) and the centre of the torus, $\Delta W = W_{\mathrm{crit}} - W_{\mathrm{center}}$, takes the largest values for plus-family marginally bound accretion discs. In black-hole backgrounds, the maximal value corresponds to the disc corotating the extreme Kerr black hole ($y = 0$), $\Delta W \approx 0.549$ (Abramowicz et al., 1978), and with the cosmological parameter y growing up to $y_{\mathrm{c(KdS)}} \doteq 0.059$ tends to zero.

Rotation of the background influences the shape of tori: the corotating discs are thicker and more extended than the counterrotating ones, generating narrower funnel where highly collimated relativistic streams of particles – jets are most probably created.

Here, we shall present the results concerning the structure of equipotential surfaces in barotropic perfect fluid tori with uniform distribution of the specific angular momentum, $\ell(r, \theta) = \mathrm{const}$,[1] rotating in the Kerr–de Sitter naked-singularity backgrounds, thoroughly published in Slaný and Stuchlík (2005). In Section 2, general theory of equilibrium configurations of barotropic perfect fluid orbiting in a stationary and axisymmetric background is outlined, in Section 3, Kerr–de Sitter spacetimes admitting stable equatorial circular orbits of test particles and the properties of such orbits are briefly discussed. Structure of equipotential surfaces determining the equilibrium configurations of barotropic fluid in the Kerr–de Sitter naked-singularity background is presented in detail in Section 4. In "Concluding remarks" (Section 5), the properties of the tori around naked singularities are summarized and compared with those in the black-hole backgrounds.

2 EQUILIBRIUM CONFIGURATIONS OF BAROTROPIC PERFECT FLUID

Analytic theory of equilibrium configurations of rotating perfect fluid bodies was developed by Boyer (1965) and than studied by many authors. The main result of the theory, known as "Boyer's condition," states that the boundary of any stationary, barotropic, perfect fluid

[1] Tori with $\ell(r, \theta) = \mathrm{const}$ are marginally stable (Seguin, 1975) and capable of producing maximal luminosity at all (Abramowicz et al., 1980). Moreover, topological properties of the equipotential surfaces seem to be rather independent on the distribution of the specific angular momentum $\ell(r, \theta)$ (see Kozłowski et al., 1978; Abramowicz et al., 1978; Jaroszyński et al., 1980; Abramowicz et al., 1980; Abramowicz, 1998; Stuchlík et al., 2000). In more realistic situations we can expect that, at large distances, such thick discs will transform into the thin discs with Keplerian distribution of the specific angular momentum, which were discussed in Stuchlík and Slaný (2004b).

body has to be an equipotential surface. In this section we briefly discuss its application to the relativistic test perfect fluid orbiting in a stationary and axisymmetric way in a stationary, axisymmetric background (Abramowicz et al., 1978; Kozłowski et al., 1978; Stuchlík et al., 2000; Slaný and Stuchlík, 2005).

In the standard Boyer–Lindquist coordinates the spacetime is described by the line element

$$\mathrm{d}s^2 = g_{tt}\,\mathrm{d}t^2 + 2g_{t\phi}\,\mathrm{d}t\mathrm{d}\phi + g_{\phi\phi}\,\mathrm{d}\phi^2 + g_{rr}\,\mathrm{d}r^2 + g_{\theta\theta}\,\mathrm{d}\theta^2 \tag{1}$$

satisfying the properties of stationarity and axial symmetry, i.e., $\partial_t g_{\mu\nu} = \partial_\phi g_{\mu\nu} = 0$. Further, we shall consider test perfect fluid moving in the azimuthal direction only and forming the toroidal configurations (discs). Its 4-velocity vector field U^μ has only two non-zero components U^t, U^ϕ which can be the functions of coordinates r, θ, and the stress-energy tensor field has the well known form

$$T^{\mu\nu} = (\epsilon + p)U^\mu U^\nu + pg^{\mu\nu}\,, \tag{2}$$

where ϵ and p are the total energy density and the pressure measured in the frame co-moving with the element of the fluid. The angular velocity and the specific angular momentum of the rotating fluid are defined in terms of the 4-velocity field as:

$$\Omega = \frac{U^\phi}{U^t}, \qquad \ell = -\frac{U_\phi}{U_t}\,. \tag{3}$$

These definitions lead to the relation between Ω and ℓ in the form

$$\Omega = -\frac{\ell g_{tt} + g_{t\phi}}{\ell g_{t\phi} + g_{\phi\phi}}\,. \tag{4}$$

The equation of motion of the fluid, i.e., the relativistic Euler equation, obtained by the projection of the conservation law $\nabla_\mu T^{\mu\nu} = 0$ onto the hypersurface orthogonal to the 4-velocity U^μ, has the axially symmetric form

$$\frac{\partial_i p}{\epsilon + p} = -\partial_i(\ln U_t) + \frac{\Omega\,\partial_i \ell}{1 - \Omega\ell}\,, \tag{5}$$

where $i = r, \theta$ and

$$(U_t)^2 = \frac{g_{t\phi}^2 - g_{tt}g_{\phi\phi}}{g_{tt}\ell^2 + 2g_{t\phi}\ell + g_{\phi\phi}}\,. \tag{6}$$

For a barotropic fluid, i.e., for a body with an equation of state $p = p(\epsilon)$, the surfaces of constant pressure are given, in accordance with Boyer's approach, by the equipotential surfaces of the potential $W(r, \theta)$ defined by the relations (Abramowicz et al., 1978)

$$\int_0^p \frac{\mathrm{d}p}{\epsilon + p} = \ln(U_t)_{\mathrm{in}} - \ln(U_t) + \int_{\ell_{\mathrm{in}}}^{\ell} \frac{\Omega\,\mathrm{d}\ell}{1 - \Omega\ell} \equiv W_{\mathrm{in}} - W\,, \tag{7}$$

where the subscript "in" refers to the inner edge of the disc. The explicit form of the potential, $W = W(r, \theta)$, is given by Eq. (7), if one specifies the metric tensor of the background and the "rotational law," i.e., the function $\Omega = \Omega(\ell)$. The simplest but also astrophysically very important is the case with uniform distribution of the specific angular momentum

$$\ell(r, \theta) = \text{const} \tag{8}$$

through the disc. In this special case the potential is given by the simple formula

$$W(r, \theta) = \ln \left(\frac{g_{t\phi}^2 - g_{tt} g_{\phi\phi}}{g_{tt}\ell^2 + 2g_{t\phi}\ell + g_{\phi\phi}} \right)^{1/2} \tag{9}$$

and is fully determined by the geometry of the background. Note that the points where $\partial_i W = 0$ correspond to free-particle (geodesic) motion due to the vanishing of the pressure-gradient forces there.

3 KERR–DE SITTER SPACETIMES ADMITTING STABLE CIRCULAR ORBITS

Stationary toroidal configurations corresponding to thick discs can exist only in the spacetimes allowing the motion along stable circular geodetical orbits. The analysis of equatorial circular geodesics in the Kerr–de Sitter spacetimes has been done in Stuchlík and Slaný (2004b) where their relevance for the thin (Keplerian) discs was also discussed. In this section we describe those characteristics of the circular geodesics which are useful for further discussion on thick discs.

The geometry of Kerr–de Sitter spacetimes is given by the line element

$$\begin{aligned} \mathrm{d}s^2 = &- \frac{\Delta_r}{I^2 \rho^2} (\mathrm{d}t - a \sin^2\theta \, \mathrm{d}\phi)^2 \\ &+ \frac{\Delta_\theta \sin^2\theta}{I^2 \rho^2} \left[a \, \mathrm{d}t - (r^2 + a^2) \, \mathrm{d}\phi \right]^2 + \frac{\rho^2}{\Delta_r} \, \mathrm{d}r^2 + \frac{\rho^2}{\Delta_\theta} \, \mathrm{d}\theta^2 \, , \end{aligned} \tag{10}$$

where

$$\Delta_r = r^2 - 2Mr + a^2 - \tfrac{1}{3}\Lambda r^2 (r^2 + a^2) \, , \tag{11}$$
$$\Delta_\theta = 1 + \tfrac{1}{3}\Lambda a^2 \cos^2\theta \, , \tag{12}$$
$$I = 1 + \tfrac{1}{3}\Lambda a^2 \, , \tag{13}$$
$$\rho^2 = r^2 + a^2 \cos^2\theta \tag{14}$$

and geometric units ($c = G = 1$) are used. The spacetime is specified by three parameters: central mass (M), rotational parameter (a) corresponding to the specific angular momentum of the central object, and positive cosmological constant (Λ). It is convenient to introduce the dimensionless "cosmological parameter"

$$y = \tfrac{1}{3}\Lambda M^2 \tag{15}$$

and reformulate relations (10)–(14) into the completely dimensionless form by putting $M = 1$ hereafter. The spacetime is stationary, axially symmetric and asymptotically de Sitter.

The spacetime horizons are determined by the condition $\Delta_r = 0$ giving the relation

$$y = y_{\mathrm{h}}(r; a) \equiv \frac{r^2 - 2r + a^2}{r^2(r^2 + a^2)} \tag{16}$$

determining implicitly radii of the horizons. Local extrema of the function $y_{\mathrm{h}}(r; a)$ are given by the relation

$$a^2 = a^2_{\mathrm{ex(h)}}(r) \equiv \frac{r}{2}\left[1 - 2r + (8r + 1)^{1/2}\right] . \tag{17}$$

Function $a^2_{\mathrm{ex(h)}}(r)$ has one extreme (maximum)

$$a^2 = a^2_{\mathrm{crit}} = \frac{3}{16}\left(3 + 2\sqrt{3}\right) \doteq 1.21202 \tag{18}$$

at $r = r_{\mathrm{crit}} = (3 + 2\sqrt{3})/4$. We can conclude that for $0 < a^2 < a^2_{\mathrm{crit}}$ the function $y_{\mathrm{h}}(r; a)$ has two local extrema, $y_{\mathrm{min}}(a)$ and $y_{\mathrm{max}}(a)$; for $a^2 = a^2_{\mathrm{crit}}$ these extrema coincide. Black-hole spacetimes exist for $y_{\mathrm{min}}(a) \leq y \leq y_{\mathrm{max}}(a)$. In general, three horizons (the inner and the outer of the black hole, $r_{\mathrm{h}-}$ and $r_{\mathrm{h}+}$, and the cosmological one, r_{c}) exist. If $y = y_{\mathrm{min}}(a)$, $r_{\mathrm{h}-} = r_{\mathrm{h}+} < r_{\mathrm{c}}$, which corresponds to the extreme black hole. If $y = y_{\mathrm{max}}(a)$, $r_{\mathrm{h}-} < r_{\mathrm{h}+} = r_{\mathrm{c}}$, which corresponds to the marginal naked singularity, as two dynamical regions are joined together. If $y < y_{\mathrm{min}}(a)$ or $y > y_{\mathrm{max}}(a)$, naked-singularity spacetimes occur. Note that for $0 < a < 1$, $y_{\mathrm{min}}(a) < 0$. If $a^2 = a^2_{\mathrm{crit}}$, the "ultra-extreme" case occurs ($r_{\mathrm{h}-} = r_{\mathrm{h}+} = r_{\mathrm{c}}$), corresponding to a naked-singularity case, and we obtain maximal value of the cosmological parameter enabling the existence of black holes to be:

$$y = y_{\mathrm{crit}} = \frac{16}{(3 + 2\sqrt{3}\,)^3} \doteq 0.05924 . \tag{19}$$

For $a^2 > a^2_{\mathrm{crit}}$, the cosmological horizon exists only, and the Kerr–de Sitter geometry describes a naked-singularity spacetime.

As in the Kerr spacetimes, also in the Kerr–de Sitter spacetimes we can distinguish two families of equatorial circular geodesics denoted $+$ (plus) or $-$ (minus), if the spacetime admits circular geodesics.[2] Angular velocity on such (Keplerian) orbits is given by the simple formula

$$\Omega_{\mathrm{K}\pm} = \frac{1}{a \pm r^{3/2}/(1 - yr^3)^{1/2}} \tag{20}$$

revealing that no circular orbits can exist behind the "static radius"

$$r = r_{\mathrm{s}} \equiv y^{-1/3} , \tag{21}$$

[2] For more detailed view into the problem of existence and properties of the equatorial circular geodesics in the Kerr–de Sitter spacetimes see Stuchlík and Slaný (2004b).

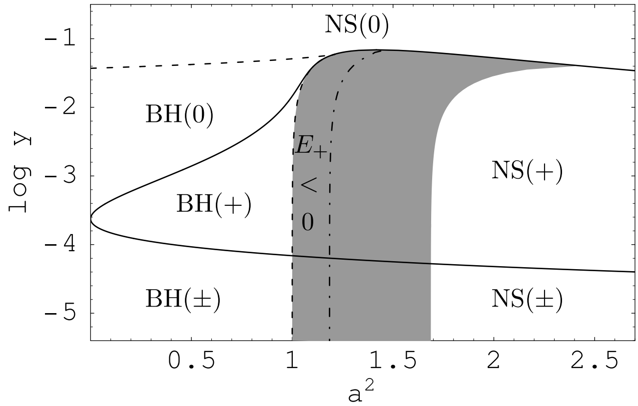

Figure 1. Classification of the Kerr–de Sitter spacetimes according to the existence of stable circular orbits of test particles in the equatorial plane. Dashed curve separates regions of black holes (BH) and naked singularities (NS), full curves separate spacetimes admitting either both families (±) of stable circular orbits or the plus-family (+) only or even no (0) stable circular orbits. For large values of a^2 both the full lines tend to the a^2-axis. Shaded region corresponds to the naked-singularity spacetimes admitting counterrotating stable plus-family orbits, dashed-dotted curve forms the boundary of subregion where these counterrotating stable plus-family orbits possess negative total energy (the constant of motion connected with the existence of timelike Killing vector field in the Kerr–de Sitter spacetime). (Taken from Slaný and Stuchlík, 2005.)

where $\Omega_{\mathrm{K}} = 0$. Note that the relation (21) for the static radius is independent of the rotation parameter a and coincides with the formula for the static radius at the Schwarzschild–de Sitter spacetimes. Direction of the circular geodesics can be determined from the point of view of LNRF moving in the equatorial plane with the angular velocity

$$\Omega_{\mathrm{LNRF}} = \frac{a(r^2 + a^2 - \Delta_r)}{(r^2 + a^2)^2 - a^2 \Delta_r} \,. \tag{22}$$

Orbits with $\Omega > \Omega_{\mathrm{LNRF}}$ or $\Omega < \Omega_{\mathrm{LNRF}}$ are called the corotating or the counterrotating, respectively.

In the black-hole spacetimes, all stable plus-family (minus-family) orbits are corotating (counterrotating) relative to the LNRF, whereas in the naked-singularity spacetimes with a rotational parameter low enough, in accordance with the Kerr case (Stuchlík, 1980), stable plus-family orbits lying near the ring singularity become counterrotating relative to the LNRF. More precisely, such orbits can exist in specifically chosen naked-singularity spacetimes with parameters $1 < a^2 < a^2_{\mathrm{cL}} \doteq 2.4406$ and $0 < y < y_{\mathrm{c(ms+)}} \doteq 0.06886$ (shaded region in Fig. 1). Moreover, a constant of motion E_+, connected with the stationarity of the geometry and possessing a physical meaning of specific energy of a particle on such an orbit, can be negative for the counterrotating plus-family orbits in the naked-singularity spacetimes with specifically chosen rotational parameter $1 < a^2 < a^2_{\mathrm{cE}} \doteq 1.47$ (the subregion with dashed-dotted boundary in Fig. 1) (see Stuchlík and Slaný, 2004b). All stable minus-family circular orbits are counterrotating from the point of view of LNRF in all naked-singularity spacetimes.

Discussion on stability of circular orbits against radial perturbations enables to divide the parametric Kerr–de Sitter space (a^2, y) into six regions according to the existence of stable circular orbits of both families (Stuchlík and Slaný, 2004b). The result is presented in Fig. 1 where the abbreviations BH and NS denote the black-hole and naked-singularity regions, respectively, the signs (+) and (−) correspond to the family of circular orbits which can be stable in a given region, and (0) says that no stable circular orbits are possible in the region.

4 EQUIPOTENTIAL SURFACES

The potential $W(r,\theta)$ in the Kerr–de Sitter background is given by the formulae

$$W(r,\theta) = \ln\left[\frac{\rho^2}{I^2}\frac{\varDelta_r\varDelta_\theta\sin^2\theta}{\varDelta_\theta(r^2+a^2-a\ell)^2\sin^2\theta - \varDelta_r(\ell - a\sin^2\theta)^2}\right]^{1/2} . \tag{23}$$

All relevant properties of the equipotential surfaces are described by the behaviour of the potential in the equatorial plane

$$W(r,\theta=\pi/2) = \ln\left[\frac{r^2}{I^2}\frac{\varDelta_r}{(r^2+a^2-a\ell)^2 - \varDelta_r(\ell-a)^2}\right]^{1/2} . \tag{24}$$

There are two reality conditions of the function (24), namely

$$\varDelta_r \geq 0\,, \tag{25}$$

$$(r^2+a^2-a\ell)^2 - \varDelta_r(\ell-a)^2 > 0\,. \tag{26}$$

Condition (25) can be rewritten into the relation $y \leq y_{\rm h}(r;a)$ which is satisfied in the whole stationary part of the naked-singularity background, $0 < r < r_{\rm c}$, between the ring singularity and the cosmological horizon. The second reality condition (26) is connected with a limit given by the photon motion, since it implies the inequality $\ell_{\rm ph-} < \ell < \ell_{\rm ph+}$ where

$$\ell_{\rm ph\pm}(r;a,y) = a + \frac{r^2}{a\pm\sqrt{\varDelta_r}} \tag{27}$$

correspond to the effective potentials of the photon geodesic motion (see Stuchlík and Hledík, 2000 for an alternative definition).

The local extrema of the function $W(r,\theta=\pi/2)$ lie at those radii where the specific angular momentum coincides with the specific angular momentum of test particles moving on the geodetical (Keplerian) circular orbits, i.e., where

$$\ell = \ell_{\rm K\pm}(r;a,y) \equiv \pm\frac{(r^2+a^2)(1-yr^3)^{1/2} \mp ar^{1/2}[2+r(r^2+a^2)y]}{r^{3/2}[1-(r^2+a^2)y] - 2r^{1/2} \pm a(1-yr^3)^{1/2}} . \tag{28}$$

Those extrema are the only local extrema of the function $W(r,\theta)$.

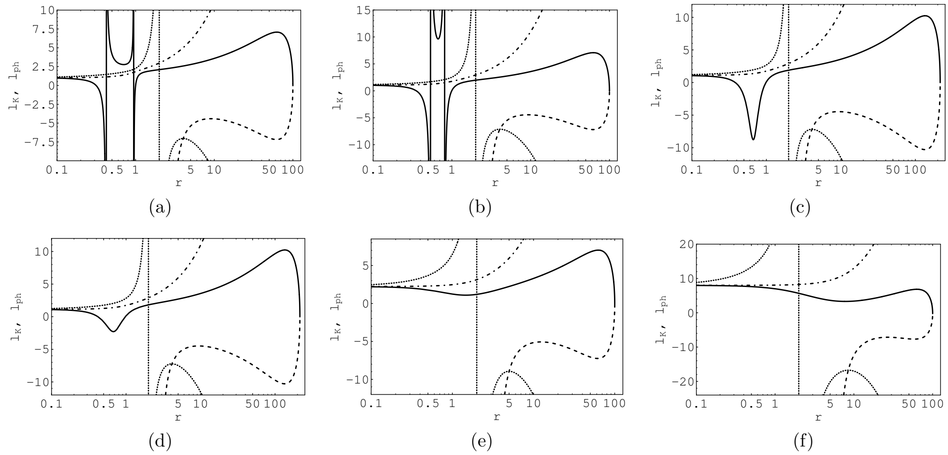

Figure 2. Keplerian specific angular momentum and the effective potential of the photon geodesic motion in some appropriately chosen Kerr–de Sitter naked-singularity spacetimes admitting stable circular geodesics of the both families. Behaviour of the functions $\ell_{K+}(r; a, y)$, $\ell_{K-}(r; a, y)$, $\ell_{ph+}(r; a, y)$ and $\ell_{ph-}(r; a, y)$ is described by the solid, dashed, dashed-dotted and dotted curves, respectively. The vertical solid and dotted straight lines correspond to the asymptotes of $\ell_{K+}(r; a, y)$ and $\ell_{ph-}(r; a, y)$, respectively. The rising (descending) part(s) of ℓ_{K+} and the descending (rising) part(s) of ℓ_{K-} correspond to the stable (unstable) orbits. The local extrema of the functions $\ell_{K\pm}$ determine the specific angular momentum of marginally stable orbits – the inner and the outer, $\ell_{ms(i)}$ and $\ell_{ms(o)}$, respectively. The local maximum of ℓ_{ph-} determines the impact parameter of the photon circular geodesic, $\ell_{ph(c)}$. (a) $y = 10^{-6}$, $a^2 = 1.05$, (b) $y = 10^{-6}$, $a^2 = 1.15$, (c) $y = 10^{-7}$, $a^2 = 1.22$, (d) $y = 10^{-7}$, $a^2 = 1.3$, (e) $y = 10^{-6}$, $a^2 = 5$, (f) $y = 10^{-6}$, $a^2 = 64$. (Taken from Slaný and Stuchlík, 2005.)

We start discussion on the equilibrium configurations of perfect fluid in the naked-singularity backgrounds with spacetimes of the class NS($\pm$) allowing stable circular orbits of the both families. The curves of Keplerian angular momentum $\ell_{K\pm}(r; a, y)$ possess two local extrema corresponding to the inner and the outer marginally stable obit $\ell_{ms(i)}$ and $\ell_{ms(o)}$, respectively; the rising parts of $\ell_{K+}(r; a, y)$ and the descending part of $\ell_{K-}(r; a, y)$ determine stable circular orbits (Fig. 2). In naked-singularity spacetimes with the rotational parameter low enough to admit stable negative-energy orbits, the curve of $\ell_{K+}(r; a, y)$ contains two points of discontinuity corresponding to the zero-energy orbits (Figs 2a,b). In naked-singularity spacetimes where the innermost stable plus-family orbits are still counterrotating but correspond to the states with $E > 0$, the local minimum of the function $\ell_{K+}(r; a, y)$ lies in negative values of ℓ (Figs 2c,d). Behaviour of the function $\ell_{K+}(r; a, y)$ in remaining naked-singularity spacetimes (Figs 2e,f), and behaviour of Keplerian angular momentum for the minus-family orbits $\ell_{K-}(r; a, y)$ is similar to their behaviour above the outer black-hole horizon in the Kerr–de Sitter black-hole spacetimes allowing stable circular orbits of given families (Stuchlík and Slaný, 2004a; Slaný and Stuchlík, 2005).

In naked-singularity spacetimes of the class NS(+) containing stable circular orbits of the plus-family only, a special subset of spacetimes with sufficiently small values of the

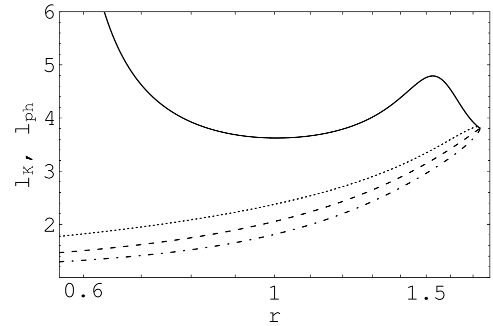

Figure 3. Keplerian specific angular momentum and the effective potential of the photon geodesic motion in the Kerr–de Sitter naked-singularity spacetime ($y = 0.061$, $a^2 = 1.24$) admitting stable circular geodesics of the plus-family with negative specific energy ($E_+ < 0$) only. Behaviour of the functions $\ell_{K+}(r; a, y)$, $\ell_{K-}(r; a, y)$, $\ell_{ph+}(r; a, y)$ and $\ell_{ph-}(r; a, y)$ is described by the solid, dashed, dashed-dotted and dotted curves, respectively. The rising part of ℓ_{K+} corresponds to the only stable circular orbits. The local extrema of the function ℓ_{K+} determine the specific angular momentum of the inner and the outer marginally stable orbit, $\ell_{ms(i)+}$ and $\ell_{ms(o)+}$, respectively. The local maximum of ℓ_{ph-} determines the impact parameter of the photon circular geodesic, $\ell_{ph(c)}$. (Taken from Slaný and Stuchlík, 2005.)

rotational parameter a and sufficiently large values of the cosmological parameter y exists, in which all stable orbits in the equatorial plane are counterrotating with negative specific energy being located between the ring singularity and the photon orbit. Corresponding behaviour of the functions $\ell_{K\pm}(r; a, y)$ and $\ell_{ph\pm}(r; a, y)$ is presented in Fig. 3.

In all of the naked-singularity spacetimes, minus-family photon circular orbits exist only,[3] corresponding to the local maximum $\ell_{ph(c)}$ of the function $\ell_{ph-}(r; a, y)$; the function $\ell_{ph+}(r; a, y)$ has no local extrema.

In most of the naked-singularity spacetimes, the necessary condition for the existence of stationary tori is the same as in the black-hole spacetimes, i.e., the specific angular momentum has to be chosen between the values of Keplerian angular momentum on the inner and the outer marginally stable orbits, $\ell \in (\ell_{ms(i)}, \ell_{ms(o)})$, of a given family, however, the exceptions exist concerning the plus-family discs in naked-singularity backgrounds with the rotational parameter low enough to admit counterrotating stable plus-family circular geodesics.

An interplay between the functions $\ell_{K\pm}(r; a, y)$ and $\ell_{ph\pm}(r; a, y)$ reveals a varied set of possible stationary disc-like configurations. First we shall consider naked-singularity spacetimes of the class NS($\pm$); this enables to cover almost all possible toroidal equilibrium configurations of perfect fluid. Next we shall consider the spacetime of the class NS($+$), in which all stable orbits are negative-energy counterrotating ones.

[3] A comprehensive analysis of the photon geodesic motion in general Kerr–Newman–de Sitter background can be found in Stuchlík and Hledík (2000).

(1) Naked-singularity spacetimes with a rotational parameter low enough to admit plus-family stable circular orbits with $E < 0$, where $\ell_{\mathrm{ms(i)+}} < \ell_{\mathrm{ms(o)+}}$ (Fig. 2a).

(i) $\ell > \ell_{\mathrm{ms(o)+}}$ Two free-particle circular orbits exist in a given disc; the inner one is unstable and the outer one is stable corresponding to the inner cusp of the equipotential surfaces and to the centre of the disc, respectively. Both the orbits are the negative-energy counterrotating ones.

(ii) $\ell_{\mathrm{ms(i)+}} < \ell < \ell_{\mathrm{ms(o)+}}$ Two pairs of circular geodesics exist, separated by a forbidden region for the occurrence of particles and fluid; boundary of the forbidden region is given by the functions $\ell_{\mathrm{ph}\pm}(r; a, y)$. The inner pair is identical with the one described in the case (1)(i). The outer pair contains the inner–stable orbit and the outer–unstable one corresponding to the centre of the second disc and to the outer cusp of the equipotential surfaces, respectively. Both the orbits are corotating.

(iii) $a < \ell < \ell_{\mathrm{ms(i)+}}$ Two corotating circular geodesics with properties identical to the second pair of the previous case (1)(ii) exist.

(iv) $\ell_{\mathrm{ms(i)-}} < \ell < a$ In a given disc, three circular geodesics exist. The innermost and the outermost ones are unstable corresponding to the inner and the outer cusp of the equipotential surfaces, respectively, the middle one is stable determining the centre of the disc. In dependence on the sign of ℓ these orbits are corotating ($\ell > 0$) or counterrotating ($\ell < 0$).

(v) $\ell_{\mathrm{ms(o)-}} < \ell_{\mathrm{ph(c)}} < \ell < \ell_{\mathrm{ms(i)-}}$ Five circular geodesics exist for the given angular momentum distribution. Counted in direction from the singularity, the second one and the fourth one are stable corresponding to two centres of the configuration, the remaining ones are unstable corresponding to the cusps. All circular geodesics counterrotate the ring singularity. In fact, the configuration consists of two counterrotating stationary tori. If $\ell_{\mathrm{ph(c)}} < \ell_{\mathrm{ms(o)-}}$, such a configuration occurs for the whole range $\ell_{\mathrm{ms(o)-}} < \ell < \ell_{\mathrm{ms(i)-}}$.

(vi) $\ell_{\mathrm{ms(o)-}} < \ell < \ell_{\mathrm{ph(c)}}$ In such a configuration, two pairs of counterrotating circular geodesics exist separated by a forbidden region for the occurrence of particles and fluid; now, the boundary of the forbidden region is given by the function $\ell_{\mathrm{ph-}}(r; a, y)$ only. This situation is similar to the case (1)(ii), however, the orbits with $E > 0$ are constituting the inner pair now. If $\ell_{\mathrm{ph(c)}} < \ell_{\mathrm{ms(o)-}}$, such a configuration does not exist.

(vii) $\ell < \ell_{\mathrm{ms(o)-}}$ This situation is identical to the case (1)(i) with one exception: the circular geodesics correspond to states with $E > 0$.

(2) Naked-singularity spacetimes with a rotational parameter low enough to admit plus-family stable circular orbits with $E < 0$, where $\ell_{\mathrm{ms(i)+}} > \ell_{\mathrm{ms(o)+}}$ (Fig. 2b). With the exception of the case (1)(ii) all the previously mentioned cases (1)(i), (1)(iii)–(1)(vii) are possible.

(3) Naked-singularity spacetimes admitting stable counterrotating plus-family orbits with $E > 0$, where $\ell_{\mathrm{ms(o)-}} < \ell_{\mathrm{ms(i)+}} < \ell_{\mathrm{ms(i)-}}$ (Fig. 2c). From the cases mentioned above, only the cases (1)(iii)–(1)(vi) are possible here and, in addition, two new ones arise:

(i) $\ell_{\mathrm{ms(o)-}} < \ell < \ell_{\mathrm{ms(i)+}} < \ell_{\mathrm{ph(c)}}$ Two circular geodesics exist in a given disc; the inner one is stable and the outer one is unstable corresponding to the centre of the disc and to the outer cusp of the equipotential surfaces, respectively. Both the orbits are the counterrotating ones and the disc is separated from the ring singularity by the forbidden region for the occurrence of matter determined by the photon potential.

(ii) $\ell_{\mathrm{ms(o)}-} < \ell_{\mathrm{ph(c)}} < \ell < \ell_{\mathrm{ms(i)}+}$ In a given disc, three circular geodesics exist. The innermost and the outermost ones are unstable corresponding to the inner and the outer cusps of the equipotential surfaces, respectively, the middle one is stable determining the centre of the disc. All the orbits are the counterrotating ones. The same situation occurs when $\ell_{\mathrm{ph(c)}} < \ell_{\mathrm{ms(o)}-} < \ell < \ell_{\mathrm{ms(i)}+}$.

(4) Naked-singularity spacetimes admitting stable counterrotating plus-family orbits with $E > 0$, where $\ell_{\mathrm{ms(i)}-} < \ell_{\mathrm{ms(i)}+} < 0$ (Fig. 2d). The cases (1)(iii), (1)(iv), (3)(i), (3)(ii) could occur in such a spacetime. Moreover, if $\ell_{\mathrm{ph(c)}} < \ell_{\mathrm{ms(o)}-}$ the case (3)(i) is impossible.

(5) Naked-singularity spacetimes admitting corotating stable plus-family orbits[4] where $\ell_{\mathrm{ms(o)}+} > a$ (Fig. 2e). The same situation as in (4) with one exception: the case (1)(iv) can be the corotating only.

(6) Naked-singularity spacetimes where $\ell_{\mathrm{ms(o)}+} < a$ (Fig. 2f). Just two possibilities, the corotating one (1)(iv) and its counterrotating analogy (3)(ii), could occur in such a spacetime.

(7) naked-singularity spacetimes of the class NS(+), in which all stable orbits are counterrotating with $E < 0$ (Fig. 3).

(i) $\ell_{\mathrm{ms(i)}+} < \ell_{\mathrm{ph(c)}} < \ell < \ell_{\mathrm{ms(o)}+}$ The situation is similar to the case (1)(iv) but all three geodetical orbits are counterrotating only.

(ii) $\ell_{\mathrm{ms(i)}+} < \ell < \ell_{\mathrm{ph(c)}}$ The situation is similar to the case (1)(i). If $\ell_{\mathrm{ph(c)}} < \ell_{\mathrm{ms(i)}+}$, such a configuration does not exist.

The presented analysis gives some insight into the behaviour of the potential $W(r,\theta)$ in the naked-singularity backgrounds. In effort to cover up all the possible toroidal configurations, we present in Fig. 4, where the Kerr–Schild coordinate x instead of the Boyer–Lindquist coordinate r is used[5], the behaviour of the function $W(r, \theta = \pi/2)$ in appropriately chosen spacetimes (each of them has been already discussed in terms of behaviour of the Keplerian angular momentum, see Figs 2 and 3) and only for the values of specific angular momentum ℓ enabling the existence of stationary discs. The local maxima correspond to the cusps of the equipotential surfaces and the local minima correspond to the centres of the discs. We can see that both the accretion discs (Figs 4a,d,e,j,k,m,p,q,s) and the excretion ones (Figs 4c,f,l,o,r) could exist in naked-singularity backgrounds too. Moreover, some naked-singularity backgrounds admit the configurations with two discs (Figs 4b,g–i,n). The inner disc is always a counterrotating accretion disc but the outer accretion or excretion disc is corotating in some cases, and counterrotating in the other cases. Region between the discs either contains the forbidden region for the occurrence of the fluid given by the photon potential through the relation $\ell = \ell_{\mathrm{ph}\pm}$ (Figs 4b,n), or can be filled by an accretion flow from the outer accretion disc (Figs 4g,h), or corresponds to a non-stationary outer part of the inner accretion disc (Fig. 4i). In the cases where both the accretion and the excretion discs are possible, a limiting value of the parameter ℓ separating the accretion

---

[4] The counterrotating ones belong to the minus-family only.

[5] Relation between the Boyer–Lindquist coordinates r, θ and the Kerr–Schild coordinates x, y, z is given through the expressions: $x^2 + y^2 = (r^2 + a^2)\sin^2\theta$, $z = r\cos\theta$ indicating that in the equatorial plane ($\theta = \pi/2$) and for $y = 0$ the Kerr–Schild coordinate $x = \pm(r^2 + a^2)^{1/2}$.

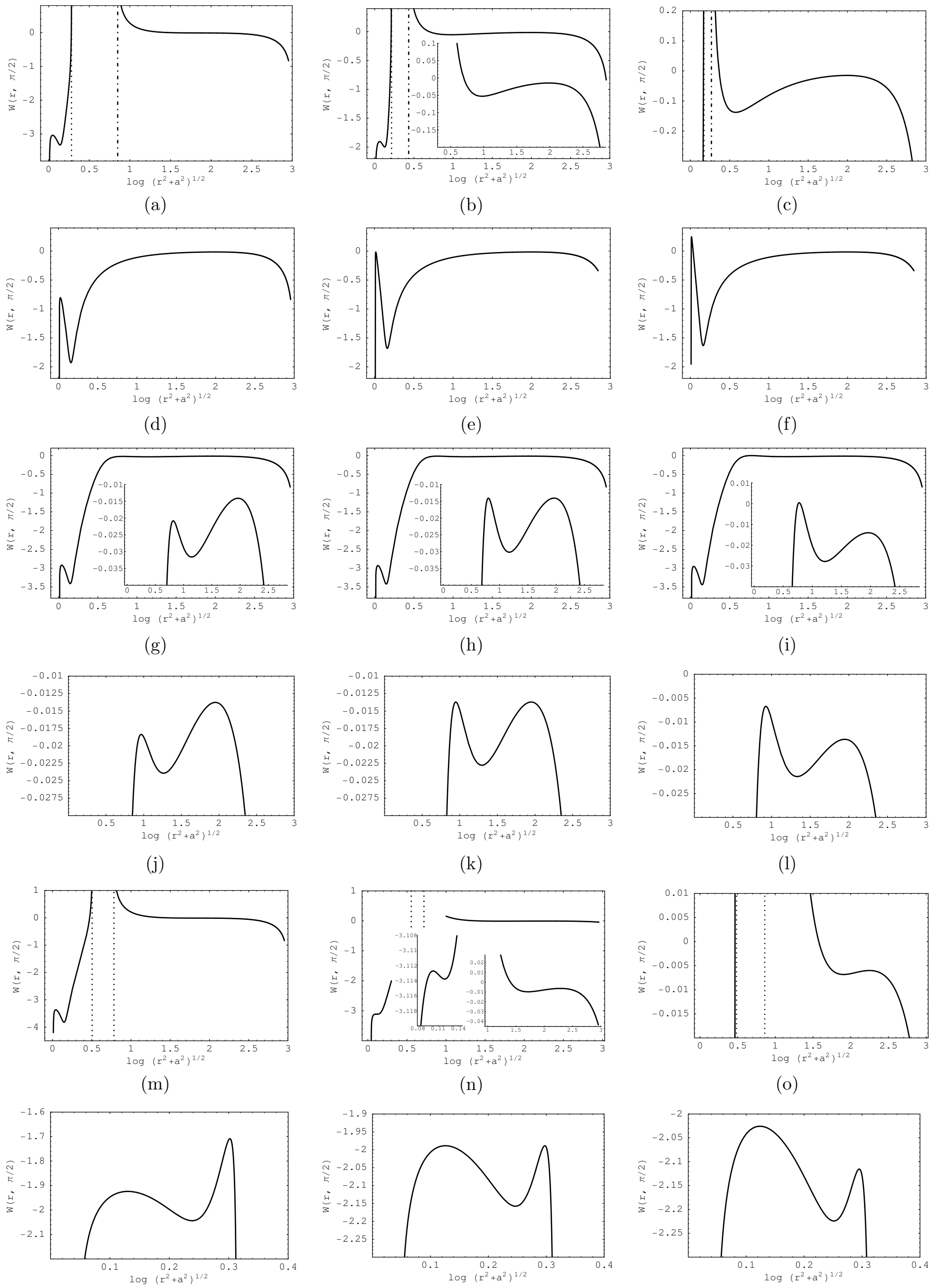

(a) (b) (c)
(d) (e) (f)
(g) (h) (i)
(j) (k) (l)
(m) (n) (o)
(p) (q) (r)

Continued on the next page.

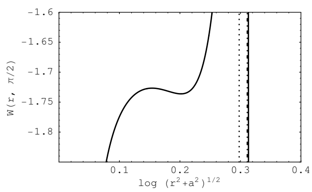

(s)

Figure 4. Behaviour of the potential $W(r, \theta = \pi/2)$ in the appropriately chosen Kerr–de Sitter naked-singularity backgrounds. The values of constant specific angular momentum ℓ were chosen to cover up all the possible disc-like configurations in naked-singularity backgrounds and are referred to the discussion presented above. A region in between the non-solid vertical lines, determined by the conditions $\ell = \ell_{\mathrm{ph}+}(r; a, y)$ (dashed-dotted lines) and $\ell = \ell_{\mathrm{ph}-}(r; a, y)$ (dotted lines), is the "forbidden region." (a) $y = 10^{-6}$, $a^2 = 1.05$, $\ell = 8$; $\ell \in$ (1)(i) case. (b) $y = 10^{-6}$, $a^2 = 1.05$, $\ell = 3.5$; $\ell \in$ (1)(ii) case. (c) $y = 10^{-6}$, $a^2 = 1.05$, $\ell = 2.5$; $\ell \in$ (1)(iii) case. (d) $y = 10^{-6}$, $a^2 = 1.05$, $\ell = 0.5$; $\ell \in$ (1)(iv) case, $\ell < \ell_{\mathrm{mb}+}$. (e) $y = 10^{-6}$, $a^2 = 1.05$, $\ell \doteq 0.84193$; $\ell \in$ (1)(iv) case, $\ell = \ell_{\mathrm{mb}+}$. (f) $y = 10^{-6}$, $a^2 = 1.05$, $\ell = 0.9$; $\ell \in$ (1)(iv) case, $\ell > \ell_{\mathrm{mb}+}$. (g) $y = 10^{-6}$, $a^2 = 1.05$, $\ell = -4.65$; $\ell \in$ (1)(v) case, $\ell > \ell_{\mathrm{mb}-}$. (h) $y = 10^{-6}$, $a^2 = 1.05$, $\ell \doteq -4.71940$; $\ell \in$ (1)(v) case, $\ell = \ell_{\mathrm{mb}-}$. (i) $y = 10^{-6}$, $a^2 = 1.05$, $\ell = -4.85$; $\ell \in$ (1)(v) case, $\ell < \ell_{\mathrm{mb}-}$. (j) $y = 10^{-6}$, $a^2 = 5$, $\ell = -5.3$; $\ell \in$ (3)(ii) case, $\ell > \ell_{\mathrm{mb}-}$. (k) $y = 10^{-6}$, $a^2 = 5$, $\ell \doteq -5.38545$; $\ell \in$ (3)(ii) case, $\ell = \ell_{\mathrm{mb}-}$. (l) $y = 10^{-6}$, $a^2 = 5$, $\ell = -5.5$; $\ell \in$ (3)(ii) case, $\ell < \ell_{\mathrm{mb}-}$. (m) $y = 10^{-6}$, $a^2 = 1.05$, $\ell = -8$; $\ell \in$ (1)(vii) case. (n) $y = 10^{-7}$, $a^2 = 1.22$, $\ell = -7.5$; $\ell \in$ (1)(vi) case. (o) $y = 10^{-7}$, $a^2 = 1.22$, $\ell = -9$; $\ell \in$ (3)(i) case. (p) $y = 0.061$, $a^2 = 1.24$, $\ell = 4.1$; $\ell \in$ (7)(i) case, $\ell < \ell_{\mathrm{mb}+}$. (q) $y = 0.061$, $a^2 = 1.24$, $\ell \doteq 4.25561$; $\ell \in$ (7)(i) case, $\ell = \ell_{\mathrm{mb}+}$. (r) $y = 0.061$, $a^2 = 1.24$, $\ell = 4.35$; $\ell \in$ (7)(i) case, $\ell > \ell_{\mathrm{mb}+}$. (s) $y = 0.061$, $a^2 = 1.24$, $\ell = 3.7$; $\ell \in$ (7)(ii) case. (Taken from Slaný and Stuchlík, 2005.)

discs from the excretion ones corresponds to the specific angular momentum of a particle on the marginally bound circular geodesic, ℓ_{mb}.

Meridional sections through the equipotential surfaces of the equilibrium configurations just mentioned are depicted in Fig. 5. Like in the black-hole backgrounds, the boundary of the shaded regions (corresponding to stationary discs) is formed by the critical closed equipotential surface self-crossing in the cusp(s).

The case **(a)** corresponds to the counterrotating accretion disc with well-defined inner edge on the position of the inner cusp; the equipotential surface with the outer cusp does not exist. Specific energy of the fluid elements in the centre and on the inner edge (where the fluid follows the geodesic motion) is negative and we can expect that every fluid element in the disc has energy $E < 0$. Moreover, no open equipotential surface going out from the singularity and corresponding to the outflow of matter in the form of "jets" is connected with such a configuration.

The case **(b)** contains two discs; the inner one is the counterrotating negative-energy accretion disc with the critical equipotential surface self-crossing in the inner cusp and the outer one corresponds to the corotating excretion disc with the critical equipotential surface self-crossing in the outer cusp. Region between the discs is the "forbidden region" and no matter can escape from the inner disc to form "jets," as seen from the behaviour of the equipotential surfaces.

The case **(c)** corresponds to the corotating excretion disc with the critical equipotential surface self-crossing in the outer cusp. The structure of the open equipotential surfaces together with the existence of the "forbidden region" near the ring singularity disables the possibility of infall of matter from the disc onto the singularity.

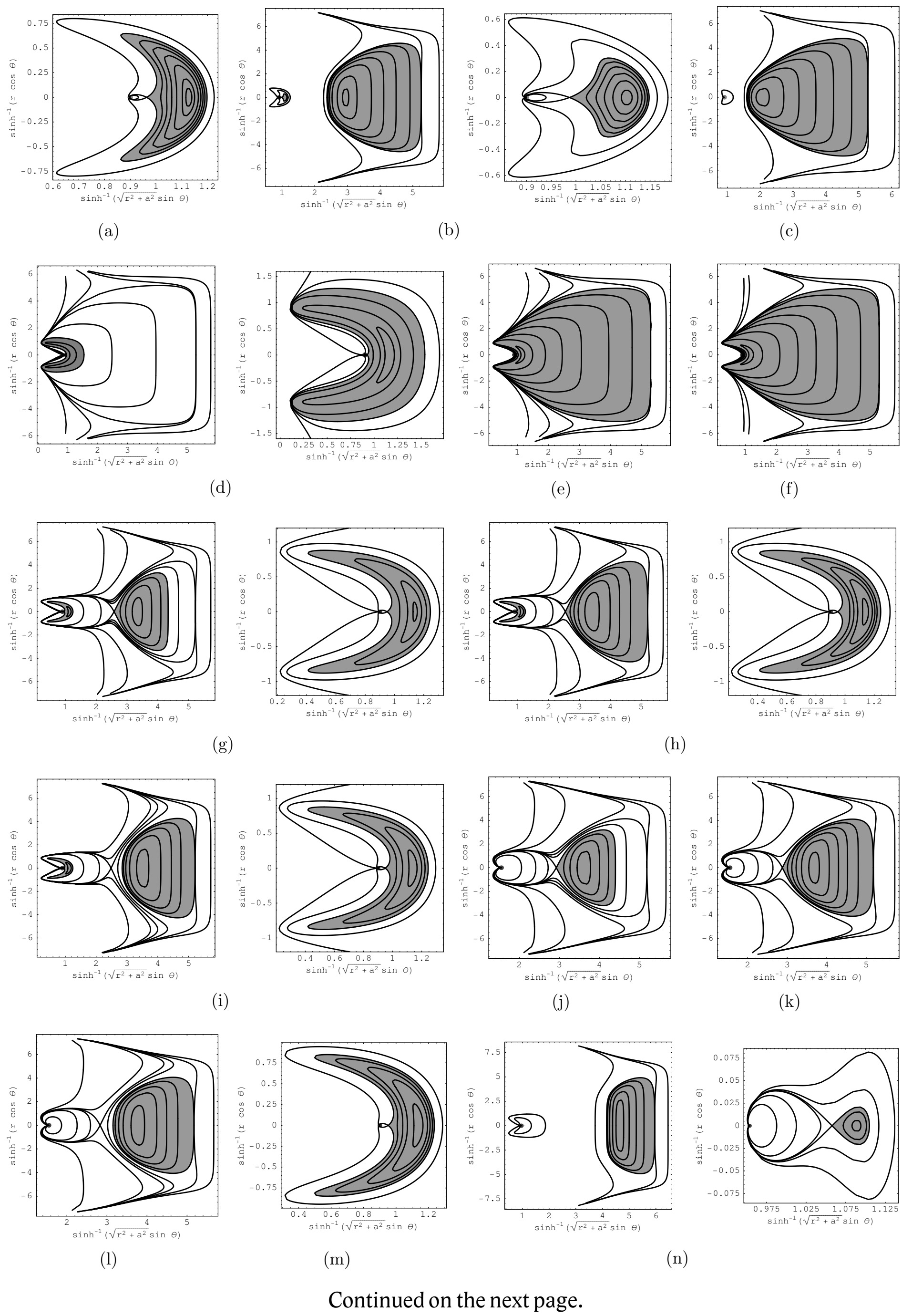

Continued on the next page.

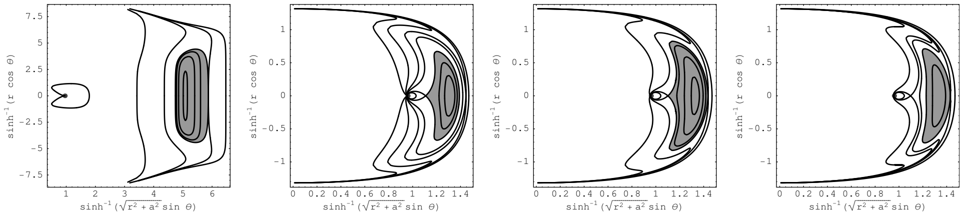

(o) (p) (q) (r)

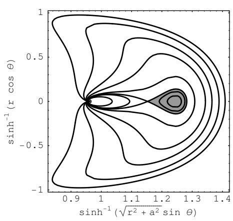

(s)

Figure 5. Equipotential surfaces (meridional sections) for the cases described in Fig. 4. Shaded regions containing closed equipotential surfaces correspond to the possible toroidal configurations; the last closed surface (critical surface) is self-crossing in the cusp(s) which naturally determines the edge(s) of a disc. The Kerr–Schild coordinates together with the scale of axes were chosen to show clearly the whole range of a disc including the ring singularity (the gray point on the left in the equatorial plane) as well as the region near the static radius. In the cases (b), (d), (g)–(i) and (n), the inner region near the ring singularity is enlarged in the right figure. A detailed discussion of depicted stationary configurations is presented in the text. (Taken from Slaný and Stuchlík, 2005.)

Cases **(d)–(f)** correspond to the configurations well-known from the black-hole backgrounds.

The case **(d)** represents the corotating accretion disc where the last closed equipotential surface is self-crossing in the inner cusp. There is another critical surface self-crossing in the outer cusp, but this surface is open. The fluid between the critical surfaces is not in hydrostatic equilibrium and falls directly onto the singularity.

The case **(e)** corresponds to the corotating marginally bound accretion disc. The critical equipotential surface contains two cusps; the inner/outer cusp determines the inner/outer edge of the disc and the outflows of matter through the outer cusp as well as the infalls through the inner cusp caused by a violation of hydrostatic equilibrium are possible.

The case **(f)** corresponds to the corotating excretion disc since the last closed equipotential surface contains the outer cusp in which the surface becomes open. The critical surface with the inner cusp is open and the region between the critical surfaces is filled up by other open surfaces disabling, in fact, accretion of matter onto the singularity.

Cases **(g)–(i)** contain two counterrotating discs and the region between them is not forbidden for the occurrence of matter. The inner disc is always the accretion disc with the inner cusp only; the critical equipotential surface is marginally closed and self-crossing in this cusp.

In the case **(g)**, the outer disc is the accretion disc as the marginally closed critical surface with the inner cusp is present, but the open critical surface with the outer cusp also exists. The matter from the outer disc as well as from the region between the critical surfaces can flow through the inner cusp (after overfilling the critical surface) and a throat formed by open equipotential surfaces onto the singularity. If some sufficiently strong dissipative processes are present during such infall, the matter could fill the inner accretion disc.

In the case **(h)**, the outer disc is the marginally bound accretion disc where the boundary is given by the critical surface with two cusps and the outflow of matter through the both cusps is equally probable. Again, if the dissipative processes, present in the accretion flow, efficiently drain the energy from the accreting matter, it could feed the inner accretion disc instead of a direct infall through the throat onto the singularity.

In the case **(i)**, the outer disc is the excretion disc and the outflow through the outer cusp of the last closed (critical) surface is only possible. The critical equipotential surface with the inner cusp is open and the region between the critical surfaces contains open surfaces only.

Cases **(j)–(l)** represent the counterrotating analogy of the cases (d)–(f), the case (m) is the plus-energy analogy of the case (a) and the cases (n), (o) are the fully counterrotating analogy of the cases (b), (c), respectively.

Cases **(p)–(s)** have some common properties with the case (a), especially that the matter following geodetical motion at the centre and in the cusp(s) of the potential possesses negative energy (and we can expect that every fluid element in the disc has energy $E < 0$) and that the configuration is imprisoned by a photon shell around the singularity. As a consequence, no open equipotential surfaces corresponding to “jets” of matter from the configuration into the outer space exist.

The case **(p)** corresponds to the counterrotating negative-energy accretion disc since the last closed surface is self-crossing in the inner cusp. Another critical surface self-crossing in the outer cusp is open.

The case **(q)** corresponds to the counterrotating negative-energy marginally bound accretion disc since the last closed surface is self-crossing in both the cusps.

The case **(r)** corresponds to the counterrotating negative-energy excretion disc; the last closed surface is self-crossing in the outer cusp. Another critical surface self-crossing in the inner cusp is open and there is no possibility for accretion onto the singularity.

The case **(s)** is very similar to the case (a), and also corresponds to the counterrotating negative-energy accretion disc, since there is only one critical surface which is, moreover, marginally closed and self-crossing in the inner cusp.

5 CONCLUDING REMARKS

Influence of a repulsive cosmological constant, or equivalently a vacuum/dark energy, on the structure of toroidal configurations of test perfect fluid orbiting the Kerr–de Sitter naked singularities allowing, at least, stable circular orbits of the plus-family ($0 < y < y_{\mathrm{c(ms+)}} \doteq 0.06886$) can be summarized in the following way. In naked-singularity backgrounds with the rotational parameter $a^2 > a^2_{\mathrm{cL}} \doteq 2.4406$, or even for $a^2 > 27/16 \doteq 1.6875$ (corresponding to the Kerr limit, Stuchlík, 1980), if the cosmological parameter y is not very large, typically $y < 10^{-4}$, the situation is similar to those in the black-hole backgrounds (Stuchlík and Slaný, 2004a; Slaný and Stuchlík, 2005):

(1) Stationary tori exist for the range of specific angular momentum ℓ between the values corresponding to the specific angular momenta of the inner and the outer marginally stable circular orbit, $\ell \in (\ell_{\mathrm{ms(i)}}, \ell_{\mathrm{ms(o)}})$, as such values of ℓ enable the existence of closed

equipotential surfaces. Moreover, the equipotential surface with the outer cusp always exists.

(2) For $\ell \in (\ell_{\mathrm{ms(i)}}, \ell_{\mathrm{mb}})$, where ℓ_{mb} denotes the specific angular momentum of marginally bound circular orbit, the last closed surface is self-crossing in the inner cusp and the configuration corresponds to the accretion disc. Equipotential surface with the outer cusp is open and matter from the region between the critical surfaces contributes to the accretion flow along the inner cusp. When the critical surface with the outer cusp is overfilled, an outflow of matter through the outer cusp begins to complement the accretion inflow, having a capability to regulate the accretion.

(3) For $\ell \in (\ell_{\mathrm{mb}}, \ell_{\mathrm{ms(o)}})$, the last closed surface is self-crossing in the outer cusp and the configuration corresponds to the excretion disc. The equipotential surface with the inner cusp, if such a surface exists, is open and separated from the critical surface with the outer cusp by additional open surfaces which, in fact, disable accretion onto the naked singularity.

(4) For $\ell = \ell_{\mathrm{mb}}$, the last closed surface is self-crossing in both cusps and the configuration corresponds to the marginally bound accretion disc.

In naked-singularity backgrounds with the rotational parameter low enough, especially for $a^2 < a^2_{\mathrm{cE}} \doteq 1.47$, and typically for $a^2 < 32/27 \doteq 1.1852$ (corresponding to the Kerr limit (Stuchlík, 1980) which holds sufficiently well for $y < 10^{-4}$), exceptions and additional possibilities exist:

(1) If $\ell_{\mathrm{ms(i)+}} < \ell_{\mathrm{ms(o)+}}$, stationary discs exist for an arbitrary value of the specific angular momentum ℓ. Spacetimes where $\ell_{\mathrm{ms(i)+}} > \ell_{\mathrm{ms(o)+}}$ admit no stationary discs for the specific angular momentum ℓ satisfying the relation $\ell_{\mathrm{ms(i)+}} > \ell > \ell_{\mathrm{ms(o)+}}$. For the remaining values of ℓ, the stationary configurations always exist.

(2) Moreover, for $\ell > \ell_{\mathrm{ms(o)+}} > \ell_{\mathrm{ms(i)+}}$ or $\ell > \ell_{\mathrm{ms(i)+}} > \ell_{\mathrm{ms(o)+}}$, the configuration corresponds to the counterrotating accretion disc with matter in states with $E < 0$. The disc is isolated from the outer space by the region without any equipotential surfaces. Consequently, no open equipotentials describing the jets are present. The inner parts including the ring singularity are screened by the disc itself. For $\ell < \ell_{\mathrm{ms(o)-}} < \ell_{\mathrm{ph(c)}}$ or $\ell < \ell_{\mathrm{ph(c)}} < \ell_{\mathrm{ms(o)-}}$, the configuration corresponds to a counterrotating accretion disc with matter in states with $E > 0$.

(3) In the part of naked-singularity spacetimes of the class NS(+) with sufficiently large values of the cosmological parameter y (very close to $y_{\mathrm{c(ms+)}}$), in which all stable plus-family circular orbits are counterrotating with negative specific energy, the stationary tori exist for $\ell \in (\ell_{\mathrm{ms(i)+}}, \ell_{\mathrm{ms(o)+}})$. Together with closed equipotential surfaces the equipotential surface with the inner cusp always exists. We can expect that all fluid elements in the torus have negative energy ($E < 0$). For $\ell_{\mathrm{ms(i)+}} < \ell < \ell_{\mathrm{mb+}}$ the configuration corresponds to the counterrotating negative-energy accretion disc, for $\ell_{\mathrm{mb+}} < \ell < \ell_{\mathrm{ms(o)+}}$ the configuration corresponds to the counterrotating negative-energy excretion disc, and for $\ell = \ell_{\mathrm{mb+}}$ the configuration corresponds to the counterrotating negative-energy marginally bound accretion disc with both accretion and excretion outflows from the torus. Since the outer marginally bound circular orbit in the equatorial plane is located under the photon circular orbit, $r_{\mathrm{mb(o)+}} < r_{\mathrm{ph(c)}}$, the whole torus is cut off from the outer space by the photon shell.

(4) Special values of the specific angular momentum $\ell = \text{const}$ can lead to stationary configurations with two discs. The inner one is always the counterrotating accretion disc (for $\ell_{\text{ms(o)}+} > \ell > \ell_{\text{ms(i)}+} > a$ matter in the disc is in the states with $E < 0$; otherwise the matter is in the states with $E > 0$), but the outer disc can be, in dependence on the value of ℓ, the corotating or the counterrotating excretion disc, as well as the counterrotating accretion disc. The region between the discs can be a region forbidden for matter, if $\ell = \text{const}$ has common points with any of the functions $\ell_{\text{ph}\pm}(r; a, y)$. However, in the case of two counterrotating accretion discs, the region between the discs is filled by the matter falling from the outer disc through its inner cusp onto the ring singularity. If, in addition, some efficient dissipative processes are present in the accretion flow from the outer disc, the matter could fill the inner accretion disc, rather than to be directly falling onto the ring singularity. If the inner accretion disc has already been created, it could shield the ring singularity from direct infall of accreting material coming from the outer disc.

(5) The potential difference between the boundary and the centre of the torus, $\Delta W = W_{\text{crit}} - W_{\text{center}}$, grows unlimitedly, $\Delta W \to \infty$, for the plus-family marginally bound accretion discs orbiting a naked singularity approaching the extreme-hole state, independently of the cosmological parameter $y < y_{\text{c(KdS)}}$.

ACKNOWLEDGEMENTS

The present work has been supported by Czech Grants GAČR 205/03/1147 and MSM 4781305903.

REFERENCES

Abramowicz, M. A. (1998), Physics of black hole accretion, in M. A. Abramowicz, G. Björnsson and J. E. Pringle, editors, *Theory of Black Hole Accretion Disks*, pp. 50–60, Cambridge University Press, Cambridge.

Abramowicz, M. A., Calvani, M. and Nobili, L. (1980), *Astrophys. J.*, **242**, p. 772.

Abramowicz, M. A., Calvani, M. and Nobili, L. (1983), Runaway instability in accretion disks orbiting black holes, *Nature*, **302**, p. 597.

Abramowicz, M. A., Jaroszyński, M. and Sikora, M. (1978), Relativistic accreting disks, *Astronomy and Astrophysics*, **63**(1–2), pp. 221–224, URL `http://adsabs.harvard.edu/journals_service.html`.

Bahcall, N., Ostriker, J. P., Perlmutter, S. and Steinhardt, P. J. (1999), The cosmic triangle: Revealing the state of the universe, *Science*, **284**, pp. 1481–1488.

Boyer, R. H. (1965), *Proc. Cambridge Phil. Soc.*, **61**, p. 527.

de Felice, F. and Yunqiang, Y. (2001), Turning a black hole into a naked singularity, *Classical Quantum Gravity*, **18**, pp. 1235–1244.

Hledík, S. and Stuchlík, Z., editors (2004), *Proceedings of RAGtime 4/5: Workshops on black holes and neutron stars, Opava, 14–16/13–15 October 2002/2003*, Silesian University in Opava, Opava, ISBN 80-7248-242-4.

Jaroszyński, M., Abramowicz, M. A. and Paczyński, B. (1980), Supercritical accretion disks around black holes, *Acta Astronom.*, **30**, pp. 1–34.

Kolb, E. W. and Turner, M. S. (1990), *The Early Universe*, Addison-Wesley, Redwood City, California, ISBN 0-201-11603-0, the Advanced Book Program.

Kozłowski, M., Jaroszyński, M. and Abramowicz, M. A. (1978), The analytic theory of fluid disks orbiting the Kerr black hole, *Astronomy and Astrophysics*, **63**(1–2), pp. 209–220, URL `http://adsabs.harvard.edu/article_service.html`.

Nishida, S., Lanza, A., Eriguchi, Y. and Abramowicz, M. A. (1997), *Monthly Notices Roy. Astronom. Soc.*, **278**, p. L41.

Novikov, I. D. and Thorne, K. S. (1973), Black hole astrophysics, in C. D. Witt and B. S. D. Witt, editors, *Black Holes*, p. 343, Gordon and Breach, New York–London–Paris.

Penrose, R. (1969), Gravitational collapse: The role of general relativity, *Nuovo Cimento B*, **1**(special number), pp. 252–276.

Rezzolla, L. (2004), Nonlinear dynamics of thick discs in Schwarzschild–de Sitter spacetimes, in Hledík and Stuchlík (2004), pp. 151–165.

Rezzolla, L., Zanotti, O. and Font, J. A. (2003), Dynamics of thick discs around Schwarzschild-de Sitter black holes, *Astronomy and Astrophysics*, **412**, p. 603.

Seguin, F. H. (1975), *Astrophys. J.*, **197**, p. 745.

Slaný, P. and Stuchlík, Z. (2005), Relativistic thick discs in the Kerr–de Sitter backgrounds, *Classical Quantum Gravity*, **22**, pp. 3623–3651.

Spergel, D. N., Verde, L., Peiris, H. V., Komatsu, E., Nolta, M. R., Bennett, C. L. et al. (2003), First Year Wilkinson Microwave Anisotropy Probe (WMAP) Observations: Determination of Cosmological Parameters, *Astrophys. J. Suppl.*, **148**, p. 175.

Stuchlík, Z. (1980), Equatorial circular orbits and the motion of the shell of dust in the field of a rotating naked singularity, *Bull. Astronom. Inst. Czechoslovakia*, **31**(3), pp. 129–144.

Stuchlík, Z. (2005), Influence of the Relict Cosmological Constant on Accretion Discs, *Modern Phys. Lett. A*, **20**(8), pp. 561–575.

Stuchlík, Z. and Hledík, S. (1999), Some properties of the Schwarzschild–de Sitter and Schwarzschild–anti-de Sitter spacetimes, *Phys. Rev. D*, **60**(4), p. 044006 (15 pages), URL `http://ojps.aip.org/journal_cgi/dbt?KEY=PRVDAQ&Volume=60&Issu%e=4`.

Stuchlík, Z. and Hledík, S. (2000), Equatorial photon motion in the Kerr–Newman spacetimes with a non-zero cosmological constant, *Classical Quantum Gravity*, **17**(21), pp. 4541–4576, ISSN 0264-9381/00, URL `http://www.iop.org/EJ/S/UNREG/1NOryEzmtf2ZMVyFDaUGbw/toc/0264%-9381/17/21`.

Stuchlík, Z. and Slaný, P. (2004a), Accretion discs in the Kerr–de Sitter spacetimes, in Hledík and Stuchlík (2004), pp. 205–237.

Stuchlík, Z. and Slaný, P. (2004b), Equatorial circular orbits in the Kerr–de Sitter spacetimes, *Phys. Rev. D*, **69**, p. 064001, ISSN 1094-1622, `gr-qc/0307049`.

Stuchlík, Z., Slaný, P. and Hledík, S. (2000), Equilibrium configurations of perfect fluid orbiting Schwarzschild–de Sitter black holes, *Astronomy and Astrophysics*, **363**(2), pp. 425–439, ISSN 0004-6361 (printed version), 1432-0746 (parallel-to-print version), URL `http://link.springer.de/link/service/journals/00230/tocs/t036%3002.htm`.

Török, G. (2005a), A possible 3 : 2 orbital epicyclic resonance in QPO frequencies of Sgr A*, *Astronomy and Astrophysics*, **440**(1), pp. 1–4.

Török, G. (2005b), QPOs in microquasars and Sgr A*: measuring the black hole spin, *Astronom. Nachr.*, **326**(9), pp. 856–860, `astro-ph/0510669`.

Wilson, D. B. (1984), *Nature*, **312**, p. 620.

Proceedings of *RAGtime 6/7: Workshops on black holes and neutron stars, Opava, 16–18/18–20 September, 2004/2005*
S. Hledík and Z. Stuchlík, editors, Silesian University in Opava, Czech Republic, 2005, pp. 189–208

Excitation of oscillations by a small inhomogeneity on the surface of a neutron star

Zdeněk Stuchlík and Stanislav Hledík

Institute of Physics, Faculty of Philosophy & Science, Silesian University in Opava, Bezručovo nám. 13, CZ-746 01 Opava, Czech Republic

ABSTRACT

Properties of the gravitational perturbation force caused by a small inhomogeneity located on the surface of a neutron star are studied. The oscillating perturbation force in both the accretion disc rotating around the star and in the interior of a differentially rotating star is determined. Both vertical and radial components of the force are given and their relations are discussed. The frequency of the oscillations is given by the difference of the frequency of the rotation of the star surface, and the orbital frequency in the disc (the frequency of rotation of matter in the star interior). Outside the star, in the disc, the vertical and radial forces vary with the same phase. Inside a differentially rotating star, the variations of the forces are in the opposite phase in an internal part of the star, while they are in the same phase in an external layer of the star. In an intermediate part of the star, an additional oscillatory change appears. Is is shown that the anharmonic character of the oscillatory forces is limited to the seventh non-negligible harmonics. For completeness, we present the perturbation force generated by a symmetric accretion column.

1 INTRODUCTION

Quasiperiodic oscillations (QPOs) of X-ray brightness have been observed in a number of binary systems containing neutron stars (see van der Klis, 2000 for a review) and black holes (McClintock and Remillard, 2004). In the QPOs the spectrum often shows twin peaks with frequencies correlated to the X-ray intensity. The ratio of the twin peak frequencies observed in black-hole systems is exactly, or almost exactly 3 : 2 (Abramowicz et al., 2004b), while in the neutron star systems the ratio is concentrated around 3 : 2 within an interval much wider than in the black-hole systems, and even some anticorrelation effect between sources has been recognized quite recently by Abramowicz et al. (2005b). Therefore, the resonant oscillatory model (Abramowicz and Kluźniak, 2001) seems to be the most promising in explaining QPOs in both black-hole and neutron star binary systems (Abramowicz and Kluźniak, 2004) and even in Sgr A* (Török, 2005a,b). A simultaneous occurrence of the resonant phenomena (parametric and forced) at different radii of the accretion disc enables, in some special cases, exact prediction of the black hole spin due to the corresponding triples of observed frequencies with special rational ratios (Stuchlík and Török, 2005). However, some other possibilities, as the warped disc oscillations (Kato and Fukue, 1980;

80-7248-334-X

Kato, 2004b,a) or simple p-mode oscillations of fluid tori (Rezzolla, 2004) still cannot be excluded.

It was shown that both the parametric resonance and forced resonance with beat (combinational) frequencies between vertical and radial disc oscillations at the epicyclic frequencies can well explain the observed data for all of the microquasars with twin peak QPOs that were considered so far (Török et al., 2005; Török and Stuchlík, 2005); moreover, the parametric resonance predictions for the values of the black hole spin and its relation to the frequency-mass dependence are in a good agreement with the observational best-fit line (McClintock and Remillard, 2004; Abramowicz et al., 2004a). The parametric resonance has been treated in a non-linear regime using multi-scale approach (Horák et al., 2004; Horák, 2004). The relation between the magnitude and frequency ratio has been derived in this approach which could be a good starting point for explaining the anticorrelation effect observed in the case of QPOs in neutron star binary systems (Abramowicz et al., 2005b,a).

In order to start up the oscillations and the resonance phenomena, it is necessary to fulfil some initial conditions. The conditions should be of both internal and external origin, and, usually, one could expect an interplay of both internal and external "ignition" mechanisms. The external mechanism for excitation of the oscillations could come from the gravitational perturbation force caused by a "mountain" on the surface of the neutron star. We shall consider influence of such a mountain in an accretion disc orbiting the neutron star in its equatorial plane. For completeness, behaviour of the perturbational force of the mountain will be determined also in the interior of the star – for simplicity we focus our attention to the forces acting in the equatorial plane, again. Such a study could be interesting in connection to generation of the oscillation modes and gravitational waves in the interior of a differentially rotating neutron star.

The frequency of the force caused by the gravitational surface perturbation of a homogeneous neutron star is given by the difference of the orbital frequency of the disc and the neutron star surface (Petri, 2005). In the interior of the neutron star, the force can be relevant, if the star is rotating differentially. Then, basically, the frequency of the perturbing force is given by the difference of the frequencies in the surface of the star and in its interior, but some additional frequencies could arise inside the star, as we shall see. In Section 2, we determine both the vertical and radial component of the gravitational force given by an isolated "mountain" located on the surface of the neutron star and acting at a given radius of the accretion disc rotating around the neutron star or inside the differentially rotating neutron star, while in Section 3, analogous formulae for the symmetric accretion column are derived. Concluding remarks are presented in Section 4. For simplicity, we use here purely Newtonian approach in treating the gravitational perturbation force.

2 GRAVITATIONAL FORCE OF AN ISOLATED MOUNTAIN

In order to obtain an intuitional understanding of the possible external excitation mechanisms of the accretion discs oscillations, we determine both the vertical and radial component of the gravitational force generated by an isolated mountain on the surface of a neutron star, acting at a given radius of the accretion disc rotating around the neutron star. Further, we shall determine the oscillatory parts of the force.

We assume a homogenous and isotropic neutron star of mass M_{A} and radius R_{A} rotating around its rotation axis with angular velocity Ω_{A}, with the symmetry plane of the accretion disc being located at the plane orthogonal to the rotation axis, as can be expected up to radii $R \sim 10^3\, R_{\mathrm{A}}$ because of the Bardeen–Petterson effect (Bardeen and Petterson, 1975).

A mountain generating the anisotropic gravitational perturbative force is assumed to be a point-like source of mass m, located on the surface of the star at a position determined by the latitudinal angle θ_{A}.

We use the spherical coordinates (R, θ, φ), the origin of the coordinate system coincides with the centre of the neutron star. The angular velocity profile of the accretion disc is denoted by $\Omega_{\mathrm{d}}(r)$. In the case of thin (or slim) discs, the profile is Keplerian, i.e., $\Omega_{\mathrm{d}}(r) = \Omega_{\mathrm{K}}(r)$ (Novikov and Thorne, 1973; Abramowicz et al., 1992). For thick discs, the angular velocity profile is determined by the distribution of the specific angular momentum (Kozłowski et al., 1978; Jaroszyński et al., 1980). The angular velocity inside the star is assumed in a general form $\Omega_{\mathrm{i}} = \Omega_{\mathrm{i}}(r, \theta)$.

We shall determine the radial and vertical components of the gravitational force of the perturbative sources in purely Newtonian way. For simplicity, the force will be determined in the equatorial plane, i.e., in the symmetry plane of the disc, which is surely quite correct for the thin, Keplerian discs, and gives good estimates for thick (slim) discs and in the interior of the star. The time evolution of the perturbing force components will be determined for a fixed point on the rotating accretion disc which will be characterized by the coordinates $(R, \theta = \pi/2, \varphi = \Omega_{\mathrm{d}} t)$, with the natural restriction put on the radial coordinate $R_{\mathrm{A}} < R < 10^3\, R_{\mathrm{A}}$. In the interior of the star, we again consider the equatorial plane ($\theta = \pi/2$) and $0 < R < R_{\mathrm{A}}$. We give both the total forces and their oscillatory parts.

Here, and henceforth, we shall consider the force acting on a unit mass element of the accretion disc (or the neutron star) located at a given radius R of symmetry plane of the disc, which is corotating with the disc (or the neutron star). Using the purely Newtonian approach, we obtain the time dependent vertical component of the perturbing gravitational force to be given by the relation

$$F_{\mathrm{AV}}(t) = \frac{Gm}{R_{\mathrm{A}}^2}\left(\frac{R_{\mathrm{A}}}{R}\right)^3 \cos\theta_{\mathrm{A}}\left[1 - 2\frac{R_{\mathrm{A}}}{R}\sin\theta_{\mathrm{A}}\cos\omega_{\mathrm{A}} t + \left(\frac{R_{\mathrm{A}}}{R}\right)^2\right]^{-3/2}, \tag{1}$$

while the time dependent radial component of the force is given by

$$F_{\mathrm{AR}}(t) = \frac{Gm}{R_{\mathrm{A}}^2}\left(\frac{R_{\mathrm{A}}}{R}\right)^2 \left(1 - \frac{R_{\mathrm{A}}}{R}\sin\theta_{\mathrm{A}}\cos\omega_{\mathrm{A}} t\right) \times \left[1 - 2\frac{R_{\mathrm{A}}}{R}\sin\theta_{\mathrm{A}}\cos\omega_{\mathrm{A}} t + \left(\frac{R_{\mathrm{A}}}{R}\right)^2\right]^{-3/2}, \tag{2}$$

where the angular velocity is given by

$$\omega_{\mathrm{A}} \equiv |\Omega_{\mathrm{A}} - \Omega_{\mathrm{d}}| \tag{3}$$

in the disc, and by

$$\omega_{\mathrm{A}} \equiv |\Omega_{\mathrm{A}} - \Omega_{\mathrm{i}}(R, \theta = \pi/2)| \tag{4}$$

inside the neutron star. The forces are oscillatory, but the oscillations have an anharmonic character. This means that in the Fourier analysis we could find some additional frequencies related to ω_{A}.

Introducing variable $x \equiv R_{\mathrm{A}}/R$, the local extrema of the oscillating forces are given by the relations:

$$\frac{\partial F_{\mathrm{AV}}}{\partial t} = \frac{Gm}{R_{\mathrm{A}}^2} \frac{3x^4 \sin\theta_{\mathrm{A}} \cos\theta_{\mathrm{A}} \sin\omega_{\mathrm{A}} t}{(1 - 2x \sin\theta_{\mathrm{A}} \cos\omega_{\mathrm{A}} t + x^2)^{5/2}} = 0\,, \tag{5}$$

$$\frac{\partial F_{\mathrm{AR}}}{\partial t} = \frac{Gm}{R_{\mathrm{A}}^2} \frac{x^3(1 - 2x \sin\theta_{\mathrm{A}} \cos\omega_{\mathrm{A}} t + x^2)^{1/2}}{\left(1 - 2x \sin\theta_{\mathrm{A}} \cos\omega_{\mathrm{A}} t + x^2\right)^{5/2}} \times \omega_{\mathrm{A}} \sin\theta_{\mathrm{A}} \sin\omega_{\mathrm{A}} t(-2 + x \sin\theta_{\mathrm{A}} \cos\omega_{\mathrm{A}} t + x^2)\,. \tag{6}$$

Clearly, the local extreme points of both F_{V} and F_{R} are given in the expected standard way by the condition independent of the radial position and θ_{A}

$$\sin\omega_{\mathrm{A}} t = 0\,. \tag{7}$$

However, for the radial force F_{R}, there are additional extrema depending on the radial position and θ_{A} by the relation

$$\cos\omega_{\mathrm{A}} t = \frac{2 - x^2}{x \sin\theta_{\mathrm{A}}}\,. \tag{8}$$

Clearly, outside the neutron star, i.e., in the disc, where $0 < x < 1$ ($R_{\mathrm{A}} < R$), these extrema are irrelevant, but inside the star ($x > 1$), the extrema are relevant in the internal of x related to the angle θ_{A}, through the inequality

$$-1 \leq \frac{2 - x^2}{x \sin\theta_{\mathrm{A}}} \leq 1\,. \tag{9}$$

The behaviour of F_{V} and F_{R} is illustrated in Fig. 1 for $x \in (0, 1)$, i.e., in the disc, and in Fig. 2 for $x > 1$, i.e., inside the neutron star (assuming $\omega_{\mathrm{A}} = \mathrm{const}$, i.e., $\Omega_{\mathrm{i}} = \mathrm{const} \neq \Omega_{\mathrm{A}}$). It should be noted that above the interval of x with additional extrema of the radial force F_{R}, the both forces F_{V} and F_{R} are varying in the same phase, while under the interval, in the central part of the neutron star, the extremum of the radial force F_{R} is shifted in half of the period and the forces vary in the opposite phase. This behaviour of the radial component of the perturbation force could imply interesting consequences in generating the oscillatory modes of the star and related gravitational waves.

The vertical force oscillates around the mean value (given by $\cos\omega_{\mathrm{A}} t = 0$)

$$F_{\mathrm{AV(mean)}} = \frac{Gm}{R^2} \left(\frac{R_{\mathrm{A}}}{R}\right)^3 \cos\theta_{\mathrm{A}} \left[1 + \left(\frac{R_{\mathrm{A}}}{R}\right)^2\right]^{-3/2} \tag{10}$$

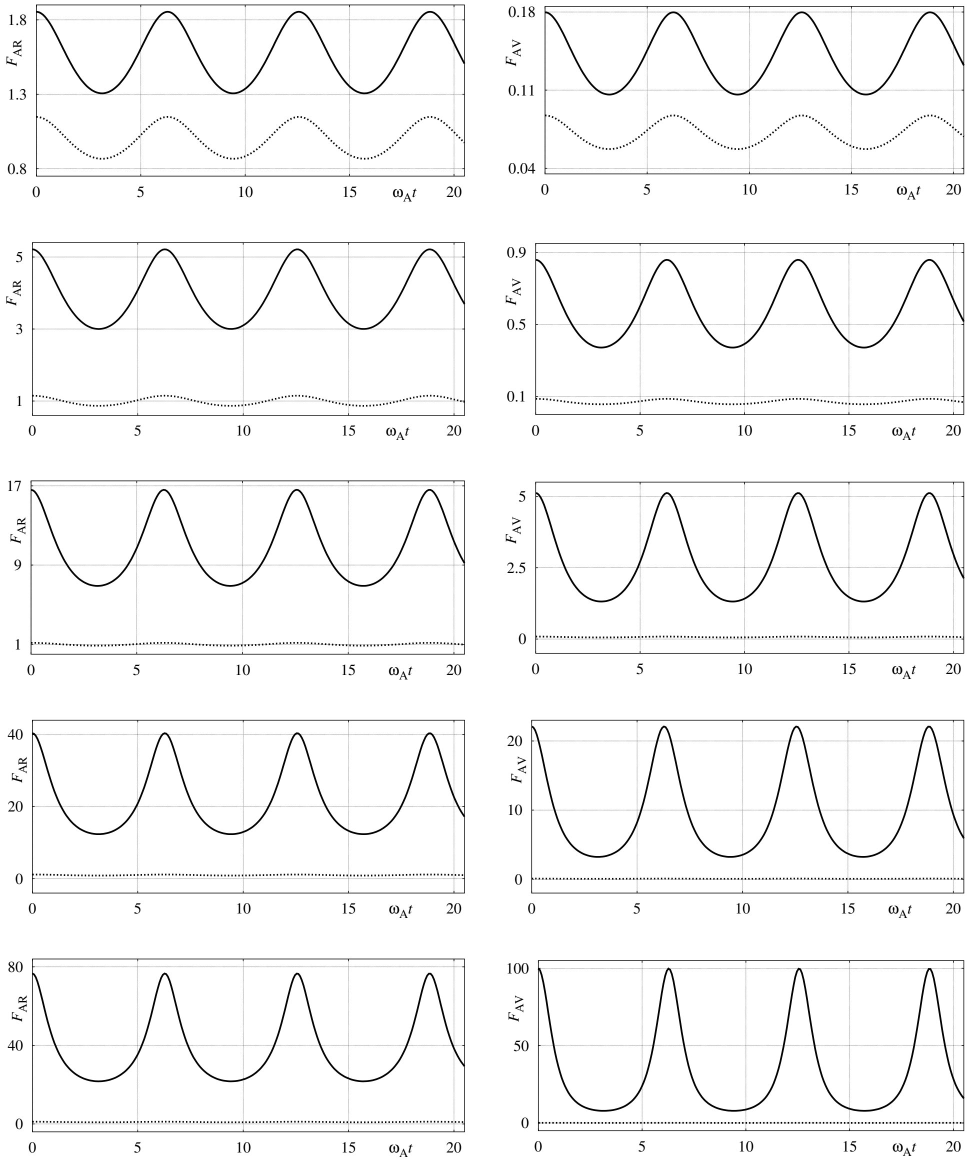

Figure 1. The oscillatory radial (*left column*) and vertical (*right column*) gravitational forces generated by an inhomogeneity (a mountain) located on the surface of a rotating neutron star, and acting outside the star onto elements of an equatorial accretion disc. The mountain is assumed to be located at $\theta_{\mathrm{A}} = 45°$. The oscillatory forces (at $R = 8\,R_{\mathrm{A}}, 5\,R_{\mathrm{A}}, 3\,R_{\mathrm{A}}, 2\,R_{\mathrm{A}}, 1.25\,R_{\mathrm{A}}$ from top to bottom, full curves) have generally an anharmonic character and are given at some typical radii in the vicinity of the neutron star. They are compared to the behaviour of the forces at $R = 10\,R_{\mathrm{A}}$ (dashed curves), where the oscillations approach harmonic character. Notice that the vertical and radial forces oscillations are mutually in phase which does not change when approaching the surface $R = R_{\mathrm{A}}$ from above.

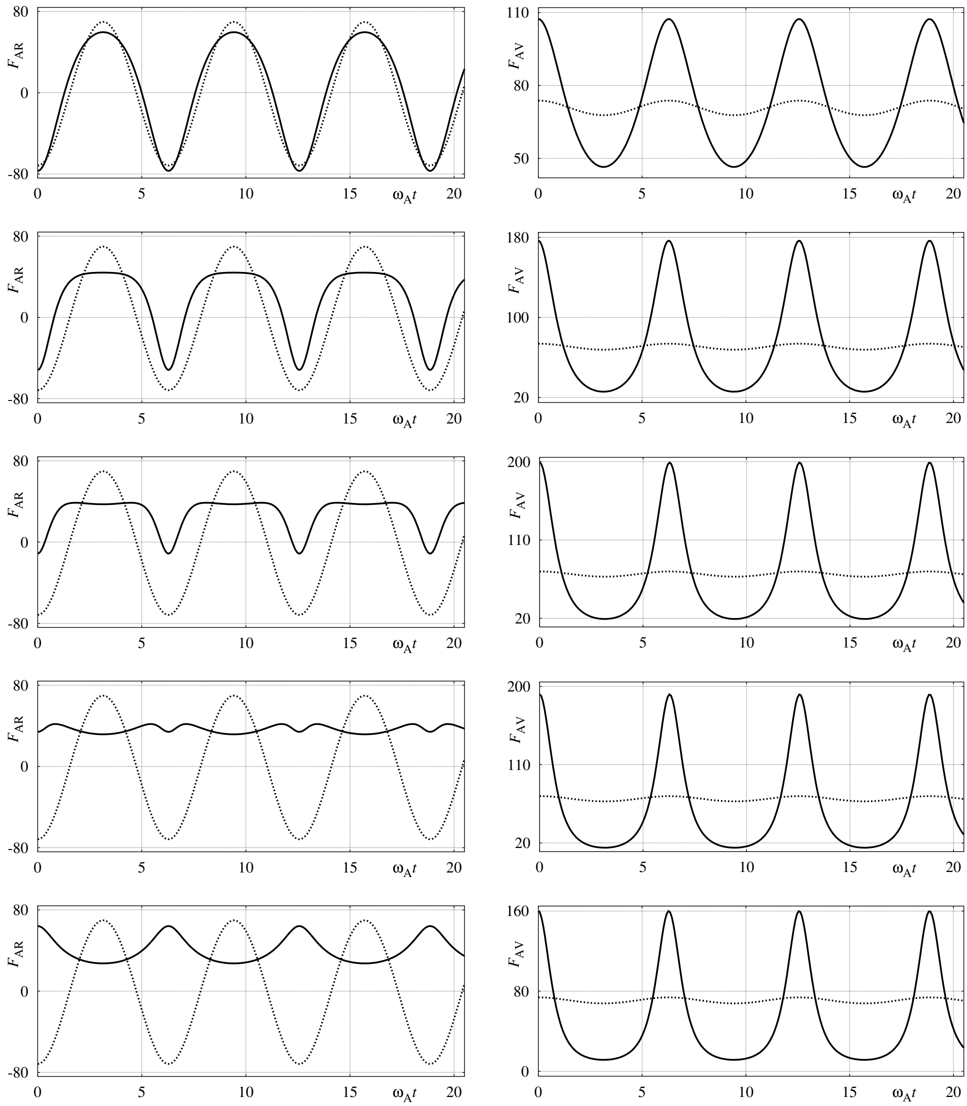

Figure 2. The oscillatory radial (*left column*) and vertical (*right column*) gravitational forces generated by a mountain on the surface of a differentially rotating neutron star, and acting inwards the star in its equatorial plane. The mountain is assumed at $\theta_A = 45°$. The oscillatory forces have an anharmonic character again. They are given at some typical radii (at $R = R_A/5$, $R_A/2$, $R_A/1.5$, $R_A/1.2$, $R_A/1.01$ from top to bottom, full curves) and compared to the nearly harmonically oscillating forces at $R = R_A/50$ (dashed curves). Notice that the vertical and radial forces are mutually in opposite phase near the centre ($R \lesssim R_A \sin\theta_A$), while in some intermediate interval of radii $R \sim R_A \sin\theta_A$, the character of the radial force oscillations becomes more complex (see the cases of $x = 1.5, 1.2$). Further approaching the surface from below ($R \gtrsim R_A \sin\theta_A$) leads to in-phase varying of both components, although they retain strongly anharmonic character.

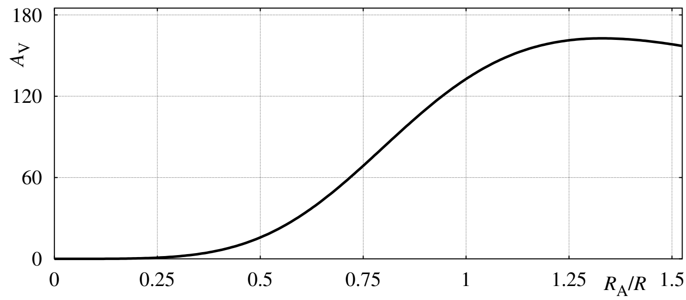

Figure 3. The amplitude of the vertical oscillatory force in terms of the inverse radius $x = R_A/R$ given for $\theta_A = 45°$. Outside the neutron star ($R_A/R < 1$), the amplitude grows monotonically with R descending, while inside the neutron star ($R_A/R > 1$), the vertical amplitude reaches a maximum given by θ_A.

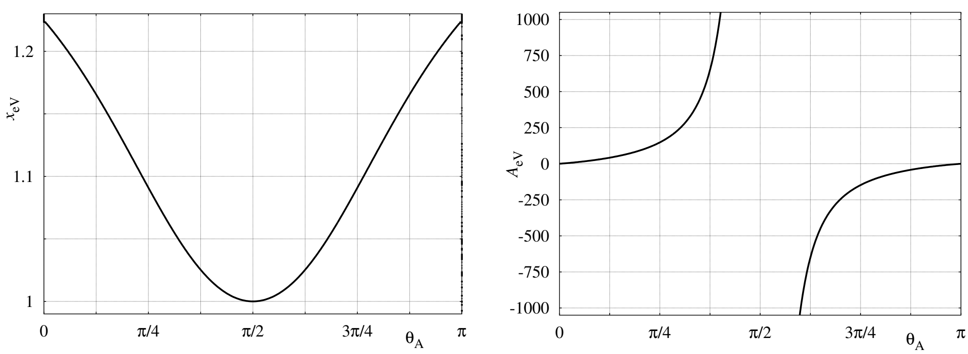

Figure 4. The extrema of the amplitude of the oscillatory vertical force. *Left panel:* the radii $x_{eV}(\theta_A)$. *Right panel:* the related extremal values of $A_{eV}(\theta_A)$. The positive and negative branches render the direction of the vertical force.

with the frequency ω_A and amplitude $A_V \equiv F_{AV(max)} - F_{AV(mean)}$ given by the relation

$$A_V = \frac{Gm}{R_A^2}\left(\frac{R_A}{R}\right)^3 \cos\theta_A \left\{\left[1 - 2\frac{R_A}{R}\sin\theta_A + \left(\frac{R_A}{R}\right)^2\right]^{-3/2} - \left[1 + \left(\frac{R_A}{R}\right)^2\right]^{-3/2}\right\}. \quad (11)$$

The behaviour of the amplitude of the oscillatory vertical force $A_V(x, \theta_A)$ is illustrated in Fig. 3. The local extrema of the function $A_V(x_{eV}, \theta_A)$ are determined by the condition

$$\frac{x^2 - 2 + x\sin\theta_A}{x^2 - 2} = \left(\frac{1 - 2x\sin\theta_A + x^2}{1 + x^2}\right)^{5/2}. \quad (12)$$

The radii of the extrema x_{eV} and of the related extremal values A_{eV} are given in Fig. 4. The radial force oscillates around the mean value

$$F_{AR(mean)} = \frac{Gm}{R_A^2}\left(\frac{R_A}{R}\right)^2\left[1+\left(\frac{R_A}{R}\right)^2\right]^{-3/2} \tag{13}$$

with the frequency ω_A and amplitude

$$A_R = \frac{Gm}{R_A^2}\left(\frac{R_A}{R}\right)^2\left\{\frac{1-\frac{R_A}{R}\sin\theta_A}{\left[1-2\frac{R_A}{R}\sin\theta_A+\left(\frac{R_A}{R}\right)^2\right]^{3/2}}-\frac{1}{\left[1+\left(\frac{R_A}{R}\right)^2\right]^{3/2}}\right\}. \tag{14}$$

The behaviour of the amplitude of the oscillatory radial force $A_R(x, \theta_A)$ varying with the frequency ω_A given by Eq. (7) is illustrated in Fig. 5. The local extrema of the function

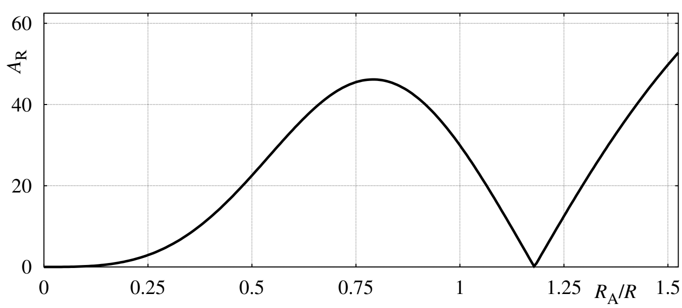

Figure 5. The amplitude of the radial oscillatory force in terms of the inverse radius $x = R_A/R$ determined for $\theta_A = 45°$. The amplitude has at least one local maximum outside the neutron star and it reaches a local minimum with the zero value inside the star.

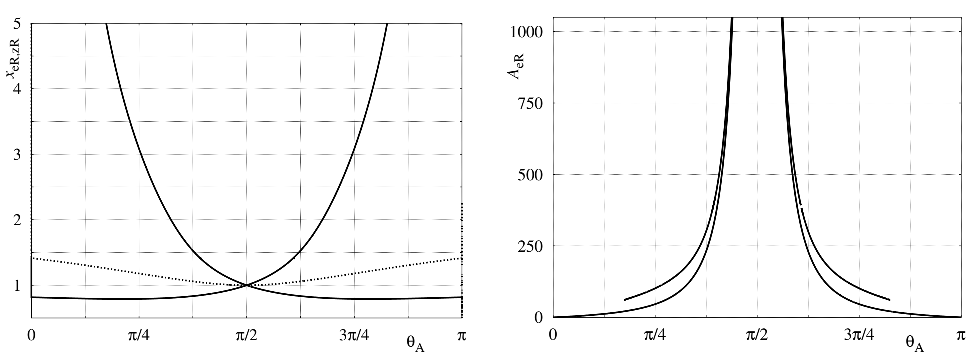

Figure 6. The extrema of the amplitude of the oscillatory radial force. *Left panel:* the radii $x_{eR}(\theta_A)$ (full curve) and $x_{zR}(\theta_A)$ (dashed curve). *Right panel:* the related extreme values of $A_{eR}(\theta_A)$.

$A_{\mathrm{R}}(x_{\mathrm{eR}}, \theta_{\mathrm{A}})$ are determined by the condition

$$\frac{x^2 - 2 + x\sin\theta_{\mathrm{A}}(4 - 3x\sin\theta_{\mathrm{A}})}{x^2 - 2} = \left(\frac{1 - 2x\sin\theta_{\mathrm{A}} + x^2}{1 + x^2}\right)^{5/2} . \tag{15}$$

The special case of $A_{\mathrm{R}}(x_{\mathrm{zR}}, \theta_{\mathrm{A}}) = 0$ is determined by the condition

$$1 - x\sin\theta_{\mathrm{A}} = \left(\frac{1 - 2x\sin\theta_{\mathrm{A}} + x^2}{1 + x^2}\right)^{3/2} . \tag{16}$$

The radii of the extrema x_{eR}, the zero radial amplitude x_{zR} and of the related extremal values A_{eR} are given in Fig. 6.

In the case when we can assume $R \gg R_{\mathrm{A}}$, we arrive at the simple formulae for both the total force and the amplitude of the oscillatory force. The oscillations now have harmonic character. There is

$$F_{\mathrm{AV}}(t) \sim \frac{Gm}{R_{\mathrm{A}}^2}\left(\frac{R_{\mathrm{A}}}{R}\right)^3 \cos\theta_{\mathrm{A}}\left(1 + 3\frac{R_{\mathrm{A}}}{R}\sin\theta_{\mathrm{A}}\cos\omega_{\mathrm{A}}t\right) , \tag{17}$$

$$F_{\mathrm{AR}}(t) \sim \frac{Gm}{R_{\mathrm{A}}^2}\left(\frac{R_{\mathrm{A}}}{R}\right)^2 \left(1 + 2\frac{R_{\mathrm{A}}}{R}\sin\theta_{\mathrm{A}}\cos\omega_{\mathrm{A}}t\right) . \tag{18}$$

The amplitude of the harmonically oscillating part of the forces reads

$$A_{\mathrm{V}} \sim 3\frac{Gm}{R_{\mathrm{A}}^2}\left(\frac{R_{\mathrm{A}}}{R}\right)^4 \sin\theta_{\mathrm{A}}\cos\theta_{\mathrm{A}} , \tag{19}$$

$$A_{\mathrm{R}} \sim 2\frac{Gm}{R_{\mathrm{A}}^2}\left(\frac{R_{\mathrm{A}}}{R}\right)^3 \sin\theta_{\mathrm{A}} . \tag{20}$$

The shift of the anharmonic oscillation to the harmonic one can be directly seen in Fig. 1. Of course, a similar shift occurs in the limit of $R/R_{\mathrm{A}} \to 0$ (Fig. 2).

3 GRAVITATIONAL FORCE OF A SYMMETRIC ACCRETION COLUMN

Now, we assume two mountains located at the poles of the magnetic axis having the same mass m_{D}, with the angle between the axis and the equatorial plane θ_{A}. Clearly, we can use the results obtained for the isolated mountain case and combine them properly. In fact, we can use the simple relations

$$F_{\mathrm{DV}}(t) = F_{\mathrm{AaV}}(t) - F_{\mathrm{AbV}}(t) , \qquad F_{\mathrm{DR}}(t) = F_{\mathrm{AaR}}(t) + F_{\mathrm{AbR}}(t) , \tag{21}$$

where F_{AaV}, F_{AaR} (F_{AbV}, F_{AbR}) give the vertical and radial forces of the mountain above (below) the equatorial plane. The azimuthal angle in the expressions for the F_{Aa} and F_{Ab}

forces is shifted by $\varphi = \pi$. Therefore, we arrive at the following results. The vertical force is given by the relation

$$F_{\mathrm{DV}}(t) = \frac{Gm_{\mathrm{D}}}{R_{\mathrm{A}}^2}\left(\frac{R_{\mathrm{A}}}{R}\right)^3 \cos\theta_{\mathrm{A}} \left\{\left[1 - 2\frac{R_{\mathrm{A}}}{R}\sin\theta_{\mathrm{A}}\cos\omega_{\mathrm{A}}t + \left(\frac{R_{\mathrm{A}}}{R}\right)^2\right]^{-3/2} - \right.$$
$$\left. - \left[1 + 2\frac{R_{\mathrm{A}}}{R}\sin\theta_{\mathrm{A}}\cos\omega_{\mathrm{A}}t + \left(\frac{R_{\mathrm{A}}}{R}\right)^2\right]^{-3/2}\right\}, \quad (22)$$

and the radial force is

$$F_{\mathrm{DR}}(t) = \frac{Gm_{\mathrm{D}}}{R_{\mathrm{A}}^2}\left(\frac{R_{\mathrm{A}}}{R}\right)^2 \left\{\frac{1 - \frac{R_{\mathrm{A}}}{R}\sin\theta_{\mathrm{A}}\cos\omega_{\mathrm{A}}t}{\left[1 - 2\frac{R_{\mathrm{A}}}{R}\sin\theta_{\mathrm{A}}\cos\omega_{\mathrm{A}}t + \left(\frac{R_{\mathrm{A}}}{R}\right)^2\right]^{3/2}} + \right.$$
$$\left. + \frac{1 + \frac{R_{\mathrm{A}}}{R}\sin\theta_{\mathrm{A}}\cos\omega_{\mathrm{A}}t}{\left[1 + 2\frac{R_{\mathrm{A}}}{R}\sin\theta_{\mathrm{A}}\cos\omega_{\mathrm{A}}t + \left(\frac{R_{\mathrm{A}}}{R}\right)^2\right]^{3/2}}\right\}. \quad (23)$$

These are, again, anharmonically oscillating forces, but frequency of the radial force is doubled because of the symmetry of the accretion columns. Introducing variable $x \equiv R_{\mathrm{A}}/R$, the local extrema of the oscillating forces are given by the relations

$$\frac{\partial F_{\mathrm{DV}}}{\partial t} = -\frac{Gm_{\mathrm{D}}}{R_{\mathrm{A}}^2} 3x^4\omega_{\mathrm{A}}\sin\theta_{\mathrm{A}}\cos\theta_{\mathrm{A}}\sin\omega_{\mathrm{A}}t$$
$$\times\left[(1 - 2x\cos\theta_{\mathrm{A}}\cos\omega_{\mathrm{A}}t + x^2)^{-5/2} + (1 + 2x\cos\theta_{\mathrm{A}}\cos\omega_{\mathrm{A}}t + x^2)^{-5/2}\right], \quad (24)$$

$$\frac{\partial F_{\mathrm{DR}}}{\partial t} = \frac{Gm_{\mathrm{D}}}{R_{\mathrm{A}}^2} x^3\cos\theta_{\mathrm{A}}\sin\omega_{\mathrm{A}}t\left[\frac{-2 + x\cos\theta_{\mathrm{A}}\cos\omega_{\mathrm{A}}t + x^2}{(1 - 2x\cos\theta_{\mathrm{A}}\cos\omega_{\mathrm{A}}t + x^2)^{5/2}}\right.$$
$$\left. + \frac{2 + x\cos\theta_{\mathrm{A}}\cos\omega_{\mathrm{A}}t + x^2}{(1 + 2x\cos\theta_{\mathrm{A}}\cos\omega_{\mathrm{A}}t + x^2)^{5/2}}\right]. \quad (25)$$

The vertical force oscillates around the mean value $F_{\mathrm{DV(mean)}} = 0$ with frequency ω_{A} and amplitude

$$D_{\mathrm{V}} = \frac{Gm_{\mathrm{D}}}{R_{\mathrm{A}}^2}\left(\frac{R_{\mathrm{A}}}{R}\right)^3\cos\theta_{\mathrm{A}}\left\{\left[1 - 2\frac{R_{\mathrm{A}}}{R}\sin\theta_{\mathrm{A}} + \left(\frac{R_{\mathrm{A}}}{R}\right)^2\right]^{-3/2} - \right.$$
$$\left. - \left[1 + 2\frac{R_{\mathrm{A}}}{R}\sin\theta_{\mathrm{A}} + \left(\frac{R_{\mathrm{A}}}{R}\right)^2\right]^{-3/2}\right\}. \quad (26)$$

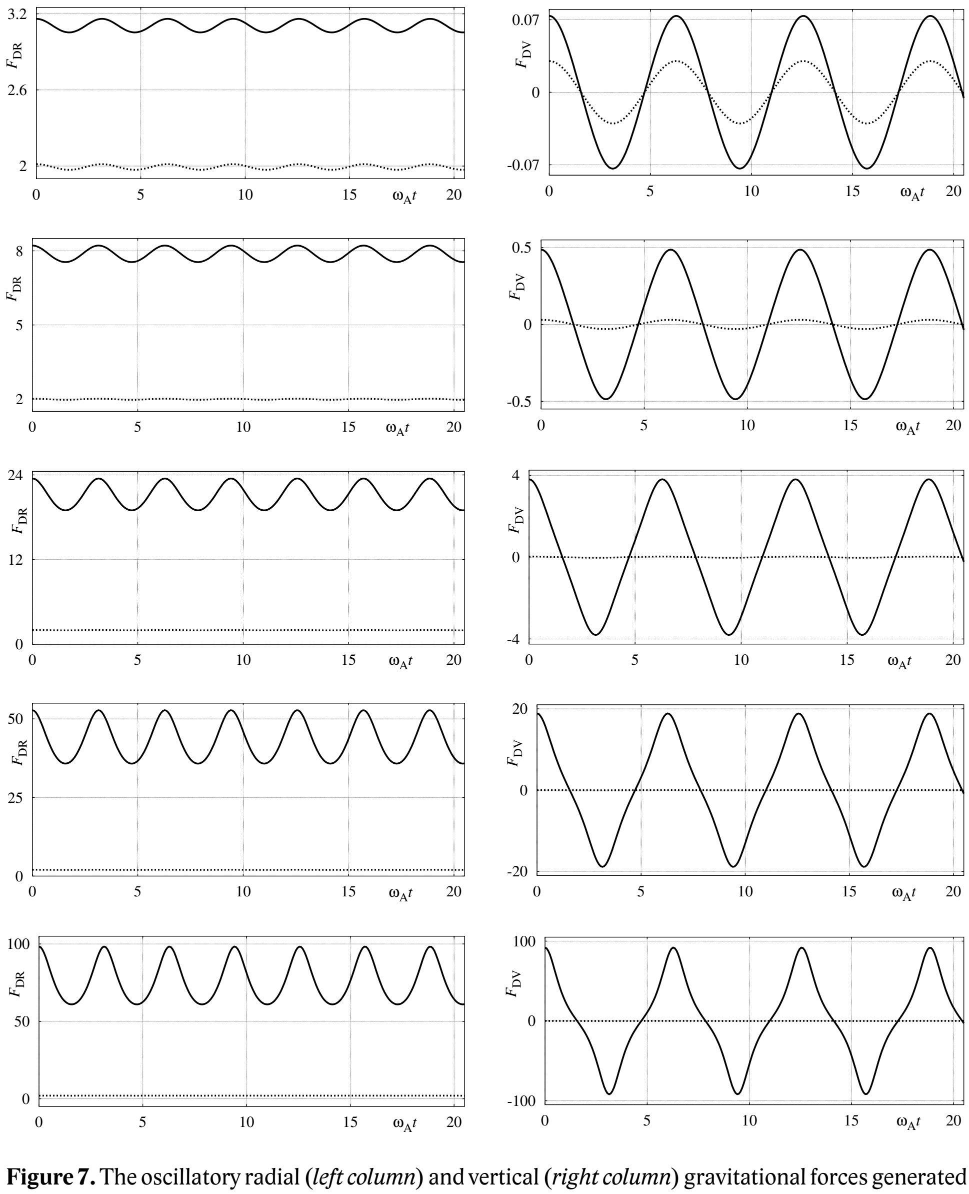

Figure 7. The oscillatory radial (*left column*) and vertical (*right column*) gravitational forces generated by two inhomogeneities (mountains) of equal masses located at the poles of the magnetic axis ($\theta_A = 45°, 135°$, and $\Delta\varphi_A = 180°$) on the surface of a rotating neutron star, and acting outside the star onto elements of an equatorial accretion disc. The oscillatory forces have generally only slightly anharmonic character and are given at some typical radii in vicinity of the neutron star (at $R = 8\,R_A, 5\,R_A, 3\,R_A, 2\,R_A, 1.25\,R_A$ from top to bottom, full curves). They are always compared to the behaviour of the forces at $R = 10\,R_A$ (dashed curves), where the oscillations approach harmonic character. Notice the double frequency of the radial component compared to the vertical one, and that the phase does not change when approaching the surface $R = R_A$ from above.

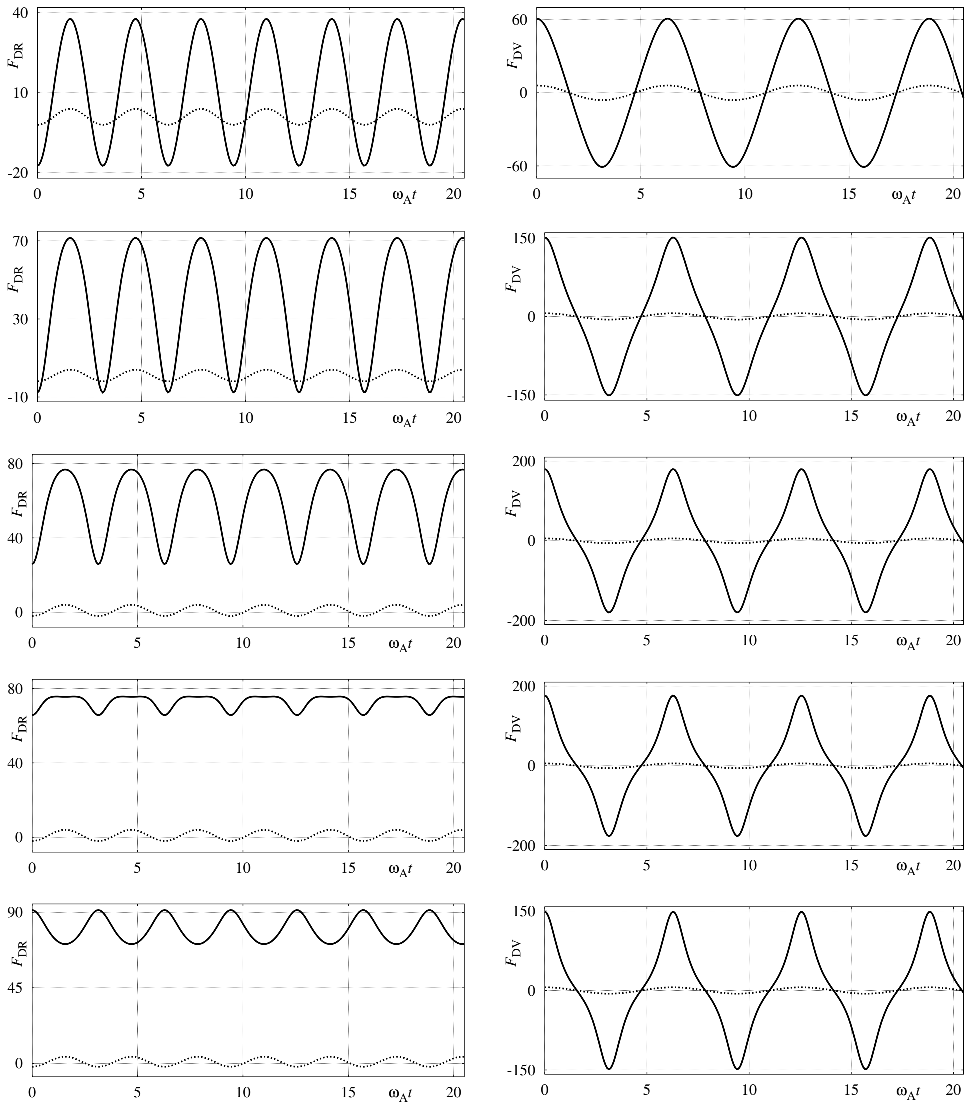

Figure 8. The oscillatory radial (*left column*) and vertical (*right column*) gravitational forces generated by two inhomogeneities (mountains) of equal masses located at the poles of the magnetic axis ($\theta_{\rm A} = 45°$, $135°$, and $\Delta\varphi_{\rm A} = 180°$) on the surface of a differentially rotating neutron star, and acting inside the star in its equatorial plane. The oscillatory forces have an anharmonic character again. They are given at some typical radii (at $R = R_{\rm A}/5$, $R_{\rm A}/2$, $R_{\rm A}/1.5$, $R_{\rm A}/1.2$, $R_{\rm A}/1.01$ from top to bottom, full curves) and compared to the nearly harmonically oscillating forces at $R = R_{\rm A}/50$ (dashed curves). Notice the double frequency of the radial component compared to the vertical one. The phase of the vertical component does not change when approaching the surface $R = R_{\rm A}$ from below, while the radial one changes its phase by π after passing the intermediate interval around $R \sim R_{\rm A} \sin\theta_{\rm A}$, in which its character is rather complex.

The radial force oscillates around the mean value

$$F_{\mathrm{DR(mean)}} = \frac{2Gm_{\mathrm{D}}}{R_{\mathrm{A}}^2}\left(\frac{R_{\mathrm{A}}}{R}\right)^2\left[1+\left(\frac{R_{\mathrm{A}}}{R}\right)^2\right]^{-3/2} \tag{27}$$

with the frequency $\omega_{\mathrm{DR}} = 2\omega_{\mathrm{A}}$ and the amplitude

$$D_{\mathrm{R}} = \frac{Gm_{\mathrm{D}}}{R_{\mathrm{A}}^2}\left(\frac{R_{\mathrm{A}}}{R}\right)^2\left\{\frac{1-\frac{R_{\mathrm{A}}}{R}\sin\theta_{\mathrm{A}}}{\left[1-2\frac{R_{\mathrm{A}}}{R}\sin\theta_{\mathrm{A}}+\left(\frac{R_{\mathrm{A}}}{R}\right)^2\right]^{3/2}} - \frac{2}{\left[1+\left(\frac{R_{\mathrm{A}}}{R}\right)\right]^{3/2}} + \right.$$
$$\left. + \frac{1+\frac{R_{\mathrm{A}}}{R}\sin\theta_{\mathrm{A}}}{\left[1+2\frac{R_{\mathrm{A}}}{R}\sin\theta_{\mathrm{A}}+\left(\frac{R_{\mathrm{A}}}{R}\right)^2\right]^{3/2}}\right\}. \tag{28}$$

The behaviour of F_{DV} and F_{DR} is illustrated in Fig. 7 for $x \in (0, 1)$, i.e., in the disc, and in Fig. 8 for $x > 1$, i.e., inside the neutron star.

Under assumption $R_{\mathrm{A}}/R \ll 1$, we obtain harmonically oscillating forces. The vertical force is given in the form

$$F_{\mathrm{DV}}(t) \sim 6\frac{Gm_{\mathrm{D}}}{R_{\mathrm{A}}^2}\left(\frac{R_{\mathrm{A}}}{R}\right)^4 \sin\theta_{\mathrm{A}}\cos\theta_{\mathrm{A}}\cos\omega_{\mathrm{A}}t \tag{29}$$

implying the amplitude of the oscillating force

$$D_{\mathrm{V}} \sim 3\frac{Gm_{\mathrm{D}}}{R_{\mathrm{A}}^2}\left(\frac{R_{\mathrm{A}}}{R}\right)^4 \sin 2\theta_{\mathrm{A}}\,. \tag{30}$$

The radial force is given by the relation

$$F_{\mathrm{DR}}(t) \sim \frac{Gm_{\mathrm{D}}}{R_{\mathrm{A}}^2}\left(\frac{R_{\mathrm{A}}}{R}\right)^2\left[2-3\left(\frac{R_{\mathrm{A}}}{R}\right)^2\left(1-8\sin^2\theta_{\mathrm{A}}\sin^2\omega_{\mathrm{A}}t\right)\right]; \tag{31}$$

the amplitude of the oscillations of the force is given by

$$D_{\mathrm{R}} \sim 24\frac{Gm_{\mathrm{D}}}{R_{\mathrm{A}}^2}\left(\frac{R_{\mathrm{A}}}{R}\right)^4 \sin^2\theta_{\mathrm{A}}\,, \tag{32}$$

and we clearly see that the frequency of the radial oscillations must be twice of the corresponding rotational frequency.

4 CONCLUDING REMARKS

The analysis of the behaviour of the vertical and radial components of the gravitational perturbative force generated by an isolated mountain located on the surface of a neutron star

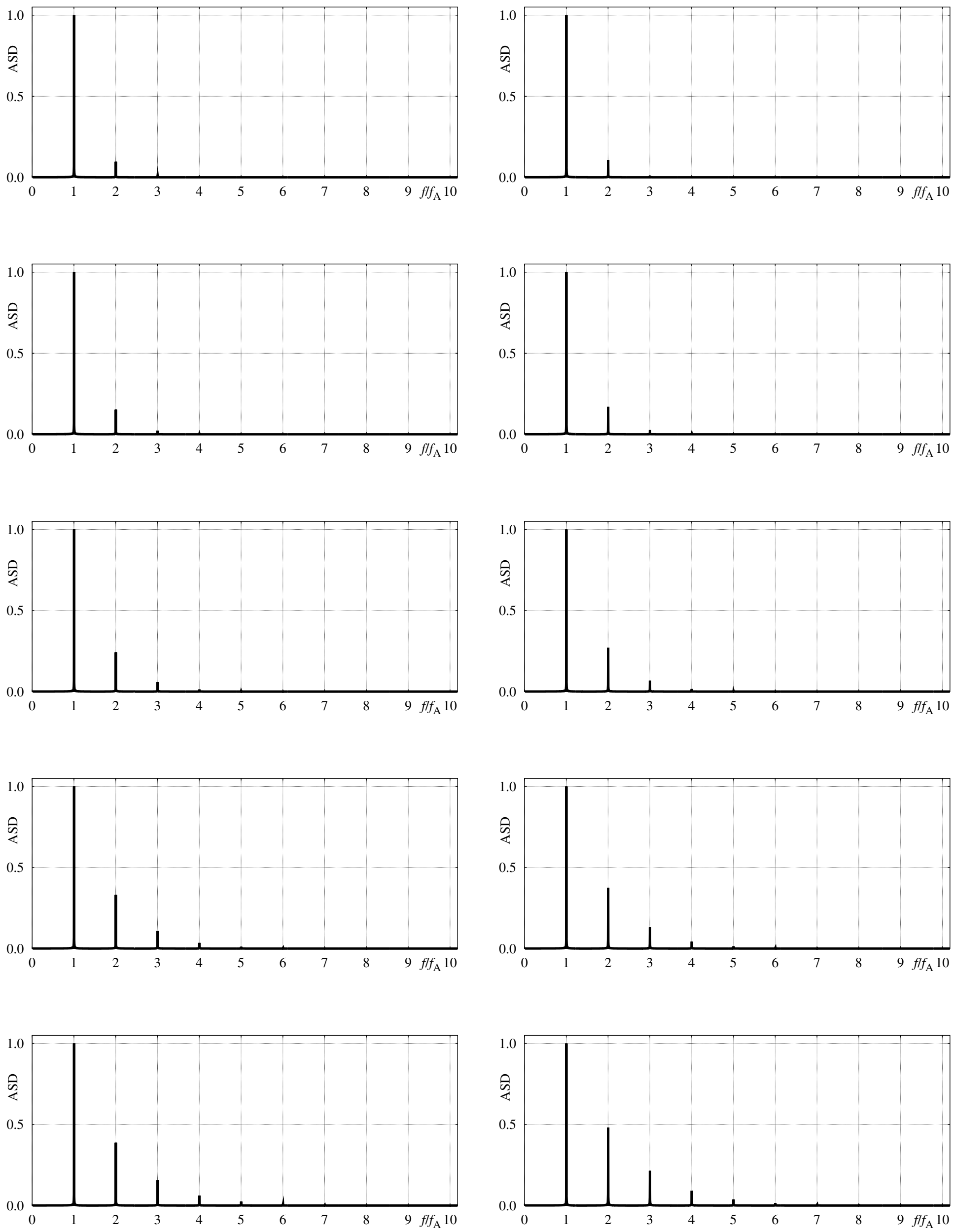

Figure 9. Fourier amplitude spectral density corresponding to oscillations of the radial (*left column*) and vertical (*right column*) components of gravitational force discussed in Fig. 1. The zero-frequency peak (corresponding to constant part of the force) is cut off and the peaks are normalized to the maximum of 1. Higher harmonics become noticeable when approaching the surface from above ($R \lesssim 3R_A$) for both radial and vertical force, which is in accordance with the discussion in Fig. 1.

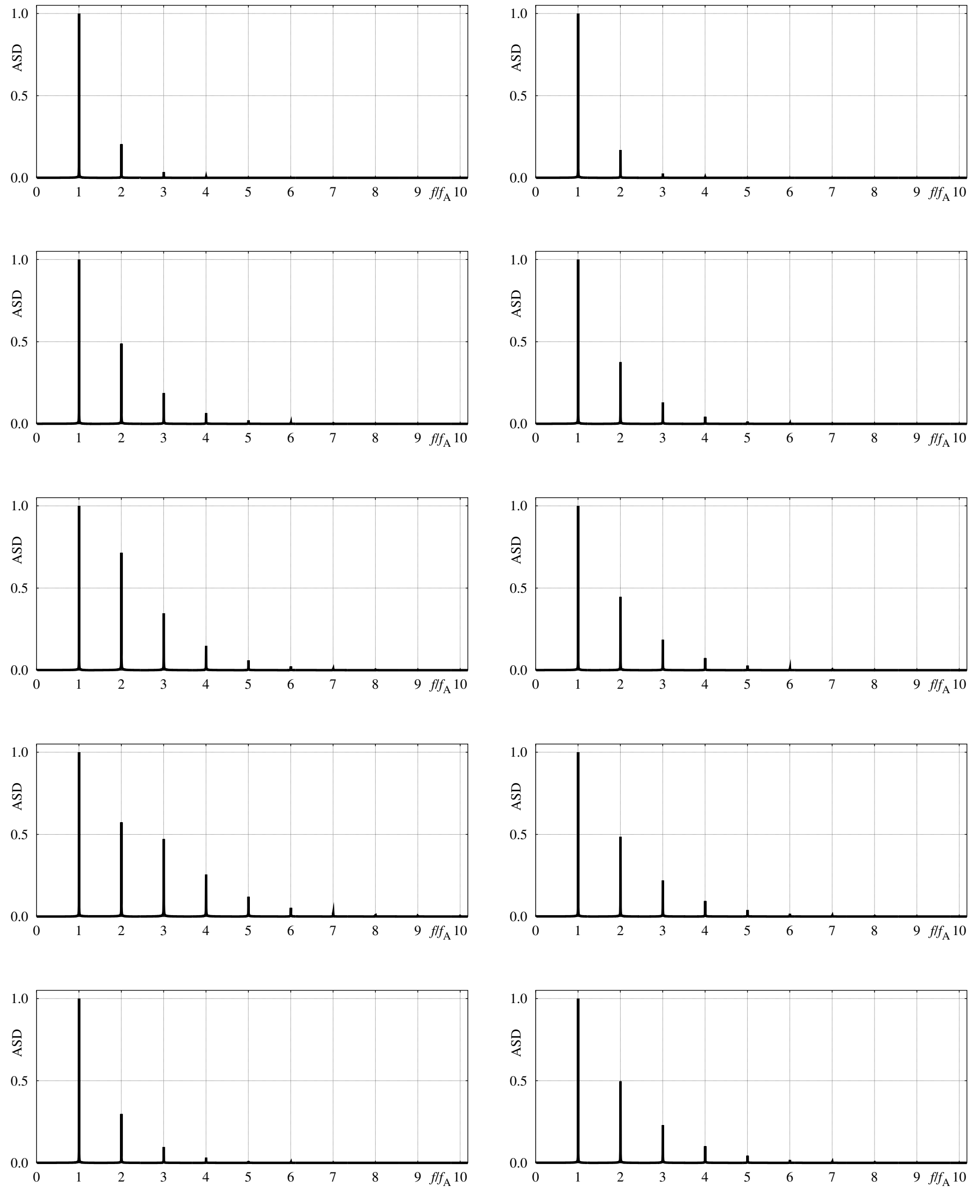

Figure 10. Fourier amplitude spectral density corresponding to oscillations of the radial (*left column*) and vertical (*right column*) components of gravitational force discussed in Fig. 2. The zero-frequency peak (corresponding to constant part of the force) is cut off and the peaks are normalized to the maximum of 1. Higher harmonics of the vertical component become more recognizable when approaching the surface from below ($R \gtrsim R_\mathrm{A}/5$), while higher harmonics of the radial component are well developed around the intermediate interval around $R \sim R_\mathrm{A} \sin\theta_\mathrm{A}$ and vanish towards the centre and the surface of the star. This is in accordance with the discussion in Fig. 2.

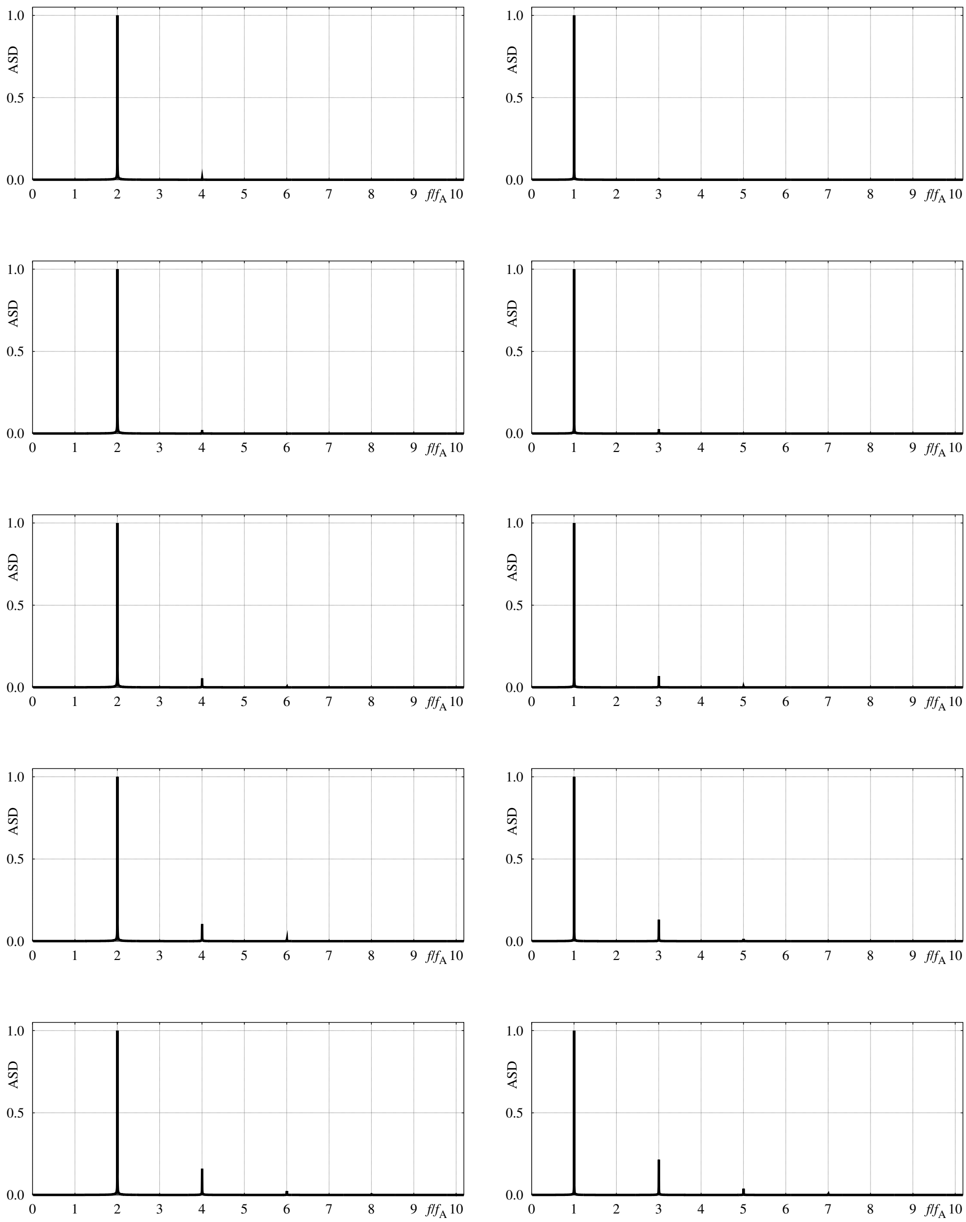

Figure 11. Fourier amplitude spectral density corresponding to oscillations of the radial (*left column*) and vertical (*right column*) components of gravitational force discussed in Fig. 7. The zero-frequency peak (corresponding to constant part of the force) is cut off and the peaks are normalized to the maximum of 1. Symmetrization of the mountains makes the higher harmonics negligible compared to the case of isolated mountain. Notice the frequency doubling of the radial force. This is in accordance with the discussion in Fig. 7.

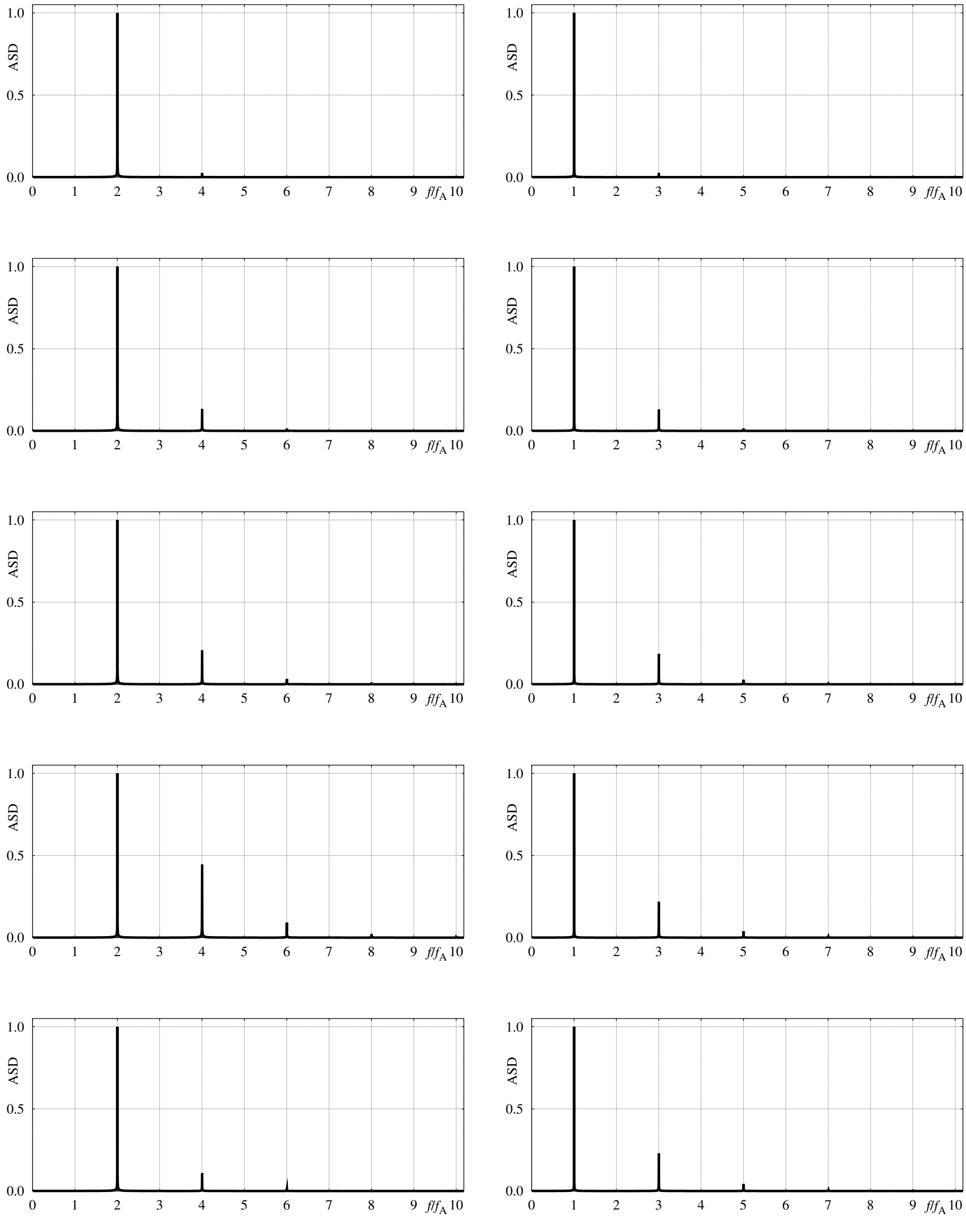

Figure 12. Fourier amplitude spectral density corresponding to oscillations of the radial (*left column*) and vertical (*right column*) components of gravitational force discussed in Fig. 8. The zero-frequency peak (corresponding to constant part of the force) is cut off and the peaks are normalized to the maximum of 1. Symmetrization of the mountains makes the higher harmonics negligible compared to the case of isolated mountain, with the exception of the intermediate interval around $R \sim R_A \sin\theta_A$. Notice the frequency doubling of the radial force. This is in accordance with the discussion in Fig. 8.

brings interesting results. We have discussed time variations of the forces in the equatorial plane related to the rotation axis of the star in both exterior and interior of the star. In the exterior, where a corotating accretion disc is assumed, the vertical and radial force oscillate with the same phase, and have an anharmonic character. In the interior of the star, the character of the oscillatory vertical and radial forces is more complex than in the exterior, if we assume a differentially rotating star, i.e., the angular velocity in the interior being different than the angular velocity of the neutron star surface. In some layer under the star surface, the oscillations of the vertical and radial forces are in the same phase, while near the centre of the star, the oscillations are in the opposite phase. Further, there is a special intermediate region, located nearby $R \sim R_{\mathrm{A}} \sin\theta_{\mathrm{A}}$, where the oscillations are modulated in such a way that there are additional local extrema, given by Eq. (8), i.e., dependent on the radial coordinate R and the angle θ_{A}. This force, oscillating in a non-standard way, could generate oscillations of a differentially rotating neutron star is some unexpected manner deserving further investigation. Of course, it is interesting to consider not only influence of an isolated mountain, but also of two mountains (accretion columns) symmetrically located at the poles of the neutron star magnetic field which is misaligned with the axis of rotation of the star. We give here the relevant formulae for the vertical and radial force and their local extrema, and postpone discussion to future studies. Nevertheless, we would like to stress an important new phenomenon, namely that the radial force always oscillates with frequency doubled in comparison with oscillations of the vertical one.

Going down from $R \sim 10\,R_{\mathrm{A}}$ to $R \sim 1.25\,R_{\mathrm{A}}$ in the equatorial disc, the amplitude of the radial (vertical) oscillatory force grows by factor of 10^2 (10^3).

Fourier analysis of the oscillatory vertical and radial forces (in Figs 9–12 we use amplitude spectral density instead of power spectral density, which is more relevant for the excitation of the oscillations and can better emphasize faint higher harmonics, see, e.g., Press et al., 1997) shows that higher harmonics up to seventh are non-negligible in the case of isolated mountain and the radial component around the region $R \sim \theta_{\mathrm{A}}$ inside the neutron star, while in the case of symmetric accretion columns higher harmonics are more suppressed and occur in odd multiples of the basic frequency for the vertical oscillations, which is caused by "triangular" shape of the oscillations.

We can conclude that an isolated mountain can lead to more complex phenomena in excitation of oscillations in both equatorial discs and interior of differentially rotating stars. Both situations are under more detailed study at present.

ACKNOWLEDGEMENTS

The present work was supported by the Czech grant MSM 4781305903.

REFERENCES

Abramowicz, M. A., Barret, D., Bursa, M., Horák, J., Kluźniak, W., Rebusco, P. and Török, G. (2005a), A note on the slope-shift anticorrelation in the neutron star kHz QPOs data, pp. 1–9, this volume.

Abramowicz, M. A., Barret, D., Bursa, M., Horák, J., Kluźniak, W., Rebusco, P. and Török, G. (2005b), The correlations and anticorrelations in QPO data, *Astronom. Nachr.*, **326**(9), pp. 864–866.

Abramowicz, M. A. and Kluźniak, W. (2001), A precise determination of black hole spin in GRO J1655−40, *Astronomy and Astrophysics*, **374**, p. L19, `astro-ph/010507`.

Abramowicz, M. A. and Kluźniak, W. (2004), Interpreting black hole QPOs, in P. Karet, F. K. Lamb and J. H. Swank, editors, *X-ray Timing 2003: Rossi and Beyond.*, volume 714, pp. 21–28, NY: American Institute of Physics, Melville, `astro-ph/0312396`.

Abramowicz, M. A., Kluźniak, W., McClintock, J. E. and Remillard, R. A. (2004a), The Importance of Discovering a 3 : 2 Twin-Peak Quasi-periodic Oscillation in an Ultraluminous X-Ray Source, or How to Solve the Puzzle of Intermediate-Mass Black Holes, *Astrophys. J. Lett.*, **609**, pp. L63–L65.

Abramowicz, M. A., Kluźniak, W., Stuchlík, Z. and Török, G. (2004b), Twin peak QPOs frequencies in microquasars and Sgr A*. The resonance and other orbital models, in Hledík and Stuchlík (2004), pp. 1–23.

Abramowicz, M. A., Lanza, A., Spiegel, E. A. and Szuszkiewicz, E. (1992), Vortices on accretion disks, *Nature*, **356**, p. 41.

Bardeen, J. M. and Petterson, J. A. (1975), The Lense–Thirring effect and accretion disks around Kerr black holes, *Astrophys. J. Lett.*, **195**, p. L65.

Hledík, S. and Stuchlík, Z., editors (2004), *Proceedings of RAGtime 4/5: Workshops on black holes and neutron stars, Opava, 14–16/13–15 October 2002/2003*, Silesian University in Opava, Opava, ISBN 80-7248-242-4.

Horák, J. (2004), General aspects of nonlinear resonance 3 : 2 in QPO context, in Hledík and Stuchlík (2004), pp. 91–110, `astro-ph/0408092`.

Horák, J., Abramowicz, M. A., Karas, V. and Kluźniak, W. (2004), Of NBOs and kHz QPOs: a Low-Frequency Modulation in Resonant Oscillations of Relativistic Accretion Disks, *Publ. Astronom. Soc. Japan*, **56**, p. 819.

Jaroszyński, M., Abramowicz, M. A. and Paczyński, B. (1980), Supercritical accretion disks around black holes, *Acta Astronom.*, **30**, pp. 1–34.

Kato, S. (2004a), Mass and Spin of GRS 1915+105 Based on a Resonance Model of QPOs, *Publ. Astronom. Soc. Japan*, **56**(5), pp. L25–L28.

Kato, S. (2004b), Resonant Excitation of Disk Oscillations by Warps: A Model of kHz QPOs, *Publ. Astronom. Soc. Japan*, **56**(5), pp. 905–922.

Kato, S. and Fukue, J. (1980), Trapped Radial Oscillations of Gaseous Disks around a Black Hole, *Publ. Astronom. Soc. Japan*, **32**(3), pp. 377–388.

Kozłowski, M., Jaroszyński, M. and Abramowicz, M. A. (1978), The analytic theory of fluid disks orbiting the Kerr black hole, *Astronomy and Astrophysics*, **63**(1–2), pp. 209–220, URL `http://adsabs.harvard.edu/article_service.html`.

McClintock, J. E. and Remillard, R. A. (2004), Black Hole Binaries, in W. H. G. Lewin and M. van der Klis, editors, *Compact Stellar X-Ray Sources*, Cambridge University Press, Cambridge, `astro-ph/0306213`.

Novikov, I. D. and Thorne, K. S. (1973), Black hole astrophysics, in C. D. Witt and B. S. D. Witt, editors, *Black Holes*, p. 343, Gordon and Breach, New York–London–Paris.

Petri, J. (2005), Forced oscillations in a hydrodynamical accretion disk and QPOs, *Astronomy and Astrophysics*.

Press, W. H., Teukolsky, S. A., Vetterling, W. T. and Flannery, B. P. (1997), *Numerical Recipes in C: The Art of Scientific Computing*, Cambridge University Press, Cambridge, 2nd edition, ISBN 0-521-43108-5, URL `http://www.nr.com/`.

Rezzolla, L. (2004), A new simple model for high frequency quasiperiodic oscillations in black hole candidates, in P. Karet, F. K. Lamb and J. H. Swank, editors, *X-ray Timing 2003: Rossi and Beyond*, volume 714, p. 36, NY: American Institu of Physics, Melville.

Stuchlík, Z. and Török, G. (2005), On the possibility of precise determination of black hole spin in the framework of resonance models, pp. 253–263, this volume.

Török, G. (2005a), A possible 3 : 2 orbital epicyclic resonance in QPOs frequencies of Sgr A*, *Astronomy and Astrophysics*, **440**(1), pp. 1–4.

Török, G. (2005b), QPOs in microquasars and Sgr A*: measuring the black hole spin, *Astronom. Nachr.*, **326**(9), pp. 856–860, `astro-ph/0510669`.

Török, G., Abramowicz, M. A., Kluźniak, W. and Stuchlík, Z. (2005), The orbital resonance model for twin peak kHz quasi periodic oscillations in microquasars, *Astronomy and Astrophysics*, **436**(1), pp. 1–8, `astro-ph/0401464`.

Török, G. and Stuchlík, Z. (2005), Radial and vertical epicyclic frequencies of Keplerian motion in the field of Kerr naked singularities. Comparison with the black hole case and possible instability of naked singularity accretion discs, *Astronomy and Astrophysics*, **437**(3), pp. 775–788, `astro-ph/0502127`.

van der Klis, M. (2000), Millisecond Oscillations in X-ray Binaries, *Annual Review of Astronomy and Astrophysics*, **38**, pp. 717–760.

Proceedings of *RAGtime 6/7: Workshops on black holes and neutron stars, Opava, 16–18/18–20 September, 2004/2005*
S. Hledík and Z. Stuchlík, editors, Silesian University in Opava, Czech Republic, 2005, pp. 209–222

Radial pulsations and dynamical stability of spherically symmetric perfect fluid configurations in spacetimes with a nonzero cosmological constant

Zdeněk Stuchlík[a] and Stanislav Hledík[b]

Institute of Physics, Faculty of Philosophy & Science, Silesian University in Opava,
Bezručovo nám. 13, CZ-746 01 Opava, Czech Republic
[a]`Zdenek.Stuchlik@fpf.slu.cz`
[b]`Stanislav.Hledik@fpf.slu.cz`

ABSTRACT

The equation governing small radial oscillations and the related Sturm–Liouville eigenvalue equation for eigenmodes of the oscillations are determined for spherically symmetric configurations of perfect fluid in spacetimes with a nonzero cosmological constant. The Sturm–Liouville equation is then applied in the cases of spherically symmetric configurations with uniform distribution of energy density and polytropic spheres. It is shown that a repulsive cosmological constant rises the critical adiabatic index and decreases the critical radius under which the dynamical instability occurs.

1 INTRODUCTION

The recent cosmological observations (Bahcall et al., 1999) indicate that the repulsive effective cosmological constant $\Lambda > 0$ has a significant role in both the very early universe during the inflationary era (Linde, 1990) and in the present universe (Spergel et al., 2003) because of the accelerated expansion of the Universe. Of course, the magnitude of the effective cosmological constant $\Lambda > 0$ differs by many orders in the recent era and the very early era of the expansion, the origin of the effective cosmological constant can be different, but its repulsive gravitational effect can be treated in the same way. The influence of $\Lambda > 0$ on the black-hole (naked singularity) backgrounds was treated in a number of papers (Stuchlík et al., 2000; Krauss, 1998). The internal Schwarzschild spacetimes with $\Lambda \neq 0$ and uniform distribution of energy density were given in Stuchlík (2000) for star-like configurations and extended to more general situations in Böhmer (2004a,b). The polytropic and adiabatic spheres were preliminary treated and compared by Stuchlík (2005); Stuchlík and Hledík (2005b); Hledík et al. (2004). Neutron star models with regions of nuclear matter described by different relativistic equations of state that are matched together were also treated extensively, e.g., by Østgaard (2001); Urbanec et al. (2005). Their stability can be grounded on energetic considerations (Tooper, 1964), but it is more

80-7248-334-X

suitable to treat it in the dynamical way pioneered by Chandrasekhar (1964). Here, we shall present generalization of the dynamical treatment of the perfect fluid configurations stability to the case of spacetimes with $\Lambda \neq 0$. In Section 2, the dynamical equation for the radial pulsations of spherically symmetric perfect fluid configurations is derived under the assumption of adiabatic pulsations, and the related boundary conditions are specified in a way corresponding to the treatment presented in Misner et al. (1973). Then the Sturm–Liouville equation for the eigenfrequencies of pulsation eigenmodes is given. In Section 3, the Sturm–Liouville equation is treated for the configurations with uniform energy density distribution and for some polytropic spheres, using some special choice of the trial function. Concluding remarks are presented in Section 4. For completeness, we consider also the case of an attractive cosmological constant ($\Lambda < 0$).

2 RADIAL PULSATIONS AND STURM–LIOUVILLE EQUATION

In the standard Schwarzschild coordinates (t, r, θ, φ), the spacetime of the pulsating, spherically symmetric configuration is given by the spacetime element

$$\mathrm{d}s^2 = -\mathrm{e}^{2\Phi}\,\mathrm{d}t^2 + \mathrm{e}^{2\Psi}\,\mathrm{d}r^2 + r^2(\mathrm{d}\theta^2 + \sin^2\theta\,\mathrm{d}\varphi^2)\,, \tag{1}$$

where the metric coefficients are taken in the general form

$$\Psi = \Psi(r, t)\,, \qquad \Phi = \Phi(r, t)\,. \tag{2}$$

The matter inside the configuration is assumed to be a perfect fluid with $\rho(r, t)$ being the energy density and $p(r, t)$ being the isotropic pressure.

The equilibrium (static) configuration about which the configuration pulsate is determined by the functions $\Phi_0(r)$, $\Psi_0(r)$, $\rho_0(r)$, $p_0(r)$ satisfying the Einstein gravitational equations in the form

$$\frac{1}{r^2}\left(r\mathrm{e}^{-\Psi_0}\right)' + \Lambda = -\frac{8\pi G}{c^4}\,\rho_0\,, \tag{3}$$

$$-\frac{1}{r^2} + \frac{\mathrm{e}^{-\Psi_0}}{r^2} + \frac{\Phi_0'\mathrm{e}^{-\Psi_0}}{r} + \Lambda = \frac{8\pi G}{c^4}\,p_0\,, \tag{4}$$

$$\frac{1}{2}\,\mathrm{e}^{-\Psi_0}\left(\Phi_0'' + \frac{\Phi_0'^2}{2} + \frac{\Phi_0' - \Psi_0'}{r} - \frac{\Phi_0'\Psi_0'}{2}\right) + \Lambda = \frac{8\pi G}{c^4}\,p_0 \tag{5}$$

which determine the unperturbed state; here, the prime denotes $\mathrm{d}/\mathrm{d}r$.

The oscillating configuration (with perturbed quantities) is determined by the Einstein equations in the form

$$\frac{1}{r^2}\left[1-\left(r\mathrm{e}^{\Phi}\right)'\right]-\Lambda=\frac{8\pi G}{c^4}\,T_t^t\,, \tag{6}$$

$$\frac{\mathrm{e}^{\Psi}-1}{r^2}-\frac{\Phi'}{r}-\Lambda=\frac{8\pi G}{c^4}\,T_r^r\,, \tag{7}$$

$$\frac{\mathrm{e}^{-\Psi}}{2}\left[\left(\ddot{\Psi}+\frac{\dot{\Psi}^2}{2}-\frac{\dot{\Psi}\dot{\Phi}}{2}\right)-\left(\Phi''+\frac{\Phi'^2}{2}+\frac{\Phi'-\Psi'}{r}-\frac{\Phi'\Psi'}{2}\right)\right]-\Lambda=\frac{8\pi G}{c^4}\,T_\theta^\theta\,, \tag{8}$$

$$\mathrm{e}^{-\Psi}\,\frac{\dot{\Psi}}{r_0}=\frac{8\pi G}{c^4}\,T_t^r\,. \tag{9}$$

Here, prime denotes partial derivative with respect to radius and dot denotes partial derivative with respect to time.

For pulsations of a small amplitude, the metric coefficients $\Psi(r,t)$ and $\Phi(r,t)$ and the thermodynamic variables $\rho(r,t)$, $p(r,t)$ and $n(r,t)$ (n being the number density) as measured in the fluid's rest frame can be described by their small Euler variations. Thus, in general we define

$$q(r,t)=q_0(r)+\delta q(r,t)\,, \tag{10}$$

where $\delta q\equiv(\delta\Phi,\delta\Psi,\delta\rho,\delta p,\delta n)$. The pulsation is given by the radial displacement ξ of the fluid from the equilibrium position

$$\xi=\xi(r,t)\,. \tag{11}$$

The *Euler perturbations* δq are related to the *Lagrangian perturbations* Δq measured by an observer who moves with the pulsating fluid by the relation

$$\Delta q(r,t)=q(r+\xi(r,t),t)-q_0(r)\approx\delta q+q_0'\xi\,. \tag{12}$$

The pulsation, i.e., the evolution of the perturbation function, is governed by the Einstein gravitational equations which have to be combined with the energy-momentum conservation, baryon conservation, and the laws of thermodynamics. All the equations have to be *linearized* relative to the displacement from static equilibrium configuration. We have to obtain the dynamic equation for the fluid displacement $\xi(t,r)$ and the set of *initial-value equations* expressing the perturbation functions $\delta\Phi$, $\delta\Psi$, $\delta\rho$, δp, δn in terms of the displacement function $\xi(t,r)$. The cosmological constant is not perturbed as we do not assume any relation of the cosmological constant to matter. We shall perform the dynamical stability analysis following the method of Misner et al. (1973).

2.1 Baryon conservation – energy density and pressure perturbations

First, we express the velocity of the fluid element in terms of the displacement. Following Misner et al. (1973); Chandrasekhar (1964), we define

$$\frac{u^r}{u^t}=\frac{\partial\xi}{\partial t}\equiv\dot{\xi}\,. \tag{13}$$

Because the number of baryons of the fluid has to be conserved, the conservation law has to be satisfied in the general form

$$\left(nu^{\mu}\right)_{;\mu} = 0 \tag{14}$$

that can be expressed in the form

$$\frac{\mathrm{d}(\Delta n)}{\mathrm{d}\tau} = -n\left(u^{\mu}{}_{;\mu}\right) \tag{15}$$

and using the linearized expressions

$$u^{t} = \mathrm{e}^{-\Psi_0}\,(1 - \delta\Phi)\ , \qquad u^{r} = \dot{\xi}\mathrm{e}^{-\Phi_0}\,, \tag{16}$$

we arrive to the equation

$$\Delta n = n_0\left[\frac{1}{r^2\mathrm{e}^{\Psi_0}}\left(r^2\mathrm{e}^{\Phi_0}\xi\right)' + \delta\Lambda\right]. \tag{17}$$

Assuming adiabatic pulsations, the Lagrange variables in number density and pressure are related by the adiabatic index γ through the relation

$$\gamma \equiv \left(\frac{\partial\ln p}{\partial\ln n}\right)_s = \frac{n}{p}\frac{\Delta p}{\Delta n}\,, \tag{18}$$

and we arrive to the initial value equation for δp in the form

$$\delta p = -\gamma p_0\left[\frac{\left(r^2\mathrm{e}^{\Psi_0}\xi\right)'}{r^2\mathrm{e}^{\Psi_0}} + \delta\Psi\right] - \xi p_0'\,. \tag{19}$$

Notice that in terms of the Euler variables, there is (Chandrasekhar, 1964):

$$\gamma = \left(p\,\frac{\partial n}{\partial p}\right)^{-1}\left[n - (\rho + p)\frac{\partial n}{\partial\rho}\right].$$

The projection of the energy-momentum conservation law $T^{\mu\nu}{}_{;\nu} = 0$ onto the 4-velocity u^{μ} gives the local energy conservation law in the form

$$\Delta\rho = \frac{\rho_0 + p_0}{n_0}\,\Delta n \tag{20}$$

implying the initial-value equation for $\delta\rho$ in the form

$$\delta\rho = -(\rho_0 + p_0)\left[\frac{\left(r^2\mathrm{e}^{\Psi_0}\xi\right)'}{r^2\mathrm{e}^{\Psi_0}} + \delta\Psi\right] - \xi\rho_0'\,. \tag{21}$$

2.2 Metric coefficient perturbations

The perturbed stress energy tensor has linearized components

$$T_{rt} = -(\rho_0 + p_0)\, \mathrm{e}^{\Psi_0 - \Phi_0} \dot{\xi} \,, \qquad T_{rr} = p_0 + \delta p \,. \tag{22}$$

The linearized form of Eq. (9), i.e., $G_{tr} = (8\pi G/c^4) T_{tr}$, then implies the initial-value equation for $\delta\Lambda$ in the form

$$\delta\Lambda = -4\pi\, (\rho_0 + p_0)\, r \mathrm{e}^{2\Psi_0 \xi} = -\left(\Psi_0' + \Phi_0'\right) \xi \,, \tag{23}$$

while Eq. (7), i.e., $G_{rr} = (8\pi G/c^4) T_{rr}$, implies the initial-value equation for $\delta\Phi$:

$$\delta\Phi' = -\frac{\gamma}{r}\left(4\pi p_0 - \frac{\Lambda}{2}\right) \mathrm{e}^{2\Psi_0 + \Phi_0} \left(r^2 \mathrm{e}^{-\Psi_0} \xi\right)' + \frac{4\pi G}{c^4}\left[p_0' - (\rho_0 + p_0)\right] \mathrm{e}^{2\Psi_0} \xi \,. \tag{24}$$

2.3 Pulsation dynamic equation and boundary conditions

Evolution of the fluid displacement $\xi(t, r)$ is determined by the Euler equation for the 4-acceleration a_μ of the fluid elements, which is given by the projection of the energy-momentum conservation law $T^{\mu\nu}{}_{;\nu} = 0$ onto the plane orthogonal to u^μ:

$$(\rho + p) a_\mu = -p_{,\mu} - u_\mu u^\nu p_{,\nu} \,. \tag{25}$$

In the linearized form, Eq. (25) has the only nonzero component

$$a_r = \Phi_0' + \delta\Phi' + \mathrm{e}^{2(\Psi_0 - \Phi_0)} \ddot{\xi} \,. \tag{26}$$

Using the initial-value equations and introducing a renormalized displacement function

$$\zeta \equiv r^2 \mathrm{e}^{-\Phi_0} \xi \,, \tag{27}$$

we arrive at the dynamic equation governing the pulsations in the form

$$W \ddot{\zeta} = \left(P \zeta'\right)' + Q \zeta \tag{28}$$

with the functions $W(r)$, $P(r)$, $Q(r)$ determined for the equilibrium configuration by the relations

$$W \equiv (\rho_0 + p_0) \frac{1}{r^2}\, \mathrm{e}^{3\Psi_0 + \Phi_0} \,, \tag{29}$$

$$P \equiv \gamma p_0 \frac{1}{r^2}\, \mathrm{e}^{\Psi_0 + 3\Phi_0} \,, \tag{30}$$

$$Q \equiv \mathrm{e}^{\Psi_0 + 3\Phi_0} \left[\frac{(p_0')^2}{\rho_0 + p_0} \frac{1}{r^2} - \frac{4 p_0'}{r^3} - (\rho_0 + p_0) \left(\frac{8\pi G}{c^4} p_0 - \Lambda \right) \frac{\mathrm{e}^{2\Psi_0}}{r^2} \right] . \tag{31}$$

The boundary conditions must guarantee that the displacement function cannot result in a divergent energy density and pressure perturbations at the centre of the sphere, and therefore, ξ/r is finite for $r \to 0$. Further, the Lagrange variations of the pressure must keep the condition $p = 0$ at the surface of the configuration at the radius R, i.e., there is

$$\Delta p = -\gamma p_0 \frac{\mathrm{e}^{\Phi_0}}{r^2} \left(r^2 \mathrm{e}^{-\Phi_0} \xi\right)' \to 0 \qquad \text{as} \qquad r \to R \,. \tag{32}$$

2.4 Sturm–Liouville equation and dynamical stability of equilibrium configurations

The linear stability analysis can be realized by the standard assumption of the displacement decomposition

$$\zeta(r,t) = \zeta(r)\mathrm{e}^{\mathrm{i}\omega t}\,. \tag{33}$$

Then the dynamic equation reduces to the Sturm–Liouville equation and the related boundary conditions in the form

$$\left(P\zeta'\right)' + (Q + \omega^2 W)\zeta = 0\,, \tag{34}$$

$$\frac{\zeta}{r^3} \qquad \text{is finite as} \qquad r \to 0\,, \tag{35}$$

$$\gamma p_0 \frac{\mathrm{e}^{\Phi_0}}{r^2}\zeta' \to 0 \qquad \text{as} \qquad r \to R\,. \tag{36}$$

The Sturm–Liouville equation (34) and the boundary conditions determine eigenfrequencies ω_j and corresponding eigenmodes $\zeta_i(r)$, where $i = 1, 2, \ldots, n$. The physically interesting stable configurations have discrete spectrum of the normal radial modes; the i-th mode has i nodes between the centre and the surface of the configuration. The eigenvalue Sturm–Liouville (SL) problem can be expressed in the variational form of Misner et al. (1973) as the extremal values of

$$\omega^2 = \frac{\int_0^R \left(P\zeta'^2 - Q\zeta^2\right)\,\mathrm{d}r}{\int_0^R W\zeta^2\,\mathrm{d}r} \tag{37}$$

determine the eigenfrequencies ω_i and the corresponding functions $\zeta_i(r)$ are the eigenfunctions that have to satisfy the orthogonality relation

$$\int_0^R \mathrm{e}^{3\Psi_0 - \Phi_0}(p_0 + \rho_0) r^2 \xi^{(i)} \xi^{(j)}\,\mathrm{d}r = 0\,. \tag{38}$$

The absolute minimum value of Eq. (37) represents the squared frequency of the fundamental mode of pulsation. If it is negative, the configuration in unstable, as $\mathrm{e}^{\mathrm{i}\omega t}$ grows exponentially with time, if it is positive, the configuration is stable against adiabatic, radial perturbations. Therefore, a sufficient condition for the dynamical instability is the vanishing of the right hand side of Eq. (37) for a trial function satisfying the boundary conditions (Misner et al., 1973; Chandrasekhar, 1964). We shall test the SL problem in the next section for two simple cases.

Using the condition $\omega^2 = 0$ for the marginally stable configurations, we can deduce from Eq. (37) a formula giving the critical value of the adiabatic index γ_c assuming it is constant through the configuration. The formula takes the general form

$$\gamma_\mathrm{c} = \frac{\int_0^R \frac{\mathrm{e}^{\Psi_0 + 3\Phi_0}}{r^2}\left[\frac{(p_0')^2}{\rho_0 + p_0} - \frac{4p_0'}{r} - (\rho_0 + p_0)\left(\frac{8\pi G}{c^4}p_0 - \Lambda\right)\mathrm{e}^{2\Psi_0}\right]\zeta^2\,\mathrm{d}r}{\int_0^R \frac{p_0}{r^2}\mathrm{e}^{\Psi_0 + 3\Phi_0}\zeta'^2\,\mathrm{d}r}\,. \tag{39}$$

We shall give the critical adiabatic index for the special cases of the uniform and polytropic spheres in the next section.

3 DYNAMICAL INSTABILITY OF POLYTROPIC SPHERES

The Sturm–Liouville equation (34) can be used to determine the dynamical instability of spherical configurations of perfect fluid with any equation of state. Here, we shall restrict our attention to the polytropic spheres, concentrating on the special case of uniform density configurations and the spheres with the polytropic index $n = 3$.

3.1 Uniform density spheres

For spheres with uniform distribution of energy density $\rho = $ const and radius R, the Einstein structure equations can be integrated in terms of elementary functions (Stuchlík, 2000). It is useful to express the metric coefficients and the pressure in terms of the new variables

$$y^2 = 1 - \frac{r^2}{a^2}\,, \qquad y_1^2 = 1 - \frac{R^2}{a^2}\,, \tag{40}$$

with the characteristic dimension of the configuration a related to the energy density by the relation

$$a^2 = \frac{3c^4}{8\pi G\rho(1+\lambda)}\,, \tag{41}$$

where

$$\lambda = \frac{\rho_{\mathrm{vac}}}{\rho}\,, \qquad \rho_{\mathrm{vac}} = \frac{\Lambda c^4}{8\pi G}\,. \tag{42}$$

Then the metric coefficients $\mathrm{e}^{2\Phi}$ and $\mathrm{e}^{2\Psi}$ can be given by the formulas

$$\mathrm{e}^{2\Phi} = \frac{[3y_1 - y(1-2\lambda)]^2}{4(1+\lambda)^2}\,, \tag{43}$$

$$\mathrm{e}^{2\Psi} = \frac{1}{y^2}\,, \tag{44}$$

and the pressure distribution is given by

$$p = \frac{\rho(1-2\lambda)(y-y_1)}{3y_1 - (1-2\lambda)y}\,. \tag{45}$$

In the special case of $\lambda = -1$, there is $1/a^2 = 0$, and the solution must be given in a special way. There is

$$\mathrm{e}^{2\Psi} = 1\,, \qquad \mathrm{e}^{\Phi} = 1 + \frac{3GM}{2c^2R}\left(\frac{r^2}{R^2} - 1\right), \tag{46}$$

with

$$M = \frac{4\pi}{3c^2}\,\rho R^3\,, \tag{47}$$

and the pressure distribution is given by

$$p = \frac{\frac{3\rho GM}{c^2}}{2R - \frac{3GM}{c^2}} \frac{1 - \frac{r^2}{R^2}}{1 + \frac{\frac{3GM}{c^2}}{2R - \frac{3GM}{c^2}} \frac{r^2}{R^2}} . \tag{48}$$

In order to have realistic configurations with positive pressure, the condition

$$R > \frac{9GM}{2c^2(2-\lambda)} = \frac{9r_g}{4(2-\lambda)} \tag{49}$$

must be satisfied.

Considering the repulsive cosmological constant only, $\lambda > 0$, we will discuss the stability of the spheres. (Of course, except the case of $\lambda = -1$, all of the derived formulae could be applied in the case of attractive cosmological constant, $\lambda < 0$.) Introducing the variables

$$x = \frac{r}{a} , \qquad x_1 = \frac{R}{a} , \tag{50}$$

the Sturm–Liouville variational equation (37) takes the form

$$\begin{aligned} \omega^2 a^2 y_1 \int_0^{x_1} \frac{\bar{\zeta}^2 \,\mathrm{d}x}{x^2 y^3} &= \frac{y_1}{4(1+\lambda)^2} \int_0^{x_1} \frac{(1-2\lambda)^2(2y^2-1) - 9y_1^2}{x^2 y^3} \bar{\zeta}^2 \,\mathrm{d}x \\ &+ \frac{\gamma}{8} \frac{(1-2\lambda)}{(1+\lambda)^3} \int_0^{x_1} \left(\bar{\zeta}'\right)^2 \frac{(y-y_1)\,[3y_1 - (1-2\lambda)\,y]^2}{x^2 y} \,\mathrm{d}x , \end{aligned} \tag{51}$$

where

$$\bar{\zeta} \equiv x^2 \mathrm{e}^{-\Phi} \xi , \qquad \bar{\zeta}' = \frac{\mathrm{d}\bar{\zeta}}{\mathrm{d}x} . \tag{52}$$

Using the Chandrasekhar trial function (Chandrasekhar, 1964)

$$\xi \equiv x \mathrm{e}^{\Phi} , \qquad \bar{\zeta} \equiv x^3 , \tag{53}$$

we render the Sturm–Liouville variational equation to the form

$$\begin{aligned} a^2 \omega^2 y_1 \int_0^{x_1} \frac{x^4}{y^3} \,\mathrm{d}x &= \frac{y_1}{4(1+\lambda)^2} \int_0^{x_1} \left[(1-2\lambda)^2 \left(2y^2 - 1\right) - 9y_1^2\right] \frac{x^4}{y^3} \,\mathrm{d}x \\ &+ \frac{9\gamma}{8} \frac{(1-2\lambda)}{(1+\lambda)^3} \int_0^{x_1} (y-y_1)[3y_1 - (1-2\lambda)\,y]^2 \frac{x^2}{y} \,\mathrm{d}x . \end{aligned} \tag{54}$$

By the standard substitution

$$x = \sin\theta , \qquad y = \cos\theta, \qquad \theta_1 = \arcsin\frac{R}{a} , \tag{55}$$

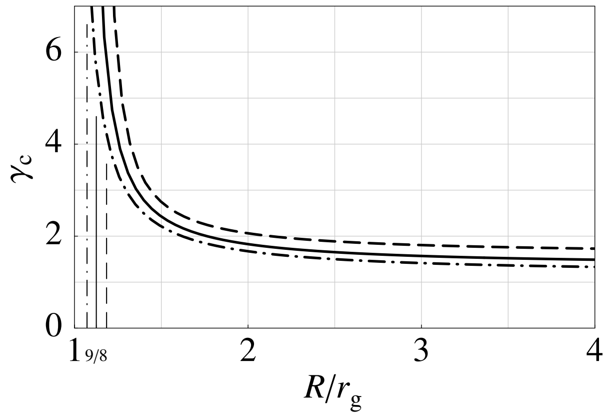

Figure 1. Dependence of the critical value of adiabatic index γ_c on sphere radius R. *Full curve:* vanishing cosmological constant $\lambda = 0$; then γ_c diverges as $R \to 9r_g/8$ from above. *Dashed curve:* positive cosmological constant $\lambda = 0.1$, the point of divergence is shifted to $1.18421 > 9/8$ according to (49), and $\gamma_{c,\lambda>0} > \gamma_{c,\lambda=0}$. *Dashed-dotted curve:* negative cosmological constant $\lambda = -0.1$, the point of divergence is shifted to $1.07143 < 9/8$ according to (49), and $\gamma_{c,\lambda<0} < \gamma_{c,\lambda=0}$.

the Sturm–Liouville equation can be transfered into the form convenient for direct integration

$$
\begin{aligned}
(\omega a)^2 \cos\theta_1 &\int_0^{\theta_1} \frac{\sin^4\theta}{\cos^2\theta}\,\mathrm{d}\theta \\
&= \frac{\cos\theta_1}{4\,(1+\lambda)^2} \int_0^{\theta_1} \left[(1-2\lambda)^2 \left(2\cos^2\theta - 1\right) - 9\cos^2\theta_1\right] \frac{\sin^4\theta}{\cos^2\theta}\,\mathrm{d}\theta \\
&+ \frac{9\gamma}{8}\frac{(1-2\lambda)}{(1+\lambda)^3} \int_0^{\theta_1} (\cos\theta - \cos\theta_1)\,[3\cos\theta_1 - (1-2\lambda)\cos\theta]^2 \sin^2\theta\,\mathrm{d}\theta\,. \qquad (56)
\end{aligned}
$$

The critical value of the adiabatic index γ_c, given by the condition $\omega = 0$, can then be determined by direct integration of the r.h.s. of the Sturm–Liouville equation (34). The results are illustrated in Fig. 1.

As shown by Chandrasekhar (1964), the most interesting results are obtained in the limit of $\theta_1 \to 0$, because in such situations the chosen trial functions tend to proper solutions.

Assuming $\theta_1 \to 0$, the Sturm–Liouville equation reduces into the form

$$
\begin{aligned}
(\omega a)^2 = \frac{1}{2(1+\lambda)^2} \Bigg\{ &(1+\lambda)\left[3\gamma\,(1-2\lambda) - 4\left(1-\frac{\lambda}{2}\right)\right] \\
&- \frac{{\theta_1}^2}{14}\,[18\gamma(1-2\lambda)(3+\lambda) - 53 - 40\lambda(1-\lambda)] \Bigg\} \qquad (57)
\end{aligned}
$$

and we arrive to a simple asymptotic formula for the critical adiabatic index

$$\gamma_{\mathrm{c}} = \frac{2(2-\lambda)}{3(1-2\lambda)} + \frac{19-4\lambda(13-7\lambda)}{42(1-2\lambda)(1+\lambda)}\frac{R^2}{a^2}\,. \tag{58}$$

Using the relation for the gravitational radius of the configuration,

$$\frac{R^2}{a^2} = (1+\lambda)\frac{2GM}{c^2R} = (1+\lambda)\,\frac{r_{\mathrm{g}}}{R}\,, \tag{59}$$

the condition of instability takes the form

$$\gamma < \gamma_{\mathrm{c}} \equiv \frac{2(2-\lambda)}{3(1-2\lambda)} + \frac{19-4\lambda(13-7\lambda)}{42(1-2\lambda)(1+\lambda)}\frac{r_{\mathrm{g}}}{R}\,. \tag{60}$$

In the case of vanishing cosmological constant ($\lambda = 0$), we arrive at the well known result (Chandrasekhar, 1964)

$$\gamma < \gamma_{\mathrm{c}} \equiv \frac{4}{3} + \frac{19}{42}\frac{r_{\mathrm{g}}}{R}\,. \tag{61}$$

3.2 Polytropic spheres

The polytropic spheres are characterized by the equation of state

$$p = K\rho^{1+\frac{1}{n}} \tag{62}$$

where n is the polytropic index and K is a constant related to a concrete sphere. The spheres are characterized by the relativistic parameter giving ratio of the central pressure and energy density

$$\sigma = \frac{p_{\mathrm{c}}}{\rho_{\mathrm{c}}c^2}\,. \tag{63}$$

The density and pressure profiles are given by the relations (Tooper, 1964; Stuchlík, 2002)

$$\rho = \rho_{\mathrm{c}}\theta^n\,, \qquad p = p_{\mathrm{c}}\theta^{n+1}\,, \tag{64}$$

where $\theta(x)$ is a function of the dimensionless radius

$$x \equiv \frac{r}{L}\,, \qquad L \equiv \left[\frac{\sigma(n+1)c^2}{4\pi G\rho_{\mathrm{c}}}\right]^{\frac{1}{2}}\,, \tag{65}$$

where L determines the characteristic length scale of the configuration. The Einstein equations imply that the function $\theta(x)$ and the "mass" function $v(x) \equiv m(x)/M$ are determined by the set of differential equations (Stuchlík and Hledík, 2005a)

$$x^2\frac{\mathrm{d}\theta}{\mathrm{d}x}\frac{1-2\sigma(n+1)\left(v(x)x^{-1}+\frac{1}{3}\lambda x^2\right)}{1+\sigma\theta} + v(x) - \frac{2\lambda}{3}x^3 = -\sigma x\theta\frac{\mathrm{d}v}{\mathrm{d}x}\,, \tag{66}$$

$$\frac{\mathrm{d}v}{\mathrm{d}x} = x^2\theta^n\,. \tag{67}$$

The edge of the configuration is located at the first solution $\theta(x_1) = 0$ of Eqs (66) and (67). The radius and mass of the configuration are determined by x_1 and $v(x_1)$ through the relations

$$R = Lx_1 \,, \tag{68}$$

$$M = 4\pi L^3 \rho_c v(x_1) = \frac{c^2}{G} L\sigma(n+1)v(x_1) \,. \tag{69}$$

The radial metric coefficient is then given by

$$e^{-2\Psi} = 1 - 2\sigma(n+1)\left[\frac{v(x)}{x} + \frac{\lambda}{3}x^2\right] \tag{70}$$

while the temporal metric coefficient is

$$e^{2\Phi} = (1+\sigma\theta)^{-2(n+1)}\left\{1 - 2\sigma\,(n+1)\left[\frac{v(x_1)}{x_1} + \frac{\lambda}{3}x_1^2\right]\right\} \,. \tag{71}$$

The variational Sturm–Liouville equation for dynamical stability of the polytropic spheres with respect to radial pulsations now takes the form (assuming γ constant in the configuration)

$$\omega^2 L^2 \rho_c c^2 \int_0^{x_1} e^{3\Psi+\Phi}\theta^n(1+\sigma\theta)\bar{\zeta}^2\,\frac{dx}{x^2} = \gamma\sigma\rho_c c^2 \int_0^{x_1} e^{\Psi+3\Phi}\theta^{n+1}\left(\frac{d\bar{\zeta}}{dx}\right)^2\frac{dx}{x^2} \tag{72}$$

$$- \sigma(n+1)\rho_c c^2 \int_0^{x_1} e^{\Psi+3\Phi}\left\{\theta^n\frac{d\theta}{dx}\frac{4}{x}\left[\frac{\sigma(n+1)x}{1+\sigma\theta}\frac{d\theta}{dx} - 1\right]\right. \tag{73}$$

$$\left. - 2(1+\sigma\theta)\theta^n\left(\sigma\theta^{n+1} - \lambda\right)e^{2\Psi}\right\}\bar{\zeta}^2\,\frac{dx}{x^2} \,. \tag{74}$$

The relation of derivatives of p and Φ is transfered into the form

$$\frac{d\Phi}{dx} = -\frac{2(n+1)\sigma}{1+\sigma\theta}\frac{d\theta}{dx} \,. \tag{75}$$

Following Chandrasekhar (1964), it is convenient to use the trial functions

$$\xi_1 = xe^{\Phi/2} \,, \qquad \xi_2 = x \,, \tag{76}$$

yielding

$$\bar{\zeta}_1 = x^3 e^{-\Phi/2} \,, \qquad \bar{\zeta}_2 = x^3 e^{-\Phi} \,. \tag{77}$$

The critical value of the adiabatic index can be determined by numerical integration only. The results are given in Fig. 2.

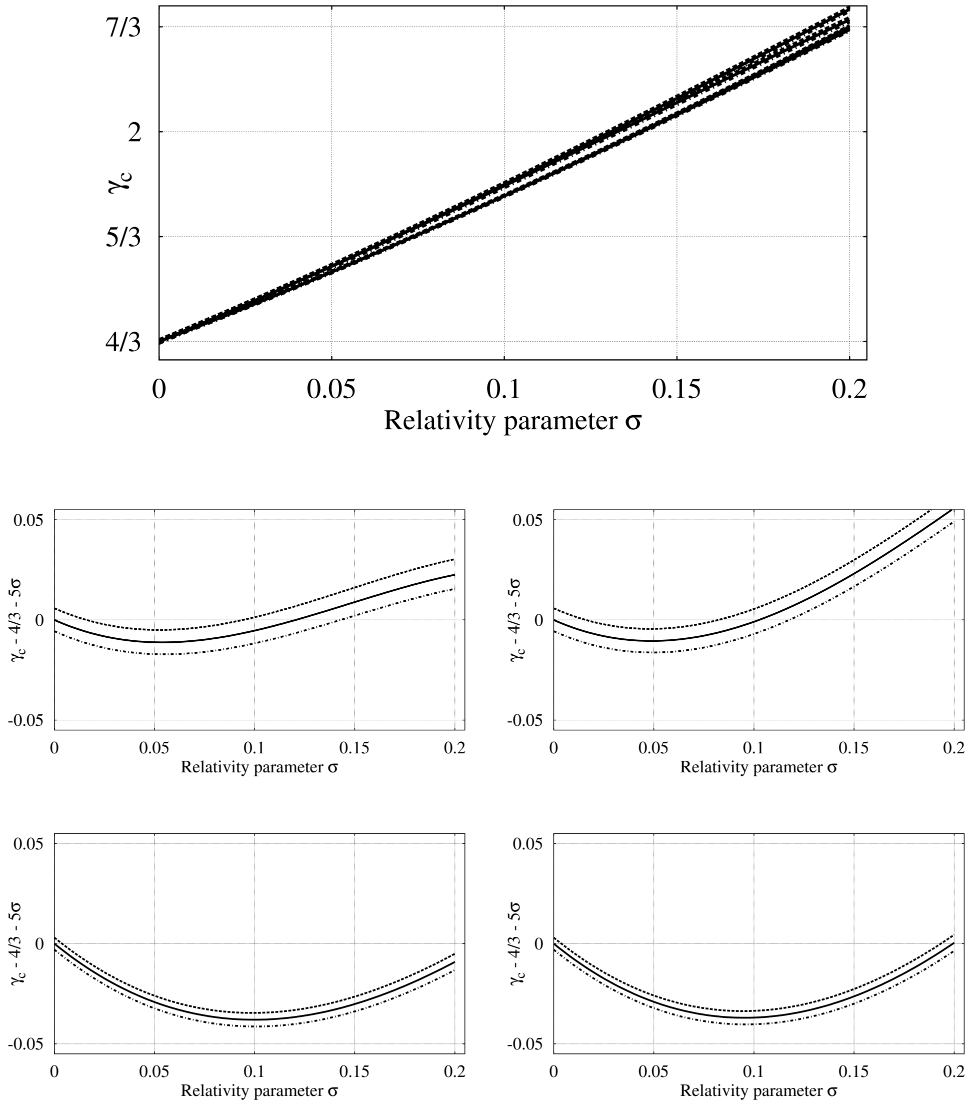

Figure 2. Dependence of the critical value of adiabatic index $\gamma_c(\sigma; n, \lambda)$ on relativistic parameter σ defined by Eq. (63). *Top panel:* Regardless of the value of polytropic index $n = 3, 1.5$ and cosmological parameter $\lambda = 0, \pm 0.0007$, within the interval $\sigma \in \langle 0, 0.2 \rangle$ the dependence pursues common, approximately linear trend: $\gamma_c(\sigma; n, \lambda) \approx 4/3 + 5\sigma$. *Remaining panels:* Deviation of the dependence $\gamma_c(\sigma; n, \lambda)$ from the common trend for $n = 3$ (*middle row*) and $n = 1.5$ (*bottom row*), numerically calculated for Chandrasekhar trial functions (76). *Left column:* using trial function ξ_1, *right column:* using trial function ξ_2. Full curves correspond to vanishing cosmological constant, while dashed (dashed-dotted) curves correspond to positive (negative) cosmological constant expressed in terms of cosmological parameter $\lambda = \pm 0.0007$.

4 CONCLUDING REMARKS

We consider the role of a nonzero cosmological constant in the problem of dynamical instability of spherically symmetric configurations of perfect fluid. The Sturm–Liouville variational equation for eigenmodes of radial pulsations of general spherically symmetric perfect fluid configurations is derived and then applied in two special cases of spheres with uniform distribution of energy density (Stuchlík, 2000), and of the polytropic spheres (Stuchlík and Hledík, 2005b). The case of uniform spheres can be properly taken as a test bed of the dynamical instability problem – although these solutions of the Einstein equations are of rather artificial character, they reflect quite well the basic properties of very compact objects (Glendenning, 1988). Moreover, analysis of their properties can be given in terms of elementary functions.

It is shown by Chandrasekhar (1964) that the critical value of the adiabatic index is about $\gamma = 4/3$ in the case of uniform spheres and it is influenced by the ratio of the radius of the sphere and its gravitational radius (given by its mass). We generalize these results, showing that the positive (negative) cosmological constant is rising (lowering) the critical adiabatic index.

In fact, for the onset of the dynamical instability the inequality

$$R < R_{\mathrm{c}} \equiv \frac{2GM}{c^2} \frac{19 - 4\lambda(13 - 7\lambda)}{42\left[\gamma - \frac{2(2-\lambda)}{3(1-2\lambda)}\right]} \tag{78}$$

must be satisfied, as follows from Eq. (60). When γ will be slightly higher than $4(1 - \lambda/2)/[3(1 - 2\lambda)]$, the dynamical instability occurs when the configuration is contracted under the critical radius R_{c}. Similar phenomena are observed in the case of polytropic spheres, when the instability analysis can be realized numerically.

ACKNOWLEDGEMENTS

The present work was supported by the Czech grant MSM 4781305903.

REFERENCES

Bahcall, N., Ostriker, J. P., Perlmutter, S. and Steinhardt, P. J. (1999), The cosmic triangle: Revealing the state of the universe, *Science*, **284**, pp. 1481–1488.

Böhmer, C. G. (2004a), Eleven spherically symmetric constant density solutions with cosmological constant, *Gen. Relativity Gravitation*, **36**, p. 1039.

Böhmer, C. G. (2004b), Static perfect fluid balls with given equation of state and cosmological constant, *General Relativity and Quantum Cosmology*, pp. 1219–1225, `gr-qc/0409030`.

Chandrasekhar, S. (1964), The dynamical instability of gaseous masses approaching the Schwarzschild limit in general relativity, *Astrophys. J.*, **140**, p. 417.

Glendenning, N. K. (1988), *Phys. Rev. C*, **37**, p. 2733.

Hledík, S., Stuchlík, Z. and Mrázová, K. (2004), Comparison of general relativistic polytropic and adiabatic fluid spheres with a repulsive cosmological constant, in S. Hledík and Z. Stuchlík, editors, *Proceedings of RAGtime 4/5: Workshops on black holes and neutron stars, Opava, 14–16/13–15 October 2002/2003*, pp. 75–89, Silesian University in Opava, Opava, ISBN 80-7248-242-4.

Krauss, L. M. (1998), The end of the age problem, and the case for a cosmological constant revisited, *Astrophys. J.*, **501**(2), pp. 461–466, URL `http://cdsaas.u-strasbg.fr:2001/ApJ/journal/issues/ApJ/v501n2%/37388/37388.html`.

Linde, A. D. (1990), *Particle Physics and Inflationary Cosmology*, Gordon and Breach, New York.

Misner, C. W., Thorne, K. S. and Wheeler, J. A. (1973), *Gravitation*, Freeman, San Francisco.

Østgaard, E. (2001), Internal structure of neutron stars, in S. Hledík and Z. Stuchlík, editors, *Proceedings of RAGtime 2/3: Workshops on black holes and neutron stars, Opava, 11–13/8–10 October 2000/01*, pp. 73–102, Silesian University in Opava, Opava, ISBN 80-7248-131-2, URL `http://uf.fpf.slu.cz/rag/`.

Spergel, D. N., Verde, L., Peiris, H. V., Komatsu, E., Nolta, M. R., Bennett, C. L., Halpern, M., Hinshaw, G., Jarosik, N., Kogut, A., Limon, M., Meyer, S. S., Page, L., Tucker, G. S., Weiland, J. L., Wollack, E. and Wright, E. L. (2003), First Year Wilkinson Microwave Anisotropy Probe (WMAP) Observations: Determination of Cosmological Parameters, *Astrophys. J. Suppl.*, **148**, p. 175, `astro-ph/0302209`.

Stuchlík, Z. (2000), Spherically symmetric static configurations of uniform density in spacetimes with a non-zero cosmological constant, *Acta Phys. Slovaca*, **50**(2), pp. 219–228, ISSN 0323-0465/00.

Stuchlík, Z. (2002), The role of a repulsive cosmological constant in astrophysical processes, in O. Semerák, J. Podolský and M. Žofka, editors, *Gravitation: Following the Prague Inspiration (A Volume in Celebration of the 60th Birthday of Jiří Bičák)*, pp. 27–83, World Scientific, New Jersey, London, Singapore, Hong Kong, ISBN 981-238-093-0.

Stuchlík, Z. (2005), Spherically symmetric steady and adiabatic flow of perfect fluid in the Schwarzschild–de Sitter spacetimes, in preparation.

Stuchlík, Z. and Hledík, S. (2005a), Excitation of oscillations by a small inhomogeneity on the surface of a neutron star, pp. 189–208, this volume.

Stuchlík, Z. and Hledík, S. (2005b), General relativistic polytropes with a nonzero cosmological constant, in preparation.

Stuchlík, Z., Slaný, P. and Hledík, S. (2000), Equilibrium configurations of perfect fluid orbiting Schwarzschild–de Sitter black holes, *Astronomy and Astrophysics*, **363**(2), pp. 425–439, ISSN 0004-6361 (printed version), 1432-0746 (parallel-to-print version), URL `http://link.springer.de/link/service/journals/00230/tocs/t036%3002.htm`.

Tooper, R. F. (1964), General relativistic polytropic fluid spheres, *Astrophys. J.*, **140**(2), pp. 434–459.

Urbanec, M., Miller, J. and Stone, J. R. (2005), Matching of equations of state: influence on calculated neutron star models, pp. 357–362, this volume.

S. Hledík and Z. Stuchlík, editors, Silesian University in Opava, Czech Republic, 2005, pp. 223–230

Friedman models with the superstring dark energy

Zdeněk Stuchlík and Martin Kološ

Institute of Physics, Faculty of Philosophy & Science, Silesian University in Opava, Bezručovo nám. 13, CZ-746 01 Opava, Czech Republic

ABSTRACT
The Friedman models of the Universe with the superstring dark energy are constructed. According to the spacetime foam approach the stringy dark energy appears to be inversely proportional to the cosmic scale factor. Evolution of the Friedman models is discussed under this assumption and compared with the standard models.

1 INTRODUCTION

The evolution of the cosmic scale factor a in dependence on the cosmic time t is given by the Friedman equations of the standard cosmology (Misner et al., 1973)

$$3\frac{\dot{a}^2+k}{a^2} = 8\pi\rho\,, \tag{1}$$

$$-2\frac{\ddot{a}}{a^2} - \frac{\dot{a}^2+k}{a^2} = 8\pi p\,, \tag{2}$$

where $\dot{} \equiv \mathrm{d}/\mathrm{d}t$. It is assumed that the energy density ρ and pressure p of the perfect fluid representing the matter content of the Universe fulfil the special simple kind of barotropic equation of state

$$p = w\rho\,. \tag{3}$$

Combining (1) and (2), we obtain the dynamic Friedman equation

$$\frac{\ddot{a}}{a} = -\frac{4\pi}{3}(\rho + 3p) \tag{4}$$

implying that the gravitational the force is given by $\rho + 3p$, and the pressure contributes substantially the force. It follows from (4) that for $\rho + 3p < 0$ the expansion of the Universe must be accelerated.

Recent observations (Riess et al., 2004; Spergel et al., 2003) show that expansion of the Universe at the present era is accelerated. From Friedman equation (4) it follows that there must be some special form of matter (energy) with $w < -1/3$ in the equation of state. This is called dark energy. The observations imply that the dark energy forms about 70% of the total mass of the Universe. It is curious that a form of energy, about which we know so few, forms nearly all the content of the Universe.

80-7248-334-X

2 DARK ENERGY FROM SUPERSTRING THEORY

In Ellis et al. (2000)[1] superstring theory has been applied in the framework of the spacetime foam approach to quantization of gravity and one of the most interesting results of this approach is that energy of vacuum is varying with the cosmological time like $1/t^2$. Therefore, in the stringy spacetime foam approach the vacuum energy behaviour resembles elasticity of spacetime and the dark energy looks like the cosmological "constant" that changes with the cosmological time and the scale factor of the expanding Universe according to the law

$$\Lambda(t) = \frac{\Lambda(0)}{t^2} \sim \frac{1}{a(t)} . \tag{5}$$

Therefore, it is interesting to consider a specific form of dark energy with density changing with scale factor according to the law

$$\rho_{\mathrm{DE(stringy)}} \sim \frac{1}{a(t)} . \tag{6}$$

We shall treat the cosmological models under assumption of the presence of the stringy dark energy and standard general relativistic equations of evolution of the Universe.

3 EVOLUTION OF THE FRIEDMAN MODELS WITH THE STRINGY DARK ENERGY

We assume the Universe containing the dust ($p_{\mathrm{d}} = 0$) with energy density $\rho_{\mathrm{d}} > 0$ and dark energy with $\rho_{\mathrm{DE}} > 0$. The Friedman Eqs (1) and (2) then take the form

$$3\frac{\dot{a}^2 + k}{a^2} = 8\pi\rho_{\mathrm{d}} + 8\pi\rho_{\mathrm{DE}} , \tag{7}$$

$$-2\frac{\ddot{a}}{a^2} - \frac{\dot{a}^2 + k}{a^2} = -\frac{16\pi}{3}\rho_{\mathrm{DE}} . \tag{8}$$

Further, we assume the Big Bang beginning of the Universe with $a(t)$ continuously growing with the cosmic time. The scale factor is tuned by the conditions $a(0) = 0$ and $a(T_0) = 1$, where t_0 denotes the age of the Universe.

The solutions of the Friedman equations can be appropriately characterized by introducing an effective potential depending on the scale factor $a(t)$. Writing the Friedman Eq. (7) in the form

$$\dot{a}^2 = \frac{8\pi}{3}\frac{\epsilon}{a} + \frac{8\pi}{3}\sigma a - k , \tag{9}$$

where ϵ and σ are constant during the expansion of the Universe and introducing the constants $X = 8\pi\epsilon/3$ and $Y = 8\pi\sigma/3$, Eq. (9) can be given in the form corresponding to the motion in an effective potential

$$\left(\frac{\mathrm{d}a}{\mathrm{d}t}\right)^2 = \frac{X}{a} + Ya - k = E^2 - V^2(a) . \tag{10}$$

---

[1] For another version of this approach see, e.g., Lopez and Nanopulos (1995).

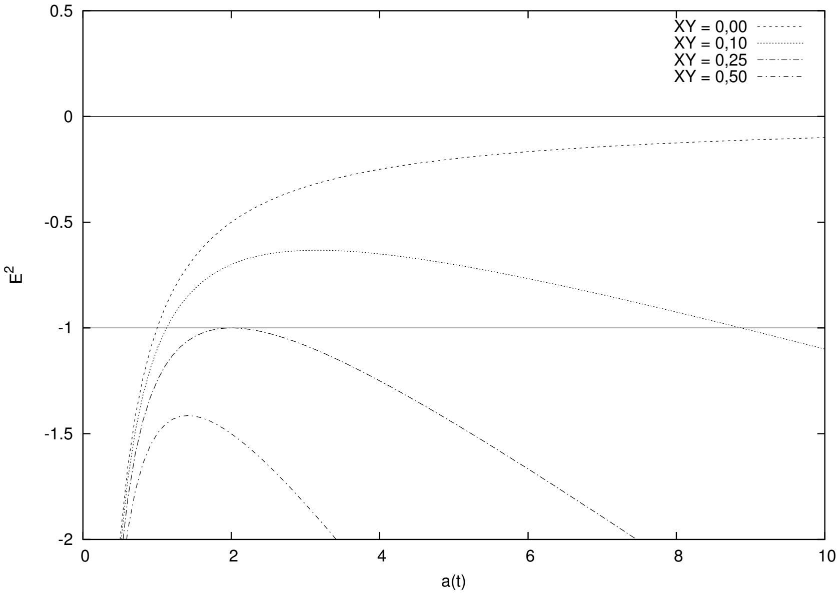

Figure 1. The effective potential determining evolution of the scale factor in the Universe with the stringy dark energy.

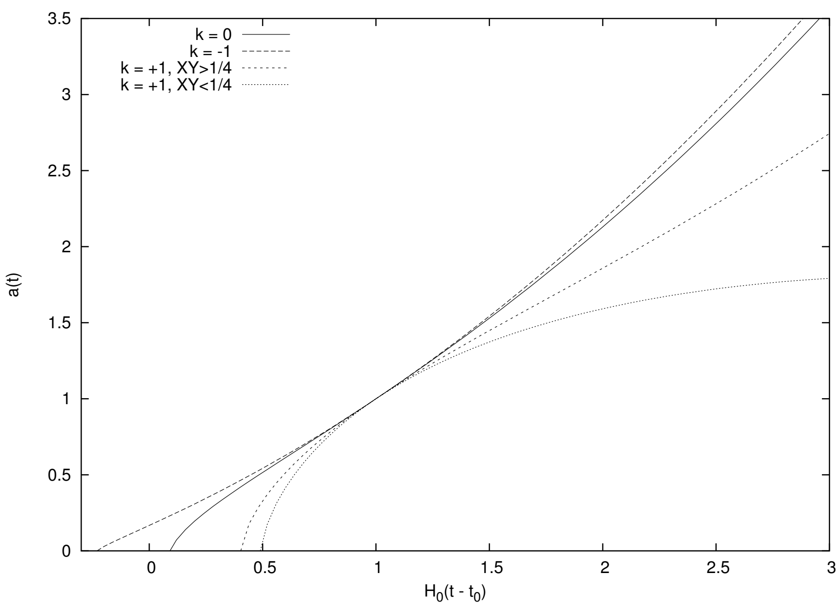

Figure 2. Evolution of the scale factor $a(t)$ of the Universe with the stringy dark energy, given for different values of the curvature term.

The equation describes motion with energy $E^2 = -k$ in the effective potential

$$V^2(a) = -\frac{X}{a} - Ya\,. \tag{11}$$

The motion determined by the potential $V^2(a)$ is possible if $E^2 > V^2(a)$. The motion is limited by the turning points given by

$$\left(\frac{\mathrm{d}a}{\mathrm{d}t}\right)^2 = 0\,, \tag{12}$$

i.e., by $E = V(a)$. The behaviour of the effective potential is given in Fig. 1 for some typical values of the evolution constants. Now, it is possible to determine the behaviour of the scale factor for a given parameter k and initial values of ρ_{d}, ρ_{DE}.

The open Universe ($k = -1$) and the flat Universe ($k = 0$) will be always expanding. The closed Universe ($k = +1$) will be expanding forever if $XY > 1/4$. In the closed Universe with $XY < 1/4$ the expansion is converted into contraction at the turning point.

The solutions of Eq. (9) are given in Fig. 2. The explicit form of the solution can be given in two ways.

3.1 Direct integration

Equation (9) gives the scale factor evolution in the implicit form $t = t(a)$. The differential equation of the first order (9) is separable and the solution can be determined in terms of elliptic integrals. We obtain the equation

$$t(a) = \int \sqrt{\frac{a}{Ya^2 - ka + X}}\,\mathrm{d}a\,, \tag{13}$$

that can be expressed in the form

$$t(a) = \int \sqrt{\frac{a}{(a-A)(a-B)}}\,\mathrm{d}a\,, \tag{14}$$

where

$$A = \frac{k + \sqrt{k^2 - 4XY}}{2Y} \qquad \text{and} \qquad B = \frac{k - \sqrt{k^2 - 4XY}}{2Y}\,, \tag{15}$$

are the roots of the polynomial of Eq. (13). For $k = 0$ both roots are imaginary and $A = -B$. In the case of $k = \pm 1$ the roots are real for $XY < 1/4$, while they are complex for $XY > 1/4$.[2] The scale factor can then be given in an implicit form by the relation

$$t(a) = 2\sqrt{B}\,(\mathrm{E}[\varphi, k] - \mathrm{F}[\varphi, k])\,, \tag{16}$$

[2] The special case of $XY = 1/4$ is not considered here.

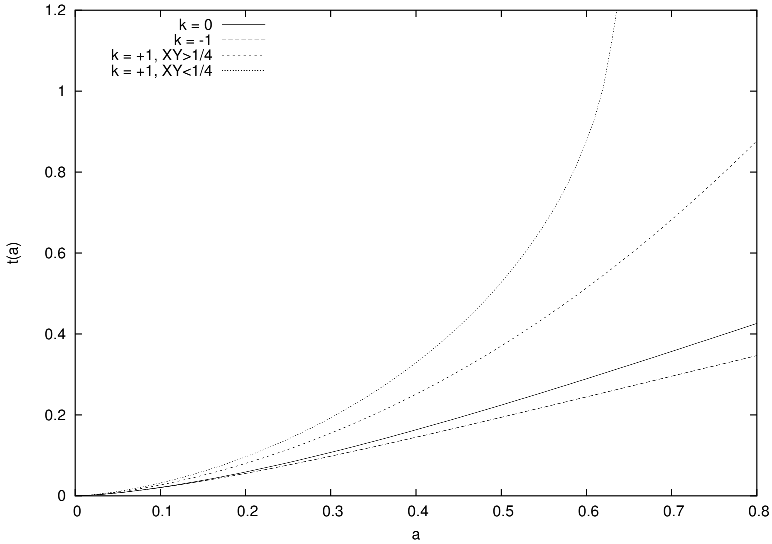

Figure 3. The cosmic time given as a function of the scale factor. Now, the expansion of the models is synchronized at the Big Bang, instead of the present time t_0, as is done in Fig. 2.

where

$$\varphi = \mathrm{i}\,\mathrm{argsinh}\left(\sqrt{-\frac{a}{A}}\right) \qquad \text{and} \qquad k = \frac{A}{B}\,. \tag{17}$$

The functions $\mathrm{F}[\varphi, k]$ and $\mathrm{E}[\varphi, k]$ are the elliptic integrals of the first and the second kind defined in the standard way by

$$\mathrm{F}[\varphi, k] = \int_0^{\varphi} \frac{\mathrm{d}\varphi}{\sqrt{1 - k^2 \sin^2 \varphi}}\,, \tag{18}$$

$$\mathrm{E}[\varphi, k] = \int_0^{\varphi} \sqrt{1 - k^2 \sin^2 \varphi}\,\mathrm{d}\varphi\,. \tag{19}$$

The dependence of the scale factor on the cosmic time $a = a(t)$ is implicitly given by Eq. (16) – for the given values of the curvature parameter k, the function $a(t)$ is determined numerically and illustrated in Fig. 3.

3.2 A parametric integration

The scale factor and the cosmic time can be given in the parametric form

$$a = a(\alpha)\,, \tag{20}$$

$$t = t(\alpha)\,, \tag{21}$$

where α is an appropriately chosen parameter; it is so called development angle. If the parameterization given by

$$dt = \sqrt{a}\, d\alpha\,, \tag{22}$$

is chosen,[3] the integral in Eq. (14) is transformed into the form

$$\alpha(a) = \int \sqrt{\frac{1}{(a-A)(a-B)}}\, da\,, \tag{23}$$

which leads to elementary functions, not elliptic integrals. In the case of $k = 0$, the evolution of the scale factor in terms of the new parameter α is determined by

$$a(\alpha) = \sqrt{\frac{X}{Y}} \sinh\left(\sqrt{Y}\alpha\right)\,. \tag{24}$$

Equation (22) then determines the function $t(\alpha)$ in the form

$$t(\alpha) = 2\sqrt{\mathrm{i}}\,\sqrt[4]{XY}\,\mathrm{E}\left[\frac{\pi}{4} - \frac{\sqrt{-Y}\,\alpha}{2}, 2\right]\,, \tag{25}$$

where, of course, the elliptic integral of the second kind appears.

4 COMPARISON WITH THE STANDARD MODELS

We shall compare there types of the Friedman cosmological models.

(a) The model containing the dusty matter only.
(b) The model with addition of the repulsive cosmological constant $\rho_\Lambda = \text{const} > 0$.
(c) The model with addition of the stringy dark energy characterized by $\rho_{\text{DE}} \sim 1/a(t)$.

Equation (1) can be expressed in the form

$$1 = \Omega_{\text{DE}} + \Omega_{\text{d}} + \Omega_k\,, \tag{26}$$

where

$$\Omega_{\text{i}} = \rho_{\text{i}}/\rho_{\text{crit}}\,; \qquad \rho_{\text{crit}} = 3H/8\pi G\,. \tag{27}$$

There exists an extremal point in the evolution of the scale factor just when $H = \dot{a}/a = 0$. Using this condition we arrive in the case of three models considered here to the relations

(a) $$\Omega_{k(0)}a + \Omega_{\text{d}(0)} = 0\,, \tag{28}$$
(b) $$\Omega_{\text{DE}(0)}a^3 + \Omega_{k(0)}a + \Omega_{\text{d}(0)} = 0\,, \tag{29}$$
(c) $$\Omega_{\text{DE}(0)}a^2 + \Omega_{k(0)}a + \Omega_{\text{d}(0)} = 0\,. \tag{30}$$

---
[3] We can also consider parameterizations given by the relations $dt = (a-A)^{-1/2}\, d\alpha$ and $dt = [a/(a-A)]^{1/2}\, d\alpha$.

Therefore, the turning point in the evolution of $a(t)$ exist, if there is a positive root of Eqs (28)–(30). When considering $\Omega_{\mathrm{d}(0)} > 0$ and $\Omega_{\mathrm{DE}(0)} > 0$, we can conclude that for the curvature factors of $k = -1$ a $k = 0$ the scale factor $a(t)$ grows forever. For $k = +1$ the behaviour of $a(t)$ is more complicated. In the case (a), the closed Universe always collapse, however in the cases (b) and (c), it is possible even for $k = +1$ that there exist models expanding forever.

Finally, we determine the age of the Universe as given by the three models considered above. For the dusty model and the the dusty model with the repulsive cosmological constant, we can use the standard results (Misner et al., 1973). In the case of the dusty model with the stringy dark energy, the age is given by the formula

$$t_0 = \frac{1}{H_0}\int_0^1 \frac{a\,\mathrm{d}a}{\left(\Omega_{\mathrm{DE}(0)}a^3 + \Omega_{k(0)}a^2 + \Omega_{\mathrm{d}(0)}a\right)^{1/2}}\,. \tag{31}$$

Taking into account recently given values of the cosmic parameters[4] the age of the Universe according to the considered models is given by

(a) $t_0 = 11.3 \times 10^9$ years, (32)

(b) $t_0 = 13.5 \times 10^9$ years, (33)

(c) $t_0 = 12.7 \times 10^9$ years. (34)

The age of the model with stringy dark energy (c) is between the age of the model with the repulsive cosmological constant (b) and the age of the standard dusty model (a).

5 CONCLUSIONS

The Friedman dusty model of the Universe with the stringy dark (vacuum) energy is discussed and compared with the standard model, and the model with the repulsive cosmological constant. The special dependence of the stringy vacuum energy density on the scale factor of the Universe causes an interesting and strong shift of the stringy model properties in comparison with both the other models, as the role of the dark energy grows with the redshift factor. Then the age of the stringy models is between the ages of the standard model and the $\Lambda > 0$ model. Further, the beginning of the dominance of the stringy dark energy shifts to higher redshift in comparison with the repulsive cosmological constant. It follows from the Fig. 4 that this happens for the redshift factor higher about twice in comparison with the case of the repulsive cosmological constant. For the stringy model the scale factor dependence on the cosmic time is between those of the standard model and the model with the cosmological constant.

[4] $\Omega_{\mathrm{DE}(0)} = 0.7$, $\Omega_{\mathrm{d}(0)} = 0.3$, $k = 0$, $H_0 = 1/14 \times 10^{-9}$ years $= 1/42 \times 10^{-16}$ s.

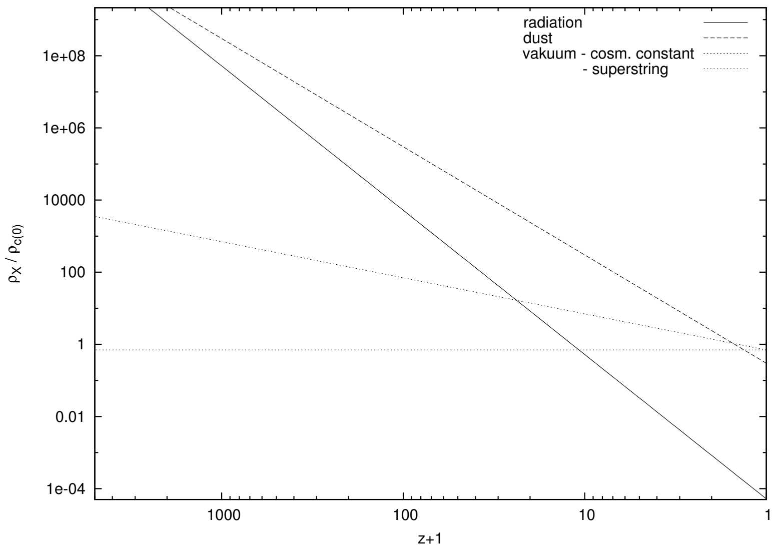

Figure 4. Evolution of the energy content of the Universe in terms of the redshift $z = 1/a(t) - 1$. The evolution is given for the dust, radiation, vacuum energy and stringy dark energy.

ACKNOWLEDGEMENTS

The present work was supported by Czech grants MSM 4781305903, GAČR 202/03/1147 and by the Committee for Collaboration of Czech Republic with CERN. One of the authors (Z. S.) would like to acknowledge the perfect hospitality at the CERN's Theory Division where part of the work was realized.

REFERENCES

Ellis, J., Mavromatos, N. E. and Nanopoulos, D. V. (2000), Time-Dependent Vacuum Energy Induced by D-Particle Recoil, *Gen. Relativity Gravitation*, **32**(5), pp. 943–958, ISSN 0001-7701, `gr-qc/9810086`, URL `http://oldwww.math.uni-potsdam.de/grg/`.

Lopez, J. L. and Nanopulos, D. V. (1995), A new cosmological constant model, *ACT-25/94*, `hep-ph/9501293`.

Misner, C. W., Thorne, K. S. and Wheeler, J. A. (1973), *Gravitation*, Freeman, San Francisco.

Riess, A. G. et al. (2004), Type Ia Supernova Discoveries at $z > 1$ From the Hubble Space Telescope: Evidence for Past Deceleration and Constraints on Dark Energy Evolution, *Astrophys. J.*, **123**, p. 145, `astro-ph/0402512`.

Spergel, D. N., Verde, L., Peiris, H. V., Komatsu, E., Nolta, M. R., Bennett, C. L., Halpern, M., Hinshaw, G., Jarosik, N., Kogut, A., Limon, M., Meyer, S. S., Page, L., Tucker, G. S., Weiland, J. L., Wollack, E. and Wright, E. L. (2003), First Year Wilkinson Microwave Anisotropy Probe (WMAP) Observations: Determination of Cosmological Parameters, *Astrophys. J. Suppl.*, **148**, p. 175, `astro-ph/0302209`.

Proceedings of *RAGtime 6/7: Workshops on black holes and neutron stars, Opava, 16–18/18–20 September, 2004/2005*
S. Hledík and Z. Stuchlík, editors, Silesian University in Opava, Czech Republic, 2005, pp. 231–240

Swiss cheese model with the superstring dark energy

Zdeněk Stuchlík and Martin Kološ

Institute of Physics, Faculty of Philosophy & Science, Silesian University in Opava,
Bezručovo nám. 13, CZ-746 01 Opava, Czech Republic

ABSTRACT
The Swiss cheese model of the Universe with the superstring dark energy is constructed. The junction conditions are shown to be fulfilled and time evolution of the matching hypersurface of the internal Schwarzschild spacetime and homogeneous external Friedman Universe is studied.

1 INTRODUCTION

One of the crucial problems of cosmology is modelling of gravitational bound systems in the expanding Friedman Universe. The simplest model of spherically symmetric gravitationally bound systems immersed in an expanding Universe is in the fully non-linear general relativistic regime described by the Einstein–Straus model of the Universe, which is also called Swiss cheese model (Einstein and Straus, 1945). A hole in the cheese represents the vacuum metric around gravitationally bounded object and cheese is the whole Universe (see Fig. 1). Precisely speaking, the Einstein–Strauss model is a Schwarzschild metric smoothly connected to the Friedman Universe.

Recent observations (Riess et al., 2004; Spergel et al., 2003) show that at its present period the expansion of the Universe is accelerated. The Friedman equations (Misner et al., 1973) imply that there must be some special form of energy governed by equation of state $p = w\rho$ with $w < -1/3$. This form of energy is called dark energy. At present, the dark energy forms about 70% of the total mass-energy of the Universe (Ostriker and Steinhardt, 1995).

We can use the effective cosmological constant in order to describe the dark energy. Then the Swiss cheese model becomes to be an Einstein–Strauss–de Sitter model and we use Schwarzschild–de Sitter metric to describe the vacuum spacetime around the gravitationally bounded object (Stuchlík, 1983, 1984, 2002).

In Ellis et al. (2000), the superstring theory has been applied to the spacetime foam ideas and one of the most interesting results is that energy of vacuum is varying with the cosmic time like $1/T^2$. Therefore, in the stringy spacetime foam model the vacuum energy behaviour resembles elasticity of spacetime and the dark energy looks like the cosmological constant that changes with the cosmological time and the scale factor of the expanding

80-7248-334-X

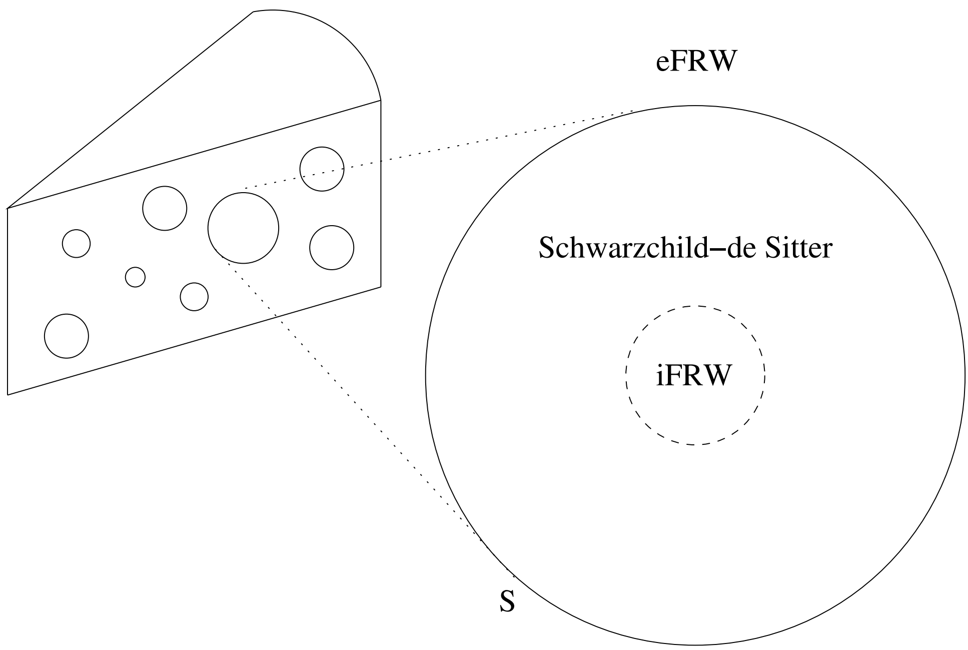

Figure 1. Einstein–Straus–de Sitter vakuola model, sometimes called Swiss cheese model, which describes gravitationally bound structure in the expanding Universe.

Universe according to the law

$$\Lambda(T) = \frac{\Lambda(0)}{T^2} \sim \frac{1}{a(T)} \,. \tag{1}$$

Therefore, we shall consider a specific form of dark energy with density changing with scale factor according to

$$\rho_{\mathrm{DE(stringy)}} \sim \frac{1}{a(T)} \,. \tag{2}$$

2 CONSTRUCTION OF THE STRINGY ESDS MODEL

In the standard ESdS model (Stuchlík, 1983, 1984, 2002), the vacuum spacetime around the gravitationally bounded object is described by the Schwarzschild–de Sitter metric. In the stringy dark energy model, there is the fundamental problem. Can we use the SdS metric also for $\Lambda = \Lambda(a)$? Of course, the exact model must be treated in the full set of equations for the stringy cosmological model. However, we can use an approximative approach based on the general relativistic equations.[1] If $\Lambda(a)$ is changing slowly, then $\Lambda(a) \approx$ const for some time, and the SdS metric can be used and its evolution can be integrated with $\Lambda = \Lambda(a)$. So we will be using SdS like metric in the form

$$\mathrm{d}s^2 = -\mathcal{A}^2(r,a)\,\mathrm{d}t^2 + \mathcal{A}^{-2}(r,a)\,\mathrm{d}r^2 + r^2(\mathrm{d}\theta^2 + \sin^2\theta\,\mathrm{d}\varphi)\,, \tag{3}$$

where

$$\mathcal{A}^2(r,a) = 1 - \frac{2M}{r} - \frac{1}{3}\Lambda(a)r^2\,. \tag{4}$$

The outer Friedman Universe is described by the Robertson–Walker geometry. Its line element in the standard comoving coordinates reads

$$\mathrm{d}s^2 = -\mathrm{d}T^2 + a^2(T)\left[\mathrm{d}\chi^2 + \Sigma_k^2(\chi)(\mathrm{d}\theta^2 + \sin^2\theta\,\mathrm{d}\varphi)\right]\,, \tag{5}$$

where

$$\Sigma_k(\chi) = \begin{cases} \sin\chi & \text{for} \quad k = +1\,, \\ \chi & \text{for} \quad k = 0\,, \\ \sinh\chi & \text{for} \quad k = -1\,. \end{cases} \tag{6}$$

The evolution of the scale factor is given by the cosmological term with the same dependence as that in the SdS metric (see Stuchlík and Kološ, 2005). In the Swiss cheese model we are matching the Friedman part $\chi > \chi_\mathrm{b}$ to the SdS part $r < r_\mathrm{b}$ and $t < t_\mathrm{b}$ through the hypersurface $\mathcal{S}_\mathrm{F} = \mathcal{S}_\mathrm{S} = \mathcal{S}$. On the hypersurface $\mathcal{S}$ freely falling test particle are moving with $\chi = \chi_\mathrm{b}$ and follow radial geodesics in the SdS spacetime $r = r_\mathrm{b}(\tau)$. The circumference of the main circles on the space slices of the hypersurface $\mathcal{S}$ (for $T =$ const) are given by

$$2\pi r_\mathrm{b} = 2\pi a(T)\,\Sigma_k(\chi_\mathrm{b})\,. \tag{7}$$

Then the induced metric (Misner et al., 1973) at the hypersurface $\mathcal{S}$ in the SdS geometry is given by

$$^{(3)}\mathrm{d}s_-^2 = -\mathrm{d}\tau^2 + r_\mathrm{b}^2(\tau)(\mathrm{d}\theta^2 + \sin^2\theta\,\mathrm{d}\varphi)\,, \tag{8}$$

where τ is the proper time of freely falling observers on $\mathcal{S}$. In the Friedman part the induced metric on $\mathcal{S}$ is given by

$$^{(3)}\mathrm{d}s_+^2 = -\mathrm{d}T^2 + a^2(T)\Sigma_k^2(\chi)(\mathrm{d}\theta^2 + \sin^2\theta\,\mathrm{d}\varphi)\,. \tag{9}$$

---

[1] We assume that $\Lambda(a)$ changes is synchronized way at the SdS spacetime, as it is a part of the Swiss cheese Universe in which the dark energy evolution is given by the evolution of the scale factor. Such an assumption is correct at least up to the time when the matching surface crosses the cosmological horizon of the SdS spacetime.

3 THE JUNCTION CONDITIONS AT THE MATCHING HYPERSURFACE $\mathcal{S}$

Necessary condition for smooth metric junction (Misner et al., 1973) is $\mathrm{d}s_+^2 \stackrel{\mathcal{S}}{=} \mathrm{d}s_-^2$ across the hypersurface $\mathcal{S}$. In our case we have spherical symmetry, therefore smoothness of metric across $\mathcal{S}$ means synchronization of proper times on the hypersurface $\mathcal{S}$

$$-\mathrm{d}T^2 \stackrel{\mathcal{S}}{=} -\mathcal{A}^2(r,a)\,\mathrm{d}t^2 + \mathcal{A}^{-2}(r,a)\,\mathrm{d}r^2 = -\mathrm{d}\tau^2\,, \tag{10}$$

i.e., we synchronize proper time of radial geodesics τ with cosmic time T on $\mathcal{S}$. The proper time τ of the radial geodesics in SdS spacetime is given by

$$\mathrm{d}\tau = \pm\left[-\mathcal{A}^2(r_\mathrm{b}) + \mathcal{E}_\mathrm{b}^2\right]^{-1/2}\mathrm{d}r\,, \tag{11}$$

where $\mathcal{E}_\mathrm{b}$ is the covariant energy of the geodesic ($\mathcal{E}_\mathrm{b}^2 = u_t^2$). We can write the first Friedman equation in the form (Misner et al., 1973)

$$\dot{a}^2 = \frac{8\pi}{3}\frac{\epsilon}{a} + \frac{1}{3}\Lambda(a)a^2 - k\,, \tag{12}$$

where $\epsilon = \rho_\mathrm{M} a^{-3}$ is a constant through the cosmic history. Now we can express the cosmic time T in the form

$$\mathrm{d}T = \pm\left(\frac{a_0}{a} - \frac{1}{3}\Lambda(a)a^2 - k\right)^{1/2}\mathrm{d}a\,, \tag{13}$$

where $a_0 = 8\pi\epsilon/3$. The proper time at the both sides of the matching surface reads

$$\mathrm{d}\tau = \pm\left[\frac{2M}{r_\mathrm{b}} + \frac{1}{3}\Lambda(a)r_\mathrm{b}^2 - \left(1-\mathcal{E}_\mathrm{b}^2\right)\right]^{-1/2}\mathrm{d}r\,, \tag{14}$$

$$\mathrm{d}T = \pm\left[\frac{a_0}{a} + \frac{1}{3}\Lambda(a)a^2 - k\right]^{-1/2}\mathrm{d}a\,. \tag{15}$$

This implies junction conditions that are independent on the function $\Lambda = \Lambda(a)$:

$$r_\mathrm{b} = a(T)\Sigma_k(\chi_\mathrm{b})\,, \tag{16}$$

$$2M = a_0\Sigma_k^3(\chi_\mathrm{b})\,, \tag{17}$$

$$1 - \mathcal{E}_\mathrm{b}^2 = k\Sigma_k^2(\chi_\mathrm{b})\,. \tag{18}$$

Of course, there junction conditions hold in the Einstein–Straus model, or in the ESdS model with the cosmological constant too (Stuchlík, 1984).

Junction of two spacetimes can be divided on two categories: surface layers and boundary surfaces. For boundary surfaces we must fulfil extra junction condition $[K_{ij}] = 0$, where K_{ij} is the extrinsic curvature. In Gaussian normal coordinates $\boldsymbol{e}_j \cdot \boldsymbol{n} = g_{in} = 0$ and for timelike hypersurface $\mathcal{S}$, the extrinsic curvature is given by

$$K_{ij} = -\tfrac{1}{2}g_{ij,n}\,. \tag{19}$$

The extrinsic curvature K_{ij}^{+} of the hypersurface $\mathcal{S}$ in the Friedman part of the model is given by the unit normal vector to the surface $\chi = \chi_{\mathrm{b}} = \mathrm{const}$

$$\boldsymbol{n} = \frac{1}{a}\frac{\partial}{\partial \chi}\,, \tag{20}$$

and according to (19), we arrive at the formula

$$K_{ij}^{+} = -\frac{1}{2a}\, g_{ij,\chi}\,. \tag{21}$$

We thus find the nonzero components in the form

$$K_{\theta\theta}^{(+)} = \frac{1}{\sin^2\theta} K_{\phi\phi}^{(+)} = -a(T)\,\Sigma_k(\chi_{\mathrm{b}})\frac{\mathrm{d}\Sigma_k(\chi_{\mathrm{b}})}{\mathrm{d}\chi}\,. \tag{22}$$

In the interior SdS spacetime, the 4-velocity of test particles of the hypersurface $\mathcal{S}$ is given by

$$\boldsymbol{u}_{(\mathrm{b})} = u_{(\mathrm{b})}^{t}\frac{\partial}{\partial t} + u_{(\mathrm{b})}^{r}\frac{\partial}{\partial r}\,, \tag{23}$$

where

$$u_{(\mathrm{b})}^{t} = \mathcal{E}_{\mathrm{b}}\mathcal{A}^{-2}(r_{\mathrm{b}})\,, \tag{24}$$

$$u_{(\mathrm{b})}^{r} = \left[\mathcal{E}_{\mathrm{b}}^{2} - \mathcal{A}^{2}(r_{\mathrm{b}})\right]^{1/2}\,. \tag{25}$$

The unit normal vector to the hypersurface $\mathcal{S}$ in the SdS spacetime reads

$$\boldsymbol{n}_{(\mathrm{b})} = n^{t}\frac{\partial}{\partial t} + n^{r}\frac{\partial}{\partial r}\,. \tag{26}$$

The hypersurface $\mathcal{S}$ is timelike then 4-vector $\boldsymbol{n}$ fulfils the condition $\boldsymbol{n}\cdot\boldsymbol{n} = 1$. The components n^t and n^r are determined by the condition

$$\boldsymbol{n}\cdot\boldsymbol{u}_{(b)} = n^{t}u_{(\mathrm{b})t} + n^{r}u_{(\mathrm{b})r} = 0\,, \tag{27}$$

which implies

$$n^{t} = u_{(\mathrm{b})r} = \mathcal{A}^{-2}(r_{\mathrm{b}})u_{(\mathrm{b})}^{r}\,, \tag{28}$$

$$n^{r} = -u_{(\mathrm{b})t} = \mathcal{E}\,. \tag{29}$$

According to Eq. (19), extrinsic curvature K_{ij}^{-} of hypersurface $\mathcal{S}$ in the inner SdS spacetime is then given by

$$K_{\theta\theta}^{(-)} = \frac{1}{\sin^2\theta}K_{\phi\phi}^{(-)} = -r_{\mathrm{b}}(T)\mathcal{E}_{\mathrm{b}}\,. \tag{30}$$

Using the junction condition (18), we arrive at

$$K_{\theta\theta}^{(-)} = \frac{1}{\sin^2\theta}\,K_{\phi\phi}^{(-)} = -r_{\mathrm{b}}(T)\left[1 - k\Sigma_k^{2}(\chi_{\mathrm{b}})\right]^{1/2}\,. \tag{31}$$

Now it is clear that Eqs (31) and (22) coincide for all three curvature parameters k, and the junction condition $[K_{ij}] = 0$ is satisfied. This means that there is no energy-momentum tensor on the hypersurface $\mathcal{S}$, i.e.,

$$S_{ij} = 0\,. \tag{32}$$

We can conclude that it is possible to construct Einstein–Straus–de Sitter model of the Universe for arbitrary dependence $\Lambda = \Lambda(a)$. The junction hypersurface $\mathcal{S}$ is only boundary surface, there is no energy-momentum tensor on $\mathcal{S}$.

4 PHYSICAL INTERPRETATION OF THE JUNCTION CONDITIONS

The first junction condition – Eq. (16) – expresses the fact that the circumference of main circles at the matching surface is the same if measured in SdS spacetime and the Friedman Universe.

When inserting the SdS spacetime into the Friedman Universe, it is necessary to have mass of the SdS part equal to mass which will be contained in a ball with radius χ_b. This is realized by the second junction condition (17)

$$2M = a_0 \Sigma_k^3(\chi_\mathrm{b}) = \tfrac{8}{3}\pi\epsilon a^3(T)\Sigma_k^3(\chi_\mathrm{b}) = 2M^*\,, \tag{33}$$

where $2M^*$ is mass of a ball with radius $a^3(T)\Sigma_k^3(\chi_\mathrm{b})$ and density ϵ. Of course, this condition is strongly restricting for use of ESdS vakuola for modelling of gravitationally bound systems.

The last condition (18) expresses the fact that the junction is realized without surface layer ($[K_{ij}] = 0$)

$$\mathcal{E}_\mathrm{b} = \left[1 - k\,\Sigma_k^2(\chi_\mathrm{b})\right]^{1/2}\,. \tag{34}$$

We know that $\Sigma_k^2(\chi_\mathrm{b}) > 0$ for all three curvature parameters k and this implies that covariant energy of the geodesic satisfies conditions

$$\mathcal{E}_\mathrm{b}^2 \begin{cases} < 1 & \text{for} \quad k = +1\,, \\ = 1 & \text{for} \quad k = 0\,, \\ > 1 & \text{for} \quad k = -1\,. \end{cases} \tag{35}$$

5 EXPANSION OF THE MATCHING HYPERSURFACE $\mathcal{S}$

According to Stuchlík and Schee (2004), expansion of the matching hypersurface $\mathcal{S}$ can influence the effectiveness of the Rees–Sciama effect on the temperature fluctuation in CMB. This effect is growing if speed of the junction hypersurface $\mathcal{S}$ is growing and can be very strong when it is approaching the speed of light.

Speed of the junction hypersurface $\mathcal{S}$ as measured by the static SdS observers is given by (for details, see Stuchlík, 1984)

$$v_\mathrm{b}(r_\mathrm{b}) = \tanh\alpha = \pm\left[1 - {\mathcal{E}_\mathrm{b}}^{-2}\mathcal{A}^2(r_\mathrm{b})\right]^{1/2}\,. \tag{36}$$

This speed approaches the light speed ($v_{\mathrm{b}}(r_{\mathrm{b}}) = 1$) at radii, where

$$\mathcal{A}^2(r_{\mathrm{b}}) = 0\,, \tag{37}$$

which is the condition giving loci of the event horizons. Therefore, the junction surface velocity reaches the speed of light when the surface is crossing the cosmological horizon of the SdS spacetime.

In the stringy model of the dark energy, we introduce a new constant Q by the relation

$$\Lambda(a) = \frac{K}{a(T)} = \frac{K\,\Sigma_k(\chi_{\mathrm{b}})}{r_{\mathrm{b}}} = \frac{Q}{r_{\mathrm{b}}}\,. \tag{38}$$

Then the metric factor takes the form

$$\mathcal{A}^2(r_{\mathrm{b}}) = 1 - \frac{2M}{r_{\mathrm{b}}} - \frac{1}{3}Qr_{\mathrm{b}}\,. \tag{39}$$

The velocity of the junction surface can be expressed in the form

$$v_{\mathrm{b}}(r_{\mathrm{b}}) = \pm\left[1 - \mathcal{E}_{\mathrm{b}}^{-2}\mathcal{A}^2(r_{\mathrm{b}})\right]^{1/2} = \pm\left[1 - \mathcal{E}_{\mathrm{b}}^{-2}\left(1 - \frac{2M}{r_{\mathrm{b}}} - \frac{1}{3}Qr_{\mathrm{b}}\right)\right]^{1/2}\,. \tag{40}$$

The horizons of the vacuum spacetime are located at radii

$$r_{\mathrm{h(b,c)}} = \frac{3}{2Q}\left(1 \pm \sqrt{1 - \frac{8}{3}QM}\right)\,, \tag{41}$$

where the condition $QM < 3/8$ must be satisfied. Clearly, the loci of the horizons change with the evolution of the dark energy and scale factor. For all values of k, the minimum of $v_{\mathrm{b}}(r_{\mathrm{b}})$ is located at

$$r_{\mathrm{b(e)}} = \sqrt{\frac{6M}{Q}}\,. \tag{42}$$

For $k = +1$, the velocity $v_{\mathrm{b}}(r_{\mathrm{b}})$ has zero points giving limits on validity of the model. The zero points are given by

$$r_{0(\pm)} = \frac{3}{2Q}\left[\left(1 - \mathcal{E}_{\mathrm{b}}^2\right) \pm \sqrt{\left(\mathcal{E}_{\mathrm{b}}^2 - 1\right)^2 - \frac{8}{3}QM}\right]\,. \tag{43}$$

The behaviour of the speed $v_{\mathrm{b}}(r_{\mathrm{b}})$ is given for all of the three versions of the ES vakuola model. The results are illustrated for some representative values of the cosmological constant and Q constant, respectively. The Einstein–Straus model (without dark energy) is represented in Fig. 2, ESdS (cosmological constant) in Fig. 3 and the Swiss cheese model with the stringy dark energy in Fig. 4.

We can see that in the stringy Swiss cheese model the speed of the junction hypersurface reaches the light speed at 20 times larger r_{b} value than in the ESdS case (compare Fig. 3 with Fig. 4). This means that in the stringy Swiss cheese model the influence on the CMB temperature fluctuations is much smaller than in the ESdS model.

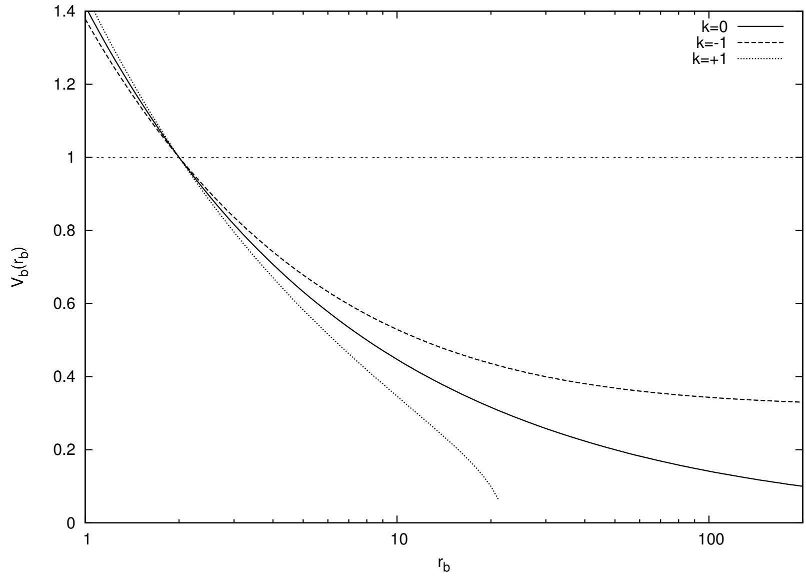

Figure 2. Speed of the junction hypersurface $\mathcal{S}$ in the Einstein–Straus model. Radial coordinate r_{b} is in mass units.

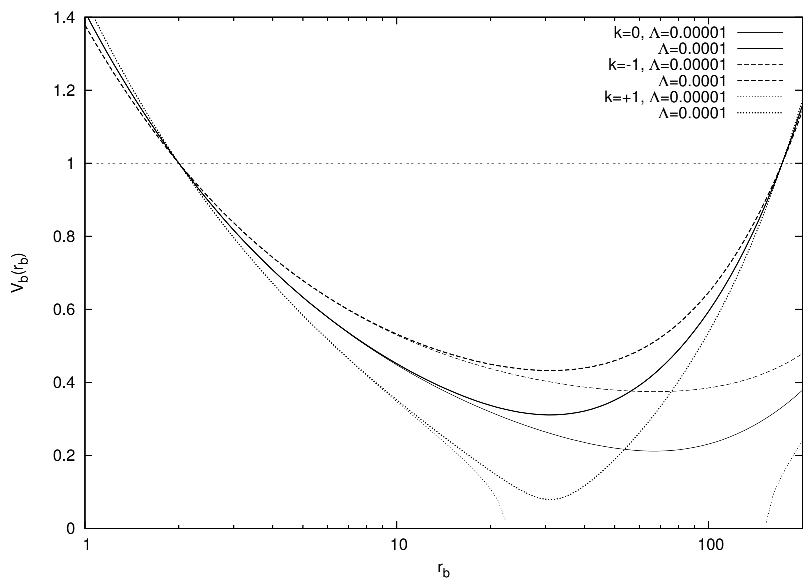

Figure 3. Speed of junction hypersurface $\mathcal{S}$ in the ESdS model with cosmological constant, for different values of Λ.

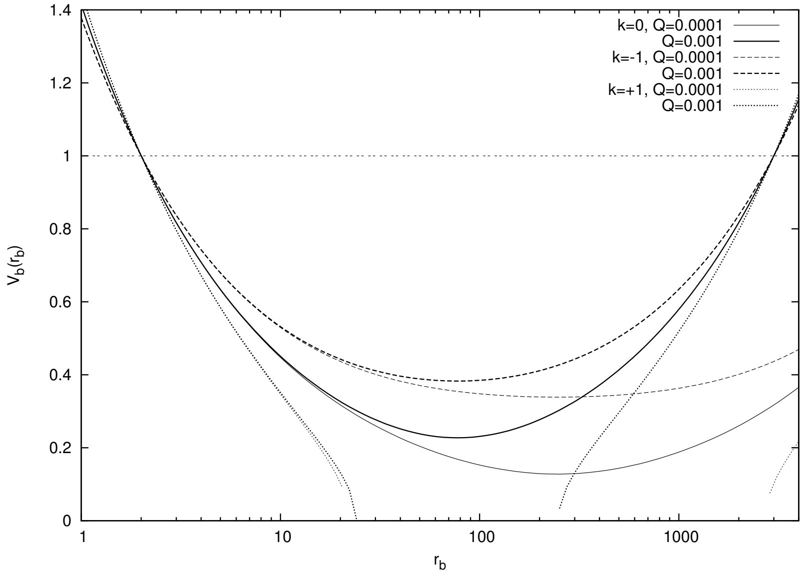

Figure 4. Speed of junction hypersurface $\mathcal{S}$ in the Swiss cheese model with dark energy form superstring, for different values of Q.

6 CONCLUSIONS

We have shown that it is possible to construct the Swiss cheese model with the dark energy depending on the scale factor $a(T)$, using the Schwarzschild–de Sitter like spacetime. The junction hypersurface $\mathcal{S}$ is only boundary surface, and there is zero energy-momentum tensor on the hypersurface $\mathcal{S}$.

In future cosmic evolution, the influence of the stringy dark energy model on CMB temperature fluctuations is smaller then in the model with the repulsive cosmological constant, while in the past it should be stronger.

ACKNOWLEDGEMENTS

The present work was supported by Czech grants MSM 4781305903, GAČR 202/03/1147 and by the Committee for Collaboration of Czech Republic with CERN. One of the authors (Z. S.) would like to acknowledge the perfect hospitality at the CERN's Theory Division where part of the work was realized.

REFERENCES

Einstein, A. and Straus, E. G. (1945), The influence of the expansion of space on the gravitation fields surrounding the individual stars, *Rev. Modern Phys.*, **17**(2–3), pp. 120–124, Corrections and additional remarks to our paper (1945), ibid. **18**, pp. 148–149.

Ellis, J., Mavromatos, N. E. and Nanopoulos, D. V. (2000), Time-Dependent Vacuum Energy Induced by D-Particle Recoil, *Gen. Relativity Gravitation*, **32**(5), pp. 943–958, ISSN 0001-7701, `gr-qc/9810086`, URL `http://oldwww.math.uni-potsdam.de/grg/`.

Misner, C. W., Thorne, K. S. and Wheeler, J. A. (1973), *Gravitation*, Freeman, San Francisco.

Ostriker, J. P. and Steinhardt, P. J. (1995), *Nature*, **377**, p. 600.

Riess, A. G. et al. (2004), Type Ia Supernova Discoveries at $z > 1$ From the Hubble Space Telescope: Evidence for Past Deceleration and Constraints on Dark Energy Evolution, *Astrophys. J.*, **123**, p. 145, `astro-ph/0402512`.

Spergel, D. N., Verde, L., Peiris, H. V., Komatsu, E., Nolta, M. R., Bennett, C. L., Halpern, M., Hinshaw, G., Jarosik, N., Kogut, A., Limon, M., Meyer, S. S., Page, L., Tucker, G. S., Weiland, J. L., Wollack, E. and Wright, E. L. (2003), First Year Wilkinson Microwave Anisotropy Probe (WMAP) Observations: Determination of Cosmological Parameters, *Astrophys. J. Suppl.*, **148**, p. 175, `astro-ph/0302209`.

Stuchlík, Z. (1983), The motion of test particles in black-hole backgrounds with non-zero cosmological constant, *Bull. Astronom. Inst. Czechoslovakia*, **34**(3), pp. 129–149.

Stuchlík, Z. (1984), An Einstein–Strauss–de Sitter model of the universe, *Bull. Astronom. Inst. Czechoslovakia*, **35**(4), pp. 205–215.

Stuchlík, Z. (2002), The role of a repulsive cosmological constant in astrophysical processes, in O. Semerák, J. Podolský and M. Žofka, editors, *Gravitation: Following the Prague Inspiration (A Volume in Celebration of the 60th Birthday of Jiří Bičák)*, pp. 27–83, World Scientific, New Jersey, London, Singapore, Hong Kong, ISBN 981-238-093-0.

Stuchlík, Z. and Kološ, M. (2005), Friedman models with the superstring dark energy, pp. 223–230, this volume.

Stuchlík, Z. and Schee, J. (2004), Influence of a relict vacuum energy on the Rees–Sciama effect, in S. Hledík and Z. Stuchlík, editors, *Proceedings of RAGtime 4/5: Workshops on black holes and neutron stars, Opava, 14–16/13–15 October 2002/2003*, pp. 187–203, Silesian University in Opava, Opava, ISBN 80-7248-242-4.

Proceedings of *RAGtime 6/7: Workshops on black holes and neutron stars, Opava, 16–18/18–20 September, 2004/2005*
S. Hledík and Z. Stuchlík, editors, Silesian University in Opava, Czech Republic, 2005, pp. 241–252

Equilibrium of spinning test particles in equatorial plane of Kerr–de Sitter spacetimes

Zdeněk Stuchlík[a] and Jiří Kovář[b]

Institute of Physics, Faculty of Philosophy & Science, Silesian University in Opava,
Bezručovo nám. 13, CZ-746 01 Opava, Czech Republic
[a]`Zdenek.Stuchlik@fpf.slu.cz`
[b]`Jiri.Kovar@fpf.slu.cz`

ABSTRACT
Equilibrium conditions and spin dynamics of spinning test particles are discussed in the stationary and axially symmetric Kerr–de Sitter black-hole or naked-singularity spacetimes. The general equilibrium conditions are established, but due to their great complexity, the detailed discussion of the equilibrium conditions and spin dynamics is presented only in the simple and most relevant case of equilibrium positions in the equatorial plane of the spacetimes. It is shown that due to the combined effect of the rotation of the source and the cosmic repulsion the equilibrium is spin dependent in contrast to the spherically symmetric spacetimes.

1 INTRODUCTION

Motion of test particles describes in an illustrative way properties of black-hole and naked-singularity spacetimes. The motion of uncharged and spinless test particles is governed by geodesic equations and directly determines the geodesic structure of the spacetimes. Charged test particles can test combined gravitational and electromagnetic field of these backgrounds, their motion is determined by the Lorentz equation. If the test particles possess also spin, their equations of motion are more complex in comparison with the spinless particles, because of the interaction of the spin with the curvature of the spacetime given by the Riemann tensor (Papapetrou, 1951; Pirani, 1956). Moreover, the spin dynamics has also to be considered. In the absence of an electromagnetic field of the background, the spin dynamics is determined by the Fermi–Walker transport equation.

Studies of the equilibrium positions and conditions (equilibrium hereinafter) of charged test particles give direct information on interplay of the gravitational and electromagnetic forces acting in the charged (Reissner–Nordström and Kerr–Newman) backgrounds (Bičák et al., 1989; Bonnor, 1993; Balek et al., 1989; Aguirregabiria et al., 1995; Stuchlík et al., 1999). In the simplest Schwarzschild backgrounds, the equilibrium of test particles is impossible, because only the gravitational attraction is acting here. However, the presence of a repulsive cosmological constant allows the equilibrium of even uncharged particles. Further, it was shown that in the Schwarzschild–de Sitter (SdS) backgrounds, the equilibrium

80-7248-334-X

of spinning test particles is independent of the particle spin being restricted to the static radius, where the gravitational attraction is just balanced by the cosmic repulsion (Stuchlík, 1999). The equilibrium is spin-independent also in the Reissner–Nordström–de Sitter spacetimes (Stuchlík and Hledík, 2001). Of course, the equilibrium is spin dependent in the rotating Kerr spacetimes due to the interaction of the spin of the particle and the black hole (Aguirregabiria et al., 1995).

We focus onto more complicated case of stationary and axially symmetric spacetimes around rotating black holes or naked singularities in the universe with the recently indicated repulsive cosmological constant, i.e., on Kerr–de Sitter (KdS) spacetimes, in order to extend the preliminary studies and to better understand the combined effects of the rotation of the source and the cosmic repulsion. For comparison, restriction of our results to the pure Kerr and SdS spacetimes is also included. Because of the complexity of general equilibrium conditions, the detailed discussion is restricted only to the case of the equatorial plane of the KdS spacetimes.

2 EQUATIONS OF MOTION AND SPIN DYNAMICS

The motion of a spinning test particle of mass m with 4-velocity u^{λ} and spin tensor $S^{\mu\nu}$ in an arbitrary gravitational field has been studied by Papapetrou (1951). Such particle deviates from its geodesic motion and moves along a different orbit due to the spin-curvature interaction. Introducing the Pirani spin supplementary condition (Pirani, 1956)

$$S^{\mu\nu}u_{\nu} = 0 \tag{1}$$

and the covariant spin vector

$$S_{\sigma} = \tfrac{1}{2}\epsilon_{\rho\mu\nu\sigma}u^{\rho}S^{\mu\nu}\,, \tag{2}$$

the motion is governed by the equation

$$m\frac{\mathrm{D}u^{\alpha}}{\mathrm{d}\tau} = -\epsilon^{\alpha\mu\nu\beta}\frac{\mathrm{D}^2u_{\beta}}{\mathrm{d}\tau^2}S_{\mu}u_{\nu} + \frac{1}{2}\epsilon^{\lambda\mu\rho\sigma}R^{\alpha}{}_{\nu\lambda\mu}u^{\nu}u_{\sigma}S_{\rho}\,, \tag{3}$$

where $\epsilon_{\rho\mu\nu\sigma}$ is the Levi-Civita completely antisymmetric tensor, $\mathrm{D}/\mathrm{d}\tau$ denotes the covariant derivate along the vector field u^{α}, i.e.,

$$\frac{\mathrm{D}u^{\alpha}}{\mathrm{d}\tau} = u^{\beta}\left(\partial_{\beta}u^{\alpha} + \Gamma^{\alpha}_{\beta\gamma}u^{\gamma}\right)\,, \tag{4}$$

whereas $\Gamma^{\alpha}_{\beta\gamma}$ denotes coefficients of the affine connection of the background and $R^{\alpha}{}_{\nu\lambda\mu}$ is the Riemann tensor describing the background on which particle moves. The test particle is assumed to be so small in size and in mass not to modify the background. Clearly, we obtain the geodesic motion in the case of spinless particles. Notice that by construction of the spin vector (2), S^{σ} is permanently orthogonal to the 4-velocity u^{σ}, i.e.,

$$S^{\sigma}u_{\sigma} = 0\,. \tag{5}$$

Dynamics of the spin vector is then given by a relatively simple equation of the Fermi–Walker transport

$$\frac{\mathrm{D}S_\alpha}{\mathrm{d}\tau} = u_\alpha \frac{\mathrm{D}u^\beta}{\mathrm{d}\tau} S_\beta \,. \tag{6}$$

3 KERR–DE SITTER SPACETIMES

KdS spacetimes are stationary and axially symmetric solutions of Einstein's equations with a non-zero cosmological constant Λ. In the standard Boyer–Lindquist coordinates $(t, \varphi, r, \vartheta)$ and geometric units $(c = G = 1)$, the line element of the KdS geometry is given by the relation

$$\begin{aligned} \mathrm{d}s^2 = {} & \frac{a^2 \Delta_\vartheta \sin\vartheta^2 - \Delta_r}{I^2\rho^2}\mathrm{d}t^2 + \frac{2a\sin\vartheta^2\left[\Delta_r - (a^2+r^2)\Delta_\vartheta\right]}{I^2\rho^2}\mathrm{d}t\mathrm{d}\varphi \\ & + \frac{\sin\vartheta^2\left[(a^2+r^2)^2\Delta_\vartheta - a^2\Delta_r\sin\vartheta^2\right]}{I^2\rho^2}\mathrm{d}\varphi^2 + \frac{\rho^2}{\Delta_r}\mathrm{d}r^2 + \frac{\rho^2}{\Delta_\vartheta}\mathrm{d}\vartheta^2 \,, \end{aligned} \tag{7}$$

where

$$\Delta_r = r^2 - 2Mr + a^2 - \tfrac{1}{3}\Lambda r^2(r^2+a^2) \,, \tag{8}$$

$$\Delta_\vartheta = 1 + \tfrac{1}{3}\Lambda a^2 \cos^2\vartheta \,, \tag{9}$$

$$I = 1 + \tfrac{1}{3}\Lambda a^2 \,, \tag{10}$$

$$\rho^2 = r^2 + a^2\cos^2\vartheta \tag{11}$$

and the mass M, specific angular momentum a, and cosmological constant Λ are parameters of the spacetime. Using the dimensionless cosmological parameter $\lambda = \Lambda M^2/3$ and putting $M = 1$, the coordinates t, r, the line element $\mathrm{d}s^2$, and the parameter a are expressed in units of M and become dimensionless.

The stationary regions of the spacetimes, determined by the relation $\Delta_r(r; a^2, \lambda) \geq 0$, are limited by the inner and outer black-hole horizons at $r_{\mathrm{h}-}$ and $r_{\mathrm{h}+}$ and by the cosmological horizon at r_c. Spacetimes containing three horizons are black-hole (BH) spacetimes, while spacetimes containing one horizon (the cosmological horizon exists for any choice of the spacetime parameters) are naked-singularity (NS) spacetimes (Stuchlík and Slaný, 2004). The radii of horizons are, due to the relation $\Delta_r(r; a^2, \lambda) = 0$, given by solutions of the equation

$$a^2 = a^2_\mathrm{h}(r;\lambda) \equiv \frac{r^2 - 2r - \lambda r^4}{\lambda r^2 - 1} \,. \tag{12}$$

For a fixed value of λ, the number of solutions of this equation (horizons) depends on the number of positive local extrema of the function $a^2_\mathrm{h}(r;\lambda)$ (see Fig. 1). The extrema are located at the radii implicitly determined (due to the condition $\partial_r a^2_\mathrm{h}(r;\lambda) = 0$) by the relation

$$\lambda = \lambda_\mathrm{he}(r) \equiv \frac{2r + 1 - \sqrt{8r+1}}{2r^3} \,, \tag{13}$$

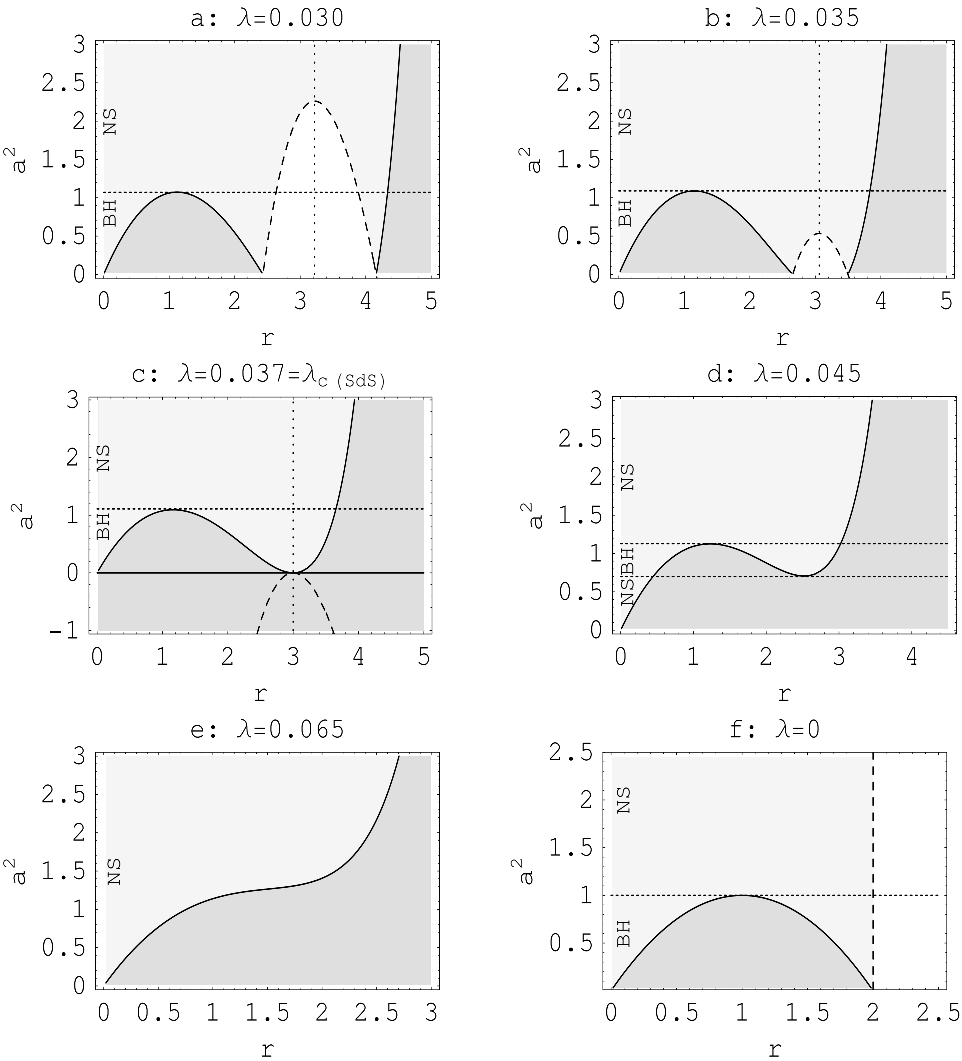

Figure 1. Location of the event horizons and static limit surfaces in the equatorial plane of the KdS spacetimes. The function $a_{\mathrm{h}}^2(r;\lambda)$ (solid) determines the loci of horizons; the function $a_{\mathrm{s}}^2(r;\lambda)$ (dashed) determines the radii of static limit surfaces. We give examples of different types of behaviour of $a_{\mathrm{h}}^2(r;\lambda)$ and $a_{\mathrm{s}}^2(r;\lambda)$ in dependence on the value of λ discussed in the text. Panels (a)–(e) concern the KdS spacetimes and for comparison the panel (f) concerns the Kerr spacetimes. The function $a_{\mathrm{h}}^2(r;\lambda)$ separates the dynamic regions (dark gray) and the stationary regions (light gray and white) of the spacetimes. The function $a_{\mathrm{s}}^2(r;\lambda)$ separates the ergosphere (light gray) and the other stationary regions of the spacetimes where the existence of the equilibrium is possible (white). For given values of λ and a^2, the horizons and static limit surfaces (respectively) are determined by the solutions of the equations $a^2 = a_{\mathrm{h}}^2(r;\lambda)$ and $a^2 = a_{\mathrm{s}}^2(r;\lambda)$ (respectively). Note that in the panel (c), the irrelevant negative function $a_{\mathrm{s}}^2(r;\lambda)$ is illustrated.

whereas the maximum of the function $\lambda_{\mathrm{he}}(r)$ is located at $r_{\mathrm{c}} = (3 + 2\sqrt{3})/4$ and takes the critical value $\lambda_{\mathrm{c(KdS)}} \doteq 0.05924$. Assuming the behaviour of the function $a^2_{\mathrm{h}}(r;\lambda)$, we can distinguish three different cases.

$0 < \lambda < \lambda_{\mathrm{c(KdS)}}$ There are two local extrema of the function $a^2_{\mathrm{h}}(r;\lambda)$, denoted as $a^2_{\mathrm{h,max}}(\lambda)$ and $a^2_{\mathrm{h,min}}(\lambda)$ and determined by the relations (12) and (13), whereas the local minimum $a^2_{\mathrm{h,min}}(\lambda)$ becomes positive (relevant) for $\lambda > \lambda_{\mathrm{c(SdS)}} \equiv 1/27 \doteq 0.03704$. Thus for $a^2 > a^2_{\mathrm{h,max}}(\lambda)$ or for $a^2 < a^2_{\mathrm{h,min}}(\lambda)$, there is one solution of Eq. (12) and only NS spacetimes exist. For $a^2 < a^2_{\mathrm{h,max}}(\lambda)$ and $a^2 > a^2_{\mathrm{h,min}}(\lambda)$, there are three solutions of the Eq. (12) and BH spacetimes exist (see Figs 1a-d).

$\lambda = \lambda_{\mathrm{c(KdS)}}$ The local extrema $a^2_{\mathrm{h,max}}(\lambda)$ and $a^2_{\mathrm{h,min}}(\lambda)$ coalesce at r_{c} and take the value $a^2_{\mathrm{c}} \doteq 1.21202$. Then there is only one solution of the equation (12) for all $a^2 > 0$ and only NS spacetimes exist.

$\lambda > \lambda_{\mathrm{c(KdS)}}$ There are no extrema of the function $a^2_{\mathrm{h}}(r;\lambda)$ and thus there is only one solution of the equation (12) for all $a^2 > 0$ and only NS spacetimes exist (see Fig. 1e).

The degenerate cases corresponding to extreme black holes or naked singularities are given in Stuchlík and Slaný (2004). In the case of Kerr spacetimes ($\lambda = 0$), there are BH spacetimes for $a^2 \leq 1$ and NS spacetimes for $a^2 > 1$ (see Fig. 1e) (Misner et al., 1973) and in the case of SdS spacetimes ($a^2 = 0$), there are only BH spacetimes for $\lambda \leq \lambda_{\mathrm{c(SdS)}}$ (Stuchlík and Hledík, 1999).

For our purposes, i.e., determination of equilibrium positions of particles, it is necessary to determine behaviour of the ergosphere (for definition see, e.g., Misner et al., 1973). The ergosphere of the KdS spacetimes, determined by the relation $g_{tt} > 0$, is limited by the static limit surfaces, given by the equation $g_{tt} = 0$. In the equatorial plane, the radii of these surfaces $r_{\mathrm{s}-}$ (inner) and $r_{\mathrm{s}+}$ (outer) are given by solutions of the equation

$$a^2 = a^2_{\mathrm{s}}(r;\lambda) \equiv \frac{r - 2 - \lambda r^3}{\lambda r}\,. \tag{14}$$

Again, for a fixed value of λ, the possible number of solutions of this equation (static limit surfaces) depends on the number of positive local extrema of the function $a^2_{\mathrm{s}}(r;\lambda)$ (see Fig. 1). We can find (due to the condition $\partial_r(a^2_{\mathrm{s}}(r;\lambda) = 0)$ the only extremum of the function taking the value

$$a^2_{\mathrm{s,max}}(\lambda) = \lambda^{-2/3}\left(\lambda^{-1/3} - 3\right)\,. \tag{15}$$

It is located at the so-called static radius

$$r = r_{\mathrm{stat}} \equiv \lambda^{-1/3}\,, \tag{16}$$

where (in the equatorial plane) the gravitational attraction is balanced by the cosmological repulsion independently of the rotational parameter a (Stuchlík and Slaný, 2004). There is $a^2_{\mathrm{s,max}}(\lambda_{\mathrm{c(SdS)}}) = 0$, while it becomes positive for $\lambda < \lambda_{\mathrm{c(SdS)}}$ and diverges for $\lambda \to 0$. Further, we have to distinguish the cases when the static limit surfaces do exist or do not exist in the BH spacetimes. The critical values of the rotational and cosmological parameters are given by the relation

$$a^2_{\mathrm{h,max}}(\lambda) = a^2_{\mathrm{s,max}}(\lambda) \tag{17}$$

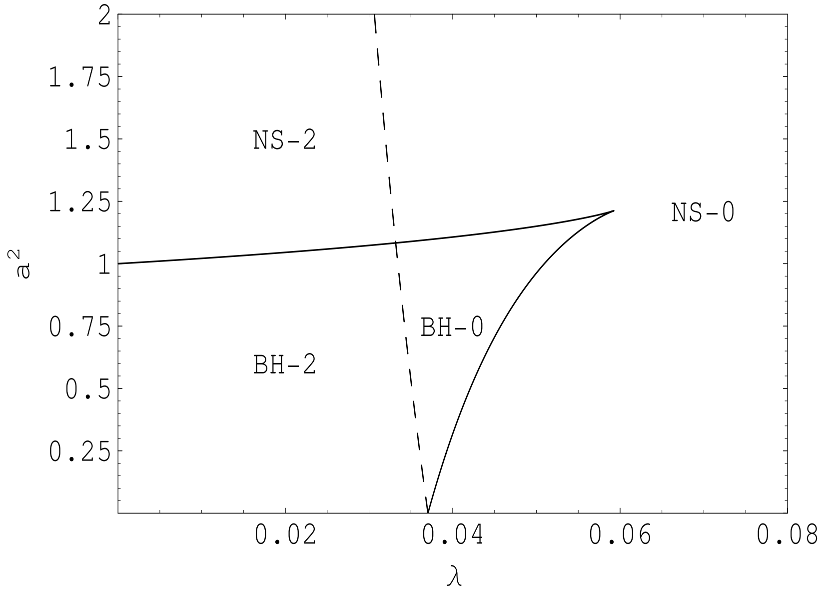

Figure 2. Classification of the KdS spacetimes. The parametric plane (λ, a^2) is divided by the functions $a^2_{\mathrm{h,max}}(\lambda)$ (upper solid), $a^2_{\mathrm{h,min}}(\lambda)$ (lower solid), and $a^2_{\mathrm{s,max}}(\lambda)$ (dashed) into four regions corresponding to the classes of KdS spacetimes BH-2, BH-0, NS-2, and NS-0 differing in the number of horizons and static limit surfaces (expressed by the digit) in the equatorial plane.

and found to be $a^2_{\mathrm{e,BH}} \doteq 1.08317$ and $\lambda_{\mathrm{e,BH}} \doteq 0.03319$. Assuming the behaviour of the function $a^2_{\mathrm{s}}(r; \lambda)$, we can summarize the number of static limit surfaces in the KdS spacetimes.

$\boldsymbol{\lambda < \lambda_{\mathrm{c(SdS)}}}$ There are two static limit surfaces for $a^2 < a^2_{\mathrm{s,max}}(\lambda)$, one static limit surface for $a^2 = a^2_{\mathrm{s,max}}(\lambda)$, and none static limit surface for $a^2 > a^2_{\mathrm{s,max}}(\lambda)$ (see Figs 1a,b). If $\lambda < \lambda_{\mathrm{e,BH}}$, the static limit surface exists in all the BH spacetimes, and in NS spacetimes with $a^2 < a^2_{\mathrm{s,max}}(\lambda)$ and it does not exist for $a^2 > a^2_{\mathrm{s,max}}(\lambda)$ in the NS spacetimes (see Fig. 1a). If $\lambda_{\mathrm{e,BH}} < \lambda < \lambda_{\mathrm{c(SdS)}}$, the static limit surface exists for BH spacetimes with $a^2 < a^2_{\mathrm{s,max}}(\lambda)$ and do not exist for the BH and NS spacetimes with $a^2 > a^2_{\mathrm{s,max}}(\lambda)$ (see Fig. 1b).

$\boldsymbol{\lambda \geq \lambda_{\mathrm{c(SdS)}}}$ There are no static limit surfaces for all $a^2 > 0$ (see Figs 1c–e).

Clearly, if no static limit surface exists in the KdS spacetimes, the equilibrium is impossible there. In the case of the Kerr spacetimes, there is the only static limit surface at $r = 2$ independently of a^2 (see Fig. 1f) and in the case of the SdS spacetimes, there is no static limit surface and no ergosphere.

According to the given discussion, the KdS spacetimes can be divided into four classes BH-2, BH-0, NS-2, and NS-0 (see Fig. 2) differing in the number of horizons and static limit surfaces (expressed by the digit) in the equatorial plane.

4 GENERAL EQUILIBRIUM CONDITIONS

In order to consider the equilibrium of a spinning test particle, we must find conditions which guarantee that the equations of motion (3), and the equations of spin dynamics (6), along with the orthonormality relation (5), are simultaneously satisfied for the 4-velocity u^α corresponding to a stationary particle in the background under consideration.

Since the particle is at the "rest," its 4-velocity has the only non-zero time component that is given by the relations

$$u^\alpha = \frac{1}{\sqrt{-g_{tt}}}\,\delta^t_\alpha\,, \qquad \frac{\mathrm{d}u^\alpha}{\mathrm{d}\tau} = u^\beta\,\partial_\beta u^\alpha = 0\,. \tag{18}$$

Thus, naturally, the equilibrium is possible only outside the static limit surfaces (outside ergosphere) where $g_{tt} < 0$, whereas such regions occur only in the stationary regions, where $\Delta_r > 0$. The orthogonality of the spin and the 4-velocity implies that $S_t = 0$, i.e., only space components of the spin vector are non-zero. Thus the spin dynamics equation (6) reduces to the form

$$\frac{\mathrm{D}S_\alpha}{\mathrm{d}\tau} = \left[u_\alpha \Gamma^i_{tt}(u^t)^2\right] S_i\,, \tag{19}$$

which implies

$$\frac{\mathrm{d}S_\alpha}{\mathrm{d}\tau} = \left[\Gamma^i_{\alpha t}u^t + u_\alpha \Gamma^i_{tt}(u^t)^2\right] S_i\,. \tag{20}$$

Therefore, in the KdS geometry, the spin dynamics of particles in equilibrium is given by the relations

$$\frac{\mathrm{d}S_t}{\mathrm{d}\tau} = 0\,, \qquad \frac{\mathrm{d}S_r}{\mathrm{d}\tau} = u^t\,\Gamma^\varphi_{rt}S_\varphi\,, \qquad \frac{\mathrm{d}S_\vartheta}{\mathrm{d}\tau} = u^t\,\Gamma^\varphi_{\vartheta t}S_\varphi\,, \tag{21}$$

$$\frac{\mathrm{d}S_\varphi}{\mathrm{d}\tau} = u^t\left[\left(\Gamma^r_{\varphi t} - \frac{g_{t\varphi}}{g_{tt}}\Gamma^r_{tt}\right)S_r + \left(\Gamma^\vartheta_{\varphi t} - \frac{g_{t\varphi}}{g_{tt}}\Gamma^\vartheta_{tt}\right)S_\vartheta\right]. \tag{22}$$

The second derivative of the 4-velocity (18) can be rewritten as

$$\frac{\mathrm{D}^2u_\alpha}{\mathrm{d}\tau^2} = (u^t)^2\Gamma^\beta_{t\alpha}\Gamma^\gamma_{\beta t}u_\gamma\,, \tag{23}$$

which in the KdS geometry reduces to the following components

$$\frac{\mathrm{D}^2u_t}{\mathrm{d}\tau^2} = -u^t\left[\left(\Gamma^r_{tt}\Gamma^t_{rt} + \Gamma^\vartheta_{tt}\Gamma^t_{\vartheta t}\right) + \frac{g_{t\varphi}}{g_{tt}}\left(\Gamma^r_{tt}\Gamma^\varphi_{rt} + \Gamma^\vartheta_{tt}\Gamma^\varphi_{\vartheta t}\right)\right], \tag{24}$$

$$\frac{\mathrm{D}^2u_\varphi}{\mathrm{d}\tau^2} = -u^t\left[\left(\Gamma^r_{\varphi t}\Gamma^t_{rt} + \Gamma^\vartheta_{\varphi t}\Gamma^t_{\vartheta t}\right) + \frac{g_{t\varphi}}{g_{tt}}\left(\Gamma^r_{\varphi t}\Gamma^\varphi_{rt} + \Gamma^\vartheta_{\varphi t}\Gamma^\varphi_{\vartheta t}\right)\right], \tag{25}$$

$$\frac{\mathrm{D}^2u_r}{\mathrm{d}\tau^2} = 0\,, \qquad \frac{\mathrm{D}^2u_\vartheta}{\mathrm{d}\tau^2} = 0\,. \tag{26}$$

The first derivate of the 4-velocity reduces to

$$\frac{\mathrm{D}u^\alpha}{\mathrm{d}\tau} = (u^t)^2 \Gamma^\alpha_{tt}\,, \tag{27}$$

which in the KdS spacetimes yields

$$\frac{\mathrm{D}u^t}{\mathrm{d}\tau} = 0\,, \qquad \frac{\mathrm{D}u^\varphi}{\mathrm{d}\tau} = 0\,, \qquad \frac{\mathrm{D}u^r}{\mathrm{d}\tau} = (u^t)^2 \Gamma^r_{tt}\,, \qquad \frac{\mathrm{D}u^\vartheta}{\mathrm{d}\tau} = (u^t)^2 \Gamma^\vartheta_{tt}\,. \tag{28}$$

The equilibrium conditions can be obtained by using Eqs (3), (24)–(26), and (28). They are too long to be explicitly written and discussed in a general case, as well as the spin dynamics Eqs (21)–(22). Therefore we restrict our attention to the most important case of the equatorial plane of the KdS spacetimes, which gives, moreover, a relatively simple results.

5 EQUILIBRIUM CONDITIONS IN EQUATORIAL PLANE OF KERR–DE SITTER SPACETIMES

As we noticed in Section 3, the equatorial equilibrium is possible in the spacetimes admitting static limit surfaces, and outside the ergosphere of these spacetimes, i.e., in the region where

$$a^2 < a^2_{\mathrm{s}}(r;\lambda)\,, \tag{29}$$

equivalently $a^2 - \Delta_r < 0$ or $r_{\mathrm{s}-} < r < r_{\mathrm{s}+}$. Generally, we thus assume $\lambda < \lambda_{\mathrm{crit(SdS)}}$ and $a^2 < a^2_{\mathrm{s,max}}(\lambda)$. Using the Eqs (21)–(22), we obtain the following spin dynamics equations

$$\frac{\mathrm{d}S_t}{\mathrm{d}\tau} = \frac{\mathrm{d}S_\vartheta}{\mathrm{d}\tau} = 0\,, \tag{30}$$

$$\frac{\mathrm{d}S_r}{\mathrm{d}\tau} = u^t \frac{a(1-r^3\lambda)}{r^2\Delta_r} S_\varphi\,, \tag{31}$$

$$\frac{\mathrm{d}S_\varphi}{\mathrm{d}\tau} = u^t \frac{a(1-r^3\lambda)\Delta_r}{r^2 I^2 (a^2-\Delta_r)} S_r\,. \tag{32}$$

The equation of motion (3) implies relevant conditions for $\alpha = r$ and $\alpha = \vartheta$ only. By using Eqs (24)–(26) and (28) we arrive at

$$S_\vartheta = m\frac{r^2(1-\lambda r^3)(a^2-\Delta_r)}{a[\lambda^2 r^6 + \lambda(r^3+3a^2 r) - 3r + 7](1+\lambda a^2)}\,, \tag{33}$$

$$\frac{S_r a \Delta_r [\lambda^2 r^6 - \lambda(5r^3 + 3ra^2) + 3r - 5]}{r^4(a^2-\Delta_r)^2} = 0\,. \tag{34}$$

Thus, outside the ergosphere, in the equatorial plane, the equilibrium of spinning test particles requires, due to the Eq. (30), $S_\vartheta = \mathrm{const}$ given by the Eq. (33). The conditions (31)–(34) can be discussed in the following way.

$\boldsymbol{S_r = 0}$ The condition (34) is automatically satisfied. Equation (32) requires $S_\varphi = \text{const}$ and the condition (31), where $\mathrm{d}S_r/\mathrm{d}\tau = 0$, implies that for

- $S_\varphi \neq 0$, the equilibrium is possible only at the static radius r_{stat} (only if r_{stat} satisfies the condition (29)) with the spin S_ϑ given by the equation (33), i.e., $S_\vartheta = 0$
- $S_\varphi = 0$, the equilibrium is possible at all the radii satisfying the condition (29) with the spin given by the function $S_\vartheta(r; a, \lambda)$ determined by Eq. (33). In the case of spinless particles ($S_\vartheta = 0$), the equilibrium is possible at the static radius only and there is no equilibrium possible at the radii, where the function S_ϑ diverges. Note that in the case of $a^2 = a^2_{\text{s,max}}(\lambda) = \lambda^{-2/3}(\lambda^{-1/3} - 3)$, the condition (33) would allow the equilibrium independent of the spin S_ϑ at r_{stat}. But this is the limit case of the spacetimes which does not satisfy the condition $a^2 < a^2_{\text{s}}(r; \lambda)$. The static radius r_{stat} is the radius where the static limit surfaces coalesce for $a^2 = a^2_{\text{s,max}}(\lambda)$ (see Figs 1a,b). We give the behaviour of the function S_ϑ for a few specifically chosen values of λ and a in Fig. 3.

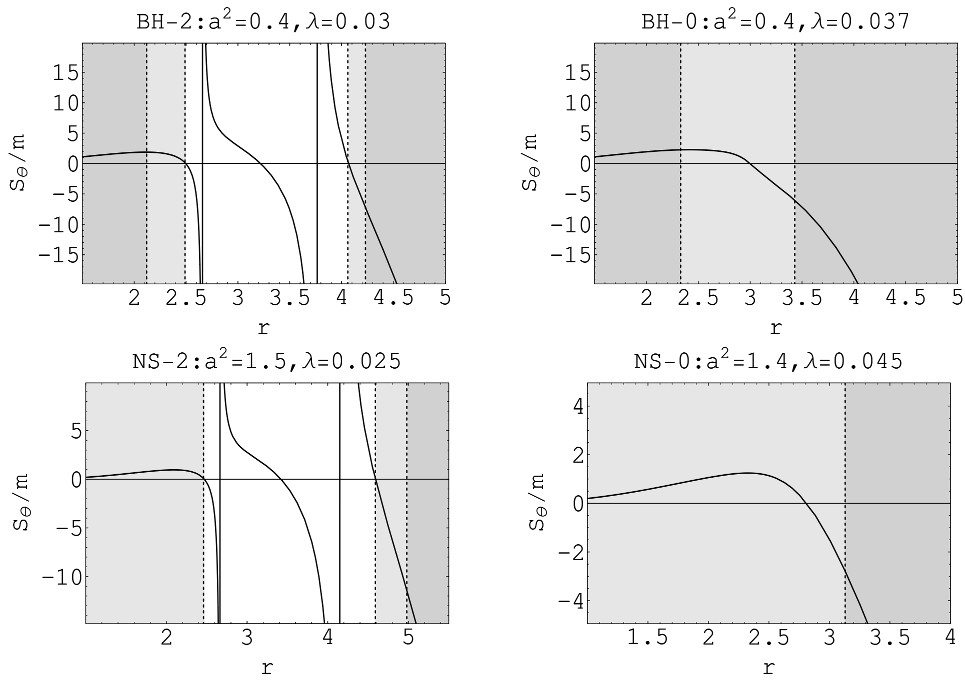

Figure 3. Function $S_\vartheta(r; a, \lambda)$ determining the magnitude and orientation of the latitudinal component of the spin vector of spinning particle in equilibrium at the radius r for given values of the parameters a^2 and λ in the case of $S_\varphi = 0$. The function vanishes at the radii of static limit surfaces, denoted by the dashed lines between the light gray and white regions, and at the static radius. The horizons of the spacetimes are denoted by the dashed lines between the dark gray and light gray regions. The divergence of the function is denoted by the vertical lines. We give four examples of the behaviour of the function for values of the parameters corresponding to the given classification of the KdS spacetimes (see Fig. 2). Note that the function $S_\vartheta(r; a, \lambda)$ is not relevant in the gray regions.

$S_r \neq 0$ The condition (34) is satisfied at the radii given by solutions of the equation

$$a^2 = a^2_{\mathrm{eq}}(r;\lambda) \equiv \frac{\lambda^2 r^6 - 5\lambda r^3 + 3r - 5}{3\lambda r}\,. \tag{35}$$

But there is $a^2_{\mathrm{eq}}(r;\lambda) \geq a^2_{\mathrm{s}}(r;\lambda)$ for all positive values of r, thus there is no equilibrium in this case.

5.1 Kerr and Schwarzschild–de Sitter cases

In the equatorial plane of the Kerr spacetimes, the equilibrium of spinning test particles is also possible only outside the ergosphere, i.e., in the region with $r > 2$. The limit case ($\lambda = 0$) of the equilibrium conditions (30)–(34) implies that the equilibrium requires $S_\vartheta = \mathrm{const}$, as well as in the KdS spacetimes.

$S_r = 0$ The condition (34) is automatically satisfied. The condition (32) implies $S_\varphi = const$ and the condition (31), where $\mathrm{d}S_r/\mathrm{d}\tau = 0$, is satisfied only in the case of $S_\varphi = 0$. Then the equilibrium is possible at all the radii satisfying the conditions $r > 2$ with spin given by the function

$$S_\vartheta = m\frac{r^3(2-r)}{a(7-3r)}\,. \tag{36}$$

Note that there is no equilibrium possible for $S_\vartheta = 0$ (spinless case), because of the restriction $r > 2$.

$S_r \neq 0$ The condition (34) implies the solution $r = 5/3$, which does not satisfy the condition $r > 2$ and then there is no equilibrium in this case.

In the SdS spacetimes, the limit case ($a = 0$) of the equilibrium conditions (30)–(34) implies that the equilibrium is possible only at the static radius. The spin can be arbitrary and it will be time independent. Of course, because of the the spherical symmetry of the SdS spacetimes, this result holds for any central plane of the spacetime.

6 CONCLUSIONS

The combined effect of the rotation of the source and the cosmic repulsion enriches significantly the properties of the test particle equilibrium in the KdS spacetimes not only for the spinning particles, but also for the non-spinning particles.

In the case of non-spinning particles (the equilibrium of which is given by the geodetical structure of the spacetimes), the equilibrium position is allowed in the equatorial plane at the static radii, determined by the spacetime parameters only. The static radius $r_{\mathrm{stat}} = \lambda^{-1/3}$, i.e., it is independent of the rotational parameter and coincides formally with the SdS formula (Stuchlík, 1999). The equatorial equilibrium is possible at r_{stat} for any KdS BH or NS admitting existence of the static limit surfaces (see Fig. 2), but it is not possible in any Kerr spacetimes. Notice, however, that the particles in equilibrium in the equatorial plane are rotating relative to the locally non-rotating frames (Stuchlík and Slaný, 2004).

The equilibrium of spinning particles in the equatorial plane of the KdS spacetimes is spin-dependent in contrast to the case of spherically symmetric SdS and Reissner–Nordström–de Sitter spacetimes (Stuchlík, 1999; Stuchlík and Hledík, 2001). It is possible at the static radius of the KdS spacetimes allowing existence of static limit surfaces, if $S_\varphi = \text{const} \neq 0$, $S_r = S_\vartheta = 0$, i.e., spin directed in the φ-direction. If $S_\vartheta = \text{const} \neq 0$ and $S_\varphi = S_r = 0$, the equilibrium is possible at the radii outside the ergosphere with the spin component S_ϑ determined by Eq. (33).

For comparison, the equilibrium positions are briefly summarized in the next table, in the cases of the SdS, Kerr, and KdS spacetimes, in dependence on the spin components.

S_r	S_φ	S_ϑ	**SdS**	**Kerr**	**KdS**
$=0$	$=0$	$=0$	r_{stat}	—	r_{stat}
		$\neq 0$	r_{stat}	$r = r(S_\vartheta, a)$	$r = r(S_\vartheta, a, \lambda)$
	$\neq 0$	$=0$	r_{stat}	—	r_{stat}
		$\neq 0$	r_{stat}	—	—
$\neq 0$	arbitr.	arbitr.	r_{stat}	—	—

ACKNOWLEDGEMENTS

The present work was supported by the Czech grant MSM 4781305903.

REFERENCES

Aguirregabiria, J. M., Chamorro, A., Suinaga, J. and Vishveshwara, C. V. (1995), Equilibrium of a charged test particle in the Kerr–Newman spacetime, *Classical Quantum Gravity*, **12**(3), p. 699, URL http://www.iop.org/EJ/S/UNREG/1NOryEzmtf2ZMVyFDaUGbw/toc/0264%-9381/12/3.

Balek, V., Bičák, J. and Stuchlík, Z. (1989), The motion of the charged particles in the field of rotating charged black holes and naked singularities – II. The motion in the equatorial plane, *Bull. Astronom. Inst. Czechoslovakia*, **40**(3), pp. 133–165.

Bičák, J., Stuchlík, Z. and Balek, V. (1989), The motion of charged particles in the field of rotating charged black holes and naked singularities – I. The general features of the radial motion and the motion along the axis of symmetry, *Bull. Astronom. Inst. Czechoslovakia*, **40**(2), pp. 65–92.

Bonnor, W. B. (1993), The equilibrium of a charged test particle in the field of a spherical charged mass in general relativity, *Classical Quantum Gravity*, **10**(10), p. 2077, URL http://www.iop.org/EJ/S/UNREG/1NOryEzmtf2ZMVyFDaUGbw/toc/0264%-9381/10/10.

Misner, C. W., Thorne, K. S. and Wheeler, J. A. (1973), *Gravitation*, Freeman, San Francisco.

Papapetrou, A. (1951), *Proc. Roy. Soc. London Ser. A*, **209**, p. 248.

Pirani, R. A. E. (1956), *Acta Phys. Polon. A*, **15**, p. 389.

Stuchlík, Z. (1999), Equilibrium of spinning test particles in the Schwarzschild–de Sitter spacetimes, *Acta Phys. Slovaca*, **49**(3), pp. 319–324, ISSN 0323-0465/99.

Stuchlík, Z., Bičák, J. and Balek, V. (1999), The shell of incoherent charged matter falling onto a charged rotating black hole, *Gen. Relativity Gravitation*, **31**(1), pp. 53–71, ISSN 0001-7701.

Stuchlík, Z. and Hledík, S. (1999), Some properties of the Schwarzschild–de Sitter and Schwarzschild–anti-de Sitter spacetimes, *Phys. Rev. D*, **60**(4), p. 044006 (15 pages), URL `http://ojps.aip.org/journal_cgi/dbt?KEY=PRVDAQ&Volume=60&Issu%e=4`.

Stuchlík, Z. and Hledík, S. (2001), Equilibrium of a charged spinning test particle in Reissner–Nordström backgrounds with a nonzero cosmological constant, *Phys. Rev. D*, **64**(10), p. 104016 (12 pages), ISSN 1089-4918, URL `http://link.aps.org/abstract/PRD/v64/e104016`.

Stuchlík, Z. and Slaný, P. (2004), Equatorial circular orbits in the Kerr–de Sitter spacetimes, *Phys. Rev. D*, **69**, p. 064001, ISSN 1094-1622, `gr-qc/0307049`.

Proceedings of *RAGtime 6/7: Workshops on black holes and neutron stars, Opava, 16–18/18–20 September, 2004/2005*
S. Hledík and Z. Stuchlík, editors, Silesian University in Opava, Czech Republic, 2005, pp. 253–263

On the possibility of precise determination of black hole spin in the framework of resonance models

Zdeněk Stuchlík and Gabriel Török

Institute of Physics, Faculty of Philosophy & Science, Silesian University in Opava, Bezručovo nám. 13, CZ-746 01 Opava, Czech Republic

ABSTRACT
It is highly probable that a non-linear resonance between some modes of oscillations in the accretion discs around black holes and neutron stars can play a crucial role in exciting detectable modulations of the X-ray flux. Detailed studies of the resonance models revealed that several of such non-linear resonances are possible in nearly Keplerian discs in strong gravity. Moreover, this idea seems to be strongly supported by observations – in all four microquasars showing twin peak QPOs (quasiperiodic oscillations), the ratio of frequency peaks is 3 : 2. In principle, using known frequencies of the twin peaks and the known mass of the central black hole, the *black-hole spin can be determined*. This was already done for the presently known sources and few miscellaneous resonance models. Details of excitation mechanisms of eventual resonances are still not fully explained, nevertheless one can imagine that not only one resonance could be excited in the accretion disc. Thus, if two such different resonances are present (by an accident or because of some causal connection), the black hole spin can be precisely determined independently of the knowledge of the black hole mass, for some specific cases discussed here.

Keywords: compact objects – X-ray variability – theory – observations

1 INTRODUCTION

Quasiperiodic oscillations (QPOs) of X-ray brightness had been observed at low (Hz) and high (kHz) frequencies in many Galactic low-mass X-ray binaries containing neutron stars or black holes (see, e.g., McClintock and Remillard, 2004; van der Klis, 2000). Some of the quasi periodic oscillations (QPOs) are in the kHz range and often come in pairs ($\nu_{\rm up}$, $\nu_{\rm down}$) of *twin peaks*[1] in the Fourier power spectra. Since the peaks of high frequencies are close to the orbital frequency of the marginally stable circular orbit representing the inner edge of Keplerian discs orbiting black holes (or neutron stars), the strong gravity effects must be relevant in explaining high frequency QPOs (Abramowicz et al., 2004b).

[1] More often called *double peaks*, but the authors prefer the term twin peaks coined by Lynch and Frost (1990).

80-7248-334-X

Before the twin peak kHz QPOs have been discovered in microquasars (first by Strohmayer, 2001), and the 3 : 2 ratio pointed out (first by Abramowicz and Kluźniak, 2001), Kluźniak and Abramowicz (2000) suggested on theoretical grounds that these QPOs should have rational ratios, because of the resonances in oscillations of nearly Keplerian accretion disks. It seems that the resonance hypothesis is now well supported by observations, and that in particular the 3 : 2 ratio ($2\nu_{\mathrm{up}} = 3\nu_{\mathrm{down}}$) is seen most often in twin peak QPOs in low mass X-ray binaries – black hole and neutron star sources. In addition, there is even some evidence of the same 3 : 2 ratio in the X-ray spectra of the Galaxy centre black hole in Sgr A* (Abramowicz et al., 2004a; Aschenbach, 2004; Török, 2005).

According to the resonance hypothesis (Kluźniak and Abramowicz, 2000), the two modes in resonance should have eigenfrequencies ν_{r} (equal to the radial epicyclic frequency) and ν_{v} (equal to the vertical epicyclic frequency ν_θ or to the Keplerian frequency ν_{K}); see Abramowicz and Kluźniak (2004) and Török et al. (2005) for recent review. While models based on the *parametric resonance* identify the two observed frequencies of the twin peak (ν_{up}, ν_{down}) directly with the eigenfrequencies of a resonance, models based on the *forced resonance* allows to observe combinational (beat) frequencies of the modes. Both parametric and forced resonance models make clear and precise predictions about the values of observed frequencies in connection with spin and mass of the observed object (at least in the case of black holes). Figure 1 and Table 1 (from Török et al., 2005) show the estimate of black hole specific internal angular momentum (sometimes, we call this quantity shortly the black hole *spin*) given by few possible models for microquasars with observed twin peak QPOs. Although the observed frequencies are consistent with several (but not every) resonance models, the most probable and natural explanation for the presence of 3 : 2 ratio is

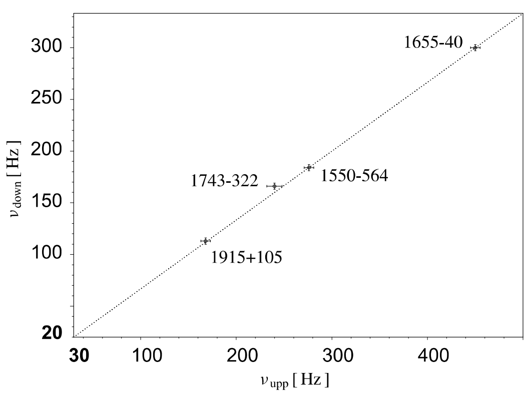

Figure 1. In all four microquasars with X-ray twin peak kHz QPOs discovered, $\nu_{\mathrm{up}}/\nu_{\mathrm{down}} = 3/2$. (From Török et al., 2005.)

	Type of resonance	Spin estimate
standard	parametric	0.97
standard	3:1 forced	0.53
standard	2:1 forced	0.35
Keplerian	parametric	—
Keplerian	3:1 forced	0.48
Keplerian	2:1 forced	0.35

Table 1. Estimate of the black hole spin for the three microquasars resulting from miscellaneous resonance models. Displayed value is averaged by the fit $\nu_{\mathrm{up}} \sim 1/M$; for the details and exact numbers corresponding to the particular microquasars see Török et al. (2005). Shaded field stress the estimate for the 3 : 2 parametric (or internal) resonance. (From Török et al., 2005.)

the 3 : 2 parametric (or *internal*) resonance (Abramowicz and Kluźniak, 2004; Török et al., 2005).

In this article we briefly remind some essential points of the orbital resonance models and then we discuss the possibility and consequences of the situation in which not only one resonance is excited in the disc. We assume that both the parametric and forced resonance could occur simultaneously at different parts of a Keplerian accretion disc. Then, under the assumption that the upper (bottom) observed frequencies can be the same, we are able to find the internal angular momentum of the black hole in dependence on the ratio of the tripled observed frequencies and independently of the black hole mass. Of course, in such case the black hole mass can be determined from the magnitude of the observed frequencies.

2 DIGEST OF ORBITAL RESONANCE MODELS

Two main groups of orbital resonance models exist. Both of them are related to the epicyclic frequencies of the equatorial circular test particle motion. The epicyclic frequencies can be relevant both for the thin, Keplerian discs (Kato et al., 1998) and for thick, toroidal discs (Rezzolla, 2004; Šrámková, 2005).

2.1 Internal parametric resonance

The first one, the internal resonance model, is based on the idea of *parametric resonance* between vertical and radial epicyclic oscillations with the frequencies $\nu_\theta = \omega_\theta/2\pi$ and $\nu_{\rm r} = \omega_{\rm r}/2\pi$. The parametric resonance is described by the Mathieu equation (Landau and Lifshitz, 1976)

$$\delta\ddot{\theta} + \omega_\theta^2[1 + h\cos(\omega_{\rm r} t)]\,\delta\theta = 0\,. \tag{1}$$

Theory behind the Mathieu equation implies that a parametric resonance is excited when

$$\frac{\omega_{\rm r}}{\omega_\theta} = \frac{\nu_{\rm r}}{\nu_\theta} = \frac{2}{n}\,, \qquad n = 1, 2, 3, \ldots \tag{2}$$

and is strongest for the smallest possible value of n (Landau and Lifshitz, 1976). Because there is $\nu_{\rm r} < \nu_\theta$ near black holes, the smallest possible value for the parametric resonance is $n = 3$, which means that $2\nu_\theta = 3\nu_{\rm r}$. This explains the observed 3 : 2 ratio, assuming $\nu_{\rm up} = \nu_\theta$ and $\nu_{\rm down} = \nu_{\rm r}$. Note that the same condition (2) holds also for the internal resonance in a system with conserved energy.

2.2 Forced resonance

Models based on the *forced resonance* come from the idea of a forced non-linear oscillator, when the relation of the latitudinal (vertical) and radial oscillations is given by the formulae

$$\delta\ddot{\theta} + \omega_\theta^2\,\delta\theta + [\text{non linear terms in } \delta\theta] = g(r)\cos(\omega_0 t)\,, \tag{3}$$

$$\delta\ddot{r} + \omega_{\rm r}^2\,\delta r + [\text{non linear terms in } \delta\theta, \delta r] = h(r)\cos(\omega_0 t)\,, \tag{4}$$

Table 2. Relation for observed frequencies for standard ($\nu_\mathrm{v} = \nu_\theta$) and "Keplerian" ($\nu_\mathrm{v} = \nu_\mathrm{K}$) resonances.

	Theory			Observed frequencies	
	Type of resonance	$n\nu_\mathrm{r} = m\nu_\mathrm{v}$			
		n	m	ν_up	ν_down
standard	parametric	3	2	ν_θ	ν_r
	3 : 1 forced	3	1	ν_θ	$\nu_\theta - \nu_\mathrm{r}$
	2 : 1 forced	2	1	$\nu_\theta + \nu_\mathrm{r}$	ν_θ
Keplerian	parametric	3	2	ν_K	ν_r
	3 : 1 forced	3	1	ν_K	$\nu_\mathrm{K} - \nu_\mathrm{r}$
	2 : 1 forced	2	1	$\nu_\mathrm{K} + \nu_\mathrm{r}$	ν_K

with

$$\omega_\theta = \frac{p}{q}\,\omega_\mathrm{r}\,, \tag{5}$$

where p, q are small natural numbers and ω_0 is the frequency of the external force.[2] The non-linear terms allow the presence of combination (beat) frequencies in resonant solutions for $\delta\theta(t)$ and $\delta r(t)$ (see, e.g., Landau and Lifshitz, 1976), which in the simplest case give

$$\omega_- = \omega_\theta - \omega_\mathrm{r}\,, \qquad \omega_+ = \omega_\theta + \omega_\mathrm{r}\,. \tag{6}$$

Such resonances can produce the observable frequencies in the 3 : 2 ratio as well as in other rational ratios (note that one of the cases which give 3 : 2 observed ratio is also the "direct" case of $p : q = 3 : 2$ corresponding to the same frequencies and radius as in the case of 3 : 2 parametric resonance).

Another, so called *"Keplerian" resonance* model, takes into account possible parametric or forced resonances between radial epicyclic frequency ν_r and Keplerian orbital frequency ν_K.

Main relations for some of the resonance models briefly mentioned above are summarized in the Table 2. Of course, there is an additional possibility how to compose the resonance models, based on the combinations of the oscillations with the vertical epicyclic frequency ν_θ and the Keplerian orbital frequency ν_K and its beat frequencies involving the radial epicyclic frequency ν_r.

[2] E.g., the gravitational perturbative forces are discussed, for the case of a neutron star with "mountains" or accretion columns, and a binary partner of the neutron star or a black hole, in Stuchlík and Hledík (2005).

3 DETERMINATION OF THE SPIN FROM RESONANCE MODELS

It is well known that the formulae for the vertical epicyclic frequency ν_θ and the radial epicyclic frequency ν_r take in the gravitational field of a rotating Kerr black hole (with the mass M and spin a) the form (e.g., Nowak et al., 1999)

$$\nu_\theta^2 = \alpha_\theta\, \nu_\mathrm{K}^2\,, \qquad \nu_\mathrm{r}^2 = \alpha_\mathrm{r}\nu_\mathrm{K}^2\,, \tag{7}$$

where the Keplerian frequency and related dimensionless epicyclic frequencies are given by the formulae

$$\begin{aligned}
\nu_\mathrm{K} &= \frac{1}{2\pi}\left(\frac{GM_0}{r_\mathrm{G}^3}\right)^{1/2}\left(x^{3/2}+a\right)^{-1}\,,\\
\alpha_\theta &= 1 - 4ax^{-3/2} + 3a^2x^{-2}\,,\\
\alpha_\mathrm{r} &= 1 - 6x^{-1} + 8ax^{-3/2} - 3a^2x^{-2}\,.
\end{aligned} \tag{8}$$

Here $x = r/(GM/c^2)$ is the dimensionless radius, expressed in terms of the gravitational radius of the black hole. For a particular resonance $n:m$, the equation

$$n\nu_\mathrm{r} = m\nu_\mathrm{v}\,; \quad \nu_\mathrm{v} \in \{\nu_\theta, \nu_\mathrm{K}\} \tag{9}$$

determines the dimensionless resonance radius $x_{n:m}$ as a function of the spin a.

From the known mass of the central black hole (e.g., low-mass in the case of binary systems or hi-mass in the case of supermassive black holes), the observed twin peak frequencies (ν_up, ν_down), and the Eqs (7) and (9) imply the black hole spin, consistent with different types of resonances with the beat frequencies taken into account. This procedure was first applied to the microquasar GRO 1655−40 by Abramowicz and Kluźniak (2001), more recently to the other three microquasars (Abramowicz and Kluźniak, 2004; Török et al., 2005) and also to the Galaxy centre black hole (Török, 2005). Quantitative results of this analysis are reminded partially in the Table 1.

4 MULTIPLE RESONANCES AND THEIR OBSERVATIONAL CONSEQUENCES

The very probable interpretation of twin peak frequencies observed in microquasars is the 3 : 2 parametric resonance, however, generally it is not unlikely that more than one resonance could be excited in the disc at the same time under different internal conditions.

In principle, in any case of this type, one can determine both the spin and mass of black hole just only from the eventually observed set of frequencies. However, the obvious difficulty would be to identify the right combination of resonances and its relation to the observed set.

Here we consider the special case of two different resonances determined by a doubled ratio of natural numbers $n:m$ and $p:q$. Such resonances are located at the corresponding radii $r_{n:m}, r_{p:q}$ and characterized by observable set of frequencies resulting from the relevant resonance modes (forced or parametric). Thus, the generic relation $n:m\ :\ p:q$ *fixes the* *rotational parameter of the central black hole*. It is reasonable (because of arguments mentioned above) to assume that one of this excited resonances is a $3:2$ parametric (internal) resonance. Such situation is described by the generic relation $3:2:p:q$ and equivalent observable frequencies are in relation $3:2:s:t$ where s, t are the relevant numbers determined by the combinational frequencies given by the ratio $p:q$ establishing the radius where the forced resonance of the epicyclic frequencies, or the epicyclic and Keplerian frequencies, is realized.

4.1 Characteristic sets of frequencies with the duplex frequency

In some specific situations, for some specific values of the central black hole spin, the bottom (top) frequencies observed at the radii $r_{3:2}$ (or, generally, $r_{n:m}$) and $r_{p:q}$ are identical. Now, we assume the specific situation with coefficients q being equal to m or p being equal to n. The first case of the "bottom identity" $3:2:p$ describes the situation with two resonances having common radial epicyclic frequency while the second case $3:2:q$ of the "top identity" describes the situation with two resonances having common vertical epicyclic frequency. These two possibilities are in principle allowed by the nonmonotonicity of the epicyclic frequencies (7) discussed in detail in Török and Stuchlík (2005a).

It is rather familiar piece of knowledge that the radial epicyclic frequency has the global maximum for any Kerr black hole, however also the vertical epicyclic frequency is not monotonic if the spin is sufficiently high (see, e.g., Kato et al., 1998; Perez et al., 1997). For the Kerr black-hole spacetimes, the locations $\mathcal{R}_{\mathrm{r}}(a)$, $\mathcal{R}_{\theta}(a)$ of maxima of the epicyclic frequencies ν_{r}, ν_{θ} are implicitly given by the conditions (Török and Stuchlík, 2005a)

$$\beta_j(x,a) = \frac{1}{2}\frac{\sqrt{x}}{x^{3/2}+a}\,\alpha_j(x,a)\,, \tag{10}$$

where $j \in \{r, \theta\}$, and

$$\alpha_{\mathrm{r}}(x,a) \equiv \frac{1}{x^2} - 2\frac{a}{x^{5/2}} + \frac{a^2}{x^3}\,, \tag{11}$$

$$\alpha_{\theta}(x,a) \equiv \frac{a}{x^{5/2}} - \frac{a^2}{x^3}\,. \tag{12}$$

For any black hole spin, the extrema of the radial epicyclic frequency $\mathcal{R}_{\mathrm{r}}(a)$ must be located above the marginally stable orbit. On the other hand, the latitudinal extrema $\mathcal{R}_{\theta}(a)$ are located above the photon (marginally bound or marginally stable) circular orbit only if the limits on the black hole spin $a > 0.748$ $(0.852, 0.952)$ are satisfied (Török and Stuchlík, 2005b). This means that while the "bottom identity" could happen for any black hole spin a, the "top identity" can arise only for $a \sim 1$. (The schematic sketches of the special cases of the triples of the observed frequencies are in the "direct" cases, with no beat frequencies involved, illustrated in Fig. 2.)

In both cases of the "identities," one frequency in resulting observable set must be *doubled*. The common radial (vertical) frequency has to be the lower (upper) one. The discussion is complicated by the possibility to consider corresponding (combinational) beat frequencies, when $\nu_{\mathrm{up}} = \nu_{\theta} + \nu_{\mathrm{r}}$, $\nu_{\mathrm{down}} = \nu_{\theta} - \nu_{\mathrm{r}}$.

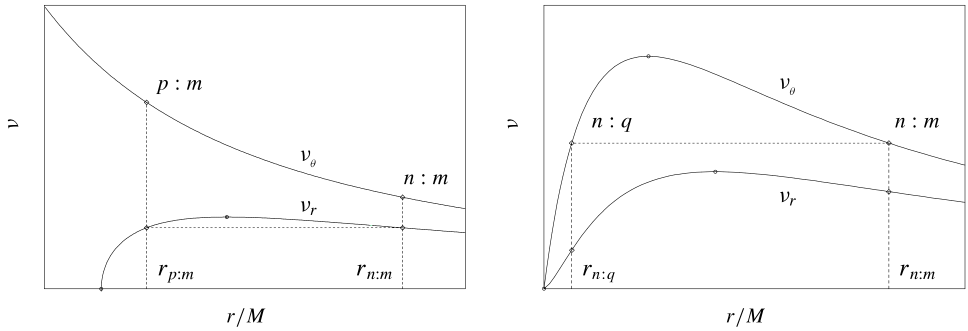

Figure 2. *Left panel:* locations of the two different resonances with natural coefficients $n:m$ and $p:q$ for the specific case of $q = m$, figure is plotted for the Schwarzschild black hole ($a = 0$). *Right panel:* locations of the two different resonances with natural coefficients $n:m$ and $p:q$ for the specific case of $p = n$, figure is plotted for the extremal Kerr black hole ($a = 1$). For both schematic figures, the position of $n:m$ is particularly chosen at location of 3 : 2 resonance.

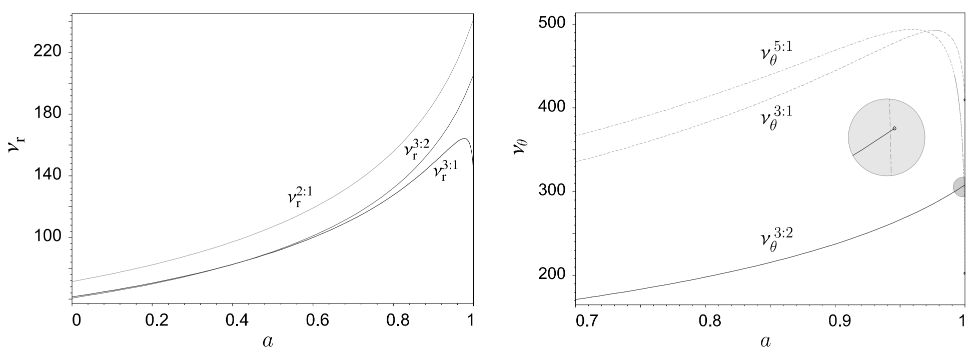

Figure 3. *Left panel:* The functions $\nu_{\rm r}^{p:q}(a)$ for the smallest $p, q = 1, 2, 3$. *Right panel:* Functions $\nu_\theta^{p:q}(a)$ for 3 : 2, 3 : 1, 5 : 1.

We have checked the functions $\nu_{\rm r}^{p:q}(a)$ in relation to $\nu_{\rm r}^{3:2}(a)$ for the smallest values of $p, q = 1, 2, 3$. While for a 2 : 1 resonance the "bottom identity" is not possible, the curves $\nu_{\rm r}^{3:1}(a)$, $\nu_{\rm r}^{3:2}(a)$ cross at $a \doteq 0.44$ and the set of frequencies resulting from common radial epicyclic frequency could be generated (see Fig. 3 – left panel). For the "top identity" with equal vertical epicyclic frequencies there is no "identity" possible if p, q are restricted to $1, 2, 3$; however, e.g., for a 4 : 1 or 5 : 1 resonances the "top identity" could be realized in the black hole backgrounds with the spin $a \sim 0.999$ (see Fig. 3 – right panel).

In Table 3 we present sets of the observable frequencies which can result from the coincidence of the 3 : 2 parametric and 3 : 1 forced resonance, if the spin has the specific value $a = 0.44$. Analogical analysis is given in Table 4 for the case of extremely high spin $a \doteq 0.999$ and the "top identity" of the 3 : 2 parametric resonance and the 4 : 1 or 5 : 1 forced resonances.

Table 3. The type of sets resulting for the "bottom identity" ($a \sim 0.44$) of 3 : 2 parametric and 3 : 1 forced resonance.

$\nu_{\rm up}$	$\nu_{\rm middle}$	$\nu_{\rm down}$	characteristic set
$\nu_\theta^{3:1}$	$\nu_\theta^{3:2}$	$\nu_{\rm r}$	$6:3:\mathbf{2}$
$\nu_\theta^{3:1}+\nu_{\rm r}$	$\nu_\theta^{3:2}$	$\nu_{\rm r}$	$8:3:\mathbf{2}$
$\nu_\theta^{3:1}-\nu_{\rm r}^{3:1}$	$\nu_\theta^{3:2}$	$\nu_{\rm r}$	$4:3:\mathbf{2}$

Table 4. The type of sets resulting for the "top identity" ($a \sim 0.999$) of 3:2 parametric and 4:1 or 5:1 forced resonance.

$\nu_{\rm up}$	$\nu_{\rm middle}$	$\nu_{\rm down}$	characteristic set
ν_θ	$\nu_{\rm r}^{3:2}$	$\nu_{\rm r}^{4:1}$	$\mathbf{12}:8:3$
$\nu_\theta+\nu_{\rm r}^{4:1}$	ν_θ	$\nu_{\rm r}^{3:2}$	$15:\mathbf{12}:8$
ν_θ	$\nu_\theta-\nu_{\rm r}^{4:1}$	$\nu_{\rm r}^{3:2}$	$\mathbf{12}:9:8$
ν_θ	$\nu_{\rm r}^{3:2}$	$\nu_{\rm r}^{5:1}$	$\mathbf{15}:10:3$
$\nu_\theta+\nu_{\rm r}^{5:1}$	ν_θ	$\nu_{\rm r}^{3:2}$	$18:\mathbf{15}:10$
ν_θ	$\nu_\theta-\nu_{\rm r}^{5:1}$	$\nu_{\rm r}^{3:2}$	$\mathbf{15}:12:10$

5 CONCLUSIONS

The resonant model of QPOs predicts that both the internal parametric resonance and a forced resonance can be excited in the both thin and thick accretion discs rotating around black holes or neutron stars and that the resonant non-linear phenomena can occur between oscillations with the vertical and radial epicyclic or with the orbital (Keplerian) frequency. It is possible that the resonances are excited for different internal reasons, at different radii on the accretion disc, and pairs of the resonant frequencies could occur in general situations. Even in this case one can determine both the spin and mass of the black hole but it would be rather difficult to identify relevant combination of resonances. However, for special values of the black hole specific internal angular momentum (spin), the bottom (upper) epicyclic frequencies could be equal at different radii, since there exist local extrema of the radial profiles of both the epicyclic frequencies in the Kerr black hole spacetimes. We have shown that in such situations, the ratio of the triples of the epicyclic frequencies, or their combinations given by beat frequencies, is directly related to the black hole spin, independently of the black hole mass. Such a possibility of direct measurement of the the black hole spin is very important because of relatively high uncertainties in observational estimates of the black hole mass, necessary for determination of the black hole spin in general resonant phenomena (Török et al., 2005) or in black hole spin determinations based on the measurements of profiled spectral lines (Laor, 1991; Bao and Stuchlík, 1992; Karas et al., 1992).

The relation between the tripled frequency ratios and the black hole spin is presented in the Tables 3 and 4 in the basic possible cases of the bottom and top identities.

Of course, it is necessary to consider also the possibility to obtain a tripled frequencies with the same ratio when taking into account some beat frequencies or relating the two epicyclic and the orbital frequency.[3] Such possibilities are under study at present.

The discussed possibility of precise determination of the black hole spin is based on special situations when tripled frequencies are observed with characteristic ratios given by the spin of the black hole, independently of its mass. The mass of the black hole is related to the magnitude of the observed frequency triple. Of course, such a method can work only accidentally, for the properly taken values of the black hole spin. Nevertheless, it is worth to make careful search of the predicted frequency ratios in the observational data, because an accidental success in the search could help much in understanding the other related phenomena, if the spin is found precisely.

ACKNOWLEDGEMENTS

This work was supported by the Czech grant MSM 4781305903.

REFERENCES

Abramowicz, M. A. and Kluźniak, W. (2001), A precise determination of black hole spin in GRO J1655−40, *Astronomy and Astrophysics*, **374**, p. L19, `astro-ph/010507`.

Abramowicz, M. A. and Kluźniak, W. (2004), Interpreting black hole QPOs, in P. Karet, F. K. Lamb and J. H. Swank, editors, *X-ray Timing 2003: Rossi and Beyond.*, volume 714, pp. 21–28, NY: American Institute of Physics, Melville, `astro-ph/0312396`.

Abramowicz, M. A., Kluźniak, W., McClintock, J. E. and Remillard, R. A. (2004a), The Importance of Discovering a 3 : 2 Twin-Peak Quasi-periodic Oscillation in an Ultraluminous X-Ray Source, or How to Solve the Puzzle of Intermediate-Mass Black Holes, *Astrophys. J. Lett.*, **609**, pp. L63–L65.

Abramowicz, M. A., Kluźniak, W., Stuchlík, Z. and Török, G. (2004b), Twin peak QPOs frequencies in microquasars and Sgr A*. The resonance and other orbital models, in Hledík and Stuchlík (2004), pp. 1–23.

Aschenbach, B. (2004), Measuring mass and angular momentum of black holes with high-frequency quasi-periodic oscillations, *Astronomy and Astrophysics*, **425**, pp. 1075–1082, `astro-ph/0406545`.

[3] Or considering the possibility of vertical precession resonance introduced by Bursa (2005). In this relation it is interesting that for the black hole spin $a \sim 0.8$ this resonance could occur at the same orbit as the 3 : 1 epicyclic resonance (see Fig. 5 in Török and Stuchlík, 2005a).

Bao, G. and Stuchlík, Z. (1992), Accretion disk self-eclipse – X-ray light curve and emission line, *Astrophys. J.*, **400**, pp. 163–169.

Bursa, M. (2005), High-frequency QPOs in GRO J1655−40: Constraints on resonance models by spectral fits, pp. 39–45, this volume.

Hledík, S. and Stuchlík, Z., editors (2004), *Proceedings of RAGtime 4/5: Workshops on black holes and neutron stars, Opava, 14–16/13–15 October 2002/2003*, Silesian University in Opava, Opava, ISBN 80-7248-242-4.

Karas, V., Vokrouhlický, D. and Polnarev, A. G. (1992), In the vicinity of a rotating black hole – A fast numerical code for computing observational effects, *Monthly Notices Roy. Astronom. Soc.*, **259**, pp. 569–575.

Kato, S., Fukue, J. and Mineshige, S. (1998), Black-hole accretion disks, Kyoto University Press, Kyoto, Japan.

Kluźniak, W. and Abramowicz, M. A. (2000), The physics of kHz QPOs – strong gravity's coupled anharmonic oscillators, submitted in Phys. Rev. Lett., `astro-ph/0105057`.

Landau, L. D. and Lifshitz, E. M. (1976), *Mechanics*, Pergamon Press, Oxford, 3rd edition.

Laor, A. (1991), Line profiles from a disk around a rotating black hole, *Astrophys. J.*, **376**, pp. 90–94.

Lynch, D. and Frost, M. (1990), Twin Peaks, television series, URL `http://www.lynchnet.com/tp/`.

McClintock, J. E. and Remillard, R. A. (2004), Black Hole Binaries, in W. H. G. Lewin and M. van der Klis, editors, *Compact Stellar X-Ray Sources*, Cambridge University Press, Cambridge, `astro-ph/0306213`.

Nowak, M., Lehr, D. and Björnsson, G. (1999), , in M. A. Abramowicz, G. Bjöornsson and J. E. Pringle, editors, *Theory of Black Hole Accretion Disks*, Cambridge University Press, Cambridge.

Perez, C. A., Silbertgleit, A. S., Wagoner, R. V. and Lehr, D. E. (1997), Relativistic Diskoseismology. I. Analytical Results for Gravity Modes, *Astrophys. J.*, **476**(2), p. 589, URL `http://www.journals.uchicago.edu/ApJ/journal/contents/ApJ/v47%6n2.html`.

Rezzolla, L. (2004), Nonlinear dynamics of thick discs in Schwarzschild–de Sitter spacetimes, in Hledík and Stuchlík (2004), pp. 151–165.

Šrámková, E. (2005), Epicyclic oscillation modes of a Newtonian, non-slender torus, *Astronom. Nachr.*, **326**(9), pp. 835–837.

Strohmayer (2001), Discovery of a 450 Hz Quasi-periodic Oscillation from the Microquasar GRO J1655−40 with the Rossi X-Ray Timing Explorer, *Astrophys. J. Lett.*, **552**(1), pp. L49–L54, URL `http://www.journals.uchicago.edu/ApJ/journal/issues/ApJL/v552%n1/015001/015001.html`.

Stuchlík, Z. and Hledík, S. (2005), Excitation of oscillations by a small inhomogeneity on the surface of a neutron star, pp. 189–208, this volume.

Török, G. (2005), A possible 3 : 2 orbital epicyclic resonance in QPOs frequencies of Sgr A*, *Astronomy and Astrophysics*, **440**(1), pp. 1–4.

Török, G., Abramowicz, M. A., Kluźniak, W. and Stuchlík, Z. (2005), The orbital resonance model for twin peak kHz quasi periodic oscillations in microquasars, *Astronomy and Astrophysics*, **436**(1), pp. 1–8, `astro-ph/0401464`.

Török, G. and Stuchlík, Z. (2005a), Epicyclic frequencies of Keplerian motion in Kerr spacetimes, pp. 315–338, this volume.

Török, G. and Stuchlík, Z. (2005b), Radial and vertical epicyclic frequencies of Keplerian motion in the field of Kerr naked singularities. Comparison with the black hole case and possible instability of naked singularity accretion discs, *Astronomy and Astrophysics*, **437**(3), pp. 775–788, `astro-ph/`

0502127.

van der Klis, M. (2000), Millisecond Oscillations in X-ray Binaries, *Annual Review of Astronomy and Astrophysics*, **38**, pp. 717–760.

Proceedings of *RAGtime 6/7: Workshops on black holes and neutron stars, Opava, 16–18/18–20 September, 2004/2005*
S. Hledík and Z. Stuchlík, editors, Silesian University in Opava, Czech Republic, 2005, pp. 265–280

Trapping of neutrinos in the internal Schwarzschild–(anti-)de Sitter spacetimes

Zdeněk Stuchlík, Martin Urbanec and Gabriel Török

Institute of Physics, Faculty of Philosophy & Science, Silesian University in Opava, Bezručovo nám. 13, CZ-746 01 Opava, Czech Republic

ABSTRACT
Extremely compact objects ($R < 3GM/c^2$) contain null geodesics that are captured by the object. Certain part of neutrinos produced in their interior will therefore be trapped, thus influencing neutrino luminosity of the objects and their thermal evolution. This effect was investigated for the interior Schwarzschild spacetimes with the uniform distribution of energy density by Stuchlík, Z., Török, G., Hledík, S. and Urbanec, M. (2005), Neutrino trapping in extremely compact objects, *Classical Quantum Gravity*, submitted. We will investigate here influence of the cosmological constant on the trapping phenomena. We use again the simplest model for interior of such objects based on the interior Schwarzschild–(anti-)de Sitter spacetimes. We determine behaviour of the trapping coefficients, i.e., "global" one representing influence on the neutrino luminosity and "local" one representing influence on the cooling process.

1 INTRODUCTION

It is well known that in the internal Schwarzschild spacetimes of uniform energy density (Schwarzschild, 1916) with radius $R < 3GM/c^2$, bound null geodesics must exist being concentrated around the stable circular null geodesic (Stuchlík et al., 2001; Abramowicz et al., 1993). It follows immediately from the behaviour of the effective potential of null geodesics in the exterior, vacuum Schwarzschild spacetimes, determining the unstable null circular geodesics at the radius $r_{\rm ph} = 3GM/c^2$ (see, e.g., Misner et al., 1973), that any spherically symmetric, static non-singular interior spacetime with radius $R < r_{\rm ph}$ admits existence of bound null geodesics. We call objects (stars) admitting existence of bound null geodesics – extremely compact objects (stars). Note that, in principle, the bound null geodesics could exist also in objects having $R > 3GM/c^2$, e.g., in some composite polytropic spheres (Nilsson and Ugla, 2000). The realistic equations of state admitting the existence of the extremely compact objects were found and investigated, e.g., in Nilsson and Ugla (2000); Hledík et al. (2004); Østgaard (2001); Abramowicz et al. (1997), for both neutron stars and quark stars.

80-7248-334-X

The existence of bound null geodesics in extremely compact objects has interesting astrophysical consequences, e.g., the trapped modes of gravitational waves influencing some instabilities in these objects (Abramowicz et al., 1997; Abramowicz, 1999).

We consider another interesting problem – namely, the problem of neutrinos trapped by the strong gravitational field of extremely compact objects, which can be important at least for two reasons. First, the neutrino flow from extremely compact stars as measured by distant observers should be suppressed. Second, trapped neutrinos, being restricted to a layer extending from some radius, depending on details of the structure of the extremely compact stars, up to their surface, can influence cooling of the extremely compact stars. The cooling process could even be realized in a "two-temperature" regime, when the temperature profile in the interior of the star with no trapped neutrinos differs from the profile established in the external layer with trapped neutrinos (Stuchlík et al., 2005). For the neutrino dominated period of the cooling process, one can speculate that some part of the external layer near the radius of the stable null circular geodesic, where the trapping of neutrinos reaches highest efficiency, will reach a higher temperature than is the temperature in the interior of the star. This effect can lead to an inflow of heat from the "overheated" external layer to the interior of the star through other "agents" than the neutrino flow. Such a heat flow could influence the structure of extremely compact stars, maybe, some special "self-organized" structures could develop due to the assumed heat flow. Then properties of the extremely compact stars could be modified in comparison with the standard picture given in Glendenning (2000); Weber and Glendenning (1992); Weber (1999).

Of course, all of these ideas deserve very sophisticated analytical estimates and detailed numerical simulations. The first step in considering the role of trapped neutrinos in extremely compact stars is estimation of the efficiency of the trapping effect by considering the number of trapped neutrinos in comparison to all neutrinos produced in the extremely compact objects. The influence on the neutrino luminosity of the star is given by a luminosity trapping coefficient relating the total number of trapped neutrinos and the total number of radiated neutrinos (per unit time of distant observers). The influence on the cooling process is given by two "cooling" trapping coefficients: a "local" one given by ratio of trapped and radiated neutrinos at any radius where the trapping occurs, and the "global" one giving ratio of trapped and radiated neutrinos (per unit time of distant observers) integrated over whole the region where the trapping occurs.

The trapping was considered in the internal Schwarzschild spacetime with uniform distribution of energy density (but a nontrivial pressure profile) and isotropic and uniform distribution of local neutrino luminosity, when all the calculations can be realized in terms of elementary functions only (Stuchlík et al., 2005). Here we shall extend the estimations to the internal Schwarzschild–(anti-)de Sitter spacetimes with the uniform distribution of energy density, in order to obtain information on the influence of a nonzero cosmological constant on the effect. The trapping and "cooling" coefficients introduced in Stuchlík et al. (2005) are given here by numerical integration.

In Section 2, we summarize properties of the internal Schwarzschild–(anti-)de Sitter spacetime. In Section 3, null geodesics of the spacetime are described in terms of properly given effective potential. In Section 4, the trapping of neutrinos is determined. In Section 5, the efficiency coefficients of the trapping are defined for both the total neutrino luminosity and neutrino cooling process, and determined numerically for the internal

Schwarzschild–(anti-)de Sitter spacetime. In Section 6, concluding remarks are presented. We shall use the geometric units, if not stated otherwise. For simplicity, we assume zero rest energy of neutrinos and the period of evolution of the compact stars, when the temperature is low enough that the motion of neutrinos is determined by the null geodesics of the spacetime.

2 INTERIOR SCHWARZSCHILD–(ANTI-)DE SITTER SPACETIME

In standard Schwarzschild coordinates (t, r, θ, φ) the line element for interior Schwarzschild-(anti)de Sitter spacetime with uniform energy density ρ reads

$$\mathrm{d}s^2 = -\mathrm{e}^{2\Phi(r)}\,\mathrm{d}t^2 + \mathrm{e}^{2\Psi(r)}\,\mathrm{d}r^2 + r^2(\mathrm{d}\theta^2 + \sin^2\theta\,\mathrm{d}\varphi^2)\,. \tag{1}$$

The temporal and radial components of metric tensor are given by relations

$$\begin{aligned}(-g_{tt})^{1/2} &= \mathrm{e}^{\Phi} = AY_1 - BY(r)\,,\\ (g_{rr})^{1/2} &= \mathrm{e}^{\Psi} = \frac{1}{Y(r)}\,,\end{aligned} \tag{2}$$

where

$$Y(r) = \left(1 - \frac{r^2}{a^2}\right)^{1/2}, \tag{3}$$

$$Y_1 = Y(R) = \left(1 - \frac{R^2}{a^2}\right)^{1/2}, \tag{4}$$

$$\frac{1}{a^2} = \frac{2M}{R^3} + \frac{\Lambda}{3}\,, \tag{5}$$

$$A = \frac{9M}{6M + \Lambda R^3}\,, \tag{6}$$

$$B = \frac{3M - \Lambda R^3}{6M + \Lambda R^3}\,. \tag{7}$$

In the presented relations R is total radius of the star, M is the mass of the star and Λ is the cosmological constant. The parameter a represents the curvature of the internal spacetime; it is the radius of the embedding diagram of its equatorial plane $t = \mathrm{const}$ section into 3D Euclidean space (Stuchlík et al., 2001).

We express all the quantities in terms of M, i.e., in dimensionless form: $r/M \to r$, $a/M \to a, x \equiv R/M, y \equiv M^2\Lambda/3$, when we obtain the relations

$$\begin{aligned}a^2 &= \frac{x^3}{2 + yx^3}\,, \qquad Y_1 = \left(\frac{x - 2 - yx^3}{x}\right)^{1/2},\\ A &= \frac{3}{2 + yx^3}\,, \qquad B = \frac{1 - yx^3}{2 + yx^3}\,.\end{aligned} \tag{8}$$

We can see that if $2+yx^3 = 0$, i.e., $y = -2/x^3$, then $Y(r) = 1$, $A-B = 1$ and so $e^{\Psi(r)} = 1$ while

$$e^{\Phi(r)} = 1 + \frac{3M}{2R}\left(\frac{r^2}{R^2} - 1\right) \tag{9}$$

and spacetime has a very simple form.

In terms of the tetrad formalism the metric (1) reads

$$ds^2 = -[\omega^{(t)}]^2 + [\omega^{(r)}]^2 + [\omega^{(\theta)}]^2 + [\omega^{(\phi)}]^2 \,, \tag{10}$$

where

$$\omega^{(t)} = e^{\Phi}\, dt \,, \qquad \omega^{(r)} = e^{\Psi}\, dr \,, \qquad \omega^{(\theta)} = r\, d\theta \,, \qquad \omega^{(\phi)} = r \sin\theta\, d\phi \,. \tag{11}$$

Tetrad of 4-vectors $e^{\mu}_{(\alpha)} = [\omega^{(\alpha)}_{\mu}]^{-1}$ is then given by

$$\boldsymbol{e}_{(t)} = \frac{1}{e^{\Phi}}\frac{\partial}{\partial t} \,, \qquad \boldsymbol{e}_{(r)} = \frac{1}{e^{\Psi}}\frac{\partial}{\partial r} \,, \qquad \boldsymbol{e}_{(\theta)} = \frac{1}{r}\frac{\partial}{\partial \theta} \,, \qquad \boldsymbol{e}_{(\phi)} = \frac{1}{r\sin\theta}\frac{\partial}{\partial \phi} \,. \tag{12}$$

Tetrad components of 4-momentum of a test particle or a photon are determined by the projections $p_{(\alpha)} = p_{\mu} e^{\mu}_{(\alpha)}$, $p^{(\alpha)} = p^{\mu}\omega^{(\alpha)}_{\mu}$ which give quantities measured by the local observers.

3 NULL GEODESICS, IMPACT PARAMETER AND EFFECTIVE POTENTIAL

For neutrinos moving along null geodesics, the geodesic equation holds together with the normalization condition

$$\frac{Dp^{\mu}}{d\lambda} = 0 \,, \qquad p^{\mu} p_{\mu} = 0 \,. \tag{13}$$

Due to the existence of two Killing vector fields: the temporal $\partial/\partial t$ one, and the azimuthal $\partial/\partial\varphi$, two conserved components of 4-momentum must exist:

$$E = -p_t \,, \qquad L = p_{\varphi} \,. \tag{14}$$

Here E is the energy and L is the axial angular momentum. All particles move in the central planes. For a single particle, we can set this plane to be equatorial ($\theta = \pi/2 = \text{const}$). For null-geodetical motion, the impact parameter $\ell = L/E$ is useful.

The relevant equation governing the radial motion then reads

$$(p^r)^2 = e^{-2(\Phi+\Psi)} E^2 \left(1 - e^{2\Phi}\frac{\ell}{r^2}\right) . \tag{15}$$

The radial motion is restricted by an effective potential defined for the internal and the external spacetime separately in the form

$$\ell^2 \le V_{\text{eff}} = \begin{cases} V_{\text{eff}}^{\text{int}} = \dfrac{a^2[1 - Y^2(r)]}{[AY_1 - BY(r)]^2} & \text{for} \quad r \le R \,, \\ V_{\text{eff}}^{\text{ext}} = \dfrac{r^3}{r - 2 - yr^3} & \text{for} \quad r \ge R \,. \end{cases} \tag{16}$$

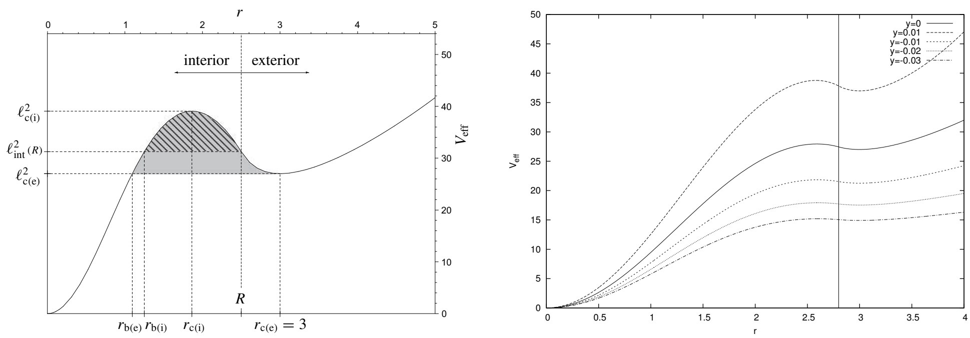

Figure 1. Detailed behaviour of effective potential (left, $R = 2.8M$, $\Lambda = 0$, taken from Stuchlík et al., 2005) and influence of cosmological parameter y (right, $R = 2.8M$).

The behaviour of the effective potential is represented in Fig. 1. We have to find $r_{\mathrm{b(i)}}$, where the value of effective potential is equal to its value at surface of the star, and to find $r_{\mathrm{b(e)}}$ where the value of effective potential is equal to its value at $r = 3$. The relevant values of the impact parameter are given in the equations

$$\ell^2_{\mathrm{i}} = \frac{x^2}{Y_1^2} = \frac{x^3}{x - 2 - yx^3}\,, \tag{17}$$

$$\ell^2_{\mathrm{e}} = \frac{27}{1 - 27y}\,. \tag{18}$$

From relation (16) for $V_{\mathrm{eff}}^{\mathrm{int}}$, we obtain $Y(r)$ to be given by the condition

$$V_{\mathrm{eff}}^{\mathrm{int}} = \frac{a^2[1 - Y^2(r)]}{[AY_1 - BY(r)]} = \ell^2_{\mathrm{i(e)}}\,, \tag{19}$$

and then from relation (3) by inverse transformation we get $r_{\mathrm{b(i)}}$ or $r_{\mathrm{b(e)}}$

$$r^2 = a^2[1 - Y^2(r)]\,. \tag{20}$$

First we find $r_{\mathrm{b(i)}}$ respectively $Y(r_{\mathrm{b(i)}})$. From equality of the effective potential and ℓ^2_{i} we obtain condition

$$\frac{a^2[1 - Y^2(r)]}{[AY_1 - BY(r)]^2} = \frac{x^2}{Y_1^2} \tag{21}$$

leading to quadratic equation in terms of $Y(r)$ that gives two solutions

$$Y_{\pm}(r_{\mathrm{b(i)}}) = \frac{2x^2ABY_1 \pm \sqrt{D}}{2(a^2Y_1^2 + x^2B^2)}\,, \tag{22}$$

where

$$D = 4x^4A^2B^2Y_1^2 - 4(a^2Y_1^2 + x^2B^2)Y_1^2(x^2A^2 - a^2)\,. \tag{23}$$

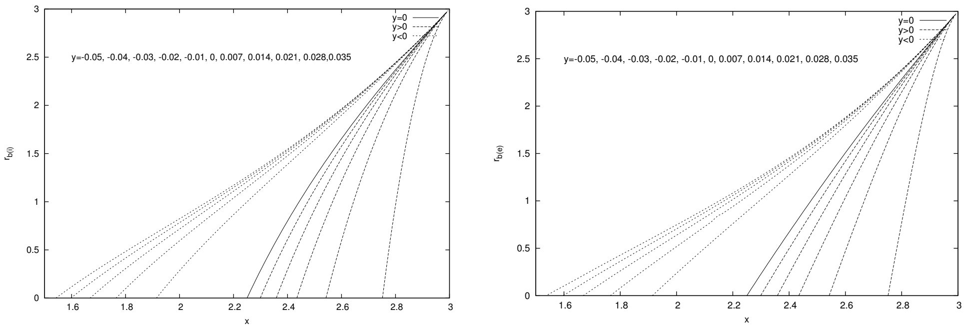

Figure 2. Dependence of total $r_{b(i)}$ (left) and $r_{b(e)}$ (right) for some values of cosmological parameter y, $-0.05 < y < 0.035$.

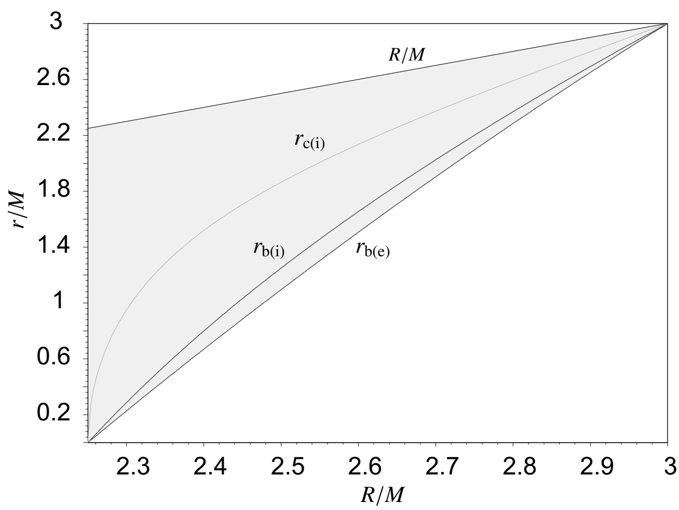

Figure 3. The dependence of the radii determining the trapped neutrinos $r_{b(e)}$, $r_{b(i)}$ and $r_{c(i)}$ giving radius of the stable circular photon orbit, on the radius R. The relations for the variable $Y(r)$ are converted into relations for r taken from Stuchlík et al. (2005).

After some simplifications we obtain the relevant solution in the form

$$Y(r_{b(i)}) = Y_1 \frac{9 - 2x - yx^4}{2x - 3 + yx^3(x - 6)}, \tag{24}$$

the other is the trivial solution $Y(r_{b(i)}) = Y_1$. The relevant solution $r_{b(i)}$ is shown in Fig. 2 for some values of cosmological parameter y.

Now we determine $r_{b(e)}$, respectively $Y(r_{b(e)})$, from equality of effective potential (for star interior) with ℓ_e^2:

$$\frac{a^2[1 - Y^2(r)]}{[AY_1 - BY(r)]^2} = \frac{27}{1 - 27y}. \tag{25}$$

We obtain quadratic equation in terms of $Y(r)$, having two solutions

$$Y_{\pm}(r_{\mathrm{b(e)}}) = \frac{54ABY_1 \pm \sqrt{D}}{2[27B^2 + a^2(1-27y)]}, \tag{26}$$

where

$$D = 54^2A^2B^2Y_1^2 - 4[27B^2 + a^2(1-27y)][27A^2Y_1^2 - a^2(1-27y)]. \tag{27}$$

We need $0 < r_{\mathrm{b(e)}} < x$; it can be shown that if $yx^3 > -2$, then Y_+ is the relevant solution while if $yx^3 < -2$, then Y_- is the relevant solution. Now, we can get $r_{\mathrm{b(e)}}$ from $Y(r_{\mathrm{b(e)}})$ numerically. The solution of $r_{\mathrm{b(e)}}(x, y)$ is shown in Fig. 2.

Circular null geodesics are given by the local extrema of effective potential ($\partial V_{\mathrm{eff}}/\partial r = 0$), which in the internal spacetime yields for their radius the relation

$$Y(r_{\mathrm{c(i)}}) = \frac{B}{AY_1}. \tag{28}$$

The radius $r_{\mathrm{c(i)}}$ is explicitly given by

$$r^2_{\mathrm{c(i)}} = a^2\frac{A^2a^2 - A^2R^2 - B^2a^2}{A^2(a^2 - R^2)}, \tag{29}$$

and it is illustrated in Fig. 3

4 TRAPPING OF NEUTRINOS

In the case of extremely compact static objects described by the internal Schwarzschild–(anti-)de Sitter spacetime, stable bound null geodesics exist (see Fig. 1), i.e., some part of produced neutrinos is prevented from escaping these static objects. For the unit mass $M = 1$, the relation (28) implies the impact parameter which corresponds to the local maximum of the effective potential $V^{\mathrm{int}}_{\mathrm{eff}}$ at $r_{\mathrm{c(i)}}$, where the stable circular null geodesics of the internal Schwarzschild–(anti-)de Sitter spacetimes are located, to be given by

$$\ell^2_{\mathrm{c(i)}} = \frac{x^3}{x - 2 - yx^3}. \tag{30}$$

The local minimum of $V^{\mathrm{ext}}_{\mathrm{eff}}$ at $r_{\mathrm{c(e)}} = 3$ corresponds to the unstable circular null geodesics of the external vacuum Schwarzschild–(anti-)de Sitter spacetime, with $\ell^2_{\mathrm{c(e)}} = 27/(1 - 27y)$ (see Fig. 1).

4.1 Regions of trapping

Bound neutrinos (depicted by the shaded area in Fig. 1) may generally appear outside the extremely compact objects, but they are trapped by the strong gravitational field of these objects and they enter them again. Therefore, we divide the trapped neutrinos into two families:

• "Internal" bound neutrinos (upper (shaded) part of the shadow area with impact parameter between $\ell^2_{\text{int}}(R)$ and $\ell^2_{\text{c(i)}}$): their motion is restricted inside the object.
• "External" bound neutrinos (lower part of the shadow area with impact parameter between $\ell^2_{\text{c(e)}}$ and $\ell^2_{\text{int}}(R)$): may leave the object, but they re-enter the object.

Pericentra for both the marginally bound ($r_{\text{b(e)}}$) and "internal" marginally bound neutrinos ($r_{\text{b(i)}}$) can be obtained from Eqs (26) or (24), see Fig. 3 for the graphical representation in the case of $y = 0$. For completeness, we show also loci $r_{\text{c(i)}}$ of the stable circular null geodesic.

Bound neutrinos with mean free path $\gg R$ (this condition can be fulfilled in a few days old neutron star, see Shapiro and Teukolsky, 1983; Weber and Glendenning, 1992) will slow down the cooling. Of course, they will be re-scattered due to finiteness of the mean free path. An eventual scattering of trapped neutrinos will cause change of their impact parameter, therefore, some of them will escape the extremely compact star, suppressing thus the slow down of the cooling process in the region of neutrino trapping. However, the "external" bound neutrinos have certain portion of their orbit outside the compact star where no interaction with matter is possible; this fact, on the other hand, "suppress the suppression" of the cooling timescale retardation. Clearly, the scattering effect of the trapped neutrinos is a complex process deserving sophisticated numerical code based on the Monte Carlo method (we expect modelling of this effect in future). Only neutrinos produced above or at $r_{\text{b(e)}}$ are subject to this effect; those produced below $r_{\text{b(e)}}$ freely escape to infinity.

4.2 Directional angles

Considering (without loss of generality, as stated just above) an equatorial motion, we can define the *directional angle* relative to the outward pointed radial direction measured in the emitor system (i.e., the local system of static observers in the internal spacetime) by the standard relations

$$\sin\psi = \frac{p^{(\phi)}}{p^{(t)}}, \qquad \cos\psi = \frac{p^{(r)}}{p^{(t)}}, \tag{31}$$

where

$$p^{(\alpha)} = p^{\mu}\omega^{(\alpha)}_{\mu}, \qquad p_{(\alpha)} = p_{\mu}e^{\mu}_{(\alpha)} \tag{32}$$

are the neutrino momentum component as measured by the static observers. Besides conserving components (13), and $p_\theta = 0$, Eq. (15) implies

$$p_r = \pm E\mathrm{e}^{\Psi-\Phi}\left(1 - \mathrm{e}^{2\Phi}\frac{\ell^2}{r^2}\right). \tag{33}$$

For the directional angles we thus obtain relations

$$\sin\psi = \alpha(r, R, \Lambda)\,\frac{\ell}{r}, \qquad \cos\psi = \pm\left(1 - \sin^2\psi\right)^{1/2}, \tag{34}$$

where

$$\alpha(r, R, \Lambda) = AY_1 - BY(r)\,. \tag{35}$$

The interval of relevant radii is given by $r \in (r_{\mathrm{b(e)}}, R)$. The directional angle limit for the bound neutrinos is determined by the impact parameter $\ell^2_{\mathrm{c(e)}} = 27/(1-27y)$. We arrive at the relation

$$\sin\psi_{\mathrm{e}}(r, R) = \alpha(r, R, \Lambda)\left(\frac{27}{1-27y}\right)^{1/2}. \tag{36}$$

The directional angle limit for the "internal" bound neutrinos is determined by Eq. (30) and yields the relations

$$\sin\psi_{\mathrm{i}}(r, R, \Lambda) = \alpha(r, R, \Lambda)\left(\frac{x^3}{x-2-yx^3}\right)^{1/2}. \tag{37}$$

Apparently, the condition $\psi_{\mathrm{i}} > \psi_{\mathrm{e}}$ holds at any given radius $r < R$.

4.3 Local escaped to produced neutrinos ratio

We assume that neutrinos are locally produced by isotropically emitting sources. Then escaped-to-produced-neutrinos ratio depends on a geometrical argument only. It is determined by the solid angle 2Ω corresponding to escaping neutrinos (also inward emitted neutrinos must be involved because even these neutrinos can be radiated away), see Fig. 4.

Let N_{p}, N_{e} and N_{b} denote, respectively, the number of produced, escaped and trapped neutrinos per unit time of an external static observer at infinity. In order to determine the global correction factors

$$\mathcal{E}(R, \Lambda) \equiv \frac{N_{\mathrm{e}}(R, \Lambda)}{N_{\mathrm{p}}(R, \Lambda)}\,, \qquad \mathcal{B}(R, \Lambda) \equiv \frac{N_{\mathrm{b}}(R, \Lambda)}{N_{\mathrm{p}}(R, \Lambda)} = 1 - \mathcal{E}(R, \Lambda)\,, \tag{38}$$

it is necessary to introduce the local correction factor for escaping neutrinos at a given radius $r \in (r_{\mathrm{b(e)}}, R)$. Because of the assumption of isotropic emission of neutrinos in the frame of the static observers, the solid angle[1] $\Omega_{\mathrm{e}}(\Psi_{\mathrm{e}})$ determines fully the ratio of escaped-produced neutrinos. The escaping solid angle is given by

$$\Omega_{\mathrm{e}}(\Psi_{\mathrm{e}}) = \int_0^{\Psi_{\mathrm{e}}}\int_0^{2\pi} \sin\Psi\,\mathrm{d}\Psi\,\mathrm{d}\phi = 2\pi(1-\cos\Psi_{\mathrm{e}}) \tag{39}$$

and the escaping correction factor

$$\epsilon(r, R, \Lambda) = \frac{\mathrm{d}N_{\mathrm{e}}(r, \Lambda)}{\mathrm{d}N_{\mathrm{p}}(r, \Lambda)} = \frac{2\Omega(\psi_{\mathrm{e}}(r, R, \Lambda))}{4\pi} = 1 - \cos\psi_{\mathrm{e}}(r, R, \Lambda)\,, \tag{40}$$

---

[1] In the case of non-isotropic emission of neutrinos, we should take $\Omega_{\mathrm{e}}(\Psi_{\mathrm{e}}) = \int_0^{\Psi_{\mathrm{e}}}\int_0^{2\pi} p(\Psi)\sin\Psi\,\mathrm{d}\Psi\,\mathrm{d}\phi$ with $p(\Psi)$ being directional function of the emission (scattering) process.

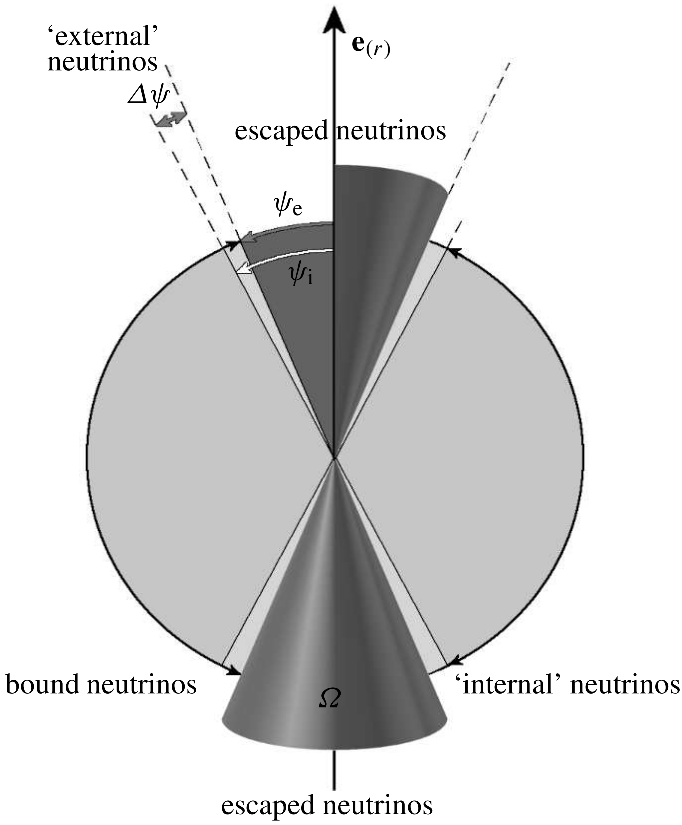

Figure 4. Schematic illustration of the bound-escape ratio at a radius $r \in (r_{b(e)}, R)$ of an internal Schwarzschild spacetime. Direction of the neutrino motion with respect to the static observers is related to $e_{(r)}$ giving the outward oriented radial direction. Taken from Stuchlík et al. (2005).

while the complementary factor for trapped neutrinos

$$\beta(r, R, \Lambda) = 1 - \epsilon(r, R, \Lambda) = \frac{dN_b(r, \Lambda)}{dN_p(r, \Lambda)} = \cos\psi_e(r, R, \Lambda)\,. \tag{41}$$

Notice that we consider production and escaping rates at a given radius r, but the radius R of the compact object and the cosmological constant enter the relation as it determines the escaping directional angle. The coefficient $\beta(r, R, \Lambda)$ determines local efficiency of the neutrino trapping, i.e., the ratio of the trapped and produced neutrinos at any given radius $r \in (r_{b(e)}, R)$. Its profile is shown for some representative values of R and Λ in Fig. 5. The local maxima of the function $\beta(r, R, \Lambda)$ (with R, Λ being fixed) are given by the condition $\partial\beta/\partial r = 0$ which is satisfied at radius $r = r_{c(i)}$ with $r_{c(i)}$ being determined by Eq. (29). This implies coincidence with the radius of the stable circular null geodesic, as anticipated intuitively. In Fig. 5, the maxima are depicted explicitly.

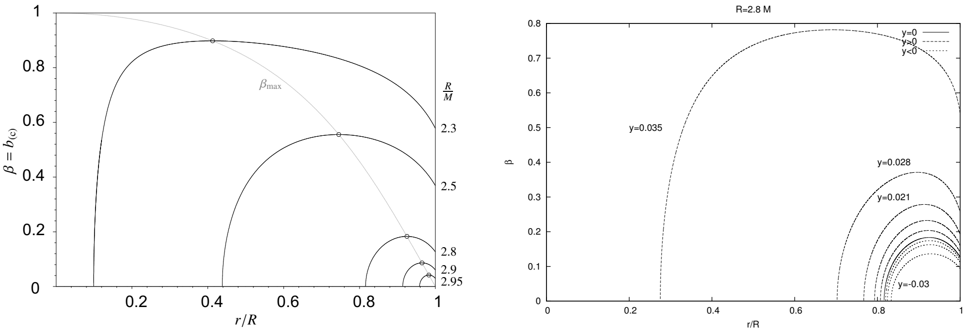

Figure 5. Local coefficient of cooling β (left, $\Lambda = 0$, some values of R taken from Stuchlík et al., 2005) and influence of cosmological parameter y (right, $R = 2.8M$).

4.4 Neutrino production rates

Generally, the neutrino production is a very complex process depending on detailed structure of an extremely compact object. We can express the locally defined neutrino production rate in the form

$$\mathcal{I}(r\{\mathcal{A}\}) = \frac{\mathrm{d}N(r\{\mathcal{A}\})}{\mathrm{d}\tau(r)}\,, \tag{42}$$

where $\mathrm{d}N$ is the number of interactions at radius r, τ is the proper time of the static observer at the given r, $\{\mathcal{A}\}$ is the full set of quantities relevant for the production rate. We can write that

$$\mathrm{d}N(r) = n(r)\Gamma(r)\mathrm{d}V(r)\,, \tag{43}$$

where $n(r)$, $\Gamma(r)$ and $\mathrm{d}V(r)$ are the number density of particles entering the neutrino production processes, the neutrino production rate and the proper volume element at the radius r, respectively. Both $n(r)$ and $\Gamma(r)$ are given by detailed structure of the extremely compact objects, $\mathrm{d}V(r)$ is given by the spacetime geometry.

Here, considering the uniform energy density internal Schwarzschild stars (for requirements of more realistic model see, e.g., Østgaard, 2001; Weber, 1999), we shall assume the local production rate to be proportional to the energy density, i.e., we assume uniform production rate as measured by the local static observers; of course, from the point of view of static observers at infinity, the production rate will not be distributed uniformly. (According to Glendenning, 2000, such toy model could be reasonable good starting point for more realistic calculations.)

Therefore, in internal Schwarzschild spacetime we can write the local neutrino production rate in the form

$$\mathcal{I}(r) \propto \rho = \mathrm{const} \tag{44}$$

or

$$\mathcal{I} = \frac{\mathrm{d}\mathcal{N}}{\mathrm{d}\tau}\,, \qquad \frac{\mathrm{d}\mathcal{N}(r)}{\mathrm{d}\tau} \propto \rho(r) \propto \mathrm{const}\,. \tag{45}$$

The local neutrino production rate related to the distant static observers is then given by the relation including the time-delay factor

$$I = \frac{\mathrm{d}N}{\mathrm{d}t} = \mathcal{I}\mathrm{e}^{\Phi(r)} . \tag{46}$$

Now, the number of neutrinos produced at a given radius in a proper volume $\mathrm{d}V$ per unit time of a distant static observer is given by the relation

$$\mathrm{d}N_\mathrm{p}(r) = I(r)\,\mathrm{d}V(r) = 4\pi\mathcal{I}\mathrm{e}^{\Phi(r)+\Psi(r)}r^2\,\mathrm{d}r . \tag{47}$$

Integrating through whole the compact object (from 0 to R) we arrive to the global neutrino production rate in the form

$$N_\mathrm{p}(R) = 4\pi\mathcal{I}\int_0^R \Big[AY_1Y^{-1}(r) - B\Big] r^2\,\mathrm{d}r . \tag{48}$$

In an analogical way, we can give the expressions for the global rates of escaping and trapping of the produced neutrinos:

$$N_\mathrm{e}(R) = 4\pi\mathcal{I}\int_{r_{\mathrm{b(e)}}}^R (1-\cos\psi_\mathrm{e}(r,R,\Lambda))\Big[AY_1Y^{-1}(r) - B\Big] r^2\,\mathrm{d}r + N_\mathrm{p}(r_{\mathrm{b(e)}}) , \tag{49}$$

$$N_\mathrm{b}(R) = 4\pi\mathcal{I}\int_{r_{\mathrm{b(e)}}}^R \cos\psi_\mathrm{e}(r,R,\Lambda)\Big[AY_1Y^{-1}(r) - B\Big] r^2\,\mathrm{d}r , \tag{50}$$

where $r_{\mathrm{b(e)}}$ is the radius given by Eq. (26) and $\cos\Psi_\mathrm{e}(r, R)$ is determined by Eq. (36).

5 EFFICIENCY OF NEUTRINO TRAPPING

In order to characterize the trapping of neutrinos in extremely compact stars, we introduce some coefficients giving the efficiency of the trapping effect in connection to the total neutrino luminosity and the cooling process in the period of the evolution of the star corresponding to the geodetical motion of neutrinos.

5.1 Trapping coefficient of total neutrino luminosity

The influence of the trapping effect on the total neutrino luminosity of extremely compact stars can be appropriately given by the coefficient $\mathcal{B}_\mathrm{L}$ relating the number of neutrinos produced inside the whole compact star during unit time of distant observers and the number of those produced neutrinos that will be captured by the extremely strong gravitational field of the star. The luminosity trapping coefficient is therefore given by the relation

$$\mathcal{B}_\mathrm{L}(R) = \frac{N_\mathrm{b}}{N_\mathrm{p}} , \tag{51}$$

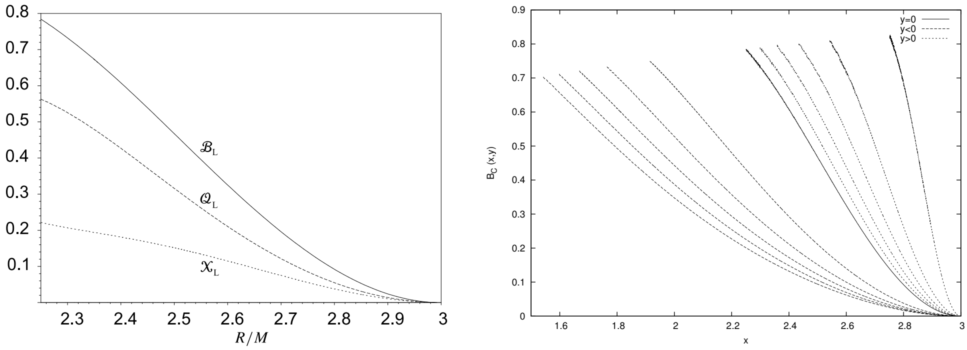

Figure 6. Behaviour of global luminosity coefficient $\mathcal{B}_{\mathrm{L}}$ (left, $\Lambda = 0$ taken from Stuchlík et al., 2005) and influence of cosmological parameter y (right).

and the complementary luminosity "escaping" coefficient is determined by the simple formula

$$\mathcal{E}_{\mathrm{L}}(R) = 1 - \mathcal{B}_{\mathrm{L}}(R)\,, \tag{52}$$

whereN_{b}, N_{p} are given by relations (50), (48).

We can, moreover, define other global characteristic coefficients. For the "internal" neutrinos with motion restricted to the interior of the star, we introduce a coefficient

$$\mathcal{Q}_{\mathrm{L}}(R) = \frac{N_{\mathrm{e}}}{N_{\mathrm{p}}} \tag{53}$$

and for the "external" neutrinos, we can use a complementary coefficient

$$\mathcal{X}_{\mathrm{L}} = \frac{N_{\mathrm{ext}}}{N_{\mathrm{p}}} = \mathcal{B}_{\mathrm{L}} - \mathcal{Q}_{\mathrm{L}}\,. \tag{54}$$

The results are illustrated for all the coefficients $\mathcal{B}_{\mathrm{L}}(R)$, $\mathcal{E}_{\mathrm{L}}(R)$, $\mathcal{Q}_{\mathrm{L}}(R)$ and $\mathcal{X}_{\mathrm{L}}(R)$ in Fig. 6.

5.2 Trapping coefficient of neutrino cooling process

The efficiency of the influence of neutrino trapping on the cooling process is most effectively described by the local coefficient of trapping b_{c} relating the captured and produced neutrinos at a given radius of the star, i.e., we can define

$$b_{\mathrm{c}} \equiv \beta(r;\, R)\,. \tag{55}$$

The local cooling coefficient is therefore given in Fig. 5 for some typical values of R. As intuitively expected, the maximum of $b_{\mathrm{c}}(r;\, R)$ for a given R is located at the radius of the stable null circular geodesic.

Further, the cooling process could be appropriately described in a complementary manner by a global coefficient for trapping, restricted to the "active" zone, where the trapping of

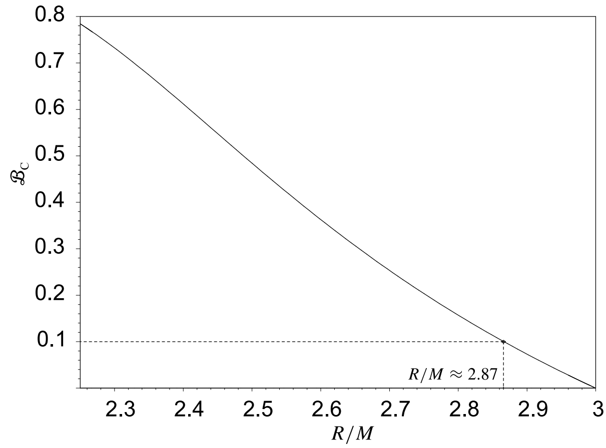

Figure 7. Behaviour of the coefficient $\mathcal{B}_c$. It is explicitly shown that $\mathcal{B}_c \sim 10\,\%$ for $R = 2.87M$. Taken from Stuchlík et al. (2005).

neutrinos occurs. The cooling global trapping coefficient is thus defined by the relation

$$\mathcal{B}_c(R) = \frac{N_b}{N_{p(red)}}\,, \tag{56}$$

where N_b is given by Eq. (50), while $N_{p(red)}$ reads

$$N_{p(red)} = N_p(R) - N_p(r_{b(e)})\,, \tag{57}$$

where $N_p(R)$ is given by Eq. (48) and $N_p(r_{b(e)})$ is the number of neutrinos produced in the internal region of the star where no trapping occurs $0 < r < r_{b(e)}$.

In an analogical way, we can define the global cooling trapping coefficient for the "internal" neutrinos by the relation

$$\mathcal{Q}_c(R) = \frac{N_i}{N_{p(red)}}\,. \tag{58}$$

The behaviour of the global "cooling" coefficient $\mathcal{B}_c$ is shown in Fig. 7.

6 CONCLUSIONS

The detailed discussion of results for $\Lambda = 0$ can be found in Stuchlík et al. (2005). We would like to point out some of the interesting and important ones.

It is important that the trapping of neutrinos is shown to be relevant even for the internal Schwarzschild–(anti-)de Sitter spacetimes with radius only moderately smaller than $R_{crit} = r_{ph} = 3GM/c^2$. Therefore, it is worth to continue detailed studies of trapped neutrinos in realistic models of extremely compact neutron stars or quark stars, when we usually expect radii R moderately smaller than r_{ph}. The surface redshift for the extremely compact stars with $R = 3M$ is $z_{\mathrm{min}} = 0.732$; the realistic models give maximum value of $z \sim 0.8$ (Weber, 1999). (Of course, some models admit existence of objects with radii R close to the critical value of $9GM/4c^2$, see, e.g., Nilsson and Ugla, 2000.) Recently, we are extending the estimates of the trapping process to the cases of the polytropic and adiabatic spherical objects and realistic models of extremely compact neutron stars and quark stars.

Because the effect of trapping of neutrinos is a cumulative one, we can expect its relevance in realistic models of extreme compact objects. It is under study now, how the trapping will influence the cooling process in some simple models of quark stars with a relatively simple "bag" equation of state, and how the cooling of such a quark star will be modified by cumulation of neutrinos in the zone of trapping.

The effect of cosmological constant Λ is shown in Figs 2, 5 and 6. The quite important result is that the maxima of $\mathcal{B}_{\mathrm{c}}$ (which correspond to minima of allowed radii of the object) depend on the cosmological constant Λ. Of course, with the presently observed values of the relict repulsive cosmological constant, its influence on the trapping phenomena is negligible, however, the situation could be different for hypothetical strange quark configurations in the early universe, where the cosmological constant could be much higher than its present value is.

ACKNOWLEDGEMENTS

The present work was supported by the Czech grant MSM 4781305903.

REFERENCES

Abramowicz, M. A. (1999), Gravitational radiation in optical geometry applied to supercompact stars, *Phys. Rep.*, **311**, p. 325.

Abramowicz, M. A., Anderson, N., Bruni, M., Ghosh, P. and Sonego, S. (1997), Gravitational waves from ultracompact stars: the optical geometry view of trapped modes, *Classical Quantum Gravity*, **14**, p. L189.

Abramowicz, M. A., Miller, J. and Stuchlík, Z. (1993), Concept of radius of gyration in general relativity, *Phys. Rev. D*, **47**(4), pp. 1440–1447, ISSN 1089-4918, URL `http://link.aps.org/abstract/PRD/v47/p1440`.

Glendenning, N. K. (2000), *Compact Stars: Nuclear Physics, Particle Physics, and General Relativity*, Springer-Verlag, New York.

Hledík, S., Stuchlík, Z. and Mrázová, K. (2004), Comparison of general relativistic polytropic and adiabatic fluid spheres with a repulsive cosmological constant, in S. Hledík and Z. Stuchlík, editors, *Proceedings of RAGtime 4/5: Workshops on black holes and neutron stars, Opava, 14–16/13–15 October 2002/2003*, pp. 75–89, Silesian University in Opava, Opava, ISBN 80-7248-242-4.

Misner, C. W., Thorne, K. S. and Wheeler, J. A. (1973), *Gravitation*, Freeman, San Francisco.

Nilsson, U. S. and Ugla, C. (2000), General Relativistic Stars: Polytropic Equations of State, `gr-qc/0002022v1`.

Østgaard, E. (2001), Internal structure of neutron stars, in S. Hledík and Z. Stuchlík, editors, *Proceedings of RAGtime 2/3: Workshops on black holes and neutron stars, Opava, 11–13/8–10 Oc-*

tober 2000/01, pp. 73–102, Silesian University in Opava, Opava, ISBN 80-7248-131-2, URL `http://uf.fpf.slu.cz/rag/`.

Schwarzschild, K. (1916), Über das Gravitationsfeld einer Kugel aus inkompressibler Flussigkeit nach der Einsteinschen Theorie, *Sitzber. Deut. Akad. Wiss. Berlin, Kl. Math.-Phys. Tech.*, pp. 424–434.

Shapiro, S. L. and Teukolsky, S. A. (1983), *Black Holes, White Dwarfs and Neutron Stars: The Physics of Compact Objects*, John Wiley & Sons, New York, ISBN 0-471-87316-0.

Stuchlík, Z., Hledík, S., Šoltés, J. and Østgaard, E. (2001), Null geodesics and embedding diagrams of the interior Schwarzschild–de Sitter spacetimes with uniform density, *Phys. Rev. D*, **64**(4), p. 044004 (17 pages), URL `http://ojps.aip.org/journal_cgi/dbt?KEY=PRVDAQ&Volume=64&Issu%e=4`.

Stuchlík, Z., Török, G., Hledík, S. and Urbanec, M. (2005), Neutrino trapping in extremely compact objects, *Classical Quantum Gravity*, submitted.

Weber, F. (1999), *Pulsars as Astrophysical Laboratories for Nuclear and Particle Pysics*, Institute of Physics Publishing, London.

Weber, F. and Glendenning, N. K. (1992), *Astrophys. J.*, **390**, p. 541.

Proceedings of *RAGtime 6/7: Workshops on black holes and neutron stars, Opava, 16–18/18–20 September, 2004/2005*
S. Hledík and Z. Stuchlík, editors, Silesian University in Opava, Czech Republic, 2005, pp. 281–293

A manifestation of the Kozai mechanism in the galactic nuclei

Ladislav Šubr[1] and Vladimír Karas[2]

[1]Charles University in Prague, Faculty of Mathematics and Physics, V Holešovičkách 2, Praha, Czech Republic
[2]Astronomical Institute, Czech Academy of Sciences, Boční II 1401, CZ-141 31 Praha 4, Czech Republic

ABSTRACT
We study stellar trajectories in a dominating central potential perturbed by an axisymmetric source of gravity. We aim this model to galactic nuclei where the motion of stars on the shortest time-scale is governed by gravity of a central supermassive black hole. The perturbation to its gravitational field is assumed to be due to an accretion disc or a gaseous torus. A hydrodynamical drag of the disc on the stellar trajectories is also considered. We discuss different observable consequences of the perturbed stellar trajectories. In particular, we examine to what degree the relativistic perihelion precession inhibits the effect of Kozai oscillations.

1 INTRODUCTION

We consider a model of galactic nuclei that consists of three main components: a supermassive black hole, an axially symmetric accretion disc or a torus, and a dense stellar cluster. In the innermost region, $r \lesssim 10^6\,R_{\rm g}$ ($R_{\rm g} \equiv GM_\bullet/c^2$), a dominating source of the gravitational field is the black hole with the mass $10^6\,{\rm M}_\odot \lesssim M_\bullet \lesssim 10^9\,{\rm M}_\odot$. An accretion disc plays a crucial role in our model, being a source of non-spherical perturbation to the gravitational field and, simultaneously, perturbing stellar trajectories via hydrodynamical drag during their repetitive passages through it. The stellar cluster is treated in a simple way as a collisionless ensemble, which is a relevant approximation when the processes which we discuss act on time-scales orders of magnitude shorter than relaxation time $t_{\rm r}$. We, however, do consider an averaged spherically symmetric component of the gravitational field due to the stellar cusp as it may considerably alter the results.

The periodical oscillations of orbital elements due to the axially symmetric perturbation to the central potential is known in the celestial mechanics as the Kozai mechanism (Kozai, 1962; Lidov, 1961). We introduce briefly the classical approach to the Kozai mechanism in the following Section together with a discussion of relativistic corrections. In Section 3 we suggest possible observable consequences of the Kozai mechanism in galactic nuclei. Discussion and prospects of the future work are summarized in Section 4.

80-7248-334-X

2 NOTES ON KOZAI APPROXIMATION

Motion in the central Keplerian potential is highly degenerate – in the Delaunay variables, the Hamiltonian of a gravitationally bound two-body system is a function of single action (generalized momentum) which implies that only one conjugated angle (cyclic generalized coordinate) varies in time. In other words, only the mean anomaly along the Keplerian ellipse varies in time, while the semi-major axis, eccentricity and orientation of the ellipse are conserved. An additional perturbing term in the potential, V_{p}, may decrease the degeneracy and, consequently, lead to temporal variations of other orbital elements. The perturbation theory of the celestial mechanics aims to describe temporal evolution of the orbital elements while discarding the information about the "fast" variable (mean anomaly). This is achieved by looking for such a canonical action–angle variables for which the Hamiltonian is independent (up to some order of accuracy) upon the action(s) conjugated to the fast variable(s).

The Kozai approximation is implicitly based on an assumption of the existence of a third integral of motion in addition to the orbital energy expressed in terms of semi-major axis a and z-component of the specific angular momentum given by the Kozai integral $c \equiv \sqrt{1-e^2}\cos i = L_z/L_{\max}$, where i is the angle between direction of the star angular momentum and the symmetry axis. Within the framework of the so called "averaging" procedure the third integral appears to be an average $\bar{V}_{\mathrm{p}}$ of the perturbing potential over the mean motion cycle (see e.g. Morbidelli, 2002). Then, the orbital evolution in the space of the averaged orbital elements (e, ω) should be periodic and follow a contour of constant $\bar{V}_{\mathrm{p}}$. In the following, we will consider two different sources for which the perturbing potential can be given analytically:

(i) a ring of radius R_{d} and mass M_{d} which can represent either a molecular torus or an averaged potential of a point-like mass orbiting around the central black hole on a circular orbit (the latter case corresponds exactly to the configurations considered originally by Lidov and Kozai). The perturbing potential reads:

$$V_{\mathrm{r}}(R, z) = -\frac{2GM_{\mathrm{d}}}{\pi}\frac{K(k)}{B}\,, \tag{1}$$

where $B^2(R,z) \equiv z^2 + (R+R_{\mathrm{d}})^2$, $k(R,z) \equiv 4RR_{\mathrm{d}}/B^2(R,z)$ and $K(k)$ stands for a complete elliptic integral of the first kind.

(ii) a razor-thin disc with constant surface density of the finite outer radius R_{d} and mass M_{d}:

$$V_{\mathrm{d}}(R, z) = \frac{2GM_{\mathrm{d}}}{\pi R_{\mathrm{d}}^2} \times \left[\Theta(R-R_{\mathrm{d}})\pi|z| - B\,E(k) - \frac{R_{\mathrm{d}}^2 - R^2}{B^2}K(k) - \frac{R_{\mathrm{d}}-R}{R_{\mathrm{d}}+R}\frac{z^2}{B}\Pi(\alpha^2;k)\right], \tag{2}$$

where B, k and $K(k)$ are defined as above, $\alpha^2 \equiv 4R_{\mathrm{d}}R/(R_{\mathrm{d}}+R)^2$ and $E(k)$ and $\Pi(\alpha^2;k)$ are complete elliptic integrals of the second and the third kind, respectively.

In both cases we have verified by means of direct numerical integration that the assumption about the existence of the third integral of motion is valid for sufficiently small values of

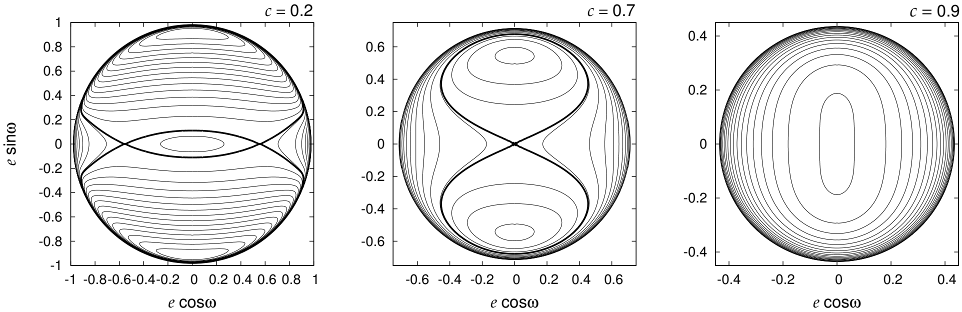

Figure 1. Three different topologies of contours of constant averaged disturbing potential $\bar{V}_{\rm p}$ in the space of orbital elements e (radial coordinate) and ω (polar coordinate) for the disc with constant surface density. Parameters common for all panels are: $M_{\rm d} = 0.01\,M_{\bullet}$, $R_{\rm d} = 2\times10^{6}\,R_{\rm g}$ and $a = 0.98\times10^{6}\,R_{\rm g}$; corresponding value of the Kozai integral is indicated above each panel. Except for the separatrices, which are accentuated with thick lines, values of $\bar{V}_{\rm d}$ are equally spaced; the steps are different for the individual cases, however.

semi-major axis compared to $R_{\rm d}$. Trajectories in the (e,ω) space can, in general, form quite a rich family of different topologies, depending on the shape of the perturbing potential and values of the semi-major axis a and Kozai integral c. In our computations we met three qualitatively different variants: in Fig. 1 they were constructed for a disc of constant surface density with identical set of the orbital parameters in all panels, except for the value of c. In the case of the ring-like source, only two topologies (those identified by $c = 0.7$ and 0.9) have occurred in our calculations.

Even for the analytical potentials (1) and (2), an analytical form of the the third integral of motion is not known. For the case of the potential due to the ring the quadrupole approximation leads to equations for the orbital inclination i, eccentricity e and argument of the pericentre ω (see, e.g., Kiseleva et al., 1998):

$$T_{\rm K}\sqrt{1-e^2}\,\frac{{\rm d}i}{{\rm d}t} = -\frac{15}{8}\,e^2\sin2\omega\sin i\cos i\,, \tag{3}$$

$$T_{\rm K}\sqrt{1-e^2}\,\frac{{\rm d}e}{{\rm d}t} = \frac{15}{8}\,e(1-e^2)\sin2\omega\sin^2 i\,, \tag{4}$$

$$T_{\rm K}\sqrt{1-e^2}\,\frac{{\rm d}\omega}{{\rm d}t} = \frac{3}{4}\left\{2(1-e^2)+5\sin^2\omega\left[e^2-\sin^2 i\right]\right\}\,. \tag{5}$$

Here, $T_{\rm K} \equiv \frac{4}{3}(M_{\bullet}/M_{\rm d})(R_{\rm d}/a)^3P$ is a characteristic time of the Kozai oscillations (expressed in terms of orbit semi-major axis a and period $P = 2\pi\sqrt{GM_{\bullet}}\,a^{3/2}$). The equations (3)–(5) imply conservation of two variables:

$$c = \sqrt{1-e^2}\,\cos i \qquad \text{and} \tag{6}$$

$$Q = \left[5e^2\sin^2\omega + 2(1-e^2)\right]\sin^2 i\,. \tag{7}$$

Ivanov et al. (2005) discuss a modified set of equations relevant for the system which consists of a dominating central mass $M_{\bullet}$, a secondary point-like mass on a circular orbit and a spherically symmetric power-law stellar cusp. Its potential causes the apsidal precession of orbits which can be described by an additional term on the right-hand side of Eq. (5):

$$\left(\frac{\mathrm{d}\omega}{\mathrm{d}t}\right)_{*} = -K\,\frac{M_{*}(a)}{M_{\bullet}}\,\frac{\sqrt{1-e^2}}{P}\,, \tag{8}$$

where K is a dimensionless constant of the order of unity and $M_{*}(a)$ is the mass of the stellar cluster enclosed within the radius a. This term leads to a modification of the integral Q:

$$Q = e^2\left(5\sin^2 i + \kappa - 2\right)\,. \tag{9}$$

Parameter $\kappa(a)$ is defined as:

$$\kappa \equiv K\,\frac{T_{\mathrm{K}}}{P}\,\frac{M_{*}(a)}{M_{\bullet}} = \frac{2}{3\pi}\,K\,\frac{M_{*}(a)}{M_{\mathrm{d}}}\,. \tag{10}$$

2.1 Relativistic corrections

The oscillations of the orbital elements may be considerably weakened in the regime of strong gravity by the effect of the relativistic pericentre advance. One way how to incorporate this effect is to add an appropriate term to the right-hand side of the Kozai equation (5):

$$\left(\frac{\mathrm{d}\omega}{\mathrm{d}t}\right)_{\mathrm{GR}} = \frac{R_{\mathrm{g}}}{a(1-e^2)}\,\frac{6\pi}{P}\,. \tag{11}$$

In the applications where direct numerical integration of the equations of motion is more convenient we use pseudo-Newtonian potential (Paczyński and Wiita, 1980) to mimic the effects of the general relativity:

$$V(r) = -\frac{GM_{\bullet}}{r-2R_{\mathrm{g}}} = -\frac{GM_{\bullet}}{r} - \frac{2GM_{\bullet}R_{\mathrm{g}}}{r(r-2R_{\mathrm{g}})} \equiv -\frac{GM_{\bullet}}{r} + V_{\mathrm{PN}}(r)\,. \tag{12}$$

It is straightforward to treat the term V_{PN} as another perturbation to the central Keplerian potential in the Kozai approximation. Being spherically symmetric, this perturbation does not affect conservation of all three components of the angular momentum, and so the contours of the averaged perturbation potential $\bar{V}_{\mathrm{PN}}$ in the (e, ω) space form a concentric circles. Hence, it is natural to expect that adding V_{PN} to any of the axisymmetric perturbations V_{r} or V_{d} will tend to smear the structure of the $\bar{V}_{\mathrm{p}} = \mathrm{const}$ contours, i.e., it decreases amplitude of the eccentricity oscillations.

The influence of the relativistic pericentre advance increases when the trajectory gets closer to the centre. It can be estimated quantitatively by comparison of the characteristic time $T_{\mathrm{K}}\sqrt{1-e^2}$ of the Kozai oscillations and the period T_{E} of the relativistic effect:

$$\frac{T_{\mathrm{K}}\sqrt{1-e^2}}{T_{\mathrm{E}}} = 4\frac{M_{\bullet}}{M_{\mathrm{d}}}\left(\frac{R_{\mathrm{d}}}{a}\right)^3\frac{R_{\mathrm{g}}}{a(1-e)}\,\frac{\sqrt{1-e^2}}{1+e}\,. \tag{13}$$

The Kozai oscillations will be considerably suppressed for small a. Hence, setting $T_{\mathrm{K}}=T_{\mathrm{E}}$ we further estimate a minimal value of semi-major axis which ensures substantial oscillations of eccentricity (using an approximation $e\rightarrow 1 \Rightarrow e+1\approx 2$; Hopman et al., 2006):

$$a_{\min}\approx (M_{\bullet}/M_{\mathrm{d}})^{2/7}\,R_{\mathrm{d}}^{6/7}\,R_{\mathrm{g}}^{2/7}\,R_{\mathrm{p}}^{-1/7}\,. \tag{14}$$

Here, we replaced eccentricity of the orbit by its pericentre $R_{\mathrm{p}}\equiv a(1-e)$ which is convenient for the discussion of Section 3.1.

3 APPLICATIONS IN THE CONTEXT OF GALACTIC NUCLEI

3.1 Tidal disruptions

Stars are assumed to be disrupted by the tidal forces from central black hole when they reach the tidal radius:

$$R_{\mathrm{t}}\equiv\left(\frac{M_{\bullet}}{M_{*}}\right)^{1/3}R_{*}\approx 2.2\left(\frac{M_{\bullet}}{10^{8}\,\mathrm{M}_{\odot}}\right)^{-2/3}\left(\frac{M_{*}}{\mathrm{M}_{\odot}}\right)^{-1/3}\left(\frac{R_{*}}{\mathrm{R}_{\odot}}\right)R_{\mathrm{g}}\,. \tag{15}$$

Such an event could lead to observable effects, hence, it is desirable to study the probability that a star from a given ensemble will be on the orbit with the pericentre comparable to R_{t}. In a spherically symmetric cluster a condition $R_{\mathrm{p}}\lesssim R_{\mathrm{t}}$ defines a loss cone in the stellar cluster:

$$L\lesssim L_{\min}\,. \tag{16}$$

Presence of an axially symmetric perturbation, however, violates conservation of the total angular momentum, keeping only its z-component conserved. Hence, the condition (16) should be replaced with

$$L_{z}\lesssim L_{\min}\,, \tag{17}$$

which leads to substantial increase of the loss cone and, therefore, increased probability to observe effects of the star-black hole close encounters.

Analytical analysis of the structure of the phase space for the case of the central mass $M_{\bullet}$ surrounded by a power-law stellar cluster ($n(r)\propto r^{-\alpha}$) and the axisymmetric perturbation due to the secondary mass M_{d} was given in Ivanov et al. (2005). The stellar disruption rate due to the Kozai effect is estimated as:

$$\dot{M}_{\max}\approx\left(\frac{q}{0.01}\right)^{4/3}\left(\frac{M_{\bullet}}{10^{7}\,\mathrm{M}_{\odot}}\right)^{5/3}\left(\frac{R_{\mathrm{h}}}{1\mathrm{pc}}\right)^{-2}\,\mathrm{M}_{\odot}\,\mathrm{yr}^{-1}\,, \tag{18}$$

where $q\equiv M_{\mathrm{d}}/M_{\bullet}$ and R_{h} is the characteristic radius of the stellar cusp.

In the following paragraphs we present another approach which is based on a direct numerical integration of the equations of motion with the aid of knowledge of the topology of the $\bar{V}_{\mathrm{p}}=\mathrm{const}$ contours. This method gives more accurate results and it can be used for different geometry of the source of the perturbing potential.

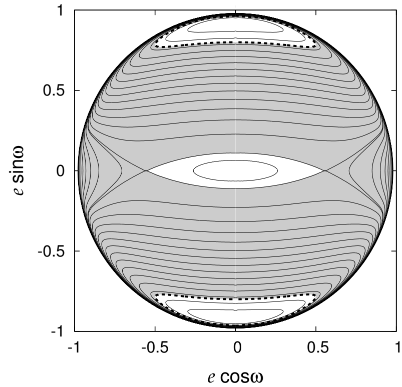

Figure 2. Area of the space of initial parameters (e, ω) from which the trajectory will reach eccentricity ≥ 0.965 at some stage during the evolution. Thick dotted line represents the orbit which reaches the limiting value of eccentricity at $\omega = \pi/2$. Axisymmetric perturbation to the central gravity is due to the disc of constant surface density, $M_\mathrm{d} = 0.01\, M_\bullet$, $R_\mathrm{d} = 2 \times 10^6\, R_\mathrm{g}$; fixed integrals of motion are $a = 0.98 \times 10^6\, R_\mathrm{g}$ and $c = 0.2$.

Let us consider a distribution function D_f of the stellar cluster to be determined in variables (a, c, e, ω). Evaluation of a fraction $\mathcal{F}(r_\mathrm{min})$ of stars that reach the centre below r_min at some stage of the orbital evolution can be performed in two steps: First, determine a corresponding fraction $\mathcal{F}(a, c; r_\mathrm{min})$ of stars with fixed a and c then integrate this function on a grid in the (a, c) space to obtain $\mathcal{F}(r_\mathrm{min})$. The first step requires to integrate numerically only one or two trajectories with suitably chosen initial conditions. The first trajectory is started with $e = 1 - r_\mathrm{min}/a$ and $\omega = \pi/2$ and it determines one boundary in the space of e and ω. Another one may be necessary to integrate if the separatrices in the (e, ω) space are crossed to determine boundary of region of rotation with small eccentricities. Initial value of eccentricity of this second trajectory is found by starting several integrations with $\omega = 0$ and evaluation of $\mathrm{d}e/\mathrm{d}t$. The trajectory with largest eccentricity and negative $\mathrm{d}e/\mathrm{d}t$ is selected. Example of this procedure is sketched in Fig. 2 where we plot contours of constant $\bar{V}_\mathrm{d}$ together with numerical solution of the equations of motion for $(e_0, \omega_0) = (0.965, \pi/2)$. Another trajectory with $(e_0, \omega_0) = (0.543, 0)$ was integrated as a boundary of the region of rotation with small eccentricities. Any orbit starting from the same values of a and c and arbitrary e and ω from the shaded area will reach the centre within r_min at some moment. Hence, integration of D_f over this area gives $\mathcal{F}(a, c; r_\mathrm{min})$.

The integration would be straightforward if the perturbing potential were not present – in that case, the relevant region in the (e, ω) space is an interval between $e_\mathrm{min} \equiv 1 - r_\mathrm{min}/a < e < \sqrt{1 - c^2}$. Let us consider a simple distribution function with random distribution of the ellipses' orientation: $D_\mathrm{f}(a, e, i, \omega) \propto a^{1/4} e \sin i$. Transformation $(a, e, x, \omega) \rightarrow (a, e, c, \omega)$ gives:

$$D_\mathrm{f}(a, e, c, \omega) \propto a^{1/4} \frac{e}{\sqrt{1 - e^2}} \tag{19}$$

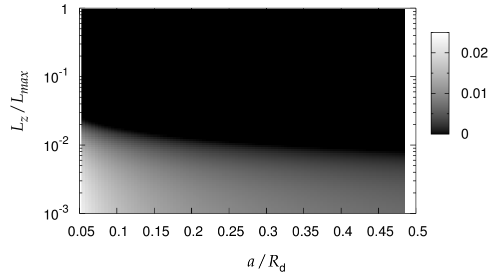

Figure 3. Fraction $\mathcal{F}(a, c; r_{\rm min})$ of stars with pericentre below $r_{\rm min} = 100\ R_{\rm g}$ as a function of two integrals of motion is expressed by means of levels of shade. Only the central mass determines the stellar trajectories in this case. Distribution of eccentricities is $\propto e$; semi-major axis is in units of $R_{\rm d} = 6.8 \times 10^6\ R_{\rm g}$.

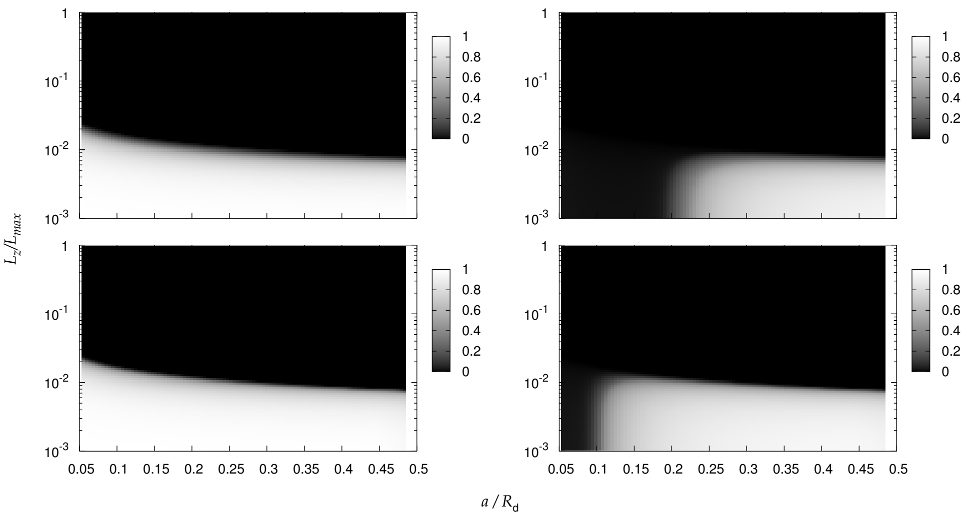

Figure 4. Same as Fig. 3 but for an ensemble in the compound gravitational field of the central mass and non-spherical perturbation. In the first row, perturbation is due to the ring, while in the second row it is due to the disc of the constant surface density. Panels on the left side were calculated with Newtonian description of the potential of the central point-like source, while panels on the right side were calculated with the pseudo-Newtonian potential (12).

and the fraction $\mathcal{F}(a, c; r_{\rm min})$ is then:

$$\mathcal{F}(a, c; r_{\rm min}) = \frac{\sqrt{1 - e_{\rm min}^2} - c}{1 - c}\,. \tag{20}$$

We plot this function in Fig. 3 for $a \in \langle 3.4 \times 10^5\ R_{\rm g}, 3.4 \times 10^6\ R_{\rm g}\rangle$ and $r_{\rm min} = 100\ R_{\rm g}$. Next, in Fig. 4 we show $\mathcal{F}(a, c; r_{\rm min})$ obtained numerically for the system perturbed by the gravity of the ring or the disc. In both cases we also present alternative variant when the pseudo-Newtonian correction to the central potential is considered. Comparing Figs 3 and 4 we see that $\mathcal{F}(a, c, r_{\min})$ is raised approximately by a factor of 100 due to the Kozai mechanism. In accordance with the estimate (14) the effect of the relativistic pericentre advance breaks the Kozai mechanism below certain value of a where $\mathcal{F}$ drops to values similar to the case without the non-spherical perturbation. The disc-like source of the perturbing potential competes more successfully with the perturbing relativistic effect. It can be understood from the fact that this source is still close enough to the orbit even for smaller a.

Integrated fraction for the perturbing potential due to the ring is shown in Fig. 5. In the left panel, we plot $\mathcal{F}(r_{\min})$, for fixed parameters $M_\bullet = 3.5 \times 10^6\,\mathrm{M}_\odot$, $M_\mathrm{d} = 0.01\,M_\bullet$ and $R_\mathrm{h} = R_\mathrm{d} = 6.8 \times 10^6\,R_\mathrm{g} = 1.2\,\mathrm{pc}$. The parameters are chosen to correspond to the case of the Galactic centre, where the source of the axisymmetric perturbation is thought be the circumnuclear molecular disc (CND). Three curves are given for clear comparison of the importance of different effects – the Kozai oscillations rise $\mathcal{F}$ with respect to an unperturbed case by approximately two orders of magnitude. On the other hand, adding the pseudo-Newtonian correction to the central potential decreases the number of potentially tidally disrupted star by a factor $\gtrsim 2$. It can be also seen from the Figure that the influence of the relativistic effect increases with decreasing $r_{\min}$ (in this case the function was not evaluated for $r_{\min} < 20 R_\mathrm{g}$ for "technical" reasons, related to the definition of initial conditions).

In the right panel of Fig. 5 we demonstrate increasing strength of the relativistic pericentre advance with increasing mass of the black hole. In this example we scale the length parameters with $M_\bullet$ according to the empirical $M_\bullet$-σ relation (Tremaine et al., 2002):

$$\frac{M_\bullet}{10^8\,\mathrm{M}_\odot} \approx \left(\frac{\sigma}{200\,\mathrm{km\,s^{-1}}}\right)^4 . \tag{21}$$

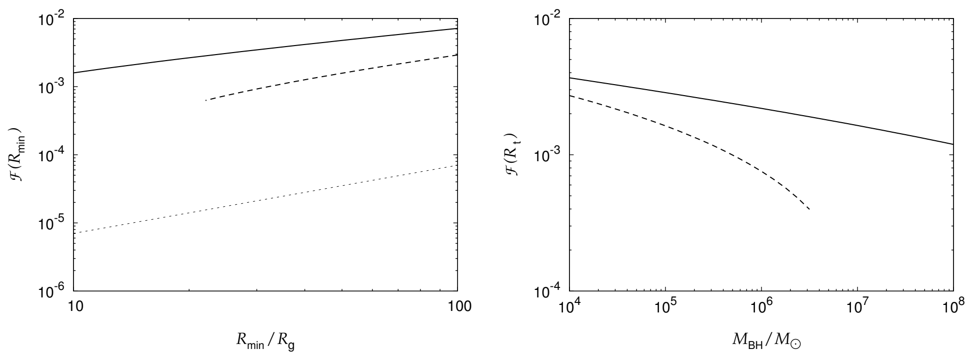

Figure 5. Fraction of stars from a stellar cluster that reach the centre within $r_{\min}$ at some stage of the orbital evolution. *Left:* $\mathcal{F}$ as a function of $r_{\min}$ for the parameters of the system relevant for the Galactic centre. *Right:* $\mathcal{F}(R_\mathrm{t})$ for different values of the black hole mass $M_\bullet$; length parameters are scaled with $M_\bullet$ according to relations (15) and (22). In both panels the solid line corresponds to the Newtonian treatment of the gravity of the black hole, while the dashed one was calculated with the Paczyński–Wiita description of the central mass potential. Thin dotted line in the left panel stands for the referential case without the axisymmetric perturbing potential.

Setting $R_\mathrm{h} = GM_\bullet/\sigma^2$ we further obtain:

$$R_\mathrm{h} = 2.25 \times 10^6 \left(\frac{M_\bullet}{10^8\,\mathrm{M}_\odot}\right)^{-1/2} R_\mathrm{g} = 11 \left(\frac{M_\bullet}{10^8\,\mathrm{M}_\odot}\right)^{1/2} \mathrm{pc}\,. \tag{22}$$

Like in the previous case we locate the ring-like source of the perturbing potential on the outer edge of the stellar cusp: $R_\mathrm{d} = R_\mathrm{h}$. Finally, $R_\mathrm{min} = R_\mathrm{t}$ scales with $M_\bullet$ according to the relation (15).

Kozai mechanism may cause substantially enhanced tidal stellar disruptions and produce episodes of enhanced gas supply towards the black hole and, consequently, increased accretion rate. This period, however, is limited by the characteristic time of the Kozai cycle (typically less than 1 Myr) during which the enlarged loss cone is emptied. The enhanced disruption rate may be prolonged if the orientation of the Kozai perturber continuously changes in time. This could be e.g. due to the precession in the large-scale non-spherical galactic potential. An interesting consequence of the tidal disruptions due to the Kozai mechanism is the fact, that the stars disrupted at the moment of maximal eccentricity during their Kozai cycle reach the centre with small inclinations with respect to the plane of the source of the perturbing potential, hence, giving naturally rise of the accretion disc.

Squeezars

In addition to stars which are directly disrupted, a similar number comes as close as $\lesssim 3\,R_\mathrm{t}$ to the black hole. These stars survive the interaction with the black hole, but do experience a strong tidal interaction (Alexander and Morris, 2003). The energy $\Delta E_t(R_\mathrm{p})$ per orbit invested in these tides comes at expense of the orbital energy and is of order

$$\Delta E_\mathrm{t}(b) \;=\; \frac{GM_*^2}{R_*}\, T(b^{3/2})\, b^{-6} \tag{23}$$

(Press and Teukolsky, 1977). Here, $T(b)$ is a dimensionless function of $b \equiv R_\mathrm{p}/R_\mathrm{t}$, which can be estimated numerically, see, e.g., Alexander and Kumar (2001).

The tidal energy will be radiated by the star, because it becomes hotter and puffs up. In the context of the Galactic centre this process is discussed in Alexander and Morris (2003). There is a possibility that the number of tidally heated stars is increased if the stellar orbits are perturbed by an axisymmetric perturbation via the Kozai mechanism (Hopman et al., 2006, work in progress).

3.2 Young stars in the vicinity of Sgr A*

There is a strong evidence that the centre of our Galaxy harbours a supermassive black hole of mass $M_\bullet \approx 3 \times 10^6\,\mathrm{M}_\odot$ (Genzel et al., 2003). It is identified with radio source Sagittarius A* which is assumed to emerge from a accretion disc with highly sub-Eddington accretion rate. The black hole dominates the gravitational potential within a distance of few parsecs. A central stellar cluster in this region consists mainly of old stellar population and has a power-law density profile $\rho(r) \propto r^{-1.8}$, which is consistent with models of a relaxed cluster under a dominance of a central mass. There are, however, also young stellar populations with age $\lesssim$ 10 Myr in the innermost regions. They form two mutually perpendicular rings at radial distances 0.01 pc $\lesssim r \lesssim$ 0.1 pc. In addition, there are several so called S-stars on highly eccentric orbits with semi-major axes below 0.01 pc. The S2 star, which is the most tightly bound to the central black hole, has a semi-major axis $a \approx 0.004\,\mathrm{pc} \approx 2.5 \times 10^4\, R_{\mathrm{g}}$ and eccentricity $e \approx 0.87$ (Ghez et al., 2003).

The S-stars represent one of the challenging mysteries of the contemporary astrophysics: Tidal forces from the central black hole inhibit stellar formation at the distances where the S-stars are observed. The most optimistic estimates admit star formation at a distance of $\gtrsim$ 0.1 pc from the centre (Vollmer and Duschl, 2001). Hence, it is necessary to find a mechanism capable of transporting stars by at least a factor of ten closer to the centre within their lifetime. The effect of two body relaxation and mass segregation, which in general lets massive stars sink towards the centre and sends lighter stars outward, acts on much longer time-scales and could hardly work within the presented context. Therefore, various scenarios of transportation have been suggested relying on an additional component perturbing (gravitationally) the stellar orbits. Portegies-Zwart et al. (2003) proposed that the core of an infalling dense young stellar cluster would dissolve in the strong tidal field setting some of its members to tightly bound orbits. This mechanism could be even more efficient if the cluster is gravitationally bound to an intermediate mass black hole (Hansen and Milosavljević, 2003). The stars may also be captured individually due to close encounters with members of a dense cluster of stellar mass black holes tightly bound to the central supermassive black hole (Alexander and Livio, 2004). However, none of the models suggested so far is widely accepted yet as they either are not able to reconcile all aspects of the observed young stellar population or require a component that is not observationally confirmed at the current time.

In Šubr and Karas (2005) we proposed an alternative model based on simultaneous gravitational and hydrodynamical drag of a gaseous environment on orbiting stars, which is assumed to form a flattened, disc-like structure. While the direct star-disc hydrodynamical interaction causes continuous dissipation of the star's orbital energy, gravity of the disc leads to periodical changes of the orbital elements, which may substantially increase the efficiency of the hydrodynamical drag.

Let us consider the topology of $\bar{V}_{\mathrm{d}}$ contours corresponding to low values of Kozai integral $c \equiv \sqrt{1-e^2}\,\cos i$. In this case, we can find initial values of orbital parameters e and ω which lead to dramatically different orbit evolution. Starting with $\omega = 0$ and eccentricity slightly less than the value corresponding to the crossing of the separatrices (≈ 0.39 for the example in Fig. 1) leads to rather small variations of eccentricity along an isocontour confined within the inner region bound by the separatrices. On the other hand, starting with the same ω and eccentricity slightly larger leads to large oscillations with maximum $\approx \sqrt{1-c^2}$. We now need a mechanism that allows an orbit to cross the separatrix. This could be provided by hydrodynamical interaction with the disc that is also responsible for the gravitational perturbation.

We model this interaction as an instantaneous kick to the star's velocity at the moment of crossing the equatorial plane. The change of the linear momentum is determined from the momentum conservation law under assumption that the star expels material from the disc lying on its trajectory and accelerates it to its own velocity. Repetitive passages through the disc lead to monotonical dissipation of the orbital energy together with circularisation and

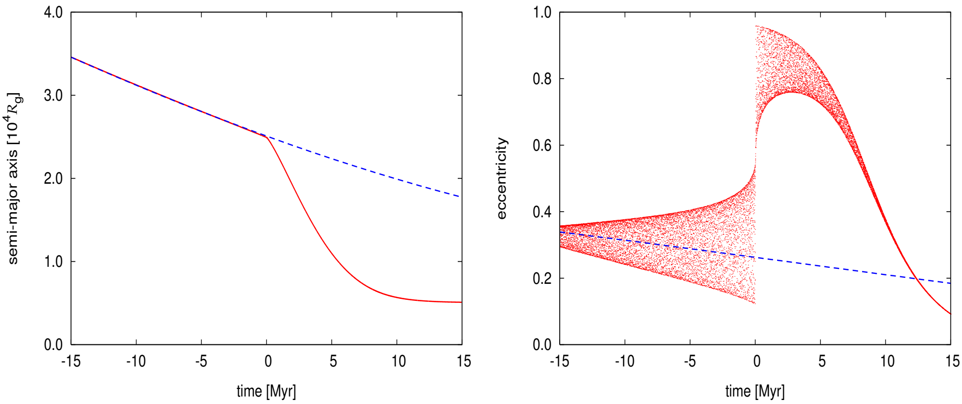

Figure 6. Temporal evolution of semi-major axis and eccentricity of the orbit of a star interacting with the disc. Dashed line corresponds to evolution omitting the disc gravity. Solid line (dots in the right panel) represents a simulation where both the hydrodynamical and gravitational interaction were considered. Kozai oscillations can be deduced from the finite interval of possible eccentricities at each moment, nevertheless, they are not explicitly visible as this effect acts on the time-scale of several thousands of years. Zero time was set to the moment when the orbit crosses the separatrix.

inclination decay (towards corotation). The rate of decay is strongly dependent upon initial conditions – highly eccentric counterrotating orbits sink towards the centre several orders of magnitude faster than circular orbits with low inclination. Hence, the orbital decay slows down in time (Rauch, 1995; Vokrouhlický and Karas, 1998a; Šubr and Karas, 1999).

The gravity of the disc may considerably alter the picture. On the time-scale of hundreds or thousands orbital periods the star follows the lines of constant $\bar{V}$ in the (e, ω) space. On an even longer time-scale, it slowly migrates across them due to the energy dissipation caused by the hydrodynamical star-disc interaction. Moreover, the topology of contours continuously changes as it depends on the semi-major axis and the z-component of angular momentum. Hence, it may happen that the orbit passes through a separatrix, which leads to a fast increase of eccentricity. An example of this evolution is plotted in Fig. 6 where we show an orbit evolving due to both the hydrodynamical and gravitational influence of the disc which has a constant surface density. It starts with a moderate eccentricity and orientation nearly perpendicular to the disc. The parameters were chosen such that after switching to the high eccentricity state, its orbital parameters roughly correspond to values reported for the S2 star. Due to the excited eccentricity, the dissipative interaction with the disc becomes more efficient and the orbital decay is accelerated with respect to the model which omits disc gravity. The trajectory shown in Fig. 6 nicely manifests the key features of the proposed mechanism, but it is not a suitable model of transportation of the S2 star to its current orbit due to the rather slow decay. The decay can be accelerated by an order of magnitude provided the star crosses the separatrix with negative L_z which leads to a flipping of the orbit towards counterrotation at the phases of high eccentricity and, consequently, to strong energy dissipation. Examples of such orbits decaying from $a \sim 10^5\,R_g$ to $\sim 10^4\,R_g$ in a few millions years can be found in Šubr and Karas (2005).

4 CONCLUSIONS

There is an observational evidence that galactic nuclei, spherically symmetric to the first approximation, host components which produce a non-spherical, roughly axially symmetric, perturbation to the gravitational potential. In the centre of our Galaxy there are already several of them: two stellar rings formed by young He I stars with $a < 0.1$pc and a molecular ring or disc with inner radius of ~ 1.5 pc. Another source of the axial perturbation could be a secondary black hole in the Galactic centre as suggested recently by Maillard et al. (2004). (However, this option is rather speculative; see Schödel et al., 2005, for discussion.) Even if the perturbing mass is small compared to the mass of the central black hole, $M_{\rm d} \lesssim 0.01\, M_{\bullet}$, it may considerably alter orbits of some stars from the central stellar cluster, changing periodically their eccentricities between moderate and extreme values. These changes, though very fast in comparison with the two-body relaxation time, take place on more than thousand years time-scale and, therefore, cannot be directly observed. Nevertheless, the tidal interactions of the stars with the central black hole which may occur at the phase of maximal eccentricity are likely to produce observable effects – tidal disruptions or tidal heating. We estimate that up to 10^4 stars from an initially spherically symmetric cluster may have undergone strong tidal interaction with the central black hole in the Galactic centre due to the Kozai oscillations. They could manifest themselves as decaying squeezars or they may have been disrupted a few millions years ago providing a material for the formation of the He I stars that are observed nowadays. We also suggest that the S-stars may have been transported to the close vicinity of the black hole by the compound action of the Kozai mechanism and a dissipative drag due to the flattened gaseous environment.

We have shown that for a proper determination of the number of orbits which may lead to the tidal effects a post-Newtonian corrections to the gravity of the central mass have to be taken into account. For the sake of simplicity we used Paczyński–Wiita description of the central mass potential which provides pericentre advance, the most important effect of general relativity in the presented context. Nevertheless, this potential does not produce quantitatively exact value of the pericentre advance and, therefore, a comparison with fully general relativistic orbits is desirable.

ACKNOWLEDGEMENTS

Authors acknowledge a financial support from the grant of the Charles University Prague (GAUK 299/2004).

REFERENCES

Alexander, T. and Kumar, P. (2001), *Astrophys. J.*, **549**, p. 948.

Alexander, T. and Livio, M. (2004), *Astrophys. J.*, **606**, p. L24.

Alexander, T. and Morris, M. (2003), *Astrophys. J.*, **590**, p. L25.

Genzel, R., Schödel, R., Ott, T., Eisenhauer, F. et al. (2003), *Astrophys. J.*, **594**, p. 812.

Ghez, A. M., Duchêne, G., Matthews, K., Hornstein, D., Tanner, A., Larkin, J., Morris, M., Becklin, E. E., Salim, S., Kremenek, T., Thompson, D., Soifer, B. T., Neugebauer, G. and McLean, I. (2003), *Astrophys. J.*, **586**, p. L127.

Hansen, B. M. S. and Milosavljević, M. (2003), *Astrophys. J.*, **593**, p. L80.

Hopman, C., Šubr, L. and Alexander, T. (2006), in preparation.

Ivanov, P. B., Polnarev, A. G. and Saha, P. (2005), *Monthly Notices Roy. Astronom. Soc.*, **358**, p. 1361.

Kiseleva, L. G., Eggleton, P. P. and Mikkola, S. (1998), *Monthly Notices Roy. Astronom. Soc.*, **300**, p. 292.

Kozai, Y. (1962), *Astronom. J.*, **67**, p. 591.

Lidov, M. L., editor (1961), *Isskust. Sputniky Zemly 8*, Acad. of Sci. USSR.

Maillard, J. P., Paumard, T., Stolovy, S. and Rigaut, F. (2004), *Astronomy and Astrophysics*, **423**, p. 125.

McMillan, L. W., McDermott, P. N. and Taam, R. E. (1987), *Astrophys. J.*, **318**, p. 261.

Morbidelli, A. (2002), *Modern Celestial Mechanics*, Taylor and Francis.

Paczyński, B. and Wiita, P. J. (1980), *Astronomy and Astrophysics*, **88**(1–2), pp. 23–31.

Peebles, P. J. E. (1972), *Astrophys. J.*, **178**, p. 371.

Portegies-Zwart, S. F., McMillan, S. L. W. and Gerhard, O. (2003), *Astrophys. J.*, **593**, p. 352.

Press, W. H. and Teukolsky, S. A. (1977), *Astrophys. J.*, **213**, p. 183.

Rauch, K. P. (1995), *Monthly Notices Roy. Astronom. Soc.*, **275**, p. 628.

Schödel, R., Eckart, A., Iserlohe, C., Genzel, R. and Ott, T. (2005), *Astrophys. J. Lett.*, **625**, p. L111, `astro-ph/0504474`.

Šubr, L. and Karas, V. (1999), An orbiter crossing an accretion disc, *Astronomy and Astrophysics*, **352**, pp. 452–458, URL `http://adsbit.harvard.edu/cgi-bin/nph-journal_query?volume=35%2&plate_select=NO&page=452&plate=&cover=&journal=A2BA..&db_key=ALL`.

Šubr, L. and Karas, V. (2005), *Astronomy and Astrophysics*, **433**, p. 405.

Tremaine, S., Gebhardt, K., Bender, R., Bower, G. et al. (2002), *Astrophys. J.*, **574**, p. 740.

Vokrouhlický, D. and Karas, V. (1998a), *Monthly Notices Roy. Astronom. Soc.*, **293**, p. L1.

Vokrouhlický, D. and Karas, V. (1998b), *Monthly Notices Roy. Astronom. Soc.*, **298**, p. 53.

Vollmer, B. and Duschl, W. J. (2001), *Astronomy and Astrophysics*, **377**, p. 1016.

Proceedings of *RAGtime 6/7: Workshops on black holes and neutron stars, Opava, 16–18/18–20 September, 2004/2005*
S. Hledík and Z. Stuchlík, editors, Silesian University in Opava, Czech Republic, 2005, pp. 295–300

On time-dependent spectra of black-hole accretion discs

Jiří Svoboda

Charles University in Prague, Faculty of Mathematics and Physics, V Holešovičkách 2, Praha, Czech Republic

ABSTRACT

We report on a research project in which we intend to employ time-dependent spectra of black hole accretion discs and use them in order to map the intensity distribution across the disc surface. The intrinsically narrow spectral line emitted from an accretion disc around a massive central object is broadened by the Doppler effect and gravitational redshift. The changes of spectral line profiles are discussed and examples of predicted spectra are presented. We illustrate the essential differences between the classical calculation and a relativistic approximation. The relativistic approximation for frequency shift g-factor is employed in Pecháček, T., Dovčiak, M., Karas, V. and Matt, G. (2005), The relativistic shift of narrow spectral features from black-hole accretion discs, *Astronomy and Astrophysics*, **441**, pp. 855–861. We also discuss possibilities offered by time-dependent spectra. An idea of mapping of an accretion disc is mentioned. On the basis of knowledge about the spectrum we can determine positions of bright radiating spots on the disc. And consequently from the spot's orbit it is possible to find out the mass of the central object.

1 INTRODUCTION

Recent observations especially from space-based instruments suggest that supermassive black holes exist in nuclei of many galaxies. This fact increases the chance to "observe" a black hole, i.e., to reveal its presence and measure its physical properties. The value of the mass of black holes in active galactic nuclei (AGN) is estimated to 10^6–$10^9 M_\odot$. A convenient way to study black holes is by using radiation from the gas around. When there is a lot of material in a black hole neighbourhood it spirals around the black hole and slowly falls down to the horizon. Nonzero value of angular momentum of incoming material leads to a formation of the accretion disc. From observations of accretion discs we can deduce the evidence of existing black hole. We also can measure important parameters of the black hole, especially its mass. Active galactic nuclei are good candidates in which a formation of a massive black hole and an accretion disc can be observed. High luminosity of AGN is caused by the conversion of the gravitational potential energy to radiation by some friction in accreting material. The most of radiation is coming from the innermost regions of the accretion disc, as studied by Fabian et al. (1989). These authors introduced

80-7248-334-X

the relationship between radiation flux density distribution on the disc and the radius:

$$I(R) \approx \frac{1}{R^{\alpha}}\,, \tag{1}$$

where α is a parameter. We consider $\alpha = 2$, respectively $\alpha = 3$ and compare both dependencies.

We focus on the problem of predicted spectra, namely, the possibility to reveal the distribution of local emissivity across the disc plane by comparing the predicted spectra against time dependent observations. We consider the intrinsic spectral line as a δ-function in energy:

$$I(R, E) = I_0 \delta(E - E_0) R^{-\alpha}\,. \tag{2}$$

Because of the rotation around the central object the radial velocity of accreting material RV (velocity from an observer) is changing with the position on the disc. Its value depends on the radius from the centre and also on the azimuth. In the Newtonian approximation the resulting spectral line is double peaked (Marsch and Horne, 1988). When the radiation comes from the strong gravity field relativistic phenomena have to be taken into account. The double-peaked character is preserved but the blue peak becomes much higher than the red one and the redshift is appreciably bigger than the blueshift, so the spectral line is broadened more to the lower frequencies. This is caused by gravitational redshift while the increase of the blue peak is due to abberation and Doppler effect. In observations this spectral line profile was first clearly seen in ASCA data (Tanaka et al., 1995) and has been confirmed by many other observations.

On the base of studying the AD spectral line there is one interesting way how to determine the black hole parameters. Imagine some radiating spot existing at some radius on the accretion disc and surviving at least a significant part of an orbit. Assuming Keplerian rotation the orbital period corresponds to the radius. By the 3rd Kepler's law the orbital period is also linked with the mass of the central object. So the observations of some radiating spot on the disc lead consequently to the determination of the black hole mass. Good time-resolution of the observation instruments is needed to recognize that spot in the spectrum. The present-day X-ray probes do not reach required accuracy but with new projects such as Constellation X observatory with 100-times greater sensitivity there is a good chance to acquire spectra with demanded time-resolution. More details about analysing time dependent spectra is mentioned in the Section 4. The basic relationships and approximations used to simplify the problem are introduced in Section 2. In Section 3 the calculated profiles for a radiating ring and for discs are shown.

2 CALCULATIONS

To calculate the spectral line profile we make several assumptions. First, we assume that the accretion disc is geometrically thin and optically thick. Next, the rate of the accretion was neglected, so the velocity in the radial direction to the central object was set to zero. We consider only the azimuthal velocity of the accreting material. A good approximation of the value of this velocity is the Keplerian velocity which is given by a familiar relationship:

$$\Omega_{\mathrm{Kep}} \equiv \sqrt{\frac{GM}{R^3}} \, . \tag{3}$$

For simplicity we show the resulting profiles for Schwarzschild metrics, we have no magnetic fields in our considerations and we assume the radiation to be isotropic. To the computation we use geometrized units $c = G = 1$, R in units of R_{g}, where R_{g} is the gravitational radius ($R_{\mathrm{g}} = GM/c^2$). The azimuthal angle φ is set to zero when the radiating material is maximally receding. In this convention, the direction to the observer is $\varphi = 3\pi/2$. The value of radius is from the interval $R \in \langle 6, 40 \rangle$. The lower limit is a natural choice because $6R_{\mathrm{g}}$ is the last stable orbit in the Schwarzschild spacetime.

To describe how the observed spectral line profile looks like it is useful to introduce the frequency shift g-factor defined as

$$g(R, \varphi, \theta_0) \equiv \frac{E_{\mathrm{o}}}{E_{\mathrm{e}}} = \frac{p_{\mathrm{o}\mu} U_{\mathrm{o}}^{\mu}}{p_{\mathrm{e}\mu} U_{\mathrm{e}}^{\mu}} \, , \tag{4}$$

which includes all effects of the special and the general theory of relativity. This factor needs to be computed numerically or it requires rather complicated analytical calculations, however, rather accurate approximations are also available. We used the approximation derived by Pecháček et al. (2005)

$$g = \frac{\sqrt{R(R-3)}}{R + \sqrt{R-2} + 4(1 - \sin\varphi \sin\theta_0)^{-1} \cos\varphi \sin\theta_0} \, . \tag{5}$$

3 COMPUTED SPECTRAL LINE PROFILES

In Fig. 1 (left panels) the spectral line of a radiating ring is shown in the Newtonian approximation. There are three curves for three different angles of the inclination of the disc. The standard convention is that the inclination angle is zero when the plane of the disc is perpendicular to the observer's direction. It is obvious the bigger inclination angle the bigger frequency shift. In the second figure there is the same plot but for the relativistic radiating ring. In fact, it represents a radiation of a spot on an accretion disc around a black hole over one orbit.

On the x-axis there is the frequency shift g, on the y-axis there is the radiation flux in arbitrary units, which is normalized in the sense that the sum of all additions gives one.

If we compare both profiles it is clear on the first sight that the relativistic approximation breaks down the symmetry by increasing of the blue peak's height. The gravitational redshift which broadens the spectral line to the red is also apparent.

Figure 2 presents the spectral line profiles for the whole accretion discs. For an illustration accretion discs with two dependencies of the radiation flux density distribution $I(R)$ on the radius are compared (an accretion disc with $I(R) \approx 1/R^2$ on the left and with $I(R) \approx 1/R^3$ on the right).

The resulting spectra are appreciably more diffused which is a direct consequence of the geometry. At the fixed frequency-shift a value of the flux corresponds to the length

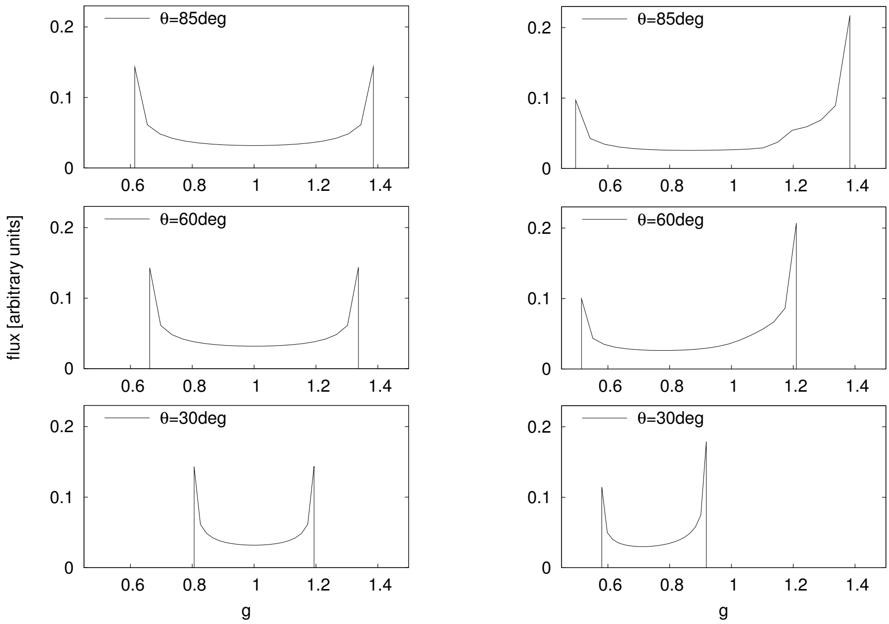

Figure 1. Spectral line profiles of a radiating ring at radius $R = 6R_{\mathrm{g}}$ influenced only by the Newtonian Doppler effect (left) and the relativistic approximation (right).

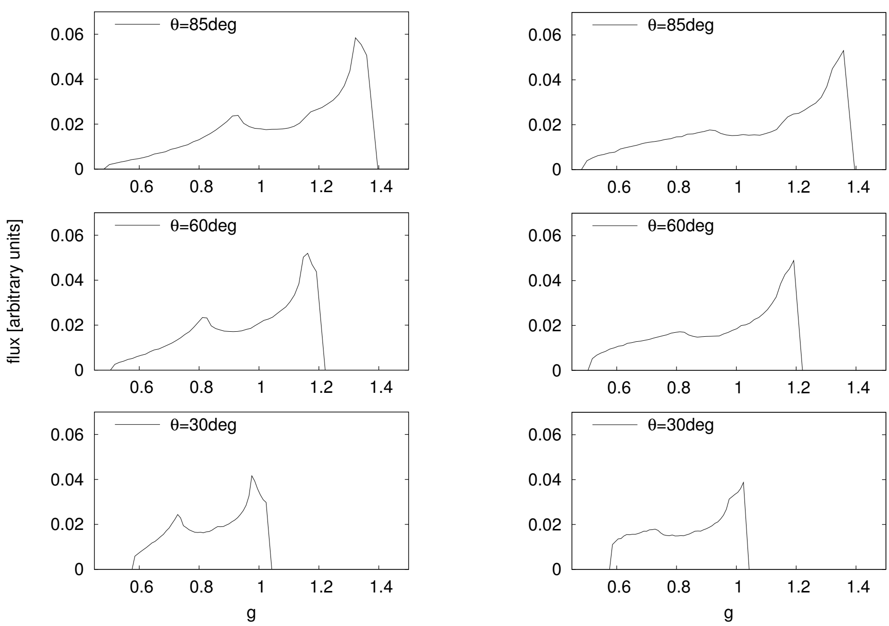

Figure 2. Spectral line profiles of AD with $I(R) \approx 1/R^2$ (left) and with $I(R) \approx 1/R^3$ (right).

of a curve joining the points on the disc with the same values of the shift. The difference between approximations of $I(R) \approx 1/R^{\alpha}$ is such that the bigger value of a parameter α the more contributions to the wings of the spectral line. The wings are namely formed by a radiation from the innermost parts of the disc while radiation from the outer region assigns less frequency shift. The maximal frequency shift is linked with the radius by the approximations mentioned above.

4 TIME-DEPENDENT SPECTRA

One can imagine the spectrum of an accretion disc as some mean profile on which a contribution from a circulating bright spot may be occasionally superposed. While Fig. 1 showed a continuum subtracted spectrum of a spot after integration over the whole orbital period, Fig. 3 illustrates time evolution of the spectral line profile. The quantity T represents time in units of orbital periods.

But it is difficult to recognize the contribution of the spot in the total observed spectrum. With time dependent spectra we have bigger chance to find an orbiting spot in the spectra and by mentioned familiar relationships to determine such an important characteristic of a black hole as its mass.

If there is a hot bright spot on the disc its radiation appears in the spectrum as a δ-function moving with time through the disc spectrum. The turn-over points of that δ-function are correlated to the radius of the spot if we consider Keplerian velocity as a good approximation of the azimuthal motion. It is because the maximally receding, respectively approaching, material contributes to the spectrum in the extremal shifts. If we establish the value of the inclination angle by an independent way then the maximal radial velocity is just the orbital Keplerian velocity times the sine of the inclination angle.

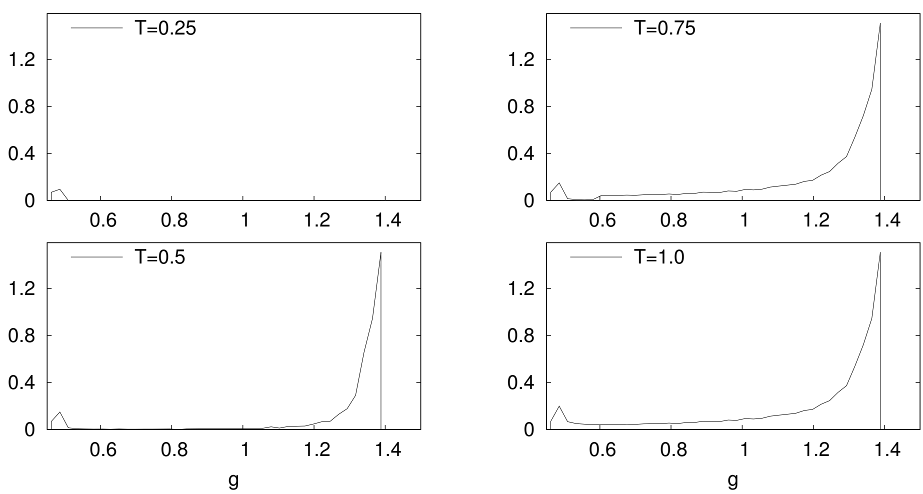

Figure 3. Time evolution of a spectral line of a spot at $R = 6R_{\mathrm{g}}$ on a disc with the inclination $\Theta_0 = 85°$.

5 CONCLUSION

The spectral line profiles of radiating rings and discs circulating around a massive black hole were shown. We have illustrated how the predicted spectral line profiles differ from the Newtonian ones. We mentioned a method to determine the mass of a black hole on the base of studying an observed spectrum. A feasible way to estimate the black hole mass employs the time-dependent spectra, assuming there is a hot spot on the disc orbiting with the Keplerian velocity. Current measurements do not reach the required resolution but this could be achieved in future.

ACKNOWLEDGEMENTS

First of all I would like to thank to Dr. Vladimír Karas who leads me in my work and significantly helps me. I would also like to thank to Dr. Ladislav Šubr for valuable advice. Our research is supported by the grant number GAUK 299/2004.

REFERENCES

Dovčiak, M., Bianchi, S., Guainazzi, M., Karas, V. and Matt, G. (2004), *Monthly Notices Roy. Astronom. Soc.*, **350**, p. 745.

Fabian, A. C., Rees, M. J., Stella, L. and White, N. E. (1989), *Monthly Notices Roy. Astronom. Soc.*, **238**, p. 729.

Marsch, T. R. and Horne, K. (1988), *Monthly Notices Roy. Astronom. Soc.*, **235**, p. 269.

Pecháček, T., Dovčiak, M., Karas, V. and Matt, G. (2005), The relativistic shift of narrow spectral features from black-hole accretion discs, *Astronomy and Astrophysics*, **441**, pp. 855–861.

Tanaka, Y., Nandra, K., Fabian, A. C., Inoue, H., Otani, C., Dotani, T., Hayashida, K., Iwasawa, K., Kii, T., Kunieda, H., Makino, F. and Matsuoka, M. (1995), *Nature*, **375**, p. 659.

Proceedings of *RAGtime 6/7: Workshops on black holes and neutron stars, Opava, 16–18/18–20 September, 2004/2005*
S. Hledík and Z. Stuchlík, editors, Silesian University in Opava, Czech Republic, 2005, pp. 301–313

Long gamma-ray bursts: (current) theory and observation

Paul A. Taylor

Oxford Astrophysics, Denys Wilkinson Building, Keble Road, Oxford OX1 3RH, UK
ptaylor@astro.ox.ac.uk

ABSTRACT
Gamma-ray bursts (GRBs) represent an intersection in many astro-fields, and a more complete understanding of their basic processes will have a broad impact in many areas. Long-duration GRBs (LGRBs) represent a final stage in the evolution of massive stars, and have been directly linked to supernovae; they may also explain events such as X-ray flashes. Due to their high energies, LGRBs have been observed out to cosmological distances, redshift $z > 6.2$; as short lived massive stars, they trace out star forming regions and give valuable information about galactic evolution through a large range of epochs. They have even been recommended as having properties of "standard candles," for testing cosmology to far greater depths than Type Ia SNe. Finally, LGRBs are an interesting test ground for general relativity. We discuss some observed properties, recent theoreties and problems in the field, in relation to such topics as GRB progenitors, the collapsar model, host galaxies, and jet phenomena.

Keywords: gamma-ray burst – supernova – collapsar – neutron star – black hole – accretion disk – relativistic jets – afterglows

1 INTRODUCTION

The GRB phenomena were first reported by Klebesadel et al. (1973) using data from the Vela satellites. The study consisted of 16 bursts lasting up to 30 s and which were detected in a range of 0.2–1.5 MeV. Since then, the number of observed GRBs has risen into the thousands, with burst durations spanning more than 5 orders of magnitude. Several new telescopes, and particularly multi-wavelength observations, have increased our understanding of the phenomena.

The Compton Gamma-ray Observatory (CGRO) was launched in 1991, carrying the Burst and Transient Experiment (BATSE) and the Energetic Gamma-Ray Experiment Telescope (EGRET) specifically designed for detecting gamma-rays. Observations and analyses have determined that GRBs occur at cosmological distances (Metzger et al., 1997) and are some of the most energetic events in the universe, with total energy typically $\approx 10^{51}$ ergs. The gamma-rays themselves are emitted in highly collimated, polar jets (Kulkarni et al.,

80-7248-334-X

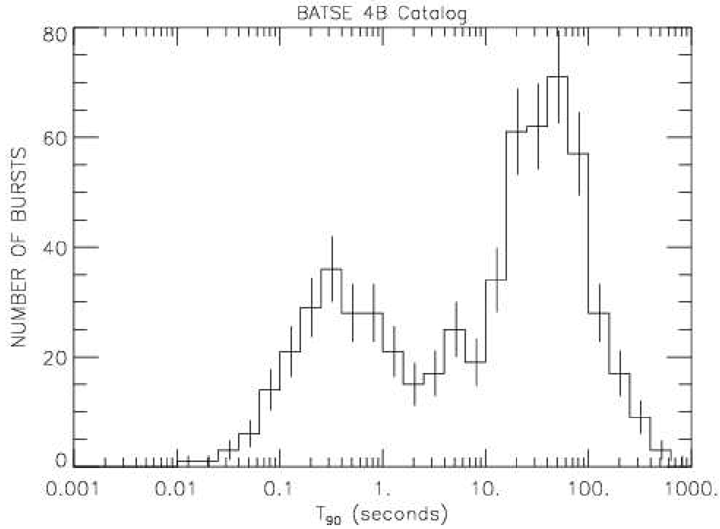

Figure 1. Duration distribution of sources in the BATSE 4B Catalog (Meegan et al., 2005). The total Catalog contained over 2000 GRBs, with durations based on the time during which 90% of an event's fluence occured, T_{90}. This sample shows a strong bimodality of two near-Gaussian distributions. Even today, nearly two-thirds of all observed GRBs are long duration bursts.

1999) with Lorentz factors $\Gamma \approx 10^2$–10^3. Observations to date of temporal duration, spectral hardness ratios and host galaxies confirm a bimodal distribution for the population (see Fig. 1): short duration bursts (SGRBs, < 2 s) and long duration bursts (LGRBs, > 2 s), with distinct progenitor scenarios for each class.

Throughout their history, models for GRBs have ranged from primordial black holes (BHs) evaporating to energy released from the cusp of a cosmic string to fast neutron stars (NSs) wandering through the Oort Clouds (Nemiroff, 1994). More recent trends have settled upon compact object collisions (NS-NS, BH-NS) as a leading candidate for producing SGRBs (e.g., Ruffert and Janka, 1999; Fryer, 1999), and the core-collapse of a massive star for producing LGRBs (e.g., Woosley and MacFadyen, 1999), which we discuss further in this paper.

Current tools for analyzing GRBs obtain multiwavelength spectra: the European Space Agency's Integral, a multi-instrument launched in 2002, contains X-ray and optical telescopes as well as a gamma-ray camera. In late 2004, the NASA's Swift Satellite went into orbit. Its onboard Burst Alert Telescope (BAT) detects and acquires locations for GRBs, and then quickly (within $\approx$20 s) focuses an X-ray Telescope (XRT) and Ultraviolet/Optical Telescope (UVOT) on the region to detect afterglows. Swift is the most sensitive gamma-ray detector built to date; its goals are to give data about GRB environments and their host galaxies out to high redshift, to study short durations bursts (determining if their relative paucity is physical or detection biased), to study the interaction of the GRB blastwave with host environs via afterglows, and to add information on GRB progenitors and the physical mechanisms behind the different classes- all of which should lead to better constrained theoretical models.

We discuss here observed properties, recent theories and problems in the field of LGRBs. First, we discuss the recent association of LGRBs with Type Ic SNe; in the next section, we discuss the collapsar model which comes from this association; we then discuss topics in relativistic jets and afterglows; we discuss current studies of LGRB host galaxies; finally, we discuss briefly cosmological implications.

2 GRB-SN-HN CONNECTION

A major breakthrough in understanding the mechanism of LGRBs came with the association of GRBs and core-collapse (Type Ic) SNe. First, occuring the same day as and within the error box of GRB980425, a very luminous optical transient was discovered with the BeppoSAX satellite and determined to be a Type Ic SN, SN1998bw (Galama et al., 1998). The event was particularly bright, with a kinetic energy $\approx 2 \times 10^{52}$ ergs, of roughly an order of magnitude greater than previous Type Ic SNe, and subsequently dubbed a "hypernova" (HN) (Iwamoto et al., 1998). Its optical properties were best matched by a progenitor $\approx 40\,M_\odot$ with a $13.8\,M_\odot$ $C + O$ core and producing $0.7\,M_\odot$ Ni_{56} with a slightly asymmetric explosion. Based on the estimated $2.9\,M_\odot$ size of the compact remnant, the end result was presumed to be a black hole.

In 2003, definitive proof of a SN-GRB connection was made by the identification of a SN bump in the afterglow of GRB030329 (Stanek et al., 2003), one of the brightest GRBs yet observed. The spectrum of SN2003dh was that of a Type Ic SN and also very similar to that of SN1998bw. A comparison of light curves taken from SN2003dh and GRB030329 is shown in Fig. 2 (Stanek et al., 2003). The broad lines observed in the ejecta indicated that early time expansion velocities were $> 30{,}000\,\mathrm{km\,s^{-1}}$; again, this event was classified as a HN.

These associations led to the acceptance of the so-called "collapsar model" for gamma-ray bursts from the model used originally for core-collapse SNe (Woosley, 1993). Briefly, the scenario involves a rotating, massive star ($M > 30\,M_\odot$) collapsing to form a black hole from its core and a centrifugally supported disk which accretes onto the black hole. The method of powering the gamma-ray production is unknown, but most proposed mechanisms required BH-disk interaction. One further requirement of the model is that any H or He envelope is removed by the time of production, otherwise the jet energy would be dissipated into kinetic energy (known as the baryon massloading problem). Strong winds may play a role, as well as a SN event, particularly one that is polarized along the axis of rotation.

One of the strongest physical features linking the two events is asphericity. This is a necessary feature in gamma-ray bursts where large amounts of energy are released in polar jets. It is also observed in many of the associated HNe, and with many Type Ic SNe in general, and may best explain the range of SN Ic line profiles, due to viewing angle effects (see Fig. 3) (Mazzali et al., 2005). If viewed along the polar/jet direction, iron is observed moving at a higher velocity than oxygen, which is represented by a narrow line due to its perceived perpendicular motion. If observed closer to the equatorial plane, then oxygen shows double lines from Doppler shifts toward and away from the observer. Viewing angle

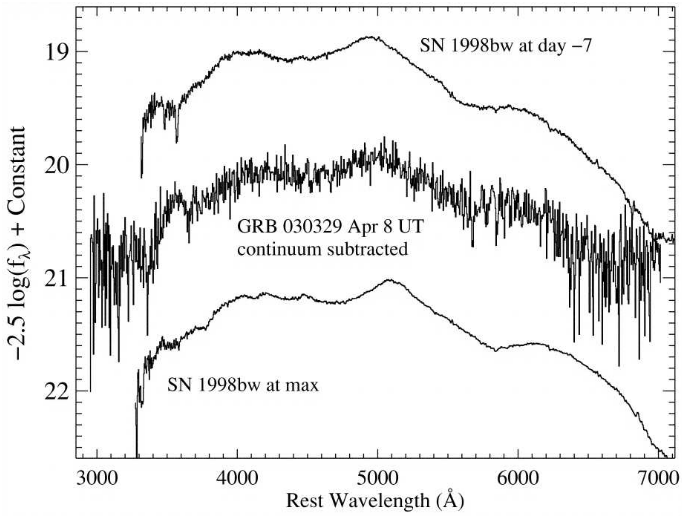

Figure 2. Comparison of spectra of SN1998bw and GRB030329 from Stanek et al. (2003); the features match quite well, leaving little doubt of a direct association of the two events.

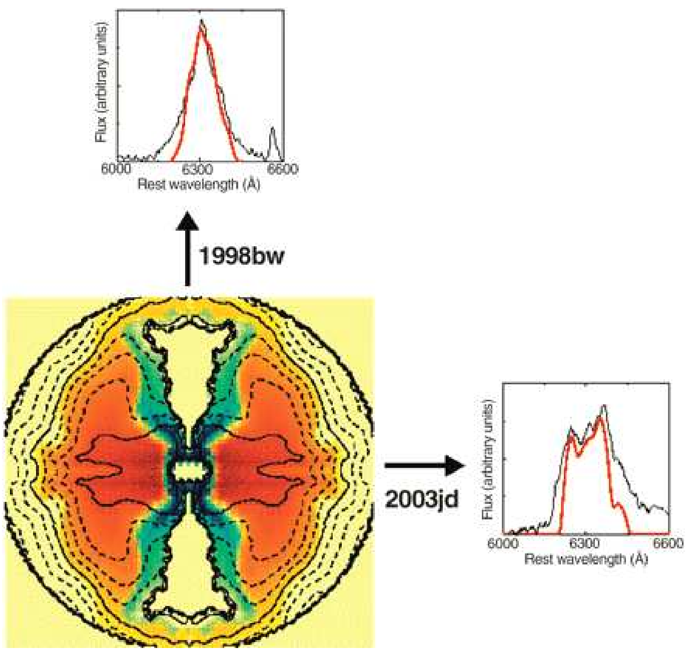

Figure 3. A comparison of viewing angles for asymmetric HN explosion, as for SN1998bw and SN2003dh, computed from a 2D model by Mazzali et al. (2005). Iron is predominantly ejected along the polar axes, and oxygen along and near the equatorial plane.

effects also mean that several SNe/HNe observations may actually be gamma-ray bursts that are not observed along the poles of emission.

Podsiadlowski et al. (2004) calculated the galactic rates for both HNe and LGRBs, taking into account viewing angle effects; they found roughly comparable rates (within large margins), that both events had a galactic rate of 10^{-6} to $10^{-5}\,\mathrm{yr}^{-1}$ – a very suggestive coincidence. These rates are orders of magnitude lower than the galactic rate of SNe Type Ic, suggesting that special circumstances are required for the very energetic events, some of which are addressed in the current collapsar models.

3 THE COLLAPSAR MODEL

In the current "collapsar model" for LGRBs, the original star forms a black hole via a two step process: first, the system collapses to a neutron star surrounded by a massive disk with a SN explosion; then, the neutron star quickly accretes matter to form a black hole, with the dense disk remaining. Finally, some kind of interaction between the disk and black hole creates the ultra-relativistic (Lorentz factor $>$ 100) gamma-ray jets. Very few specifics of the process are understood, and several models are proposed for jet production.

3.1 The progenitor

GRB observations and afterglow spectra, in addition to the association with HNe/SNeIC, give several requirements for the progenitors of these collapsars. Firstly, the progenitors are certainly massive, so that the iron core is nearly the size of a BH, $\approx 2\,\mathrm{M}_\odot$ or so. Most models employ progenitors with the initial mass range of $>$ 25–30 $\mathrm{M}_\odot$, (Woosley and MacFadyen, 1999; Fryer and Heger, 2000); 2D simulations by Fryer (1999) showed that a star with initial mass $> 40\,\mathrm{M}_\odot$ forms a BH directly with no intermediate NS, suggesting a maximum progenitor size for this two-step collapse version of the model.

Secondly, the SN/HN connection requires the star must be stripped of any H or He envelope (Heger and Woosley, 2003). This condition also helps in accommodating the aforementioned baryon loading problem for the system *a priori*. Most progenitors utilize Wolf-Rayet stars or bare helium stars that have been stripped of their envelopes either by companions or by winds (Heger and Woosley, 2003; Chevalier and Li, 1999; Petrovic et al., 2005).

Rotation plays an important and not-fully-understood role in these systems as well. It is agreed that in order to prevent a prompt collapse to a BH, the $\approx 2\,\mathrm{M}_\odot$ Fe core must be rotating rapidly enough that the specific angular momentum near its edge, j_c, is greater than that of the last stable orbit around a BH of the same mass: $j_\mathrm{c} \geq \sqrt{6}\,GM/c \approx 2 \times 10^{16}(M/2\mathrm{M}_\odot)\,\mathrm{cm}^2\,\mathrm{s}^{-1}$ (Podsiadlowski et al., 2004; Petrovic et al., 2005). Likewise, most mechanisms for generating gamma-ray jets from a BH require rapid rotation (Fryer et al., 1999). Rotation also results in non-spherical symmetry for the system, both from centrifugal forces and from restricting convective regions along the rotation axis due to instability criterion (Fryer and Heger, 2000). But the other effects of rotation are debated, such as on the core bounce after the collapse. Due to the introduced centrifugal force, the core bounce is weakened, lessening the explosion (Mönchmeyer and Müller, 1989);

however, rotation yields asymmetric convective layers where neutrinos heat more efficiently, increasing the explosion in these parts (Yamada and Sato, 1994; Fryer and Heger, 2000). In general, it is assumed that the progenitors are rapidly rotating, although the full range of effects of rotation, such as chemical mixing and convective instabilities, are not well determined.

In general, 1- and 2-dimension hydrodynamic simulations which have been performed omit the full inclusion of magnetic fields and full general relativity (GR). Some more recent models investigate both: for inclusion of GR effects in prompt collapse, see recent papers by Shibata and Sekiguchi (2005); Sekiguchi and Shibata (2005); for GR effects in the proto-NS, (e.g., Fryer and Heger, 2000; Heger and Woosley, 2003). GR considerations would be important particularly in the later stages of collapse during BH formation, and in any adjustment to Kerr spacetime in the presence of a massive disk. Such interesting considerations are for future studies.

Strong magnetic fields should in principle reduce stellar rotation rates significantly by enforcing rigid rotation with frozen-in field lines (Spruit, 2002). And the majority of mechanisms suggested for producing the gamma-ray jets themselves (e.g., neutrino annihilation Paczyński, 1990; Popham et al., 1999) and the Blandford–Znajek mechanism (Blandford and Znajek, 1977; Lee et al., 2000; Popham et al., 1999), discussed below), require strong magnetic fields during the BH/disk stage. It is often assumed (in models) that the magnetic fields are negligible in the proto-NS and gain in size via flux conservation in the shrinking system, as well as magnetic torques from differential rotation and dynamo transport (Petrovic et al., 2005; Spruit, 2002).

Although each of these arguments may work in principle, a consistent model is more difficult to achieve. Maintaining a large angular momentum to support a disk is difficult, as strong magnetic fields work against differential rotation, and the ejection of a large envelope loses large amounts of angular momentum from the star. One solution to this angular momentum problem is a binary merger progenitor: massive helium stars interact with quasi-conservative mass transfer and enter a common envelope inspiral; the stars eject the common envelope and merge. Preliminary models have shown that some stars evolved by this channel may have up to an order of magnitude greater core angular momentum than the single massive star progenitor (Fryer and Heger, 2005). The binary merger channel may be a viable solution to including the various progenitor requirements.

3.2 The central engine

In the collapsar model discussed in this paper, the gamma-rays are produced after the system's second collapse, when a massive accretion torus surrounds a BH (Popham et al., 1999). There are different mechanisms for converting the matter into gamma rays (Woosley and MacFadyen, 1999), the two leading candidates being neutrino annihilation and the Blandford–Znajek (B-Z) process.

The model for neutrino annihilation was proposed for both neutron star mergers and failed SN explosions from a massive Wolf–Rayet star (Jaroszyński, 1996; Popham et al., 1999). Briefly, neutrinos are produced in the massive disk and annihilate near the system's axis of rotation, where the density of matter is low, avoiding the baryon loading problem. Neutrino annihilation produces a high energy $e^{\pm}$ plasma in a narrow jet. The BH must have high angular momentum ($a = J/M_{\rm BH} \approx 1$) with a torus described by a nearly constant specific angular momentum profile. However, amidst other difficulties, the efficiency of neutrino production and annihilation required to power GRBs is mainly considered too high to be a plausible mechanism for producing gamma-ray jets.

The more currently favoured model for GRB jet production (e.g., Lee et al., 2000) uses magnetohydrodynamics (MHD). In 1977, Blandford and Znajek (1977) proposed that the interaction between a BH and massive disk, mediated by a large magnetic field, would convert rotational energy from the BH (Blandford and Znajek, 1977) into a Poynting-flux dominated jet. For estimates of the energetics in GRB discussions, the B-Z effect yields (Thorne et al., 1986):

$$\dot{E}_{\rm jet} \approx 10^{50} a^2 \left(\frac{M_{\rm BH}}{3\,{\rm M}_\odot}\right)^2 \left(\frac{B}{B^{15}\,{\rm G}}\right)^2 \,{\rm erg\,s^{-1}}\,, \tag{1}$$

where $a = J/M_{\rm BH}$ is the Kerr spin parameter of the BH, $M_{\rm BH}$ is the mass of the BH, and B is the magnetic field strength in the BH/disk. It has been shown that the convection-driven dynamo of Thompson and Duncan (1993) can just manage to produce a B-field of this necessary magnitude. Even with this large field, the accretion rate must be quite high to explain observed GRB energies, requiring a very dense disk. It is not known whether it is possible to establish a disk of necessary density.

4 JETS AND AFTERGLOWS

In 1997, targeted by the Italian-Dutch X-ray satellite, Beppo-SAX, the first optical afterglows from a GRB, GRB 970228, were obtained using a number of groundbased telescopes and the Hubble Space Telescope (HST). The observed spectra matched well with a GRB model composed of a simple blastwave from a “fireball” colliding into the surrounding medium, decelerating and releasing energy (Wijers et al., 1997). The bulk Lorentz factor ($\Gamma > 10^3$, Rees and Meszaros, 1992) of the relativistic fireball decreased in time as $t^{-3/8}$ for the observers frame, and the observed spectrum was due to resulting synchrotron radiation.

“Afterglows” of radiation from the LGRBs are observed in wavelengths such as X-ray to optical. The jet afterglows are quite important for revealing properties of the GRB- it is from the afterglows that host galaxies and redshifts typically determined. Rhoads (1997) noted that the lateral expansion of a GRB jet will create a steepening or break in the declining afterglow spectrum which is related to the jet’s Lorentz factor. This phenomenon occurs simultaneously across multi-wavelength spectra (see Fig. 4, Tagliaferri et al., 2005). The jet collimation is given in terms of its minimum opening angle, Ω, which in our observer rest frame is given by $\Omega \approx \Gamma^{-1}$ if the photons are assumed to be emitted isotropically in the rest frame of the radiating matter. This is the Ω which we would always observe for gamma-rays, even with less collimation. By measuring the abrupt shift in the afterglow spectrum to lower frequencies, therefore, one may determine the opening angle/Lorentz factor, as has been done for several GRBs (as in Wei and Lu, 2002).

An important and unresolved issue is the structure of the relativistic jets. The leading candidate jet models are: a uniform (or “top-hat”) model (Panaitescu and Meszaros, 1999), where the energy per solid angle and Lorentz Γ are constant through the opening angle and

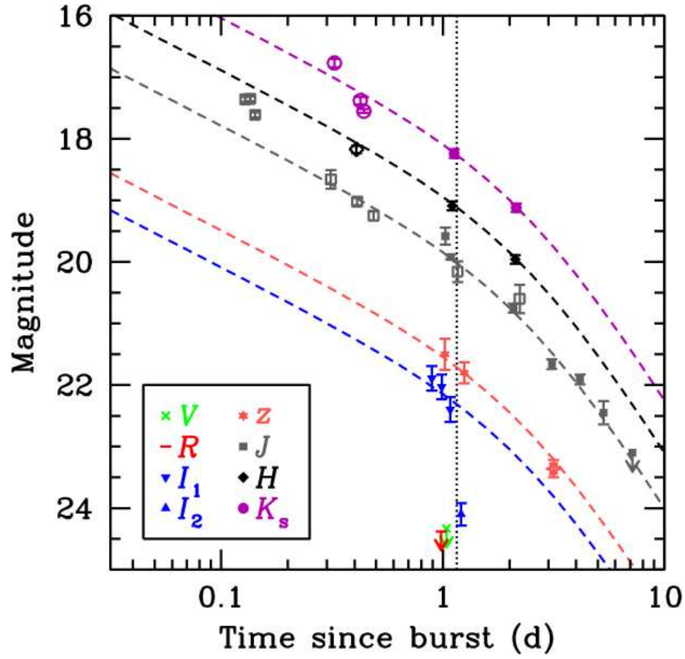

Figure 4. From Tagliaferri et al. (2005), the light curve of recent GRB 050904. Dashed lines represent best fit lines in J band, which is used for the other bands. The multiwavength steepening or break due to the jet phenomenon is apparent.

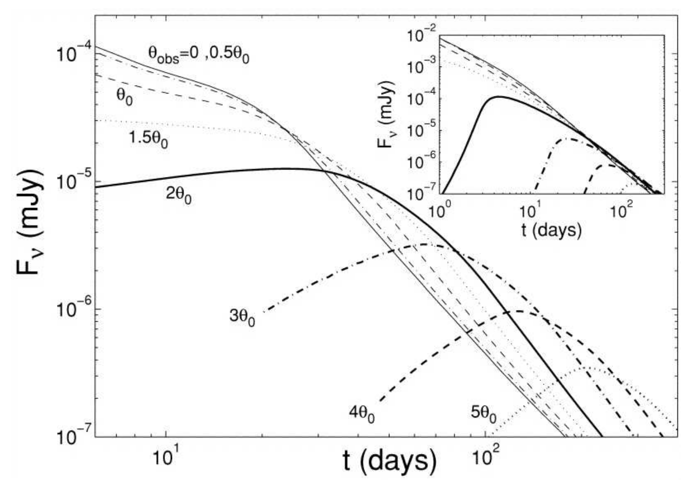

Figure 5. From (Granot et al., 2002), the calculated effect on flux over time depending on the observers viewing angle of a uniform jet. θ_O and $\theta_{\rm obs}$ are the opening angle and observer's angle from centre, respectively.

drop off sharply at the edge; and the universal structured jet (USJ) model (Lipunov et al., 2001), where the energy per solid angle falls off with the square of the angle from a central core value. In the latter model, all GRB jets are essentially identical (Nakar et al., 2004), but slight differences in viewing angle result in very different light curves. Some authors propose that gamma-ray bursts viewed far off-axis may explain events such as X-ray flashes (Lamb et al., 2004).

Because of the uncertain nature of the physical circumstellar material (whether it is a remnant of a stellar wind or cleared by a SN shell, depending on evolutionary paths),

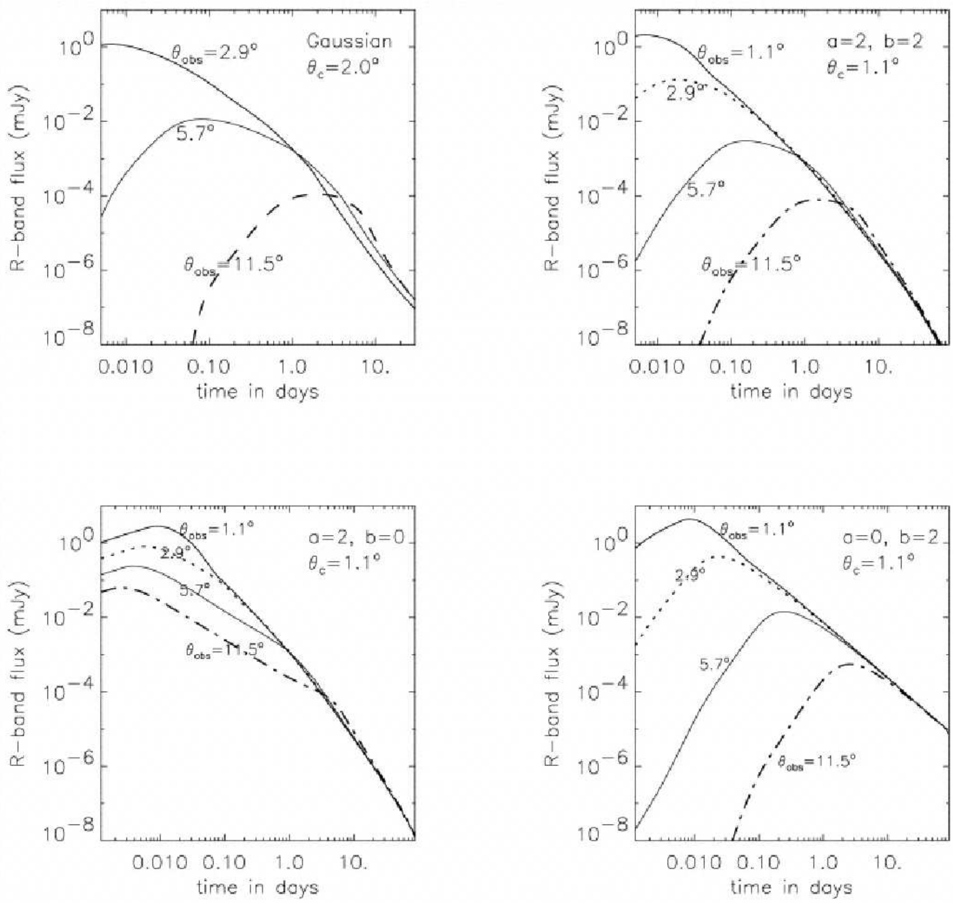

Figure 6. From (Kumar and Granot, 2003), these diagrams show the variety of viewing angle effects on the R-band afterglow of prescribed models of uniformly structured jets (and one Gaussian); the initial energy per solid angle and Lorentz Γ are assumed to follow a power-law model, with the "a" and "b" parameters representing the steepness of each factor, respectively. The circumstellar material is assumed to be of uniform density. Note the differences between both models and viewing angles.

and also because the viewing angles are uncertain, it is difficult to determine the precise nature of the jet. Fig. 5 (Granot et al., 2002) shows the variation of uniform jet for different opening angles, and Fig. 6 (Kumar and Granot, 2003) shows some of the different afterglow results for the structured jet at various opening angles, with model parameters described in the caption. Comparisons with physical afterglows have not yet selected one jet model definitively, in part because of the large uncertainties of environment and viewing angles.

5 GRB HOST GALAXIES

Most evidence connects LGRBs to the collapse of massive stars. Given their high energies and the short lifespan of massive stars, LGRBs become natural candidates for studying star formation histories. Moreover, gamma-rays are not subject to dust absorption (though parts of their afterglows are), and have been observed out to redshift $z > 6$, making them important in the study of the evolution of galaxies as well.

Floc'h et al. (2003) studied GRB host galaxies by identifying counterparts to optical afterglows, most with redshift $z < 1.6$. Typically, hosts belonged to the population of blue, faint galaxies with high star formation rate (SFR). The study also suggested that LGRBs were preferentially located in regions of low-metalicity; this bias is explainable with the collapsar model, as lower metalicity in a stellar envelope reduces mass loss and also angular momentum loss.

Simulations of large-scale structure formation (Courty et al., 2004) have identified host candidates as young, low-mass galaxies ($M < 10^{10}\,M_\odot$ with low to moderate star formation rate, of order a few $M_\odot$/year. These results were in agreement with optical observations of LGRB hosts at $z \approx 1$, typically blue subluminous galaxies, with SFR $= 1$–$50\,M\,\mathrm{yr}^{-1}$ (e.g. Chary et al., 2002) and host mass, M, in the range 2×10^8–$4 \times 10^{10}\,M_\odot$. It was found that assigning LGRB hosts to the most active galaxies with high SFR was inconsistent with observations. Instead, LGRB host galaxies were the most efficient at star-forming, having high and consistent specific star-formation rates, SFR/M. While most observed LGRB were $z \lesssim 1$, the simulations showed the efficiency of low-mass galaxies to be fairly constant with redshift. Thus, observational studies of LGRB hosts would be biased towards higher mass objects, due to the faintness of the low-mass galaxies.

A very recent survey of 37 LGRB host galaxies using the Hubble Space Telescope (HST) was performed by Conselice et al. (2005). The aim was to study the structural properties and sizes of LGRB host galaxies, and to compare those galaxies with non-GRB hosts at the same redshift in the Hubble Deep Field (HDF). For all galaxies, the model-independent CAS (concentration, asymmetry, clumpiness) parameters were used to determine morphological class: E/S0, spiral, and irregular/peculiar/merging (e.g., Schade et al., 1995; Abraham et al., 1996). The results showed that LGRB host galaxies occur in all types of field galaxies, not solely restricted to irregulars. Approximately 68% of the host galaxies were CAS-associated with spirals or peculiar/merging galaxies, and the remaining 32% early type or forming early type elliptical galaxies.

As to the evolution of galaxies, at $z < 1.2$, LGRB host galaxies were significantly smaller (Petrosian radius of 6.5 ± 5.2 kpc or 4.5 ± 1.5 kpc, depending on sample) than the typical HDF galaxies (Petrosian radius of 12.0 ± 8.5). For $z > 1.2$, the average Petrosian radius for LGRB hosts was 6.8 ± 4.0 kpc, fairly similar to the average HDF galaxy with Petrosian radius of 7.1 ± 2.0 kpc. Thus, the size of LGRB host galaxies does not appear to vary significantly with redshift. However, the concentration parameter of the hosts did vary; in the sample with $z > 1.2$, LGRB hosts had a significantly higher concentration of light than similar redshift HDF galaxies. At lower redshifts, the concentrations decreased in the host galaxies. This suggests that the high redshift host galaxies may be either massive or blue compact galaxies, different than the host galaxies at low redshift, but still those with high star formation rates.

6 COSMOLOGICAL IMPLICATIONS?

The most distant LGRB observed to date is one recently seen at redshift $z = 6.29$ (Tagliaferri et al., 2005). As bright events seen out to large distances, LGRBs have been sought after to measure cosmology. Several empirical relations have been derived. One such proposal (Ghirlanda et al., 2004) relates the observed peak energy, $E^{\mathrm{obs}}_{\mathrm{peak}}$, to the collimation-corrected energy $E_{\gamma,\mathrm{iso}}$:

$$E^{\mathrm{obs}}_{\mathrm{peak}}(1+z) \propto E^{0.7}_{\gamma,\mathrm{iso}}\,. \tag{2}$$

Another empirical relation utilizes the temporal behaviour of bursts. A variability parameter, V, is defined for bursts using statistical methods (Reichart et al., 2001). Interestingly (perhaps) is the fact that luminosity and variability scale together by the relation, $L \approx V^{3.3}$, somewhat analogous to existing Cepheid-variability relations, and provides a possible distance indicator. We shall have to wait and see if these patterns continue to exist in the Swift-era of observations, as more LGRBs with measured redshifts are detected, and if any physical explanation evolves, before measuring cosmology with them.

7 CONCLUSIONS

Remarkable progress has been made in the field of LGRBs in recent years, particularly due to the multi-wavelength nature of observations once the gamma-ray are detected. Afterglows have been necessary to determine the LGRB association with with SNe-HNe events and redshift measures, and hopefully will yield more results to constrain the progenitor's evolution and central engine mechanism. The brightness and distance of observed LGRBs make them valuable in the field of galactic evolution and, perhaps, in cosmology. The next few years should see a remarkable influx of data from the Swift satellite and multi-wavelength follow-ups, and in addition increase our understanding of SGRBs as well as LGRBs.

As our theoretical understanding of GRBs develops, we wait to see whether, "The world is more complicated than most of our theories make it out to be," (Edmund C. Berkeley) or whether we shall take consolation in the fact that, "Nature uses as little as possible of anything" (Johannes Kepler).

ACKNOWLEDGEMENTS

Thanks to my supervisors at Oxford, John C. Miller and Philipp Podsiadlowski.

REFERENCES

Abraham, R. G. et al. (1996), *Monthly Notices Roy. Astronom. Soc.*, **279**, p. L47.

Blandford, R. D. and Znajek, R. L. (1977), *Monthly Notices Roy. Astronom. Soc.*, **179**, p. 433.

Chary, R., Becklin, E. E. and Armus, L. (2002), *Astrophys. J.*, **566**, p. 299.

Chevalier, R. and Li, Z. (1999), *Astrophys. J. Lett.*, **520**, p. 29.

Conselice, C. J. et al. (2005), *Astrophys. J.*, **633**, p. 29.

Courty, S. et al. (2004), *Monthly Notices Roy. Astronom. Soc.*, **354**, p. 581.

Floc'h, L. et al. (2003), *Astronomy and Astrophysics*, **400**, p. 499.

Fryer, C. (1999), *Astrophys. J.*, **522**, p. 413.

Fryer, C. and Heger, A. (2000), *Astrophys. J.*, **541**, p. 1033.

Fryer, C., Woosley, S. and Hartmann, D. (1999), *Astrophys. J.*, **526**, p. 152.

Fryer, C. L. and Heger, A. (2005), *Astrophys. J.*, **623**, p. 302.

Galama, T. J. et al. (1998), *Nature*, **395**, p. 670.

Ghirlanda, G., Ghisellini, G. and Lazzati, D. (2004), *Astrophys. J.*, **616**, p. 331.

Granot, J. et al. (2002), *Astrophys. J. Lett.*, **570**, p. 61.

Heger, A. and Woosley, S. (2003), in *(UCSC)AIP Conf. Proc.*, volume 662, pp. 214–216.

Iwamoto, K. et al. (1998), *Nature*, **395**, p. 672.

Jaroszyński, M. (1996), *Astronomy and Astrophysics*, **305**, p. 839.

Klebesadel, R., Strong, I. and Olson, R. (1973), *Astrophys. J. Lett.*, **182**, p. 85.

Kulkarni, S. R. et al. (1999), *Nature*, **398**, p. 389.

Kumar, P. and Granot, J. (2003), *Astrophys. J.*, **591**, p. 1075.

Lamb, D. Q., Donaghy, T. Q. and Graziani, C. (2004), *New Astronomy Reviews*, **48**, p. 459.

Lee, H., Wijers, R. and Brown, G. (2000), *Phys. Rep.*, **325**, p. 83.

Lipunov, V. M., Postnov, K. A. and Prokhorov, M. E. (2001), *Astronom. Rep.*, **45**, p. 236.

Mazzali, P. et al. (2005), *Science*, **308**, p. 1284.

Meegan, C. et al. (2005), Current BATSE Gamma-Ray Burst Catalog, URL `http://www.batse.msfc.nasa.gov/data/grb/catalog/`.

Metzger, M. R. et al. (1997), *Nature*, **387**, p. 879.

Mönchmeyer, R. and Müller, E. (1989), in Ögelman and van den Heuvel, editors, *Timing Neutron Stars*, volume 262 of *NATO ASI Ser. C*, p. 549, NATO, NY:ASI.

Nakar, E., Granot, J. and Guetta, D. (2004), *Astrophys. J. Lett.*, **606**, p. 37.

Nemiroff, R. J. (1994), in *AIP Conf. Proc.*, volume 307, p. 730.

Paczyński, B. (1990), *Astrophys. J.*, **363**, p. 218.

Panaitescu, A. and Meszaros, P. (1999), *Astrophys. J.*, **526**, p. 707.

Petrovic, J. et al. (2005), *Astronomy and Astrophysics*, **435**, p. 247.

Podsiadlowski, P. et al. (2004), *Astrophys. J. Lett.*, **607**, pp. 17–20.

Popham, R., Woosley, S. and Fryer, C. (1999), *Astrophys. J.*, **518**, p. 356.

Rees, M. and Meszaros, P. (1992), *Monthly Notices Roy. Astronom. Soc.*, **258P**, p. 41.

Reichart, D. et al. (2001), *Astrophys. J.*, **552**, p. 57.
Rhoads, J. (1997), *Astrophys. J. Lett.*, **487**, p. 1.
Ruffert, M. and Janka, H.-T. (1999), *Astronomy and Astrophysics*, **344**, p. 573.
Schade, D. et al. (1995), *Astrophys. J. Lett.*, **451**, p. 1.
Sekiguchi, Y. and Shibata, M. (2005), *Phys. Rev. D*, **71**, p. 084013, `astro-ph/0504567`.
Shibata, M. and Sekiguchi, Y. (2005), *Phys. Rev. D*, **71**, p. 024014, `astro-ph/0412243`.
Spruit, H. (2002), *Astronomy and Astrophysics*, **381**, p. 923.
Stanek, K. Z. et al. (2003), *Astrophys. J. Lett.*, **591**, p. 17.
Tagliaferri, G. et al. (2005), *Astronomy and Astrophysics*, **443L**, p. 1.
Thompson, C. and Duncan, R. (1993), *Astrophys. J.*, **408**, p. 194.
Thorne, K. S., Price, R. H. and MacDonald, D. A. (1986), *Black Holes: The Membrane Paradigm*, Yale Univ. Press.
Wei, D. and Lu, T. (2002), *Monthly Notices Roy. Astronom. Soc.*, **332**, p. 994.
Wijers, R., Rees, M. and Meszaros, P. (1997), *Monthly Notices Roy. Astronom. Soc.*, **288L**, p. 51.
Woosley, S. (1993), *Astrophys. J.*, **405**, p. 273.
Woosley, S. E. and MacFadyen, A. I. (1999), *Astronomy and Astrophysics*, **138**, p. 499.
Yamada, S. and Sato, K. (1994), *Astrophys. J.*, **434**, p. 268.

Proceedings of *RAGtime 6/7: Workshops on black holes and neutron stars, Opava, 16–18/18–20 September, 2004/2005*
S. Hledík and Z. Stuchlík, editors, Silesian University in Opava, Czech Republic, 2005, pp. 315–338

Epicyclic frequencies of Keplerian motion in Kerr spacetimes

Gabriel Török and Zdeněk Stuchlík

Institute of Physics, Faculty of Philosophy & Science, Silesian University in Opava, Bezručovo nám. 13, CZ-746 01 Opava, Czech Republic

ABSTRACT

Relativistic Keplerian orbital frequency (ν_K) and the related epicyclic frequencies (radial ν_r, vertical ν_θ) play an important role in the physics of accretion discs orbiting Kerr black holes. We examine in detail their properties in Kerr spacetimes and discuss some possible observational implications resulting from their behaviour in the black hole case. Characteristics of the fundamental orbital frequencies of Keplerian motion are also analysed with the intention to find the phenomena which could observationally distinguish a hypothetical naked singularity from black holes. We explore the significant differences in behaviour of the epicyclic frequencies. These suggest that oscillations of discs orbiting Kerr black holes and naked singularities could be very different, and the information, given through X-ray variability of the source, could distinguish between the naked singularities and the black holes *in general*.

Keywords: black holes – naked singularities – theory – observations
X-ray variability

1 INTRODUCTION

Quasiperiodic oscillations (QPOs) of X-ray brightness have been observed at low (Hz) and high (kHz) frequencies in some low-mass X-ray binaries containing neutron stars or black holes; for a review articles see, e.g., McClintock and Remillard (2004) in the case of black hole binaries and van der Klis (2000) in the case of neutron star binaries. Since the observed high frequencies are close to the orbital frequency of the marginally stable circular geodesic representing the inner edge of Keplerian discs orbiting black holes (or neutron stars), strong gravity effects must be relevant if trying to explain high frequency QPOs (Abramowicz et al., 2004b). In the context of *discs oscillations* (Okazaki et al., 1987; Nowak and Wagoner, 1991, 1992) both the warped discs (trapped) oscillations (Kato and Fukue, 1980; Kato, 2004b) and resonant oscillations (Abramowicz and Kluźniak, 2001; Abramowicz et al., 2004b) has been considered for explaining QPOs.

In the case of microquasars containing stellar mass black holes, the observed ratio of the twin peak frequencies is exactly, or almost exactly, 3 : 2; therefore, some resonant effects are probably involved in oscillating accretion discs of microquasars (Kluźniak and

80-7248-334-X

Abramowicz, 2000, 2001).[1] It was shown that the parametric resonance of vertical and radial oscillations at epicyclic frequencies related to the Keplerian motion could be the most probable explanation of the observed microquasars phenomena (Török et al., 2005). On the other hand, the forced resonance of the epicyclic frequencies or some other kind of resonance with ratios given by small integral numbers, e.g., 2 : 1, 3 : 1, 5 : 2, etc. could also explain observed QPOs frequencies (with the same 3 : 2 ratio), if combinational ("beat") frequencies are considered (Abramowicz and Kluźniak, 2001; Török et al., 2005; Aschenbach, 2004). The puzzle of this 3 : 2 ratio kHz frequencies has still not been definitely solved and other possible explanations, like warped-disc oscillations (see Kato, 2004a) or simple p-mode oscillations (Rezzolla, 2004), can not be excluded.

The mechanisms for triggering the oscillations in epicyclic frequencies were treated successfully both for thin (see Kato et al., 1998) and thick discs (e.g., Matsumoto et al., 1989; Abramowicz et al., 2003b; Rezzolla, 2004; Šrámková, 2005). Nevertheless, sophisticated three-dimensional magnetohydrodynamic simulations (3-MHD) of accretion flows usually do not show any twin peak kHz QPOs resembling those observed (Igumenshchev et al., 2003; de Villiers et al., 2003 and others). Only very recently Kato (2004c) has reported a view of the 3 : 2 twin peaks in 3-MHD simulations.

In addition, it has recently been shown by Bursa et al. (2004) that the possible resonant oscillations of the torus could be directly observable in X-ray modulation when they occur in the inner parts of accretion flow around a black hole or neutron star, even if the source of radiation is steady and perfectly axisymmetric.

Apparently, the vertical and radial epicyclic frequencies of the Keplerian motion play a crucial role for both thin Keplerian discs and thick toroidal discs. Their properties have been extensively studied in the case of accretion discs orbiting Kerr black holes both in works mentioned above and in many others, yet continue to be very hot outstanding topic in recent astrophysics. On the other hand, it is natural to extend the concept of disc oscillations in the epicyclic frequencies around other physical objects.

According to the cosmic censorship hypothesis (Penrose, 1969) and the uniqueness black-hole theorems (Carter, 1973), the result of the gravitational collapse of a sufficiently massive rotating body is a rotating Kerr black hole, rather than a Kerr naked singularity. Although the cosmic censorship is a plausible hypothesis, there is some evidence against it. In modelling the collapse of rotating stars, it was shown that in some situations mass shedding and gravitational radiation will not reduce the angular momentum of the star enough to lead to the formation of a Kerr black hole (Miller and de Felice, 1985). Some 2D numerical models of collapsing, rotating supermassive objects imply that a Kerr-like naked singularity could develop from objects when rotating rapidly enough (Nakamura et al., 1987).

It is generally believed that black holes are stable against perturbations that would transfer them into naked singularities (Bardeen, 1973; Thorne, 1974; Wald, 1974; Cohen and Gautreau, 1979; Israel, 1986; de Felice and Yu, 1986). However, recently presented gedanken experiments concerning electrically charged, Reissner–Nordström black holes

[1] Interestingly, the same 3 : 2 ratio seems to be present in the case of neutron stars sources, indicating the same origin of the observed quasiperiodic oscillations (Abramowicz et al., 2003a; Belloni et al., 2005; Bulik, 2005; Abramowicz et al., 2005; see also Fig. 10).

put this belief in doubt. It was shown that an extreme Reissner–Nordström black hole could be transformed into a Kerr–Newman naked singularity by capturing a flat and electrically neutral spinning body that plunges in radially with its spin aligned to the radial direction (de Felice and Yu, 2001). Moreover, the possible existence of naked singularities is supported by general mathematical studies concerning scalar fields around Reissner–Nordström naked singularities (see, e.g., Stalker and Tahvildar-Zadeh, 2004).

Therefore, naked-singularity spacetimes related to the black-hole spacetimes with a nonzero charge and/or rotation parameter could be considered conceivable models for some exotic Galactic binary systems or, on much higher scale, of quasars and active galactic nuclei, so they, too, deserve some attention. Of particular interest are those effects that could observationally distinguish a naked singularity from black holes. Therefore, we shall discuss here in detail the properties of the vertical and radial epicyclic frequencies of the Keplerian circular motion in the field of Kerr black holes and naked singularities, in order to find astrophysically relevant differences between the black-hole and naked-singularity cases.

2 EPICYCLIC OSCILLATIONS OF KEPLERIAN DISCS

In the case of oscillating Keplerian discs three orbital frequencies are relevant: Keplerian orbital frequency $\nu_{\mathrm{K}} = \Omega_{\mathrm{K}}/2\pi$, radial epicyclic frequency $\nu_{\mathrm{r}} = \omega_{\mathrm{r}}/2\pi$, and vertical epicyclic frequency $\nu_\theta = \omega_\theta/2\pi$. For discs orbiting Kerr black holes or naked singularities, corresponding angular velocities Ω_{K}, ω_{r}, ω_θ are given by the well-known formulae (e.g., Nowak and Lehr, 1998),

$$\Omega_{\mathrm{K}} = \left(\frac{GM_0}{r_{\mathrm{G}}^3}\right)^{1/2} \left(x^{3/2} + a\right)^{-1}, \tag{1}$$

$$\omega_{\mathrm{r}}^2 = \alpha_{\mathrm{r}}\, \Omega_{\mathrm{K}}^2\,, \tag{2}$$

$$\omega_\theta^2 = \alpha_\theta\, \Omega_{\mathrm{K}}^2\,, \tag{3}$$

where

$$\alpha_{\mathrm{r}}(x, a) \equiv 1 - 6x^{-1} + 8ax^{-3/2} - 3a^2x^{-2}\,, \tag{4}$$

$$\alpha_\theta(x, a) \equiv 1 - 4ax^{-3/2} + 3a^2x^{-2}\,, \tag{5}$$

and x is introduced as dimensionless radial coordinate

$$x = r/M\,. \tag{6}$$

We use Boyer–Lindquist coordinates (t, r, θ, ϕ). We rescale the central object mass with $M = GM_0/c^2 = r_{\mathrm{G}}$ and the central object angular momentum with $a = J_0c/GM_0^2$. Here, the parameters M_0 and J_0 give the mass and the internal angular momentum of the Kerr black hole or naked singularity.

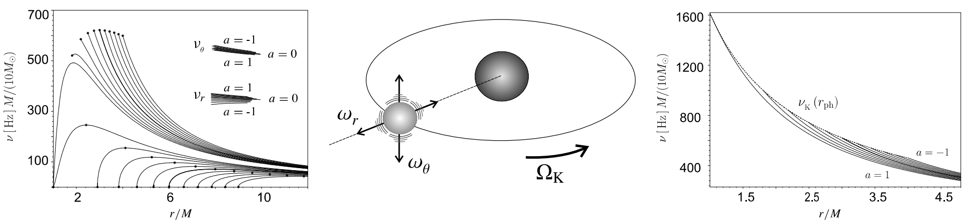

Figure 1. In the gravitational field of a central object, test particle on a circular orbit starts oscillate after a small perturbation. Frequencies of these oscillations (radial ν_{r} and vertical ν_θ) are fundamentally different in Newton's and Einstein's gravity. In Newtonian physics these epicyclic frequencies must always be equal to the Keplerian frequency of circular orbit and the resulting trajectory is an ellipse, while in Einstein's theory they differ and the trajectory is not closed. *Left panel* shows behaviour of these epicyclic frequencies while right one illustrate behaviour of the Keplerian frequency ν_{K}. For both *left* and *right panel* the curves are spaced by 0.2 in a.

In the limit of the Schwarzschild black holes ($a = 0$), we arrive at

$$\alpha_{\mathrm{r}}(x) = 1 - \frac{6}{x}\,, \tag{7}$$

$$\alpha_\theta(x) = 1\,, \tag{8}$$

so that $\Omega_{\mathrm{K}}(x) = \omega_\theta(x)$. In the field of Kerr black holes ($a \neq 0$), there is

$$\Omega_{\mathrm{K}}(x, a) > \omega_\theta(x, a) > \omega_{\mathrm{r}}(x, a) \tag{9}$$

in the range where the frequencies are well defined (Fig. 1 – right panel).

The properties of Ω_{K}, ω_{r}, ω_θ for Kerr black-hole spacetimes are reviewed, e.g., in Kato et al. (1998). We can summarize that

- the Keplerian frequency is a monotonically decreasing function of radius for the whole range of black hole rotational parameter $a \in (-1, 1)$[2] in astrophysically relevant radii above the photon orbit (Fig. 1 – left panel);
- for slowly rotating black holes the vertical epicyclic frequency is a monotonically decreasing function of radius in the same radial range as well; however, for rapidly rotating black holes this function has a maximum (Fig. 1 – left panel);
- the radial epicyclic frequency has a local maximum for all $a \in (-1, 1)$ (Fig. 1 – left panel).

For Kerr naked singularities the behaviour of the epicyclic frequencies is different. In the next sections we show that the vertical frequency can have two local extrema, and the radial one even three. For completeness, we shall discuss the properties of the functions $\Omega_{\mathrm{K}}(x, a)$, $\omega_{\mathrm{r}}(x, a)$, and $\omega_\theta(x, a)$ for both naked singularities and black holes.

[2] Here and henceforth values of $a > 0$ correspond to corotating orbits, while $a < 0$ give counterrotating orbits.

Obviously, all three frequencies (1)–(3) have the general form,

$$\nu = \left(\frac{GM_0}{r_G^3}\right)^{1/2} f(x,a) \doteq 32.3 \left(\frac{M_0}{\mathrm{M}_\odot}\right)^{-1} f(x,a)\,\mathrm{kHz}\,. \tag{10}$$

Thus for the reader's convenience we express the frequency as ν [Hz] $M/(10\,\mathrm{M}_\odot)$ in every quantitative plot of frequency dependence on the radial coordinate (6); i.e., displayed *value* is the frequency relevant for a central object with a mass of $10\,\mathrm{M}_\odot$, which could be simply rescaled for another mass by just dividing the displayed *value* by the respective mass in units of ten solar mass.

3 PROPERTIES OF THE EPICYCLIC FREQUENCIES

First, it is important to find the range of relevance for the functions $\Omega_K(x,a)$, $\omega_r(x,a)$, and $\omega_\theta(x,a)$ above the event horizon located at

$$x_+ = 1 + \sqrt{1-a^2} \tag{11}$$

for black holes, and above the ring singularity located at

$$x = 0 \quad (\theta = \pi/2) \tag{12}$$

for naked singularities.

The circular geodesics in the field of Kerr black holes were discussed in Bardeen et al. (1972), while in the case of Kerr naked singularities the circular geodesics were discussed in Stuchlík (1980). We can summarize that circular geodesics can exist in the range of

$$x \in (x_{ph}(a), \infty)\,, \tag{13}$$

where

$$x_{ph}(a) = 2\left[1 + \cos\left(\tfrac{2}{3}\arccos(-a)\right)\right] \tag{14}$$

gives loci of photon circular geodesics. Stable circular geodesics, relevant for the Keplerian, thin accretion discs exist in the range of

$$x \in (x_{ms}(a), \infty)\,, \tag{15}$$

where $x_{ms}(a)$ denotes the radius of the marginally stable orbit, determined (in an implicit form) by the relation

$$1 - 6x^{-1} + 8ax^{-3/2} - 3a^2x^{-2} = 0\,, \tag{16}$$

which coincides with the condition

$$\alpha_r(x,a) = 0\,. \tag{17}$$

For toroidal, thick accretion discs the unstable circular geodesics can be relevant in the range

$$x_{\mathrm{mb}} \leq x_{\mathrm{in}} < x < x_{\mathrm{ms}} , \tag{18}$$

being stabilized by pressure gradients in the tori. Here,

$$x_{\mathrm{mb}} = 2 - a + 2\sqrt{1-a} \tag{19}$$

is the radius of the marginally bound circular geodesic that is the lower limit for the inner edge of thick discs (Kozłowski et al., 1978; Krolik and Hawley, 2002).

Clearly, the Keplerian orbital frequency is well defined up to $x = x_{\mathrm{ph}}(a)$. However, ω_{r} is well defined, if $\alpha_{\mathrm{r}} \geq 0$, i.e., at $x \geq x_{\mathrm{ms}}(a)$, and $\omega_{\mathrm{r}}(x) = 0$ at x_{ms}. We can also show that for $x \geq x_{\mathrm{ph}}$, there is $\alpha_\theta \geq 0$; i.e., the vertical frequency ω_θ is well defined at $x > x_{\mathrm{ph}}$.

3.1 Local extrema of epicyclic frequencies

Denoting by $\mathcal{R}_{\mathrm{K}}, \mathcal{R}_{\mathrm{r}}, \mathcal{R}_\theta$ the local extrema of Keplerian ν_{K} and epicyclic ν_{r}, ν_θ frequencies, we can give the extrema by the condition

$$\frac{\partial}{\partial r}\nu_i = 0 \quad \Leftrightarrow \quad \frac{\partial}{\partial x}\nu_i = 0 \quad \text{for} \quad \mathcal{R}_i , \qquad i \in \{\mathrm{K}, \mathrm{r}, \theta\} , \tag{20}$$

where x is dimensionless coordinate (6). From (1)–(3), we find that the corresponding derivatives[3] are

$$\Omega_{\mathrm{K}}' = -\frac{3}{2}\sqrt{\frac{GM_0}{r_G^3}}\,\frac{\sqrt{x}}{(x^{3/2}+a)^2} , \tag{21}$$

$$\omega_j' = \frac{3}{2}\left[\frac{2\beta_j}{\sqrt{\alpha_j}} - \frac{\sqrt{\alpha_j x}}{(x^{3/2}+a)}\right]\Omega_{\mathrm{K}} , \tag{22}$$

$$\alpha_j' = 6\beta_j/\alpha_j , \tag{23}$$

where $j \in \{r, \theta\}$, and

$$\beta_{\mathrm{r}}(x,a) = \frac{1}{x^2} - 2\frac{a}{x^{5/2}} + \frac{a^2}{x^3} , \tag{24}$$

$$\beta_\theta(x,a) = \frac{a}{x^{5/2}} - \frac{a^2}{x^3} . \tag{25}$$

Clearly, $\Omega_{\mathrm{K}}' < 0$ for $x > 0$; i.e., the Keplerian frequency is a monotonically decreasing function of the radial coordinate for any value of the rotational parameter a.

[3] After introducing $'$ as $\mathrm{d}/\mathrm{d}r$.

Relations (20) and (22) imply the condition determining extrema $\mathcal{R}_j(a)$ of the epicyclic frequencies:

$$\beta_j(x,a) = \frac{1}{2}\frac{\sqrt{x}}{x^{3/2}+a}\,\alpha_j(x,a)\,, \qquad j \in \{r,\theta\}\,. \tag{26}$$

Because we have checked that in the case of counterrotating orbits ($a < 0$), the extrema $\mathcal{R}_\theta$ are located under the photon circular orbit and the extrema $\mathcal{R}_\mathrm{r}$ are just extensions of the $\mathcal{R}_\mathrm{r}$ for corotating case ($a < 0$), we focus mainly on the case of corotating orbits in the next discussion. In Figs 2 (3) we show curves $\mathcal{R}_\mathrm{r}^k(a), k \in \{1,2,3\}$ ($\mathcal{R}_\theta^l(a), l \in \{1,2\}$) implicitly determined by the relations (26); indices k, l denote different branches of the solution of (26). The radial epicyclic frequency has one local maximum for Kerr black holes

$$-1 \le a \le 1\,, \tag{27}$$

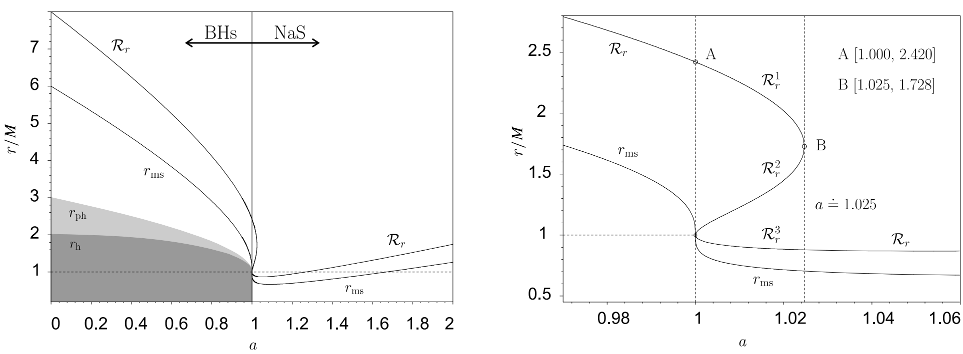

Figure 2. *Left panel:* The locations $\mathcal{R}_\mathrm{r}^i$ of the radial epicyclic frequency local extrema. *Right panel:* detailed view. Here, in the next Fig. 3 and henceforth we use the following convention for both kinds of extrema of the radial ($\mathcal{R}_\mathrm{r}^i$) and the vertical ($\mathcal{R}_\theta^i$) epicyclic frequencies: odd or missing superscript denotes a local maximum and even-numbered one means a local minimum. The question whether in the case of naked singularities the maximum is global one can be addressed by the left panel in Fig. 6.

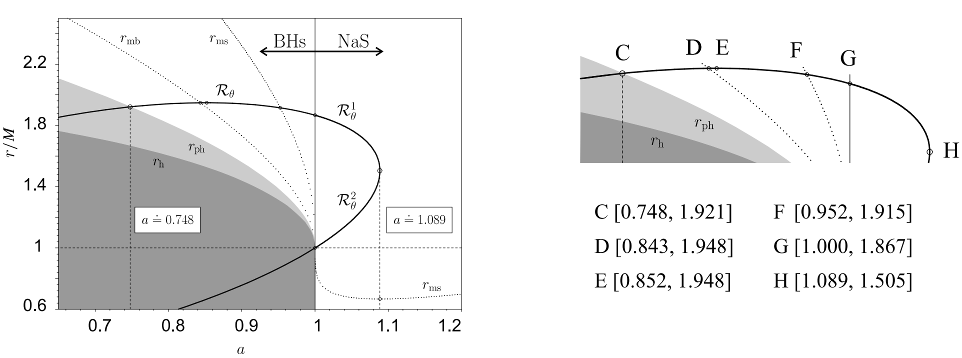

Figure 3. The locations $\mathcal{R}_\theta^i$ of the vertical epicyclic frequency local extrema. The right panel gives exact information about the positions of important points.

but it has two local maxima and one local minimum for Kerr naked singularities with

$$1 < a < a_{c(r)} \doteq 1.025\,, \tag{28}$$

and again one local maximum for

$$a \geq a_{c(r)} \quad \text{and} \quad a < -1\,. \tag{29}$$

The vertical epicyclic frequency has a local maximum at $x > x_{\mathrm{ph}}$ for Kerr black holes with

$$a > a_{\mathrm{ph}(\theta)} \doteq 0.748\,, \tag{30}$$

and at $x > x_{\mathrm{ms}}$ for

$$a > a_{\mathrm{ms}(\theta)} \doteq 0.952\,. \tag{31}$$

The local maximum of $\omega_\theta(x, a)$ is relevant in resonant effects for $a > a_{\mathrm{ms}(\theta)}$. Note that $\mathcal{R}_\theta$ has a maximum at

$$a_{\max(\mathcal{R}_\theta)} \doteq 0.852\,; \tag{32}$$

therefore, the situation with function $\omega_\theta(x, a)$ is more complicated than seems to be indicated in Fig. 1: for high values of the black hole rotational parameter a, curves $\omega_\theta(x, a)$ cross each other as is shown in the left panel of Fig. 4, while Fig. 1 does not show such detail because of hi-spacing between curves. In the Kerr naked singularity spacetimes, the function $\omega_\theta(x, a)$ has a local minimum and a local maximum for

$$1 < a < a_{c_\theta} \doteq 1.089\,, \tag{33}$$

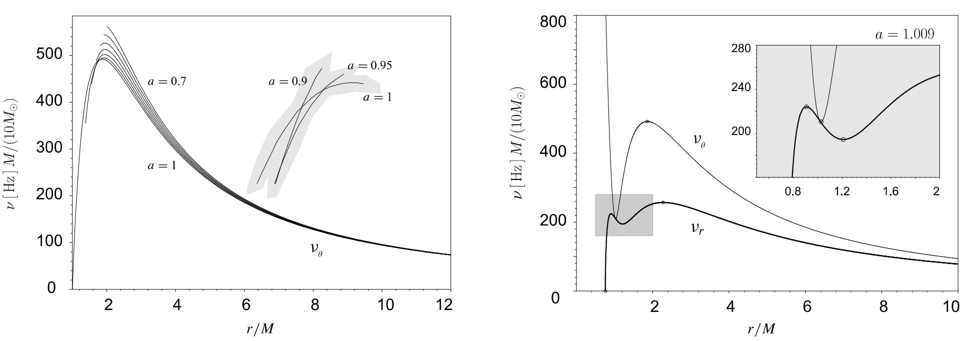

Figure 4. *Left panel:* "unlikely" effects resulting from the existence maxima of $\mathcal{R}_\theta$ (the point E on Fig. 3). Curves $\nu_\theta(r)$ after $a \doteq 0.852$ cross each other (curves *differ* in rotational parameter here by 0.05), see also Fig. 1 for comparison. The *right panel* displays an example of epicyclic frequency behaviour for Kerr naked singularity with $a = 1.009$; all allowed extrema are present. Note that the minimum ν_θ is very close but not identical to the *point of contact*, which is also present (see Subsection 3.4 for details).

and has no astrophysically relevant local extrema for

$$a \geq a_{c_\theta} \quad \text{and} \quad a < -1\,. \tag{34}$$

Using properties of $\mathcal{R}_{\rm r}(a)$ and $\mathcal{R}_\theta(a)$, we can conclude that two qualitatively different types of behaviour exist for the epicyclic frequencies in the Kerr black-hole spacetimes along with three qualitatively different types of their behaviour in the Kerr naked-singularity spacetimes. Examples of the behaviour of the epicyclic frequencies for Kerr black holes are given in Fig. 1 (see also Fig. A1).

An example of the behaviour of the epicyclic frequencies in Kerr naked-singularity spacetimes is shown in Fig. 4 (right panel) for the case when all the local extrema mentioned above are present, while for an example of the case when the number of the local extrema is lowest, see Fig. 8. The complete set of figures systematically representing the evolution of the character of the epicyclic frequencies with rotational parameter increasing is included in the Appendix which consists of Figs A1 (black holes) and A2 (naked singularities); the evolution of derivatives (22) and of the ratio $\nu_\theta/\nu_{\rm r}$ of the epicyclic frequencies is also included. This set of figures represents classification of the Kerr spacetimes according to the properties of the epicyclic frequencies that is fully given in Section 4. Note that in the black-hole case it is important to distinguish the cases when the local maximum of $\nu_\theta(x, a)$ is located above $x_{\rm ms}$, and under $x_{\rm ms}$.

Clearly, the behaviour of the epicyclic frequencies substantially differs for Kerr naked singularities in comparison with Kerr black holes.

3.2 Ratio of epicyclic frequencies

The ratio of epicyclic frequencies ν_θ and $\nu_{\rm r}$ needs to be defined well for some models of QPOs (e.g., Abramowicz et al., 2004b; Kato, 2004b). It is well known (see, e.g., Kato et al., 1998) that for the Kerr black holes ($-1 \leq a \leq 1$) the inequality

$$\omega_{\rm r}(x, a) < \omega_\theta(x, a) \tag{35}$$

holds, i.e., the equation

$$\omega_{\rm r}(x, a) = \omega_\theta(x, a) \tag{36}$$

does not have any real solution in the whole range of black hole rotational parameter $a \in (-1, 1)$ and

$$\frac{\nu_\theta}{\nu_{\rm r}} > 1 \tag{37}$$

for any Kerr black hole. Furthermore, this ratio is a monotonic function of radius for any fixed $a \in (-1, 1)$ (see Fig. 5 – left panel). However, the situation is different for Kerr naked singularities, see Section 3.4.

3.3 Implications for the orbital resonance models in the field of Kerr black holes

The orbital resonance models for QPOs proposed by Abramowicz and Kluźniak (2001); Abramowicz et al. (2004b) are particularly based on resonance between epicyclic frequencies which are excited at a well defined *resonance radius* $r_{p:q}$ given by the condition

$$\frac{\omega_\theta}{\omega_\mathrm{r}}(a, r_{p:q}) = \frac{p}{q}\,, \tag{38}$$

where $p:q$ is $3:2$ in the case of *parametric resonance* and arbitrary rational ratio of two small integral numbers $(1, 2, 3, \ldots)$ in the case of *forced resonances*. Notice that in the case of arbitrary forced resonance the combinational ("beat") frequencies could also be observed including the $3:2$ ratio (Abramowicz and Kluźniak, 2001; Török et al., 2005). Such resonance radii are monotonically decreasing functions of the rotational parameter a (see Fig. 5 – left panel). Resulting resonant frequencies are given generally as a linear combination of epicyclic frequencies at $r_{p:q}$. In Török et al. (2005) it is reported that the resonant frequencies (both observed frequencies, the *upper* and the *lower*) are not monotonic function of a for the case of $3:1$ and $5:1$ $(5:2)$ forced resonance models, while for other resonance model ratios (e.g., $2:1, 3:2$), it is a monotonic function of the rotational parameter a.

For the observational consequences, it is important to determine the limiting value of the frequency ratios $\omega_\theta/\omega_\mathrm{r} = p/q$, which separates the monotonic and non-monotonic dependence of the resonant frequencies on the rotational parameter.

Indeed, this monotonicity of some resonant frequencies results from the non-monotonic character of the epicyclic frequencies. It is known that the radial epicyclic frequency has a local maximum at $r_{\max(\mathrm{r})} \equiv \mathcal{R}_\mathrm{r}$ for $a \in (-1, 1)$ and its value $\nu_{\mathrm{r}(\max)}(a)$ increases with the rotational parameter (see Fig. 1 – right panel). Moreover, outside its maxima it is monotonically decreasing with the radius. From the left panel of Fig. 5, we conclude that $r_{p:q}(a)$ must be a *monotonically decreasing function* of a. If the horizontal line representing some ratio $p:q$ is fixed, then this figure implies a necessarily monotonically decreasing function $r_{p:q}(a)$. Because of this, the resulting resonant frequency, which is just multiple of the radial frequency, must be monotonically increasing for $r_{p:q}$ located outside (or at) the maximum of the radial epicyclic frequency.

For Schwarzschild black holes the ratio between the epicyclic frequencies at the radius of maximal radial frequency is exactly $\nu_\theta/\nu_\mathrm{r} = 2$ $(x = 8)$ and then changes slightly with the rotational parameter growing to reach the value $\nu_\theta/\nu_\mathrm{r} \sim 1.8$ for extremely rotating Kerr black hole $(a = 1)$. This gives the limit in the sense that for $p:q > 1.8$, the radius $r_{p:q}$ is certainly located above the maximum of ν_r.

On the other hand, an analogical consideration shows that ν_θ (or ν_r, if the resonance condition (38) is satisfied) is surely decreasing with the rotational parameter, if $r_{p:q}$ is located under the location of the maximum of ν_θ. The ratio of the epicyclic frequencies at the maximum of ν_θ is shown in the left bottom panel of Fig. 5. Its minimum is reached for extremely rotating Kerr black holes at $\nu_\theta/\nu_\mathrm{r}(r_{\max}) \sim 2.18$. It means that for black holes the resonance is surely non-monotonic if $p/q \geq 2.18$.

It is clear from the discussion above that the limit for non-monotonicity must be located between the values of $p/q \in (1.8, 2.18)$. We numerically checked the loci of eventual non-monotonicity and find that the limit is very close to the upper value; i.e., nonmonotonicity of

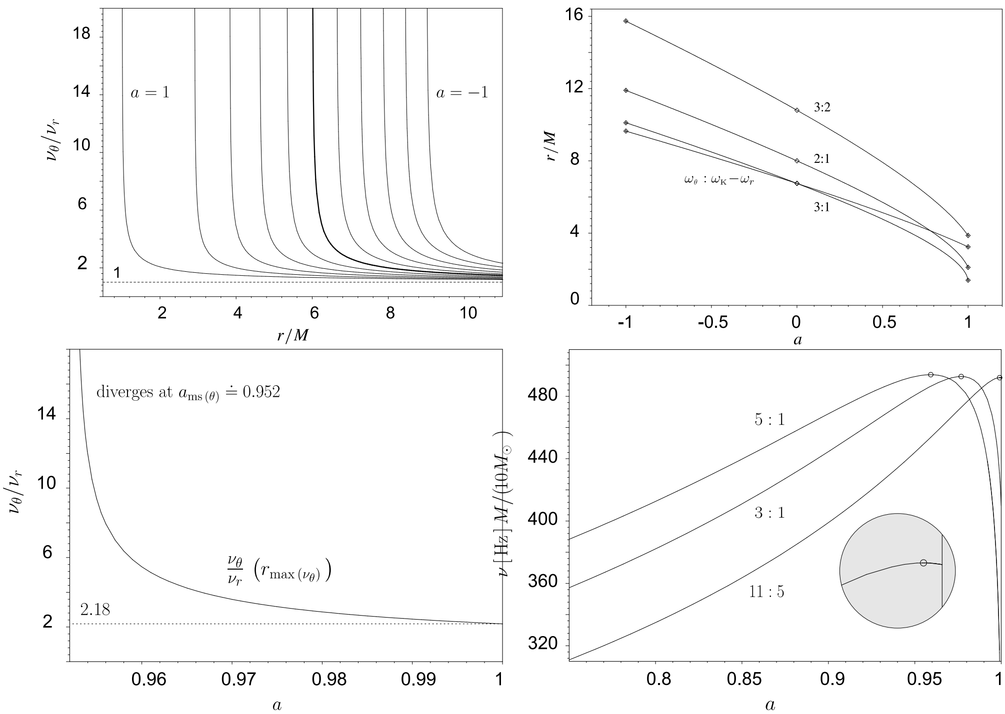

Figure 5. *Left top panel:* the behaviour of ratio $\nu_\theta/\nu_\mathrm{r}$ of the epicyclic frequencies, with curves spaced by 0.2 in rotational parameter. *Right top panel:* Location of three epicyclic resonances and resonance between vertical epicyclic frequency and periastron precession frequency recently introduced by Bursa (2005). *Left bottom panel:* the ratio between epicyclic frequencies at maxima of ν_θ. *Right bottom panel:* the examples of the behaviour of frequency ν_θ for three cases of forced resonances with $p/q = 5$, 3, and 2.2.

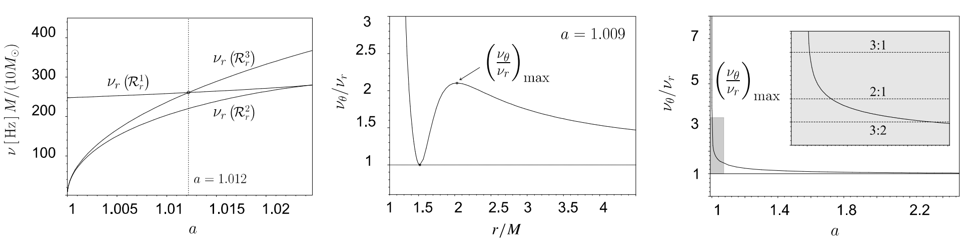

Figure 6. *Left panel:* the radial epicyclic frequency at particular extrema as a function of rotational parameter a between $a = 1$ and $a = 1.025$. We can see that for $a < 1.012$ the global maximum is situated at $\mathcal{R}_\mathrm{r}^1(a)$ while for $a > 1.012$ it is at $\mathcal{R}_\mathrm{r}^3(a)$. The *middle panel* exposes the behaviour of the function $\nu_\theta/\nu_\mathrm{r}(x)$ typical for Kerr naked singularities. With increasing parameter a the local maximum of this function is shifted to higher radii. The *right panel* illustrates that the value of maximum $\nu_\theta/\nu_\mathrm{r}$ is rapidly decreasing with the rotational parameter growing. The upper limit for unambiguity of a resonance in the case of $p:q = 3:1$, $2:1$ and $3:2$ is denoted.

the function $\nu_\theta/\nu_\mathrm{r}(r_{p:q}, a)$ in dependence on a is relevant for forced resonances with

$$p : q \geq 2.18\,. \tag{39}$$

Figure 5 (right bottom panel) illustrates this limit by examples of behaviour of $\nu_\theta\,(a, r_{p:q})$ for three different forced resonances, which embody the non-monotonic (in the sense described above).

3.3.1 The black hole spin and $\mathbf{1/}M$ *scaling in the resonance models*

It is well known and often argued that relativistic orbital frequencies scale inversely with the mass as $\nu \sim c/r_\mathrm{G} \sim 1/M$ (see, e.g., Abramowicz et al., 2004a, 2005). On the other hand, these frequencies depend on other parameters of the metric as well whereas in the case of Kerr spacetimes the only one remaining parameter is the black hole spin which strongly affects such simple $1/M$ scaling.

The influence of the spin on the $1/M$ scaling is illustrated in Fig. 7 – we can immediately see that for Kerr spacetimes the role of the spin on the observed frequencies in the resonant phenomena is *crucial*.

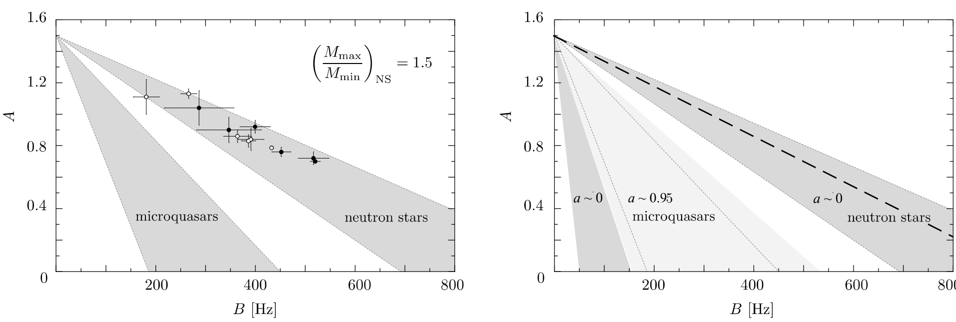

Figure 7. The influence of the Kerr spacetime spin on the parametric resonance frequencies. *Left (adopted from Abramowicz et al., 2005):* 12 neutron star sources in the slope-shift diagram (particular source is approximated by linear relation $\nu_\mathrm{upp} = A\nu_\mathrm{down} + B$). Mass of the neutron stars vary in factor of about 1.5 under the assumption that eigenfrequencies of the resonance scale inversely with the mass. Shaded microquasars area is denoted for frequencies observed in low mass black hole binaries. *Right:* If the observed frequencies for the 3 : 2 parametric epicyclic resonance are identified directly with the eigenfrequencies and assuming that the neutron star spacetimes are given by the Schwarzschild metric, we obtain the typical neutron star mass $\sim 1\mathrm{M}_\odot$ (dashed line). Of course this is rather approximate estimate as the spacetime description is not quite realistic. Nevertheless, we can rescale the A–B diagram directly for microquasars as their mass is known, being in the interval 6–18 $\mathrm{M}_\odot$ (dark shaded region $\sim$ 100 Hz). Taking into account the black hole spin, this region is substantially shifted into the light shaded area $a \sim 0.95$, which is plotted for the same range of the mass, but the frequency is rescaled with the spin at the orbit fixed by the condition $\nu_\theta/\nu_\mathrm{r} = 3 : 2$. We note that analogical rescaling can be done for the vertical precession resonance (Bursa, 2005) and spin $\sim$0.7, but the typical neutron star mass would be about two times higher.

3.4 Strong resonant frequency

It is shown in Section 3 that for Kerr naked singularities with $a > a_{c(\theta)} \doteq 1.089$ the behaviour of epicyclic frequencies is formally similar to Kerr black holes. However, for any naked singularity with $a \geq 1$, the epicyclic frequencies (2), (3) can satisfy the equality condition

$$\omega_r(a, x) = \omega_\theta(a, x) \tag{40}$$

giving a *strong resonant phenomenon*,[4] which occurs at the critical radius

$$x_{sr} = a^2 \quad (a \geq 1)\,. \tag{41}$$

This means that for any Kerr naked singularity the epicyclic frequency ratio $\nu_\theta/\nu_r(r)$ is a nonmonotonic function that reaches value 1 at the point given by (41) (see Fig. 6 – middle panel). The loci of this point are compared with locations of some other important points as shown in Fig. 8 – the right panel; while the left panel shows an example that illustrates radial extension of the strong resonant phenomenon.

Using the relation (41) in (2), (3) we find a strong resonant frequency that, in terms of the corresponding angular velocity, reads

$$\omega_{sr} \equiv \omega_r(a, a^2) = \omega_\theta(a, a^2) = \left(\frac{GM_0}{r_G^3}\right)^{1/2} \frac{\sqrt{a^2-1}}{a^2\left(a^2+1\right)}\,, \tag{42}$$

and the frequency can be expressed in the form

$$\nu_{sr} = 32.3 \left(\frac{M_\odot}{M}\right) \frac{\sqrt{a^2-1}}{a^2(1+a^2)}\ \text{kHz}\,. \tag{43}$$

[4] Intuitively clear attribution is well founded in the last Subsection 3.6.

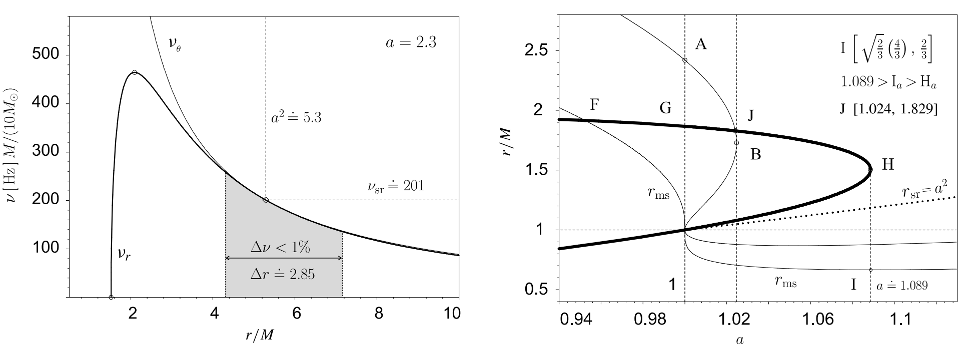

Figure 8. *Left panel:* behaviour of epicyclic frequencies for $a = 2.3$, the region where frequencies are identical with accuracy of 1%. The *right panel* illustrates the location of the strong resonant frequency (dotted curve a^2) in relation to extrema of epicyclic frequencies (thin curve $\mathcal{R}^k_r$, thick one $\mathcal{R}^l_\theta$). The critical radius is always located (in radial order) between the first maximum of ω_r and the minimum of ω_θ (if these exist). The notation of the important points [A. . . J] accords with Figs 2, 3.

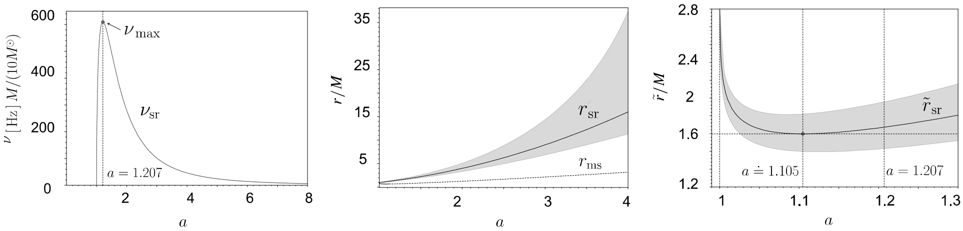

Figure 9. *Left panel:* the behaviour of strong resonant frequency shows remarkable maximum for the rotational parameter $a \sim 1.2$. From the *middle panel* we can see the evolution of area (around critical radius) where epicyclic frequencies are close, while the *right panel* shows the same in the proper distance to marginally stable orbit.

We note that this strong-resonance phenomenon represents a crucial difference between Kerr naked singularities and the case of Kerr black holes for which the ratio $\omega_\theta/\omega_{\rm r}(r)$ is determined as a monotonic function for fixed a (Fig. 5 – left panel).

The behaviour of the epicyclic frequency ratio $\omega_\theta/\omega_{\rm r}(r)$ typical of Kerr naked singularities is shown in Fig. 6 (middle panel). In right panel in Fig. 6 we plot the value of the local extrema of the ratio $\omega_\theta/\omega_{\rm r}$ as a function of the rotational parameter a. For high values of the rotational parameter, the radial and vertical epicyclic frequencies are very close each other in large radial range around $r_{\rm sr}$. This example is given in Fig. 8 (left panel). We plot the strong-resonance frequency as a function of the rotational parameter in Fig. 9 (left panel). It approaches zero value for an extremely rotating Kerr black hole and has a maximum for naked singularities with rotational parameter

$$a_{\rm src} \doteq 1.207\,, \tag{44}$$

with the corresponding value of the epicyclic frequency determined by the relation

$$\nu_{\rm src} \doteq 6.1\left(\frac{M}{\mathrm{M}_\odot}\right)^{-1}\ \mathrm{kHz}\,. \tag{45}$$

In the middle panel of Fig. 9, location of the critical radius $x_{\rm sr} = a^2$ is shown together with location of the marginally stable orbit and extension of the *instability* region of r (see Section 3.6), where the difference between values of the radial and vertical epicyclic frequencies is smaller then 1%. However, for the values of rotational parameter $a \sim 1$, it is more convenient to express the region of the disc with 1% difference of the epicyclic frequencies in terms of the proper radial distance $\tilde{r}$, which has direct physical meaning. There is

$$\tilde{r} = \int_{r_0}^{r_1} \sqrt{g_{rr}}\,\mathrm{d}r\,, \tag{46}$$

where g_{rr} denotes the radial metric coefficient of the Kerr metric in the standard Boyer–Lindquist coordinates; the distance is measured from the inner edge of the thin discs located at $r_{\rm ms}$. The result is represented by the right panel in Fig. 9; we found that the strong-resonance is closest to the inner edge of the Keplerian disc for a naked singularity with

$$a_{\tilde{\rm r}} \doteq 1.105\,. \tag{47}$$

For this value of the rotational parameter, the strong resonant frequency is

$$\nu_{\rm sr\,in} \doteq 4.3 \left(\frac{M}{{\rm M}_\odot}\right)^{-1}\ {\rm kHz}\,, \tag{48}$$

which is about 70% of the maximum at $a_{\rm sr\,max}$ given by (45). However, the critical radius is always located outside of the innermost part of the disc (see Fig. 8, right panel).

3.5 Implication for other resonant effects

For Kerr naked singularities with any rotational parameter a, the ratio $\omega_\theta/\omega_{\rm r} < (\omega_\theta/\omega_{\rm r})_{\rm max}$ being fixed can appear at three different radii. This kind of behaviour results from the existence of the strong resonance frequency ($\omega_\theta = \omega_{\rm r}$) for any Kerr naked singularity; i.e., it is not restricted to the cases when local extrema of ω_θ, $\omega_{\rm r}$ exist. This implies an important consequence for the resonant phenomena: in the case of slowly rotating Kerr naked singularities, an eventual resonance orbit $r_{p:q}$ (with p, q being small integral numbers) is defined ambiguously. In the range of frequencies $(\omega_\theta/\omega_{\rm r})_{\rm max}(a) \geq \omega_\theta/\omega_{\rm r} \geq 1$, the resonant effects with the same rational ratio $p:q$ can occur at three different radii $r_{p:q}$. Using the behaviour of the function $(\omega_\theta/\omega_{\rm r})_{\rm max}(a)$ (Fig. 6 – right panel) we can conclude that three radii $r_{p:q}$ could occur in the field of Kerr naked singularities with $a \leq 1.0012$ for $p:q \leq 3:1$, with $a \leq 1.012$ for $p:q \leq 2:1$, and with $a \leq 1.062$ for $p:q \leq 3:2$.

3.6 Possible instability of the accretion disc around Kerr naked singularities

The orbital resonance model (Kluźniak and Abramowicz, 2002) demonstrates that *fluid accretion flows* admit two linear quasi-incompressible modes of oscillations, vertical and radial, with corresponding eigenfrequencies equal to vertical and radial epicyclic frequencies for free particles. In a particular model of slender torus, the general properties of these modes can be shown: the vertical mode corresponds to a periodic displacement in which the whole torus moves as a rigid body up and down the equatorial plane and each fluid element has a vertical velocity that periodically changes in time, but does not depend on the position. The frequency of the vertical mode is equal to the vertical epicyclic frequency that a ficticious free particle orbiting at the circle of maximum pressure in the torus equilibrium position would have. Behaviour of the radial mode is similar to the vertical one, and in the linear regime these two modes are formally uncoupled. Kluźniak and Abramowicz (2002) argue that in the case of more realistic description that includes non-linear effects given by pressure and dissipation, these effects couple the two epicyclic modes that may result in a *resonance*.

One possible resonance, the *parametric resonance*, seems to be the most probable explanation of the 3 : 2 double peak kHz QPOs observed in some galactic microquasars

(Abramowicz et al., 2004b). The effect itself is described by the Mathieu equation (Landau and Lifshitz, 1976). After denoting the time derivative $\mathrm{d}/\mathrm{d}t$ by dot, we obtain the relation

$$\delta\ddot{\theta} + \omega_\theta^2\,[1 + h\cos(\omega_\mathrm{r} t)]\,\delta\theta = 0\,, \tag{49}$$

which can be formally derived by considering small deviations of fluid streamlines from planar circular motion governed by a set of equations (Rebusco, 2004; Horák, 2004)

$$\begin{aligned} \delta\ddot{r} + \omega_\mathrm{r}^2\,\delta r &= \omega_\mathrm{r}^2 f_\mathrm{r}(\delta r, \delta\theta, \delta\dot{r}, \delta\dot{\theta})\,, \\ \delta\ddot{\theta} + \omega_\theta^2\,\delta\theta &= \omega_\theta^2 f_\theta(\delta r, \delta\theta, \delta\dot{r}, \delta\dot{\theta})\,, \end{aligned} \tag{50}$$

for a particular choice of f_r and f_θ, corresponding to

$$\delta\ddot{r} + \omega_r^2\,\delta r = 0\,, \quad \delta\ddot{\theta} + \omega_\theta^2\,\delta\theta = -\omega_\theta^2\,\delta\theta\delta r\,. \tag{51}$$

From the theory of the Mathieu equation it is known that the parametric resonance is then excited when[5]

$$\frac{\omega_\mathrm{r}}{\omega_\theta} = \frac{\nu_\mathrm{r}}{\nu_\theta} = \frac{2}{n}, \quad n = 1, 2, 3, \ldots \tag{52}$$

The effect is strongest for the smallest possible value of n (Landau and Lifshitz, 1976). Because in the field of black holes $\nu_\mathrm{r} < \nu_\theta$ (see Section 3), the smallest possible value for resonance is $n = 3$, i.e., $2\nu_\theta = 3\nu_\mathrm{r}$, which explains the 3 : 2 ratio observed in microquasars very well (Abramowicz and Kluźniak, 2004; Török et al., 2005).

As shown above, the point where radial epicyclic frequency equals vertical epicyclic frequency exists for any Kerr naked singularity. Obviously, at such a point the Eq. (52) is satisfied ($\nu_\mathrm{r}/\nu_\theta = 1/1 = 2/n$; $n = 2$), and the parametric resonance (between the radial and vertical epicyclic frequency) eventually excited at this point is the strongest possible parametric resonance excited between the epicyclic frequencies in the field of Kerr naked singularities. Such 2 : 2 resonance must also be stronger than the 3 : 2 parametric resonance in the black hole case (Landau and Lifshitz, 1976).

From this, and from the fact that the radial region with epicyclic frequencies that are nearly equal is rather large, one can expect that at this region both radial and vertical oscillations could be strongly amplified, leading to an instability of the accretion disc.[6]

4 CONCLUSIONS

For counterrotating Keplerian orbits, properties of the epicyclic frequencies are the same for all Kerr black holes and naked singularities. Radial epicyclic frequency always has a local maximum, while the vertical epicyclic frequency has no local extrema at $x > x_\mathrm{ph}$.

[5] We note that the same condition holds for *internal resonance*, which describes systems with conserved energy (Horák, 2004).

[6] Such a claim is motivated by experience from known situations related to the parametric or forced resonance in complex non-linear systems observed in Earth physics (Landau and Lifshitz, 1976). Examples of mathematically possible resonances causing damaging bridges, wings, etc. with no specific physical coupling mechanism known are discussed in Nayfeh and Mook (1979).

On the other hand, for corotating Keplerian orbits, properties of the epicyclic frequencies strongly depend on the rotational parameter of the Kerr spacetimes. The most important difference between spacetimes with $a < 1$ and $a > 1$ is the change of inequality

$$\omega_\theta(x) > \omega_{\rm r}(x) \quad (a < 1) \quad \to \quad \omega_\theta(x) \geq \omega_{\rm r}(x) \quad (a > 1)\,. \tag{53}$$

We have also to distinguish different possibilities according to the existence and relative locations of the local extrema of the epicyclic frequencies.

In the case of Kerr black holes, the classification according to the properties of the epicyclic frequencies is given in the following way:

BH1 (Fig. A1a, $0 < a < 0.748$) $\omega_{\rm r}(x,a)$ has one local maximum, $\omega_\theta(x,a)$ has no local extrema above the photon circular orbit $x_{\rm ph}$.
BH2 (Fig. A1b, $0.748 < a < 0.952$) $\omega_{\rm r}(x,a)$ with one local maximum, $\omega_\theta(x,a)$ with one local maximum at $x < x_{\rm ms}$.
BH3 (Fig. A1c, $0.952 < a < 1$) $\omega_{\rm r}(x,a)$ with one local maximum, $\omega_\theta(x,a)$ with one local maximum at $x > x_{\rm ms}$.

In all the cases, the function $(\omega_\theta/\omega_{\rm r})(x,a)$ which is relevant for resonant effects, has a monotonic (descending) character (Fig. A1). Therefore, for a given rotational parameter a, there is only one radius allowed for any $p:q$ resonance. However, we have shown that the resulting resonant frequencies are nonmonotonic functions of a for $p:q > 2.18$, which could contradict eventual spin estimate in some resonance models. In addition, curve $\mathcal{R}_\theta(a)$ has a local maximum at $a \doteq 0.852$ so we can conclude that the functions $\omega_\theta(x,a_1)$, $\omega_\theta(x,a_2)$ with a_1, a_2 fixed and higher than $a \simeq 0.85$ cross each other, which can be also of observational interest.

In the case of Kerr naked singularities, the classification is given as follows:

NaS1 (Fig. A2a, $1 < a < 1.012$) $\omega_{\rm r}(x,a)$ has two local maxima and one local minimum between the maxima; $\omega_{\rm r(max)}(x_{\rm r(in)},a) < \omega_{\rm r(max)}(x_{\rm r(out)},a) < \omega_{\theta\rm (max)}$, where $x_{\rm r(in)} \equiv \mathcal{R}^3_{\rm r}$, $x_{\rm r(out)} \equiv \mathcal{R}^1_{\rm r}$. $\omega_\theta(x,a)$ has one local minimum and one local maximum. There is $x_{\theta\rm (max)} \equiv \mathcal{R}^1_\theta < x_{\rm r(out)}$.
NaS2 (Fig. A2b, $1.012 < a < 1.024$) $\omega_{\rm r}(x,a)$ has two local maxima and a local minimum in between, $\omega_{\rm r(max)}\,(x_{\rm r(out)},a) < \omega_{\rm r(max)}(x_{\rm r(in)},a) < \omega_{\theta\rm (max)}$. $\omega_\theta(x,a)$ has one local minimum and one local maximum, with $x_{\theta\rm (max)} < x_{\rm r(out)}$.
NaS3 (Fig. A2c, $1.024 < a < 1.025$) The same as in NaS2, but with $x_{\theta\rm (max)} > x_{\rm r(out)}$.
NaS4 $1.025 < a < 1.047$ $\omega_{\rm r}(x,a)$ with one local maximum. $\omega_\theta(x,a)$ with one local minimum and one local maximum; $\omega_{\theta\rm (max)} \geq \omega_{\rm r(max)}$.
NaS5 (Fig. A2d, $1.047 < a < 1.089$) The same as NaS4, but with $\omega_{\theta\rm (max)} < \omega_{\rm r(max)}$.
NaS6 (Fig. A2e, $a > 1.089$ $\omega_{\rm r}(x,\ a)$) with one local maximum, $\omega_\theta(x,a)$ with no local extrema. This class is formally similar to the class BH1, but with the crucial exception of the point $x_{\rm sr}$.

We conclude that the properties of the radial and vertical epicyclic frequencies of the Keplerian motion in the case of Kerr naked singularities differ substantially from the case of Kerr black holes, which can have strong observational consequences for both resonant phenomena and the stability of accretion discs around Kerr naked singularities.

Properties of the epicyclic frequencies and general resonant phenomena in the case of oscillations in the discs around Kerr naked singularities are substantially different from the black hole case not only for spacetimes with $a \in (1, 1.025)$, as the strong resonance effect can occur for any Kerr naked singularity. The strong resonant frequency of disc oscillations around Kerr naked singularities always arise at the descending part of the function $\omega_{\mathrm{r}}(x, a)$, in vicinity of a local minimum of ω_θ, if this exists; i.e., it is always located above the innermost part of the disc. We stress that this phenomenon represents the strongest parametric resonance between the epicyclic frequencies possible in the field of Kerr naked singularities, stronger than in the case of Kerr black holes. Moreover, the area where the effect occurs is large which implies strong influence on the stability of the Keplerian disc itself.

It follows from the existence of the strong resonant frequency that the function $(\omega_\theta/\omega_{\mathrm{r}})(x, a)$ has the same character for all Kerr naked singularities with one local maximum $(\omega_\theta/\omega_{\mathrm{r}})_{\max} > 1$, and one local minimum at $(\omega_\theta/\omega_{\mathrm{r}})_{\min}\,(x_{\mathrm{sr}} = a^2, a) = 1$ corresponding to the strong resonant frequency. Because of this, some resonant effects can occur at three different radii $r_{p:q}$ with the same rational ratio $p : q$; i.e., resonant effects with the same ratios could be induced by very different physical phenomena at different parts of the accretion disc.

We stress that the strong resonant frequency represents the phenomenon which we searched for in particular – i.e., the effect which could clearly indicate whether an observed X-ray is emitted from the accretion disc orbiting a naked singularity. If the resonant explanation of black-hole double peak QPOs is right, for naked singularities one can expect that *the 1 : 1 strong resonance* should significantly modulate in X-ray spectra one *unique peak* instead of two different peaks.

The observational data from microquasars, i.e., the low mass binary systems containing a black hole, indicate strongly the relevance of the exact 3 : 2 resonance phenomena (Török et al., 2005). The recent results concerning analysis of data from neutron star binaries bring a strong support for the relevance of the 3 : 2 phenomena in this systems as well. Although, the situation is more complex than for the case of accreting black holes, as twin peak kHz QPOs with frequency ratios different from 3 : 2 are observed in the neutron star binary systems. For a given source, the frequency ratios are concentrated around the value of 1.5 (Abramowicz et al., 2003a; Belloni et al., 2005; Bulik, 2005) and the linear fits of particular sources in the ν-ν plane seem to be anticorrelated (Abramowicz et al., 2005). An important clue to understanding the resonant phenomena in the neutron-star systems was found quite recently by one of authors (GT, work with Didier Barret in preparation). For the few atoll sources considered so far the energy contained in the upper frequency oscillations is higher then in the lower frequency oscillations when the frequency position is below the intersection of Bursa line[7] with 3 : 2 line, the energy is balanced when the source is passing this intersection and the higher energy is contained in the lower oscillations when frequencies are above this intersection (see Fig. 10).

This observational phenomenon could indicate a significant role of the parametric resonance and its possible combination with forced resonances, caused, e.g., by an accretion

[7] Linear fit of the source in ν-ν plane (see, e.g., Abramowicz et al., 2005).

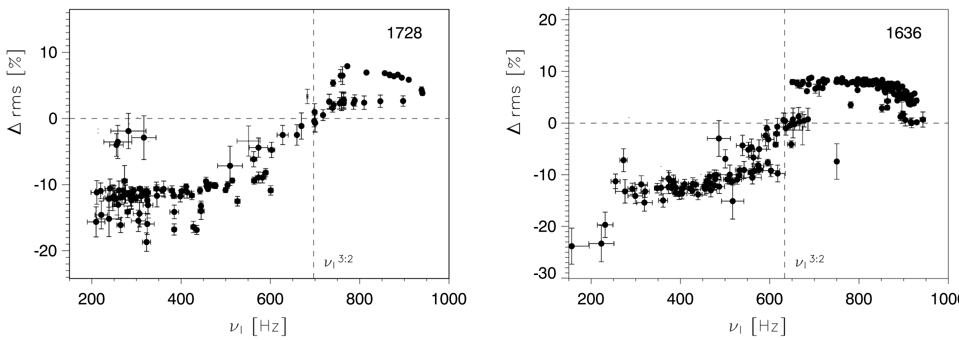

Figure 10. Illustration of the neutron star binary case from the present work of one of the authors (GT) and Didier Barret (following Barret et al., 2005). The plotted is difference between rms amplitudes of the lower and upper peak of the kHz QPO frequencies for two neutron star atoll sources 4U 1728−34 and 4U 1636−53 (colours denote different groups of data). Note that the Δrms changes its sign when the source is passing *critical point* where upper QPO frequency is 1.5 times higher than lower one.

column on the surface of an accreting neutron star. In principle, such forcing can "pump" more energy into the upper (lower) frequency; the modelling of the forced resonant phenomena in combination with parametric resonance is under the study now. On the other hand, in the black-hole systems, the gravitational forcing can be caused by the binary partner only, being in some situations weaker in the vicinity of the central body than in the case of a neutron star accretion column, except the case of close binary systems. Therefore, in black hole systems only the parametric resonance seems to be relevant. Of course, the perturbing force acting in the accretion disc can also be of magnetic origin.

Finally, we should note that in difference to 3 : 2 resonance in the black hole and neutron star case, the resonant 1 : 1 phenomena allowed for Kerr naked singularities do not have any circumstantial evidence in the observation till this time.

ACKNOWLEDGEMENTS

This work was supported by the Czech grant MSM 4781305903. We thank Prof. Marek Abramowicz and Jiří Horák for discussions. We also thank the hospitality at Nordita (Copenhagen).

REFERENCES

Abramowicz, M. A., Barret, D., Bursa, M., Horák, J., Kluźniak, W., Rebusco, P. and Török, G. (2005), A note on the slope-shift anticorrelation in the neutron star kHz QPOs data, pp. 1–9, this volume.

Abramowicz, M. A., Bulik, T., Bursa, M. and Kluźniak, W. (2003a), Evidence for a 2 : 3 resonance in Sco X-1 kHz QPOs, *Astronomy and Astrophysics*, **404**, pp. L21–L24.

Abramowicz, M. A., Karas, V., Kluźniak, W., Lee, W. and Rebusco, P. (2003b), Non-Linear Resonance in Nearly Geodesic Motion in Low-Mass X-Ray Binaries, *Publ. Astronom. Soc. Japan*, **55**(2), pp. 467–471, URL `http://pasj.asj.or.jp/v55/n2/550214/550214-frame.html`.

Abramowicz, M. A. and Kluźniak, W. (2001), A precise determination of black hole spin in GRO J1655−40, *Astronomy and Astrophysics*, **374**, p. L19, `astro-ph/010507`.

Abramowicz, M. A. and Kluźniak, W. (2004), Interpreting black hole QPOs, in P. Karet, F. K. Lamb and J. H. Swank, editors, *X-ray Timing 2003: Rossi and Beyond.*, volume 714, pp. 21–28, NY: American Institute of Physics, Melville, `astro-ph/0312396`.

Abramowicz, M. A., Kluźniak, W., McClintock, J. E. and Remillard, R. A. (2004a), The Importance of Discovering a 3 : 2 Twin-Peak Quasi-periodic Oscillation in an Ultraluminous X-Ray Source, or How to Solve the Puzzle of Intermediate-Mass Black Holes, *Astrophys. J. Lett.*, **609**, pp. L63–L65.

Abramowicz, M. A., Kluźniak, W., Stuchlík, Z. and Török, G. (2004b), Twin peak QPOs frequencies in microquasars and Sgr A*. The resonance and other orbital models, in Hledík and Stuchlík (2004), pp. 1–23.

Aschenbach, B. (2004), Measuring mass and angular momentum of black holes with high-frequency quasi-periodic oscillations, *Astronomy and Astrophysics*, **425**, pp. 1075–1082, `astro-ph/0406545`.

Bardeen, J. M. (1973), Timelike and null geodesics in the Kerr metric, in C. D. Witt and B. S. D. Witt, editors, *Black Holes*, p. 215, Gordon and Breach, New York–London–Paris.

Bardeen, J. M., Press, W. H. and Teukolsky, S. A. (1972), Rotating black holes: locally nonrotating frames, energy extraction, and scalar synchrotron radiation, *Astrophys. J.*, **178**, pp. 347–369.

Barret, D., Olive, J.-F. and Miller, M. C. (2005), An abrupt drop in the coherence of the lower kilohertz QPO in 4U 1636−536, *Monthly Notices Roy. Astronom. Soc.*, **361**, pp. 855–860.

Belloni, T., Méndez, M. and Homan, J. (2005), The distribution of kHz QPO frequencies in bright low mass X-ray binaries, *Astronomy and Astrophysics*, **437**, pp. 209–216.

Bulik, T. (2005), The statistics of Sco X-1 kHZ QPOs, *Astronom. Nachr.*, **326**(9), pp. 861–863.

Bursa, M. (2005), High-frequency QPOs in GRO J1655−40: Constraints on resonance models by spectral fits, pp. 39–45, this volume.

Bursa, M., Abramowicz, M. A., Karas, V. and Kluźniak, W. (2004), The Upper Kilohertz Quasi-periodic Oscillation: A Gravitationally Lensed Vertical Oscillation, *Astrophys. J. Lett.*, **617**, pp. L45–L48, `astro-ph/0406586`.

Carter, B. (1973), Black hole equilibrium states, in C. D. Witt and B. S. D. Witt, editors, *Black Holes*, p. 57, Gordon and Breach, New York–London–Paris.

Cohen, J. M. and Gautreau, R. (1979), Naked singularities, event horizons, and charged particles, *Phys. Rev. D*, **19**, pp. 2273–2279.

de Felice, F. and Yu, Y. (1986), in R. Ruffini, editor, *Proc. IV Marcell Grossman Meeting*.

de Felice, F. and Yu, Y. (2001), Turning a black hole into a naked singularity, *Classical Quantum Gravity*, **18**(7), pp. 1235–1244.

de Villiers, J. P., Hawley, J. F. and Krolik, J. H. (2003), Magnetically Driven Accretion Flows in the Kerr Metric I: Models and Overall Structure, astro-ph/0307260.

Hledík, S. and Stuchlík, Z., editors (2004), *Proceedings of RAGtime 4/5: Workshops on black holes and neutron stars, Opava, 14–16/13–15 October 2002/2003*, Silesian University in Opava, Opava, ISBN 80-7248-242-4.

Horák, J. (2004), General aspects of nonlinear resonance 3 : 2 in QPO context, in Hledík and Stuchlík (2004), pp. 91–110, `astro-ph/0408092`.

Igumenshchev, I. V., Narayan, R. and Abramowicz, M. A. (2003), Three-dimensional Magneto-hydrodynamic Simulations of Radiatively Inefficient Accretion Flows, *Astrophys. J.*, **592**(2), pp. 1042–1059.

Israel, W. (1986), , in H. Sato and T. Nakamura, editors, *Proc. 14th Yamada Conf.*

Kato, S. (2004a), Mass and Spin of GRS 1915+105 Based on a Resonance Model of QPOs, *Publ. Astronom. Soc. Japan*, **56**(5), pp. L25–L28.

Kato, S. (2004b), Resonant Excitation of Disk Oscillations by Warps: A Model of kHz QPOs, *Publ. Astronom. Soc. Japan*, **56**(5), pp. 905–922.

Kato, S. and Fukue, J. (1980), Trapped Radial Oscillations of Gaseous Disks around a Black Hole, *Publ. Astronom. Soc. Japan*, **32**(3), pp. 377–388.

Kato, S., Fukue, J. and Mineshige, S. (1998), Black-hole accretion disks, Kyoto University Press, Kyoto, Japan.

Kato, Y. (2004c), 2:3 Twin Quasi-Periodic Oscillations in Magnetohydrodynamic Accretion Flows, *Publ. Astronom. Soc. Japan*, **56**(5), pp. 931–937.

Kluźniak, W. and Abramowicz, M. A. (2000), The physics of kHz QPOs – strong gravity's coupled anharmonic oscillators, submitted in Phys. Rev. Lett.

Kluźniak, W. and Abramowicz, M. A. (2001), Strong-Field Gravity and Orbital Resonance in Black Holes and Neutron Stars – kHz Quasi-Periodic Oscillations (QPO), *Acta Physica Polonica B*, **32**, pp. 3605–3612, URL `http://th-www.if.uj.edu.pl/acta/vol32/t11.htm`.

Kluźniak, W. and Abramowicz, M. A. (2002), , astro-ph/020331.

Kozłowski, M., Jaroszyński, M. and Abramowicz, M. A. (1978), The analytic theory of fluid disks orbiting the Kerr black hole, *Astronomy and Astrophysics*, **63**(1–2), pp. 209–220, URL `http://adsabs.harvard.edu/article_service.html`.

Krolik, J. H. and Hawley, J. F. (2002), Where Is the Inner Edge of an Accretion Disk around a Black Hole?, *Astrophys. J.*, **573**(2), pp. 754–763, URL `http://www.journals.uchicago.edu/ApJ/journal/issues/ApJ/v573n%2/55306/55306.html`.

Landau, L. D. and Lifshitz, E. M. (1976), *Mechanics*, Pergamon Press, Oxford, 3rd edition.

Matsumoto, R., Kato, S. and Honma, F. (1989), , in *NATO ASIC Proc. 290: Theory of Accretion Disks*, volume 167.

McClintock, J. E. and Remillard, R. A. (2004), Black Hole Binaries, in W. H. G. Lewin and M. van der Klis, editors, *Compact Stellar X-Ray Sources*, Cambridge University Press, Cambridge, `astro-ph/0306213`.

Miller, J. C. and de Felice, F. (1985), Gravitational collapse and rotation, *Astrophys. J.*, **298**, p. 474.

Nakamura, T., Oohara, K. and Kojima, Y. (1987), *Progr. Theoret. Phys. Suppl.*, **90**, p. 1.

Nayfeh, A. H. and Mook, D. T. (1979), *Nonlinear Oscillations*, Wiley-interscience, New York.

Nowak, M. A. and Lehr, D. E. (1998), Stable oscillations of black hole accretion discs, in M. A. Abramowicz, G. Björnsson and J. E. Pringle, editors, *Theory of Black Hole Accretion Disks*, pp. 233–253, Cambridge University Press, Cambridge, `astro-ph/9812004`.

Nowak, M. A. and Wagoner, R. V. (1991), Diskoseismology: Probing accretion disks. i, *Astrophys. J.*, **378**, p. 656.

Nowak, M. A. and Wagoner, R. V. (1992), Diskoseismology: Probing accretion disks. ii, *Astrophys. J.*, **393**, p. 697.

Okazaki, A. T., Kato, S. and Fukue, J. (1987), Global Trapped Oscillations of Relativistic Accretion Disks, *Publ. Astronom. Soc. Japan*, **39**(3), pp. 457–473.

Penrose, R. (1969), Gravitational collapse: The role of general relativity, *Nuovo Cimento B*, **1**(special number), pp. 252–276.

Rebusco, P. (2004), , Laurea thesis, Univerzity of Trieste, Trieste.

Rezzolla, L. (2004), Nonlinear dynamics of thick discs in Schwarzschild–de Sitter spacetimes, in Hledík and Stuchlík (2004), pp. 151–165.

Šrámková, E. (2005), Epicyclic oscillation modes of a Newtonian, non-slender torus, *Astronom. Nachr.*, **326**(9), pp. 835–837.

Stalker, J. G. and Tahvildar-Zadeh, A. S. (2004), *Classical Quantum Gravity*, **21**, pp. 2831–2848.

Stuchlík, Z. (1980), Equatorial circular orbits and the motion of the shell of dust in the field of a rotating naked singularity, *Bull. Astronom. Inst. Czechoslovakia*, **31**(3), pp. 129–144.

Thorne, K. S. (1974), Disk-Accretion onto a Black Hole. II. Evolution of the Hole, *Astrophys. J.*, **191**, p. 507.

Török, G., Abramowicz, M. A., Kluźniak, W. and Stuchlík, Z. (2005), The orbital resonance model for twin peak kHz quasi periodic oscillations in microquasars, *Astronomy and Astrophysics*, **436**(1), pp. 1–8, `astro-ph/0401464`.

van der Klis, M. (2000), Millisecond Oscillations in X-ray Binaries, *Annual Review of Astronomy and Astrophysics*, **38**, pp. 717–760.

Wald, R. M. (1974), , *Ann. Phys.*, **83**, p. 548.

APPENDIX A: CLASSIFICATION OF THE KERR SPACETIMES (DUE TO EPICYCLIC FREQUENCIES)

a) $a = 0.5 \in (0, 0.748) \equiv \text{BH1}$

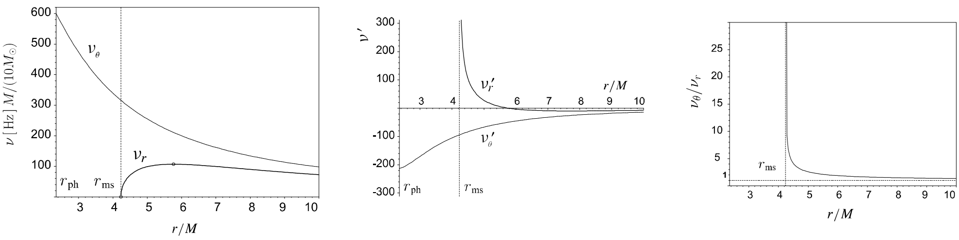

b) $a = 0.85 \in (0.748, 0.952) \equiv \text{BH2}$

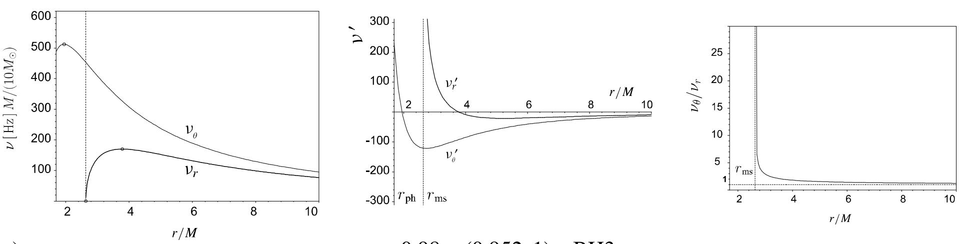

c) $a = 0.98 \in (0.952, 1) \equiv \text{BH3}$

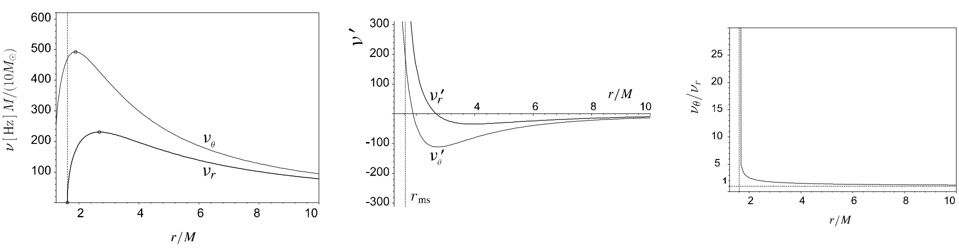

d) degenerated case of $a = 1$

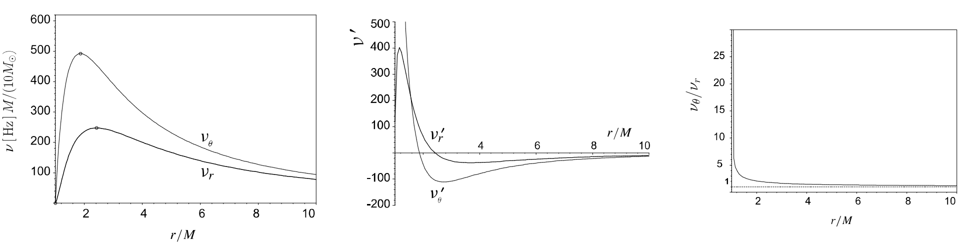

Figure A1. Classification of the Kerr black-hole spacetimes. The behaviour of the epicyclic frequencies (left panel), their first derivatives (middle panel), and their ratio $\nu_\theta/\nu_\mathrm{r}$ (right panel) are shown for four representative values of rotational parameter a, including the extreme Kerr black hole, the left margin of plots is always situated at the photon circular orbit r_ph, while the marginally stable orbit r_ms is denoted by a dashed vertical line.

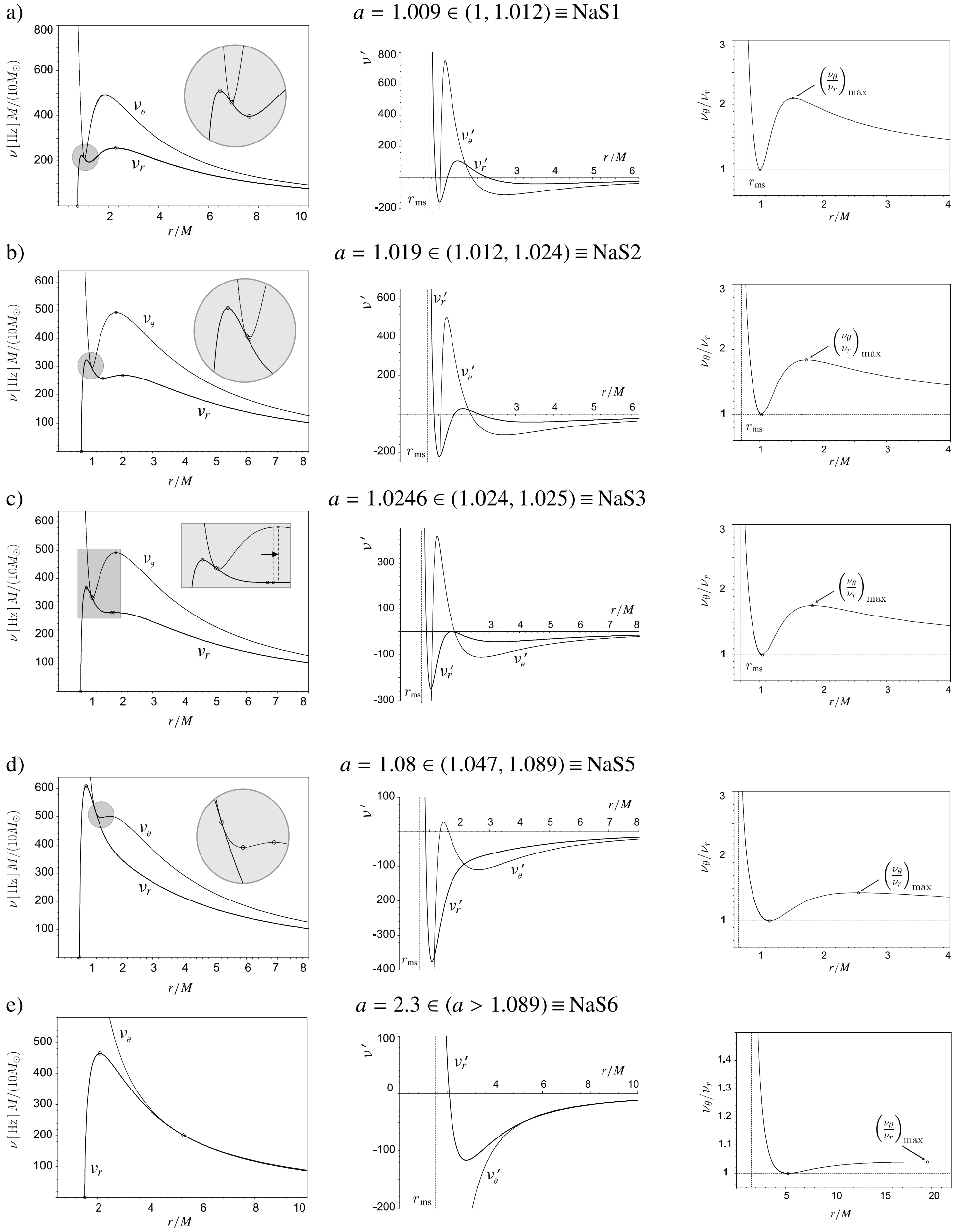

Figure A2. Classification of the Kerr naked-singularity spacetimes. The behaviour of the epicyclic frequencies (left panel), their first derivatives (middle panel), and their ratio $\nu_\theta/\nu_\mathrm{r}$ (right panel) are shown for five representative values of rotational parameter a. An example of the class NaS4 which differs from the class NaS3 by the absence of the "radial pair" maximum–minimum is not shown.

Proceedings of *RAGtime 6/7: Workshops on black holes and neutron stars, Opava, 16–18/18–20 September, 2004/2005*
S. Hledík and Z. Stuchlík, editors, Silesian University in Opava, Czech Republic, 2005, pp. 339–356

The latitudinal and radial geodetical motion in Kerr–de Sitter spacetime

Kamila Truparová Plšková and Zdeněk Stuchlík

Institute of Physics, Faculty of Philosophy & Science, Silesian University in Opava,
Bezručovo nám. 13, CZ-746 01 Opava, Czech Republic

ABSTRACT
The discussion of the latitudinal and radial photon motion in the Kerr–de Sitter (KdS) spacetime is examined by using the "Chinese boxes" technique. Only the case with a positive cosmological constant is considered. The latitudinal motion is discussed by using a new motion constant Q vanishing for motion in the equatorial plane. This will be more comfortable for the next discussion of the photon off-equatorial motion in KdS spacetime. For the radial motion an "effective potential" governing the photon radial motion is used, circular photon orbits are determined and their stability is discussed.

1 INTRODUCTION

Wide range of cosmological observations (Ostriker and Steinhardt, 1995; Spergel et al., 2003) indicate that recent Universe is dominated by a dark energy that can effectively be described by a repulsive ($\Lambda > 0$) cosmological constant. The properties of the black hole (or related spherically symmetric, static spacetime naked singularity) spacetimes with ($\Lambda > 0$) were studied extensively for Schwarzschild–de Sitter spacetime (SdS: Stuchlík, 1983; Stuchlík and Hledík, 1999), Reissner–Nordström–de Sitter (RNdS: Stuchlík and Hledík, 2001, 2002), axisymmetric rotating Kerr–de Sitter (KdS: Stuchlík and Calvani, 1991; Stuchlík and Slaný, 2004; Stuchlík, 2005) and Kerr–Newman–de Sitter (KNdS: Stuchlík and Hledík, 2000). Basic properties of the geometry and its relation to the geodesic motion are thus mapped.

However, recent observations of quasiperiodic oscillations (QPOs) in the vicinity of the black hole in the centre of our Galaxy (Aschenbach, 2004) and the proposal of observing QPOs coming from the central parts of active galactic nuclei with giant black holes (Abramowicz and Kluźniak, 2004; Török et al., 2005; Török, 2005a,b), where the effects of ($\Lambda > 0$) could be relevant and observable, calls for a detailed study of the optical effects in KdS spacetimes that could be appropriate to describe the spacetime structure in such situations. The special case of the equatorial photon motion was treated in Stuchlík and Hledík (2000). Here we start our investigation of the off-equatorial general photon motion in the KdS spacetimes. First, we present discussion of the latitudinal motion in terms of the motion constant Q vanishing for the equatorial motion. Then the radial motion in the

80-7248-334-X

equatorial plane is discussed and a classification of the KdS spacetimes is given relative to the properties of the equatorial photon motion. In a forthcoming paper the off-equatorial radial motion will be treated for the case of KdS black holes using the results obtained in the present work.

2 KERR–DE SITTER SPACETIMES

The Kerr–de Sitter (KdS) solution of the Einstein equations represents black holes and naked singularities in spacetime with a non-zero cosmological constant that is repulsive ($\Lambda > 0$). This spacetime is asymptotically de Sitter and contains one cosmological horizon, behind which the spacetime must be dynamic. By using standard Boyer–Lindquist coordinates (t, r, θ, ϕ) and geometric units ($c = G = 1$) the KdS geometry is given by the line element

$$\mathrm{d}s^2 = -\frac{\Delta_r}{I^2\rho^2}\left(\mathrm{d}t - a\sin^2\theta\,\mathrm{d}\phi\right)^2 + \frac{\Delta_\theta\sin^2\theta}{I^2\rho^2}\left[a\,\mathrm{d}t - (r^2+a^2)\,\mathrm{d}\phi\right]^2 \tag{1}$$

$$+\frac{\rho^2}{\Delta_r}\,\mathrm{d}r^2 + \frac{\rho^2}{\Delta_\theta}\,\mathrm{d}\theta^2\,, \tag{2}$$

where

$$\Delta_r = \left(1 - \tfrac{1}{3}\Lambda r^2\right)\left(r^2+a^2\right) - 2Mr\,, \tag{3}$$

$$\Delta_\theta = 1 + \tfrac{1}{3}\Lambda a^2\cos^2\theta\,, \tag{4}$$

$$I = 1 + \tfrac{1}{3}\Lambda a^2\,, \tag{5}$$

$$\rho^2 = r^2 + a^2\cos^2\theta\,. \tag{6}$$

M is the mass of the central black hole, a is its specific angular momentum ($a = J/M$) and $\Lambda > 0$ is the repulsive cosmological constant. In spacetimes with the cosmological constant, it is convenient to introduce a new dimensionless cosmological parameter

$$y = \tfrac{1}{3}\Lambda M^2 \tag{7}$$

and redefine the following quantities: $s/M \rightarrow s, t/M \rightarrow t, r/M \rightarrow r$ and $a/M \rightarrow a$; so we express these quantities in units of M.

The loci of event horizons are given by the condition $\Delta_r = 0$, from which we obtain (Stuchlík and Slaný, 2004)

$$y_{\mathrm{h}}(r; a) \equiv \frac{r^2 - 2r + a^2}{r^2(r^2+a^2)}\,. \tag{8}$$

The function y_{h} diverges at $r = 0$ and for $r \rightarrow \infty$ it approaches to zero. For $a^2 > 0$ and $r \rightarrow 0$ holds $y_{\mathrm{h}} \rightarrow \infty$, for $a^2 = 0$ and $r \rightarrow 0$ the function $y_{\mathrm{h}} \rightarrow -\infty$.

The zero points of $y_{\mathrm{h}}(r; a)$ are determined by

$$a^2 = a^2_{\mathrm{z(h)}}(r) \equiv 2r - r^2\,. \tag{9}$$

The zeros of $a^2_{\mathrm{z(h)}}(r)$ are located at $r = 0$ and $r = 2$. The extreme (maximum) of $a^2_{\mathrm{z(h)}}(r)$ is located at $r = 1$ with $a^2_{\mathrm{z(h)}}(r = 1) = 1$. This corresponds to the extreme Kerr black hole.

The local extrema of $y_{\mathrm{h}}(r; a)$ are determined by the condition $(\partial y_{\mathrm{h}}/\partial r = 0)$, which gives us

$$a^2 = a^2_{\mathrm{ex(h)}\pm}(r) \equiv \frac{1}{2}\left\{-2r^2 + r \pm \sqrt{r^2(8r+1)}\right\} . \tag{10}$$

The function $a^2_{\mathrm{ex(h)}+}$ has one extreme at $r = 1.61603$ with $a^2_{\mathrm{ex(h)}+}(r = 1.61603) = 1.21202$. The zero points are located at $r = 0$ and $r = 3$.

The Carter equations in separated and integrated form can be used as the equations of latitudinal and radial motion of test particles and photons (Carter, 1973; Stuchlík, 2002).

3 LATITUDINAL MOTION OF TEST PARTICLES AND PHOTONS

The Carter equation of the latitudinal motion is given by the well known formula

$$\rho^2 \frac{\mathrm{d}\theta}{\mathrm{d}\lambda} = \pm\sqrt{W(\theta; K, y, a, m, E, \Phi)} , \tag{11}$$

where

$$W(\theta) = (K - a^2m^2\cos^2\theta)(1 + ya^2\cos^2\theta) - \frac{(IaE\sin^2\theta - I\Phi)^2}{\sin^2\theta} . \tag{12}$$

E and Φ are the constants of the motion connected with symmetries of the geometry, λ is the affine parameter along the geodesics. The constant of the motion E and Φ cannot be interpreted as energy and the axial component of the angular momentum in infinity, since the geometry is not asymptotically flat, but is asymptotically de Sitter. The discussion of the latitudinal motion in terms of the constant of motion K is given in great detail in Stuchlík (1983). However, for our purposes of discussing general motion of photons, a new motion constant can conveniently be introduced by the relation

$$Q = K - (1 + ya^2)^2(aE - \Phi)^2 . \tag{13}$$

Then

$$\begin{aligned} W(\theta) = {} & Q(1 + ya^2\cos^2\theta) \\ & + \cos^2\theta\left\{I^2\left[a^2E^2 - \frac{\Phi^2}{\sin^2\theta} + ya^2(aE - \Phi)^2\right] - a^2m^2(1 + ya^2\cos^2\theta)\right\} . \end{aligned} \tag{14}$$

Notice that $Q = 0$ for the motion in the equatorial plane, where $\theta = \pi/2$. In order to find the character of the latitudinal motion, the loci of turning points (where $\mathrm{d}\theta/\mathrm{d}\lambda = 0$) must be found. From Eq. (11) we obtain condition

$$W(\theta) = 0 , \tag{15}$$

which implies the turning points to be where

$$Q = Q_{\mathrm{t}} \equiv \cos^2\theta \left\{ a^2m^2 - \frac{(1+ya^2)^2}{1+ya^2\cos^2\theta}\left[a^2E^2 - \frac{\Phi^2}{\sin^2\theta} + ya^2(aE-\Phi)^2 \right] \right\}. \qquad (16)$$

$Q_{\mathrm{t}}(\theta;\, E, \Phi, a, m, \Lambda)$ represents a five-parameter family of curves in the Q-θ plane. The latitudinal motion is allowed for $Q > Q_{\mathrm{t}}$, where $W(\theta) \geq 0$.

It is advantageous to introduce new parameters (constants of motion):

$$q_{\mathrm{t}} = \frac{Q_{\mathrm{t}}}{(aE)^2}\,, \qquad (17)$$

$$b = \frac{\Phi}{aE}\,, \qquad (18)$$

$$\gamma = \frac{E}{m}\,, \qquad (19)$$

and for simplicity we denote $\Delta_\theta = 1 + ya^2\cos^2\theta$. Then the five-parameter family reduces to four-parameter family,

$$q_{\mathrm{t}}(\theta;\, y, a, \gamma, b) = \cos^2\theta \left\{ \frac{1}{\gamma^2} - \frac{I^2}{\Delta_\theta}\left[1 - \frac{b^2}{\sin^2\theta} + ya^2(1-b)^2 \right] \right\}. \qquad (20)$$

Behaviour of this family of curves can be studied by "Chinese boxes" technique. We find the regions of reality of the function q_{t}, its local extrema and its divergences. First we shall study the case of non-zero rest mass particles ($m \neq 0$) and after that we shall study the geodesics motion of photons ($m = 0$). Note that it is clear from Eq. (20) that the behaviour of the curves q_{t} and all their characteristics must be symmetric with respect to the equatorial plane ($\theta = \pi/2$).

3.1 Test particles

The zero points of q_{t} are located at $\theta = \pi/2$ and θ satisfying the condition

$$b = b_{\mathrm{z}\pm}(\theta;\, y, a, \gamma) \equiv \frac{-ya^2\sin^2\theta \pm \sin^2\theta\sqrt{y^2a^4 - \left(\frac{\Delta_\theta}{I^2\gamma^2} - I\right)\frac{1-ya^2\sin^2\theta}{\sin^2\theta}}}{1-ya^2\sin^2\theta}\,. \qquad (21)$$

The reality condition of the function $b_{\mathrm{z}\pm}$ is given by the relation

$$y^2a^4 - \left(\frac{\Delta_\theta}{I^2\gamma^2} - I\right)\frac{1-ya^2\sin^2\theta}{\sin^2\theta} \geq 0\,, \qquad (22)$$

from which we obtain

$$\gamma^2 \geq \gamma^2_{\mathrm{zrc}}(\theta;\, y, a) \equiv \frac{1-ya^2\sin^2\theta}{(1+ya^2)^2}\,. \qquad (23)$$

The reality condition of γ^2_{zrc} then implies

$$a^2 < a^2_{\mathrm{zrc}}(\theta; y) \equiv \frac{1}{y \sin^2\theta}\,. \tag{24}$$

This function has one extreme (minimum) located at $\theta = \pi/2$, where $a^2_{\mathrm{zrc}}(\pi/2, y) = 1/y$ and diverges at $\theta = 0, \pi$.

The extrema of γ^2_{zrc} are located at $\theta = 0, \pi$ (two maxima given by $\gamma^2_{\mathrm{zrc}}(\theta = 0, \pi; y, a) = 1/(1 + ya^2)^2$) and $\theta = \pi/2$ (minimum given by $\gamma^2_{\mathrm{zrc}}(\pi/2; y, a) = (1 - ya^2)/(1 + ya^2)^2$). The zero points of γ^2_{zrc} are located at

$$\theta_{\mathrm{zzrc}} = \arcsin\sqrt{\frac{1}{ya^2}}\,. \tag{25}$$

The marginal value of θ, where $b_{\mathrm{z}+} = b_{\mathrm{z}-}$, is located at

$$\theta_{\mathrm{mz}} = \arcsin\sqrt{\frac{1 - \gamma^2(1 + ya^2)^2}{ya^2}}\,. \tag{26}$$

The zero points of both functions $b_{\mathrm{z}+}$ and $b_{\mathrm{z}-}$ are determined by the condition

$$\gamma^2 = \gamma^2_{\mathrm{zz}\pm}(\theta; y, a) \equiv \frac{1 + ya^2\cos^2\theta}{(1 + ya^2)^3}\,. \tag{27}$$

The extrema of $\gamma^2_{\mathrm{zz}\pm}$ are located at $\theta = 0, \pi$ – maxima with

$$\gamma^2_{\mathrm{zz}\pm}(\theta = 0, \pi; y, a) = \frac{1}{(1 + ya^2)^2} \tag{28}$$

and at $\theta = \pi/2$ – minimum with

$$\gamma^2_{\mathrm{zz}\pm}(\theta = \pi/2; y, a) = \frac{1}{(1 + ya^2)^3}\,. \tag{29}$$

The extrema of $q_{\mathrm{t}}(\theta; y, a, \gamma)$ are given by the relation

$$b = b_{\mathrm{ex}\pm}(\theta; y, a, \gamma) \equiv \frac{\sin^2\theta\left[-ya^2\sin^2\theta \pm \sqrt{1 - \frac{1+ya^2\cos 2\theta}{\gamma^2 I^2}}\right]}{1 + ya^2\cos 2\theta}\,. \tag{30}$$

The reality condition is given by

$$\gamma^2 \geq \gamma^2_{\mathrm{Rex}}(\theta; y, a) \equiv \frac{1 + ya^2\cos 2\theta}{(1 + ya^2)^2}\,. \tag{31}$$

The extrema of γ^2_{Rex} are at $\theta = 0, \pi$ – maximum with

$$\gamma^2_{\mathrm{Rex}}(\theta = 0, \pi; y, a) = \frac{1}{1 + ya^2} \tag{32}$$

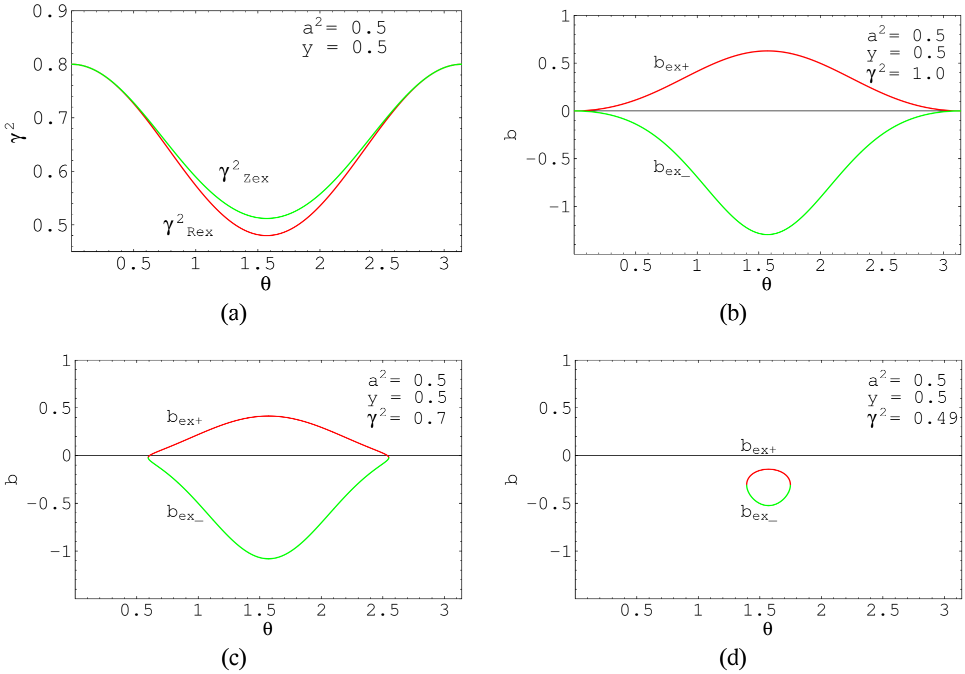

Figure 1. Behaviour of curves $\gamma^2_{\rm Zex}$, $\gamma^2_{\rm Rex}$ (a) and $b_{\rm ex\pm}$ (b)–(d) for given typical values of γ^2.

and at $\theta = \pi/2$ – minimum with

$$\gamma^2_{\rm Rex}(\theta = \pi/2; y, a) = \frac{1 - ya^2}{(1 + ya^2)^2}\,. \tag{33}$$

Behaviour of curves $\gamma^2_{\rm Rex}$, $\gamma^2_{\rm Zex}$ is illustrated in Fig. 1a. The marginal values, where $b_{\rm ex+} = b_{\rm ex-}$, are at $\theta_{\rm mex}$ determined by

$$\theta_{\rm mex} = \frac{1}{2}\arccos\left[\frac{\gamma^2(1 + ya^2)^2 - 1}{ya^2}\right]. \tag{34}$$

The zero points of $b_{\rm ex\pm}$ are at $\theta = 0$, π and at θ given by the condition

$$\gamma^2 = \gamma^2_{\rm Zex}(\theta; y, a) \equiv \frac{\Delta^2_\theta}{I^3} = \frac{(1 + ya^2\cos^2\theta)^2}{(1 + ya^2)^3}\,. \tag{35}$$

The zero points of $\gamma^2_{\rm Zex}$ are given by the function

$$a^2_{\rm zZex}(\theta; y) = -\frac{1}{y\cos 2\theta}\,, \tag{36}$$

which has its extrema located at $\theta = 0, \pi/2, \pi$ and diverges at $\theta = \pi/4, 3\pi/4$. The values of the extrema are common at $\theta = 0$ and $\theta = \pi$, where

$$\gamma^2_{\mathrm{Zex}}(\theta = 0, \pi; y, a) = \frac{1}{1 + ya^2}\,. \tag{37}$$

For $\theta = \pi/2$, there is

$$\gamma^2_{\mathrm{Zex}}(\theta = \pi/2; y, a) = \frac{1}{(1 + ya^2)^3}\,. \tag{38}$$

The character of the extrema of γ^2_{Zex} is given by the relation between a and y. At $\theta = \pi/2$ the extreme is a minimum for arbitrary values of a and y.

Behaviour of the functions γ^2_{Rex} and γ^2_{Zex} can be divided into two parts according to the relation between a and y.

3.1.1 $y \in \langle 0, 1/a^2\rangle$

The extreme at $\theta = \pi/2$ is always positive, Fig. 1a, and

$$\gamma^2_{\mathrm{Rex}}(\theta = \pi/2) < \gamma^2_{\mathrm{Zex}}(\theta = \pi/2) < \gamma^2_{\mathrm{Rex}}(\theta = 0)\,. \tag{39}$$

This three values separate the range of γ^2 into four parts.

For $\gamma^2 > \gamma^2_{\mathrm{Rex}}(0)$, the curves of $b_{\mathrm{ex}\pm}$ are defined everywhere, Fig. 1b.

For $\gamma^2 \in (\gamma^2_{\mathrm{Zex}}(\pi/2), \gamma^2_{\mathrm{Rex}}(0))$ the curves of $b_{\mathrm{ex}\pm}$ are defined just for $\theta \in \langle\theta_{\mathrm{m}}, \pi/2)$ and have got two zero points, Fig. 1c.

For $\gamma^2 \in (\gamma^2_{\mathrm{Rex}}(\pi/2), \gamma^2_{\mathrm{Zex}}(\pi/2))$ the curves of $b_{\mathrm{ex}\pm}$ are defined for $\theta \in \langle\theta_{\mathrm{m}}, \pi/2)$ too, but have no zero points and their values are negative, Fig. 1d.

The curves of $b_{\mathrm{ex}\pm}$ are not defined for $\gamma^2 < \gamma^2_{\mathrm{Rex}}(\pi/2)$.

- First we will discuss the case $b = 0$. There are three cases possible. For $\gamma^2 > \gamma^2_{\mathrm{Rex}}(0)$, the extrema of q_{t} are located at $\theta = 0, \pi/2, \pi$, Fig. 2a. The curve of $b_{\mathrm{ex}\pm}$ is defined for all θ and its zero values are located at $\theta = 0, \pi$, where the minima of q_{t} appear. For $\gamma^2 \in \langle\gamma^2_{\mathrm{Zex}}(\pi/2), \gamma^2_{\mathrm{Rex}}(0)\rangle$, there exist two another extrema (minima) located at specified θ, Fig. 2b. It is easy to find that the vortical motion is allowed there (Bičák and Stuchlík, 1976). The third case occurs for $\gamma^2 < \gamma^2_{\mathrm{Zex}}(\pi/2)$ and the extrema are located at $\theta = 0, \pi/2, \pi$, Fig. 2c. The vortical motion is not possible in this case.
- If $b \neq 0$ and the $b = \mathrm{const}$ line intersects the curves of $b_{\mathrm{ex}\pm}$, the function of q_{t} has one maximum at $\theta = \pi/2$ (the orbits are not stable here) and two minima, Fig. 2d. The vortical motion is allowed in this case.
- If $b \neq 0$ and the $b = \mathrm{const}$ line does not intersect the curves of $b_{\mathrm{ex}\pm}$ (or if the curves are not defined), then the curve of q_{t} has got just one extreme (minimum) at $\theta = \pi/2$, Fig. 2e. The equatorial orbits are stable.

Behaviour of the "effective potential" of the latitudinal motion, related to the constant of motion Q, is represented in Fig. 2 in typical situations. Note that the orbital motion means that the particle crosses the equatorial plane, while the vortical motion is restricted above or below the equatorial plane. It is important to distinguish these families of orbits in connection with modelling accretion discs located in the equatorial plane.

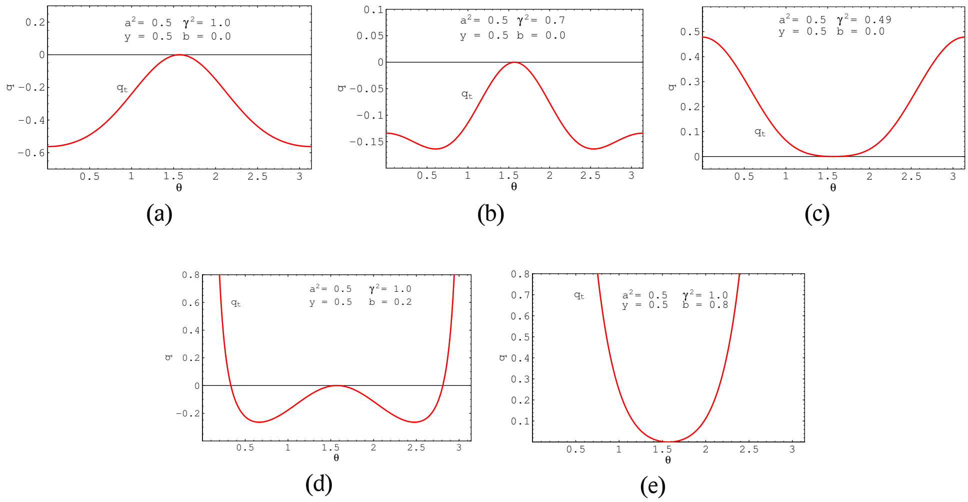

Figure 2. Behaviour of q_t for given values of a, γ, y, b.

3.1.2 $y \in \langle 1/a^2, \infty)$

The values of $\gamma^2_{\mathrm{Rex}}(\pi/2) = (1 - ya^2)/(1 + ya^2)^2$ are negative for this range of y, Fig. 3a. The zero points of $\gamma^2_{\mathrm{Rex}}(\pi/2)$ are located at $\theta_{\mathrm{zero}} = [\arccos(-1/ya^2)]/2$ and γ^2_{Rex} is defined for $\theta \in \langle 0, \theta_{\mathrm{zero}}) \cup (\pi - \theta_{\mathrm{zero}}, \pi\rangle$. The function $b_{\mathrm{ex}-}$ diverges at θ_{zero}. The curve γ^2_{Zex} is defined for all values of θ.

There exist three sets of γ^2. First range is for $\gamma^2 > \gamma^2_{\mathrm{Rex}}(0)$. The curves $b_{\mathrm{ex}\pm}$ are defined for all θ and the null points of $b_{\mathrm{ex}+}$ are located at $\theta = 0, \pi$, Fig. 3b. The second range is for $\gamma^2 \in (\gamma^2_{\mathrm{Zex}}(\pi/2), \gamma^2_{\mathrm{Rex}}(0))$. The functions $b_{\mathrm{ex}\pm}$ are defined at a limited range of θ, Fig. 3c. The third range is for $\gamma^2 \in (0, \gamma^2_{\mathrm{Zex}}(\pi/2))$. The values of $b_{\mathrm{ex}+}$ have got negative values, only (Fig. 3d).

Behaviour of q_t for $b > b_{\mathrm{ex}-}(\pi/2)$ and $b < b_{\mathrm{ex}+}(\pi/2)$ is illustrated in Fig. 4a. The vortical motion is allowed, and the motion in the equatorial plane is unstable.

For $b \in (b_{\mathrm{ex}+}(\pi/2), b_{\mathrm{ex}-}(\pi/2))$ the motion in the equatorial plane is stable, Fig. 4b.

We can divide the special case $b = 0$ into three cases according to the value of γ^2. For $\gamma^2 > \gamma^2_{\mathrm{Rex}}(0)$ the extrema are at $\theta = 0, \pi/2, \pi$. The zero point is at $\theta = \pi/2$ only, Fig. 4c. For the case where $\gamma^2 \in \langle \gamma^2_{\mathrm{Zex}}(\pi/2), \gamma^2_{\mathrm{Rex}}(0)\rangle$, there are two another extrema at θ, which are the solution of the equation $b_{\mathrm{ex}+} = 0$, Fig. 4d. In the case $\gamma^2 \in \langle 0, \gamma^2_{\mathrm{Zex}}(\pi/2)\rangle$ the motion in equatorial plane is stable, Fig. 4e.

3.2 Photons

Assuming $m = 0$, we arrive at the three-parameter family of curves

$$q_t(\theta; b, y, a) = \cos^2\theta \left\{ -\frac{I^2}{\Delta_\theta}\left[1 - \frac{b^2}{\sin^2\theta} + ya^2(1-b)^2\right]\right\} . \tag{40}$$

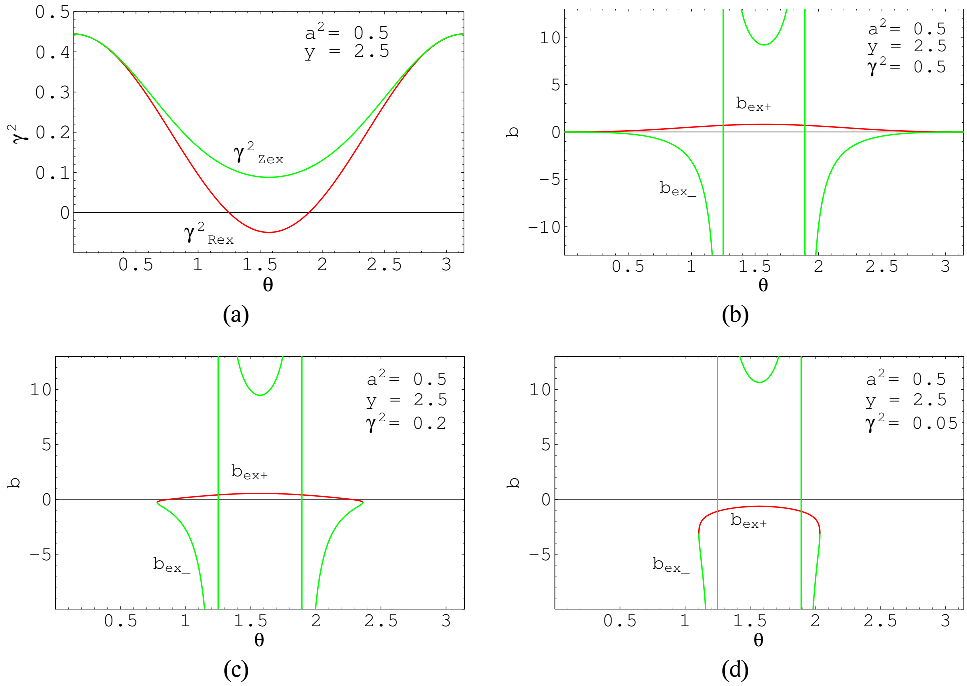

Figure 3. Behaviour of curves γ^2_{Zex}, γ^2_{Rex} (a) and $b_{\mathrm{ex}\pm}$ (b)–(d) for given values of γ^2.

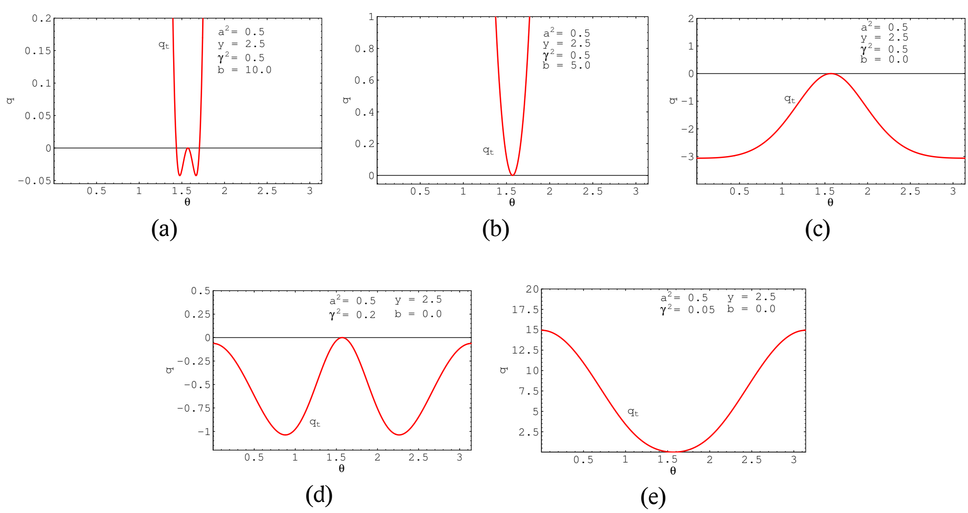

Figure 4. Behaviour of q_{t} for given values of a, γ, y, b.

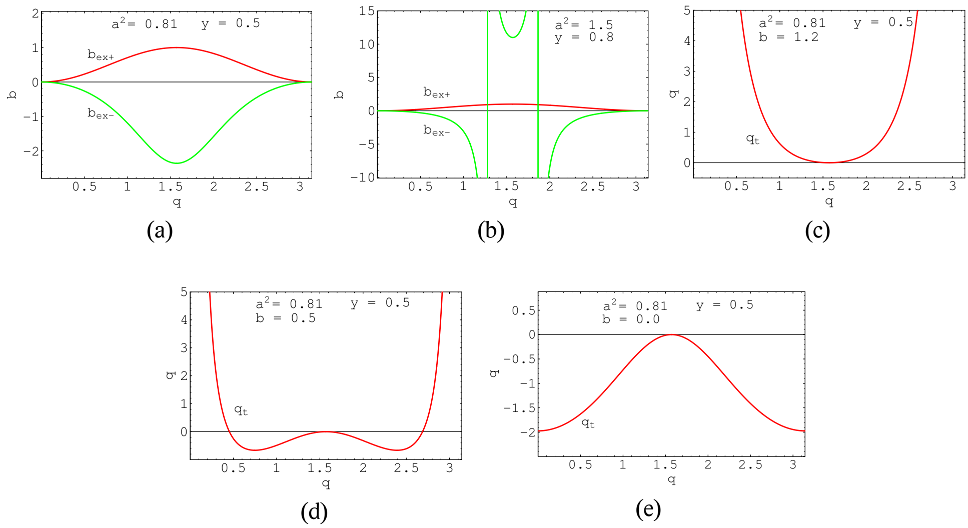

Figure 5. Behaviour of $b_{\mathrm{ex}\pm}$ and q_{t} for photons in spacetimes, where $y < 1/a^2$, and for given values of a, y, b.

The loci of extrema of $q_{\mathrm{t}}(\theta; b, y, a)$ are at $\theta = \pi/2$ and in the b-θ plane they are described by the equations

$$b_{\mathrm{ex}+} = \sin^2\theta\,, \tag{41}$$

and

$$b_{\mathrm{ex}-} = -\frac{(1 + ya^2)\sin^2\theta}{1 + ya^2\cos 2\theta}\,. \tag{42}$$

It is interesting that $b_{\mathrm{ex}+}$ does not depend on y and a. The extrema of $b_{\mathrm{ex}\pm}$ are located at $\theta = 0, \pi/2, \pi$. At $\theta = \pi/2$, $b_{\mathrm{ex}+}(\pi/2, y) = 1$ (a maximum) and $b_{\mathrm{ex}-}(\pi/2, y) = -(1+ya^2)/(1-ya^2)$ (a minimum). The common points are located at $\theta = 0, \pi$. Behaviour of curves $b_{\mathrm{ex}\pm}$ is illustrated in Fig. 5a.

3.2.1 $\quad y \in \langle 0, 1/a^2\rangle$

The value of $b_{\mathrm{ex}-}(\pi/2, y)$ is always negative for this range of y.

For $b > 1$ and $b < (1 + ya^2)/(ya^2 - 1)$ the characteristic section of $q_{\mathrm{t}}(\theta; b, y, a)$ is illustrated in Fig. 5c. The curves of $b = \text{const}$ do not intersect the curves of $b_{\mathrm{ex}\pm}$, and that is why the curve of q_{t} has just one extreme, which is zero and it is located at $\theta = \pi/2$. The latitudinal motion is allowed in region where $q \geq q_{\mathrm{t}}$.

For $b \in (0, 1)$, the section of $q_{\mathrm{t}}(\theta; b, y, a)$ is given by Fig. 5d. The curves of $b = \text{const}$ intersect $b_{\mathrm{ex}\pm}$ at two points, therefore, two other extrema arise, located at $\theta =$

$\arcsin(\pm\sqrt{b})$. The minima of q_t correspond to the stable orbits and permit the existence of the so called PNC photons (Bičák and Stuchlík, 1976). The orbit at $\theta = \pi/2$ is unstable.

For $b \in (b_{ex-}(\pi/2), 0)$, the behaviour of q_t will be nearly the same, only the location of the minima of q_t will be shifted.

The special case $b = 0$ is illustrated in Fig. 5e.

3.2.2 $y > 1/a^2$

The extreme of $b_{ex-}(\pi/2)$ will be positive, Fig. 5b. The function of b_{ex-} has two points of discontinuity at θ_n and $\pi - \theta_n$, where

$$\theta_n = \frac{1}{2}\arccos\left(-\frac{1}{ya^2}\right). \tag{43}$$

The discussion of behaviour of q_t will be the same as in the case $y > 1/a^2$ of the motion of test particles.

4 EQUATORIAL MOTION OF PHOTONS

The Carter equation for radial motion in the equatorial plane can be written in the form

$$\rho^2\frac{dr}{d\lambda} = \pm\sqrt{R(r; y, a, E)}, \tag{44}$$

where (for photons)

$$R(r; y, a, E) = I^2\left\{\left[(r^2 + a^2)E - a\Phi\right]^2 - \Delta_r(aE - \Phi)^2\right\}. \tag{45}$$

4.1 The effective potential of the radial motion

The motion of photons is independent of the constant of the motion E. The equatorial motion is fully governed by the impact parameter $l = \Phi/E$, $E \neq 0$. However, it is convenient to introduce a redefined impact parameter

$$X \equiv \frac{\Phi}{E} - a. \tag{46}$$

Then

$$R(r; y, a, E, X) = I^2E^2\left[(r^2 - aX)^2 - \Delta_r X^2\right]. \tag{47}$$

In the dynamic regions, where $\Delta_r < 0$, there is $R(r) > 0$, and there are no turning points of the radial motion. In the stationary regions, where $\Delta_r \geq 0$, the turning points of the radial motion exist and they are determined by the "effective potential" (Stuchlík and Hledík, 2000).

$$X_\pm(r; y, a) = \frac{r^2}{a \mp \sqrt{\Delta_r}}. \tag{48}$$

In the following discussion of the behaviour of $X_\pm$, we will assume $a \geq 0$.

In the regions, where $a^2 - \Delta_r > 0$ (and $X_+ > 0$), the radial motion is allowed, if

$$X > X_+(r; y, a) \qquad \text{or} \qquad X < X_-(r; y, a) \,. \tag{49}$$

In the regions, where $a^2 - \Delta_r < 0$ (and $X_+ < 0$), the radial motion is allowed, if

$$X > X_+(r; y, a) \qquad \text{and} \qquad X < X_-(r; y, a) \,. \tag{50}$$

We will use the "Chinese boxes" technique, as in the case of discussion of the latitudinal motion, and we will concentrate on the behaviour of the potential in the regions where $r > 0$.

First, we will discuss the reality condition of the effective potential. The potential is well defined in stationary regions, where $\Delta_r \geq 0$. At the boundaries $\Delta_r = 0$ the common points are located. These points are thus located at the event horizons of the geometry. One more common point exist at $r = 0$, it is the only point, where both potentials $X_\pm(r; y, a) = 0$.

At the event horizons ($r = r_\mathrm{h}$), there is

$$X_\pm(r_\mathrm{h}) = \frac{{r_\mathrm{h}}^2}{a} \,. \tag{51}$$

The local extrema of the effective potential determine the loci and impact parameters of the circular photon orbits. They are given by condition $\partial X_\pm / \partial r = 0$, which implies the relation

$$y = y_{\mathrm{ex}\pm}(r; a) \equiv \frac{1}{a^2 r^2} \left\{ -r(r+3) \pm 2\sqrt{r(3r^2 + a^2)} \right\} \,. \tag{52}$$

For $r \to \infty$, both $y_{\mathrm{ex}\pm} \to -1/a^2$.

The reality of these functions is given by $\sqrt{r(3r^2 + a^2)} \geq 0$, from which we obtain

$$a^2 \geq a^2_{\mathrm{r(ex)}} \equiv -3r^2 \,. \tag{53}$$

There are no divergent points of $y_{\mathrm{ex}\pm}$. The zero points of $y_{\mathrm{ex}\pm}$, which determine photon circular orbits in the Kerr spacetimes, are given by

$$a^2 = a^2_{\mathrm{z(ex)}}(r) \equiv \frac{r(r - 3^2)}{4} \,. \tag{54}$$

The function $a^2_{\mathrm{z(ex)}}(r)$ diverges for $r \to \infty$, the zeros are located at $r = 3$ and the extrema are for $r = 1$ (maximum) where $a^2_{\mathrm{z(ex)}}(r = 1) = 1$ and for $r = 3$ (minimum and zero point together).

The local extrema of the function $y_{\mathrm{ex}\pm}$ are given by

$$a^2 = a^2_{\mathrm{ex(ex)}\pm}(r) \equiv \frac{1}{2} \left\{ -2r^2 + r \pm \sqrt{r^2(8r+1)} \right\} \equiv a^2_{\mathrm{ex(h)}\pm}(r) \,. \tag{55}$$

Therefore, the local extrema of the functions $y_\mathrm{h}(r; a)$ and $y_{\mathrm{ex}\pm}(r; a)$ coincide.

Finally we determine the divergent points of the effective potential. Only $X_+(r; y, a)$ can diverge. The loci of divergent points are given by the relation

$$y = y_{\mathrm{d}}(r; a) \equiv \frac{r-2}{r(r^2+a^2)} \,. \tag{56}$$

For $r \to \infty$, this function goes to zero from above. The function $y_{\mathrm{d}}(r; a)$ diverges for $r \to 0$, where $y_{\mathrm{d}} \to -\infty$. The zero point is located at $r = 2$.

The local extrema of $y_{\mathrm{d}}(r; a)$ are determined by

$$a^2 = a^2_{\mathrm{ex(d)}}(r) \equiv r^2(r-3) \,. \tag{57}$$

The function of $a^2_{\mathrm{ex(d)}}(r)$ has no divergent point, the zero point is located at $r = 3$ and its local extreme is at $r = 2$ (minimum). This function is positive for $r \geq 3$.

4.2 Classification

We propose a classification of the Kerr–de Sitter spacetime according to the properties of the effective potential $X_\pm(r; y, a)$ governing the photon motion in the equatorial plane. We use the systematic study of the properties of the functions founded in a few last pages. The important features of the classification will be the number of the event horizons, the number of divergences of the effective potential and the number of its local extrema.

For $y > 0$ a cosmological horizon exists behind which the spacetime is dynamic. The effective potential is well defined up to the cosmological horizon.

For the separating the black hole and naked singularity spacetimes the criterion of the number of event horizons is important. The event horizons are determined by the function $y_{\mathrm{h}}(r; a)$. As you can see from the behaviour of $y_{\mathrm{h}}(r; a)$ at least one event horizon must exist in spacetime with $a^2 > 0$ and it is a cosmological horizon. The black-hole horizon can exists, if $y_{\mathrm{h}}(r; a)$ has local extrema. The extrema are given by function $a^2_{\mathrm{ex(h)+}}$ which has its maximum at $r = 1.61603$ with the corresponding critical value

$$a^2_{\mathrm{crit}} = 1.21202 \,. \tag{58}$$

So the black-hole spacetimes can exist for $a^2 < a^2_{\mathrm{crit}}$ and for $y \in (y_{\mathrm{hmax}}, y_{\mathrm{hmin}})$, respectively for $y \in (y_{\mathrm{hmax}}, 0)$ in case (c), see below. There are two black-hole horizons and one cosmological horizon.

If $y = y_{\mathrm{hmin}}$, the two black-hole horizons coincide and the geometry describes an extreme black hole. If $y = y_{\mathrm{hmax}}$, the outer black-hole horizon and the cosmological horizon coincide and we obtain an extreme black hole geometry again. For $y < y_{\mathrm{hmin}}$ or $y > y_{\mathrm{hmax}}$ the geometry describes the naked singularity.

The characteristic functions $a^2(r)$ which are relevant to determine the behaviour of the functions $y(r; a)$ are illustrated in Fig. 6a. We restrict ourselves to the regions where the functions $a^2(r)$ are non negative.

It follows from the behaviour of the characteristic functions $a^2(r)$ that there are three different cases of the behaviour of the characteristic functions $y(r; a)$. We denote them in the following way:

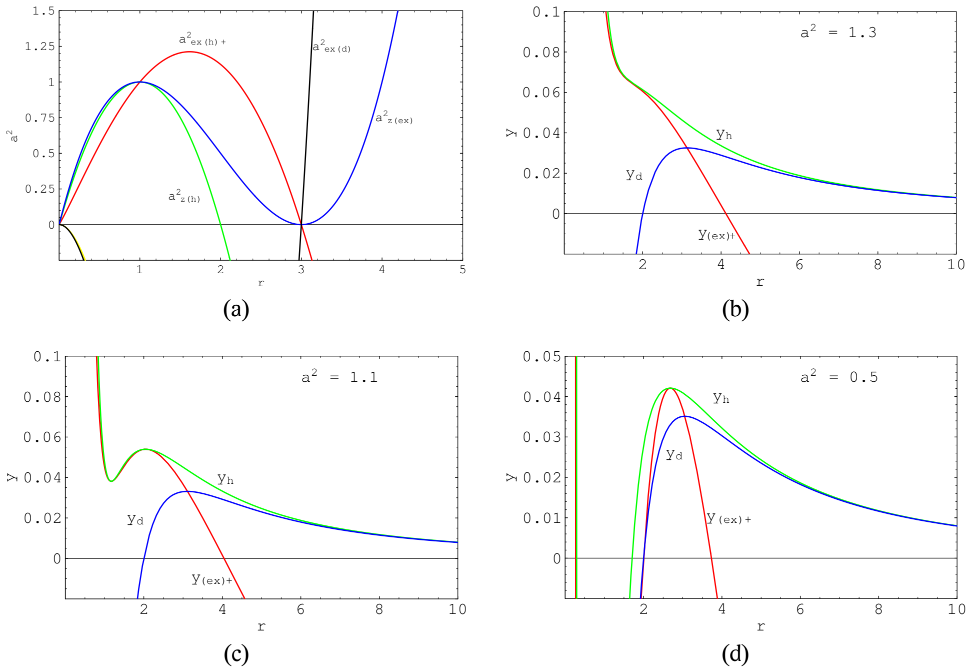

Figure 6. The characteristic functions $a^2(r)$ (a) and $y(r; a)$ for values a^2 given in (b)–(d).

(a) $a^2 > a^2_{\mathrm{ex(h)+max}} \equiv a^2_{\mathrm{ex(ex)max}}$, $a^2 > 1.21202$,
(b) $a^2 \in \langle a^2_{\mathrm{ex(h)+max}}, a^2_{\mathrm{z(h)max}} \equiv a^2_{\mathrm{z(ex)max}} \rangle$, $a^2 \in \langle 1.21202, 1 \rangle$,
(c) $a^2 \in \langle a^2_{\mathrm{z(h)max}}, 0 \rangle$, $a^2 \in \langle 1, 0 \rangle$.

4.2.1 $a^2 > a^2_{\mathrm{ex(h)+max}}$

Behaviour of the characteristic functions y_{h}, y_{d}, $y_{\mathrm{(ex)+}}$ is given in Fig. 6b and can be found from the behaviour of the characteristic functions $a^2_{\mathrm{ex(h)+}}$, $a^2_{\mathrm{ex(d)}}$, $a^2_{\mathrm{z(ex)}}$, $a^2_{\mathrm{z(h)}}$. We find that y_{d} has got one local extreme (maximum) and one zero point (always located at $r = 2$). The function $y_{\mathrm{(ex)+}}$ has got just one zero point.

Behaviour of the effective potential $X_\pm$ in this region can be divided in two cases (we don't consider negative values of y.) In both cases there exists one horizon determining the naked singularity spacetime, Figs 7a,b. In first case for $y > y_{\mathrm{dmax}}$ there will be none divergent points of the effective potential. In both cases there exists one circular orbit which is stable relative to the radial perturbations.

4.2.2 $a^2 \in \langle a^2_{\mathrm{ex(h)+max}}, a^2_{\mathrm{z(h)max}} \rangle$

Behaviour of the characteristic functions y_{h}, y_{d}, $y_{\mathrm{(ex)+}}$ is given in Fig. 6c. We find that y_{d} has got one local extreme (maximum) and one zero point (always located at $r = 2$) as in the

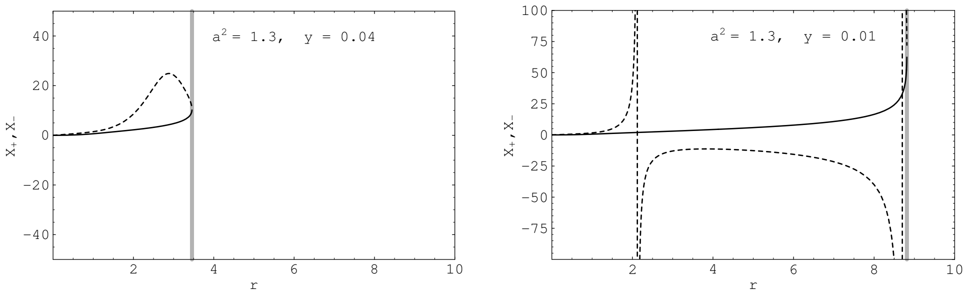

(a) (b)

Figure 7. Behaviour of the effective potential X_+ (represented by the full curves) and X_- (broken curves) for the values a^2, y given in figures. The shade bold full curve represents the event horizon.

first case. The function $y_{(\mathrm{ex})+}$ has got just one zero point and two extrema (one maximum and one minimum with positive values) common for y_h, too.

Behaviour of the effective potential $X_\pm$ can be divided into four cases.

- For $y > y_\mathrm{hmax}$ the effective potential has got one extreme (corresponding to a stable circular orbit) and one horizon determining the naked singularity spacetime, Fig. 8a. The situation will be nearly the same as for $y \in \langle y_\mathrm{hmin}, y_\mathrm{dmax}\rangle$, Fig. 8c.
- For $y \in \langle y_\mathrm{hmax}, y_\mathrm{hmin}\rangle$ there will be three horizons determining the black hole spacetime, three extrema (three stable circular orbits) and no divergent point, Fig. 8b.
- For $y \in \langle y_\mathrm{dmax}, 0\rangle$ there will be one horizon (naked singularity), two divergent points and one stable circular orbit, Fig. 8d.

4.2.3 $a^2 \in \langle a^2_{\mathrm{z(h)max}}, 0\rangle$

Behaviour of the characteristic functions y_h, y_d, $y_{(\mathrm{ex})+}$ is given in Fig. 6d. The function y_d has got the same characteristic as in the last two cases. The function $y_{(\mathrm{ex})+}$ has got three zero points and two extrema, one maximum with positive value and one minimum with negative value. Both extrema are common for $y_{(\mathrm{ex})+}$ and for y_h. The function y_h has got two zero points.

Behaviour of the effective potential $X_\pm$ can be divided into three cases.

- For $y > y_\mathrm{hmax}$ the effective potential has got one extreme (stable circular orbit) and one horizon representing the naked singularity spacetime, Fig. 9a.
- For $y \in \langle y_\mathrm{hmax}, y_\mathrm{dmax}\rangle$ there will be three horizons (black hole spacetime), three extrema (stable circular orbits) and no divergent point, Fig. 9b.
- For $y \in \langle y_\mathrm{dmax}, 0\rangle$ there will be three horizons (black hole spacetime), three extrema (stable circular orbits) and two divergent points, Fig. 9c.

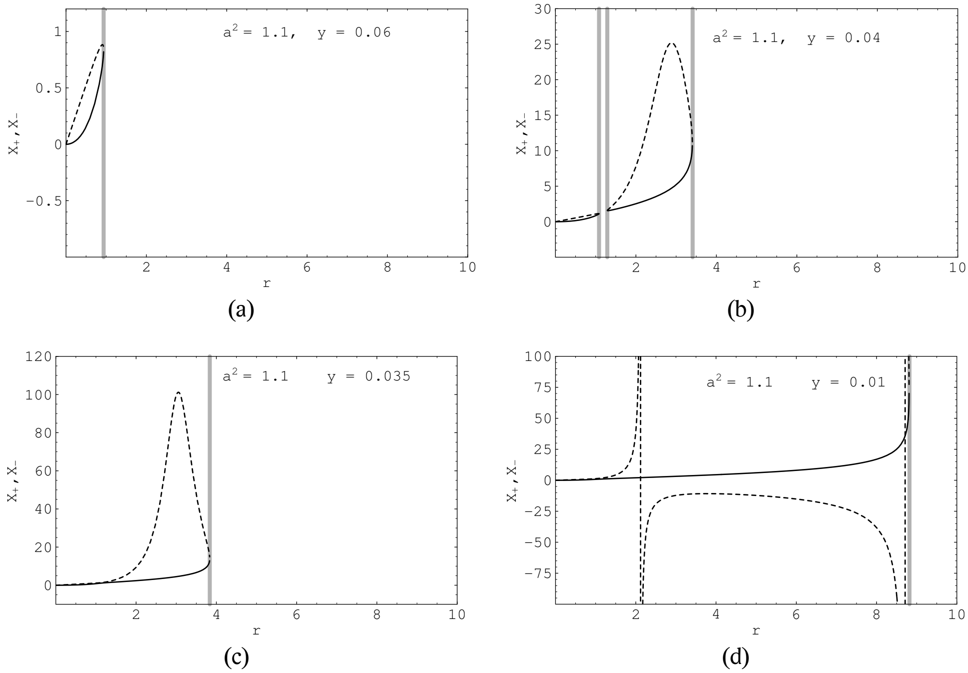

Figure 8. Behaviour of the effective potential X_+ (represented by the full curves) and X_- (broken curves) for the values a^2, y given in figures. The shade bold full curve represents the event horizon(s).

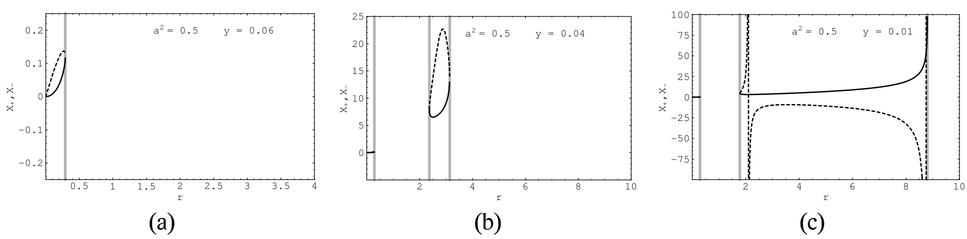

Figure 9. Behaviour of the effective potential X_+ (represented by the full curves) and X_- (broken curves) for the values a^2, y given in figures. The shade bold full curve represents the event horizon(s).

5 CONCLUDING REMARKS

We have discussed the latitudinal motion of test particles and photons in terms of the motion constant Q, which must be zero for the equatorial motion, simplifying substantially discussion of the general off-equatorial radial motion. In order to prepare a detailed study of the optical effects in the KdS black-hole spacetimes, we summarize the classification of the equatorial photon motion in the KdS black-hole spacetimes. Such a classification will be very helpful in the very complex analysis of the general, off-equatorial photon motion.

ACKNOWLEDGEMENTS

The present work was supported by the Czech grant MSM 4781305903.

REFERENCES

Abramowicz, M. A. and Kluźniak, W. (2004), Interpreting black hole QPOs, in P. Karet, F. K. Lamb and J. H. Swank, editors, *X-ray Timing 2003: Rossi and Beyond.*, volume 714, pp. 21–28, NY: American Institute of Physics, Melville, `astro-ph/0312396`.

Aschenbach, B. (2004), Measuring mass and angular momentum of black holes with high-frequency quasi-periodic oscillations, *Astronomy and Astrophysics*, **425**, pp. 1075–1082, `astro-ph/0406545`.

Bičák, J. and Stuchlík, Z. (1976), On the latitudinal and radial motion in the field of a rotating black hole, *Bull. Astronom. Inst. Czechoslovakia*, **27**(3), pp. 129–133.

Carter, B. (1973), Black hole equilibrium states, in C. D. Witt and B. S. D. Witt, editors, *Black Holes*, p. 57, Gordon and Breach, New York–London–Paris.

Ostriker, J. P. and Steinhardt, P. J. (1995), *Nature*, **377**, p. 600.

Spergel, D. N., Verde, L., Peiris, H. V., Komatsu, E., Nolta, M. R., Bennett, C. L., Halpern, M., Hinshaw, G., Jarosik, N., Kogut, A., Limon, M., Meyer, S. S., Page, L., Tucker, G. S., Weiland, J. L., Wollack, E. and Wright, E. L. (2003), First Year Wilkinson Microwave Anisotropy Probe (WMAP) Observations: Determination of Cosmological Parameters, *Astrophys. J. Suppl.*, **148**, p. 175, `astro-ph/0302209`.

Stuchlík, Z. (1983), The motion of test particles in black-hole backgrounds with non-zero cosmological constant, *Bull. Astronom. Inst. Czechoslovakia*, **34**(3), pp. 129–149.

Stuchlík, Z. (2002), The role of a repulsive cosmological constant in astrophysical processes, in O. Semerák, J. Podolský and M. Žofka, editors, *Gravitation: Following the Prague Inspiration (A Volume in Celebration of the 60th Birthday of Jiří Bičák)*, pp. 27–83, World Scientific, New Jersey, London, Singapore, Hong Kong, ISBN 981-238-093-0.

Stuchlík, Z. (2005), Influence of the Relict Cosmological Constant on Accretion Discs, *Modern Phys. Lett. A*, **20**(8), pp. 561–575.

Stuchlík, Z. and Calvani, M. (1991), Null geodesics in black hole metrics with non-zero cosmological constant, *Gen. Relativity Gravitation*, **23**, p. 507.

Stuchlík, Z. and Hledík, S. (1999), Some properties of the Schwarzschild–de Sitter and Schwarzschild–anti-de Sitter spacetimes, *Phys. Rev. D*, **60**(4), p. 044006 (15 pages), URL `http://ojps.aip.org/journal_cgi/dbt?KEY=PRVDAQ&Volume=60&Issu%e=4`.

Stuchlík, Z. and Hledík, S. (2000), Equatorial photon motion in the Kerr–Newman spacetimes with a non-zero cosmological constant, *Classical Quantum Gravity*, **17**(21), pp. 4541–4576, ISSN 0264-9381/00, URL `http://www.iop.org/EJ/S/UNREG/1NOryEzmtf2ZMVyFDaUGbw/toc/0264%-9381/17/21`.

Stuchlík, Z. and Hledík, S. (2001), Equilibrium of a charged spinning test particle in Reissner–Nordström backgrounds with a nonzero cosmological constant, *Phys. Rev. D*, **64**(10), p. 104016 (12 pages), ISSN 1089-4918, URL `http://link.aps.org/abstract/PRD/v64/e104016`.

Stuchlík, Z. and Hledík, S. (2002), Properties of the Reissner–Nordström spacetimes with a nonzero cosmological constant, *Acta Phys. Slovaca*, **52**(5), pp. 363–407, ISSN 0323-0465/02, URL `http://nic.savba.sk/sav/inst/fyzi/aps/acta02/no5/`.

Stuchlík, Z. and Slaný, P. (2004), Equatorial circular orbits in the Kerr–de Sitter spacetimes, *Phys. Rev. D*, **69**, p. 064001, ISSN 1094-1622, `gr-qc/0307049`.

Török, G. (2005a), A possible 3 : 2 orbital epicyclic resonance in QPO frequencies of Sgr A*, *Astronomy and Astrophysics*, **440**(1), pp. 1–4.

Török, G. (2005b), QPOs in microquasars and Sgr A*: measuring the black hole spin, *Astronom. Nachr.*, **326**(9), pp. 856–860, `astro-ph/0510669`.

Török, G., Abramowicz, M. A., Kluźniak, W. and Stuchlík, Z. (2005), The orbital resonance model for twin peak kHz quasi periodic oscillations in microquasars, *Astronomy and Astrophysics*, **436**(1), pp. 1–8, `astro-ph/0401464`.

Proceedings of *RAGtime 6/7: Workshops on black holes and neutron stars, Opava, 16–18/18–20 September, 2004/2005*
S. Hledík and Z. Stuchlík, editors, Silesian University in Opava, Czech Republic, 2005, pp. 357–362

Matching of equations of state: Influence on calculated neutron star models

Martin Urbanec[1], John C. Miller[2,3] and Jiřina Říkovská Stone[4,5,6]

[1]Institute of Physics, Faculty of Philosophy & Science, Silesian University in Opava, Bezručovo nám. 13, CZ-746 01 Opava, Czech Republic
[2]Department of Physics (Astrophysics), University of Oxford, Oxford, OX1 3RH, UK
[3]SISSA and INFN, Via Beirut, 34014 Trieste, Italy
[4]Department of Physics, University of Oxford, Oxford, OX1 3PU, UK
[5]Department of Chemistry and Biochemistry, University of Maryland, College Park, Maryland 20742, USA
[6]Physics Division, ORNL, Oak Ridge, TN 37831, USA

ABSTRACT
Equations of state for neutron-star matter at densities above nuclear-matter density are usually joined onto an equation of state for matter at lower densities calculated using a different physical treatment. Since the way of making the join is not clearly defined, we have tested the sensitivity of derived neutron-star models to the way in which the matching is made. We consider the joining between Skyrme equations of state for the higher densities and the Baym–Bethe–Pethick equation of state for densities between the neutron-drip point and nuclear-matter density. Three different prescriptions for making the join are tested, and it is shown that the radius of the neutron star model can depend substantially on the details of the matching, whereas the mass is almost independent of the prescription used.

1 INTRODUCTION

The interior of a neutron star consists of various types of matter. As the pressure increases moving inwards from the surface, the form and behaviour of the matter change. There is an iron crust at the surface which we describe using the Feynman–Metropolis–Teller equation of state (Feynman et al., 1949); then, with increasing pressure, progressively more neutron-rich nuclei start to appear (we use the Baym–Pethick–Sutherland equation of state for describing this, Baym et al., 1971b) and at the density $\rho_{\mathrm{drip}} = 4.3 \times 10^{11}\,\mathrm{g\,cm^{-3}}$ free neutrons start to drip from nuclei (the value is given by condition for inverse β decay). Beyond this point, free neutrons exist in equilibrium with nuclei and for this density range we use the Baym–Bethe–Pethick (BBP) equation of state (Baym et al., 1971a). At still higher densities, the nuclei merge and dissolve into a sea of free neutrons and protons together with electrons and, later, muons. In the present work, we have used three types of Skyrme force to describe the inter-particle interactions in this high-density matter.

80-7248-334-X

The way in which the transition occurs from the mixture of nuclei, neutrons and electrons to a mixture of neutrons, protons and electrons is not usually calculated in a self-consistent way; rather, separate calculations are made for the two regimes and then a join is made between the two, making a matching at some suitable pressure. The joining together of different equations of state calculated for different density ranges and using different methods is far from being a precise procedure. Ideally, one would like to have an equation of state calculated using the same methodology throughout the entire density range, thus avoiding the necessity for making artificial joins, but at present such calculations are not available. Frequently in the literature, joins have been made in a very rough way. The present work investigates the sensitivity of the calculated values for the mass and radius of neutron-star models when different types of equation-of-state matching are used.

In Section 2 we describe how we construct the neutron star models. In Section 3 we give a short overview of the equations of state being used and present the different types of matching being investigated. Section 4 contains results and conclusions.

2 NEUTRON STAR MODEL

Our simple neutron star models describe non-rotating, cold ($T = 0$) neutron stars without magnetic field. The line element in standard Schwarzschild coordinates $(t, r, \vartheta, \varphi)$ is

$$\mathrm{d}s^2 = -\mathrm{e}^{2\nu}\,\mathrm{d}t^2 + \mathrm{e}^{2\lambda}\,\mathrm{d}r^2 + r^2(\mathrm{d}\vartheta^2 + \sin^2\vartheta\,\mathrm{d}\varphi^2)\,, \tag{1}$$

where ν and λ are functions only of r. To get the equation of hydrostatic equilibrium, we need the Einstein field equation

$$G_{\mu\nu} = R_{\mu\nu} - \frac{1}{2}Rg_{\mu\nu} = \frac{8\pi G}{c^4}T_{\mu\nu}\,, \tag{2}$$

where $G_{\mu\nu}$ is Einstein tensor, $R_{\mu\nu}$ is the Ricci tensor, R is the Ricci scalar, G is the gravitational constant, c is the velocity of light and $T_{\mu\nu}$ is the energy-momentum tensor. For a perfect fluid,

$$T_\mu^\nu = (P + \rho c^2)u^\nu u_\mu + P\delta_\mu^\nu \tag{3}$$

where u^ν is the four-velocity, P is the pressure and ρc^2 is the energy density. For a spherically symmetric, static configuration, the energy-momentum tensor takes the form

$$T_\mu^\nu = (-\rho c^2, P, P, P)\,. \tag{4}$$

The conservation of energy and momentum is expressed by

$$T_{\mu;\nu}^\nu = 0\,. \tag{5}$$

The equation of hydrostatic equilibrium can be derived from Eqs (2) and (5); we get

$$\frac{\mathrm{d}P}{\mathrm{d}r} = -\frac{Gm(r)\rho}{r^2}\frac{\left(1 + P/\rho c^2\right)\left[1 + 4\pi r^3 P/m(r)c^2\right]}{1 - 2Gm(r)/rc^2}\,, \tag{6}$$

where

$$m(r) = \int_0^r 4\pi r^2 \rho \, \mathrm{d}r \tag{7}$$

is the mass inside radius r. Equation (6) is the Tolman–Oppenheimer–Volkoff (TOV) equation of hydrostatic equilibrium.

For obtaining our neutron-star models, we need to integrate Eq. (6) from the centre out to the stellar surface (where $P \to 0$). For given central conditions (central energy density ρ and the corresponding pressure P) we obtain a neutron-star model and its gross properties (mass M, radius R, total baryon number A, etc.). To integrate the TOV equation (6), we need the equation of state giving the relation between pressure and energy density.

The total number of baryons inside the object A is calculated using

$$A = \int_0^R \frac{4\pi r^2 n_\mathrm{b}(r)}{\left[1 - 2Gm(r)/rc^2\right]^{1/2}} \, \mathrm{d}r \, , \tag{8}$$

where $n_\mathrm{b}(r)$ is the baryon number density at radius r. The total number of baryons inside the star plays an important role for calculating the binding energy E_b which is given by relation $E_\mathrm{b} = (Am_0 - M)c^2$ where m_0 is the rest-mass per baryon. For a neutron star formed by collapse of an iron core, the binding energy liberated in the collapse is given approximately by this expression with m_0 taken as the mass per baryon of ^{56}Fe. Note that for having consistent values of M and A, it is necessary for P, ρ and n_b to obey the correct thermodynamic relations within the joining regime.

3 EQUATIONS OF STATE USED

As mentioned above, because of the wide range of densities and different types of matter in neutron stars, it is usually necessary to join together several different equations of state, each calculated for different restricted density regimes, except in the case of some simplified approximations such as uniform density profiles or polytropic and adiabatic equations of state (Stuchlík, 2002; Hledík et al., 2004; Mrázová et al., 2005). We here briefly summarize the equations of state used for the present work (more details can be found in the references quoted). For densities above nuclear matter density, we focus attention on equations state derived using Skyrme forces and do not include here the possible appearance of hyperons or quark matter at high densities.

The equations of state used are the following:

- Feynman–Metropolis–Teller equation of state for $7.9 \lesssim \rho \lesssim 10^4\,\mathrm{g\,cm^{-3}}$ where matter consists of e^- and $^{56}_{26}$Fe (Feynman et al., 1949)
- Baym–Pethick–Sutherland equation of state for $10^4 \lesssim \rho \lesssim 4.3 \times 10^{11}\,\mathrm{g\,cm^{-3}}$ with coulomb lattice energy corrections (Baym et al., 1971b)
- Baym–Bethe–Pethick equation of state for $4.3 \times 10^{11} \lesssim \rho \lesssim \times 10^{14}\,\mathrm{g\,cm^{-3}}$: e^-, n and equilibrium nuclei calculated using the compressible liquid drop model (Baym et al., 1971a)
- Skyrme equations of state for $\rho \gtrsim 10^{14}\,\mathrm{g\,cm^{-3}}$. We use three types of Skyrme equation of state SkI3 (Reinhard and Flocard, 1995), SkT5 (Tondeur et al., 1984), and Sly4 (Chabanat, 1995).

3.1 Skyrme equation of state

The energy of nuclear matter can be written as the integral of a density functional $\mathcal{H}$ which is a function of empirical parameters, and is given by

$$\mathcal{H} = \mathcal{K} + \mathcal{H}_0 + \mathcal{H}_3 + \mathcal{H}_{\rm eff} + \cdots , \tag{9}$$

where $\mathcal{K}$ is the kinetic-energy term, $\mathcal{H}_0$ the zero-range term $\mathcal{H}_3$ the density dependent term , $\mathcal{H}_{\rm eff}$ effective-mass dependent term. These terms are functions of nine parameters $t_0, t_1, t_2, t_3, x_0, x_1, x_2, x_3$ and α and are given by:

$$\mathcal{K} = \frac{\hbar^2}{2m}\tau , \tag{10}$$

$$\mathcal{H}_0 = \tfrac{1}{4} t_0 \left[(2+x_0)n^2 - (2x_0+1)\left(n_{\rm p}^2 + n_{\rm n}^2\right) \right] , \tag{11}$$

$$\mathcal{H}_3 = \tfrac{1}{24} t_3 n^\alpha \left[(2+x_3)n^2 - (2x_3+1)\left(n_{\rm p}^2 + n_{\rm n}^2\right) \right] , \tag{12}$$

$$\mathcal{H}_{\rm eff} = 18 \left[t_1(2+x_1) + t_2(2+x_2) \right] \tau_{\rm n} + \tfrac{1}{8} \left[t_2(2x_2+1) - t_1(2x_1+1) \right] (\tau_{\rm p} n_{\rm p} + \tau_{\rm n} n_{\rm n}) . \tag{13}$$

3.2 Matching of equations of state

The objective here is to investigate the effect of using non-optimal matching between equations of state in the different density regimes. At the joins between the three lower-density regimes, we use the matchings given by BBP but we experiment with the join between the BBP and Skyrme equations of state. For doing this, we consider a "best" matching and two rather extreme non-optimal ones. The pressure has to be continuous inside the object and so we set by hand the "matching pressure" and find corresponding densities for the BBP equation of state and for the Skyrme equation of state. The three types of matching used (see Fig. 1) are

• Low: matching at a low pressure. There is a discontinuity in density with a jump to a higher value.
• Continuous (Cont): matching at the point where both equations of state give the same value of density for the matching pressure (the "best matching").

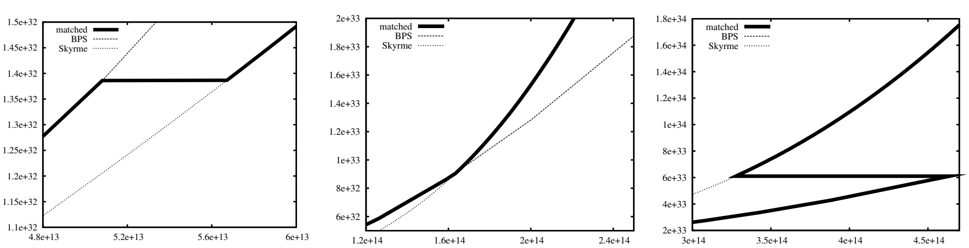

Figure 1. The three different types of matching Low, Cont (continuous) and Up (from left to right and top to bottom).

• Up: matching at a higher value of pressure. There is a discontinuity in density with a jump to a lower value.

All of the matching values of the pressure are in the range where either equation of state could reasonably be thought to be valid.

4 RESULTS AND CONCLUSIONS

The results of using the three different types of matching are shown in Figs 2–4. From Fig. 2 it can be seen that the different types of matching do not influence very much the curves of mass against central density. The curves of radius against central density (see Fig. 3)

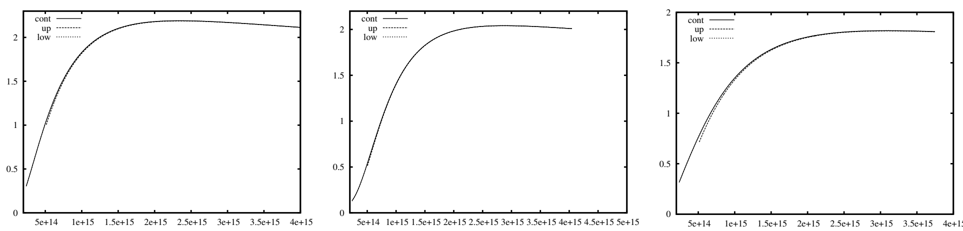

Figure 2. Behaviour of the neutron star mass M (in solar masses) as a function of the central energy density ρ_c for three Skyrme equations of state SkI3, Sly4 and SktT5 (from left to right and top to bottom).

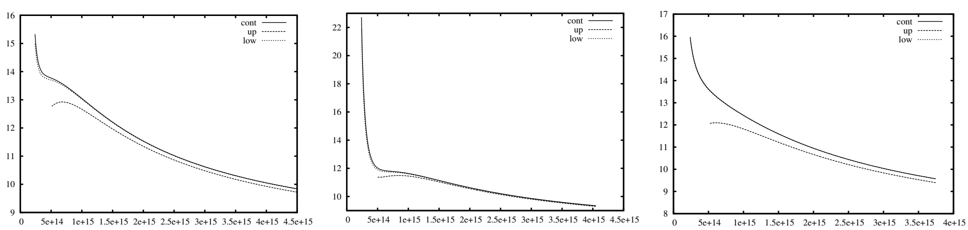

Figure 3. Behaviour of the neutron star radius R (in km) as a function of the central energy density ρ_c for three Skyrme equations of state SkI3, Sly4 and SktT5 (from left to right and top to bottom).

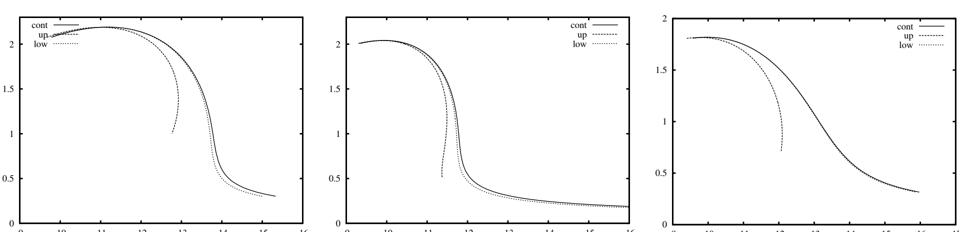

Figure 4. Behaviour of the neutron star mass M (in solar masses) as a function of the radius R (in km) for three Skyrme equations of state SkI3, Sly4 and SktT5 (from left to right and top to bottom).

are also not affected greatly if the low matching is used instead of the continuous one but they *are* significantly affected if the up matching is used. Corresponding effects are seen in the mass-radius curves (Fig. 4). Using the up matching leads to the lower mass models being more compact than they would otherwise be. The matching with continuity in the density can be thought of as being like a second order "phase transition" with the other types of matching being analogous to first order transitions. It would be very desirable to have equations of state calculated consistently with a single methodology both above and below nuclear matter density so that no artificial joining needs to be done in this region.

ACKNOWLEDGEMENTS

The present work was supported by the Czech grant MSM 4781305903.

REFERENCES

Baym, G., Bethe, H. and Pethick, C. (1971a), *Nuclear Phys. A*, **175**.

Baym, G., Pethick, C. and Sutherland, P. (1971b), *Astrophys. J.*, **170**.

Chabanat, E. (1995), Ph.D. thesis, Lyon.

Feynman, R. P., Metropolis, N. and Teller, E. (1949), *Phys. Rev.*, **75**.

Hledík, S., Stuchlík, Z. and Mrázová, K. (2004), Comparison of general relativistic polytropic and adiabatic fluid spheres with a repulsive cosmological constant, in S. Hledík and Z. Stuchlík, editors, *Proceedings of RAGtime 4/5: Workshops on black holes and neutron stars, Opava, 14–16/13–15 October 2002/2003*, pp. 75–89, Silesian University in Opava, Opava, ISBN 80-7248-242-4.

Mrázová, K., Hledík, S. and Stuchlík, Z. (2005), Games with polytropes and adiabates, pp. 109–117, this volume.

Reinhard, P. G. and Flocard, H. (1995), *Nuclear Phys. A*, **584**.

Stuchlík, Z. (2002), The role of a repulsive cosmological constant in astrophysical processes, in O. Semerák, J. Podolský and M. Žofka, editors, *Gravitation: Following the Prague Inspiration (A Volume in Celebration of the 60th Birthday of Jiří Bičák)*, pp. 27–83, World Scientific, New Jersey, London, Singapore, Hong Kong, ISBN 981-238-093-0.

Tondeur, F., Brack, M., Farine, M. and Pearson, J. M. (1984), *Nuclear Phys. A*, **420**.

Proceedings of *RAGtime 6/7: Workshops on black holes and neutron stars, Opava, 16–18/18–20 September, 2004/2005*
S. Hledík and Z. Stuchlík, editors, Silesian University in Opava, Czech Republic, 2005, pp. 363–368

The Double Pulsar J0737−3039

John Miller

SISSA, International School for Advanced Studies, Trieste, Italy
INFN, Trieste, Italy
Department of Physics (Astrophysics), University of Oxford, England
miller@sissa.it

1 OVERVIEW

The discovery of the double pulsar J0737−3039 (Burgay et al., 2003; Lyne et al., 2004) has been a very exciting event for relativistic astrophysics since measurements connected with it are giving the best direct tests so far of the validity of general relativity (see Kramer et al., 2005) and are also allowing new constraints to be placed on the equation of state of neutron star matter (see Podsiadlowski et al., 2005 and references therein). In this paper, we discuss the background to this and describe the results obtained.

2 BINARY PULSARS

So far, there are three close binary systems containing a pulsar for which the system parameters are known to high accuracy. In each case, it is thought that the companion is also a neutron star. The first of these systems to be discovered was the famous Hulse/Taylor binary pulsar PSR B1913+16 (Hulse and Taylor, 1975) which, for the first time, revealed evidence for gravitational radiation being emitted in accordance with the predictions of general relativity. The components of this system have masses of 1.441 $M_\odot$ and 1.387 $M_\odot$, the orbital period is $\sim$8 hours and the pulsar period is 59 ms. PSR B1534+12 (Wolszczan, 1991; Stairs et al., 2002) was the second one to be found and has masses 1.333 $M_\odot$ and 1.345 $M_\odot$, orbital period $\sim$ 10 hours and pulsar period 38 ms. The quite recently discovered double pulsar PSR J0737−3039 (Burgay et al., 2003; Lyne et al., 2004) has masses 1.249 $M_\odot$ and 1.338 $M_\odot$, orbital period $\sim$2.4 hours (separation less than a million kilometres) and pulsar periods 23 ms and 2.8 s. The mass measurements for these binary pulsars have much higher precision than is normally possible for astronomical measurements.

Since we will be focusing here on the double pulsar PSR J0737−3039, it is useful to list some further details of it:

- eccentricity of the binary orbit: 0.087778
- viewing angle: $\sin i = 0.9995 \pm 0.0004$
- periastron advance: 16.9 degrees/year

80-7248-334-X

- merger predicted in 85 Myr

All of the values quoted here for this system come from the paper by Kramer et al. (2005) which gives updates on values quoted previously. (As more data is accumulated with time, the derived parameter values become progressively more precise.)

3 FINDING PARAMETER VALUES FOR A BINARY PULSAR

Finding the parameter values for a binary system is actually easier for binary pulsars in close orbits than for ordinary stars because these systems contain a very accurate clock (the pulsar) and relativistic effects give extra pieces of information. Figure 1 is a schematic picture showing the geometry of the system.

From timing data giving the changing Doppler shift of the pulse-period of the observed pulsar as it moves round its orbit, it is possible to derive its *radial velocity curve* giving the variation of its projected radial velocity with time. This immediately gives the orbital period of the binary P_b and the semi-amplitude of the curve $\bar{v}_2$ also plays an important role in the following analysis. A non-zero eccentricity e of the orbit leads to a deviation of the curve away from a sinusoidal form and e can be determined from this if it is sufficiently large.

To a first approximation, the motion of these systems can be described with Newtonian theory. Using Kepler's laws, one obtains the *mass function*:

$$f(M_1) = \frac{(M_1 \sin i)^3}{(M_1 + M_2)^2} = \frac{P_b\, \bar{v}_2^3 \left(1 - e^2\right)^{3/2}}{2\pi G}$$

which can be evaluated using the above observational data. Two further pieces of information are then required in order to solve completely for the two masses, M_1 and M_2, and the

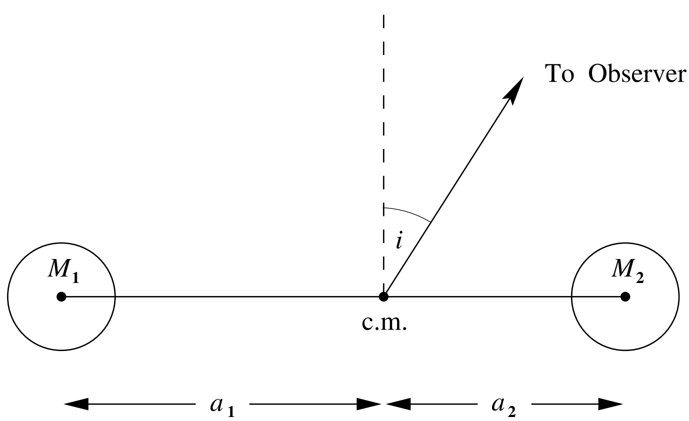

Figure 1. Schematic picture of the binary as viewed in the orbital plane of the system. The observed pulsar has mass M_2, the other star has mass M_1 and distances a_1 and a_2 are measured from the centre of mass (c.m.) of the system.

viewing angle i. (If we have the radial velocity curves for *both* objects, then we can calculate two mass functions $f(M_1)$ and $f(M_2)$, from which the mass ratio R can be determined, and only one further piece of information is then needed.) By making long-term pulsar-timing measurements, it can become possible to pick out post-Newtonian corrections to the basic Keplerian motion and these can then be used to provide the additional pieces of information required.

4 POST-KEPLERIAN PARAMETERS AND TESTING GRAVITY THEORIES

The post-Newtonian corrections mentioned above involve the so-called *post-Keplerian (PK)* parameters:

- $\dot{\omega}$ – rate of precession of the periastron
- γ – gravitational redshift parameter of the system
- $\dot{P}_b$ – rate of change of the orbital period of the binary (related to emission of gravitational waves)
- r – Shapiro time delay parameter (time)
- s – Shapiro time delay parameter (angle)

In the case of the Double Pulsar, values for all of these PK parameters have been extracted from the pulsar-timing data for the more massive component, known as Pulsar A (see Kramer et al., 2005), and have been used to determine the values of the system parameters quoted earlier. For a given post-Newtonian gravity theory, each of the PK parameters gives rise to a curve on the phase-plane for the masses of the two pulsars (with the masses of the two pulsars plotted on the two axes). Uncertainties in the measured parameter values give rise to a finite width of the allowed strip in the phase-plane related to each parameter and all of the allowed strips should intersect if the gravity theory is correct. The figure presented by Kramer et al. (2005) gives impressive confirmation of general relativity but it should be noted that gravity is here only being tested at a particular range (the range of separation of the two binary components) and that significant discrepancies might still arise on other length-scales.

5 HOW DID THE DOUBLE PULSAR EVOLVE TO ITS PRESENT STATE?

In this section we discuss how the Double Pulsar probably reached its present state and use this picture in order to derive constraints on the equation of state of neutron star matter. (A more extensive presentation of the arguments involved can be found in our paper: Podsiadlowski et al., 2005.) The suggested formation scenario must explain the following:

- The binary system was not disrupted by the supernova explosions.
- Pulsar A was spun up, giving a period in the millisecond range (23 ms).
- The binary separation became small enough so that gravitational-wave emission could start to drive a significant inspiral of the system.

- The orbital eccentricity is small, implying that there was only a small kick velocity when the second neutron star was formed.
- Pulsar B has extremely low mass, $1.249 \pm 0.001\ M_\odot$ (the smallest accurately-measured mass for any known pulsar).

Based on this, we proposed two likely evolutionary routes involving interacting binary systems with the hydrogen envelopes being stripped from both stars after their main-sequence phase. The later stages are very similar in the two scenarios, with a helium star (the progenitor of Pulsar B) transferring matter onto the already-formed Pulsar A and spinning it up. It is suggested that the subsequent supernova which produced Pulsar B was an *electron-capture* supernova which would be consistent with the very low mass of Pulsar B and with the kick velocity being small.

Electron-capture supernovae occur for helium stars when the central density of the Oxygen/Neon/Magnesium core reaches the threshold for electron captures on magnesium nuclei. The electron captures reduce the pressure in the core and lead to the onset of core collapse. This mechanism occurs for only a small mass range of helium stars and at a well-defined pre-collapse ONeMg core mass. Very little material is lost during the collapse (typically around $10^{-3}\ M_\odot$, although this is a little controversial) and so the *baryon number* of Pulsar B is known to rather good accuracy (estimated as being within about 1%,

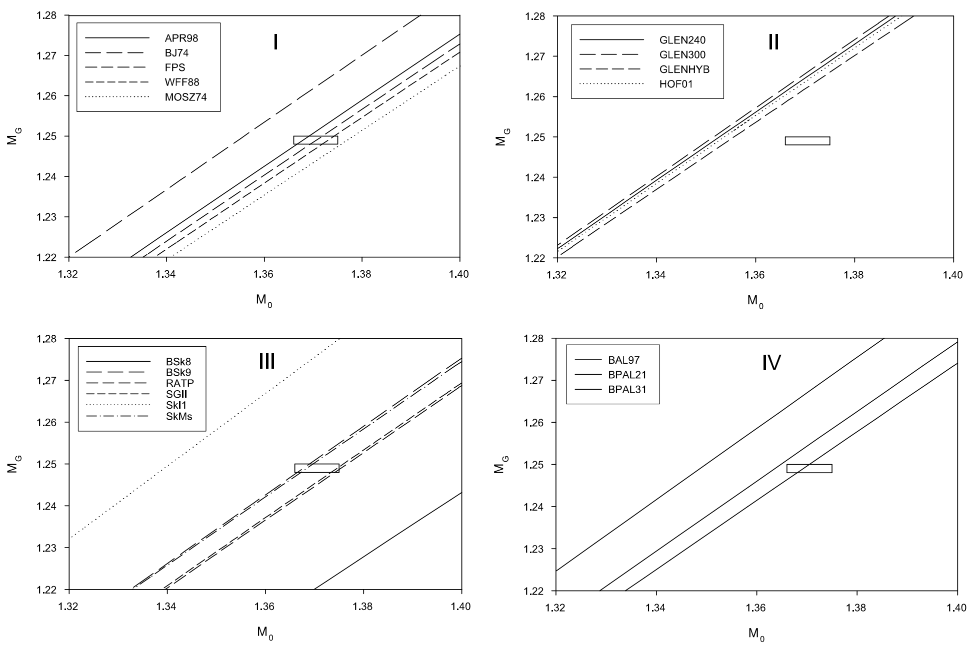

Figure 2. Relation between the gravitational mass M_G of neutron star models and their baryonic mass M_0, measured in units of the solar mass $M_\odot$, for various equations of state. The constraint which we have derived is marked by a rectangle.

taking all of the uncertainties into account). Knowing both the *baryon number* and *gravitational mass* of Pulsar B then allows constraints to be placed on the equation of state of neutron star matter since any equation of state predicts a particular relationship between these quantities. We have examined representative members from four classes of equations of state:

I Non-relativistic many-body calculations with "realistic" potentials
II Relativistic mean-field calculations including hyperons
III Non-relativistic Skyrme models
IV Some other phenomenological non-relativistic potentials

(Full details of the equations of state used are given in our paper.) Each of these gives a curve in the plane of gravitational mass M_G plotted against baryon number A which ought to intersect the "experimental" error box given by the measured gravitational mass of Pulsar B and its baryon number, derived on the basis of our assumed model. Results are shown in Fig. 2 (where, for convenience, we have plotted the "baryonic mass" M_0 rather than A itself, where M_0 is equal to A multiplied by the atomic mass unit).

It should be stressed that the constraint obtained applies *if our hypothesis about Pulsar B having been formed in an electron-capture supernova is correct*. However, we think that this hypothesis is rather well-founded and that the constraint is a plausible one. Clearly, it has some interesting consequences.

6 CONCLUSIONS

We have discussed here some implications of the very interesting observations of the double pulsar J0737−3039, noting that they lead to a very good confirmation of general relativity at the length-scales tested and also to useful constraints on the equation of state of neutron star matter *if* our hypothesis about the formation process for Pulsar B is correct. Further timing measurements may make it possible to measure the *spin-orbit coupling* correction for Pulsar A and hence to determine its *moment of inertia* I (Morrison et al., 2004). The relationship between I and M_G has a variation of $\sim 70\%$ depending on the equation of state, as compared with a variation of $\sim 5\%$ for the relationship between M_0 and M_G considered here. Any reasonably accurate measurement of I would give a very important constraint on the equation of state.

REFERENCES

Burgay, M. et al. (2003), *Nature*, **426**, p. 531.

Hulse, R. A. and Taylor, J. H. (1975), *Astrophys. J.*, **195**, p. L51.

Kramer, M. et al. (2005), `astro-ph/0503386`.

Lyne, A. G. et al. (2004), *Science*, **303**, p. 1153.

Morrison, I. A., Baumgarte, T. W., Shapiro, S. L. and Pandharipande, V. R. (2004), *Astrophys. J.*, **617**, p. 135.

Podsiadlowski, P., Dewi, J. D. M., Lesaffre, P., Miller, J. C., Newton, W. G. and Stone, J. R. (2005), *Monthly Notices Roy. Astronom. Soc.*, **361**, p. 1243.

Stairs, I. H., Thorsett, S. E., Taylor, J. H. and Wolszczan, A. (2002), *Astrophys. J.*, **581**, p. 501.
Wolszczan, A. (1991), *Nature*, **350**, p. 688.

Title: **Proceedings of RAGtime 6/7: Workshops on black holes and neutron stars, 16–18/18–20 September 2004/2005, Opava, Czech Republic**

Published by: Silesian University in Opava
Faculty of Philosophy and Science
Institute of Physics
Bezručovo nám. 13
CZ-746 01 Opava
Czech Republic

Editors: S. Hledík and Z. Stuchlík

Cover design: Otakar Karlas

1st edition

Printed by Editorial Centre of FPS SU in Opava, Czech Republic

Published in December 2005

ISBN 80-7248-334-X

Typeset in LaTeX

Název: **Proceedings of RAGtime 6/7: Workshops on black holes and neutron stars, 16–18/18–20 September 2004/2005, Opava, Czech Republic**

Nakladatel: Slezská univerzita v Opavě
Filozoficko-přírodovědecká fakulta
Ústav fyziky
Bezručovo nám. 13
CZ-746 01 Opava
Česká republika

Editoři: S. Hledík a Z. Stuchlík

Obálka: Otakar Karlas

První vydání

Tisk: Ediční středisko FPF SU v Opavě, Česká republika

Vydáno v prosinci 2005

ISBN 80-7248-334-X

Vysázeno systémem LaTeX